RICE UNIVERSITY

Discontinuous Galerkin method with a modified penalty flux for the modeling of acousto-elastic waves, coupled to rupture dynamics, in a self gravitating Earth

by

Ruichao Ye

A THESIS SUBMITTED
IN PARTIAL FULFILLMENT OF THE
REQUIREMENTS FOR THE DEGREE

Doctor of Philosophy

APPROVED, THESIS COMMITTEE:

Maarten V. de Hoop, Chair
Simons Chair in Computational and Applied Mathematics and Earth Science

Jesse Chan
Assistant Professor in Computational and Applied Mathematics

Melodie E. French
Assistant Professor in Earth, Environmental and Planetary Sciences

Alan Levander
Carey Croneis Professor in Earth, Environmental and Planetary Sciences

Fenglin Niu
Professor in Earth, Environmental and Planetary Sciences

Houston, Texas
Feburary, 2018

ABSTRACT

Discontinuous Galerkin method with a modified penalty flux for the modeling of acousto-elastic waves, coupled to rupture dynamics, in a self gravitating Earth

by

Ruichao Ye

We present a novel method to simulate the propagation of seismic waves in realistic fluid-solid materials, coupled with dynamically evolving faults, in the self-gravitating prestressed Earth. A discontinuous Galerkin method is introduced, with a modified penalty numerical flux dealing with various boundary conditions, in particular with discontinuities. This numerical scheme allows general heterogeneity and anisotropy in the materials, by avoiding the diagonalization into polarized wave constituents such as in the approach based on solving elementwise Riemann problems, while maintains the numerical accuracy with mesh and polynomial refinements. We also include the interior slip boundary conditions for dynamic ruptures coupling with nonlinear friction laws, as an approach to simulate spontaneously cracking faults. We show the well-posedness for the system of particle motion coupled with gravitation field and its perturbation, by proving the coercivity of the bilinear operator, both in the continuous and discretized polynomial space, and therefore the convergence results. A multi-rate iterative scheme is proposed to address the challenging of solving the large implicit nonlinear system, and to allow different time steps for distinct physical processes in the overall coupling problem. We give rigorous proof for the well-posedness of mathematical model and moreover the stability of the numerical methods. Numer-

ical experiments show the convergence as well as robustness in both well-established benchmark examples and realistic simulations.

Acknowledgements

I would like to extend my deepest gratitude to my advisor Dr. Maarten V. de Hoop, for his unmatched academic vision and inspiration without which this project would not have been initiated, for his years of detailed supervision without which this thesis work would not have been accomplished, and for his great patience and encouragements throughout my Ph.D. without which I would not have been enlightened with the beauty of mathematics.

Thanks are also due to my committee members, Dr. Jesse Chan, Dr. Melodie E. French, Dr. Alan Levander, and Dr. Fenglin Niu, for their constructive advice on each detailed components of this thesis work, from mathematical theories to implementations, and broadened my view in fields of geophysics as well as applied mathematics.

I would like to thank my collaborators, who have contributed to this work from various aspects. Essentially I would like to thank Dr. Kundan Kumar for extensive discussions on the rupture dynamic problem, which greatly improved my understanding of numerical analysis. I would like to thank Dr. Michel Campillo for referring me a wide range of geophysical implementations related to this thesis project. I would like to thank Dr. Jianlin Xia, for introducing me to the leading world of numerical linear algebra in three courses.

I also owe a deep gratitude to my friends and family, who have also contributed to my work from various aspects. I would like to thank my team mates for the help and encouragement in research as well as in daily life. I would like to thank my wife Xiang Li for sharing the various tastes of life, and my son Aaron Ye, who taught me the word responsibility.

Thanks are also extended to the current and formal members, ExxonMobil, PGS, Total and many other, of the Geo-Mathematical Imaging Group (GMIG), and the Simons Foundation, for financial supports of my graduate studies. I would also thank Purdue University for providing part of the education and essential computation resources for this PhD program.

Contents

Illustrations

Tables

Chapter 1

Introduction

1.1 Motivations from geophysical problems

The purpose of this thesis work is to address several main issues in numerical simulations in seismological problems. The accurate computation of waves in realistic three-dimensional Earth models represents an ongoing challenge in local, regional, and global seismology. The acousto-elastic wave propagates in both fluid and solids, which are in general anisotropic and heterogeneous. The upscaling of real Earth material can be described as piecewise smooth, namely, divided into finite number of subdomains in which material parameters are approximated by smooth functions of position. The boundaries of these subdomains are positions where coefficients vary strongly, and part of the energy is reflected, and the geometry are often recognized as geological structures of the subsurface. In particular, the scattering of waves are concerned on interior boundaries separating fluid and solids materials, such as the ocean bottom, the core-mantle-boundary (CMB) and inner-core-boundary (ICB). The impact of coupling acoustic waves to elastic ones is significant in analyzing the Earth normal modes [38].

In practice, the seismic waves can be stimulated by distinct types of sources. In seismic explorations, the sources of waves at sea are usually explosions generated by air-gun, while on land may be explosions or heavy vibrating objects. In Global Earth, natural earthquakes are consequences of rupturing faults releasing energy in prestressed materials. In the first category of applications, sources are represented kinetically by hydraulic pressure perturbations or external Cauchy boundary forces, while in the second, either kinetically as moment tensors or dynamically as interior boundary force coupling with a friction law. The study of dynamic ruptures is critical in understanding the nucleation of nature earthquakes and induced seismicity.

In many applications, a "Cowling approximation" is employed [41, 27, 94], which only accounts for unperturbed reference gravitational field, while ignoring the perturbation. However, for long period waves (greater than $\sim$100s) and free oscillation of the earth, this simplification is not valid, and one has to solve a Poisson's equation to account for the mass redistribution potential. The introduction of self-gravitation is fundamental in studying free-oscillation modes, and provide potential solution in quick detection of earthquakes.

1.2 A brief review of numerical methods

The questions of numerical implementation lies on the proper mathematical formulation of the above physical problems. The well-posedness of system of equations is not obvious, and must be rigorously proven. The discretized numerical schemes must also be analyzed to ensure stability, with numerical error well controlled with refinements.

In the past three decades, a wide variety of numerical techniques has been employed in the development of computational methods for simulating seismic waves. The most widely used one is based on the finite difference method [e.g., [107] and [166]]. This method has been applied to computing the wavefield in three-dimensional local and regional models [e.g., [67] and [118]]. The use of optimal or compact finite-difference operators has provided a certain improvement [e.g., [184] and [183]]. Methods that resort to spectral and pseudospectral techniques based on global gridding of the model have also been used both in regional [e.g., [23]] and global [e.g., [160] and [80]] seismic wave propagation and scattering problems. However, because of the use of global basis functions (polynomial: Chebyshev or Legendre, or harmonic: Fourier), these techniques are limited to coefficients which are (piecewise) sufficiently smooth. The finite difference method suffers from a limited accuracy in the presence of a free surface or surface discontinuities with topography within the model [e.g., [140] and [157]]. A procedure for the stable imposition of free-surface boundary conditions for a second-order formulation can be found in [7]. Another approach, belonging to a broader family of interface methods, handles both free surfaces [e.g., [104]] and fluid-solid interfaces [e.g., [103]] in such a way, conjectured by the authors, that enables higher-order accuracy to be obtained. [99] use summation-by-parts finite difference operators along with a weak enforcement of boundary conditions to develop a multi-block finite difference scheme which achieves higher-order accuracy for complex geometries.

A key development in the computation of seismic waves has been based on the spectral element method (SEM) [[94]]. In its original formulation, in terms of displacement [[96]], continuity of displacement and velocity is enforced everywhere within the model. In the case of a boundary between an inviscid fluid and a solid, however, the kinematic boundary condition is perfect slip; therefore, only the normal component of velocity is continuous across such a boundary, and thus this formulation is not applicable. Some classical finite-element methods (FEMs) alternatively introduce coupling conditions on fluid-solid interfaces between displacement in the solid and pressure in the fluid [e.g. [182, 15]].

The FEM and SEM are commonly (but not exclusively) based on the second-order form of the system of equations describing acousto-elastic waves. In this case, the acousto-elastic interaction is affected by coupling the respective wave equations through appropriate interface conditions. To resolve the coupling, a predictor-multicorrector iteration at each time step has been used [[92], [26]]. A computationally more efficient time stepping method for global seismic wave propagation accommodating the effects of fluid-solid boundaries, as well as transverse isotropy with a radial symmetry axis and radial models of attenuation, was proposed in [95]. It uses a velocity potential formulation and a second-order accurate Newmark time integration, in which a time step is first performed in the acoustic fluid and then in the elastic solid using interface values based on the fluid solution. Currently the SEM is used in a variety of implementations in global and regional seismic simulation, with the effects of variations in elastic parameters, density, ellipticity, topography and bathymetry, fluid-solid interfaces, anisotropy, and self-gravitation included [e.g. [24]].

In contrast to classical finite element discretizations, the Discontinous Galerkin (DG) method imposes continuity of approximate solutions between elements only weakly through a numerical flux.

The discontinuous Galerkin method has been employed for solving second-order wave equations in both the acoustic and elastodynamic settings [e.g. [137], [69], [34] and [48]]. [58] employ a central numerical flux in a DG scheme combined with a leap-frog time integration for the velocity-stress elastic-wave formulation. [54, 89] developed a non-conservative formulation with an upwind numerical flux using only the material properties from the side of the interface that is opposite to the outer normal direction. [171] derived an upwind numerical flux by solving the exact Riemann problem on interior boundaries of each element with material discontinuities based on a velocity-strain formulation of the coupled acousto-elastic equations. Recent developments in the general DG methods include the study in curved-linear elements

[28] and hybrid meshes [30], and heterogeneous in-element parameters [29]. Implementations of DG methods for high-performance computation on GPU are proposed in many recent works, for example, [30, 111].

1.3 Main contributions of this work

In this thesis we essentially give both variational and numerical frame-works for all three problems, with rigorous proof of well-posedness for continuous variational form and the stability analysis for discretized schemes.

In Chapter 2, we study the acousto-elastic wave phenomena, including scattering from fluid-solid boundaries, where the solid is allowed to be anisotropic. We develop a numerical approach with the discontinuous Galerkin method. We use a coupled first-order elastic strain-velocity, acoustic velocity-pressure formulation, and append penalty terms based on interior boundary continuity conditions to the numerical (central) flux so that the consistency condition holds for the discretized discontinuous Galerkin weak formulation. We incorporate the fluid-solid boundaries through these penalty terms and obtain a stable algorithm. Our approach avoids the diagonalization into polarized wave constituents such as in the approach based on solving elementwise Riemann problems.

In Chapter 3 and 4, we consider the dynamical evolution of spontaneous ruptures embedded in a prestressed elastic-gravitational deforming body, and governed by rate- and state-dependent friction laws. A multi-rate splitting iterative coupling scheme is proposed based on the weak form with nonlinear interior boundary conditions, for both continuous and with implicit discretization (backward Euler) in time. We introduce necessary artificial viscosity, and the convergence of the scheme to unique regularized solutions of both cases while the artificial viscosity coefficient can be chosen arbitrarily small but positive in the time-continuous case, and proportional to the time step in the discretized case. We use the proposed discontinuous Galerkin method, where the nonlinear interior boundary conditions are weakly imposed across the fault surface as numerical flux with penalty, and by an implicit-explicit Euler scheme in time. With the iterative scheme, the nonlinear sub-problem containing the friction law the time-evolving state ODE are separated in the form of Schur-complements, and solved locally as a constrained optimization problem by Gauss-Newton method. We test our algorithm on several well-established numerical examples, which illustrate the generality of our method for realistic rupture simulations.

In Chapter 5, we focus on the wave motion coupled with the self-gravitational potential. The coupling weak forms are derived from Euler-Lagrange equations, with hydrostatic prestress assumptions. The Poisson's equation governing the mass-redistribution potential couple with wave motion is solved by domain decomposition method, where the exterior solution represented by integration of fundamental solutions, and the interior problem reformulated as Poisson's equation with Robin-type boundary conditions, which is solved by structured matrices techniques. We proof well-posedness based on energy estimate, and the stability of DG discretization using error estimate.

As a completion of methodology, we discuss in Chapter 6 the unstructured mesh deformation for the application of model building and inverse problems. We introduce constraints by shape optimization of interior polyhedral boundaries and physics-based regularization. The interior boundaries, which need not be smooth, are flexible and can be chosen to be geomechanically related. The energy function is derived from the Hausdorff distance with contribution from the entire mesh and the interior boundaries. We use elastic deformation, via finite elements, as a regularization. We carry out the updating in two steps: by solving the optimization problem of energy functional including its regularization, and by modifying the outcome of the first step where necessary to ensure that basic assumptions on the mesh are satisfied. The modification entails an array of techniques including topology correction involving interior boundary contacting and breakup, edge warping and edge removal. We implement this as a feed-back mechanism from volume to interior boundary meshes optimization. Following the updating we invoke and apply a criterion of mesh quality control for coarsening, and for local multi-scale refinement in a multi-level fashion. Our physics-based regularization provides the opportunity to incorporate geodynamics in the mesh evolution.

Chapter 2

A modified penalty flux for the propagation and scattering of acousto-elastic waves

2.1 Introduction

The accurate computation of waves in realistic three-dimensional Earth models represents an ongoing challenge in local, regional, and global seismology. Here, we focus on simulating coupled acousto-elastic wave phenomena including scattering from fluid-solid boundaries, where the solid is allowed to be anisotropic, with the Discontinuous Galerkin method. Of particular interest are applications in geophysics, namely, marine seismic exploration and global Earth inverse problems using earthquake-generated seismic waves as the probing field. In the first application, we are concerned with the presence of the ocean bottom and in the second one with the core-mantle-boundary (CMB) and inner-core-boundary (ICB). Our formulation closely follows the analysis of existence of (weak) solutions of hyperbolic first-order systems of equations by [16]. We use an unstructured tetrahedral mesh with local refinement to accommodate highly heterogeneous media and complex geometries, which is also an underlying motivation for employing the Discontinuous Galerkin method from a computational point of view.

The Discontinuous Galerkin method has been employed for solving second-order wave equations in both the acoustic and elastodynamic settings [e.g. [137], [69], [34] and [48]]. [58] employ a central numerical flux in a DG scheme combined with a leap-frog time integration for the velocity-stress elastic-wave formulation. [54, 89] developed a non-conservative formulation with an upwind numerical flux using only the material properties from the side of the interface that is opposite to the outer normal direction. [171] derived an upwind numerical flux by solving the exact Riemann problem on interior boundaries of each element with material discontinuities based on a velocity-strain formulation of the coupled acousto-elastic equations.

In this work, we essentially extend the upwind flux, given by [169] for hyperbolic systems, to a penalty flux based on the boundary continuity condition for general fluid-solid interfaces. The novelties of our approach are the following: we

1. use a coupled *first-order* elastic strain-velocity, acoustic velocity-pressure formulation,

2. obtain a self-consistent Discontinuous Galerkin weak formulation *without diagonalization* into polarized wave constituents,

3. *append penalty terms*, derived from interior boundary continuity conditions, with an appropriate weight *to the numerical (central) flux* so that the consistency condition holds for the discretized Discontinuous Galerkin weak formulation,

4. *incorporate fluid-solid boundaries* through the mentioned penalty terms.

We note that the DG method is naturally adapted to well-posedness, in the sense that it makes use of coercivity of the operator defining the part of the system containing the spatial derivatives *separately* in the solid and fluid regions.

2.2 The system of equations describing acousto-elastic waves

We consider a bounded domain $\Omega \subset \mathbb{R}^3$ which is divided into solid and fluid regions, Ω_{S} and Ω_{F}, respectively. The interior boundaries include solid-solid interface Σ_{SS}, fluid-fluid interface Σ_{FF}, and fluid-solid interface Σ_{FS}, Σ_{SF} (where we distinguish whether the fluid or solid is on a particular side). We present the weak form of the coupled acousto-elastic system of equations.

Hooke's law in an elastodynamical system is expressed by relating stress, S_{ij}, and strain, E_{kl}. Assuming small deformations gives a linear relationship, that is, $S_{ij} = c_{ijkl}E_{kl}$, where c_{ijkl} is the stiffness tensor. Through the relevant symmetries, this tensor only contains 21 independent components. We use the Voigt notation which simplifies the writing of tensors while introducing $\boldsymbol{S} = (S_{11}, S_{22}, S_{33}, S_{23}, S_{12}, S_{13})^T$ and $\boldsymbol{E} = (E_{11}, E_{22}, E_{33}, E_{23}, E_{12}, E_{13})^T$. In this notation the stiffness tensor takes the form of a 6 by 6 matrix, $\boldsymbol{C}$, defined by,

$$\boldsymbol{S} = \boldsymbol{C}\boldsymbol{E}, \quad \boldsymbol{C} = \begin{bmatrix} C_{11} & C_{12} & C_{13} & 2C_{14} & 2C_{15} & 2C_{16} \\ C_{12} & C_{22} & C_{13} & 2C_{24} & 2C_{25} & 2C_{26} \\ C_{13} & C_{23} & C_{33} & 2C_{34} & 2C_{35} & 2C_{36} \\ C_{14} & C_{24} & C_{34} & 2C_{44} & 2C_{45} & 2C_{46} \\ C_{15} & C_{25} & C_{35} & 2C_{45} & 2C_{55} & 2C_{56} \\ C_{16} & C_{26} & C_{36} & 2C_{46} & 2C_{56} & 2C_{66} \end{bmatrix}. \tag{2.1}$$

The isotropic case is obtained by setting all of the C_{ij} components to zero except for $C_{11} = \lambda + 2\mu$, $C_{12} = C_{13} = C_{23} = \lambda$, $C_{44} = \mu$, $C_{55} = \mu$, and $C_{66} = \mu$; (λ, μ) are the *Lamé* parameters. Furthermore, ρ denotes the density. The anisotropic elastodynamical equations are written in terms of the strain, $\boldsymbol{E}$, and the particle velocity, $\boldsymbol{v}$,

$$\dot{\boldsymbol{E}} = \tfrac{1}{2}\left(\nabla \boldsymbol{v} + \nabla \boldsymbol{v}^T\right), \quad \rho\,\dot{\boldsymbol{v}} = \nabla \cdot (\boldsymbol{C}\boldsymbol{E}) + \boldsymbol{f} \tag{2.2}$$

in $\Omega_{\rm S}$. In fluid regions, $\Omega_{\rm F}$, we use the pressure-velocity formulation,

$$\dot{\widetilde{E}} = \nabla \cdot \widetilde{\boldsymbol{v}} - \frac{\widetilde{f}}{\widetilde{\lambda}}, \quad \widetilde{\rho}\,\dot{\widetilde{\boldsymbol{v}}} = \nabla(\widetilde{\lambda}\widetilde{E}). \tag{2.3}$$

Here, $\widetilde{P} = -\widetilde{\lambda}\widetilde{E}$ is the pressure, while we use $\widetilde{}$ to distinguish acoustic field quantities and material parameters from the elastic ones. In the above, $\widetilde{f}$ denotes a volume source density of injection and $\boldsymbol{f}$ denotes a volume source density of force.

The solid-solid, fluid-solid and fluid-fluid boundary conditions are given by

$$\boldsymbol{v}^+ - \boldsymbol{v}^- = 0 \qquad \text{and} \qquad \boldsymbol{n}\cdot(\boldsymbol{C}\boldsymbol{E})^+ - \boldsymbol{n}\cdot(\boldsymbol{C}\boldsymbol{E})^- = 0 \qquad \text{on } \Sigma_{\rm SS}, \tag{2.4a}$$

$$\boldsymbol{n}\cdot(\boldsymbol{v}^\pm - \widetilde{\boldsymbol{v}}^\mp) = 0 \qquad \text{and} \qquad \boldsymbol{n}\cdot(\boldsymbol{C}\boldsymbol{E})^\pm - (\widetilde{\lambda}\widetilde{E})^\mp\boldsymbol{n} = 0 \qquad \text{on } \Sigma_{\rm SF} \text{ and } \Sigma_{\rm FS}, \tag{2.4b}$$

$$\boldsymbol{n}\cdot(\widetilde{\boldsymbol{v}}^+ - \widetilde{\boldsymbol{v}}^-) = 0 \qquad \text{and} \qquad (\widetilde{\lambda}\widetilde{E})^+ - (\widetilde{\lambda}\widetilde{E})^- = 0 \qquad \text{on } \Sigma_{\rm FF}. \tag{2.4c}$$

The $\pm$ convention is determined by the direction of the interface normal, $\boldsymbol{n}$. The outer normal vector points in the direction of the "+" side of the interface.

We introduce test functions (tensors) $\boldsymbol{H}, \boldsymbol{w}$ in the solid regions and $\widetilde{\boldsymbol{w}}, \widetilde{H}$ in the fluid regions, which are assumed to be contained in the same spaces and satisfy the same boundary conditions as $\boldsymbol{E}, \boldsymbol{v}, \widetilde{\boldsymbol{v}}$ and $\widetilde{E}$. Using (2.2) and (2.3), we find that

$$\int_{\Omega_{\rm S}} \dot{\boldsymbol{E}} : (\boldsymbol{C}\boldsymbol{H})\,\mathrm{d}\Omega = \int_{\Omega_{\rm S}} \tfrac{1}{2}(\nabla\boldsymbol{v} + \nabla\boldsymbol{v}^T) : (\boldsymbol{C}\boldsymbol{H})\,\mathrm{d}\Omega, \tag{2.5a}$$

$$\int_{\Omega_{\rm S}} \rho\,\dot{\boldsymbol{v}}\cdot\boldsymbol{w}\,\mathrm{d}\Omega = \int_{\Omega_{\rm S}} (\nabla\cdot(\boldsymbol{C}\boldsymbol{E}))\cdot\boldsymbol{w}\,\mathrm{d}\Omega + \int_{\Omega_{\rm S}} \boldsymbol{f}\cdot\boldsymbol{w}\,\mathrm{d}\Omega, \tag{2.5b}$$

$$\int_{\Omega_{\rm F}} \dot{\widetilde{E}}\widetilde{\lambda}\,\widetilde{H}\,\mathrm{d}\Omega = \int_{\Omega_{\rm F}} (\nabla\cdot\widetilde{\boldsymbol{v}})\widetilde{\lambda}\,\widetilde{H}\,\mathrm{d}\Omega - \int_{\Omega_{\rm F}} \widetilde{f}\,\widetilde{H}\,\mathrm{d}\Omega, \tag{2.5c}$$

$$\int_{\Omega_{\rm F}} \widetilde{\rho}\,\dot{\widetilde{\boldsymbol{v}}}\cdot\widetilde{\boldsymbol{w}}\,\mathrm{d}\Omega = \int_{\Omega_{\rm F}} \nabla(\widetilde{\lambda}\widetilde{E})\cdot\widetilde{\boldsymbol{w}}\,\mathrm{d}\Omega. \tag{2.5d}$$

Assuming an outer traction-free boundary condition in (2.5b) and an outer pressure-free boundary condition in (2.5c), and applying an integration by parts, we obtain

$$\int_{\Omega_\mathrm{S}} \rho\, \dot{\boldsymbol{v}} \cdot \boldsymbol{w} \,\mathrm{d}\Omega = -\int_{\Omega_\mathrm{S}} (\boldsymbol{C}\boldsymbol{E}) : \nabla \boldsymbol{w} \,\mathrm{d}\Omega + \int_{\Sigma_\mathrm{SF}} (\boldsymbol{n} \cdot (\boldsymbol{C}\boldsymbol{E})^-) \cdot \boldsymbol{w}^- \,\mathrm{d}\Sigma + \int_{\Omega_\mathrm{S}} \boldsymbol{f} \cdot \boldsymbol{w} \,\mathrm{d}\Omega, \tag{2.6a}$$

$$\int_{\Omega_\mathrm{F}} \dot{\widetilde{E}}\widetilde{\lambda}\, \widetilde{H} \,\mathrm{d}\Omega = -\int_{\Omega_\mathrm{F}} \widetilde{\boldsymbol{v}} \cdot \nabla(\widetilde{\lambda}\widetilde{H}) \,\mathrm{d}\Omega + \int_{\Sigma_\mathrm{FS}} (\boldsymbol{n} \cdot \widetilde{\boldsymbol{v}}^-)(\widetilde{\lambda}\widetilde{H})^- \,\mathrm{d}\Sigma - \int_{\Omega_\mathrm{F}} \widetilde{f}\, \widetilde{H} \,\mathrm{d}\Omega. \tag{2.6b}$$

We use the fluid-solid boundary conditions (2.4b), replacing the fluid-solid surface integrals in (2.6a) and (2.6b) by taking the average of both sides consistent with a central flux scheme, and obtain

$$\begin{aligned} \int_{\Omega_\mathrm{S}} \rho\, \dot{\boldsymbol{v}} \cdot \boldsymbol{w} \,\mathrm{d}\Omega = &-\int_{\Omega_\mathrm{S}} (\boldsymbol{C}\boldsymbol{E}) : \nabla \boldsymbol{w} \,\mathrm{d}\Omega \\ &+ \int_{\Sigma_\mathrm{SF}} \tfrac{1}{2}((\widetilde{\lambda}\widetilde{E})^+ \boldsymbol{n} + \boldsymbol{n} \cdot (\boldsymbol{C}\boldsymbol{E})^-) \cdot \boldsymbol{w}^- \,\mathrm{d}\Sigma + \int_{\Omega_\mathrm{S}} \boldsymbol{f} \cdot \boldsymbol{w} \,\mathrm{d}\Omega, \end{aligned} \tag{2.7a}$$

$$\begin{aligned} \int_{\Omega_\mathrm{F}} \dot{\widetilde{E}}\widetilde{\lambda}\widetilde{H} \,\mathrm{d}\Omega = &-\int_{\Omega_\mathrm{F}} \widetilde{\boldsymbol{v}} \cdot \nabla(\widetilde{\lambda}\widetilde{H}) \,\mathrm{d}\Omega \\ &+ \int_{\Sigma_\mathrm{FS}} \tfrac{1}{2}(\boldsymbol{n} \cdot \boldsymbol{v}^- + \boldsymbol{n} \cdot \widetilde{\boldsymbol{v}}^+)\, (\widetilde{\lambda}\widetilde{H})^- \,\mathrm{d}\Sigma - \int_{\Omega_\mathrm{F}} \widetilde{f}\, \widetilde{H} \,\mathrm{d}\Omega. \end{aligned} \tag{2.7b}$$

This form of the equations is analogous to the one used in the spectral element method, see [27]. Applying an integration by parts, again, in (2.7), we recover the coupled strong formulation,

$$\begin{aligned} \int_{\Omega_\mathrm{S}} \rho\, \dot{\boldsymbol{v}} \cdot \boldsymbol{w} \,\mathrm{d}\Omega = &\int_{\Omega_\mathrm{S}} (\nabla \cdot (\boldsymbol{C}\boldsymbol{E})) \cdot \boldsymbol{w} \,\mathrm{d}\Omega \\ &+ \int_{\Sigma_\mathrm{SF}} \tfrac{1}{2}((\widetilde{\lambda}\widetilde{E})^+ \boldsymbol{n} - \boldsymbol{n} \cdot (\boldsymbol{C}\boldsymbol{E})^-) \cdot \boldsymbol{w}^- \,\mathrm{d}\Sigma + \int_{\Omega_\mathrm{S}} \boldsymbol{f} \cdot \boldsymbol{w} \,\mathrm{d}\Omega, \end{aligned} \tag{2.8a}$$

$$\begin{aligned} \int_{\Omega_\mathrm{F}} \dot{\widetilde{E}}\widetilde{\lambda}\widetilde{H} \,\mathrm{d}\Omega = &\int_{\Omega_\mathrm{F}} (\nabla \cdot \widetilde{\boldsymbol{v}})\widetilde{\lambda}\widetilde{H} \,\mathrm{d}\Omega \\ &+ \int_{\Sigma_\mathrm{FS}} \tfrac{1}{2}(\boldsymbol{n} \cdot (\boldsymbol{v}^+ - \widetilde{\boldsymbol{v}}^-))\, (\widetilde{\lambda}\widetilde{H})^- \,\mathrm{d}\Sigma - \int_{\Omega_\mathrm{F}} \widetilde{f}\, \widetilde{H} \,\mathrm{d}\Omega. \end{aligned} \tag{2.8b}$$

We use this system of equations together with (2.5a) and (2.5d) to develop our Discontinuous Galerkin method based approach.

2.3 Discontinuous Galerkin method with fluid-solid boundaries

The domain is partitioned into elements, D^e. We distinguish elements, ${\Omega^{\mathrm{e}}}_{\mathrm{S}}$, in the solid regions from elements, ${\Omega^{\mathrm{e}}}_{\mathrm{F}}$, in the fluid regions. Correspondingly, we distinguish fluid-fluid ($\Sigma^{\mathrm{e}}_{\mathrm{FF}}$), solid-solid ($\Sigma^{\mathrm{e}}_{\mathrm{SS}}$) and fluid-solid ($\Sigma^{\mathrm{e}}_{\mathrm{FS}}, \Sigma^{\mathrm{e}}_{\mathrm{SF}}$) faces for each element; thus the interior boundaries are decomposed as

$$\Sigma_{*\bullet} = \cup \Sigma^{\mathrm{e}}_{*\bullet}, \quad *, \bullet \in \{\mathrm{S}, \mathrm{F}\},$$

and so are the elements' boundaries: $\partial{\Omega^{\mathrm{e}}}_{\mathrm{S}} = \Sigma^{\mathrm{e}}_{\mathrm{SS}} \cup \Sigma^{\mathrm{e}}_{\mathrm{SF}}$ and $\partial{\Omega^{\mathrm{e}}}_{\mathrm{F}} = \Sigma^{\mathrm{e}}_{\mathrm{FF}} \cup \Sigma^{\mathrm{e}}_{\mathrm{FS}}$. The mesh size, h, is defined as the maximum radius of each tetrahedral's inscribed sphere.

We introduce the broken polynomial space $V_h = \bigoplus_{\Omega^{\mathrm{e}}} V_h^{\Omega^{\mathrm{e}}}$ where the local space is defined elementwise as $V_h^{\Omega^{\mathrm{e}}} = \mathrm{span}\{\phi_n(\Omega^{\mathrm{e}})\}_{n=1}^{N_p}$, with ϕ_n a set of polynomial basis further discussed in Section 2.3.2. The subscript "h" indicates the refinement of V_h with decrease in mesh size. The semi-discrete time-domain, discontinuous Galerkin formulation using a central flux yields: Find $\boldsymbol{E}_h, \boldsymbol{v}_h, \widetilde{\boldsymbol{v}}_h, \widetilde{E}_h$, with each component for each one of them in V_h such that

$$\begin{aligned}
&\int_{{\Omega^{\mathrm{e}}}_{\mathrm{S}}} \dot{\boldsymbol{E}}_h : (\boldsymbol{C}\boldsymbol{H}_h)\,\mathrm{d}\Omega + \int_{{\Omega^{\mathrm{e}}}_{\mathrm{S}}} \rho\,\dot{\boldsymbol{v}}_h \cdot \boldsymbol{w}_h\,\mathrm{d}\Omega \\
&\quad - \int_{{\Omega^{\mathrm{e}}}_{\mathrm{S}}} \tfrac{1}{2}(\nabla \boldsymbol{v}_h + \nabla \boldsymbol{v}_h^T) : (\boldsymbol{C}\boldsymbol{H}_h)\,\mathrm{d}\Omega - \int_{{\Omega^{\mathrm{e}}}_{\mathrm{S}}} (\nabla \cdot (\boldsymbol{C}\boldsymbol{E}_h)) \cdot \boldsymbol{w}_h\,\mathrm{d}\Omega \\
&\quad - \int_{\Sigma^{\mathrm{e}}_{\mathrm{SS}}} \tfrac{1}{2}[\![\boldsymbol{v}_h]\!]_{\mathrm{SS}} \cdot (\boldsymbol{n} \cdot (\boldsymbol{C}\boldsymbol{H}_h)^-)\,\mathrm{d}\Sigma - \int_{\Sigma^{\mathrm{e}}_{\mathrm{SF}}} \tfrac{1}{2}[\![\boldsymbol{v}_h]\!]_{\mathrm{SF}} \cdot (\boldsymbol{n} \cdot (\boldsymbol{C}\boldsymbol{H}_h)^-)\,\mathrm{d}\Sigma \\
&\quad - \int_{\Sigma^{\mathrm{e}}_{\mathrm{SS}}} \tfrac{1}{2}\boldsymbol{n} \cdot ([\![\boldsymbol{C}\boldsymbol{E}_h]\!]_{\mathrm{SS}}) \cdot \boldsymbol{w}_h^-\,\mathrm{d}\Sigma - \int_{\Sigma^{\mathrm{e}}_{\mathrm{SF}}} \tfrac{1}{2}\boldsymbol{n} \cdot ([\![\boldsymbol{C}\boldsymbol{E}_h]\!]_{\mathrm{SF}}) \cdot \boldsymbol{w}_h^-\,\mathrm{d}\Sigma = \int_{{\Omega^{\mathrm{e}}}_{\mathrm{S}}} \boldsymbol{f}_h \cdot \boldsymbol{w}_h\,\mathrm{d}\Omega,
\end{aligned} \tag{2.9}$$

and

$$\int_{\Omega^e{}_F} \dot{\widetilde{E}}_h \widetilde{\lambda} \widetilde{H}_h \,\mathrm{d}\Omega + \int_{\Omega^e{}_F} \widetilde{\rho}\, \dot{\widetilde{\boldsymbol{v}}}_h \cdot \widetilde{\boldsymbol{w}}_h \,\mathrm{d}\Omega$$
$$- \int_{\Omega^e{}_F} (\nabla \cdot \widetilde{\boldsymbol{v}}_h)\, \widetilde{\lambda} \widetilde{H}_h \,\mathrm{d}\Omega - \int_{\Omega^e{}_F} \nabla(\widetilde{\lambda} \widetilde{E}_h) \cdot \widetilde{\boldsymbol{w}}_h \,\mathrm{d}\Omega$$
$$- \int_{\Sigma^e_{FF}} \tfrac{1}{2}(\boldsymbol{n} \cdot [\![\widetilde{\boldsymbol{v}}_h]\!]_{FF})\, (\widetilde{\lambda} \widetilde{H}_h)^- \,\mathrm{d}\Sigma - \int_{\Sigma^e_{FS}} \tfrac{1}{2}(\boldsymbol{n} \cdot [\![\widetilde{\boldsymbol{v}}_h]\!]_{FS})\, (\widetilde{\lambda} \widetilde{H}_h)^- \,\mathrm{d}\Sigma$$
$$- \int_{\Sigma^e_{FF}} \tfrac{1}{2} [\![\widetilde{\lambda} \widetilde{E}_h]\!]_{FF} (\boldsymbol{n} \cdot \boldsymbol{w}_h^-) \,\mathrm{d}\Sigma - \int_{\Sigma^e_{FS}} \tfrac{1}{2} [\![\widetilde{\lambda} \widetilde{E}_h]\!]_{FS} (\boldsymbol{n} \cdot \boldsymbol{w}_h^-) \,\mathrm{d}\Sigma = - \int_{\Omega^e{}_F} \widetilde{f}_h\, \widetilde{H}_h \,\mathrm{d}\Omega, \tag{2.10}$$

hold for each element $\Omega^e{}_S$ or $\Omega^e{}_F$, for all test functions $\boldsymbol{H}_h, \boldsymbol{w}_h, \widetilde{\boldsymbol{w}}_h, \widetilde{H}_h \in V_h$. The notations $\boldsymbol{f}_h$ and $\widetilde{f}_h$ indicate polynomial approximation of $\boldsymbol{f}$ and $\widetilde{f}$. Here,

$$\left.\begin{aligned} [\![\boldsymbol{v}]\!]_{SS} &= \boldsymbol{v}^+ - \boldsymbol{v}^- \\ [\![\boldsymbol{CE}]\!]_{SS} &= \boldsymbol{n}\,(\boldsymbol{n} \cdot (\boldsymbol{CE})^+ - \boldsymbol{n} \cdot (\boldsymbol{CE})^-) \end{aligned}\right. \qquad \text{on } \Sigma^e_{SS}, \tag{2.11a}$$

$$\left.\begin{aligned} [\![\boldsymbol{v}]\!]_{SF} &= (\boldsymbol{n} \cdot (\widetilde{\boldsymbol{v}}^+ - \boldsymbol{v}^-))\boldsymbol{n} \\ [\![\boldsymbol{CE}]\!]_{SF} &= \boldsymbol{n}\,((\widetilde{\lambda}\widetilde{E})^+ \boldsymbol{n} - \boldsymbol{n} \cdot (\boldsymbol{CE})^-) \end{aligned}\right. \qquad \text{on } \Sigma^e_{SF} \tag{2.11b}$$

in the solid regions, while

$$\left.\begin{aligned} [\![\widetilde{\boldsymbol{v}}]\!]_{FF} &= (\boldsymbol{n} \cdot (\widetilde{\boldsymbol{v}}^+ - \widetilde{\boldsymbol{v}}^-))\boldsymbol{n} \\ [\![\widetilde{\lambda}\widetilde{E}]\!]_{FF} &= (\widetilde{\lambda}\widetilde{E})^+ - (\widetilde{\lambda}\widetilde{E})^- \end{aligned}\right. \qquad \text{on } \Sigma^e_{FF}, \tag{2.12a}$$

$$\left.\begin{aligned} [\![\widetilde{\boldsymbol{v}}]\!]_{FS} &= (\boldsymbol{n} \cdot (\boldsymbol{v}^+ - \widetilde{\boldsymbol{v}}^-))\boldsymbol{n} \\ [\![\widetilde{\lambda}\widetilde{E}]\!]_{FS} &= \boldsymbol{n} \cdot (\boldsymbol{CE})^+ \cdot \boldsymbol{n} - (\widetilde{\lambda}\widetilde{E})^- \end{aligned}\right. \qquad \text{on } \Sigma^e_{FS} \tag{2.12b}$$

in the fluid regions, using interior boundary continuity conditions. A similar formulation for Maxwell's equations, using the central flux, can be found in [75, Chapter 10, Page 434].

2.3.1 Energy function of central flux

We consider a time-dependent energy function comprising both the solid and fluid regions, $\mathcal{E}_h = \mathcal{E}_{\mathrm{S},h} + \mathcal{E}_{\mathrm{F},h}$, with

$$
\begin{aligned}
\mathcal{E}_{\mathrm{S},h} &= \tfrac{1}{2}\sum_{\mathrm{e}} \int_{\Omega^{\mathrm{e}}{}_{\mathrm{S}}} \left(\boldsymbol{E}_h : (\boldsymbol{C}\boldsymbol{E}_h) + \rho\,\boldsymbol{v}_h \cdot \boldsymbol{v}_h\right) \mathrm{d}\Omega, \\
\mathcal{E}_{\mathrm{F},h} &= \tfrac{1}{2}\sum_{\mathrm{e}} \int_{\Omega^{\mathrm{e}}{}_{\mathrm{F}}} \left(\widetilde{\lambda}\widetilde{E}_h^2 + \widetilde{\rho}\,\widetilde{\boldsymbol{v}}_h \cdot \widetilde{\boldsymbol{v}}_h\right) \mathrm{d}\Omega.
\end{aligned}
\tag{2.13}
$$

The functions in (2.13) define a norm both in the solid and in the fluid regions. Taking the time derivative and noting that $\boldsymbol{C}$ is symmetric, we have

$$
\frac{\mathrm{d}\mathcal{E}_{\mathrm{S},h}}{\mathrm{d}t} = \sum_{\mathrm{e}} \int_{\Omega^{\mathrm{e}}{}_{\mathrm{S}}} \left(\dot{\boldsymbol{E}}_h : (\boldsymbol{C}\boldsymbol{E}_h) + \rho\,\dot{\boldsymbol{v}}_h \cdot \boldsymbol{v}_h\right) \mathrm{d}\Omega, \tag{2.14}
$$

$$
\frac{\mathrm{d}\mathcal{E}_{\mathrm{F},h}}{\mathrm{d}t} = \sum_{\mathrm{e}} \int_{\Omega^{\mathrm{e}}{}_{\mathrm{F}}} \left(\dot{\widetilde{E}}_h\widetilde{\lambda}\widetilde{E}_h + \widetilde{\rho}\,\dot{\widetilde{\boldsymbol{v}}}_h \cdot \widetilde{\boldsymbol{v}}_h\right) \mathrm{d}\Omega. \tag{2.15}
$$

Starting from (2.9) and (2.10) and carrying out the summation over all the elements yields

$$
\frac{\mathrm{d}\mathcal{E}_h}{\mathrm{d}t} = \sum_{\mathrm{e}} \int_{\Omega^{\mathrm{e}}{}_{\mathrm{S}}} \boldsymbol{f}_h \cdot \boldsymbol{v}_h \,\mathrm{d}\Omega - \sum_{\mathrm{e}} \int_{\Omega^{\mathrm{e}}{}_{\mathrm{F}}} \widetilde{f}_h\,\widetilde{E}_h \,\mathrm{d}\Omega. \tag{2.16}
$$

This property is obtained as follows:

In (2.9) and (2.10) we let $\boldsymbol{H}_h = \boldsymbol{E}_h, \boldsymbol{w}_h = \boldsymbol{v}_h, \widetilde{H}_h = \widetilde{E}_h, \widetilde{\boldsymbol{w}}_h = \widetilde{\boldsymbol{v}}_h$, and obtain elementwise

$$
\begin{aligned}
&\int_{\Omega^{\mathrm{e}}{}_{\mathrm{S}}} \tfrac{1}{2}(\nabla\boldsymbol{v}_h + \nabla\boldsymbol{v}_h^T) : (\boldsymbol{C}\boldsymbol{E}_h)\,\mathrm{d}\Omega + \int_{\Omega^{\mathrm{e}}{}_{\mathrm{S}}} (\nabla\cdot(\boldsymbol{C}\boldsymbol{E}_h)) \cdot \boldsymbol{v}_h \,\mathrm{d}\Omega \\
={}& \int_{\Sigma^{\mathrm{e}}_{\mathrm{SS}}\cup\Sigma^{\mathrm{e}}_{\mathrm{SF}}} \boldsymbol{v}_h^- \cdot (\boldsymbol{n}\cdot(\boldsymbol{C}\boldsymbol{E}_h)^-)\,\mathrm{d}\Sigma,
\end{aligned}
\tag{2.17}
$$

and similarily

$$
\begin{aligned}
&\int_{\Omega^{\mathrm{e}}{}_{\mathrm{F}}} (\nabla\cdot\widetilde{\boldsymbol{v}}_h)\,\widetilde{\lambda}\widetilde{E}_h\,\mathrm{d}\Omega + \int_{\Omega^{\mathrm{e}}{}_{\mathrm{F}}} \nabla(\widetilde{\lambda}\widetilde{E}_h)\cdot\widetilde{\boldsymbol{v}}_h\,\mathrm{d}\Omega \\
={}& \int_{\Sigma^{\mathrm{e}}_{\mathrm{FF}}\cup\Sigma^{\mathrm{e}}_{\mathrm{FS}}} \boldsymbol{n}\cdot\widetilde{\boldsymbol{v}}_h^-\,(\widetilde{\lambda}\widetilde{E}_h)^-\,\mathrm{d}\Sigma.
\end{aligned}
\tag{2.18}
$$

From (2.9), (2.11), (2.14) and (2.17),

$$\frac{\mathrm{d}\mathcal{E}_{\mathrm{S},h}}{\mathrm{d}t} = \sum_{\mathrm{e}} \int_{\Omega^{\mathrm{e}}{}_{\mathrm{S}}} \boldsymbol{f}_h \cdot \boldsymbol{v}_h \,\mathrm{d}\Omega$$

$$+ \sum_{\mathrm{e}} \tfrac{1}{2} \int_{\Sigma^{\mathrm{e}}_{\mathrm{SF}}} \left(([\![\boldsymbol{v}_h]\!]_{\mathrm{SF}} + \boldsymbol{v}_h^-) \cdot (\boldsymbol{n} \cdot (\boldsymbol{C}\boldsymbol{E}_h)^-) + \boldsymbol{n} \cdot ([\![\boldsymbol{C}\boldsymbol{E}_h]\!]_{\mathrm{SF}} + (\boldsymbol{C}\boldsymbol{E}_h)^-) \cdot \boldsymbol{v}_h^- \right) \mathrm{d}\Sigma \tag{Θ_1}$$

$$+ \sum_{\mathrm{e}} \tfrac{1}{2} \int_{\Sigma^{\mathrm{e}}_{\mathrm{SS}}} \left(([\![\boldsymbol{v}_h]\!]_{\mathrm{SS}} + \boldsymbol{v}_h^-) \cdot (\boldsymbol{n} \cdot (\boldsymbol{C}\boldsymbol{E}_h)^-) + \boldsymbol{n} \cdot ([\![\boldsymbol{C}\boldsymbol{E}_h]\!]_{\mathrm{SS}} + (\boldsymbol{C}\boldsymbol{E}_h)^-) \cdot \boldsymbol{v}_h^- \right) \mathrm{d}\Sigma. \tag{Θ_2}$$

In the above,

$$\Theta_2 = \sum_{\mathrm{e}} \tfrac{1}{2} \int_{\Sigma^{\mathrm{e}}_{\mathrm{SS}}} \left(\boldsymbol{v}_h^+ \cdot (\boldsymbol{n} \cdot (\boldsymbol{C}\boldsymbol{E}_h)^-) + \boldsymbol{n} \cdot (\boldsymbol{C}\boldsymbol{E}_h)^+ \cdot \boldsymbol{v}_h^- \right) \mathrm{d}\Sigma = 0. \tag{2.19}$$

The surface integration terms cancel out when summed from both sides of the solid-solid interfaces because of the continuity condition (2.4a) and the opposite outer normal directions. We are left with the contributions from solid-fluid inner faces, Θ_1,

$$\frac{\mathrm{d}\mathcal{E}_{\mathrm{S},h}}{\mathrm{d}t} = \sum_{\mathrm{e}} \tfrac{1}{2} \int_{\Sigma^{\mathrm{e}}_{\mathrm{SF}}} \left(\widetilde{\boldsymbol{v}}_h^+ \cdot (\boldsymbol{n} \cdot (\boldsymbol{C}\boldsymbol{E}_h)^-) + (\widetilde{\lambda}\widetilde{E})^+ \boldsymbol{n} \cdot \boldsymbol{v}_h^- \right) \mathrm{d}\Sigma + \sum_{\mathrm{e}} \int_{\Omega^{\mathrm{e}}{}_{\mathrm{S}}} \boldsymbol{f}_h \cdot \boldsymbol{v}_h \,\mathrm{d}\Omega. \tag{2.20}$$

A similar result in the fluid region obtained from (2.10), (2.12), (2.15) and (2.18) yields

$$\frac{\mathrm{d}\mathcal{E}_{\mathrm{F},h}}{\mathrm{d}t} = \sum_{\mathrm{e}} \tfrac{1}{2} \int_{\Sigma^{\mathrm{e}}_{\mathrm{FS}}} \left((\boldsymbol{n} \cdot \boldsymbol{v}_h^+)(\widetilde{\lambda}\widetilde{E})^- + \boldsymbol{n} \cdot (\boldsymbol{C}\boldsymbol{E}_h)^+ \cdot \widetilde{\boldsymbol{v}}_h^- \right) \mathrm{d}\Sigma - \sum_{\mathrm{e}} \int_{\Omega^{\mathrm{e}}{}_{\mathrm{F}}} \widetilde{f}_h \, \widetilde{E}_h \,\mathrm{d}\Omega, \tag{2.21}$$

and the surface integration terms on the solid-fluid and fluid-solid interfaces in (2.20) and (2.21) cancel out due to (2.4b). Therefore (2.16) is obtained. We note that the surface integration along solid-fluid interfaces $\int_{\Sigma^{\mathrm{e}}_{\mathrm{SF}}} \frac{1}{2} \boldsymbol{n} \cdot ([\![\boldsymbol{C}\boldsymbol{E}_h]\!]_{\mathrm{SF}}) \cdot \boldsymbol{w}_h^- \,\mathrm{d}\Sigma$ and $\int_{\Sigma^{\mathrm{e}}_{\mathrm{FS}}} \frac{1}{2} (\boldsymbol{n} \cdot [\![\widetilde{\boldsymbol{v}}_h]\!]_{\mathrm{FS}}) \, (\widetilde{\lambda}\widetilde{H}_h)^- \,\mathrm{d}\Sigma$ are essential to guarantee energy conservation.

2.3.2 Nodal basis functions

The discretized solution follows an expansion, componentwise, into $N_p = N_p(N_p)$ nodal trial basis functions of order N_p, as is in [75],

$$\begin{aligned}(\boldsymbol{E}_h)_{ij}(\boldsymbol{x},t) =& \bigoplus_{\Omega^{\mathrm{e}}} \sum_{n=1}^{N_p} (\boldsymbol{E}_{h,n}^{\Omega^{\mathrm{e}}})_{ij}(t)\phi_n(\boldsymbol{x}), \\ \text{with } (\boldsymbol{E}_{h,n}^{\Omega^{\mathrm{e}}})_{ij}(t) =& (\boldsymbol{E}_h)_{ij}(\boldsymbol{x}_n,t), n = 1,2,\cdots,N_p,\end{aligned} \tag{2.22}$$

and similarly for the other fields, $\boldsymbol{v}_h, \widetilde{\boldsymbol{v}}_h, \widetilde{E}_h$. The superscript, $\boldsymbol{.}^{D^e}$, indicates a local expansion within element D^e. In the above, $\{\phi_n(\boldsymbol{x})\}_{n=1}^{N_p}$ is a set of three-dimensional Lagrange polynomials associated with the nodal points, $\{\boldsymbol{x}_n\}_{n=1}^{N_p}$ (see Figure 2.1), with each polynomial defined as

$$\phi_k(\boldsymbol{x}) = \prod_{j=1,j\neq k}^{N_p} \frac{\boldsymbol{x}-\boldsymbol{x}_j}{\boldsymbol{x}_k-\boldsymbol{x}_j}.$$

We use the warp & blend method [[168]] to determine the coordinates of nodal points in the tetrahedron by numerically minimizing the Lebesgue constant of interpolation. For an order N_p interpolation there are $N_p = \frac{1}{6}(N_p+1)(N_p+2)(N_p+3)$ nodal points.

The medium coefficients are expanded in a likewise manner

$$\begin{aligned}(\boldsymbol{C}_h)_{ij}(\boldsymbol{x}) =& \bigoplus_{\Omega^{\mathrm{e}}} \sum_{n=1}^{N_p} (\boldsymbol{C}_{h,n}^{\Omega^{\mathrm{e}}\mathrm{s}})_{ij}\phi_n(\boldsymbol{x}), \\ \text{with } (\boldsymbol{C}_{h,n}^{\Omega^{\mathrm{e}}\mathrm{s}})_{ij} =& (\boldsymbol{C}_h)_{ij}(\boldsymbol{x}_n), n = 1,2,\cdots,N_p,\end{aligned} \tag{2.23}$$

and similarly for $\rho, \widetilde{\rho}, \widetilde{\lambda}$. When refining a mesh, we expect an increase in number of elements Ω^{e} with decreased size.

2.3.3 The system of equations in matrix form

To simplify the notation in the further development of a numerical scheme, we introduce a joint matrix form of the system of equations. We map the components of $\boldsymbol{E}, \boldsymbol{v}$

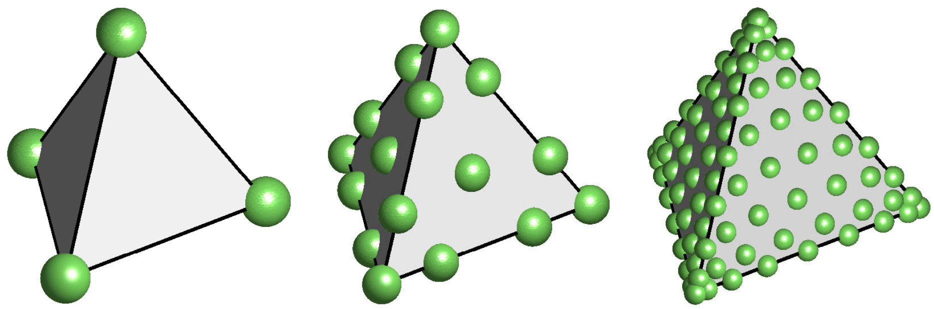

Figure 2.1 : Warp & blend tetrahedral nodal point distribution for $N_p = 1, 3, 8$. For clarity only facial nodes are illustrated.

and $\widetilde{E}, \widetilde{\boldsymbol{v}}$ to 9×1 and 4×1 matrices, respectively,

$$\boldsymbol{q} = (E_{11}, E_{22}, E_{33}, E_{23}, E_{13}, E_{12}, v_1, v_2, v_3)^T \quad \text{and} \quad \widetilde{\boldsymbol{q}} = (\widetilde{E}, \widetilde{v}_1, \widetilde{v}_2, \widetilde{v}_3)^T, \tag{2.24}$$

and, correspondingly, the components of body forces $\boldsymbol{f}$ and $\widetilde{f}$ to the matrix

$$\boldsymbol{g} = (0,0,0,0,0,0,f_1,f_2,f_3)^T \quad \text{and} \quad \widetilde{\boldsymbol{g}} = \left(-\frac{\widetilde{f}}{\widetilde{\lambda}}, 0, 0, 0\right)^T \quad .$$

Equations (2.2) and (2.3) attain the form

$$\mathcal{Q}\,\dot{\boldsymbol{q}} - \nabla \cdot (\mathcal{A}\boldsymbol{q}) = \boldsymbol{g} \quad \text{and} \quad \widetilde{\mathcal{Q}}\,\dot{\widetilde{\boldsymbol{q}}} - \nabla \cdot (\widetilde{\mathcal{A}}\widetilde{\boldsymbol{q}}) = \widetilde{\boldsymbol{g}}, \tag{2.25}$$

where

$$\mathcal{Q} = \left(\begin{array}{c|c} I_{6\times 6} & 0 \\ \hline 0 & \rho I_{3\times 3} \end{array}\right) \quad \text{and} \quad \widetilde{\mathcal{Q}} = \left(\begin{array}{c|c} 1 & 0 \\ \hline 0 & \widetilde{\rho} I_{3\times 3} \end{array}\right)$$

and

$$\mathcal{A} = (A_1, A_2, A_3) \quad \text{and} \quad \widetilde{\mathcal{A}} = (\widetilde{A}_1, \widetilde{A}_2, \widetilde{A}_3),$$

that is,

$$(\nabla \cdot (\mathcal{A}\boldsymbol{q}))_l = \partial_{x_k}((\mathcal{A}_k)_{lm}\boldsymbol{q}_m) \quad \text{and} \quad (\nabla \cdot (\widetilde{\mathcal{A}}\widetilde{\boldsymbol{q}}))_l = \partial_{x_k}((\widetilde{\mathcal{A}}_k)_{lm}\widetilde{\boldsymbol{q}}_m),$$
$$k = 1, 2, 3, \quad l, m = 1, \cdots, 9 \text{ or } 1, \cdots, 4$$

with

$$A_1 = \left(\begin{array}{cccccc|ccc} & & & & & & 1 & 0 & 0 \\ & & & & & & 0 & 0 & 0 \\ & & & \mathbf{0} & & & 0 & 0 & 0 \\ & & & & & & 0 & 0 & 0 \\ & & & & & & 0 & 0 & \frac{1}{2} \\ & & & & & & 0 & \frac{1}{2} & 0 \\ \hline C_{11} & C_{12} & C_{13} & 2C_{14} & 2C_{15} & 2C_{16} & & & \\ C_{16} & C_{26} & C_{36} & 2C_{46} & 2C_{56} & 2C_{66} & & \mathbf{0} & \\ C_{15} & C_{25} & C_{35} & 2C_{45} & 2C_{55} & 2C_{56} & & & \end{array}\right) \quad \text{and} \quad \widetilde{A}_1 = \left(\begin{array}{c|ccc} & 1 & 0 & 0 \\ \mathbf{0} & 0 & 0 & 0 \\ & 0 & 0 & 0 \\ \hline \widetilde{\lambda} & & \mathbf{0} & \end{array}\right),$$

$$A_2 = \left(\begin{array}{cccccc|ccc} & & & & & & 0 & 0 & 0 \\ & & & & & & 0 & 1 & 0 \\ & & & \mathbf{0} & & & 0 & 0 & 0 \\ & & & & & & 0 & 0 & \frac{1}{2} \\ & & & & & & 0 & 0 & 0 \\ & & & & & & \frac{1}{2} & 0 & 0 \\ \hline C_{16} & C_{26} & C_{36} & 2C_{46} & 2C_{56} & 2C_{66} & & & \\ C_{12} & C_{22} & C_{23} & 2C_{24} & 2C_{25} & 2C_{26} & & \mathbf{0} & \\ C_{14} & C_{24} & C_{34} & 2C_{44} & 2C_{45} & 2C_{46} & & & \end{array}\right) \quad \text{and} \quad \widetilde{A}_2 = \left(\begin{array}{c|ccc} & 0 & 0 & 0 \\ \mathbf{0} & 0 & 1 & 0 \\ & 0 & 0 & 0 \\ \hline \widetilde{\lambda} & & \mathbf{0} & \end{array}\right),$$

$$A_3 = \left(\begin{array}{cccccc|ccc} & & & & & & 0 & 0 & 0 \\ & & & & & & 0 & 0 & 0 \\ & & & & & & 0 & 0 & 1 \\ & & & \mathbf{0} & & & 0 & \frac{1}{2} & 0 \\ & & & & & & \frac{1}{2} & 0 & 0 \\ & & & & & & 0 & 0 & 0 \\ \hline C_{15} & C_{25} & C_{35} & 2C_{45} & 2C_{55} & 2C_{56} & & & \\ C_{14} & C_{24} & C_{34} & 2C_{44} & 2C_{45} & 2C_{46} & & \mathbf{0} & \\ C_{13} & C_{23} & C_{33} & 2C_{34} & 2C_{35} & 2C_{36} & & & \end{array}\right) \quad \text{and} \quad \widetilde{A}_3 = \left(\begin{array}{c|ccc} & 0 & 0 & 0 \\ \mathbf{0} & 0 & 0 & 0 \\ & 0 & 0 & 1 \\ \hline \widetilde{\lambda} & & \mathbf{0} & \end{array}\right).$$

We define the coefficient matrices $\mathcal{A}_n$ in the normal directions $\boldsymbol{n} = (n_1, n_2, n_3)$ as $\mathcal{A}_n = n_1 A_1 + n_2 A_2 + n_3 A_3$, thus $\mathcal{A}_n \boldsymbol{q} \equiv \boldsymbol{n} \cdot (\mathcal{A}\boldsymbol{q})$; similarly, $\widetilde{\mathcal{A}}_n = n_1 \tilde{A}_1 + n_2 \tilde{A}_2 + n_3 \tilde{A}_3$. We can also give them in the matrix form,

$$\mathcal{A}_n = \begin{pmatrix} 0 & T_{12} \\ T_{21} \cdot \boldsymbol{C} & 0 \end{pmatrix} \quad \text{and} \quad \widetilde{\mathcal{A}}_n = \begin{pmatrix} 0 & \boldsymbol{n}^T \\ \widetilde{\lambda}\boldsymbol{n} & 0 \end{pmatrix},$$

with

$$T_{12} = \begin{pmatrix} n_1 & 0 & 0 & 0 & \frac{1}{2}n_3 & \frac{1}{2}n_2 \\ 0 & n_2 & 0 & \frac{1}{2}n_3 & 0 & \frac{1}{2}n_1 \\ 0 & 0 & n_3 & \frac{1}{2}n_2 & \frac{1}{2}n_1 & 0 \end{pmatrix}^T, \quad T_{21} = \begin{pmatrix} n_1 & 0 & 0 & 0 & n_3 & n_2 \\ 0 & n_2 & 0 & n_3 & 0 & n_1 \\ 0 & 0 & n_3 & n_2 & n_1 & 0 \end{pmatrix}.$$

We introduce

$$\boldsymbol{\Lambda} = \left(\begin{array}{c|c} \boldsymbol{C} & 0 \\ \hline 0 & I_{3\times 3} \end{array}\right) \quad \text{and} \quad \widetilde{\boldsymbol{\Lambda}} = \left(\begin{array}{c|c} \widetilde{\lambda} & 0 \\ \hline 0 & I_{3\times 3} \end{array}\right).$$

In the solid regions, we write $\boldsymbol{p} = (H_{11}, H_{22}, H_{33}, H_{23}, H_{13}, H_{12}, w_1, w_2, w_3)^T$, and in the fluid regions, we write $\widetilde{\boldsymbol{p}} = (\widetilde{H}, \tilde{w}_1, \tilde{w}_2, \tilde{w}_3)^T$. The inner product $\left(\boldsymbol{q}, \boldsymbol{p}\right)_\Omega$ indicates the dot product of vectors $\boldsymbol{q}$ and $\boldsymbol{p}$ followed by integration over the domain Ω. Equation (2.9) is then rewritten, regarding the supports of basis functions $\boldsymbol{p}_h$ localized to an element $\Omega^{\mathrm{e}}{}_{\mathrm{S,F}}$, as

$$\begin{aligned}\big(\mathcal{Q}_h\dot{\boldsymbol{q}}_h,\boldsymbol{\Lambda}_h\boldsymbol{p}_h\big)_{\Omega^{\mathrm{e}}{}_{\mathrm{S}}}-\big(\nabla\cdot(\mathcal{A}_h\boldsymbol{q}_h),\boldsymbol{\Lambda}_h\boldsymbol{p}_h\big)_{\Omega^{\mathrm{e}}{}_{\mathrm{S}}}-\tfrac{1}{2}\big(\left[\!\left[\mathcal{A}_{n,h}\boldsymbol{q}_h\right]\!\right]_{\mathrm{SS}},(\boldsymbol{\Lambda}_h\boldsymbol{p}_h)^-\big)_{\Sigma^{\mathrm{e}}_{\mathrm{SS}}}\\ -\tfrac{1}{2}\big(\left[\!\left[\mathcal{A}_{n,h}\boldsymbol{q}_h\right]\!\right]_{\mathrm{SF}},(\boldsymbol{\Lambda}_h\boldsymbol{p}_h)^-\big)_{\Sigma^{\mathrm{e}}_{\mathrm{SF}}}=\big(\boldsymbol{g},\boldsymbol{\Lambda}_h\boldsymbol{p}_h\big)_{\Omega^{\mathrm{e}}{}_{\mathrm{S}}},\end{aligned}\tag{2.26}$$

$$\begin{aligned}\big(\widetilde{\mathcal{Q}}_h\dot{\widetilde{\boldsymbol{q}}}_h,\widetilde{\boldsymbol{\Lambda}}_h\widetilde{\boldsymbol{p}}_h\big)_{\Omega^{\mathrm{e}}{}_{\mathrm{F}}}-\big(\nabla\cdot(\widetilde{\mathcal{A}}_h\widetilde{\boldsymbol{q}}_h),\widetilde{\boldsymbol{\Lambda}}_h\widetilde{\boldsymbol{p}}_h\big)_{\Omega^{\mathrm{e}}{}_{\mathrm{F}}}-\tfrac{1}{2}\big(\left[\!\left[\widetilde{\mathcal{A}}_{n,h}\widetilde{\boldsymbol{q}}_h\right]\!\right]_{\mathrm{FF}},(\widetilde{\boldsymbol{\Lambda}}_h\widetilde{\boldsymbol{p}}_h)^-\big)_{\Sigma^{\mathrm{e}}_{\mathrm{FF}}}\\ -\tfrac{1}{2}\big(\left[\!\left[\widetilde{\mathcal{A}}_{n,h}\widetilde{\boldsymbol{q}}_h\right]\!\right]_{\mathrm{FS}},(\widetilde{\boldsymbol{\Lambda}}_h\widetilde{\boldsymbol{p}}_h)^-\big)_{\Sigma^{\mathrm{e}}_{\mathrm{FS}}}=\big(\widetilde{\boldsymbol{g}},\widetilde{\boldsymbol{\Lambda}}_h\widetilde{\boldsymbol{p}}_h\big)_{\Omega^{\mathrm{e}}{}_{\mathrm{F}}}.\end{aligned}\tag{2.27}$$

In the above we identify the central flux as

$$\mathcal{F}^{\mathrm{C}}_{\mathrm{S}*}=\tfrac{1}{2}\big(\left[\!\left[\mathcal{A}_n\boldsymbol{q}\right]\!\right]_{\mathrm{S}*},(\boldsymbol{\Lambda}\boldsymbol{p})^-\big)_{\Sigma^{\mathrm{e}}_{\mathrm{S}*}},\quad \widetilde{\mathcal{F}}^{\mathrm{C}}_{\mathrm{F}*}=\tfrac{1}{2}\big(\left[\!\left[\widetilde{\mathcal{A}}_n\widetilde{\boldsymbol{q}}\right]\!\right]_{\mathrm{F}*},(\widetilde{\boldsymbol{\Lambda}}\widetilde{\boldsymbol{p}})^-\big)_{\Sigma^{\mathrm{e}}_{\mathrm{F}*}},\quad *\in\{\mathrm{S},\mathrm{F}\},\tag{2.28}$$

in which we redefine

$$\begin{aligned}&\left[\!\left[\mathcal{A}_n\boldsymbol{q}\right]\!\right]_{\mathrm{SS}}=(\mathcal{A}_n\boldsymbol{q})^+-(\mathcal{A}_n\boldsymbol{q})^-,\quad \left[\!\left[\mathcal{A}_n\boldsymbol{q}\right]\!\right]_{\mathrm{SF}}=O^T(\widetilde{\mathcal{A}}_n\widetilde{\boldsymbol{q}})^+-(\mathcal{A}_n\boldsymbol{q})^-,\\ &\left[\!\left[\widetilde{\mathcal{A}}_n\widetilde{\boldsymbol{q}}\right]\!\right]_{\mathrm{FF}}=(\widetilde{\mathcal{A}}_n\widetilde{\boldsymbol{q}})^+-(\widetilde{\mathcal{A}}_n\widetilde{\boldsymbol{q}})^-,\quad \left[\!\left[\widetilde{\mathcal{A}}_n\widetilde{\boldsymbol{q}}\right]\!\right]_{\mathrm{FS}}=O\ (\mathcal{A}_n\boldsymbol{q})^+-(\widetilde{\mathcal{A}}_n\widetilde{\boldsymbol{q}})^-,\end{aligned}\tag{2.29}$$

with the map $O:\mathbb{R}^9\to\mathbb{R}^4$ given by

$$O\boldsymbol{q}=\begin{pmatrix}\boldsymbol{n}\cdot\boldsymbol{E}\cdot\boldsymbol{n}\\ (\boldsymbol{n}\cdot\boldsymbol{v})\boldsymbol{n}\end{pmatrix},\quad \text{and its adjoint}\quad O^T\widetilde{\boldsymbol{q}}=\begin{pmatrix}(\boldsymbol{n}\boldsymbol{n})\widetilde{E}\\ (\boldsymbol{n}\cdot\widetilde{\boldsymbol{v}})\boldsymbol{n}\end{pmatrix},$$

which can also be explicitly given in the matrix form

$$O=\left(\begin{array}{cccccc|ccc} n_1n_1 & n_2n_2 & n_3n_3 & n_2n_3 & n_1n_3 & n_1n_2 & & \mathbf{0} & \\ \hline & & & & & & n_1n_1 & n_1n_2 & n_1n_3\\ & & & \mathbf{0} & & & n_1n_2 & n_2n_2 & n_2n_3\\ & & & & & & n_1n_3 & n_2n_3 & n_3n_3\end{array}\right).$$

2.4 The Boundary Condition penalized numerical flux and stability

Here, we construct our penalized numerical flux. The flux is designed such that the penalized discrete counterpart of the weak form (2.26) and (2.27) satisfies the condition of non-increasing energy and guarantees a proper error estimate. We replace the central fluxes, $\mathcal{F}^{\mathrm{C}}$ and $\widetilde{\mathcal{F}}^{\mathrm{C}}$, in (2.28), by penalized fluxes, $\mathcal{F}^{\mathrm{P}}$ and $\widetilde{\mathcal{F}}^{\mathrm{P}}$, by adding penalty terms, that is:

$$\begin{aligned}
\mathcal{F}^{\mathrm{P}}_{\mathrm{S}*} =&\tfrac{1}{2}\big([\![\mathcal{A}_n\boldsymbol{q}\,]\!]_{\mathrm{S}*},(\boldsymbol{\Lambda}\boldsymbol{p})^-\big)_{\Sigma^{\mathrm{e}}_{\mathrm{S}*}}+\alpha\big(\mathcal{A}_n^{T,-}[\![\mathcal{A}_n\boldsymbol{q}\,]\!]_{\mathrm{S}*},\boldsymbol{p}^-\big)_{\Sigma^{\mathrm{e}}_{\mathrm{S}*}}\\
&=\tfrac{1}{2}\big([\![\mathcal{A}_n\boldsymbol{q}\,]\!]_{\mathrm{S}*},(\boldsymbol{\Lambda}\boldsymbol{p})^-\big)_{\Sigma^{\mathrm{e}}_{\mathrm{S}*}}+\alpha\big([\![\mathcal{A}_n\boldsymbol{q}\,]\!]_{\mathrm{S}*},(\mathcal{A}_n\boldsymbol{p})^-\big)_{\Sigma^{\mathrm{e}}_{\mathrm{S}*}},\\
\widetilde{\mathcal{F}}^{\mathrm{P}}_{\mathrm{F}*} =&\tfrac{1}{2}\big([\![\widetilde{\mathcal{A}}_n\widetilde{\boldsymbol{q}}\,]\!]_{\mathrm{F}*},(\widetilde{\boldsymbol{\Lambda}}\widetilde{\boldsymbol{p}})^-\big)_{\Sigma^{\mathrm{e}}_{\mathrm{F}*}}+\alpha\big(\widetilde{\mathcal{A}}_n^{T,-}[\![\widetilde{\mathcal{A}}_n\widetilde{\boldsymbol{q}}\,]\!]_{\mathrm{F}*},\widetilde{\boldsymbol{p}}^-\big)_{\Sigma^{\mathrm{e}}_{\mathrm{F}*}}\\
&=\tfrac{1}{2}\big([\![\widetilde{\mathcal{A}}_n\widetilde{\boldsymbol{q}}\,]\!]_{\mathrm{F}*},(\widetilde{\boldsymbol{\Lambda}}\widetilde{\boldsymbol{p}})^-\big)_{\Sigma^{\mathrm{e}}_{\mathrm{F}*}}+\alpha\big([\![\widetilde{\mathcal{A}}_n\widetilde{\boldsymbol{q}}\,]\!]_{\mathrm{F}*},(\widetilde{\mathcal{A}}_n\widetilde{\boldsymbol{p}})^-\big)_{\Sigma^{\mathrm{e}}_{\mathrm{F}*}},\quad *\in\{\mathrm{S},\mathrm{F}\}
\end{aligned}\tag{2.30}$$

with α some positive constant scalar. With this modification, (2.26) and (2.27) becomes

$$\begin{aligned}
\big(\mathcal{Q}_h\dot{\boldsymbol{q}}_h,\boldsymbol{\Lambda}_h\boldsymbol{p}_h\big)_{\Omega^{\mathrm{e}}{}_{\mathrm{S}}}-&\big(\nabla\cdot(\mathcal{A}_h\boldsymbol{q}_h),\boldsymbol{\Lambda}_h\boldsymbol{p}_h\big)_{\Omega^{\mathrm{e}}{}_{\mathrm{S}}}-\tfrac{1}{2}\big([\![\mathcal{A}_{n,h}\boldsymbol{q}_h\,]\!]_{\mathrm{S}*},(\boldsymbol{\Lambda}_h\boldsymbol{p}_h)^-\big)_{\Sigma^{\mathrm{e}}_{\mathrm{S}*}}\\
&-\alpha\big([\![\mathcal{A}_{n,h}\boldsymbol{q}_h\,]\!]_{\mathrm{S}*},(\mathcal{A}_{n,h}\boldsymbol{p}_h)^-\big)_{\Sigma^{\mathrm{e}}_{\mathrm{S}*}}=\big(\boldsymbol{g},\boldsymbol{\Lambda}_h\boldsymbol{p}_h\big)_{\Omega^{\mathrm{e}}{}_{\mathrm{S}}},
\end{aligned}\tag{2.31}$$

$$\begin{aligned}
\big(\widetilde{\mathcal{Q}}_h\dot{\widetilde{\boldsymbol{q}}}_h,\widetilde{\boldsymbol{\Lambda}}_h\widetilde{\boldsymbol{p}}_h\big)_{\Omega^{\mathrm{e}}{}_{\mathrm{F}}}-&\big(\nabla\cdot(\widetilde{\mathcal{A}}_h\widetilde{\boldsymbol{q}}_h),\widetilde{\boldsymbol{\Lambda}}_h\widetilde{\boldsymbol{p}}_h\big)_{\Omega^{\mathrm{e}}{}_{\mathrm{F}}}-\tfrac{1}{2}\big([\![\widetilde{\mathcal{A}}_{n,h}\widetilde{\boldsymbol{q}}_h\,]\!]_{\mathrm{F}*},(\widetilde{\boldsymbol{\Lambda}}_h\widetilde{\boldsymbol{p}}_h)^-\big)_{\Sigma^{\mathrm{e}}_{\mathrm{F}*}}\\
&-\alpha\big([\![\widetilde{\mathcal{A}}_{n,h}\widetilde{\boldsymbol{q}}_h\,]\!]_{\mathrm{F}*},(\widetilde{\mathcal{A}}_{n,h}\widetilde{\boldsymbol{p}}_h)^-\big)_{\Sigma^{\mathrm{e}}_{\mathrm{F}*}}=\big(\widetilde{\boldsymbol{g}},\widetilde{\boldsymbol{\Lambda}}_h\widetilde{\boldsymbol{p}}_h\big)_{\Omega^{\mathrm{e}}{}_{\mathrm{F}}},\quad *\in\{\mathrm{S},\mathrm{F}\}.
\end{aligned}\tag{2.32}$$

In Appendix 4.5 we provide a guideline how to choose an α based on an error analysis. We set $\alpha = 1/2$, in which case the energy function with the penalty terms coincides with the one using an upwind flux [169,]. For the convergence analysis, we follow [169, Section 5.1] while obtaining an error estimate.

Following the matrix form in Subsection 2.3.3, we immediately rewrite the definition of energy functions (2.13) in solid and fluid region as

$$\begin{aligned}
\mathcal{E}_{\mathrm{S},h} =&\tfrac{1}{2}\sum_{\mathrm{e}}\big(\mathcal{Q}_h\boldsymbol{q}_h,\boldsymbol{\Lambda}_h\boldsymbol{q}_h\big)_{\Omega^{\mathrm{e}}{}_{\mathrm{S}}}=\tfrac{1}{2}\sum_{\mathrm{e}}\|\boldsymbol{q}\,\|_{L^2(\Omega^{\mathrm{e}}{}_{\mathrm{S}};\mathcal{Q}_h,\boldsymbol{\Lambda}_h)}\\
\mathcal{E}_{\mathrm{F},h} =&\tfrac{1}{2}\sum_{\mathrm{e}}\big(\widetilde{\mathcal{Q}}_h\widetilde{\boldsymbol{q}}_h,\widetilde{\boldsymbol{\Lambda}}_h\widetilde{\boldsymbol{q}}_h\big)_{\Omega^{\mathrm{e}}{}_{\mathrm{F}}}=\tfrac{1}{2}\sum_{\mathrm{e}}\|\widetilde{\boldsymbol{q}}\,\|_{L^2(\Omega^{\mathrm{e}}{}_{\mathrm{F}};\widetilde{\mathcal{Q}}_h,\widetilde{\boldsymbol{\Lambda}}_h)}.
\end{aligned}\tag{2.33}$$

Here $\|\,\boldsymbol{\cdot}\,\|_{L^2(\Omega^{\mathrm{e}}{}_{\mathrm{S}};\mathcal{Q},\boldsymbol{\Lambda})}$ and $\|\,\boldsymbol{\cdot}\,\|_{L^2(\Omega^{\mathrm{e}}{}_{\mathrm{F}};\widetilde{\mathcal{Q}},\widetilde{\boldsymbol{\Lambda}})}$ are the energy norms in solid and fluid regions, and we simplify the notification without causing ambiguity by $\|\boldsymbol{\cdot}\|_{L^2(\Omega^{\mathrm{e}}{}_{\mathrm{S}};\,\mathcal{Q},\boldsymbol{\Lambda})}$ and $\|\boldsymbol{\cdot}\|_{L^2(\Omega^{\mathrm{e}}{}_{\mathrm{F}};\,\widetilde{\mathcal{Q}},\widetilde{\boldsymbol{\Lambda}})}$, respectively. We also define the energy norms in solid-solid, fluid-fluid and solid-fluid interfaces similarly as $\|\boldsymbol{\cdot}\|_{L^2(\Sigma^{\mathrm{e}}_{\mathrm{SS}})}$, $\|\boldsymbol{\cdot}\|_{L^2(\Sigma^{\mathrm{e}}_{\mathrm{FF}})}$ and $\|\boldsymbol{\cdot}\|_{L^2(\Sigma^{\mathrm{e}}_{\mathrm{SF}})}$, $\|\boldsymbol{\cdot}\|_{L^2(\Sigma^{\mathrm{e}}_{\mathrm{FS}})}$. Upon taking the penalty terms into consideration, equation (2.16) is replaced by

$$\begin{aligned}\frac{\mathrm{d}\mathcal{E}_h}{\mathrm{d}t} &+ \frac{\alpha}{2}\Big(\sum_{\mathrm{e}}\|\,[\![\mathcal{A}_{n,h}\boldsymbol{q}_h]\!]_{\mathrm{SS}}\,\|^2_{L^2(\Sigma^{\mathrm{e}}_{\mathrm{SS}})} + \sum_{\mathrm{e}}\|\,[\![\widetilde{\mathcal{A}}_{n,h}\widetilde{\boldsymbol{q}}_h]\!]_{\mathrm{FF}}\,\|^2_{L^2(\Sigma^{\mathrm{e}}_{\mathrm{FF}})} \\ &+ 2\sum_{\mathrm{e}}\|\,[\![\mathcal{A}_{n,h}\boldsymbol{q}_h]\!]_{\mathrm{SF}}\,\|^2_{L^2(\Sigma^{\mathrm{e}}_{\mathrm{SF}})}\Big) = \sum_{\mathrm{e}}\int_{\Omega^{\mathrm{e}}{}_{\mathrm{S}}}\boldsymbol{g}_h\cdot\boldsymbol{\Lambda}_h\boldsymbol{q}_h\,\mathrm{d}\Omega + \sum_{\mathrm{e}}\int_{\Omega^{\mathrm{e}}{}_{\mathrm{F}}}\widetilde{\boldsymbol{g}}_h\cdot\widetilde{\boldsymbol{\Lambda}}_h\widetilde{\boldsymbol{q}}_h\,\mathrm{d}\Omega.\end{aligned} \tag{2.34}$$

To obtain this result, in (2.31) – (2.32), we let $\boldsymbol{p}=\boldsymbol{q},\widetilde{\boldsymbol{p}}=\widetilde{\boldsymbol{q}}$. Taking the summation over all penalty terms on solid-solid interfaces yields

$$\begin{aligned}\sum_{\mathrm{e}}\big([\![\mathcal{A}_{n,h}\boldsymbol{q}_h]\!]_{\mathrm{SS}},(\mathcal{A}_{n,h}\boldsymbol{q}_h)^-\big)_{\Sigma^{\mathrm{e}}_{\mathrm{SS}}} = &\sum_{\mathrm{e}}\big((\mathcal{A}_{n,h}\boldsymbol{q}_h)^+-(\mathcal{A}_{n,h}\boldsymbol{q}_h)^-,(\mathcal{A}_{n,h}\boldsymbol{q}_h)^-\big)_{\Sigma^{\mathrm{e}}_{\mathrm{SS}}} \\ &= -\tfrac{1}{2}\sum_{\mathrm{e}}\|\,[\![\mathcal{A}_{n,h}\boldsymbol{q}_h]\!]_{\mathrm{SS}}\,\|^2_{L^2(\Sigma^{\mathrm{e}}_{\mathrm{SS}})}\end{aligned} \tag{2.35}$$

Taking the summation over all penalty terms on fluid-fluid interfaces yields

$$\sum_{\mathrm{e}}\big([\![\widetilde{\mathcal{A}}_{n,h}\widetilde{\boldsymbol{q}}_h]\!]_{\mathrm{FF}},(\widetilde{\mathcal{A}}_{n,h}\widetilde{\boldsymbol{q}}_h)^-\big)_{\Sigma^{\mathrm{e}}_{\mathrm{FF}}} = -\tfrac{1}{2}\sum_{\mathrm{e}}\|\,[\![\widetilde{\mathcal{A}}_{n,h}\widetilde{\boldsymbol{q}}_h]\!]_{\mathrm{FF}}\,\|^2_{L^2(\Sigma^{\mathrm{e}}_{\mathrm{FF}})}. \tag{2.36}$$

We rewrite the penalty terms on fluid-solid interface from the solid side as

$$\begin{aligned}&\big([\![\mathcal{A}_{n,h}\boldsymbol{q}_h]\!]_{\mathrm{SF}},(\mathcal{A}_{n,h}\boldsymbol{q}_h)^-\big)_{\Sigma^{\mathrm{e}}_{\mathrm{SF}}} \\ &\quad=\big(O^T(\widetilde{\mathcal{A}}_{n,h}\widetilde{\boldsymbol{q}}_h)^+,(\mathcal{A}_{n,h}\boldsymbol{q}_h)^-\big)_{\Sigma^{\mathrm{e}}_{\mathrm{SF}}} - \big((\mathcal{A}_{n,h}\boldsymbol{q}_h)^-,(\mathcal{A}_{n,h}\boldsymbol{q}_h)^-\big)_{\Sigma^{\mathrm{e}}_{\mathrm{SF}}},\end{aligned} \tag{2.37}$$

and from the fluid side as

$$\begin{aligned}&\big([\![\widetilde{\mathcal{A}}_{n,h}\widetilde{\boldsymbol{q}}_h]\!]_{\mathrm{FS}},(\widetilde{\mathcal{A}}_{n,h}\widetilde{\boldsymbol{q}}_h)^-\big)_{\Sigma^{\mathrm{e}}_{\mathrm{FS}}} \\ &\quad=\big(O(\mathcal{A}_{n,h}\boldsymbol{q}_h)^+,(\widetilde{\mathcal{A}}_{n,h}\widetilde{\boldsymbol{q}}_h)^-\big)_{\Sigma^{\mathrm{e}}_{\mathrm{FS}}} - \big((\widetilde{\mathcal{A}}_{n,h}\widetilde{\boldsymbol{q}}_h)^-,(\widetilde{\mathcal{A}}_{n,h}\widetilde{\boldsymbol{q}}_h)^-\big)_{\Sigma^{\mathrm{e}}_{\mathrm{FS}}} \\ &\quad=\big((\mathcal{A}_{n,h}\boldsymbol{q}_h)^+,O^T(\widetilde{\mathcal{A}}_{n,h}\widetilde{\boldsymbol{q}}_h)^-\big)_{\Sigma^{\mathrm{e}}_{\mathrm{FS}}} - \big(O^T(\widetilde{\mathcal{A}}_{n,h}\widetilde{\boldsymbol{q}}_h)^-,O^T(\widetilde{\mathcal{A}}_{n,h}\widetilde{\boldsymbol{q}}_h)^-\big)_{\Sigma^{\mathrm{e}}_{\mathrm{FS}}},\end{aligned} \tag{2.38}$$

in which the property $OO^T = I_{4\times 4}$ is used. Changing from the fluid to the solid sides yields

$$\begin{aligned}&\big(\big[\!\big[\widetilde{\mathcal{A}}_{n,h}\widetilde{\boldsymbol{q}}_h\big]\!\big]_{\mathrm{FS}}, (\widetilde{\mathcal{A}}_{n,h}\widetilde{\boldsymbol{q}}_h)^-\big)_{\Sigma^{\mathrm{e}}_{\mathrm{FS}}}\\ &\quad=\big((\mathcal{A}_{n,h}\boldsymbol{q}_h)^-, O^T(\widetilde{\mathcal{A}}_{n,h}\widetilde{\boldsymbol{q}}_h)^+\big)_{\Sigma^{\mathrm{e}}_{\mathrm{SF}}} - \big(O^T(\widetilde{\mathcal{A}}_{n,h}\widetilde{\boldsymbol{q}}_h)^+, O^T(\widetilde{\mathcal{A}}_{n,h}\widetilde{\boldsymbol{q}}_h)^+\big)_{\Sigma^{\mathrm{e}}_{\mathrm{SF}}}.\end{aligned} \tag{2.39}$$

Summation over all fluid-solid interfaces with (2.37) and (2.39),

$$\begin{aligned}&\sum_{\mathrm{e}}\big(\big[\!\big[\mathcal{A}_{n,h}\boldsymbol{q}_h\big]\!\big]_{\mathrm{SF}}, (\mathcal{A}_{n,h}\boldsymbol{q}_h)^-\big)_{\Sigma^{\mathrm{e}}_{\mathrm{SF}}} + \sum_{\mathrm{e}}\big(\big[\!\big[\widetilde{\mathcal{A}}_{n,h}\widetilde{\boldsymbol{q}}_h\big]\!\big]_{\mathrm{FS}}, (\widetilde{\mathcal{A}}_{n,h}\widetilde{\boldsymbol{q}}_h)^-\big)_{\Sigma^{\mathrm{e}}_{\mathrm{FS}}}\\ &\qquad= -\sum_{\mathrm{e}}\big\| O^T(\widetilde{\mathcal{A}}_{n,h}\widetilde{\boldsymbol{q}}_h)^+ - (\mathcal{A}_{n,h}\boldsymbol{q}_h)^-\big\|^2_{L^2(\Sigma^{\mathrm{e}}_{\mathrm{SF}})}\\ &\qquad= -\sum_{\mathrm{e}}\big\|\big[\!\big[\mathcal{A}_{n,h}\boldsymbol{q}_h\big]\!\big]_{\mathrm{SF}}\big\|^2_{L^2(\Sigma^{\mathrm{e}}_{\mathrm{SF}})}.\end{aligned} \tag{2.40}$$

Thus we obtain (2.34).

Our approach is reminiscent of earlier work, in which an upwind flux is defined by the Riemann solutions which are obtained by diagonalizing $\mathcal{A}_n$, that is, $\mathcal{A}_n = RDR^T$, on the faces of each element [[171]], and D is the diagonal matrix of eigenvalues of $\mathcal{A}_n$. The upwind flux takes the form,

$$\begin{aligned}\mathcal{F}^{\mathrm{U}}_{\mathrm{S}*} &= \big(\big[\!\big[\mathcal{A}_n\boldsymbol{q}\big]\!\big]_{\mathrm{S}*}, (\boldsymbol{\Lambda}\boldsymbol{p})^-\big)_{\Sigma^{\mathrm{e}}_{\mathrm{S}*}} + \big(\big[\!\big[(R|D|R^T)\boldsymbol{q}\big]\!\big]_{\mathrm{S}*}, (\boldsymbol{\Lambda}\boldsymbol{p})^-\big)_{\Sigma^{\mathrm{e}}_{\mathrm{S}*}},\\ \widetilde{\mathcal{F}}^{\mathrm{U}}_{\mathrm{F}*} &= \big(\big[\!\big[\widetilde{\mathcal{A}}_n\widetilde{\boldsymbol{q}}\big]\!\big]_{\mathrm{F}*}, (\widetilde{\boldsymbol{\Lambda}}\widetilde{\boldsymbol{p}})^-\big)_{\Sigma^{\mathrm{e}}_{\mathrm{F}*}} + \big(\big[\!\big[(\widetilde{R}|\widetilde{D}|\widetilde{R}^T)\widetilde{\boldsymbol{q}}\big]\!\big]_{\mathrm{F}*}, (\widetilde{\boldsymbol{\Lambda}}\widetilde{\boldsymbol{p}})^-\big)_{\Sigma^{\mathrm{e}}_{\mathrm{F}*}}, \quad * \in \{\mathrm{S},\mathrm{F}\},\end{aligned} \tag{2.41}$$

where $|\,\cdot\,|$ stands for the operaton of taking the absolute value of each entry of the diagonal matrix, that is, $|D|_{ij} = |D_{ij}|$. Our approach avoids this diagonalization, allowing general heterogeneous media with anisotropy.

2.5 Time Discretization

In this section, we discuss a time discretization that is computationally efficient for complex domains. Often, the computational meshes used to model the subsurface must contain regions where the characteristic lengths of the elements drop far below that of a wavelength because the subsurface contains very complex geometries and discontinuities. As a result, the time steps must be equally reduced to produce a stable solution. We follow two different time discretization schemes: (1) for non-complex domains, it is advantageous to use a traditional Runge–Kutta (RK) method and (2) for complex domains, a semi implicit–explicit (IMEX) method is used. The IMEX method enables the solver to perform implicit time integration in areas of oversampling, while keeping the computational efficiency of RK in regions of proper sampling.

2.5.1 Explicit Runge–Kutta

We use an explicit time integration method when the variation in element size is small. There are a variety of time-stepping methods available, however, we employ the five stage low-storage explicit Runge–Kutta (LSERK) method from [35]. LSERK is an explicit method the time-step of which is dictated by the Courant–Friedrichs–Lewy (CFL) condition. Efforts to define, quantitatively, a stable CFL condition depending on polynomial order N_p, can be found in [35]. The LSERK method is preferred over other methods because it saves memory at the cost of computation time.

2.5.2 Explicit–Implicit Runge–Kutta

When the domain in question contains complex geometries within large domains, such as rough surfaces, the resulting mesh will contain regions of oversampling relative to the relevant wavelengths. This hinders the use of an implicit time-stepping method because its accuracy depends on the size of the time step, which in turn is dependent on the region of highest spatial sampling. A natural approach is the IMEX method, (e.g. [9, 88, 125]), which allows the regions of oversampling to be integrated in time with an L-stable third-order and 3-stage Diagonally Implicit Runge–Kutta (DIRK) method, while using a fast and simple 4-stage third-order ERK method in the regions of more reasonable sampling (8–10 nodes per wavelength).

The system can be solved without requiring an interpolation at the boundary of the implicit–explicit regions. The intermediate abscissaes of each time step for implicit Runge–Kutta stages and for explicit ones are selected to equal one another so as to synchronize the explicit and implicit schemes, and the so-called Butcher matrix is calculated correspondingly. The implicit stages are solved using a multifrontal factorization.

2.6 Convergence analysis

In this section we consider the L^2 error of numerical solutions $\boldsymbol{q}_h$ and $\widetilde{\boldsymbol{q}}_h$, which satisfy (2.31)–(2.32) for any $\boldsymbol{p}_h$ and $\widetilde{\boldsymbol{p}}_h \in V_h^{N_p}$. We denote by $\pi_h^{N_p} : L^2 \mapsto V_h^{N_p}$ the L^2 projection onto the polynomial space of order N_p. We assume that $\boldsymbol{f} - \boldsymbol{f}_h = 0$ and $\widetilde{f} - \widetilde{f}_h = 0$, and no error occurs for L^2 projection of coefficient matrices, that is, $\mathcal{A} - \mathcal{A}_h = 0$, $\mathcal{Q} - \mathcal{Q}_h = 0$ and $\boldsymbol{\Lambda} - \boldsymbol{\Lambda}_h = 0$. We define $\boldsymbol{e} := \boldsymbol{q} - \boldsymbol{q}_h$ and $\widetilde{\boldsymbol{e}} := \widetilde{\boldsymbol{q}} - \widetilde{\boldsymbol{q}}_h$, where $\boldsymbol{q}$ and $\widetilde{\boldsymbol{q}}$ are the exact solutions. We also denote $\boldsymbol{\eta} := \boldsymbol{q}_h - \pi_h^{N_p}\boldsymbol{q}$, $\widetilde{\boldsymbol{\eta}} := \widetilde{\boldsymbol{q}}_h - \pi_h^{N_p}\widetilde{\boldsymbol{q}}$, and $\boldsymbol{\epsilon} := (1 - \pi_h^{N_p})\boldsymbol{q}$, $\widetilde{\boldsymbol{\epsilon}} := (1 - \pi_h^{N_p})\widetilde{\boldsymbol{q}}$; thus $\boldsymbol{e} = \boldsymbol{\epsilon} - \boldsymbol{\eta}$, $\widetilde{\boldsymbol{e}} = \widetilde{\boldsymbol{\epsilon}} - \widetilde{\boldsymbol{\eta}}$. We define the volume residuals

$$\mathrm{res}_{\mathrm{S}}(\boldsymbol{q}_h) := \boldsymbol{\Lambda}^T \left(\mathcal{Q}\dot{\boldsymbol{q}}_h - \nabla \cdot (\mathcal{A}\boldsymbol{q}_h)\right), \quad \widetilde{\mathrm{res}}_{\mathrm{F}}(\widetilde{\boldsymbol{q}}_h) := \widetilde{\boldsymbol{\Lambda}}^T \left(\widetilde{\mathcal{Q}}\dot{\widetilde{\boldsymbol{q}}}_h - \nabla \cdot (\widetilde{\mathcal{A}}\widetilde{\boldsymbol{q}}_h)\right), \tag{2.42}$$

and surface residuals

$$
\begin{aligned}
\mathrm{res}_{\mathrm{SS}}(\boldsymbol{q}_h) &:= \tfrac{1}{2}(\boldsymbol{\Lambda}^-)^T [\![\mathcal{A}_n \boldsymbol{q}_h]\!]_{\mathrm{SS}} + \alpha(\mathcal{A}_n^-)^T [\![\mathcal{A}_n \boldsymbol{q}_h]\!]_{\mathrm{SS}}, \\
\widetilde{\mathrm{res}}_{\mathrm{FS}}(\widetilde{\boldsymbol{q}}_h) &:= \tfrac{1}{2}(\widetilde{\boldsymbol{\Lambda}}^-)^T [\![\widetilde{\mathcal{A}}_n \widetilde{\boldsymbol{q}}_h]\!]_{\mathrm{FS}} + \alpha(\widetilde{\mathcal{A}}_n^-)^T [\![\widetilde{\mathcal{A}}_n \widetilde{\boldsymbol{q}}_h]\!]_{\mathrm{FS}}, \\
\mathrm{res}_{\mathrm{SF}}(\boldsymbol{q}_h) &:= \tfrac{1}{2}(\boldsymbol{\Lambda}^-)^T [\![\mathcal{A}_n \boldsymbol{q}_h]\!]_{\mathrm{SF}} + \alpha(\mathcal{A}_n^-)^T [\![\mathcal{A}_n \boldsymbol{q}_h]\!]_{\mathrm{SF}}, \\
\widetilde{\mathrm{res}}_{\mathrm{FF}}(\widetilde{\boldsymbol{q}}_h) &:= \tfrac{1}{2}(\widetilde{\boldsymbol{\Lambda}}^-)^T [\![\widetilde{\mathcal{A}}_n \widetilde{\boldsymbol{q}}_h]\!]_{\mathrm{FF}} + \alpha(\widetilde{\mathcal{A}}_n^-)^T [\![\widetilde{\mathcal{A}}_n \widetilde{\boldsymbol{q}}_h]\!]_{\mathrm{FF}}.
\end{aligned}
\tag{2.43}
$$

Using (2.31)–(2.32), it follows that $(\boldsymbol{e}, \widetilde{\boldsymbol{e}})$ satisfy

$$
\begin{aligned}
\sum_{\mathrm{e}} \int_{\Omega^{\mathrm{e}}{}_{\mathrm{S}}} \mathrm{res}_{\mathrm{S}}(\boldsymbol{e}) \cdot \boldsymbol{p}_h \, \mathrm{d}\Omega - \sum_{\mathrm{e}} \int_{\Sigma^{\mathrm{e}}_{\mathrm{SS}}} \mathrm{res}_{\mathrm{SS}}(\boldsymbol{e}) \cdot \boldsymbol{p}_h^- \, \mathrm{d}\Sigma - \sum_{\mathrm{e}} \int_{\Sigma^{\mathrm{e}}_{\mathrm{SF}}} \mathrm{res}_{\mathrm{SF}}(\boldsymbol{e}) \cdot \boldsymbol{p}_h^- \, \mathrm{d}\Sigma &= 0, \\
\sum_{\mathrm{e}} \int_{\Omega^{\mathrm{e}}{}_{\mathrm{F}}} \widetilde{\mathrm{res}}_{\mathrm{F}}(\widetilde{\boldsymbol{e}}) \cdot \widetilde{\boldsymbol{p}}_h \, \mathrm{d}\Omega - \sum_{\mathrm{e}} \int_{\Sigma^{\mathrm{e}}_{\mathrm{FS}}} \widetilde{\mathrm{res}}_{\mathrm{FS}}(\widetilde{\boldsymbol{e}}) \cdot \widetilde{\boldsymbol{p}}_h^- \, \mathrm{d}\Sigma - \sum_{\mathrm{e}} \int_{\Sigma^{\mathrm{e}}_{\mathrm{FF}}} \widetilde{\mathrm{res}}_{\mathrm{FF}}(\widetilde{\boldsymbol{e}}) \cdot \widetilde{\boldsymbol{p}}_h^- \, \mathrm{d}\Sigma &= 0,
\end{aligned}
\tag{2.44}
$$

upon setting $\mathcal{Q}_h = \mathcal{Q}$ and $\mathcal{A}_h = \mathcal{A}$. We take inner products of (2.42) and (2.43) with corresponding test functions, and immediately get, after summing up all the terms,

$$
\begin{aligned}
&\sum_{\mathrm{e}} \int_{\Omega^{\mathrm{e}}{}_{\mathrm{S}}} \mathcal{Q}\dot{\boldsymbol{q}}_h \cdot \boldsymbol{\Lambda}\boldsymbol{p}_h \, \mathrm{d}\Omega - \sum_{\mathrm{e}} \int_{\Omega^{\mathrm{e}}{}_{\mathrm{S}}} (\nabla \cdot (\mathcal{A}\boldsymbol{q}_h)) \cdot \boldsymbol{\Lambda}\boldsymbol{p}_h \, \mathrm{d}\Omega \\
&\qquad - \tfrac{1}{2}\sum_{\mathrm{e}} \int_{\Sigma^{\mathrm{e}}_{\mathrm{SS}}} [\![\mathcal{A}_n \boldsymbol{q}_h]\!]_{\mathrm{SS}} \cdot (\boldsymbol{\Lambda}\boldsymbol{p}_h)^- \, \mathrm{d}\Sigma - \tfrac{1}{2}\sum_{\mathrm{e}} \int_{\Sigma^{\mathrm{e}}_{\mathrm{SF}}} [\![\mathcal{A}_n \boldsymbol{q}_h]\!]_{\mathrm{SF}} \cdot (\boldsymbol{\Lambda}\boldsymbol{p}_h)^- \, \mathrm{d}\Sigma \\
&\qquad - \alpha\sum_{\mathrm{e}} \int_{\Sigma^{\mathrm{e}}_{\mathrm{SS}}} [\![\mathcal{A}_n \boldsymbol{q}_h]\!]_{\mathrm{SS}} \cdot (\mathcal{A}_n\boldsymbol{p}_h)^- \, \mathrm{d}\Sigma - \alpha\sum_{\mathrm{e}} \int_{\Sigma^{\mathrm{e}}_{\mathrm{SF}}} [\![\mathcal{A}_n \boldsymbol{q}_h]\!]_{\mathrm{SF}} \cdot (\mathcal{A}_n\boldsymbol{p}_h)^- \, \mathrm{d}\Sigma \\
=&\sum_{\mathrm{e}} \int_{\Omega^{\mathrm{e}}{}_{\mathrm{S}}} \mathrm{res}_{\mathrm{S}}(\boldsymbol{q}_h) \cdot \boldsymbol{p}_h \, \mathrm{d}\Omega - \sum_{\mathrm{e}} \int_{\Sigma^{\mathrm{e}}_{\mathrm{SS}}} \mathrm{res}_{\mathrm{SS}}(\boldsymbol{q}_h) \cdot \boldsymbol{p}_h^- \, \mathrm{d}\Sigma - \sum_{\mathrm{e}} \int_{\Sigma^{\mathrm{e}}_{\mathrm{SF}}} \mathrm{res}_{\mathrm{SF}}(\boldsymbol{q}_h) \cdot \boldsymbol{p}_h^- \, \mathrm{d}\Sigma,
\end{aligned}
\tag{2.45}
$$

$$
\begin{aligned}
&\sum_{\mathrm{e}} \int_{\Omega^{\mathrm{e}}{}_{\mathrm{F}}} \widetilde{\mathcal{Q}}\dot{\widetilde{\boldsymbol{q}}}_h \cdot \widetilde{\boldsymbol{\Lambda}}\widetilde{\boldsymbol{p}}_h \,\mathrm{d}\Omega - \sum_{\mathrm{e}} \int_{\Omega^{\mathrm{e}}{}_{\mathrm{F}}} (\nabla \cdot (\widetilde{\mathcal{A}}\widetilde{\boldsymbol{q}}_h)) \cdot \widetilde{\boldsymbol{\Lambda}}\widetilde{\boldsymbol{p}}_h \,\mathrm{d}\Omega \\
&\qquad - \tfrac{1}{2}\sum_{\mathrm{e}} \int_{\Sigma^{\mathrm{e}}_{\mathrm{FF}}} [\![\widetilde{\mathcal{A}}_n\widetilde{\boldsymbol{q}}_h]\!]_{\mathrm{FF}} \cdot (\widetilde{\boldsymbol{\Lambda}}\widetilde{\boldsymbol{p}}_h)^- \,\mathrm{d}\Sigma - \tfrac{1}{2}\sum_{\mathrm{e}} \int_{\Sigma^{\mathrm{e}}_{\mathrm{FS}}} [\![\widetilde{\mathcal{A}}_n\widetilde{\boldsymbol{q}}_h]\!]_{\mathrm{FS}} \cdot (\widetilde{\boldsymbol{\Lambda}}\widetilde{\boldsymbol{p}}_h)^- \,\mathrm{d}\Sigma \\
&\qquad - \alpha\sum_{\mathrm{e}} \int_{\Sigma^{\mathrm{e}}_{\mathrm{FF}}} [\![\widetilde{\mathcal{A}}_n\widetilde{\boldsymbol{q}}_h]\!]_{\mathrm{FF}} \cdot (\widetilde{\mathcal{A}}_n\widetilde{\boldsymbol{p}}_h)^- \,\mathrm{d}\Sigma - \alpha\sum_{\mathrm{e}} \int_{\Sigma^{\mathrm{e}}_{\mathrm{FS}}} [\![\widetilde{\mathcal{A}}_n\widetilde{\boldsymbol{q}}_h]\!]_{\mathrm{FS}} \cdot (\widetilde{\mathcal{A}}_n\widetilde{\boldsymbol{p}}_h)^- \,\mathrm{d}\Sigma \\
= &\sum_{\mathrm{e}} \int_{\Omega^{\mathrm{e}}{}_{\mathrm{F}}} \widetilde{\mathrm{res}}_{\mathrm{F}}(\widetilde{\boldsymbol{q}}_h) \cdot \widetilde{\boldsymbol{p}}_h \,\mathrm{d}\Omega - \sum_{\mathrm{e}} \int_{\Sigma^{\mathrm{e}}_{\mathrm{FF}}} \widetilde{\mathrm{res}}_{\mathrm{FF}}(\widetilde{\boldsymbol{q}}_h) \cdot \widetilde{\boldsymbol{p}}_h^- \,\mathrm{d}\Sigma - \sum_{\mathrm{e}} \int_{\Sigma^{\mathrm{e}}_{\mathrm{FS}}} \widetilde{\mathrm{res}}_{\mathrm{FS}}(\widetilde{\boldsymbol{q}}_h) \cdot \widetilde{\boldsymbol{p}}_h^- \,\mathrm{d}\Sigma.
\end{aligned}
\tag{2.46}
$$

We let $\boldsymbol{q}_h = \boldsymbol{p}_h = \boldsymbol{\eta}$, $\widetilde{\boldsymbol{q}}_h = \widetilde{\boldsymbol{p}}_h = \widetilde{\boldsymbol{\eta}}$, when equations (2.45) and (2.46) become

$$
\begin{aligned}
&\frac{1}{2}\frac{\mathrm{d}}{\mathrm{d}t}\sum_{\mathrm{e}}\|\boldsymbol{\eta}\|^2_{L^2(\Omega^{\mathrm{e}}{}_{\mathrm{S}})} - \alpha\sum_{\mathrm{e}} \int_{\Sigma^{\mathrm{e}}_{\mathrm{SS}}} [\![\mathcal{A}_n\boldsymbol{\eta}]\!]_{\mathrm{SS}} \cdot (\mathcal{A}_n\boldsymbol{\eta})^- \,\mathrm{d}\Sigma - \alpha\sum_{\mathrm{e}} \int_{\Sigma^{\mathrm{e}}_{\mathrm{SF}}} [\![\mathcal{A}_n\boldsymbol{\eta}]\!]_{\mathrm{SF}} \cdot (\mathcal{A}_n\boldsymbol{\eta})^- \,\mathrm{d}\Sigma \\
&\quad - \Bigg(\sum_{\mathrm{e}} \int_{\Omega^{\mathrm{e}}{}_{\mathrm{S}}} (\nabla \cdot (\mathcal{A}\boldsymbol{\eta})) \cdot \boldsymbol{\Lambda}\boldsymbol{\eta} \,\mathrm{d}\Omega + \tfrac{1}{2}\sum_{\mathrm{e}} \int_{\Sigma^{\mathrm{e}}_{\mathrm{SS}}} [\![\mathcal{A}_n\boldsymbol{\eta}]\!]_{\mathrm{SS}} \cdot (\boldsymbol{\Lambda}\boldsymbol{\eta})^- \,\mathrm{d}\Sigma \\
&\qquad\qquad + \tfrac{1}{2}\sum_{\mathrm{e}} \int_{\Sigma^{\mathrm{e}}_{\mathrm{SF}}} [\![\mathcal{A}_n\boldsymbol{\eta}]\!]_{\mathrm{SF}} \cdot (\boldsymbol{\Lambda}\boldsymbol{\eta})^- \,\mathrm{d}\Sigma\Bigg) \\
&= \sum_{\mathrm{e}} \int_{\Omega^{\mathrm{e}}{}_{\mathrm{S}}} \mathrm{res}_{\mathrm{S}}(\boldsymbol{\eta}) \cdot \boldsymbol{\eta} \,\mathrm{d}\Omega - \sum_{\mathrm{e}} \int_{\Sigma^{\mathrm{e}}_{\mathrm{SS}}} \mathrm{res}_{\mathrm{SS}}(\boldsymbol{\eta}) \cdot \boldsymbol{\eta}^- \,\mathrm{d}\Sigma - \sum_{\mathrm{e}} \int_{\Sigma^{\mathrm{e}}_{\mathrm{SF}}} \mathrm{res}_{\mathrm{SF}}(\boldsymbol{\eta}) \cdot \boldsymbol{\eta}^- \,\mathrm{d}\Sigma,
\end{aligned}
\tag{2.47}
$$

$$
\begin{aligned}
&\frac{1}{2}\frac{\mathrm{d}}{\mathrm{d}t}\sum_{\mathrm{e}}\|\widetilde{\boldsymbol{\eta}}\|^2_{L^2(\Omega^{\mathrm{e}}{}_{\mathrm{F}})} - \alpha\sum_{\mathrm{e}} \int_{\Sigma^{\mathrm{e}}_{\mathrm{FF}}} [\![\widetilde{\mathcal{A}}_n\widetilde{\boldsymbol{\eta}}]\!]_{\mathrm{FF}} \cdot (\widetilde{\mathcal{A}}_n\widetilde{\boldsymbol{\eta}})^- \,\mathrm{d}\Sigma - \alpha\sum_{\mathrm{e}} \int_{\Sigma^{\mathrm{e}}_{\mathrm{FS}}} [\![\widetilde{\mathcal{A}}_n\widetilde{\boldsymbol{\eta}}]\!]_{\mathrm{FS}} \cdot (\widetilde{\mathcal{A}}_n\widetilde{\boldsymbol{\eta}})^- \,\mathrm{d}\Sigma \\
&\quad - \Bigg(\sum_{\mathrm{e}} \int_{\Omega^{\mathrm{e}}{}_{\mathrm{F}}} (\nabla \cdot (\widetilde{\mathcal{A}}\widetilde{\boldsymbol{\eta}})) \cdot \widetilde{\boldsymbol{\Lambda}}\widetilde{\boldsymbol{\eta}} \,\mathrm{d}\Omega + \tfrac{1}{2}\sum_{\mathrm{e}} \int_{\Sigma^{\mathrm{e}}_{\mathrm{FF}}} [\![\widetilde{\mathcal{A}}_n\widetilde{\boldsymbol{\eta}}]\!]_{\mathrm{FF}} \cdot (\widetilde{\boldsymbol{\Lambda}}\widetilde{\boldsymbol{\eta}})^- \,\mathrm{d}\Sigma \\
&\qquad\qquad + \tfrac{1}{2}\sum_{\mathrm{e}} \int_{\Sigma^{\mathrm{e}}_{\mathrm{FS}}} [\![\widetilde{\mathcal{A}}_n\widetilde{\boldsymbol{\eta}}]\!]_{\mathrm{FS}} \cdot (\widetilde{\boldsymbol{\Lambda}}\widetilde{\boldsymbol{\eta}})^- \,\mathrm{d}\Sigma\Bigg) \\
&= \sum_{\mathrm{e}} \int_{\Omega^{\mathrm{e}}{}_{\mathrm{F}}} \widetilde{\mathrm{res}}_{\mathrm{F}}(\widetilde{\boldsymbol{\eta}}) \cdot \widetilde{\boldsymbol{\eta}} \,\mathrm{d}\Omega - \sum_{\mathrm{e}} \int_{\Sigma^{\mathrm{e}}_{\mathrm{FF}}} \widetilde{\mathrm{res}}_{\mathrm{FF}}(\widetilde{\boldsymbol{\eta}}) \cdot \widetilde{\boldsymbol{\eta}}^- \,\mathrm{d}\Sigma - \sum_{\mathrm{e}} \int_{\Sigma^{\mathrm{e}}_{\mathrm{FS}}} \widetilde{\mathrm{res}}_{\mathrm{FS}}(\widetilde{\boldsymbol{\eta}}) \cdot \widetilde{\boldsymbol{\eta}}^- \,\mathrm{d}\Sigma.
\end{aligned}
\tag{2.48}
$$

Adding (2.47) and (2.48), and using the energy result in Section 2.4, the terms in between parentheses on the left-hand sides of both equations cancel one another, and the penalty terms turn into quadratic forms, that is,

$$\begin{aligned}
&\frac{1}{2}\frac{\mathrm{d}}{\mathrm{d}t}\left(\sum_{\mathrm{e}}\|\boldsymbol{\eta}\|^2_{L^2(\Omega^{\mathrm{e}}{}_{\mathrm{S}};\,\mathcal{Q},\boldsymbol{\Lambda})}+\sum_{\mathrm{e}}\|\widetilde{\boldsymbol{\eta}}\|^2_{L^2(\Omega^{\mathrm{e}}{}_{\mathrm{F}};\,\widetilde{\mathcal{Q}},\widetilde{\boldsymbol{\Lambda}})}\right)\\
&\quad+\frac{\alpha}{2}\left(\sum_{\mathrm{e}}\left\|[\![\mathcal{A}_n\boldsymbol{\eta}]\!]_{\mathrm{SS}}\right\|^2_{L^2(\Sigma^{\mathrm{e}}_{\mathrm{SS}})}+\sum_{\mathrm{e}}\left\|[\![\widetilde{\mathcal{A}}_n\widetilde{\boldsymbol{\eta}}]\!]_{\mathrm{FF}}\right\|^2_{L^2(\Sigma^{\mathrm{e}}_{\mathrm{FF}})}+2\sum_{\mathrm{e}}\left\|[\![\mathcal{A}_n\boldsymbol{\eta}]\!]_{\mathrm{SF}}\right\|^2_{L^2(\Sigma^{\mathrm{e}}_{\mathrm{SF}})}\right)\\
&=\sum_{\mathrm{e}}\int_{\Omega^{\mathrm{e}}{}_{\mathrm{S}}}\mathrm{res}_{\mathrm{S}}(\boldsymbol{\eta})\cdot\boldsymbol{\eta}\,\mathrm{d}\Omega-\sum_{\mathrm{e}}\int_{\Sigma^{\mathrm{e}}_{\mathrm{SS}}}\mathrm{res}_{\mathrm{SS}}(\boldsymbol{\eta})\cdot\boldsymbol{\eta}^-\,\mathrm{d}\Sigma-\sum_{\mathrm{e}}\int_{\Sigma^{\mathrm{e}}_{\mathrm{SF}}}\mathrm{res}_{\mathrm{SF}}(\boldsymbol{\eta})\cdot\boldsymbol{\eta}^-\,\mathrm{d}\Sigma\\
&\quad+\sum_{\mathrm{e}}\int_{\Omega^{\mathrm{e}}{}_{\mathrm{F}}}\widetilde{\mathrm{res}}_{\mathrm{F}}(\widetilde{\boldsymbol{\eta}})\cdot\widetilde{\boldsymbol{\eta}}\,\mathrm{d}\Omega-\sum_{\mathrm{e}}\int_{\Sigma^{\mathrm{e}}_{\mathrm{FF}}}\widetilde{\mathrm{res}}_{\mathrm{FF}}(\widetilde{\boldsymbol{\eta}})\cdot\widetilde{\boldsymbol{\eta}}^-\,\mathrm{d}\Sigma-\sum_{\mathrm{e}}\int_{\Sigma^{\mathrm{e}}_{\mathrm{FS}}}\widetilde{\mathrm{res}}_{\mathrm{FS}}(\widetilde{\boldsymbol{\eta}})\cdot\widetilde{\boldsymbol{\eta}}^-\,\mathrm{d}\Sigma.
\end{aligned}\tag{2.49}$$

Let $\boldsymbol{p}_h=\boldsymbol{\eta}$ in (2.44), and subtract it from the right-hand side of (2.49). We note that $\boldsymbol{e}=\boldsymbol{\epsilon}-\boldsymbol{\eta}$, $\widetilde{\boldsymbol{e}}=\widetilde{\boldsymbol{\epsilon}}-\widetilde{\boldsymbol{\eta}}$, and obtain

$$\begin{aligned}
&\frac{1}{2}\frac{\mathrm{d}}{\mathrm{d}t}\left(\sum_{\mathrm{e}}\|\boldsymbol{\eta}\|^2_{L^2(\Omega^{\mathrm{e}}{}_{\mathrm{S}};\,\mathcal{Q},\boldsymbol{\Lambda})}+\sum_{\mathrm{e}}\|\widetilde{\boldsymbol{\eta}}\|^2_{L^2(\Omega^{\mathrm{e}}{}_{\mathrm{F}};\,\widetilde{\mathcal{Q}},\widetilde{\boldsymbol{\Lambda}})}\right)\\
&\quad+\frac{\alpha}{2}\left(\sum_{\mathrm{e}}\left\|[\![\mathcal{A}_n\boldsymbol{\eta}]\!]_{\mathrm{SS}}\right\|^2_{L^2(\Sigma^{\mathrm{e}}_{\mathrm{SS}})}+\sum_{\mathrm{e}}\left\|[\![\widetilde{\mathcal{A}}_n\widetilde{\boldsymbol{\eta}}]\!]_{\mathrm{FF}}\right\|^2_{L^2(\Sigma^{\mathrm{e}}_{\mathrm{FF}})}+2\sum_{\mathrm{e}}\left\|[\![\mathcal{A}_n\boldsymbol{\eta}]\!]_{\mathrm{SF}}\right\|^2_{L^2(\Sigma^{\mathrm{e}}_{\mathrm{SF}})}\right)\\
&=\sum_{\mathrm{e}}\int_{\Omega^{\mathrm{e}}{}_{\mathrm{S}}}\mathrm{res}_{\mathrm{S}}(\boldsymbol{\epsilon})\cdot\boldsymbol{\eta}\,\mathrm{d}\Omega-\sum_{\mathrm{e}}\int_{\Sigma^{\mathrm{e}}_{\mathrm{SS}}}\mathrm{res}_{\mathrm{SS}}(\boldsymbol{\epsilon})\cdot\boldsymbol{\eta}^-\,\mathrm{d}\Sigma-\sum_{\mathrm{e}}\int_{\Sigma^{\mathrm{e}}_{\mathrm{SF}}}\mathrm{res}_{\mathrm{SF}}(\boldsymbol{\epsilon})\cdot\boldsymbol{\eta}^-\,\mathrm{d}\Sigma\\
&\quad+\sum_{\mathrm{e}}\int_{\Omega^{\mathrm{e}}{}_{\mathrm{F}}}\widetilde{\mathrm{res}}_{\mathrm{F}}(\widetilde{\boldsymbol{\epsilon}})\cdot\widetilde{\boldsymbol{\eta}}\,\mathrm{d}\Omega-\sum_{\mathrm{e}}\int_{\Sigma^{\mathrm{e}}_{\mathrm{FF}}}\widetilde{\mathrm{res}}_{\mathrm{FF}}(\widetilde{\boldsymbol{\epsilon}})\cdot\widetilde{\boldsymbol{\eta}}^-\,\mathrm{d}\Sigma-\sum_{\mathrm{e}}\int_{\Sigma^{\mathrm{e}}_{\mathrm{FS}}}\widetilde{\mathrm{res}}_{\mathrm{FS}}(\widetilde{\boldsymbol{\epsilon}})\cdot\widetilde{\boldsymbol{\eta}}^-\,\mathrm{d}\Sigma.
\end{aligned}\tag{2.50}$$

Having the energy result (2.50), which corresponds with Equation (5.10) in [169], we follow the same process as described in the reference.

We apply integration by parts:

$$\begin{aligned}
\int_{\Omega^{\mathrm{e}}{}_{\mathrm{S}}}(\nabla\cdot(\mathcal{A}\boldsymbol{q}))\cdot(\boldsymbol{\Lambda}\boldsymbol{p})\,\mathrm{d}\Omega&=\int_{\Omega^{\mathrm{e}}{}_{\mathrm{S}}}(\nabla\cdot(\boldsymbol{C}\boldsymbol{E}))\cdot\boldsymbol{w}+\tfrac{1}{2}(\nabla\boldsymbol{v}+\nabla\boldsymbol{v}^T):(\boldsymbol{C}\boldsymbol{H})\,\mathrm{d}\Omega\\
&=-\int_{\Omega^{\mathrm{e}}{}_{\mathrm{S}}}(\boldsymbol{C}\boldsymbol{E}):\tfrac{1}{2}(\nabla\boldsymbol{w}+\nabla\boldsymbol{w}^T)+\boldsymbol{v}\cdot(\nabla\cdot(\boldsymbol{C}\boldsymbol{H}))\,\mathrm{d}\Omega\\
&\qquad+\int_{\Sigma^{\mathrm{e}}_{\mathrm{SS}}\cup\Sigma^{\mathrm{e}}_{\mathrm{SF}}}(\boldsymbol{n}\cdot(\boldsymbol{C}\boldsymbol{E}))^-\cdot\boldsymbol{w}^-+\boldsymbol{v}^-\cdot(\boldsymbol{n}\cdot(\boldsymbol{C}\boldsymbol{H}))^-\,\mathrm{d}\Sigma\\
&=\boxed{-\int_{\Omega^{\mathrm{e}}{}_{\mathrm{S}}}(\nabla\cdot(\mathcal{A}\boldsymbol{p}))\cdot(\boldsymbol{\Lambda}\boldsymbol{q})\,\mathrm{d}\Omega}+\int_{\Sigma^{\mathrm{e}}_{\mathrm{SS}}\cup\Sigma^{\mathrm{e}}_{\mathrm{SF}}}(\mathcal{A}_n\boldsymbol{q})^-\cdot(\boldsymbol{\Lambda}\boldsymbol{p})^-\,\mathrm{d}\Sigma,
\end{aligned}\tag{2.51}$$

and similarly

$$\int_{\Omega^{\mathrm{e}}{}_{\mathrm{F}}} (\nabla \cdot (\widetilde{\mathcal{A}}\widetilde{\boldsymbol{q}})) \cdot (\widetilde{\boldsymbol{\Lambda}}\widetilde{\boldsymbol{p}}) \, \mathrm{d}\Omega = \boxed{- \int_{\Omega^{\mathrm{e}}{}_{\mathrm{F}}} (\nabla \cdot (\widetilde{\mathcal{A}}\widetilde{\boldsymbol{p}})) \cdot (\widetilde{\boldsymbol{\Lambda}}\boldsymbol{q}) \, \mathrm{d}\Omega} + \int_{\Sigma^{\mathrm{e}}_{\mathrm{FS}} \cup \Sigma^{\mathrm{e}}_{\mathrm{FF}}} (\widetilde{\mathcal{A}}_n \widetilde{\boldsymbol{q}})^- \cdot (\widetilde{\boldsymbol{\Lambda}}\widetilde{\boldsymbol{p}})^- \, \mathrm{d}\Sigma. \tag{2.52}$$

We set $\boldsymbol{q} = \boldsymbol{\epsilon}$, $\boldsymbol{p} = \boldsymbol{\eta}$ in (2.51) and $\widetilde{\boldsymbol{q}} = \widetilde{\boldsymbol{\epsilon}}$, $\widetilde{\boldsymbol{p}} = \widetilde{\boldsymbol{\eta}}$ in (2.52). The boxed terms in (2.51) and (2.52) vanish as the projection errors $\boldsymbol{\epsilon}$ and $\widetilde{\boldsymbol{\epsilon}}$ are orthogonal to the spatial derivatives of the polynomial solutions $\boldsymbol{q}_h$ and $\widetilde{\boldsymbol{q}}_h$ by Galerkin approximation, and then the right-hand side of (2.50) becomes

$$\begin{aligned}
&\sum_{\mathrm{e}} \int_{\Omega^{\mathrm{e}}{}_{\mathrm{S}}} \mathrm{res}_{\mathrm{S}}(\boldsymbol{\epsilon}) \cdot \boldsymbol{\eta} \, \mathrm{d}\Omega - \sum_{\mathrm{e}} \int_{\Sigma^{\mathrm{e}}_{\mathrm{SS}}} \mathrm{res}_{\mathrm{SS}}(\boldsymbol{\epsilon}) \cdot \boldsymbol{\eta}^- \, \mathrm{d}\Sigma - \sum_{\mathrm{e}} \int_{\Sigma^{\mathrm{e}}_{\mathrm{SF}}} \mathrm{res}_{\mathrm{SF}}(\boldsymbol{\epsilon}) \cdot \boldsymbol{\eta}^- \, \mathrm{d}\Sigma \\
&\quad + \sum_{\mathrm{e}} \int_{\Omega^{\mathrm{e}}{}_{\mathrm{F}}} \widetilde{\mathrm{res}}_{\mathrm{F}}(\widetilde{\boldsymbol{\epsilon}}) \cdot \widetilde{\boldsymbol{\eta}} \, \mathrm{d}\Omega - \sum_{\mathrm{e}} \int_{\Sigma^{\mathrm{e}}_{\mathrm{FF}}} \widetilde{\mathrm{res}}_{\mathrm{FF}}(\widetilde{\boldsymbol{\epsilon}}) \cdot \widetilde{\boldsymbol{\eta}}^- \, \mathrm{d}\Sigma - \sum_{\mathrm{e}} \int_{\Sigma^{\mathrm{e}}_{\mathrm{FS}}} \widetilde{\mathrm{res}}_{\mathrm{FS}}(\widetilde{\boldsymbol{\epsilon}}) \cdot \widetilde{\boldsymbol{\eta}}^- \, \mathrm{d}\Sigma \\
= \; & \boxed{\sum_{\mathrm{e}} \int_{\Omega^{\mathrm{e}}{}_{\mathrm{S}}} \mathcal{Q}\dot{\boldsymbol{\epsilon}} \cdot (\boldsymbol{\Lambda}\boldsymbol{\eta}) \, \mathrm{d}\Omega + \sum_{\mathrm{e}} \int_{\Omega^{\mathrm{e}}{}_{\mathrm{F}}} \widetilde{\mathcal{Q}}\dot{\widetilde{\boldsymbol{\epsilon}}} \cdot (\widetilde{\boldsymbol{\Lambda}}\widetilde{\boldsymbol{\eta}}) \, \mathrm{d}\Omega} \qquad (\Xi_1) \\
& \boxed{\begin{aligned}
&- \sum_{\mathrm{e}} \int_{\Sigma^{\mathrm{e}}_{\mathrm{SS}}} \{\!\{ \mathcal{A}_n \boldsymbol{\epsilon} \}\!\}_{\mathrm{SS}} \cdot (\boldsymbol{\Lambda}\boldsymbol{\eta})^- \, \mathrm{d}\Sigma - \sum_{\mathrm{e}} \int_{\Sigma^{\mathrm{e}}_{\mathrm{SF}}} \{\!\{ \mathcal{A}_n \boldsymbol{\epsilon} \}\!\}_{\mathrm{SF}} \cdot (\boldsymbol{\Lambda}\boldsymbol{\eta})^- \, \mathrm{d}\Sigma \\
&- \sum_{\mathrm{e}} \int_{\Sigma^{\mathrm{e}}_{\mathrm{FF}}} \{\!\{ \widetilde{\mathcal{A}}_n \widetilde{\boldsymbol{\epsilon}} \}\!\}_{\mathrm{FF}} \cdot (\widetilde{\boldsymbol{\Lambda}}\widetilde{\boldsymbol{\eta}})^- \, \mathrm{d}\Sigma - \sum_{\mathrm{e}} \int_{\Sigma^{\mathrm{e}}_{\mathrm{FS}}} \{\!\{ \widetilde{\mathcal{A}}_n \widetilde{\boldsymbol{\epsilon}} \}\!\}_{\mathrm{FS}} \cdot (\widetilde{\boldsymbol{\Lambda}}\widetilde{\boldsymbol{\eta}})^- \, \mathrm{d}\Sigma \\
&- \alpha \sum_{\mathrm{e}} \int_{\Sigma^{\mathrm{e}}_{\mathrm{SS}}} [\![\mathcal{A}_n \boldsymbol{\epsilon}]\!]_{\mathrm{SS}} \cdot (\mathcal{A}_n \boldsymbol{\eta})^- \, \mathrm{d}\Sigma - \alpha \sum_{\mathrm{e}} \int_{\Sigma^{\mathrm{e}}_{\mathrm{SF}}} [\![\mathcal{A}_n \boldsymbol{\epsilon}]\!]_{\mathrm{SF}} \cdot (\mathcal{A}_n \boldsymbol{\eta})^- \, \mathrm{d}\Sigma \\
&- \alpha \sum_{\mathrm{e}} \int_{\Sigma^{\mathrm{e}}_{\mathrm{FF}}} [\![\widetilde{\mathcal{A}}_n \widetilde{\boldsymbol{\epsilon}}]\!]_{\mathrm{FF}} \cdot (\widetilde{\mathcal{A}}_n \widetilde{\boldsymbol{\eta}})^- \, \mathrm{d}\Sigma - \alpha \sum_{\mathrm{e}} \int_{\Sigma^{\mathrm{e}}_{\mathrm{FS}}} [\![\widetilde{\mathcal{A}}_n \widetilde{\boldsymbol{\epsilon}}]\!]_{\mathrm{FS}} \cdot (\widetilde{\mathcal{A}}_n \widetilde{\boldsymbol{\eta}})^- \, \mathrm{d}\Sigma,
\end{aligned}} \qquad (\Xi_2)
\end{aligned}$$

in which we use the following simplified notation for averaging:

$$\begin{aligned}
\{\!\{ \mathcal{A}_n \boldsymbol{q} \}\!\}_{\mathrm{SS}} &= \tfrac{1}{2}((\mathcal{A}_n \boldsymbol{q})^+ + (\mathcal{A}_n \boldsymbol{q})^-), \quad \{\!\{ \mathcal{A}_n \boldsymbol{q} \}\!\}_{\mathrm{SF}} = \tfrac{1}{2}(O^T (\widetilde{\mathcal{A}}_n \widetilde{\boldsymbol{q}})^+ + (\mathcal{A}_n \boldsymbol{q})^-), \\
\{\!\{ \widetilde{\mathcal{A}}_n \widetilde{\boldsymbol{q}} \}\!\}_{\mathrm{FF}} &= \tfrac{1}{2}((\widetilde{\mathcal{A}}_n \widetilde{\boldsymbol{q}})^+ + (\widetilde{\mathcal{A}}_n \widetilde{\boldsymbol{q}})^-), \quad \{\!\{ \widetilde{\mathcal{A}}_n \widetilde{\boldsymbol{q}} \}\!\}_{\mathrm{FS}} = \tfrac{1}{2}(O \ (\mathcal{A}_n \boldsymbol{q})^+ + (\widetilde{\mathcal{A}}_n \widetilde{\boldsymbol{q}})^-).
\end{aligned}$$

For the volume integration terms (cf. (Ξ_1)) we obtain the estimate

$$\begin{aligned}\sum_{\mathrm{e}} \| \boldsymbol{\eta} \|_{L^2(\Omega^{\mathrm{e}}{}_{\mathrm{S}};\, \mathcal{Q},\boldsymbol{\Lambda})} \| \dot{\boldsymbol{\epsilon}} \|_{L^2(\Omega^{\mathrm{e}}{}_{\mathrm{S}};\, \mathcal{Q},\boldsymbol{\Lambda})} + \sum_{\mathrm{e}} \| \widetilde{\boldsymbol{\eta}} \|_{L^2(\Omega^{\mathrm{e}}{}_{\mathrm{F}};\, \widetilde{\mathcal{Q}},\widetilde{\boldsymbol{\Lambda}})} \| \dot{\widetilde{\boldsymbol{\epsilon}}} \|_{L^2(\Omega^{\mathrm{e}}{}_{\mathrm{F}};\, \widetilde{\mathcal{Q}},\widetilde{\boldsymbol{\Lambda}})} \\ \leq \sqrt{\sum_{\mathrm{e}} \| \boldsymbol{\eta} \|^2_{L^2(\Omega^{\mathrm{e}}{}_{\mathrm{S}};\, \mathcal{Q},\boldsymbol{\Lambda})} + \sum_{\mathrm{e}} \| \widetilde{\boldsymbol{\eta}} \|^2_{L^2(\Omega^{\mathrm{e}}{}_{\mathrm{F}};\, \widetilde{\mathcal{Q}},\widetilde{\boldsymbol{\Lambda}})}} \\ \sqrt{\sum_{\mathrm{e}} \| \dot{\boldsymbol{\epsilon}} \|^2_{L^2(\Omega^{\mathrm{e}}{}_{\mathrm{S}};\, \mathcal{Q},\boldsymbol{\Lambda})} + \sum_{\mathrm{e}} \| \dot{\widetilde{\boldsymbol{\epsilon}}} \|^2_{L^2(\Omega^{\mathrm{e}}{}_{\mathrm{F}};\, \widetilde{\mathcal{Q}},\widetilde{\boldsymbol{\Lambda}})}} \;. \end{aligned} \tag{2.53}$$

For the surface integration terms (cf. (Ξ_2)), we use the symmetry in $\mathcal{A}$ and $\boldsymbol{\Lambda}$ to find that

$$(\mathcal{A}_n \boldsymbol{q})^{\pm} \cdot (\boldsymbol{\Lambda} \boldsymbol{p})^{-} = \boldsymbol{n} \cdot (\boldsymbol{C} \boldsymbol{E}\,)^{\pm} \cdot \boldsymbol{w}^{-} + \boldsymbol{n} \cdot (\boldsymbol{C} \boldsymbol{H}\,)^{-} \cdot \boldsymbol{v}^{\pm} = (\mathcal{A}_n \boldsymbol{p})^{-} \cdot (\boldsymbol{\Lambda} \boldsymbol{q})^{\pm}. \tag{2.54}$$

Thus

$$\begin{aligned} &\sum_{\mathrm{e}} \int_{\Sigma^{\mathrm{e}}_{\mathrm{SS}}} \{\{ \mathcal{A}_n \boldsymbol{\epsilon} \,\}\}_{\mathrm{SS}} \cdot (\boldsymbol{\Lambda} \boldsymbol{\eta})^{-} \, \mathrm{d}\Sigma \\ &\quad = \tfrac{1}{2} \sum_{\mathrm{e}} \int_{\Sigma^{\mathrm{e}}_{\mathrm{SS}}} (\mathcal{A}_n \boldsymbol{\epsilon})^{+} \cdot (\boldsymbol{\Lambda} \boldsymbol{\eta})^{-} \, \mathrm{d}\Sigma + \tfrac{1}{2} \sum_{\mathrm{e}} \int_{\Sigma^{\mathrm{e}}_{\mathrm{SS}}} (\mathcal{A}_n \boldsymbol{\epsilon})^{-} \cdot (\boldsymbol{\Lambda} \boldsymbol{\eta})^{-} \, \mathrm{d}\Sigma \\ &\quad = \tfrac{1}{2} \sum_{\mathrm{e}} \int_{\Sigma^{\mathrm{e}}_{\mathrm{SS}}} (\mathcal{A}_n \boldsymbol{\eta})^{-} \cdot (\boldsymbol{\Lambda} \boldsymbol{\epsilon})^{+} \, \mathrm{d}\Sigma + \tfrac{1}{2} \sum_{\mathrm{e}} \int_{\Sigma^{\mathrm{e}}_{\mathrm{SS}}} (\mathcal{A}_n \boldsymbol{\eta})^{-} \cdot (\boldsymbol{\Lambda} \boldsymbol{\epsilon})^{-} \, \mathrm{d}\Sigma \\ &\quad = \tfrac{1}{2} \sum_{\mathrm{e}} \int_{\Sigma^{\mathrm{e}}_{\mathrm{SS}}} -(\mathcal{A}_n \boldsymbol{\eta})^{+} \cdot (\boldsymbol{\Lambda} \boldsymbol{\epsilon})^{-} \, \mathrm{d}\Sigma + \tfrac{1}{2} \sum_{\mathrm{e}} \int_{\Sigma^{\mathrm{e}}_{\mathrm{SS}}} (\mathcal{A}_n \boldsymbol{\eta})^{-} \cdot (\boldsymbol{\Lambda} \boldsymbol{\epsilon})^{-} \, \mathrm{d}\Sigma \\ &\quad = \tfrac{1}{2} \sum_{\mathrm{e}} \int_{\Sigma^{\mathrm{e}}_{\mathrm{SS}}} - [[\mathcal{A}_n \boldsymbol{\eta} \,]]_{\mathrm{SS}} \cdot (\boldsymbol{\Lambda} \boldsymbol{\epsilon})^{-} \, \mathrm{d}\Sigma \quad = -\tfrac{1}{2} \sum_{\mathrm{e}} \int_{\Sigma^{\mathrm{e}}_{\mathrm{SS}}} [[\mathcal{A}_n \boldsymbol{\eta} \,]]_{\mathrm{SS}} \cdot \{\{ \boldsymbol{\Lambda} \boldsymbol{\epsilon} \,\}\}_{\mathrm{SS}} \, \mathrm{d}\Sigma, \end{aligned} \tag{2.55}$$

in which the second equality uses (2.54), and the third equality is obtained by exchanging the summation order of elements between solid-solid interfaces. Similarly, we have

$$(\widetilde{\mathcal{A}}_n \widetilde{\boldsymbol{q}})^{\pm} \cdot (\widetilde{\boldsymbol{\Lambda}} \widetilde{\boldsymbol{p}})^{-} = (\widetilde{\lambda} \widetilde{E}\,)^{\pm} \boldsymbol{n} \cdot \widetilde{\boldsymbol{w}}^{-} + (\widetilde{\lambda} \widetilde{H}\,)^{-} \boldsymbol{n} \cdot \widetilde{\boldsymbol{v}}^{\pm} = (\widetilde{\mathcal{A}}_n \widetilde{\boldsymbol{p}})^{-} \cdot (\widetilde{\boldsymbol{\Lambda}} \widetilde{\boldsymbol{q}})^{\pm}, \tag{2.56}$$

and

$$\sum_{\mathrm{e}} \int_{\Sigma^{\mathrm{e}}_{\mathrm{FF}}} \{\{ \widetilde{\mathcal{A}}_n \widetilde{\boldsymbol{\epsilon}} \,\}\}_{\mathrm{FF}} \cdot (\widetilde{\boldsymbol{\Lambda}} \widetilde{\boldsymbol{\eta}})^{-} \, \mathrm{d}\Sigma = -\tfrac{1}{2} \sum_{\mathrm{e}} \int_{\Sigma^{\mathrm{e}}_{\mathrm{FF}}} [[\widetilde{\mathcal{A}}_n \widetilde{\boldsymbol{\eta}} \,]]_{\mathrm{FF}} \cdot \{\{ \widetilde{\boldsymbol{\Lambda}} \widetilde{\boldsymbol{\epsilon}} \,\}\}_{\mathrm{FF}} \, \mathrm{d}\Sigma. \tag{2.57}$$

For fluid-solid interfaces we also have the symmetry

$$O^T(\widetilde{\mathcal{A}}_n\widetilde{\boldsymbol{q}})^+\cdot(\boldsymbol{\Lambda p})^- = (\widetilde{\lambda}\widetilde{E})^+\boldsymbol{n}\cdot\boldsymbol{w}^- + (\boldsymbol{n}\cdot(\boldsymbol{CH}\,)^-\cdot\boldsymbol{n})(\boldsymbol{n}\cdot\widetilde{\boldsymbol{v}}^+) = (\mathcal{A}_n\boldsymbol{p})^-\cdot O^T(\widetilde{\boldsymbol{\Lambda}}\widetilde{\boldsymbol{q}})^+,$$

$$O\ \ (\mathcal{A}_n\boldsymbol{q})^+\cdot(\widetilde{\boldsymbol{\Lambda}}\widetilde{\boldsymbol{p}})^- = (\boldsymbol{n}\cdot(\boldsymbol{CE}\,)^+\cdot\boldsymbol{n})(\widetilde{\boldsymbol{w}}^-\cdot\boldsymbol{n}) + (\widetilde{\lambda}\widetilde{H})^-\boldsymbol{n}\cdot\boldsymbol{v}^+ = O^T(\widetilde{\mathcal{A}}_n\widetilde{\boldsymbol{p}})^-\cdot(\boldsymbol{\Lambda q})^+, \tag{2.58}$$

and using (2.54), (2.56) and (2.58),

$$\begin{aligned}
&\sum_{\mathrm{e}}\int_{\Sigma^{\mathrm{e}}_{\mathrm{SF}}}\{\!\{\mathcal{A}_n\boldsymbol{\epsilon}\,\}\!\}_{\mathrm{SF}}\cdot(\boldsymbol{\Lambda\eta})^-\,\mathrm{d}\Sigma + \sum_{\mathrm{e}}\int_{\Sigma^{\mathrm{e}}_{\mathrm{FS}}}\{\!\{\widetilde{\mathcal{A}}_n\widetilde{\boldsymbol{\epsilon}}\,\}\!\}_{\mathrm{FS}}\cdot(\widetilde{\boldsymbol{\Lambda}}\widetilde{\boldsymbol{\eta}})^-\,\mathrm{d}\Sigma\\
&\qquad = \sum_{\mathrm{e}}\int_{\Sigma^{\mathrm{e}}_{\mathrm{SF}}}\tfrac{1}{2}(O^T(\widetilde{\mathcal{A}}_n\widetilde{\boldsymbol{\epsilon}})^+\cdot(\boldsymbol{\Lambda\eta})^- + (\mathcal{A}_n\boldsymbol{\epsilon})^-\cdot(\boldsymbol{\Lambda\eta})^-)\,\mathrm{d}\Sigma\\
&\qquad\qquad\qquad + \sum_{\mathrm{e}}\int_{\Sigma^{\mathrm{e}}_{\mathrm{FS}}}\tfrac{1}{2}(O\ \ (\mathcal{A}_n\boldsymbol{\epsilon})^+\cdot(\widetilde{\boldsymbol{\Lambda}}\widetilde{\boldsymbol{\eta}})^- + (\widetilde{\mathcal{A}}_n\widetilde{\boldsymbol{\epsilon}})^-\cdot(\widetilde{\boldsymbol{\Lambda}}\widetilde{\boldsymbol{\eta}})^-)\,\mathrm{d}\Sigma\\
&\qquad = \sum_{\mathrm{e}}\int_{\Sigma^{\mathrm{e}}_{\mathrm{SF}}}\tfrac{1}{2}((\mathcal{A}_n\boldsymbol{\eta})^-\cdot O^T(\widetilde{\boldsymbol{\Lambda}}\widetilde{\boldsymbol{\epsilon}})^+ + (\mathcal{A}_n\boldsymbol{\eta})^-\cdot(\boldsymbol{\Lambda\epsilon})^-)\,\mathrm{d}\Sigma\\
&\qquad\qquad\qquad + \sum_{\mathrm{e}}\int_{\Sigma^{\mathrm{e}}_{\mathrm{FS}}}\tfrac{1}{2}(O^T(\widetilde{\mathcal{A}}_n\widetilde{\boldsymbol{\eta}})^-\cdot(\boldsymbol{\Lambda\epsilon})^+ + (\widetilde{\mathcal{A}}_n\widetilde{\boldsymbol{\eta}})^-\cdot(\widetilde{\boldsymbol{\Lambda}}\widetilde{\boldsymbol{\epsilon}})^-)\,\mathrm{d}\Sigma\\
&\qquad = \sum_{\mathrm{e}}\int_{\Sigma^{\mathrm{e}}_{\mathrm{SF}}}\tfrac{1}{2}((\mathcal{A}_n\boldsymbol{\eta})^-\cdot O^T(\widetilde{\boldsymbol{\Lambda}}\widetilde{\boldsymbol{\epsilon}})^+ + (\mathcal{A}_n\boldsymbol{\eta})^-\cdot(\boldsymbol{\Lambda\epsilon})^-\\
&\qquad\qquad\qquad - O^T(\widetilde{\mathcal{A}}_n\widetilde{\boldsymbol{\eta}})^+\cdot(\boldsymbol{\Lambda\epsilon})^- - O^T(\widetilde{\mathcal{A}}_n\widetilde{\boldsymbol{\eta}})^+\cdot O^T(\widetilde{\boldsymbol{\Lambda}}\widetilde{\boldsymbol{\epsilon}})^+)\,\mathrm{d}\Sigma\\
&\qquad = -\sum_{\mathrm{e}}\int_{\Sigma^{\mathrm{e}}_{\mathrm{SF}}}\llbracket\mathcal{A}_n\boldsymbol{\eta}\,\rrbracket_{\mathrm{SF}}\cdot\{\!\{\boldsymbol{\Lambda\epsilon}\,\}\!\}_{\mathrm{SF}}\,\mathrm{d}\Sigma\,.
\end{aligned}\tag{2.59}$$

For the penalty terms in (Ξ_2), it is straightforward to check that

$$\sum_{\mathrm{e}}\int_{\Sigma^{\mathrm{e}}_{\mathrm{SS}}}\llbracket\mathcal{A}_n\boldsymbol{\epsilon}\,\rrbracket_{\mathrm{SS}}\cdot(\mathcal{A}_n\boldsymbol{\eta})^-\,\mathrm{d}\Sigma = -\tfrac{1}{2}\sum_{\mathrm{e}}\int_{\Sigma^{\mathrm{e}}_{\mathrm{SS}}}\llbracket\mathcal{A}_n\boldsymbol{\epsilon}\,\rrbracket_{\mathrm{SS}}\cdot\llbracket\mathcal{A}_n\boldsymbol{\eta}\,\rrbracket_{\mathrm{SS}}\,\mathrm{d}\Sigma, \tag{2.60}$$

$$\sum_{\mathrm{e}}\int_{\Sigma^{\mathrm{e}}_{\mathrm{FF}}}\llbracket\widetilde{\mathcal{A}}_n\widetilde{\boldsymbol{\epsilon}}\,\rrbracket_{\mathrm{FF}}\cdot(\widetilde{\mathcal{A}}_n\widetilde{\boldsymbol{\eta}})^-\,\mathrm{d}\Sigma = -\tfrac{1}{2}\sum_{\mathrm{e}}\int_{\Sigma^{\mathrm{e}}_{\mathrm{FF}}}\llbracket\widetilde{\mathcal{A}}_n\widetilde{\boldsymbol{\epsilon}}\,\rrbracket_{\mathrm{FF}}\cdot\llbracket\widetilde{\mathcal{A}}_n\widetilde{\boldsymbol{\eta}}\,\rrbracket_{\mathrm{FF}}\,\mathrm{d}\Sigma, \tag{2.61}$$

and

$$
\begin{aligned}
&\sum_{\mathrm{e}} \int_{\Sigma^{\mathrm{e}}_{\mathrm{SF}}} [\![\mathcal{A}_n \boldsymbol{\epsilon}]\!]_{\mathrm{SF}} \cdot (\mathcal{A}_n \boldsymbol{\eta})^- \,\mathrm{d}\Sigma + \sum_{\mathrm{e}} \int_{\Sigma^{\mathrm{e}}_{\mathrm{FS}}} [\![\widetilde{\mathcal{A}}_n \widetilde{\boldsymbol{\epsilon}}]\!]_{\mathrm{FS}} \cdot (\widetilde{\mathcal{A}}_n \widetilde{\boldsymbol{\eta}})^- \,\mathrm{d}\Sigma \\
&\quad = \sum_{\mathrm{e}} \int_{\Sigma^{\mathrm{e}}_{\mathrm{SF}}} (O^T (\widetilde{\mathcal{A}}_n \widetilde{\boldsymbol{\epsilon}})^+ \cdot (\mathcal{A}_n \boldsymbol{\eta})^- - (\mathcal{A}_n \boldsymbol{\epsilon})^- \cdot (\mathcal{A}_n \boldsymbol{\eta})^-) \,\mathrm{d}\Sigma \\
&\qquad\qquad + \sum_{\mathrm{e}} \int_{\Sigma^{\mathrm{e}}_{\mathrm{FS}}} (O \;(\mathcal{A}_n \boldsymbol{\epsilon})^+ \cdot (\widetilde{\mathcal{A}}_n \widetilde{\boldsymbol{\eta}})^- - (\widetilde{\mathcal{A}}_n \widetilde{\boldsymbol{\epsilon}})^- \cdot (\widetilde{\mathcal{A}}_n \widetilde{\boldsymbol{\eta}})^-) \,\mathrm{d}\Sigma \\
&\quad = \sum_{\mathrm{e}} \int_{\Sigma^{\mathrm{e}}_{\mathrm{SF}}} (O^T (\widetilde{\mathcal{A}}_n \widetilde{\boldsymbol{\epsilon}})^+ \cdot (\mathcal{A}_n \boldsymbol{\eta})^- - (\mathcal{A}_n \boldsymbol{\epsilon})^- \cdot (\mathcal{A}_n \boldsymbol{\eta})^- \\
&\qquad\qquad + (\mathcal{A}_n \boldsymbol{\epsilon})^- \cdot O^T (\widetilde{\mathcal{A}}_n \widetilde{\boldsymbol{\eta}})^+ - O^T (\widetilde{\mathcal{A}}_n \widetilde{\boldsymbol{\epsilon}})^+ \cdot O^T (\widetilde{\mathcal{A}}_n \widetilde{\boldsymbol{\eta}})^+) \,\mathrm{d}\Sigma \\
&\quad = -\sum_{\mathrm{e}} \int_{\Sigma^{\mathrm{e}}_{\mathrm{SF}}} [\![\mathcal{A}_n \boldsymbol{\epsilon}]\!]_{\mathrm{SF}} \cdot [\![\mathcal{A}_n \boldsymbol{\eta}]\!]_{\mathrm{SF}} \,\mathrm{d}\Sigma.
\end{aligned}
\tag{2.62}
$$

Using (2.55), (2.57), (2.59), (2.60), (2.61) and (2.62) in (Ξ_2) yields the estimate for (Ξ_2)

$$
\begin{aligned}
&\tfrac{1}{2}\sum_{\mathrm{e}} \int_{\Sigma^{\mathrm{e}}_{\mathrm{SS}}} [\![\mathcal{A}_n \boldsymbol{\eta}]\!]_{\mathrm{SS}} \cdot \Big(\{\!\{\boldsymbol{\Lambda\epsilon}\}\!\}_{\mathrm{SS}} + \alpha [\![\mathcal{A}_n \boldsymbol{\epsilon}]\!]_{\mathrm{SS}} \Big) \,\mathrm{d}\Sigma \\
&\quad + \tfrac{1}{2}\sum_{\mathrm{e}} \int_{\Sigma^{\mathrm{e}}_{\mathrm{FF}}} [\![\widetilde{\mathcal{A}}_n \widetilde{\boldsymbol{\eta}}]\!]_{\mathrm{FF}} \cdot \Big(\{\!\{\widetilde{\boldsymbol{\Lambda}}\widetilde{\boldsymbol{\epsilon}}\}\!\}_{\mathrm{FF}} + \alpha [\![\widetilde{\mathcal{A}}_n \widetilde{\boldsymbol{\epsilon}}]\!]_{\mathrm{FF}} \Big) \,\mathrm{d}\Sigma \\
&\quad + \sum_{\mathrm{e}} \int_{\Sigma^{\mathrm{e}}_{\mathrm{SF}}} [\![\mathcal{A}_n \boldsymbol{\eta}]\!]_{\mathrm{SF}} \cdot \Big(\{\!\{\boldsymbol{\Lambda\epsilon}\}\!\}_{\mathrm{SF}} + \alpha [\![\mathcal{A}_n \boldsymbol{\epsilon}]\!]_{\mathrm{SF}} \Big) \,\mathrm{d}\Sigma \\
\leq\;& \tfrac{1}{2}\sum_{\mathrm{e}} \Big(\big\| [\![\mathcal{A}_n \boldsymbol{\eta}]\!]_{\mathrm{SS}} \big\|_{L^2(\Sigma^{\mathrm{e}}_{\mathrm{SS}})} \big\| \{\!\{\boldsymbol{\Lambda\epsilon}\}\!\}_{\mathrm{SS}} \big\|_{L^2(\Sigma^{\mathrm{e}}_{\mathrm{SS}})} \\
&\qquad + \alpha \big\| [\![\mathcal{A}_n \boldsymbol{\eta}]\!]_{\mathrm{SS}} \big\|_{L^2(\Sigma^{\mathrm{e}}_{\mathrm{SS}})} \big\| [\![\mathcal{A}_n \boldsymbol{\epsilon}]\!]_{\mathrm{SS}} \big\|_{L^2(\Sigma^{\mathrm{e}}_{\mathrm{SS}})} \Big) \\
&\quad + \tfrac{1}{2}\sum_{\mathrm{e}} \Big(\Big\| [\![\widetilde{\mathcal{A}}_n \widetilde{\boldsymbol{\eta}}]\!]_{\mathrm{FF}} \Big\|_{L^2(\Sigma^{\mathrm{e}}_{\mathrm{FF}})} \Big\| \{\!\{\widetilde{\boldsymbol{\Lambda}}\widetilde{\boldsymbol{\epsilon}}\}\!\}_{\mathrm{FF}} \Big\|_{L^2(\Sigma^{\mathrm{e}}_{\mathrm{FF}})} \\
&\qquad + \alpha \Big\| [\![\widetilde{\mathcal{A}}_n \widetilde{\boldsymbol{\eta}}]\!]_{\mathrm{FF}} \Big\|_{L^2(\Sigma^{\mathrm{e}}_{\mathrm{FF}})} \Big\| [\![\widetilde{\mathcal{A}}_n \widetilde{\boldsymbol{\epsilon}}]\!]_{\mathrm{FF}} \Big\|_{L^2(\Sigma^{\mathrm{e}}_{\mathrm{FF}})} \Big) \\
&\quad + \sum_{\mathrm{e}} \Big(\big\| [\![\mathcal{A}_n \boldsymbol{\eta}]\!]_{\mathrm{SF}} \big\|_{L^2(\Sigma^{\mathrm{e}}_{\mathrm{SF}})} \big\| \{\!\{\boldsymbol{\Lambda\epsilon}\}\!\}_{\mathrm{SF}} \big\|_{L^2(\Sigma^{\mathrm{e}}_{\mathrm{SF}})} \\
&\qquad + \alpha \big\| [\![\mathcal{A}_n \boldsymbol{\eta}]\!]_{\mathrm{SF}} \big\|_{L^2(\Sigma^{\mathrm{e}}_{\mathrm{SF}})} \big\| [\![\mathcal{A}_n \boldsymbol{\epsilon}]\!]_{\mathrm{SF}} \big\|_{L^2(\Sigma^{\mathrm{e}}_{\mathrm{SF}})} \Big) \\
\leq\;& \frac{1}{2\beta} \Big(\sum_{\mathrm{e}} \big\| [\![\mathcal{A}_n \boldsymbol{\eta}]\!]_{\mathrm{SS}} \big\|^2_{L^2(\Sigma^{\mathrm{e}}_{\mathrm{SS}})} + \sum_{\mathrm{e}} \Big\| [\![\widetilde{\mathcal{A}}_n \widetilde{\boldsymbol{\eta}}]\!]_{\mathrm{FF}} \Big\|^2_{L^2(\Sigma^{\mathrm{e}}_{\mathrm{FF}})} + 2\sum_{\mathrm{e}} \big\| [\![\mathcal{A}_n \boldsymbol{\eta}]\!]_{\mathrm{SF}} \big\|^2_{L^2(\Sigma^{\mathrm{e}}_{\mathrm{SF}})} \Big) \\
&\quad + \frac{\beta}{4} \Big(\sum_{\mathrm{e}} \Big(\big\| \{\!\{\boldsymbol{\Lambda\epsilon}\}\!\}_{\mathrm{SS}} \big\|^2_{L^2(\Sigma^{\mathrm{e}}_{\mathrm{SS}})} + \alpha^2 \big\| [\![\mathcal{A}_n \boldsymbol{\epsilon}]\!]_{\mathrm{SS}} \big\|^2_{L^2(\Sigma^{\mathrm{e}}_{\mathrm{SS}})} \Big)
\end{aligned}
$$

$$+ \sum_{\mathrm{e}} \left(\left\| \{\!\{ \widetilde{\boldsymbol{\Lambda}} \widetilde{\boldsymbol{\epsilon}} \}\!\}_{\mathrm{FF}} \right\|^2_{L^2(\Sigma^{\mathrm{e}}_{\mathrm{FF}})} + \alpha^2 \left\| [\![\widetilde{\mathcal{A}}_n \widetilde{\boldsymbol{\epsilon}}]\!]_{\mathrm{FF}} \right\|^2_{L^2(\Sigma^{\mathrm{e}}_{\mathrm{FF}})} \right)$$
$$+ 2 \sum_{\mathrm{e}} \left(\left\| \{\!\{ \boldsymbol{\Lambda} \boldsymbol{\epsilon} \}\!\}_{\mathrm{SF}} \right\|^2_{L^2(\Sigma^{\mathrm{e}}_{\mathrm{SF}})} + \alpha^2 \left\| [\![\mathcal{A}_n \boldsymbol{\epsilon}]\!]_{\mathrm{SF}} \right\|^2_{L^2(\Sigma^{\mathrm{e}}_{\mathrm{SF}})} \right) \Bigg).$$

The first inequality is obtained by Cauchy–Schwarz, and the second one is based on Young's inequality with factor β (or so-called "Peter–Paul inequality"). Since

$$\begin{aligned}
\sum_{\mathrm{e}} \left\| \{\!\{ \boldsymbol{\Lambda} \boldsymbol{\epsilon} \}\!\}_{\mathrm{SS}} \right\|^2_{L^2(\Sigma^{\mathrm{e}}_{\mathrm{SS}})} &= \sum_{\mathrm{e}} \left(\tfrac{1}{2} \left\| (\boldsymbol{\Lambda}\boldsymbol{\epsilon})^+ + (\boldsymbol{\Lambda}\boldsymbol{\epsilon})^- \right\|_{L^2(\Sigma^{\mathrm{e}}_{\mathrm{SS}})} \right)^2 \\
&\le \sum_{\mathrm{e}} \tfrac{1}{4} \left(\left\| (\boldsymbol{\Lambda}\boldsymbol{\epsilon})^+ \right\|^2_{L^2(\Sigma^{\mathrm{e}}_{\mathrm{SS}})} + \left\| (\boldsymbol{\Lambda}\boldsymbol{\epsilon})^- \right\|^2_{L^2(\Sigma^{\mathrm{e}}_{\mathrm{SS}})} + 2 \left\| (\boldsymbol{\Lambda}\boldsymbol{\epsilon})^+ \right\|_{L^2(\Sigma^{\mathrm{e}}_{\mathrm{SS}})} \left\| (\boldsymbol{\Lambda}\boldsymbol{\epsilon})^- \right\|_{L^2(\Sigma^{\mathrm{e}}_{\mathrm{SS}})} \right) \\
&\le \sum_{\mathrm{e}} \tfrac{1}{2} \left(\left\| (\boldsymbol{\Lambda}\boldsymbol{\epsilon})^+ \right\|^2_{L^2(\Sigma^{\mathrm{e}}_{\mathrm{SS}})} + \left\| (\boldsymbol{\Lambda}\boldsymbol{\epsilon})^- \right\|^2_{L^2(\Sigma^{\mathrm{e}}_{\mathrm{SS}})} \right) = \sum_{\mathrm{e}} \left\| (\boldsymbol{\Lambda}\boldsymbol{\epsilon})^- \right\|^2_{L^2(\Sigma^{\mathrm{e}}_{\mathrm{SS}})}, \\
\sum_{\mathrm{e}} \left\| [\![\mathcal{A}_n \boldsymbol{\epsilon}]\!]_{\mathrm{SS}} \right\|^2_{L^2(\Sigma^{\mathrm{e}}_{\mathrm{SS}})} &= 4 \sum_{\mathrm{e}} \left(\tfrac{1}{2} \left\| (\mathcal{A}_n\boldsymbol{\epsilon})^+ + (\mathcal{A}_n\boldsymbol{\epsilon})^- \right\|_{L^2(\Sigma^{\mathrm{e}}_{\mathrm{SS}})} \right)^2 \\
&\le 4 \sum_{\mathrm{e}} \tfrac{1}{4} \left(\left\| (\mathcal{A}_n\boldsymbol{\epsilon})^+ \right\|^2_{L^2(\Sigma^{\mathrm{e}}_{\mathrm{SS}})} + \left\| (\mathcal{A}_n\boldsymbol{\epsilon})^- \right\|^2_{L^2(\Sigma^{\mathrm{e}}_{\mathrm{SS}})} + 2 \left\| (\mathcal{A}_n\boldsymbol{\epsilon})^+ \right\|_{L^2(\Sigma^{\mathrm{e}}_{\mathrm{SS}})} \left\| (\mathcal{A}_n\boldsymbol{\epsilon})^- \right\|_{L^2(\Sigma^{\mathrm{e}}_{\mathrm{SS}})} \right) \\
&\le 4 \sum_{\mathrm{e}} \tfrac{1}{2} \left(\left\| (\mathcal{A}_n\boldsymbol{\epsilon})^+ \right\|^2_{L^2(\Sigma^{\mathrm{e}}_{\mathrm{SS}})} + \left\| (\mathcal{A}_n\boldsymbol{\epsilon})^- \right\|^2_{L^2(\Sigma^{\mathrm{e}}_{\mathrm{SS}})} \right) = 4 \sum_{\mathrm{e}} \left\| (\mathcal{A}_n\boldsymbol{\epsilon})^- \right\|^2_{L^2(\Sigma^{\mathrm{e}}_{\mathrm{SS}})},
\end{aligned}$$

due to Cauchy–Schwarz followed by Young's inequality, and

$$\begin{aligned}
\sum_{\mathrm{e}} \left\| \{\!\{ \widetilde{\boldsymbol{\Lambda}} \widetilde{\boldsymbol{\epsilon}} \}\!\}_{\mathrm{FF}} \right\|^2_{L^2(\Sigma^{\mathrm{e}}_{\mathrm{FF}})} &\le \sum_{\mathrm{e}} \left\| (\widetilde{\boldsymbol{\Lambda}} \widetilde{\boldsymbol{\epsilon}})^- \right\|^2_{L^2(\Sigma^{\mathrm{e}}_{\mathrm{FF}})}, \\
\sum_{\mathrm{e}} \left\| [\![\widetilde{\mathcal{A}}_n \widetilde{\boldsymbol{\epsilon}}]\!]_{\mathrm{FF}} \right\|^2_{L^2(\Sigma^{\mathrm{e}}_{\mathrm{FF}})} &\le 4 \sum_{\mathrm{e}} \left\| (\widetilde{\mathcal{A}}_n \widetilde{\boldsymbol{\epsilon}})^- \right\|^2_{L^2(\Sigma^{\mathrm{e}}_{\mathrm{FF}})}, \\
\sum_{\mathrm{e}} \left\| \{\!\{ \boldsymbol{\Lambda} \boldsymbol{\epsilon} \}\!\}_{\mathrm{SF}} \right\|^2_{L^2(\Sigma^{\mathrm{e}}_{\mathrm{SF}})} &\le \tfrac{1}{2} \sum_{\mathrm{e}} \left\| (\boldsymbol{\Lambda}\boldsymbol{\epsilon})^- \right\|^2_{L^2(\Sigma^{\mathrm{e}}_{\mathrm{SF}})} + \tfrac{1}{2} \sum_{\mathrm{e}} \left\| (\widetilde{\boldsymbol{\Lambda}} \widetilde{\boldsymbol{\epsilon}})^- \right\|^2_{L^2(\Sigma^{\mathrm{e}}_{\mathrm{FS}})}, \\
\sum_{\mathrm{e}} \left\| [\![\mathcal{A}_n \boldsymbol{\epsilon}]\!]_{\mathrm{SF}} \right\|^2_{L^2(\Sigma^{\mathrm{e}}_{\mathrm{SF}})} &\le 2 \sum_{\mathrm{e}} \left\| (\mathcal{A}_n\boldsymbol{\epsilon})^- \right\|^2_{L^2(\Sigma^{\mathrm{e}}_{\mathrm{SF}})} + 2 \sum_{\mathrm{e}} \left\| (\widetilde{\mathcal{A}}_n \widetilde{\boldsymbol{\epsilon}})^- \right\|^2_{L^2(\Sigma^{\mathrm{e}}_{\mathrm{FS}})},
\end{aligned}$$

we get the estimate for (Ξ_2),

$$\Xi_2 \leq \frac{1}{2\beta}\left(\sum_{\mathrm{e}}\| [[\mathcal{A}_n\boldsymbol{\eta}]]_{\mathrm{SS}}\|^2_{L^2(\Sigma^{\mathrm{e}}_{\mathrm{SS}})} + \sum_{\mathrm{e}}\left\| [[\widetilde{\mathcal{A}}_n\widetilde{\boldsymbol{\eta}}]]_{\mathrm{FF}}\right\|^2_{L^2(\Sigma^{\mathrm{e}}_{\mathrm{FF}})} + 2\sum_{\mathrm{e}}\| [[\mathcal{A}_n\boldsymbol{\eta}]]_{\mathrm{SF}}\|^2_{L^2(\Sigma^{\mathrm{e}}_{\mathrm{SF}})}\right)$$
$$+\frac{\beta}{4}\Bigg(\sum_{\mathrm{e}}\left(\|(\boldsymbol{\Lambda\epsilon})^-\|^2_{L^2(\Sigma^{\mathrm{e}}_{\mathrm{SS}}\cup\Sigma^{\mathrm{e}}_{\mathrm{SF}})} + 4\alpha^2\|(\mathcal{A}_n\boldsymbol{\epsilon})^-\|^2_{L^2(\Sigma^{\mathrm{e}}_{\mathrm{SS}}\cup\Sigma^{\mathrm{e}}_{\mathrm{SF}})}\right)$$
$$+\sum_{\mathrm{e}}\left(\|(\widetilde{\boldsymbol{\Lambda}}\widetilde{\boldsymbol{\epsilon}})^-\|^2_{L^2(\Sigma^{\mathrm{e}}_{\mathrm{FF}}\cup\Sigma^{\mathrm{e}}_{\mathrm{FS}})} + 4\alpha^2\|(\widetilde{\mathcal{A}}_n\widetilde{\boldsymbol{\epsilon}})^-\|^2_{L^2(\Sigma^{\mathrm{e}}_{\mathrm{FF}}\cup\Sigma^{\mathrm{e}}_{\mathrm{FS}})}\right)\Bigg). \tag{2.63}$$

Using (2.53) and (2.63) in (2.50) yields

$$\frac{1}{2}\frac{\mathrm{d}}{\mathrm{d}t}\left(\sum_{\mathrm{e}}\|\boldsymbol{\eta}\|^2_{L^2(\Omega^{\mathrm{e}}{}_{\mathrm{S}};\,\mathcal{Q},\boldsymbol{\Lambda})} + \sum_{\mathrm{e}}\|\widetilde{\boldsymbol{\eta}}\|^2_{L^2(\Omega^{\mathrm{e}}{}_{\mathrm{F}};\,\widetilde{\mathcal{Q}},\widetilde{\boldsymbol{\Lambda}})}\right) + \left(\frac{\alpha}{2} - \frac{1}{2\beta}\right)\Bigg(\sum_{\mathrm{e}}\| [[\mathcal{A}_n\boldsymbol{\eta}]]_{\mathrm{SS}}\|^2_{L^2(\Sigma_{\mathrm{SS}})}$$
$$+\sum_{\mathrm{e}}\| [[\widetilde{\mathcal{A}}_n\widetilde{\boldsymbol{\eta}}]]_{\mathrm{FF}}\|^2_{L^2(\Sigma_{\mathrm{FF}})} + 2\sum_{\mathrm{e}}\| [[\mathcal{A}_n\boldsymbol{\eta}]]_{\mathrm{SF}}\|^2_{L^2(\Sigma_{\mathrm{SF}})}\Bigg)$$
$$\leq \sqrt{\sum_{\mathrm{e}}\|\boldsymbol{\eta}\|^2_{L^2(\Omega^{\mathrm{e}}{}_{\mathrm{S}};\,\mathcal{Q},\boldsymbol{\Lambda})} + \sum_{\mathrm{e}}\|\widetilde{\boldsymbol{\eta}}\|^2_{L^2(\Omega^{\mathrm{e}}{}_{\mathrm{F}};\,\widetilde{\mathcal{Q}},\widetilde{\boldsymbol{\Lambda}})}}\sqrt{\sum_{\mathrm{e}}\|\dot{\boldsymbol{\epsilon}}\|^2_{L^2(\Omega^{\mathrm{e}}{}_{\mathrm{S}};\,\mathcal{Q},\boldsymbol{\Lambda})} + \sum_{\mathrm{e}}\|\dot{\widetilde{\boldsymbol{\epsilon}}}\|^2_{L^2(\Omega^{\mathrm{e}}{}_{\mathrm{F}};\,\widetilde{\mathcal{Q}},\widetilde{\boldsymbol{\Lambda}})}}$$
$$+\frac{\beta}{4}\Bigg(\sum_{\mathrm{e}}\left(\|(\boldsymbol{\Lambda\epsilon})^-\|^2_{L^2(\Sigma^{\mathrm{e}}_{\mathrm{SS}}\cup\Sigma^{\mathrm{e}}_{\mathrm{SF}})} + 4\alpha^2\|(\mathcal{A}_n\boldsymbol{\epsilon})^-\|^2_{L^2(\Sigma^{\mathrm{e}}_{\mathrm{SS}}\cup\Sigma^{\mathrm{e}}_{\mathrm{SF}})}\right)$$
$$+\sum_{\mathrm{e}}\left(\|(\widetilde{\boldsymbol{\Lambda}}\widetilde{\boldsymbol{\epsilon}})^-\|^2_{L^2(\Sigma^{\mathrm{e}}_{\mathrm{FF}}\cup\Sigma^{\mathrm{e}}_{\mathrm{FS}})} + 4\alpha^2\|(\widetilde{\mathcal{A}}_n\widetilde{\boldsymbol{\epsilon}})^-\|^2_{L^2(\Sigma^{\mathrm{e}}_{\mathrm{FF}}\cup\Sigma^{\mathrm{e}}_{\mathrm{FS}})}\right)\Bigg). \tag{2.64}$$

Following [169, Section 5.1], we can finally obtain the required error estimate from (2.64). We take $\alpha = 1/2$; by choosing β sufficiently large in Young's inequality, we control the error by applying a modified Gronwall's lemma [169, p.A2007].

2.7 Computational experiments

Here, we illustrate our DG method by verifying its convergence rate and carrying out computational experiments. We use the fourth-order LSERK algorithm for time integration. For visualization of wavefields or model parameters, we write the value in the Visualization Toolkit (VTK) unstructured mesh format and visualize the result using *Paraview* [74,].

2.7.1 Convergence tests at (interior) boundaries

We carry out computational tests using wave propagation and scattering problems in 3-dimensional cubic subdomains. We first test the propagation of a plane wave in a homogeneous isotropic elastic medium, in which periodic boundary conditions are applied. We also test the free-surface boundary condition with a homogeneous isotropic elastic solid, in which both Rayleigh and Love waves are generated. We focus on the Rayleigh wave, the particle motion of which is in the plane perpendicular to the free surface. A Stoneley wave, generated at a solid-elastic interface [4,] in an unbounded domain composed of two subspaces with different material properties, is also simulated and compared with the closed-form solution following [90, Section 5.2]. For the test of our DG method at an acousto-elastic interface, we generate a Scholte wave. We refer to [171] for the closed-form solution.

The computational domains are discretized as regular tetrahedral meshes. A sufficiently small constant, $K_{\mathrm{CFL}} = 0.05$, was selected during the tests for time stepping, and a large simulation time (10 s) is choosen for the error computation. The domain geometry and boundary conditions for each test are given in Table 2.1. The relevant material parameters, that is, the Lamé parameters λ and μ, and density ρ, are given in Table 2.2. We calculate the L^2 errors for the particle velocity of the numerical solutions, which are discretized by N_p order polynomials. The magnitudes of the numerical errors at time $t = 10$ s are shown in Figure 2.2, as a function of mesh size h for different values of N_p, and least-squares fits to lines, with the estimated convergence order for each line shown in the legend. We observe that the L^2 error of

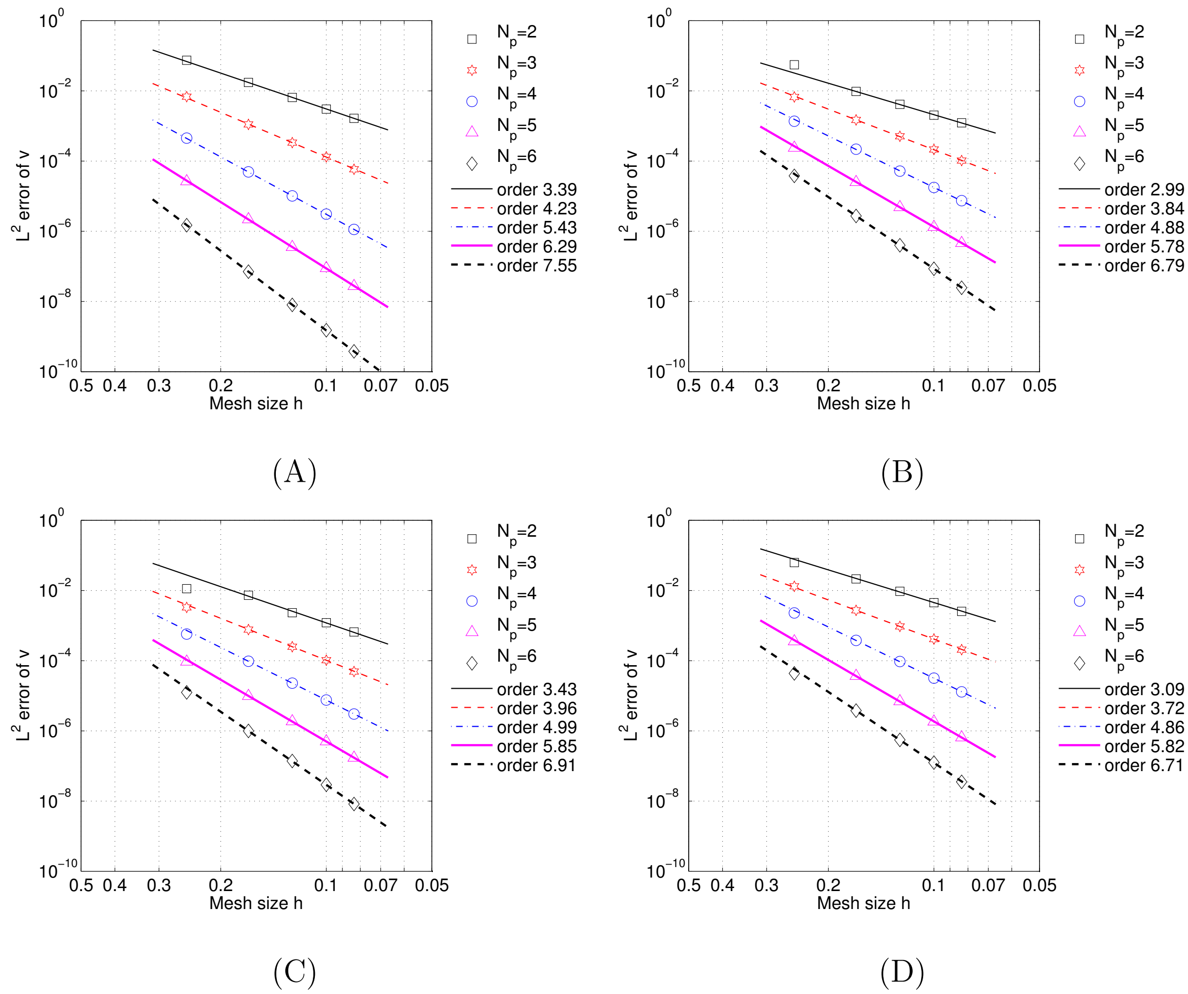

Figure 2.2 : L^2 error of partical velocity $\boldsymbol{v}$ as a function of mesh size h, for the simulation of (A) a plane wave, (B) a Rayleigh wave, (C) a Stoneley wave, and (D) a Scholte wave, for different orders $N_p = 2, 3, \cdots, 6$.

wave type	domain range (in km)	boundary conditions
plane wave	$[-1,1]\times[-1,1]\times[-1,1]$	periodic boundaries
Rayleigh wave	$[-1,1]\times[-1,1]\times[-1,1]$	free surface boundary at $x_3=\pm1$, periodic boundaries otherwise
Stoneley wave	$[-1,1]\times[-1,1]\times[-2,2]$	periodic boundaries
Scholte wave	$[-1,1]\times[-1,1]\times[-2,2]$	periodic boundaries (fluid-solid boundaries at $x_3=0,\pm2$)

Table 2.1 : Geometry and boundary conditions for the four wave types in the convergence tests.

our numerical scheme achieves a convergence rate higher than $N_p+\frac{1}{2}$. We also show a comparison of accuracies and convergence rates tested with the wave types described in this section for the upwind flux, the central flux and our penalty flux in Appendix 2.7.2.

2.7.2 Comparison of numerical flux

We compare the performance of three types of numerical flux in our DG method: the central flux (2.28), the upwind flux based on [171], and the boundary condition penalized flux (2.30). The comparisons are conducted using a Stoneley wave and a Scholte wave, with the parameter settings as in 2.7.1.

Figure 2.3 compares the accuracies and convergence rates of the penalized numer-

wave type	material properties
plane wave	$\lambda = 2.00$ GPa, $\mu = 1.00$ GPa, $\rho = 1.00$ g/cm^3
Rayleigh wave	$\lambda = 2.00$ GPa, $\mu = 1.00$ GPa, $\rho = 1.00$ g/cm^3
Stoneley wave	$\lambda = 1.20$ Gpa, $\mu = 1.20$ GPa, $\rho = 1.20$ g/cm^3, for $x_3 > 0$
	$\lambda = 3.00$ Gpa, $\mu = 1.20$ GPa, $\rho = 4.00$ g/cm^3, for $x_3 < 0$
Scholte wave	$\lambda = 1.20$ Gpa, $\mu = 1.30$ GPa, $\rho = 1.10$ g/cm^3, for $x_3 > 0$
	$\lambda = 1.11$ Gpa, $\mu = 0.00$ GPa, $\rho = 1.32$ g/cm^3, for $x_3 < 0$

Table 2.2 : Material parameters for the four wave types in the convergence tests.

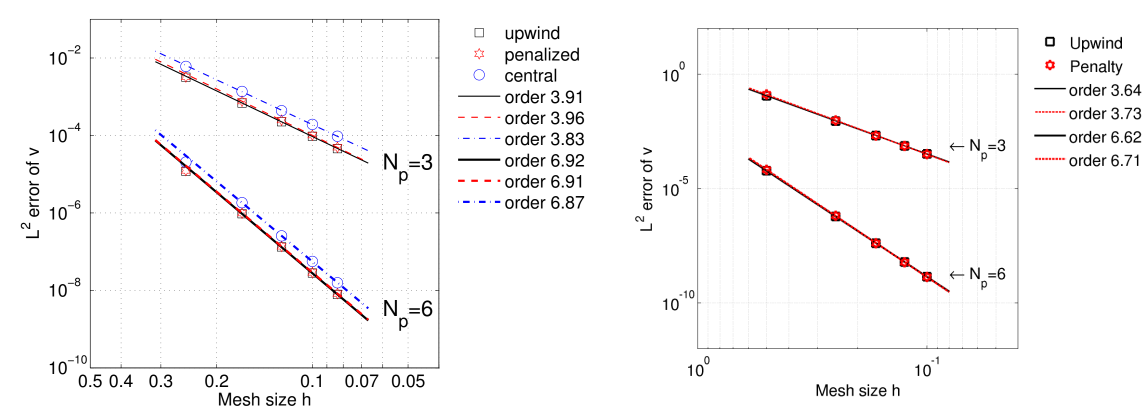

(A) (B)

Figure 2.3 : Comparison of the accuracies and convergence rates of different numerical fluxes when simulating (A) a Stoneley wave, and (B) a Scholte wave, for polynomial orders $N_p = 3$ and 6.

(A) $N_p = 3$

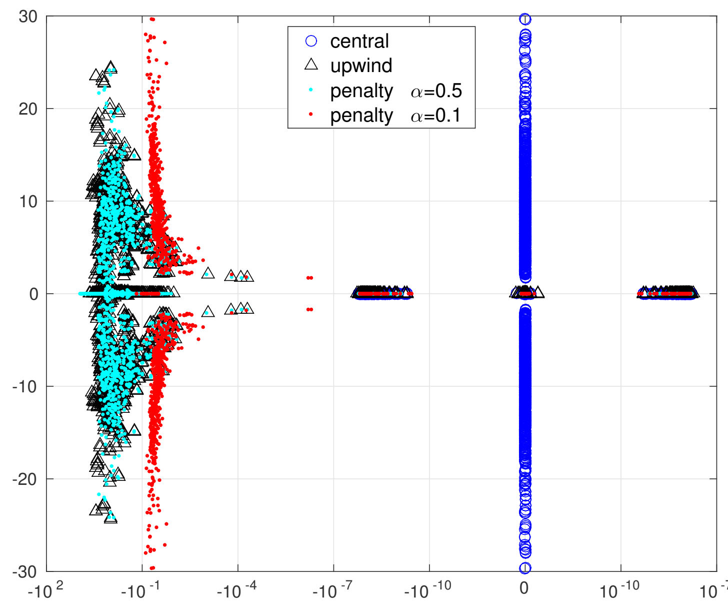

(B) $N_p = 6$

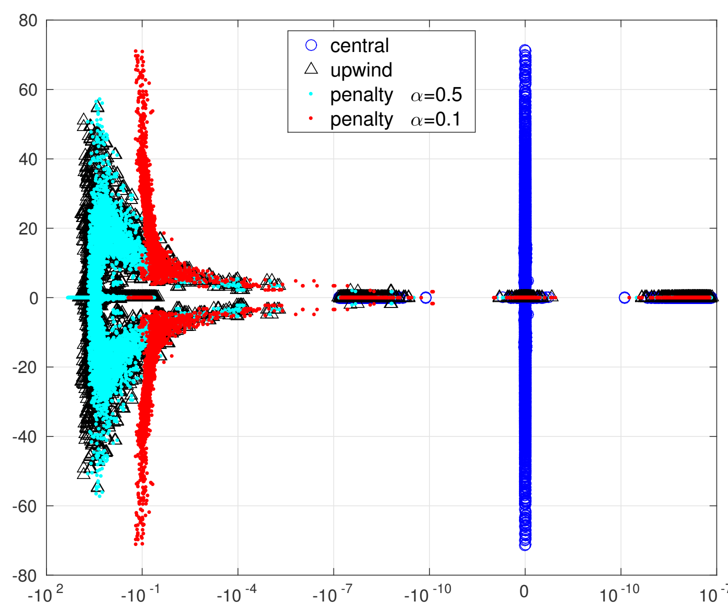

Figure 2.4 : Eigenvalue spectrum of the discretized spatial DG operator for a periodic domain solid-fluid interfaces for simulating the Scholte wave.

(A) $N_p = 3$

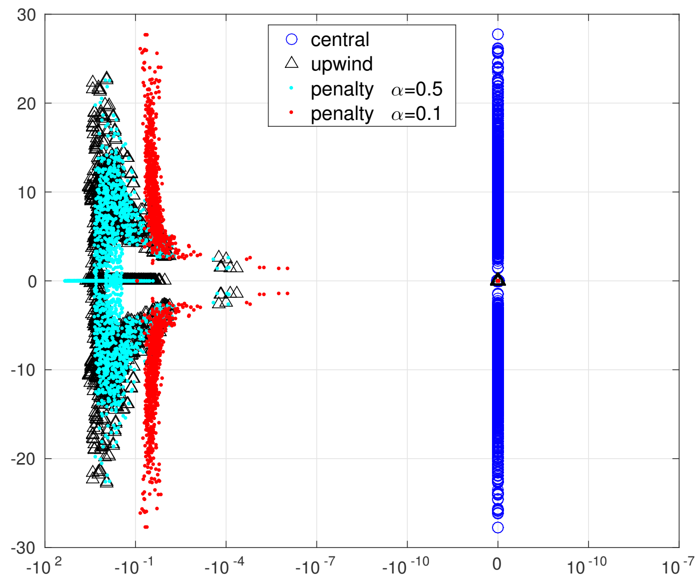

(B) $N_p = 6$

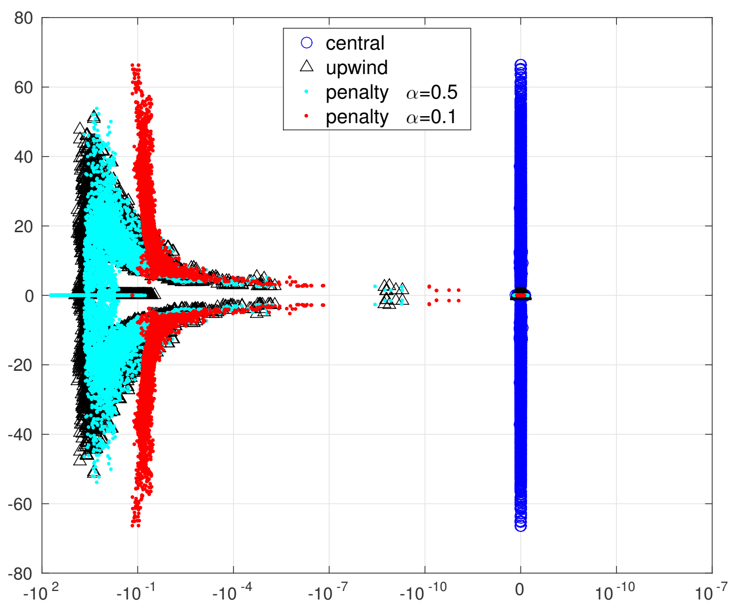

Figure 2.5 : Eigenvalue spectrum of the discretized spatial DG operator for a periodic domain solid-solid interfaces for simulating the Stoneley wave.

(A) $N_p = 3$

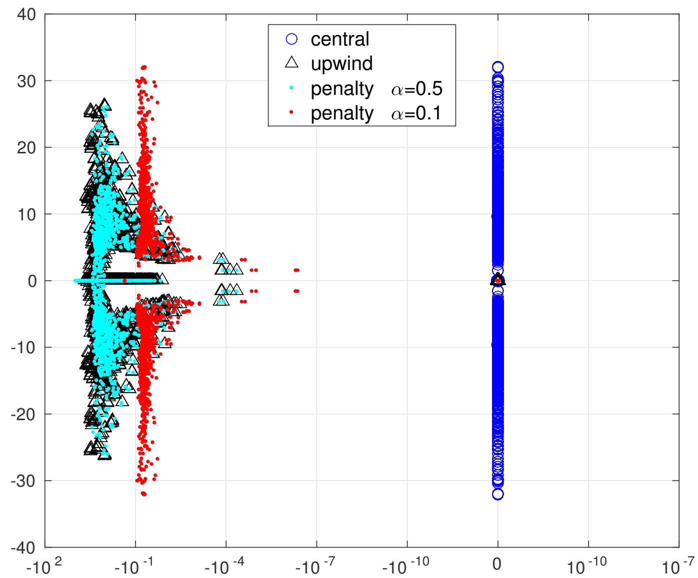

(B) $N_p = 6$

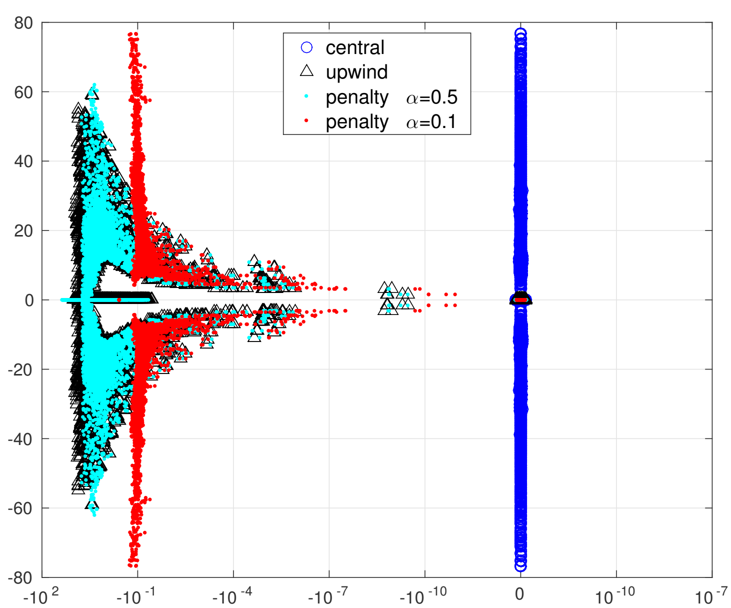

Figure 2.6 : Eigenvalue spectrum of the discretized spatial DG operator for a periodic domain with traction-free external boundary at top and bottom for simulating the Rayleigh wave.

ical fluxes with the upwind flux and the central flux when simulating the Stoneley wave and the Scholte wave, for both the lower-order case ($N_p = 3$) and the higher-order case ($N_p = 6$). We observe in Figure 2.3that the orders of convergence are essentially the same in the simulation of the Stoneley wave for the three types on fluxes (and all better than $\mathcal{O}(h^{N_p+\frac{1}{2}})$). The amplitude of error generated by penalty flux is the same as that generated by upwind flux, which is usually smaller than the central flux.

Figure 2.4–2.6 shows the eigenvalue spectrum λ_N for the three types of numerical fluxes, while the penalty coefficient takes two different values, $\alpha = 0.5$ and $\alpha = 0.1$, for polynomial order $N_p = 3$ and $N_p = 6$, on a tetrahedral mesh with a uniform mesh size $h = 0.25$ (in km). For the solid-solid and solid-fluid interior boundaries, and the external traction-free boundaries, the vanishing non-negative real parts of eigenvalues of upwind and penalized flux indicate their dissipative nature, while the purely imaginary spectrum for the central flux is consistent with energy conservation. However, rounding errors are quite more significant for the solid-fluid interfaces that generate eigenvalues with positive real-part, due to the contribution of operator O in (2.29), which result in so-called "spurious oscillations" while using the explicit Runge–Kutta method [e.g., [176]]. Moreover, the distribution of eigenvalues on the imaginary axis can not fit into the stable region of low-order (≤ 2) Runge–Kutta methods. As a consequence, the central flux have to be implemented with higher-ordered Runge–Kutta methods, with relatively small time step. On the other hands, the distribution of eigenvalues for $\alpha = 0.5$ is roughly the same as that for unwind flux, and one can obtain the freedom to choose different penalty coefficient to acheve optimal stable time step when implementing penalty scheme.

2.7.3 Homogeneous orthorhombic solid: Caustics

Here, we simulate a band-limited fundamental solution in an anisotropic elastic medium, forming caustics. The medium is orthorhombic and homogeneous. Several minerals in Earth's mantle have orthorhombic symmetry; this symmetry also appears in regions of sedimentary basins where fracture sets are commonly found in sandstone beds, shales, and granites. The material properties are selected as follows,

ρ	C_{11}	C_{22}	C_{33}	C_{44}	C_{55}	C_{66}	C_{23}	C_{13}	C_{12}	
1.0 (g/cm^3)	30.40	19.20	16.00	4.67	10.86	12.82	4.80	4.00	6.24	(GPa)

which produce a medium whose P phase velocities are 5.51 km/s, 4.38 km/s, and 4.00 km/s and S phase velocities are 2.16 km/s, 3.26 km/s, and 3.58 km/s in the principal directions (perpendicular to the symmetry planes). The computational domain is a $5 \times 5 \times 5$ (in km) cube. We place an explosive Gaussian source at the center of the cube, using a Ricker wavelet with a center frequency of 5Hz. Images of isosurfaces of the different components of the particle velocity are shown in Figure 2.7. We note the presence of caustics in one of the shear polarizations.

2.7.4 Flat isotropic fluid-solid interface: Propagation of Scholte wave

We present a model with dimensions $[0, 50] \times [0, 30] \times [0, 15]$km with a flat fluid-solid interface located at $x_3 = 7.5$km. The fluid side is homogeneous isotropic with an acoustic wave speed 1.5km/s and density 1.0g/cm^3. The solid side is homogeneous isotropic with a P-wave speed 3.0km/s and S-wave speed 1.5km/s, and density 2.5g/cm^3. The Scholte wave speed is computed numerically as 1.2455km/s [e.g., [90]]. We place an explosive source in the fluid at location (5.0, 15.0, 6.5)km, using a Ricker wavelet as the source-time series with a central frequency of 2.0Hz. A receiver is lo-

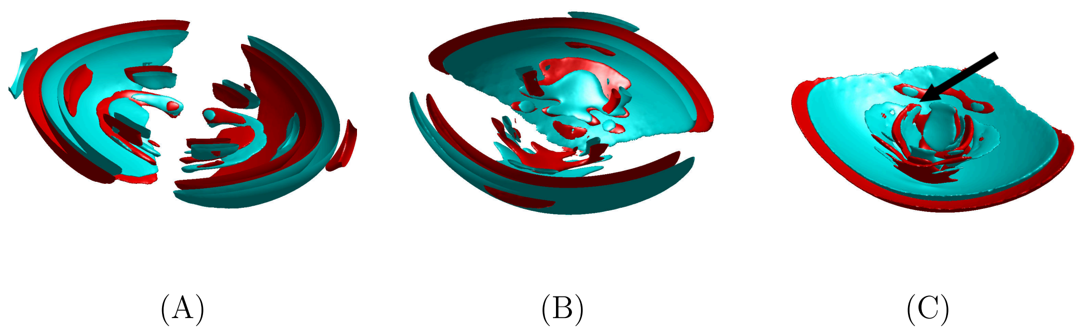

Figure 2.7 : Snapshots of the contours for the particle velocity (A) v_1, (B) v_2, and (C) v_3 at $t = 0.45s$. The black arrow in (C) indicates the shear wave front forming caustics.

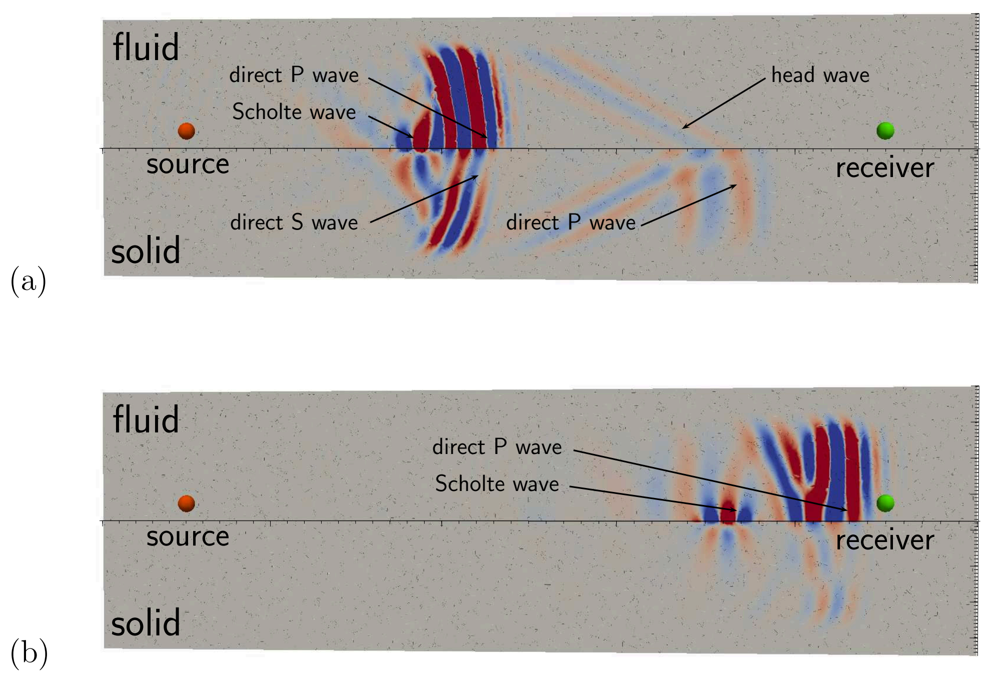

Figure 2.8 : Fluid-solid configuration visualized in the x_1–x_3 plane at $x_2 = 15.0$, with source and receiver located in the fluid. A snapshot at $t = 12s$ is shown in (a), and a snapshot at $t = 26s$ is shown in (b).

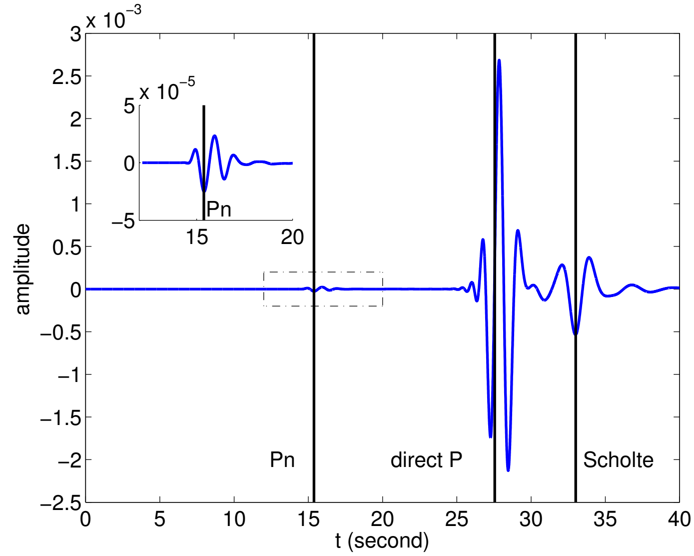

Figure 2.9 : Seismic trace from a hydrophone located at (40.0, 15.0, 6.0)km in the fluid side. Arrival times of head wave Pn, direct P waves and Scholte waves are indicated by vertical lines.

cated at (45.0, 15.0, 6.5)km and records the synthetic phases for 40 seconds. We apply convolutional perfect matching layers (CPMLs) [e.g., [93]] for all external boundaries of the model, highlighting the effects of a fluid-solid internal boundary.

Two snapshots are shown in Figure 2.8, one for the solution at $t = 12$s and the other for the solution at $t = 26$s, in which we observe the occurence of a Scholte wave which is well seperated from the body wave phases at long times. The amplitude of the Scholte wave decays exponentially with the distance from fluid-solid interface [[90]]. Figure 2.9 shows the seismogram as well as the arrival times of the head wave Pn, the direct P wave and Scholte wave. The modelled phase arrivals agree well with the travel times marked by perpendicular lines.

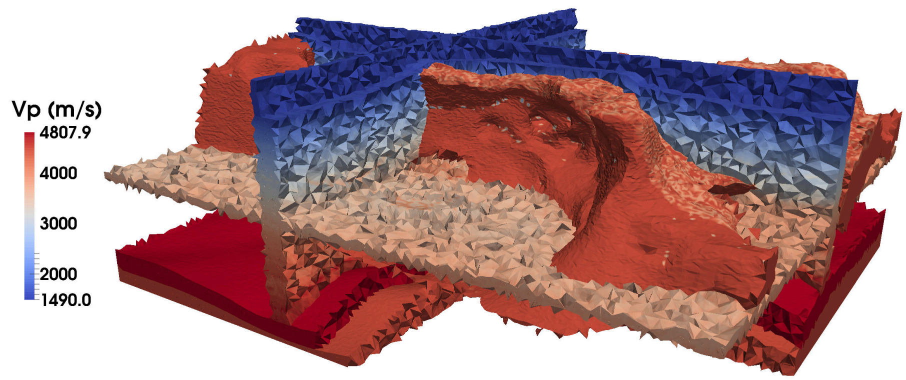

Figure 2.10 : A tetrahedral meshing for the 3D SEAM generated by segmentation and mesh deformation techniques. The color map shows the P wavespeed v_p interpolation.

2.7.5 Seismic waves in a geological structure: SEAM model

In this application, the DG method's ability to model the propagation and scattering of seismic waves in a field-scale domain with complex geological structures is demonstrated. The 3D SEAM (SEG Advanced Modeling) Phase I acoustic model is used that has heterogeneous structures and represents the sea-bed of the Gulf of Mexico [[59]]. It spans a 35 km by 40 km region of the earth's surface and has a depth of 15 km, and is discretized as a regular grid with 20m $\times$ 20m $\times$ 10m sample interval. The model has several geological features that we will use to test the robustness of the DG method. It contains a high-velocity salt body that extends through the center of the model (Figure 2.10). The rapid contrast in velocity makes the model, in the language of partial differential equations, a stiff domain. Another geometric feature is the sedimentary layering at approximately 10 km under the surface. These layers will cause multiple scattering that will lead to constructive and destructive interference.

A tetrahedral mesh with 863,973 elements of order 3 is generated adaptively start-

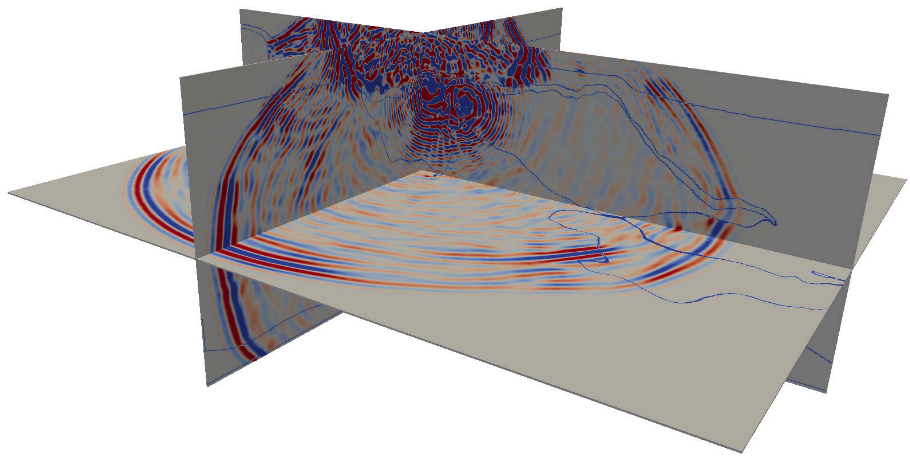

Figure 2.11 : Slices of the 3D SEAM acoustic velocity model and snapshot of pressure wave field at $t = 5.0$s, with the same viewpoint as in Figure 2.10.

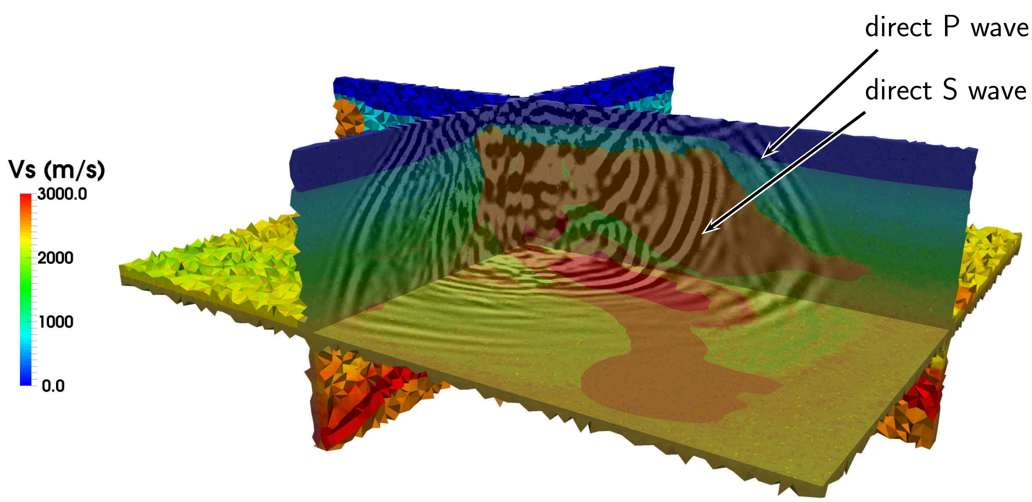

Figure 2.12 : Slices of the isotropic extension of 3D SEAM Phase I shear wavespeed model and snapshot of 3-component of particle velocity at $t = 5.0$s, with the same viewpoint as in Figure 2.10 and 2.11.

ing from the contours of the wave speed model, including the rough boundary of the salt body (Figure 2.10) and selected smooth interfaces associated with the sedimentary layers. We generate triangular isosurfaces based on domain partitioning of the wavespeed model into four primary subdomains: the ocean layer, the salt body, a high-contrast sediment layer and the sediment background. We also adaptively add vertices by tracking the contrasts of wavespeed inside each subregion. Using these, a tetrahedral mesh was created using *TetGen* [[154]]. A point source is located at the ocean bottom $(x_1, x_2, x_3) = (17.5, 15.0, 1.45)$km and the source function was a Ricker wavelet with a center frequency of 10.0 Hz. A snapshot of the acoustic pressure wave field solution is shown in Figure 2.11.

We also consider an extension of the SEAM Phase I model to isotropic elasiticity as is presented by [121]. We represent, via interpolation, the S wave speed and density on the unstructured mesh based on the four distinct subdomains, and place a point source inside the ocean layer at $(x_1, x_2, x_3) = (17.5, 15.0, 0.10)$km using a Ricker wavelet with a center frequency of 5.0 Hz. We apply a pressure-free surface boundary condition on the ocean surface, and CPMLs elsewhere. The S wavespeed and 3-component of the particle velocity are shown in Figure 2.12, in which the shear wave front can be clearly observed after the P arrivals.

2.7.6 Scattering from a rough surface: Fractured carbonate

Here, we model the reflection generated by an explosive point source from a rough surface embedded in a transversely isotropic medium. This type of medium closely resembles fractured samples of carbonate rocks [[101]]. Carbonates are abundantly found in nature. They pose many complications when working with them in the field because the physical properties vary from site to site and are strongly heterogeneous

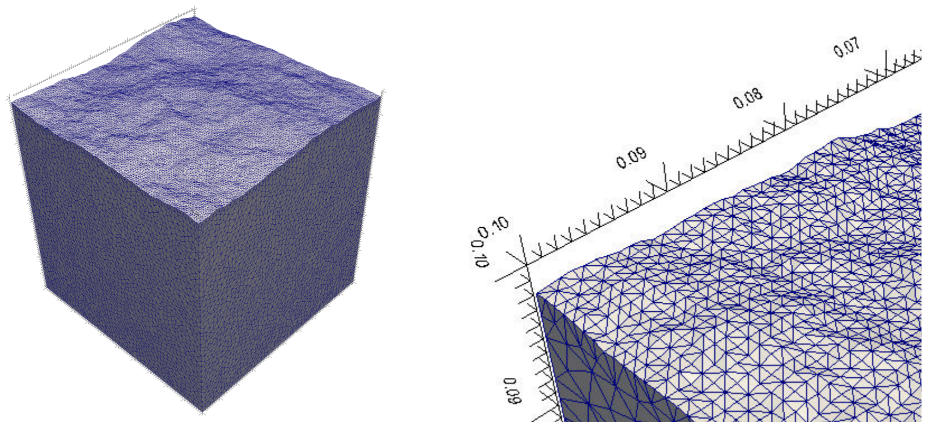

(A) (B)

Figure 2.13 : (A) Domain of the digitized rough surface. (B) Zoomed in of the mesh. The unit of the axises are in meters.

within the bulk rock. A homogeneous transversely isotropic medium can be used to model a carbonate because a variation in velocity amongst layers is the most common form of heterogeneity [[117]].

Laser profilometry was used to measure the surface roughness of an induced fracture in Austin Chalk, a carbonate rock sample. From these measurements, a profile of the surface was extracted to provide a rough boundary in an otherwise cubic domain with edge length of 0.1 m. The rough surface was placed on the top plane of the box, i.e. $x_3 = 0.1$m (Figure 2.13). The material properties were chosen such that the symmetry axis was in the $(\hat{x}_1, \hat{x}_2, \hat{x}_3) = (0, 1, 0)$ direction. P- and S-phase velocities along the axis of symmetry are 4000 m/s and 2280 m/s respectively, and are 4900 m/s and 2000 m/s respectively along the other two directions. The following table provides a list of the specific elastic constants used:

ρ	C_{11}	C_{22}	C_{33}	C_{44}	C_{55}	C_{66}	C_{23}	C_{13}	C_{12}	
1.5 (g/cm^3)	24.00	16.00	24.00	4.00	5.20	4.00	8.00	13.60	8.00	(GPa)

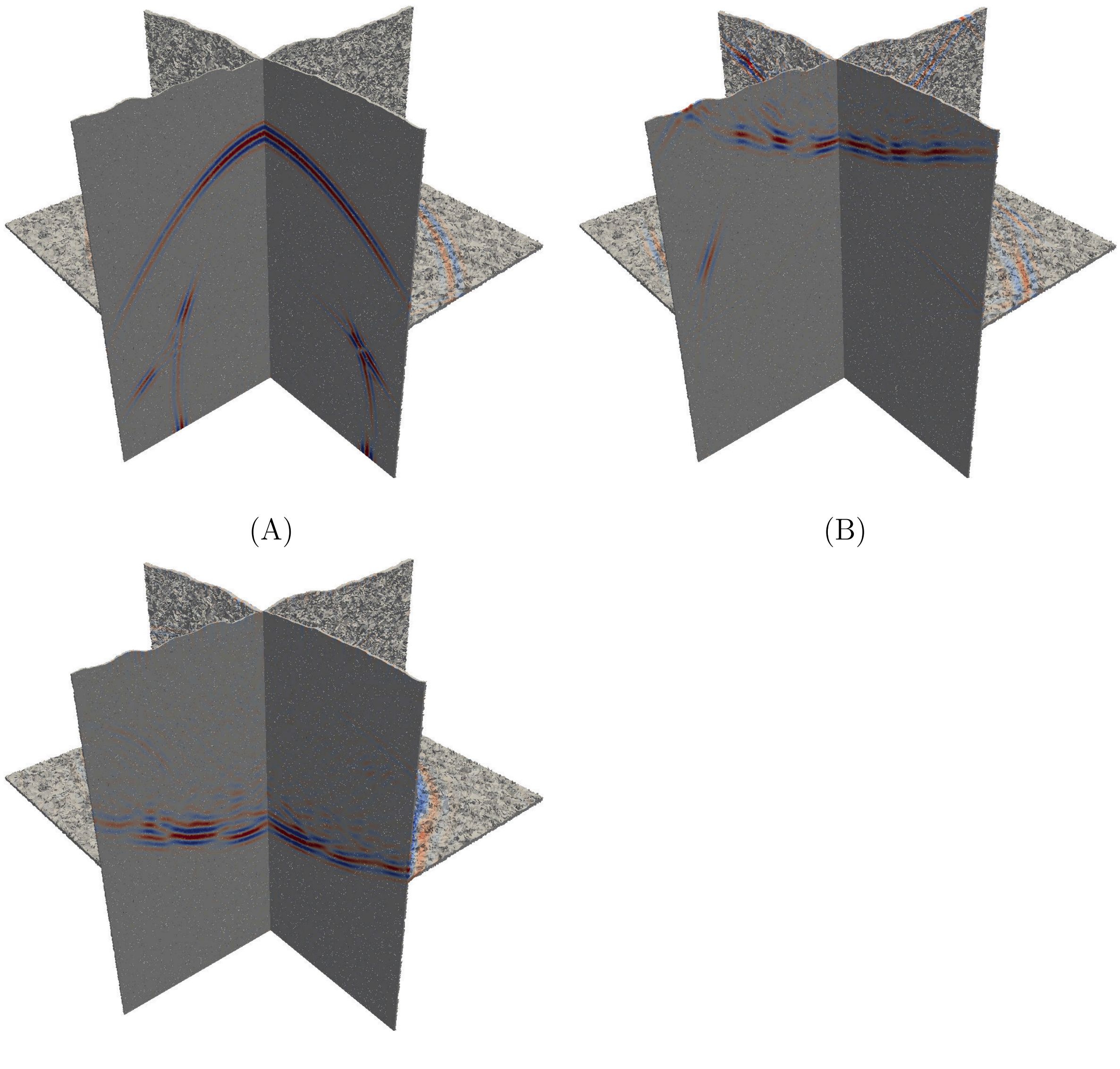

(A) (B) (C)

Figure 2.14 : Slices of the V_3 wave field after (A) 21 μs, (B) 31 μs, and (C) 41 μs from a 3D rough surface.

The tetrahedral mesh contains 686,444 elements, with $N_p = 4$. We place an explosive source at $(x_1, x_2, x_3) = (.05, .05, 0)$, using a Ricker wavelet with a central frequency of 1 MHz. Two snapshots of the wave field were taken of the 3-component of the particle velocity (Figure 2.14) that display the formation of shear-wave caustics due to anisotropy at $t = 21\mu s$, and the solutions of scattering at $t = 31\mu s$ and $t = 41\mu s$, respectively.

2.7.7 Heterogeneous anisotropic solid-fluid boundary with topography

Here, we use our DG method to simulate the wave propagation and scattering in a heterogeneous anisotropic solid-fluid configuration. The solid-fluid boundary has topography, which is well described by adaptively fitting an unstructured mesh (see Figure 2.15(a)). The model has dimensions $[0, 50] \times [0, 30] \times [0, 15]$km. The fluid side is homogeneous isotropic with an acoustic wave speed 1.5km/s and density 1.0g/cm^3. The solid side consists of a reference HTI medium component with elastic parameters given by $C_{11} = 33.75$, $C_{22} = 22.50$, $C_{33} = 13.85$, $C_{23} = 13.85$, $C_{13} = 11.44$, $C_{12} = 11.44$, $C_{44} = 4.327$, $C_{55} = 5.625$, $C_{66} = 5.625$ (GPa), and $\rho = 2.5$g/cm^3. A low-velocity lens is superimposed with its center located at (25, 15, 9)km. We place an explosive source in the fluid at location (8.0, 15.0, 6.5)km, using a Ricker wavelet as source-time series with a central frequency of 1.0Hz. We apply convolutional perfect matching layers (CPMLs) for all external boundaries of the model with the thickness of approximately two central wavelengths.

The waves are propagated for 40 seconds. Two snapshots in time of the wave field are shown; the solution at $t = 4$s (Figure 2.15 (b)) and the solution at $t = 14$s (Figure 2.15 (c)), with the occurence of a Scholte wave and seperation from body waves while propagating. We note the fomation of caustics in the solid region, caused

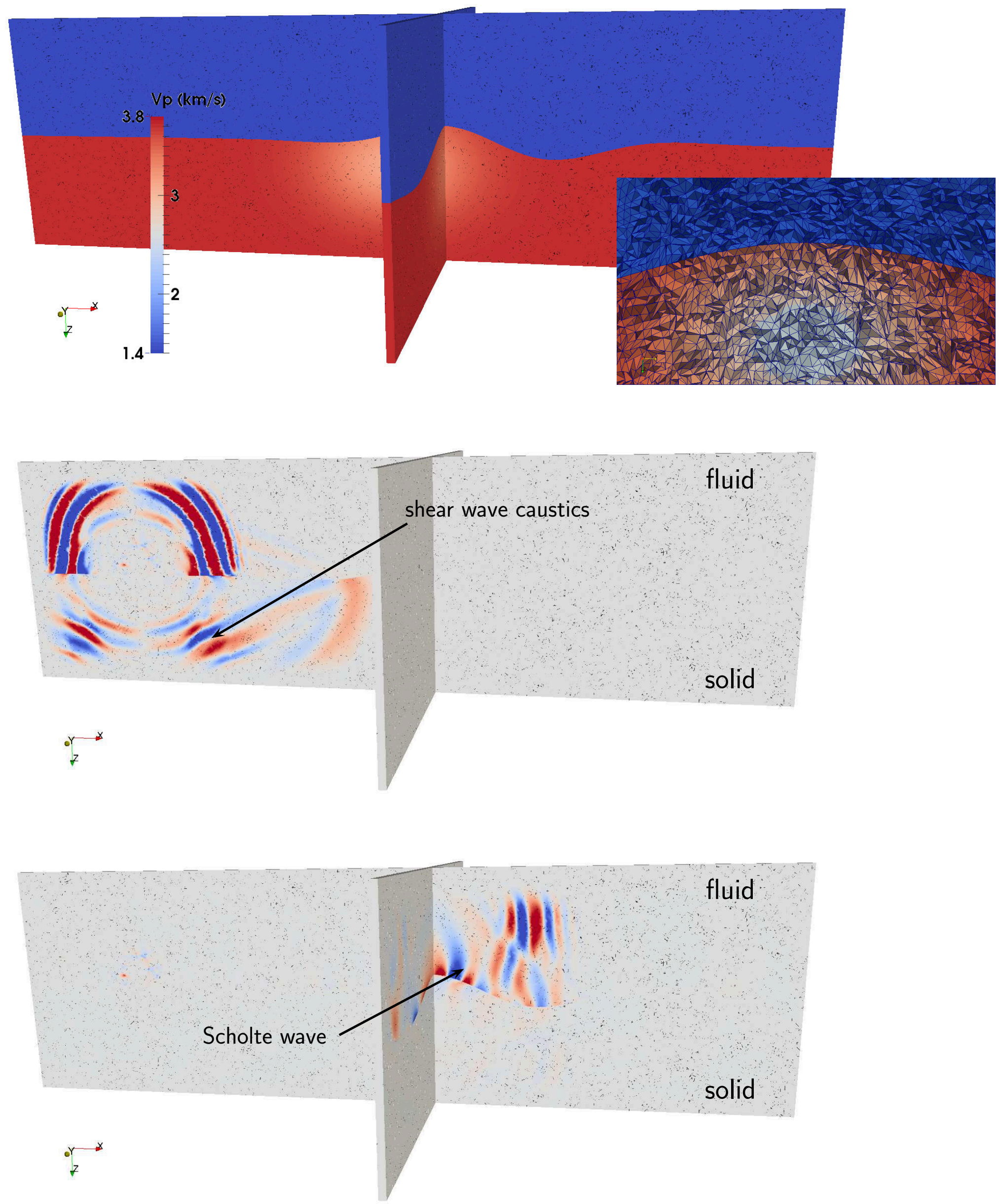

(a)

(b)

(c)

Figure 2.15 : Heterogeneous HTI solid-fluid boundary with topography. (a) 3D model setting, with color indicating quasi-P wavespeed; (b) snapshot at t=4.0s; (c) snapshot at t=18.0s.

by the anisotropy and the low-velocity lens.

2.8 Discussion

We develop a DG-method based numerical approach to simulate acousto-elastic wave phenomena. We demonstrate its ability to generate accurate solutions in domains with heterogeneous and complex geometries for long-time simulation. We briefly discuss the specifics of and differences between our and earlier developed DG methods for general acousto-elastic wave problems.

Most of the existing DG discretizations for solving the acousto-elastic system of equations in the first-order formulation make use of an upwind numerical flux derived from the elementwise solution of a Riemann problem. In [54], a Godunov upwind flux is applied upon diagonalizing the coefficient matrix in the stress-velocity formulation at element-element interfaces. Specifically, they use a "one-sided" upwind numerical flux and, to avoid elementwise numerical integration and make use of pre-calculated matrices instead, restrict the coefficients to be constant in each element. Steger-Warming flux-vector splitting in [155] is another way to obtain an exact Riemann solution for the linear system with flexibly parameterized isotropic elastic media, allowing variable coefficient within elements. The velocity-strain formulation introduced by [171] uses the Rankine-Hugoniot jump condition to obtain an upwind flux for isotropic solid-fluid interfaces while designing a uniform conservative formulation for coupled elasto-acoustic systems.

Meanwhile, there are penalty based DG schemes designed to solve numerically the second-order system of equations for the displacement. The interior penalty Galerkin method is used by [137] to solve a nonlinear parabolic system, and a symmetric interior penalty term was employed by [69] to make the stiffness matrix symmetric positive definite. [48] studies the dispersion and convergence of these interior penalty DG-method based schemes for the second-order elliptic Lamé system. [169] defines for a general hyperbolic system a flux that penalizes the fields based on their continuity.

In our DG-method based scheme, we introduce a penalized numerical flux the form of which is motivated by the interior boundary continuity conditions. The fluid-solid boundary conditions are accounted for in the coupling of elements through the fluxes. Our penalty weight does not depend on the normal direction of the interior faces of the elements, and moreover, unlike the interior penalty scheme in the second-order displacement formulation, does not depend on the mesh size either.

Chapter 3

A multi-rate iterative coupling scheme for dynamic ruptures in a weak form: well-posedness

3.1 Introduction

The study and mathematical formulation of seismic wave propagation and scattering in a uniformly rotating and self-gravitating Earth model dates back to the work of Dahlen [38, 39] and Woodhouse and Dahlen [172]. Valette [163] studied the proper weak formulation of the underlying system of equations, and De Hoop, Holman and Pham [50] completed the analysis of well-posedness also through energy estimates. The complications in this analysis arise essentially from the presence of a fluid outer core. Here, we study a different complication, namely the coupling of the system to rupture dynamics.

Kinematics of earthquake sources, which in most situations are the catastrophic failure of faults and slip, may be captured by a moment tensor (*e.g.* Dahlen and Tromp[41, Ch. 5]). The energy budget of a kinematic rupture along with a slip boundary condition was studied by Dahlen [40], without friction laws. However, in rupture dynamics friction laws play a critical role. Theoretical models of earthquake rupturing based on rate- and state friction laws and their incorporation in the elastic-gravitational system of equations describing seismic waves have been studied in recent years [105, 73, 161]. However, the rigorous mathematical, weak formulation of this and well-posedness have been open problems and are addressed, here. This weak formulation also forms the foundation of the development of numerical schemes.

The dependency of friction strength on slip rate and the evolving contact property of material, or so-called "state", have been recognized in laboratory studies and formalized by Dieterich [53], Ruina [144, 143], Rice [134], Rice and Ruina [133], and many others. Such studies were conducted on various rock types and fault gouge layers, and over a wide range of slip rates and confined normal stress. The relation between the rate and state friction laws and realistic rupture processes was discussed by Dunham et al.[55].

Originally developed in the laboratory, the rate and state friction laws have been proven to be well-posed in one-dimensional problems and to approximate rate-dependent experimental results [53, 143, 136, 135]. However, general existence or uniqueness results are absent for coupled rate and state friction with pure elasticity in both two and three dimensions. The main issue is the high-order derivative terms arising from the dependency of friction on normal stress as well as the surface divergence introduced by a dynamically slipping boundary. These also occur when using simpler slip-dependent friction laws, even for the simplest one, that is, linear slip-weakening friction. Existing proofs of well-posedness are based on simplified scenarios: By fixing the normal stress to a reference value (the Tresca model, *e.g.* [83, 82, 128, 127]), or by characterizing the normal stress with a power-relation of normal displacement (the normal compliance model, *e.g.* [109, 91, 81]). For both simplifications, existence and uniqueness can be obtained with or without (physical or artificial) viscosity. In our framework, we show that with a natural regularization which gives a slightly viscous Kelvin-Voigt material asymptotically approaching pure elasticity, more general scenarios can be resolved, where the friction force depends on normal stress following constraints no other than the ones from the relevant

Dirichlet-to-Neumann map.

At the same time, in recent years, numerical algorithms have been developed for coupled rate and state friction with pure elasticity based on the above mentioned simplifications, nonetheless producing physically reasonable results [63, 43, 11, 123, 99, 181, 120, 56]. Some numerical studies do point out that problems (like shock waves) can occur for long-time simulation, and that introducing artificial viscosity is a natural way to obtain a stable solution (*e.g.* [47, 87, 2]). However, a mathematical framework to address the well-posedness while avoiding simplifications to enable a general study of coupled rupture dynamics and seismic wave generation has been lacking so far. This is the subject of this chapter. The main result concerns the coupling that can be realized iteratively and its convergence in concert with the occurrence of two time scales.

We present a weak form of the elastic-gravitational system coupled to dynamical ruptures with rate and state friction laws. We suppress the uniform rotation in our analysis, but including this is a simple task. We obtain the equations of motion from the Euler-Lagrange equations. These comprise a hyperbolic system of second-order linear equations coupled to the friction law on some of the interior boundaries identified as faults, involving a nonlinear algebraic relation with evolution of a state variable that is represented by a time-dependent nonlinear ordinary differential equation. The multi-rate iterative coupling scheme [65] pertains to the two sub-problems mentioned above, each being solved with significantly distinct time steps. We prove that the coupling problem can be asymptotically solved within any finite time interval by introducing a regularization term through a small artificial viscosity coefficient. The coupling leads to a unique solution, which can be obtained by an iterative scheme, exploiting the Banach fixed-point theorem. The natural choice of numerical method is the discontinuous Galerkin one [177]; see, also, earlier works by de la Puente et al.(2009) [51], Tago et al.(2012) [158], and Pelties et al.(2012) [123], with formulations leading to various issues or flaws. In the next chapter, we develop such a method for the iterative coupling scheme proposed here.

The outline of this chapter is as follows. In Section 2, we give the strong formulation for particle motion and boundary conditions expressing the coupling with a friction law, and the corresponding weak formulation with necessary assumptions including the regularity of model geometry and model parameters. The empirical assumptions of friction laws are also discussed, from a mathematics point of view. We then define the appropriate energy spaces. In Section 3, we propose an iterative coupling scheme and present a proof of contraction. As a byproduct, we obtain well-posedness with a condition on the artificial viscosity. We discuss a backward Euler time discretization in Section 4. The proof of contraction implies conditions for the time step and the choice of viscosity coefficient. The main results of this chapter are Theorems 4.1 and 4.2, which indicate the impact of model geometry and model parameters on the well-posedness of the coupling problem, as well as the convergence rate of the proposed scheme. We end with some conclusions in Section 5.

3.2 Mathematical model and assumptions

We consider the problem in a finite set $\overline{\Omega} \in \mathbb{R}^3$ that stands for the interior of solid Earth (ignoring the fluid ocean layer and outer core), with a continuum of linear elastic material that follows Hooke's law, except at the rupture surface denoted by Σ_{f}. We further assume that Ω is a Lipschitz composite domain, which is defined as a disjoint union of open subsets, $\Omega = \bigcup_{k=1}^{k_0} \Omega_k$, with interior boundaries (supplemented with slip and non-slip conditions) given by

$$\Sigma = \bigcup_{1 \le k < k' \le k_0} \partial\Omega_k \cap \partial\Omega_{k'} \setminus \partial\Omega,$$

which are two-dimensional Lipschitz continuous surfaces. We note that $\Sigma_{\mathrm{f}} \subseteq \Sigma$. We have $\overline{\Omega} = \Omega \cup \Sigma \cup \partial\Omega$. The boundary of interior surface $\partial\Sigma$ is a finite union of curves of measure 0 lie on the exterior boundary $\partial\Omega$, where traction free condition (3.7) is applied. We choose $\boldsymbol{n} : \partial\Omega_k \to \mathbb{R}^3$ almost everywhere on $\Sigma \cup \partial\Omega$, as the unit normal vector of interior and exterior boundaries. It satisfies $\boldsymbol{n} \in Ł^{\infty}(\Sigma \cup \partial\Omega)^3$, and labels the two sides across of Σ by "$-$" and "$+$". The jump operator $[\![\,\cdot\,]\!]$ can be defined for any bounded Lipschitz continuous function, f say, as

$$[\![f]\!] := f^+ - f^- = f^{\overline{\Omega_k}}(x) - f^{\overline{\Omega_{k'}}}(x), \qquad \text{for } x \in \partial\Omega_k \cap \partial\Omega_{k'}, \tag{3.1}$$

where Ω_k corresponds to the region of the "$+$" side and $\Omega_{k'}$ to the region on the "$-$" side. We also define the averaging operator across Σ by $\{\!\{\,\cdot\,\}\!\}$ such that $\{\!\{f\}\!\} = \frac{1}{2}(f^+ + f^-)$ which will be used in Subsection 2.5.

3.2.1 The basic equations in the strong form

We follow Brazda et al.[18] in deriving the equation of motion in a prestressed Earth while ignoring the rotation of Earth. The gravitational potential ϕ^0 satisfies Poisson's equation

$$\Delta\phi^0 = 4\pi G\rho^0, \tag{3.2}$$

with ρ^0 the initial density distribution of Earth, and G Newton's universal constant of gravitation. The equilibrium condition for the initial steady-state is

$$\rho^0\nabla\phi^0 = \nabla \cdot \boldsymbol{T}^0, \tag{3.3}$$

where $\boldsymbol{T}^0$ is the tensor of static prestress. The equation of motion is written following [18, (5.43)] as

$$\rho^0 \ddot{\boldsymbol{u}} + \rho^0 \nabla S(\boldsymbol{u}) + \rho^0 \boldsymbol{u} \cdot (\nabla\nabla\phi^0) - \nabla \cdot (\boldsymbol{\Lambda}^{\boldsymbol{T}^0} : \nabla \boldsymbol{u}) = 0 \quad \text{in } \Omega \setminus \Sigma_{\mathrm{f}} \tag{3.4}$$

with the initial conditions given as

$$\boldsymbol{u}|_{t=0} = 0,\ \dot{\boldsymbol{u}}|_{t=0} = 0.$$

The mass redistribution potential $S(\boldsymbol{u})$ is associated with particle displacement $\boldsymbol{u}$ by

$$\Delta S(\boldsymbol{u}) = -4\pi G \nabla \cdot (\rho^0 \boldsymbol{u}), \tag{3.5}$$

and the prestressed elasticity tensor is a linear map $\boldsymbol{\Lambda}^{\boldsymbol{T}^0} : \mathbb{R}^{3\times 3} \to \mathbb{R}^{3\times 3}$ such that $(\boldsymbol{\Lambda}^{\boldsymbol{T}^0} : \nabla \boldsymbol{u})$ represents the first Piola-Kirchhoff stress perturbation. The prestressed elasticity tensor is related to the *in situ* isentropic elastic tensor $\boldsymbol{C}$ by

$$\Lambda^{\boldsymbol{T}^0}_{ijkl} = C_{ijkl} + \tfrac{1}{2}\big((T_0)_{ij}\delta_{kl} + (T_0)_{kl}\delta_{ij} + (T_0)_{ik}\delta_{jl} - (T_0)_{il}\delta_{jk} - (T_0)_{jk}\delta_{il} - (T_0)_{jl}\delta_{ik}\big).$$

The non-slipping inner interfaces yield the conventional continuous boundary conditions,

$$[\![\boldsymbol{u}]\!] = 0\,, \quad [\![\boldsymbol{n} \cdot (\boldsymbol{\Lambda}^{\boldsymbol{T}^0} : \nabla \boldsymbol{u})]\!] = 0, \quad \text{on } \Sigma \setminus \Sigma_{\mathrm{f}}, \tag{3.6}$$

and the external boundary yield the traction free condition,

$$\boldsymbol{n} \cdot (\boldsymbol{\Lambda}^{\boldsymbol{T}^0} : \nabla \boldsymbol{u})^- = 0, \quad \text{on } \partial\Omega. \tag{3.7}$$

We denote by $\boldsymbol{T}_\delta(t)$ the perturbation of the stress tensor introduced by multi-physics processes such as regional tectonics, geothermal activities, or fluid injections, which is evolving as a function of time [116, 146]. On the rupture surface Σ_{f}, the dynamic slipping boundary condition (*e.g.* [18, (4.57)]) and the force equilibrium are satisfied, which give

$$
\begin{cases}
[\![\boldsymbol{n}\cdot\boldsymbol{u}]\!] = 0, & \\
[\![\boldsymbol{\tau}_1+\boldsymbol{\tau}_2]\!] = 0, & \text{on } \Sigma_{\mathrm{f}}, \\
\boldsymbol{\tau}_{\mathrm{f}} - \big(\boldsymbol{n}\cdot(\boldsymbol{T}^0+\boldsymbol{T}_\delta)+\boldsymbol{\tau}_1+\boldsymbol{\tau}_2\big)_{\parallel} = 0, &
\end{cases}
\tag{3.8}
$$

with

$$
\begin{cases}
\boldsymbol{\tau}_1 := \boldsymbol{n}\cdot(\boldsymbol{\Lambda}^{\boldsymbol{T}^0} : \nabla\boldsymbol{u}), \\
\boldsymbol{\tau}_2 := -\nabla^{\Sigma}\cdot(\boldsymbol{u}(\boldsymbol{n}\cdot\boldsymbol{T}^0)), \\
\sigma := -\boldsymbol{n}\cdot(\boldsymbol{n}\cdot(\boldsymbol{T}^0+\boldsymbol{T}_\delta)+\boldsymbol{\tau}_1+\boldsymbol{\tau}_2), \\
\boldsymbol{s} := [\![\dot{\boldsymbol{u}}_{\parallel}]\!], \quad s := |\boldsymbol{s}\,|, \quad \tau_{\mathrm{f}} := |\boldsymbol{\tau}_{\mathrm{f}}|.
\end{cases}
\tag{3.9}
$$

In the above, σ stands for the compressive normal stress. The direction of friction force is opposite to slip velocity, following (*e.g.* [47, eq. (4)])

$$
\tau_{\mathrm{f}}\boldsymbol{s} - s\boldsymbol{\tau}_{\mathrm{f}} = 0. \tag{3.10}
$$

The nonlinear relation between s and τ_{f} are governed by a rate- and state-dependent friction law, which will be discussed in Section 3.2.2. In the above, the surface divergence is defined by $\nabla^{\Sigma}\cdot\boldsymbol{f} = \nabla\cdot\boldsymbol{f} - (\nabla\boldsymbol{f}\cdot\boldsymbol{n})\cdot\boldsymbol{n}$.

We mention an equivalent representation of the wave motion as an alternative for the above equations (5.2), (3.6), (3.8) and (3.9), based on which a mathematical formulation for the same dynamic rupture problem can be obtained following a similar route. Within this representation, the incremental Lagrangian stress tensor takes the place of the incremental Piola–Kirchhoff stress tensor, and the equation of motion is given by (*e.g.* [18, (5.52)])

$$\rho^0\ddot{\boldsymbol{u}}+\rho^0\nabla S(\boldsymbol{u})-(\nabla\cdot(\rho^0\boldsymbol{u}))\nabla\phi^0+\nabla\cdot(\boldsymbol{u}\cdot\nabla\boldsymbol{T}^0)-\nabla\cdot(\boldsymbol{\Gamma}^{\boldsymbol{T}^0}:\nabla\boldsymbol{u})=0 \quad \text{in } \Omega\backslash\Sigma_{\mathrm{f}}, \tag{3.11}$$

where $\boldsymbol{\Gamma}^{\boldsymbol{T}^0}:\mathbb{R}^{3\times 3}\to\mathbb{R}^{3\times 3}$ is a linear map such that $(\boldsymbol{\Gamma}^{\boldsymbol{T}^0}:\nabla\boldsymbol{u})$ represents the first-order Lagrangian stress perturbation, which satisfies the same boundary condition as (3.6) and (3.8), with $\boldsymbol{\tau}_1$ and $\boldsymbol{\tau}_2$ replaced by $\tilde{\boldsymbol{\tau}}_1$ and $\tilde{\boldsymbol{\tau}}_2$, given by

$$\begin{cases} \tilde{\boldsymbol{\tau}}_1 := \boldsymbol{n}\cdot(\boldsymbol{\Gamma}^{\boldsymbol{T}^0}:\nabla\boldsymbol{u}), \\ \\ \tilde{\boldsymbol{\tau}}_2 := -\boldsymbol{n}\cdot(\boldsymbol{u}\cdot\nabla^{\Sigma}\boldsymbol{T}^0)-\boldsymbol{T}^0\cdot\nabla^{\Sigma}(\boldsymbol{n}\cdot\boldsymbol{u}). \end{cases} \tag{3.12}$$

Here, the surface gradient is defined by $\nabla^{\Sigma}\boldsymbol{f}=\nabla\boldsymbol{f}-(\nabla\boldsymbol{f}\cdot\boldsymbol{n})\boldsymbol{n}$. We can apply the same coupling scheme to (3.11) and (3.12) and obtain similar well-posedness results that will be developed in Sections 3.4 and 3.5.

3.2.2 The rate and state friction law

The generally accepted class of rate- and state-dependent friction laws is based on several assumptions that are commonly observed in the laboratory. Here, we summarize the general assumptions in Subsection 3.2.2 for most existing friction laws, and the particular assumptions for composing a rate- and state-friction law in Subsection 3.2.2, following the discussion and analysis by Rice et al.[135].

Perhaps the most critical notion for the rate and state friction law is “steady state”, which is a status of relative motion for two contacting objects that lasts for a relatively long time, maintaining a constant slipping velocity under a fixed normal compressive stress. A steady friction force can be measured for various combinations of constant slip-rate and normal stress, and a time-dependent one is usually recorded during a process of switching from one steady state to another.

The general assumptions of friction laws

We review several features that are common in the experimental observations of friction laws listed in the references of this chapter, showing that

($\mathfrak{a}_1$) the instantaneous friction force is positively related to the compressive normal stress;

($\mathfrak{a}_2$) the instantaneous friction force is positively related to the magnitude of slip rate;

($\mathfrak{a}_3$) the long-term variation of friction force is accumulatively affected by the history of slip rate and compressive normal stress;

($\mathfrak{a}_4$) a steady-state friction force can be obtained with any given combination of constant slip rate and fixed compressive normal stress.

A universal representation capturing the characteristics above was proposed by Rice et al.[135, p. 1869-1870] and is given in equations (4.4)-(3.17) below. Based on assumptions ($\mathfrak{a}_1$)-($\mathfrak{a}_3$), a state variable, ψ, is introduced to measure the average contact maturity. The nonlinear relation for the magnitude of friction force, τ_{f}, defined in (3.9), can then be written in the general form of a scalar function

$$\tau_{\mathrm{f}} = \mathcal{F}(\sigma, s, \psi), \tag{3.13}$$

with

$$\frac{\partial \mathcal{F}}{\partial \sigma} \geq C_{\mathcal{F},\sigma} > 0, \quad \frac{\partial \mathcal{F}}{\partial s} \geq C_{\mathcal{F},s} > 0 \quad \text{and} \quad \frac{\partial \mathcal{F}}{\partial \psi} \geq C_{\mathcal{F},\psi} > 0. \tag{3.14}$$

We also assume that the rupture remains compressive or, in other words, the compressive normal stress σ is positive throughout the time of rupture, which correspondingly puts constraints on the initial stress $\boldsymbol{T}^0$, perturbated stress $\boldsymbol{T}_\delta$ and solutions based on (3.9). The state variable evolves with time following the ordinary differential relation,

$$\dot{\psi} + \mathcal{G}(\sigma, \dot{\sigma}, s, \psi) = 0. \tag{3.15}$$

Based on empirical rule $(\mathfrak{a}_4)$, for each pair of (σ, s) under the constraints $\dot{s} = 0$ and $\dot{\sigma} = 0$, there is a steady-state value $\psi_{\text{ss}}(\sigma, s)$ satisfying

$$\mathcal{G}(\sigma, 0, s, \psi_{\text{ss}}(\sigma, s)) = 0, \tag{3.16}$$

with the corresponding friction force denoted by

$$\tau_{\text{ss}}(\sigma, s) := \mathcal{F}(\sigma, s, \psi_{\text{ss}}(\sigma, s)). \tag{3.17}$$

The quasi-static assumption

In the notion of quasi-static state, the change of slip rate of sliding motion is sufficiently slow that the inertia of the block mass can be neglected. The Amontons-Coulomb law is usually assumed, in which the friction force τ_{f} is proportional to the compressive normal stress σ such that (*cf.* [143, eq. (4a)])

$$\tau_{\text{f}} = \sigma\, f(s, \psi), \tag{3.18}$$

with f the so-called friction coefficient. With the assumption of rapid change of the normal stress σ relative to that of the slip rate s, (4.5) is linearized (*cf.* [135, p.1870]) by

$$\dot{\psi} = -\mathcal{G}_1(\sigma, s, \psi) - \dot{\sigma}\mathcal{G}_2(\sigma, s, \psi), \tag{3.19}$$

such that the friction law can be evaluated with the observation results based on a quasi-static assumption (with sufficiently slow changes on slip rate s as well as compressive normal stress σ), while allowing studies on time-variational compressive normal stress as linear perturbations. A steady state therefore satisfies,

$$\mathcal{G}(\sigma, 0, s, \psi_{\mathrm{ss}}(\sigma, s)) \equiv \mathcal{G}_1(\sigma, s, \psi_{\mathrm{ss}}(\sigma, s)) = 0.$$

The general form of the function $\mathcal{G}_2$ is still under debate. Studies by Linker and Dieterich [102], Prakash [130], Richardson and Marone [136], Bureau et al.[20], and many others show that the effects of variable compressive normal stress upon friction state can take various forms.

By fixing the value of σ, there are further empirical results from laboratory experiments suggesting that

($\mathfrak{b}_1$) there is a characteristic length for the steady-sliding rupture evolving into the next steady state after a sudden change of slip rate, regardless of the value of slip rate;

($\mathfrak{b}_2$) the instantaneous rate-dependent friction force is approximately proportional to the logarithm of slip rate;

($\mathfrak{b}_3$) the steady state friction force is approximately proportional to the logarithm of slip rate.

We elaborate on ($\mathfrak{b}_1$) while assuming that the slip rate stays constant with value s after a sudden jump. Linearizing (3.19) as a perturbation of steady state with $\dot{\sigma} \equiv 0$ yields (*cf.* [143, eq. (7)])

$$\frac{\mathrm{d}\psi}{\mathrm{d}t} = -\frac{\partial \mathcal{G}_1}{\partial \psi}\left(\psi - \psi_{\mathrm{ss}}\right), \tag{3.20}$$

which has a solution (*cf.* [143, eq. (8)])

$$\psi(s, L/s) = \psi_{\mathrm{ss}}(s) + \big(\psi(s,0) - \psi_{\mathrm{ss}}(s)\big)\exp\left(-\frac{L}{s}\frac{\partial \mathcal{G}_1}{\partial \psi}\right), \tag{3.21}$$

in which the time is replaced by L/s, where L is the slip distance. The characteristic length is defined as $L_c := s/(\partial\mathcal{G}_1/\partial\psi)$, physically meaning that after slipping for a distance L_c under constant compressive normal stress and slip rate, the friction coefficient evolves towards steady state by a definite ratio $1/e$. Assumption ($\mathfrak{b}_1$) indicates that L_c is independent of s, and the non-negative nature of L_c and s implies that

$$\frac{\partial\mathcal{G}_1}{\partial\psi} \geq C_{\mathcal{G},\psi} \geq 0. \tag{3.22}$$

A linear slip-dependent friction law can be regarded as a trivial interpretation of assumption ($\mathfrak{b}_1$) by taking $\mathcal{G}_1$ to be a linear function of ψ with a proportionality of $1/L_c$.

However, friction law (3.18) can be specified based on Assumption ($\mathfrak{b}_2$) by (*cf.* [135, p. 1873])

$$f(s,\psi) = \left(f_0 + a\ln\left(\frac{s}{s_0}\right) + \psi\right), \tag{3.23}$$

where f_0 and s_0 are given reference values for friction coefficient and slip rate. It is usually arranged in a way such that $\psi = 0$ when $s = s_0$, and f_0 represents the friction coefficient at steady state and slip rate s_0. Assumption ($\mathfrak{b}_3$) indicates that with f given in (3.23), the steady state should take the form (*cf.* [124, p. 13,457])

$$\psi_{\text{ss}}(s) = -b\ln\left(\frac{s}{s_0}\right), \tag{3.24}$$

such that (*cf.* [124, eq. (7)])

$$f_{\text{ss}}(s) = f_0 + (a-b)\ln\left(\frac{s}{s_0}\right). \tag{3.25}$$

The sign of $a - b$ indicates whether the steady-state dependency is slip-strengthening or slip-weakening. In the above, the parameters a, b and L_c are independent of σ, s or ψ by assumption, and can be thereby evaluated at reference state σ_0, s_0 and ψ_0 [135].

3.2.3 The assumptions on material parameters and nonlinear friction laws

We give assumptions on the regularity of parameters following [50]. The reference density, ρ^0, is contained in $L^\infty(\overline{\Omega}) \cap W^{1,\infty}(\Omega)$, where $W^{1,\infty}$ is the space of C^0 functions whose weak gradient is in L^∞, and

$$\begin{cases} \rho^0(\boldsymbol{x}) \geq C_{\rho^0} > 0, & x \in \overline{\Omega} \\ \rho^0(\boldsymbol{x}) \equiv 0, & x \in \overline{\Omega}^c; \end{cases}$$

thus $\phi^0 \in H^2(\mathbb{R}^3)$ by elliptic regularity. In other words, $\nabla\nabla\phi^0 \in L^\infty(\mathbb{R}^3)^{3\times 3}$ is a symmetric matrix that is strongly elliptic. The prestress tensor $\boldsymbol{T}^0 \in L^\infty(\overline{\Omega})^{3\times 3}$ governed by (3.3) satisfies the symmetries

$$(T_0)_{ij} = (T_0)_{ji}, \quad i, j \in \{1, 2, 3\},$$

and the continuity on interfaces

$$[\![\boldsymbol{n} \cdot \boldsymbol{T}^0]\!] = 0.$$

We assume that $\boldsymbol{T}_\delta$ has the same symmetries and continuity as $\boldsymbol{T}^0$. The stiffness tensor $C_{ijkl} \in L^\infty(\overline{\Omega})^{3\times 3\times 3\times 3}$ satisfies the symmetries

$$C_{ijkl} = C_{klij} = C_{jikl} = C_{ijlk}, \quad i, j, k, l \in \{1, 2, 3\}.$$

It automatically follows that $\boldsymbol{\Lambda}^{\boldsymbol{T}^0} \in L^\infty(\overline{\Omega})^{3\times 3\times 3\times 3}$, which is also strongly elliptic and satisfies the symmetry relation

$$\Lambda^{\boldsymbol{T}^0}_{ijkl} = \Lambda^{\boldsymbol{T}^0}_{klij}, \quad i, j, k, l \in \{1, 2, 3\}.$$

For simplicity of the analysis, we use the laws of Dieterich-Ruina [135, p. 1875], which ignore the dependency on variational normal stress of the nonlinear state ODE

(4.5) *, and let $\mathcal{G} \equiv \mathcal{G}_1$, such that

$$\dot{\psi} + \mathcal{G}(s, \psi) = 0.$$

Furthermore, we assume that the nonlinear functions $\mathcal{F}$ and $\mathcal{G}$ are Lipschitz continuous and, in addition to (3.14) and (3.22), assume that

$$\begin{aligned}
&\frac{\partial \mathcal{F}}{\partial s} \geq C_{\mathcal{F},s} > 0, \quad C^{\star}_{\mathcal{F},\sigma} \geq \frac{\partial \mathcal{F}(\sigma, s, \psi)}{\partial \sigma} \geq C_{\mathcal{F},\sigma} > 0, \quad C^{\star}_{\mathcal{F},\psi} \geq \frac{\partial \mathcal{F}(\sigma, s, \psi)}{\partial \psi} \geq C_{\mathcal{F},\psi} > 0, \\
&\quad \text{and} \quad \frac{\partial \mathcal{G}_1}{\partial \psi} \geq C_{\mathcal{G},\psi} \geq 0, \quad \left| \frac{\partial \mathcal{G}(s, \psi)}{\partial s} \right| \leq C^{\star}_{\mathcal{G},s}.
\end{aligned} \tag{3.26}$$

3.3 The variational form

We bring the overall problem in a hyperbolic variational form of second order coupled with a nonlinear algebraic relation and time evolution of state on the interior slipping boundary or rupture plane. In this section, we present the procedure and give the Sobolev spaces for which well posedness holds.

3.3.1 Energy spaces, faults and trace theorem

In the Lipschitz composite domain $\Omega \in \mathbb{R}^3$, we redefine the space of square integrable functions as

$$L^2(\Omega) = \left\{ v \,\middle|\, \sum_{k=1}^{k_0} \| v \|^2_{L^2(\Omega_k)} < \infty \right\},$$

and the corresponding Sobolev spaces such as

$$H^1(\Omega) = \left\{ v \in L^2(\Omega) \,\middle|\, \nabla v \in L^2(\Omega) \right\}.$$

*The dependency of $\mathcal{G}$ on σ and $\dot{\sigma}$ does not harm the stability of the system if the Amontons-Coulomb law (3.18) is assumed, and if $\mathcal{G}$ is sufficiently smooth with regard to σ and $\dot{\sigma}$.

We denote by $C([0,T];H)$ and $C^1([0,T];H)$ the space of real-valued continuous and continuously differentiable functions from finite time interval $[0,T]$ to any Sobolev space H, with the norms

$$\begin{aligned} \| v \|_{C([0,T];H)} &:= \max_{t\in[0,T]} \| v(t) \|_H, \\ \| v \|_{C^1([0,T];H)} &:= \max_{t\in[0,T]} \| v(t) \|_H + \max_{t\in[0,T]} \| \dot{v}(t) \|_H. \end{aligned} \tag{3.27}$$

We use an equivalent norm in the space $C([0,T];H)$ depending on any positive scalar β defined as

$$\| v \|^{\star}_{C([0,T];H)} = \max_{t\in[0,T]} \left(e^{-\frac{t}{\beta}} \| v(t) \|_H \right).$$

We revisit the general trace theorem (*e.g.* [132, Theorem 1.3.1]) and rewrite it for interior boundaries. The quantities $\boldsymbol{v}^{\pm}$ related to any vector-value $\boldsymbol{v} \in H^1(\Omega)^3$ are defined in (3.1).

Lemma 3.1

Let $\Sigma_{\mathrm{f}_i} = \partial\Omega_k \cap \partial\Omega_{k'} \setminus \partial\Omega$ be a Lipschitz continuous interior boundary for two adjacent subdomains Ω_k and $\Omega_{k'}$.

(a) There exist two unique linear continuous maps (trace operators) $T_{\mathrm{f}_i^+} : H^1(\Omega_k)^3 \to H^{\frac{1}{2}}(\Sigma_{\mathrm{f}_i})^3$ and $T_{\mathrm{f}_i^-} : H^1(\Omega_{k'})^3 \to H^{\frac{1}{2}}(\Sigma_{\mathrm{f}_i})^3$, such that $T_{\mathrm{f}_i^+}(\boldsymbol{v}) = \boldsymbol{v}^+|_{\Sigma_{\mathrm{f}_i}}$ and $T_{\mathrm{f}_i^-}(\boldsymbol{v}) = \boldsymbol{v}^-|_{\Sigma_{\mathrm{f}_i}}$ for each $\boldsymbol{v} \in H^1(\Omega)^3$.

(b) There exists two linear continuous maps (extension operators) $R_{\mathrm{f}_i^+} : H^{\frac{1}{2}}(\Sigma_{\mathrm{f}_i})^3 \to H^1(\Omega_k)^3$ and $R_{\mathrm{f}_i^-} : H^{\frac{1}{2}}(\Sigma_{\mathrm{f}_i})^3 \to H^1(\Omega_{k'})^3$, such that $T_{\mathrm{f}_i^+} \circ R_{\mathrm{f}_i^+}(\boldsymbol{v}) = T_{\mathrm{f}_i^-} \circ R_{\mathrm{f}_i^-}(\boldsymbol{v}) = \boldsymbol{v}$, for each $\boldsymbol{v} \in H^{\frac{1}{2}}(\Sigma_{\mathrm{f}_i})^3$.

This lemma implies the existence of constants $C_{\mathrm{f}_i}^{\pm} > 0$ such that

$$\left\| T_{\mathrm{f}_i^+}(\boldsymbol{v}) \right\|^2_{L^2(\Sigma_{\mathrm{f}_i})} \le C_{\mathrm{f}_i^+} \| \boldsymbol{v} \|^2_{H^1(\Omega_k)} \text{ and } \left\| T_{\mathrm{f}_i^-}(\boldsymbol{v}) \right\|^2_{L^2(\Sigma_{\mathrm{f}_i})} \le C_{\mathrm{f}_i^-} \| \boldsymbol{v} \|^2_{H^1(\Omega_{k'})}, \quad \forall v \in H^1(\Omega)^3. \tag{3.28}$$

We denote by T_{f} the direct union of all $T_{\mathrm{f}_i^{\pm}}$, and $C_{\mathrm{f}} = \max_{(i,\pm)} C_{\mathrm{f}_i^{\pm}}$. We can then define the tangential jump operator $T_{\mathrm{f}_{-}^{+}}$ for interior boundaries that generates $\boldsymbol{s} = T_{\mathrm{f}_{-}^{+}}(\dot{\boldsymbol{u}})$ and yields the following lemma, which can be obtained directly from Lemma 3.1.

Lemma 3.2

Let Ω be a Lipschitz composite domain and Σ_{f} be subset of its Lipschitz continuous interior boundaries.

(a) *There exists a unique linear continuous map $T_{\mathrm{f}_{-}^{+}} : H^1(\Omega)^3 \to H^{\frac{1}{2}}(\Sigma_{\mathrm{f}})^3$ such that $T_{\mathrm{f}_{-}^{+}}(\boldsymbol{v}) = [\![\boldsymbol{v}_{\parallel}]\!]$, for each $\boldsymbol{v} \in H^1(\Omega)^3$.*

(b) *There exists a linear continuous map $R_{\mathrm{f}_{-}^{+}} : H^{\frac{1}{2}}(\Sigma_{\mathrm{f}})^3 \to H^1(\Omega)^3$ such that $T_{\mathrm{f}_{-}^{+}} \circ R_{\mathrm{f}_{-}^{+}}(\boldsymbol{v}) = \boldsymbol{v}$ for each $\boldsymbol{v} \in H^{\frac{1}{2}}(\Sigma_{\mathrm{f}})^3$.*

(c) *There exist a constant $C_{\mathrm{f}_{-}^{+}} > 0$ such that*

$$\| [\![\boldsymbol{v}_{\parallel}]\!] \|^2_{L^2(\Sigma_{\mathrm{f}})} = \left\| T_{\mathrm{f}_{-}^{+}}(\boldsymbol{v}) \right\|^2_{L^2(\Sigma_{\mathrm{f}})} \leq C_{\mathrm{f}_{-}^{+}} \| \boldsymbol{v} \|^2_{H^1(\Omega)}, \quad \forall \boldsymbol{v} \in H^1(\Omega)^3. \tag{3.29}$$

We introduce the (bounded linear) Dirichlet-to-Neumann maps [145, 14, 13] associated with the elastic wave equation (5.2),

$$\begin{aligned} \Lambda_{\boldsymbol{\Lambda}^{\boldsymbol{T}^0},\rho^0,\phi^0} &: H^{\frac{1}{2}}(\Sigma_{\mathrm{f}})^3 \ni T_{\mathrm{f}}(\boldsymbol{u}) \to \left(\boldsymbol{n} \cdot (\boldsymbol{\Lambda}^{\boldsymbol{T}^0} : \nabla \boldsymbol{u})\right)\big|_{\Sigma_{\mathrm{f}}} \in H^{-\frac{1}{2}}(\Sigma_{\mathrm{f}})^3, \\ \Lambda'_{\boldsymbol{\Lambda}^{\boldsymbol{T}^0},\rho^0,\phi^0} &: H^{\frac{1}{2}}(\Sigma_{\mathrm{f}})^3 \ni T_{\mathrm{f}}(\boldsymbol{u}) \to \left(\nabla^{\Sigma} \cdot (\boldsymbol{u}(\boldsymbol{n} \cdot \boldsymbol{T}^0))\right)\big|_{\Sigma_{\mathrm{f}}} \in H^{-\frac{1}{2}}(\Sigma_{\mathrm{f}})^3. \end{aligned}$$

Clearly,

$$\begin{aligned} \| \boldsymbol{\tau}_1 \|^2_{H^{-\frac{1}{2}}(\Sigma_{\mathrm{f}})} &= \left\| \Lambda_{\boldsymbol{\Lambda}^{\boldsymbol{T}^0},\rho^0,\phi^0} \circ T_{\mathrm{f}}\left(\boldsymbol{u}\right) \right\|^2_{H^{-\frac{1}{2}}(\Sigma_{\mathrm{f}})} \leq C_{\Lambda} \| \boldsymbol{u} \|^2_{H^{\frac{1}{2}}(\Sigma_{\mathrm{f}})}, \\ \| \boldsymbol{\tau}_2 \|^2_{H^{-\frac{1}{2}}(\Sigma_{\mathrm{f}})} &= \left\| \Lambda'_{\boldsymbol{\Lambda}^{\boldsymbol{T}^0},\rho^0,\phi^0} \circ T_{\mathrm{f}}\left(\boldsymbol{u}\right) \right\|^2_{H^{-\frac{1}{2}}(\Sigma_{\mathrm{f}})} \leq C_{\Lambda'} \| \boldsymbol{u} \|^2_{H^{\frac{1}{2}}(\Sigma_{\mathrm{f}})}. \end{aligned} \tag{3.30}$$

We have

Theorem 3.1

Let T_{f}, $T_{\mathrm{f}^{+}_{-}}$, $\Lambda_{\boldsymbol{\Lambda}^{\boldsymbol{T}^0},\rho^0,\phi^0}$ *and* $\Lambda'_{\boldsymbol{\Lambda}^{\boldsymbol{T}^0},\rho^0,\phi^0}$ *as defined above, then there exist constants* $C_I, C_I' > 0$ *such that*

$$\begin{aligned} \left(\Lambda_{\boldsymbol{\Lambda}^{\boldsymbol{T}^0},\rho^0,\phi^0} \circ T_{\mathrm{f}}\,(\boldsymbol{u})\,,\, T_{\mathrm{f}^{+}_{-}}(\boldsymbol{v})\right)_{L^2(\Sigma_{\mathrm{f}})} &\leq C_I \|\boldsymbol{u}\,\|_{H^1(\Omega)} \|\boldsymbol{v}\,\|_{H^1(\Omega)}, \\ \left(\Lambda'_{\boldsymbol{\Lambda}^{\boldsymbol{T}^0},\rho^0,\phi^0} \circ T_{\mathrm{f}}\,(\boldsymbol{u})\,,\, T_{\mathrm{f}^{+}_{-}}(\boldsymbol{v})\right)_{L^2(\Sigma_{\mathrm{f}})} &\leq C_I' \|\boldsymbol{u}\,\|_{H^1(\Omega)} \|\boldsymbol{v}\,\|_{H^1(\Omega)}, \quad \forall \boldsymbol{u}, \boldsymbol{v} \in H^1(\Omega)^3. \end{aligned} \tag{3.31}$$

Proof 3.1 Based on the Cauchy-Schwartz inequality [145],

$$\left(\Lambda_{\boldsymbol{\Lambda}^{\boldsymbol{T}^0},\rho^0,\phi^0} \circ T_{\mathrm{f}}\,(\boldsymbol{u})\,,\, T_{\mathrm{f}^{+}_{-}}(\boldsymbol{v})\right)_{L^2(\Sigma_{\mathrm{f}})} \leq \left\| \Lambda_{\boldsymbol{\Lambda}^{\boldsymbol{T}^0},\rho^0,\phi^0} \circ T_{\mathrm{f}}\,(\boldsymbol{u}) \right\|_{H^{-\frac{1}{2}}(\Sigma_{\mathrm{f}})} \left\| T_{\mathrm{f}^{+}_{-}}(\boldsymbol{v}) \right\|_{H^{\frac{1}{2}}(\Sigma_{\mathrm{f}})}. \tag{3.32}$$

Using (5.85), (3.29) and (3.30) in (3.32), we immediately obtain

$$\left(\Lambda_{\boldsymbol{\Lambda}^{\boldsymbol{T}^0},\rho^0,\phi^0} \circ T_{\mathrm{f}}\,(\boldsymbol{u})\,,\, T_{\mathrm{f}^{+}_{-}}(\boldsymbol{v})\right)_{L^2(\Sigma_{\mathrm{f}})} \leq (C_\Lambda C_{\mathrm{f}} C_{\mathrm{f}^{+}_{-}}) \|\boldsymbol{u}\,\|_{H^1(\Omega)} \|\boldsymbol{v}\,\|_{H^1(\Omega)}.$$

Thus $C_I = C_\Lambda C_{\mathrm{f}} C_{\mathrm{f}^{+}_{-}}$. We can prove the second inequality in (3.31), with $C_I' = C_{\Lambda'} C_{\mathrm{f}} C_{\mathrm{f}^{+}_{-}}$, in the same manner.

This lemma will be used in Sections 5.5.2 and 3.5. We denote by $L^2(\Omega;\rho^0)$, $L^2(\Omega;\rho^0,\phi^0)$ and $L^2(\Omega;\boldsymbol{\Lambda}^{\boldsymbol{T}^0})$ the following weighted Hilbert spaces

$$\begin{aligned} L^2(\Omega;\rho^0) &:= \left\{ \boldsymbol{u} \in \mathbb{R}^3 \,\middle|\, \sum_{k=1}^{k_0} \int_{\Omega_k} \rho^0 |\boldsymbol{u}|^2 \,\mathrm{d}\Omega < \infty \right\}; \\ L^2(\Omega;\rho^0,\phi^0) &:= \left\{ \boldsymbol{u} \in \mathbb{R}^3 \,\middle|\, \sum_{k=1}^{k_0} \int_{\Omega_k} \rho^0 (\boldsymbol{u} \cdot (\nabla\nabla\phi^0) \cdot \boldsymbol{u}) \,\mathrm{d}\Omega < \infty \right\}; \\ L^2(\Omega;\boldsymbol{\Lambda}^{\boldsymbol{T}^0}) &:= \left\{ \boldsymbol{E} \in \mathbb{R}^{3\times 3} \,\middle|\, \sum_{k=1}^{k_0} \int_{\Omega_k} \boldsymbol{E} : (\boldsymbol{\Lambda}^{\boldsymbol{T}^0} : \boldsymbol{E}) \,\mathrm{d}\Omega < \infty \right\}, \end{aligned} \tag{3.33}$$

equipped with the respective inner products

$$\begin{aligned}
\big(\boldsymbol{v}, \boldsymbol{w}\big)_{L^2(\Omega;\rho^0)} &:= \sum_{k=1}^{k_0} \int_{\Omega_k} \rho^0 (\boldsymbol{v} \cdot \boldsymbol{w}) \, \mathrm{d}\Omega; \\
\big(\boldsymbol{v}, \boldsymbol{w}\big)_{L^2(\Omega;\rho^0,\phi^0)} &:= \sum_{k=1}^{k_0} \int_{\Omega_k} \rho^0 \boldsymbol{v} \cdot (\nabla\nabla\phi^0) \cdot \boldsymbol{w} \, \mathrm{d}\Omega; \qquad (3.34) \\
\big(\boldsymbol{E}, \boldsymbol{H}\big)_{L^2(\Omega;\boldsymbol{\Lambda}^{\boldsymbol{T}^0})} &:= \sum_{k=1}^{k_0} \int_{\Omega_k} \boldsymbol{H} : (\boldsymbol{\Lambda}^{\boldsymbol{T}^0} : \boldsymbol{E}) \, \mathrm{d}\Omega.
\end{aligned}$$

The space for the weak solution, $\boldsymbol{u}$, of the coupling problem is defined by

$$V := \big\{ \boldsymbol{u} \in H^1(\Omega)^3 \cap L^2(\Omega;\rho^0) \,\big|\, [[\boldsymbol{n} \cdot \boldsymbol{u}]] = 0 \text{ on } \Sigma_{\mathrm{f}} \big\}.$$

With the assumptions introduced in Section 3.2.3, the norms $\|\boldsymbol{u}\|^2_{L^2(\Omega)}$, $\|\boldsymbol{u}\|^2_{L^2(\Omega;\rho^0)}$ and $\|\boldsymbol{u}\|^2_{L^2(\Omega;\rho^0,\phi^0)}$ are equivalent and the norms $\|\nabla\boldsymbol{u}\|^2_{L^2(\Omega)}$ and $\|\nabla\boldsymbol{u}\|^2_{L^2(\Omega;\boldsymbol{\Lambda}^{\boldsymbol{T}^0})}$ are equivalent, for all $\forall \boldsymbol{u} \in V$. We introduce positive constants $C_{\rho^0}, C_{\phi^0}, C_{\boldsymbol{\Lambda}^{\boldsymbol{T}^0}}$ and $C^\star_{\rho^0}, C^\star_{\phi^0}, C^\star_{\boldsymbol{\Lambda}^{\boldsymbol{T}^0}}$ such that

$$\begin{aligned}
C_{\rho^0}\|\boldsymbol{u}\|^2_{L^2(\Omega)} &\le \|\boldsymbol{u}\|^2_{L^2(\Omega;\rho^0)} \le C^\star_{\rho^0}\|\boldsymbol{u}\|^2_{L^2(\Omega)}, \\
C_{\phi^0}\|\boldsymbol{u}\|^2_{L^2(\Omega)} &\le \|\boldsymbol{u}\|^2_{L^2(\Omega;\rho^0,\phi^0)} \le C^\star_{\phi^0}\|\boldsymbol{u}\|^2_{L^2(\Omega)}, \qquad (3.35) \\
C_{\boldsymbol{\Lambda}^{\boldsymbol{T}^0}}\|\nabla\boldsymbol{u}\|^2_{L^2(\Omega)} &\le \|\nabla\boldsymbol{u}\|^2_{L^2(\Omega;\boldsymbol{\Lambda}^{\boldsymbol{T}^0})} \le C^\star_{\boldsymbol{\Lambda}^{\boldsymbol{T}^0}}\|\nabla\boldsymbol{u}\|^2_{L^2(\Omega)}
\end{aligned}$$

for all $\boldsymbol{u} \in V$.

3.3.2 The weak form of the system of equations and viscosity solutions

We introduce the weak form on Ω while requiring the nonlinear friction law to hold pointwise. The techniques used to prove well-posedness are classical; see, for example, Martins and Oden [109], and Ionescu et al.(2003) [82].

We introduce a convex and Gâteaux differentiable approximation to friction force $\boldsymbol{\tau}_{\mathrm{f}}$ by defining the regularized slip rate as (*cf.* [82, (30)])

$$\Psi^\varepsilon(\boldsymbol{v}) = \sqrt{|\boldsymbol{v}|^2 + \varepsilon^2} - \varepsilon,$$

for some small constant $\varepsilon > 0$, whose gradient with regard to the slip velocity is denoted by

$$\boldsymbol{D}^{\varepsilon}(\boldsymbol{v}) = \frac{\boldsymbol{v}}{\sqrt{|\boldsymbol{v}|^2 + \varepsilon^2}}.$$

We then introduce the nonlinear map $F^{\varepsilon} : H^{-\frac{1}{2}}(\Sigma_{\mathrm{f}}) \times L^2(\Sigma_{\mathrm{f}}) \times V \times V \to \mathbb{R}$ as a family of regularized friction functionals,

$$F^{\varepsilon}(\sigma, \psi, \boldsymbol{u}, \boldsymbol{v}) = \int_{\Sigma_{\mathrm{f}}} \mathcal{F}\big(\sigma, |T_{\mathrm{f}_{-}^{+}}(\boldsymbol{u})|, \psi\big) \Psi^{\varepsilon}\big(T_{\mathrm{f}_{-}^{+}}(\boldsymbol{v})\big)\, \mathrm{d}\Sigma,$$
$$\sigma \in H^{-\frac{1}{2}}(\Sigma_{\mathrm{f}}), \quad \psi \in L^2(\Sigma_{\mathrm{f}}), \quad \boldsymbol{u}, \boldsymbol{v} \in V.$$

We denote by $\boldsymbol{F}^{\varepsilon} : H^{-\frac{1}{2}}(\Sigma_{\mathrm{f}}) \times L^2(\Sigma_{\mathrm{f}}) \times V \times V \to V^*$ the derivative of F^{ε} with respect to the last variable such that

$$\big(\boldsymbol{F}^{\varepsilon}(\sigma, \psi, \boldsymbol{u}, \boldsymbol{v}), \boldsymbol{w}\big)_{L^2(\Sigma_{\mathrm{f}})} = \int_{\Sigma_{\mathrm{f}}} \mathcal{F}(\sigma, |T_{\mathrm{f}_{-}^{+}}(\boldsymbol{u})|, \psi) \boldsymbol{D}^{\varepsilon}\big(T_{\mathrm{f}_{-}^{+}}(\boldsymbol{v})\big) \cdot \boldsymbol{w}\, \mathrm{d}\Sigma,$$

which represents the regularized replacement of $\boldsymbol{\tau}_{\mathrm{f}}$.

We write (5.2)-(3.9) in the following weak form, appended with an artificial (temporal) viscosity term weighted by $\gamma > 0$ and obtain

Problem 3.1

Find $\boldsymbol{u} \in C^1([0,T]; V)$ and $\psi \in C^1([0,T]; L^2(\Sigma_{\mathrm{f}}))$ such that

$$\begin{aligned}
&\big(\ddot{\boldsymbol{u}}\,,\,\boldsymbol{w}\big)_{L^2(\Omega;\rho^0)} - \frac{1}{4\pi G}\big(\nabla S(\boldsymbol{u})\,,\,\nabla S(\boldsymbol{w})\big)_{L^2(\mathbb{R}^3)} + \big(\boldsymbol{u}\,,\,\boldsymbol{w}\big)_{L^2(\Omega;\rho^0,\phi^0)} + \big(\nabla \boldsymbol{u}\,,\,\nabla \boldsymbol{w}\big)_{L^2(\Omega;\boldsymbol{\Lambda}^{\boldsymbol{T}^0})} \\
&\qquad + \gamma\big(\dot{\boldsymbol{u}}\,,\,\boldsymbol{w}\big)_{H^1(\Omega)} + \big(\boldsymbol{F}^{\varepsilon}(\sigma, \psi, \dot{\boldsymbol{u}}, \dot{\boldsymbol{u}})\,,\,T_{\mathrm{f}_{-}^{+}}(\boldsymbol{w})\big)_{L^2(\Sigma_{\mathrm{f}})} - \Big[\Big[\big(\boldsymbol{\tau}_2\,,\,\boldsymbol{w}\big)_{L^2(\Sigma_{\mathrm{f}})}\Big]\Big] \\
&\quad = \big(\boldsymbol{n} \cdot (\boldsymbol{T}^0 + \boldsymbol{T}_{\delta})\,,\,T_{\mathrm{f}_{-}^{+}}(\boldsymbol{w})\big)_{L^2(\Sigma_{\mathrm{f}})},
\end{aligned} \tag{3.36}$$

$$\big(\dot{\psi}, \varphi\big)_{L^2(\Sigma_{\mathrm{f}})} + \big(\mathcal{G}(|T_{\mathrm{f}_{-}^{+}}(\dot{\boldsymbol{u}})|, \psi), \varphi\big)_{L^2(\Sigma_{\mathrm{f}})} = 0, \tag{3.37}$$

with

$$
\begin{cases}
\boldsymbol{\tau}_2 = -\nabla^{\Sigma} \cdot \big(\boldsymbol{u}(\boldsymbol{n} \cdot \boldsymbol{T}^0)\big), \\
\\
\sigma = -\boldsymbol{n} \cdot \big(\boldsymbol{T}^0 + \boldsymbol{T}_\delta + \{\{\boldsymbol{\Lambda}^{\boldsymbol{T}^0} : \nabla \boldsymbol{u}\}\}\big) \cdot \boldsymbol{n} - \boldsymbol{n} \cdot \boldsymbol{\tau}_2
\end{cases}
\tag{3.38}
$$

on Σ_{f} *in the sense of traces, holds for all* $\boldsymbol{w} \in V$ *and* $\varphi \in L^2(\Sigma_{\mathrm{f}})$*, with* $\varepsilon \to 0$*.*

In the above, we used the integration by parts [50, eq. (4.10)],

$$
\begin{aligned}
\int_\Omega \rho^0 \nabla S(\boldsymbol{u}) \cdot \boldsymbol{w} \,\mathrm{d}\Omega &= \frac{1}{4\pi G} \int_{\mathbb{R}^3} S(\boldsymbol{u}) \big(-4\pi G \nabla \cdot (\rho^0 \dot{\boldsymbol{w}})\big) \,\mathrm{d}\Omega \\
&= \frac{1}{4\pi G} \int_{\mathbb{R}^3} S(\boldsymbol{u}) \Delta S(\boldsymbol{w}) \,\mathrm{d}\Omega = -\frac{1}{4\pi G} \int_{\mathbb{R}^3} \nabla S(\boldsymbol{u}) \cdot \nabla S(\boldsymbol{w}) \,\mathrm{d}\Omega.
\end{aligned}
\tag{3.39}
$$

Remark 3.1

In the formulation of Problem 4.2, the boundary conditions (3.6), (3.7) and (3.8) are enforced by surface integration. Since both $\Sigma \cap \partial\Omega$ *and* $\Sigma_{\mathrm{f}} \cap (\Sigma \setminus \Sigma_{\mathrm{f}})$ *are union of curves with measure* 0*, discontinuities that occur on these curves will not appear in the variational form. Therefore, the intersection of the slipping interior boundary with continuous interior boundaries or the external boundary with the traction-free condition does not affect the well-posedness results.*

3.4 Nonlinear coupling: A splitting scheme

Here, we present a robust linearly convergent splitting scheme. There are several reasons that lead to introducing a stable splitting algorithm. First, it simplifies the stability analysis through studying the behaviors of each of the subproblems. Secondly, it enables acceleration of solving the system through introducing preconditioners for each of the subproblems. Moreover, in the time discretization, it facilitates the use of different time steps; this is critically important, since the ruptures and wave propagation take place on significantly different time scales. Thirdly, we immediately obtain a proof of well-posedness by verifying whether the iterative coupling is a contraction.

3.4.1 The robust splitting scheme

We present the nonlinear iterative scheme, which decouples the computation of the seismic wave from that of the boundary source with state ODE as two split steps, which are given below. First, the hyperbolic boundary value problem is solved in the entire volume.

Step 1 *Given* $\boldsymbol{u}^{k-1} \in C([0,T];V)$, $\sigma^{k-1}, \boldsymbol{\tau}_2^{k-1} \in C([0,T];H^{-\frac{1}{2}}(\Sigma_{\mathrm{f}}))$ *and* $\psi^{k-1} \in C([0,T];L^2(\Sigma_{\mathrm{f}}))$, *find* $\boldsymbol{u}^k \in C([0,T];V)$ *such that for all* $\boldsymbol{w} \in V$ *in* Ω,

$$\begin{aligned}
&\big(\ddot{\boldsymbol{u}}^k\,,\,\boldsymbol{w}\big)_{L^2(\Omega;\rho^0)} - \frac{1}{4\pi G}\big(\nabla S(\boldsymbol{u}^{k-1})\,,\,\nabla S(\boldsymbol{w})\big)_{L^2(\mathbb{R}^3)} + \big(\boldsymbol{u}^k\,,\,\boldsymbol{w}\big)_{L^2(\Omega;\rho^0,\phi^0)}\\
&\quad + \big(\nabla\boldsymbol{u}^k\,,\,\nabla\boldsymbol{w}\big)_{L^2(\Omega;\boldsymbol{\Lambda}^{\boldsymbol{T}^0})} + \gamma\big(\dot{\boldsymbol{u}}^k, \boldsymbol{w}\big)_{H^1(\Omega)} + \big(\boldsymbol{F}^{\varepsilon}(\sigma^{k-1}, \psi^{k-1}, \dot{\boldsymbol{u}}^k, \dot{\boldsymbol{u}}^k)\,,\,T_{\mathrm{f}_-^+}(\boldsymbol{w})\big)_{L^2(\Sigma_{\mathrm{f}})}\\
&\quad - \Big[\Big[\big(\boldsymbol{\tau}_2^{k-1}\,,\,\boldsymbol{w}\big)_{L^2(\Sigma_{\mathrm{f}})}\Big]\Big] = \big(\boldsymbol{n}\cdot(\boldsymbol{T}^0 + \boldsymbol{T}_\delta)\,,\,T_{\mathrm{f}_-^+}(\boldsymbol{w})\big)_{L^2(\Sigma_{\mathrm{f}})}
\end{aligned} \tag{3.40}$$

with the initial condition independent of k,

$$\boldsymbol{u}^k\big|_{t=0} = \dot{\boldsymbol{u}}^k\big|_{t=0} = 0. \tag{3.41}$$

Once the wavefield is computed, we update the state variable and traction on the rupture.

Step 2 *Given* $\psi^{k-1} \in C([0,T];L^2(\Sigma_{\mathrm{f}}))$ *and* $\boldsymbol{u}^k \in C([0,T];V)$, *find* $\sigma^k, \boldsymbol{\tau}_2^k \in C([0,T];H^{-\frac{1}{2}}(\Sigma_{\mathrm{f}}))$ *and* $\psi^k \in C([0,T];L^2(\Sigma_{\mathrm{f}}))$, *such that for all* $\varphi \in$

$L^2(\Sigma_{\mathrm{f}})$.

$$\begin{cases} \boldsymbol{\tau}_2^k = -\nabla^{\Sigma} \cdot \big(\boldsymbol{u}^k(\boldsymbol{n}\cdot\boldsymbol{T}^0)\big), \\ \\ \sigma^k = -\boldsymbol{n}\cdot(\boldsymbol{T}^0 + \boldsymbol{T}_\delta + \{\{\boldsymbol{\Lambda}^{\boldsymbol{T}^0} : \nabla\boldsymbol{u}^k\}\})\cdot\boldsymbol{n} - \{\{\boldsymbol{n}\cdot\boldsymbol{\tau}_2^k\}\}, \end{cases} \tag{3.42}$$

and

$$\big(\dot{\psi}^k, \varphi\big)_{L^2(\Sigma_{\mathrm{f}})} + \big(\mathcal{G}(|T_{\mathrm{f}_-^+}(\dot{\boldsymbol{u}}^k)|, \psi^k), \varphi\big)_{L^2(\Sigma_{\mathrm{f}})} = 0, \tag{3.43}$$

with the initial condition independent of k,

$$\psi^k\big|_{t=0} = \psi^0. \tag{3.44}$$

The updated variables from Step 2 are then used in computing the Neumann boundary condition in Step 1, which starts the next iteration, until convergence. In the next subsection, we give a convergence proof that involves a bound on the viscosity coefficient, γ, in terms of the material parameters and the trace inequality.

3.4.2 Convergence

We show that the splitting scheme is linearly convergent with $\lambda^{-1} \in (0,1)$ the convergence rate, within any finite time interval $[0,T]$ under certain conditions, and prove the uniqueness of solution of Problem 3.1 via the Banach fixed point theorem.

Theorem 3.2

Let the coefficients β and γ satisfy

$$\begin{aligned} &\frac{1}{\beta} \geq \max\left(\frac{\lambda C_{\mathcal{F},\psi}^{\star\,2}}{C_{\mathcal{F},s}} + \Big(\frac{C_{\mathcal{G},s}^{\star\,2}}{C_{\mathcal{F},s}} - 2C_{\mathcal{G},\psi}\Big)\,,\quad \frac{C_S C_{\rho^0}^\star}{4\pi G C_{\rho^0}},\quad \frac{C_S C_{\rho^0}^\star \lambda}{4\pi G C_{\phi^0}}\right), \\ &\gamma \geq \beta\big(((C_I + C_I')C_{\mathcal{F},\sigma}^\star)^2 + C_I'^{\,2}\big)\max\left(\Big(\frac{C_{\phi^0}}{\lambda} - \frac{C_S C_{\rho^0}^\star \beta}{4\pi G}\Big)^{-1},\quad \frac{\lambda}{C_{\boldsymbol{\Lambda}^{\boldsymbol{T}^0}}}\right). \end{aligned} \tag{3.45}$$

Then the solution of split coupling scheme (3.40)-(3.43) is a contraction within finite time interval $[0,T]$ and convergence rate $\lambda^{-1} \in (0,1)$.

Proof 3.2 We define the error vectors and scalars:

$$\boldsymbol{\epsilon}^k_{\boldsymbol{u}} := \boldsymbol{u}^k - \boldsymbol{u}, \quad \boldsymbol{\epsilon}^k_{\boldsymbol{\tau}_2} := \boldsymbol{\tau}^k_2 - \boldsymbol{\tau}_2, \quad \boldsymbol{\epsilon}^k_{\boldsymbol{F}^\varepsilon} := \boldsymbol{F}^\varepsilon(\sigma^{k-1}, \psi^{k-1}, \dot{\boldsymbol{u}}^k, \dot{\boldsymbol{u}}^k) - \boldsymbol{F}^\varepsilon(\sigma, \psi, \dot{\boldsymbol{u}}, \dot{\boldsymbol{u}}),$$

$$\epsilon^k_\sigma := \sigma^k - \sigma, \qquad \epsilon^k_\psi := \psi^k - \psi, \qquad \epsilon^k_{\mathcal{F}} := \mathcal{F}(\sigma^{k-1}, |T_{\mathrm{f}^+_-}(\dot{\boldsymbol{u}}^k)|, \psi^{k-1}) - \mathcal{F}(\sigma, |T_{\mathrm{f}^+_-}(\dot{\boldsymbol{u}})|, \psi),$$

and

$$\begin{aligned}
&\epsilon^k_{\mathcal{G}} := \mathcal{G}(\sigma^k, |T_{\mathrm{f}^+_-}(\dot{\boldsymbol{u}}^k)|, \psi^k) - \mathcal{G}(\sigma, |T_{\mathrm{f}^+_-}(\dot{\boldsymbol{u}})|, \psi)\,, \\
&\epsilon^k_s := |T_{\mathrm{f}^+_-}(\dot{\boldsymbol{u}}^k)| - |T_{\mathrm{f}^+_-}(\dot{\boldsymbol{u}})|\,, \quad \epsilon^{\varepsilon,k}_s := \sqrt{|T_{\mathrm{f}^+_-}(\dot{\boldsymbol{u}}^k)|^2 + \varepsilon^2} - \sqrt{|T_{\mathrm{f}^+_-}(\dot{\boldsymbol{u}})|^2 + \varepsilon^2} \quad .
\end{aligned}$$

It is immediate that

$$\left|\epsilon^k_s\right| \le \left|T_{\mathrm{f}^+_-}(\dot{\boldsymbol{\epsilon}}^k_{\boldsymbol{u}})\right| = \left|T_{\mathrm{f}^+}(\dot{\boldsymbol{\epsilon}}^k_{\boldsymbol{u}})_\parallel - T_{\mathrm{f}^-}(\dot{\boldsymbol{\epsilon}}^k_{\boldsymbol{u}})_\parallel\right| \le \left|T_{\mathrm{f}^+}(\dot{\boldsymbol{\epsilon}}^k_{\boldsymbol{u}})\right| + \left|T_{\mathrm{f}^-}(\dot{\boldsymbol{\epsilon}}^k_{\boldsymbol{u}})\right|, \tag{3.46}$$

which, following (5.85), gives

$$\left\|\epsilon^k_s\right\|^2_{L^2(\Sigma_{\mathrm{f}})} \le \left\|T_{\mathrm{f}^+_-}(\dot{\boldsymbol{\epsilon}}^k_{\boldsymbol{u}})\right\|^2_{L^2(\Sigma_{\mathrm{f}})} \le \left\|T_{\mathrm{f}}(\dot{\boldsymbol{\epsilon}}^k_{\boldsymbol{u}})\right\|^2_{L^2(\Sigma_{\mathrm{f}})} \le C_{\mathrm{f}}\left\|\dot{\boldsymbol{\epsilon}}^k_{\boldsymbol{u}}\right\|^2_{H^1(\Omega)}. \tag{3.47}$$

It is clear that $\epsilon^k_s\, \epsilon^{\varepsilon,k}_s \ge 0$. Subtracting (5.32) from (3.40) at iteration k yields the error estimate,

$$\begin{aligned}
&\big(\ddot{\boldsymbol{\epsilon}}^k_{\boldsymbol{u}}, \boldsymbol{w}\big)_{L^2(\Omega;\rho^0)} - \frac{1}{4\pi G}\big(\nabla S(\boldsymbol{\epsilon}^{k-1}_{\boldsymbol{u}}), \nabla S(\boldsymbol{w})\big)_{L^2(\mathbb{R}^3)} + \big(\boldsymbol{\epsilon}^k_{\boldsymbol{u}}, \boldsymbol{w}\big)_{L^2(\Omega;\rho^0,\phi^0)} + \big(\nabla\boldsymbol{\epsilon}^k_{\boldsymbol{u}}, \nabla\boldsymbol{w}\big)_{L^2(\Omega;\boldsymbol{\Lambda}^{\boldsymbol{T}^0})} \\
&\qquad + \gamma\big(\dot{\boldsymbol{\epsilon}}^k_{\boldsymbol{u}}, \boldsymbol{w}\big)_{H^1(\Omega)} + \big(\boldsymbol{\epsilon}^k_{\boldsymbol{F}^\varepsilon}\,,\, T_{\mathrm{f}^+_-}(\boldsymbol{w})\big)_{L^2(\Sigma_{\mathrm{f}})} - \Big[\Big[\big(\boldsymbol{\epsilon}^{k-1}_{\boldsymbol{\tau}_2}\,,\, \boldsymbol{w}\big)_{L^2(\Sigma_{\mathrm{f}})}\Big]\Big] = 0.
\end{aligned} \tag{3.48}$$

We let $\boldsymbol{w} = \dot{\boldsymbol{\epsilon}}^k_{\boldsymbol{u}}$, so that (3.48) implies

$$\begin{aligned}
&\frac{1}{2}\frac{\partial}{\partial t}\Big(\left\|\dot{\boldsymbol{\epsilon}}^k_{\boldsymbol{u}}\right\|^2_{L^2(\Omega;\rho^0)} + \left\|\boldsymbol{\epsilon}^k_{\boldsymbol{u}}\right\|^2_{L^2(\Omega;\rho^0,\phi^0)} + \left\|\nabla\boldsymbol{\epsilon}^k_{\boldsymbol{u}}\right\|^2_{L^2(\Omega;\boldsymbol{\Lambda}^{\boldsymbol{T}^0})}\Big) + \gamma\left\|\dot{\boldsymbol{\epsilon}}^k_{\boldsymbol{u}}\right\|^2_{H^1(\Omega)} \\
&\quad \le \frac{1}{4\pi G}\big(\nabla S(\boldsymbol{\epsilon}^{k-1}_{\boldsymbol{u}})\,,\, \nabla S(\dot{\boldsymbol{\epsilon}}^k_{\boldsymbol{u}})\big)_{L^2(\mathbb{R}^3))} - \big(\boldsymbol{\epsilon}^k_{\boldsymbol{F}^\varepsilon}\,,\, T_{\mathrm{f}^+_-}(\dot{\boldsymbol{\epsilon}}^k_{\boldsymbol{u}})\big)_{L^2(\Sigma_{\mathrm{f}})} + \Big[\Big[\big(\boldsymbol{\epsilon}^{k-1}_{\boldsymbol{\tau}_2}\,,\, \dot{\boldsymbol{\epsilon}}^k_{\boldsymbol{u}}\big)_{L^2(\Sigma_{\mathrm{f}})}\Big]\Big].
\end{aligned} \tag{3.49}$$

We denote by I_1, I_2 and I_3 the three terms on the right-hand side of (3.49). Based on [50, Page 28], we have

$$\|\nabla S(\boldsymbol{u})\|_{L^2(\mathbb{R}^3)}^2 \leq C_S \|\boldsymbol{u}\|_{L^2(\Omega;\rho^0)}^2,$$

so that

$$\begin{aligned} I_1 \leq & \frac{1}{8\pi G}\Big(\delta_1 \big\|\nabla S(\boldsymbol{\epsilon}_{\boldsymbol{u}}^{k-1})\big\|_{L^2(\mathbb{R}^3)}^2 + \frac{1}{\delta_1}\big\|\nabla S(\dot{\boldsymbol{\epsilon}}_{\boldsymbol{u}}^k)\big\|_{L^2(\mathbb{R}^3)}^2\Big) \\ \leq & \frac{C_S C_{\rho^0}^{\star}}{8\pi G}\Big(\delta_1 \big\|\boldsymbol{\epsilon}_{\boldsymbol{u}}^{k-1}\big\|_{L^2(\Omega)}^2 + \frac{1}{\delta_1}\big\|\dot{\boldsymbol{\epsilon}}_{\boldsymbol{u}}^k\big\|_{L^2(\Omega)}^2\Big). \end{aligned} \tag{3.50}$$

Meanwhile,

$$\begin{aligned} I_2 = & -\int_{\Sigma_\mathrm{f}} \bigg(\mathcal{F}\big(\sigma^{k-1}, |T_{\mathrm{f}_-^+}(\dot{\boldsymbol{u}}^k)|, \psi^{k-1}\big)\Big(\frac{|T_{\mathrm{f}_-^+}(\dot{\boldsymbol{u}}^k)|^2 - T_{\mathrm{f}_-^+}(\dot{\boldsymbol{u}}^k)\cdot T_{\mathrm{f}_-^+}(\dot{\boldsymbol{u}})}{\sqrt{|T_{\mathrm{f}_-^+}(\dot{\boldsymbol{u}}^k)|^2 + \varepsilon^2}}\Big) \\ & + \mathcal{F}\big(\sigma, |T_{\mathrm{f}_-^+}(\dot{\boldsymbol{u}})|, \psi\big)\Big(\frac{|T_{\mathrm{f}_-^+}(\dot{\boldsymbol{u}})|^2 - T_{\mathrm{f}_-^+}(\dot{\boldsymbol{u}}^k)\cdot T_{\mathrm{f}_-^+}(\dot{\boldsymbol{u}})}{\sqrt{|T_{\mathrm{f}_-^+}(\dot{\boldsymbol{u}})|^2 + \varepsilon^2}}\Big)\bigg)\,\mathrm{d}\Sigma. \end{aligned} \tag{3.51}$$

To simplify the notation in the algebraic manipulations, we let $f_1 = \mathcal{F}\big(\sigma^{k-1}, |T_{\mathrm{f}_-^+}(\dot{\boldsymbol{u}}^k)|, \psi^{k-1}\big)$, $f_2 = \mathcal{F}\big(\sigma, |T_{\mathrm{f}_-^+}(\dot{\boldsymbol{u}})|, \psi\big)$, $\boldsymbol{i} = T_{\mathrm{f}_-^+}(\dot{\boldsymbol{u}}^k)$ and $\boldsymbol{j} = T_{\mathrm{f}_-^+}(\dot{\boldsymbol{u}})$, when

$$I_2 = \int_{\Sigma_\mathrm{f}} \Big(f_1 \frac{-|\boldsymbol{i}|^2 + \boldsymbol{i}\cdot\boldsymbol{j}}{\sqrt{|\boldsymbol{i}|^2+\varepsilon^2}} + f_2 \frac{-|\boldsymbol{j}|^2 + \boldsymbol{i}\cdot\boldsymbol{j}}{\sqrt{|\boldsymbol{j}|^2+\varepsilon^2}}\Big)\,\mathrm{d}\Sigma.$$

Using the Cauchy-Schwartz inequality,

$$\boldsymbol{i}\cdot\boldsymbol{j} + \varepsilon^2 \leq \sqrt{(|\boldsymbol{i}|^2+\varepsilon^2)(|\boldsymbol{j}|^2+\varepsilon^2)},$$

and it follows that

$$\begin{aligned} & f_1 \frac{-|\boldsymbol{i}|^2 + \boldsymbol{i}\cdot\boldsymbol{j}}{\sqrt{|\boldsymbol{i}|^2+\varepsilon^2}} + f_2 \frac{-|\boldsymbol{j}|^2 + \boldsymbol{i}\cdot\boldsymbol{j}}{\sqrt{|\boldsymbol{j}|^2+\varepsilon^2}} \\ & \quad = f_1\Big(-\sqrt{|\boldsymbol{i}|^2+\varepsilon^2} + \frac{\boldsymbol{i}\cdot\boldsymbol{j}+\varepsilon^2}{\sqrt{|\boldsymbol{i}|^2+\varepsilon^2}}\Big) + f_2\Big(-\sqrt{|\boldsymbol{j}|^2+\varepsilon^2} + \frac{\boldsymbol{i}\cdot\boldsymbol{j}+\varepsilon^2}{\sqrt{|\boldsymbol{j}|^2+\varepsilon^2}}\Big) \\ & \quad \leq (f_1 - f_2)\big(-\sqrt{|\boldsymbol{i}|^2+\varepsilon^2} + \sqrt{|\boldsymbol{j}|^2+\varepsilon^2}\big). \end{aligned} \tag{3.52}$$

We note that

$$\left|\sqrt{|\boldsymbol{i}|^2+\varepsilon^2}-\sqrt{|\boldsymbol{j}|^2+\varepsilon^2}\right| \leq \big||\boldsymbol{i}|-|\boldsymbol{j}|\big|,$$

with the difference going to 0 uniformly as ε vanishes. Hence, $C_\varepsilon|\epsilon_s^k| \leq |\epsilon_s^{\varepsilon,k}| \leq |\epsilon_s^k|$, with the positive constant $C_\varepsilon \to 1$ for $\varepsilon \to 0$. Therefore, with the Lipschitz continuity of $\mathcal{F}$ expressed in (3.26),

$$\begin{aligned}
I_2 \leq & \int_{\Sigma_{\mathrm{f}}} \Big(\mathcal{F}\big(\sigma^{k-1}, |T_{\mathrm{f}_-^+}(\dot{\boldsymbol{u}}^k)|, \psi^{k-1}\big) - \mathcal{F}\big(\sigma, |T_{\mathrm{f}_-^+}(\dot{\boldsymbol{u}})|, \psi\big)\Big) \\
& \qquad\qquad \Big(\sqrt{|T_{\mathrm{f}_-^+}(\dot{\boldsymbol{u}})|^2+\varepsilon^2}-\sqrt{|T_{\mathrm{f}_-^+}(\dot{\boldsymbol{u}}^k)|^2+\varepsilon^2}\Big)\,\mathrm{d}\Sigma \\
= & -\int_{\Sigma_{\mathrm{f}}} \epsilon_{\mathcal{F}}^k\,\epsilon_s^{\varepsilon,k}\,\mathrm{d}\Sigma \approx -\int_{\Sigma_{\mathrm{f}}}\Big(\frac{\partial\mathcal{F}}{\partial s}\epsilon_s^k\,\epsilon_s^{\varepsilon,k} + \frac{\partial\mathcal{F}}{\partial\sigma}\epsilon_\sigma^{k-1}\,\epsilon_s^{\varepsilon,k} + \frac{\partial\mathcal{F}}{\partial\psi}\epsilon_\psi^{k-1}\,\epsilon_s^{\varepsilon,k}\Big)\,\mathrm{d}\Sigma \\
\leq & \int_{\Sigma_{\mathrm{f}}}\big(-C_{\mathcal{F},s}C_\varepsilon|\epsilon_s^k|^2 + C^\star_{\mathcal{F},\sigma}|\epsilon_\sigma^{k-1}||\epsilon_s^k| + C^\star_{\mathcal{F},\psi}|\epsilon_\psi^{k-1}||\epsilon_s^k|\big)\,\mathrm{d}\Sigma \\
\leq & -C_{\mathcal{F},s}C_\varepsilon\big\|\epsilon_s^k\big\|^2_{L^2(\Sigma_{\mathrm{f}})} + C^\star_{\mathcal{F},\sigma}\big(|\epsilon_\sigma^{k-1}|\,,\,|\epsilon_s^k|\big)_{L^2(\Sigma_{\mathrm{f}})} + C^\star_{\mathcal{F},\psi}\big(|\epsilon_\psi^{k-1}|\,,\,|\epsilon_s^k|\big)_{L^2(\Sigma_{\mathrm{f}})}. \\
{\scriptstyle(\varepsilon\to0)} \approx & -C_{\mathcal{F},s}\big\|\epsilon_s^k\big\|^2_{L^2(\Sigma_{\mathrm{f}})} + C^\star_{\mathcal{F},\sigma}\big(|\epsilon_\sigma^{k-1}|\,,\,|\epsilon_s^k|\big)_{L^2(\Sigma_{\mathrm{f}})} + C^\star_{\mathcal{F},\psi}\big(|\epsilon_\psi^{k-1}|\,,\,|\epsilon_s^k|\big)_{L^2(\Sigma_{\mathrm{f}})}.
\end{aligned} \tag{3.53}$$

Using Lemma 3.1 and then Young's inequality, we obtain

$$\begin{aligned}
\big(|\epsilon_\sigma^{k-1}|\,,\,|\epsilon_s^k|\big)_{L^2(\Sigma_{\mathrm{f}})} &= \Big(\big|\boldsymbol{n}\cdot\big(\mathit{\Lambda}_{\mathbf{\Lambda}\boldsymbol{T}^0,\rho^0,\phi^0} + \mathit{\Lambda}'_{\mathbf{\Lambda}\boldsymbol{T}^0,\rho^0,\phi^0}\big)\circ T_{\mathrm{f}}\,(\boldsymbol{\epsilon}_{\boldsymbol{u}}^k)\big|\,,\,\big|T_{\mathrm{f}_-^+}(\dot{\boldsymbol{\epsilon}}_{\boldsymbol{u}}^k)\big|\Big)_{L^2(\Sigma_{\mathrm{f}})} \\
&\leq (C_I + C_I')\big(\frac{1}{2\delta_2}\big\|\boldsymbol{\epsilon}_{\boldsymbol{u}}^{k-1}\big\|^2_{H^1(\Omega)} + \frac{\delta_2}{2}\big\|\dot{\boldsymbol{\epsilon}}_{\boldsymbol{u}}^k\big\|^2_{H^1(\Omega)}\big).
\end{aligned} \tag{3.54}$$

With the Cauchy-Schwartz and Young's inequalities, also

$$\big(|\epsilon_\psi^{k-1}|\,,\,|\epsilon_s^k|\big)_{L^2(\Sigma_{\mathrm{f}})} \leq \frac{1}{2\delta_3}\big\|\epsilon_\psi^{k-1}\big\|^2_{L^2(\Sigma_{\mathrm{f}})} + \frac{\delta_3}{2}\big\|\epsilon_s^k\big\|^2_{L^2(\Sigma_{\mathrm{f}})}. \tag{3.55}$$

Estimates leading to (3.54) also lead to,

$$\begin{aligned}
I_3 = \Big[\!\Big[\big(\boldsymbol{\epsilon}_{\boldsymbol{\tau}_2}^{k-1}\,,\,\dot{\boldsymbol{\epsilon}}_{\boldsymbol{u}}^k\big)_{L^2(\Sigma_{\mathrm{f}})}\Big]\!\Big] &\leq \sum_{+,-}\Big|\Big(\mathit{\Lambda}'_{\mathbf{\Lambda}\boldsymbol{T}^0,\rho^0,\phi^0}\circ T_{\mathrm{f}}\,(\boldsymbol{\epsilon}_{\boldsymbol{u}}^k)\,,\,T_{\mathrm{f}}(\dot{\boldsymbol{\epsilon}}_{\boldsymbol{u}}^k)\Big)_{L^2(\Sigma_{\mathrm{f}\pm})}\Big| \\
&\leq C_I'\big(\frac{1}{2\delta_4}\big\|\boldsymbol{\epsilon}_{\boldsymbol{u}}^{k-1}\big\|^2_{H^1(\Omega)} + \frac{\delta_4}{2}\big\|\dot{\boldsymbol{\epsilon}}_{\boldsymbol{u}}^k\big\|^2_{H^1(\Omega)}\big).
\end{aligned} \tag{3.56}$$

We subtract (3.37) from (3.43) at step k, and let $\varphi = \epsilon_\psi^k$ so that

$$\begin{aligned}\frac{1}{2}\frac{\partial}{\partial t}\big\|\epsilon_\psi^k\big\|^2_{L^2(\Sigma_\mathrm{f})} &= -\big(\epsilon_\mathcal{G}^k\,,\,\epsilon_\psi^k\big)_{L^2(\Sigma_\mathrm{f})} \le \int_{\Sigma_\mathrm{f}}\big(C^\star_{\mathcal{G},s}|\epsilon_s^k| - C_{\mathcal{G},\psi}|\epsilon_\psi^k|\big)|\epsilon_\psi^k|\,\mathrm{d}\Sigma\\ &\le \frac{C^\star_{\mathcal{G},s}}{2}\big(\frac{1}{\delta_5}\big\|\epsilon_\psi^k\big\|^2_{L^2(\Sigma_\mathrm{f})} + \delta_5\big\|\epsilon_s^k\big\|^2_{L^2(\Sigma_\mathrm{f})}\big) - C_{\mathcal{G},\psi}\big\|\epsilon_\psi^k\big\|^2_{L^2(\Sigma_\mathrm{f})},\end{aligned} \tag{3.57}$$

in which, based on (3.26),

$$|\epsilon_\mathcal{G}^k\,\epsilon_\psi^k| \approx \Big|\frac{\partial\mathcal{G}}{\partial s}\epsilon_s^k\,\epsilon_\psi^k + \frac{\partial\mathcal{G}}{\partial\psi}|\epsilon_\psi^k|^2\Big| \ge -\Big|\frac{\partial\mathcal{G}}{\partial s}\epsilon_s^k\,\epsilon_\psi^k\Big| + \frac{\partial\mathcal{G}}{\partial\psi}|\epsilon_\psi^k|^2 \ge -C^\star_{\mathcal{G},s}|\epsilon_s^k||\epsilon_\psi^k| + C_{\mathcal{G},\psi}|\epsilon_\psi^k|^2. \tag{3.58}$$

Combining (3.49)-(3.57), we get the estimate

$$\begin{aligned}&\frac{1}{2}\frac{\partial}{\partial t}\Big(C_{\rho^0}\big\|\dot{\boldsymbol{\epsilon}}_{\boldsymbol{u}}^k\big\|^2_{L^2(\Omega)} + C_{\phi^0}\big\|\boldsymbol{\epsilon}_{\boldsymbol{u}}^k\big\|^2_{L^2(\Omega)} + C_{\boldsymbol{\Lambda}^{\boldsymbol{T}^0}}\big\|\nabla\boldsymbol{\epsilon}_{\boldsymbol{u}}^k\big\|^2_{L^2(\Omega)} + \big\|\epsilon_\psi^k\big\|^2_{L^2(\Sigma_\mathrm{f})}\Big)\\ &\quad\le \frac{C_S C^\star_{\rho^0}\delta_1}{8\pi G}\big\|\boldsymbol{\epsilon}_{\boldsymbol{u}}^{k-1}\big\|^2_{L^2(\Omega)} + \big(\frac{C_I + C_I'}{2\delta_2}C^\star_{\mathcal{F},\sigma} + \frac{C_I'}{2\delta_4}\big)\big\|\boldsymbol{\epsilon}_{\boldsymbol{u}}^{k-1}\big\|^2_{H^1(\Omega)}\\ &\qquad + \frac{C^\star_{\mathcal{F},\psi}}{2\delta_3}\big\|\epsilon_\psi^{k-1}\big\|^2_{L^2(\Sigma_\mathrm{f})} + \frac{C_S C^\star_{\rho^0}}{8\pi G\delta_1}\big\|\dot{\boldsymbol{\epsilon}}_{\boldsymbol{u}}^k\big\|^2_{L^2(\Omega)} + \big(\frac{C^\star_{\mathcal{G},s}}{2\delta_5} - C_{\mathcal{G},\psi}\big)\big\|\epsilon_\psi^k\big\|^2_{L^2(\Sigma_\mathrm{f})}\\ &\qquad + \frac{1}{2}\Big((C_I + C_I')C^\star_{\mathcal{F},\sigma}\delta_2 + C_I'\delta_4 - 2\gamma\Big)\big\|\dot{\boldsymbol{\epsilon}}_{\boldsymbol{u}}^k\big\|^2_{H^1(\Omega)}\\ &\qquad + \frac{1}{2}\big(C^\star_{\mathcal{F},\psi}\delta_3 + C^\star_{\mathcal{G},s}\delta_5 - 2C_{\mathcal{F},s}\big)\big\|\epsilon_s^k\big\|^2_{L^2(\Sigma_\mathrm{f})}.\end{aligned} \tag{3.59}$$

We let $\delta_1 = 1$, $(C_I + C_I')C^\star_{\mathcal{F},\sigma}\delta_2 = C_I'\delta_4 = \gamma$ and $C^\star_{\mathcal{F},\psi}\delta_3 = C^\star_{\mathcal{G},s}\delta_5 = C_{\mathcal{F},s}$, and integrate (4.51) over $[0,t]$ with $t \le T$, whence

$$\begin{aligned}&C_{\rho^0}\big\|\dot{\boldsymbol{\epsilon}}_{\boldsymbol{u}}^k\big\|^2_{L^2(\Omega)} + C_{\phi^0}\big\|\boldsymbol{\epsilon}_{\boldsymbol{u}}^k\big\|^2_{L^2(\Omega)} + C_{\boldsymbol{\Lambda}^{\boldsymbol{T}^0}}\big\|\nabla\boldsymbol{\epsilon}_{\boldsymbol{u}}^k\big\|^2_{L^2(\Omega)} + \big\|\epsilon_\psi^k\big\|^2_{L^2(\Sigma_\mathrm{f})}\\ &\quad\le \int_0^t\Big(\frac{C_S C^\star_{\rho^0}}{4\pi G}\big\|\boldsymbol{\epsilon}_{\boldsymbol{u}}^{k-1}\big\|^2_{L^2(\Omega)} + \frac{1}{\gamma}\big(((C_I + C_I')C^\star_{\mathcal{F},\sigma})^2 + C_I'^{\,2}\big)\big\|\boldsymbol{\epsilon}_{\boldsymbol{u}}^{k-1}\big\|^2_{H^1(\Omega)}\\ &\qquad + \frac{C^{\star\,2}_{\mathcal{F},\psi}}{C_{\mathcal{F},s}}\big\|\epsilon_\psi^{k-1}\big\|^2_{L^2(\Sigma_\mathrm{f})} + \frac{C_S C^\star_{\rho^0}}{4\pi G}\big\|\dot{\boldsymbol{\epsilon}}_{\boldsymbol{u}}^k\big\|^2_{L^2(\Omega)} + \big(\frac{C^{\star\,2}_{\mathcal{G},s}}{C_{\mathcal{F},s}} - 2C_{\mathcal{G},\psi}\big)\big\|\epsilon_\psi^k\big\|^2_{L^2(\Sigma_\mathrm{f})}\Big)\,\mathrm{d}\tau\\ &\quad\le \Big(\int_0^t e^{\frac{\tau}{\beta}}\,\mathrm{d}\tau\Big)\Big(\frac{C_S C^\star_{\rho^0}}{4\pi G}\big\|\boldsymbol{\epsilon}_{\boldsymbol{u}}^{k-1}\big\|^{\star\,2}_{C([0,T];L^2(\Omega))}\\ &\qquad + \frac{1}{\gamma}\big(((C_I + C_I')C^\star_{\mathcal{F},\sigma})^2 + C_I'^{\,2}\big)\big\|\boldsymbol{\epsilon}_{\boldsymbol{u}}^{k-1}\big\|^{\star\,2}_{C([0,T];H^1(\Omega))} + \frac{C^{\star\,2}_{\mathcal{F},\psi}}{C_{\mathcal{F},s}}\big\|\epsilon_\psi^{k-1}\big\|^{\star\,2}_{C([0,T];L^2(\Sigma_\mathrm{f}))}\\ &\qquad + \frac{C_S C^\star_{\rho^0}}{4\pi G}\big\|\dot{\boldsymbol{\epsilon}}_{\boldsymbol{u}}^k\big\|^{\star\,2}_{C([0,T];L^2(\Omega))} + \big(\frac{C^{\star\,2}_{\mathcal{G},s}}{C_{\mathcal{F},s}} - 2C_{\mathcal{G},\psi}\big)\big\|\epsilon_\psi^k\big\|^{\star\,2}_{C([0,T];L^2(\Sigma_\mathrm{f}))}.\end{aligned} \tag{3.60}$$

We use the inequality,

$$\int_0^t e^{\frac{\tau}{\beta}}\,\mathrm{d}\tau = \beta\big(e^{\frac{t}{\beta}}-1\big) \le \beta e^{\frac{t}{\beta}}, \quad \forall \beta > 0,$$

and multiply both sides of (3.60) by $e^{-\frac{t}{\beta}}$, which yields

$$\begin{aligned}
&\Big(C_{\rho^0} - \frac{C_S C^\star_{\rho^0}\beta}{4\pi G}\Big)\big\|\dot{\boldsymbol{\epsilon}}^k_{\boldsymbol{u}}\big\|^{\star 2}_{C([0,T];L^2(\Omega))} + C_{\phi^0}\big\|\boldsymbol{\epsilon}^k_{\boldsymbol{u}}\big\|^{\star 2}_{C([0,T];L^2(\Omega))}\\
&\qquad + C_{\boldsymbol{\Lambda}\boldsymbol{T}^0}\big\|\nabla\boldsymbol{\epsilon}^k_{\boldsymbol{u}}\big\|^{\star 2}_{C([0,T];L^2(\Omega))} + \Big(1 - \big(\frac{C^{\star 2}_{\mathcal{G},s}}{C_{\mathcal{F},s}} - 2C_{\mathcal{G},\psi}\big)\beta\Big)\big\|\epsilon^k_\psi\big\|^{\star 2}_{C([0,T];L^2(\Sigma_{\mathrm{f}}))}\Big)\\
&\le \frac{C_S C^\star_{\rho^0}\beta}{4\pi G}\big\|\boldsymbol{\epsilon}^{k-1}_{\boldsymbol{u}}\big\|^{\star 2}_{C([0,T];L^2(\Omega))} + \frac{\beta}{\gamma}\big(((C_I + C'_I)C^\star_{\mathcal{F},\sigma})^2 + C'^{\,2}_I\big)\big\|\boldsymbol{\epsilon}^{k-1}_{\boldsymbol{u}}\big\|^{\star 2}_{C([0,T];H^1(\Omega))}\\
&\qquad + \frac{C^{\star 2}_{\mathcal{F},\psi}\beta}{C_{\mathcal{F},s}}\big\|\epsilon^{k-1}_\psi\big\|^{\star 2}_{C([0,T];L^2(\Sigma_{\mathrm{f}}))}\quad .
\end{aligned} \tag{3.61}$$

Clearly (3.61) is a contraction if (3.45) is satisfied, and a unique fixed point $(\boldsymbol{u},\psi)$ in $C^1([0,T];V\times L^2(\Sigma_{\mathrm{f}}))$ can be obtained.

Remark 3.2

To properly control the error, the parameter β should increase with the length of time interval T. For a long-time simulation, the overall time is subdivided into sufficiently small time invervals, namely,

$$[0,\delta t\,], [\delta t\,, 2\delta t\,], [2\delta t\,, 3\delta t\,], \cdots, [(N-1)\delta t\,, N\delta t\,], \quad \delta t\, := T/N,$$

and iterations are conducted within each time segment. In this way, a small β can be used in Theorem 4.1.

Remark 3.3

Based on Theorem 4.1, it is prohibited that γ takes the value of 0, in which case the uniqueness of solution for the continuous coupling problem is not guaranteed. However, γ can be a small positive number while asymptotically characterizing the physics of friction interacting with pure elasticity without viscosity.

3.5 Implicit discretization in time

We use the particle velocity $\boldsymbol{v} := \dot{\boldsymbol{u}}$, and discretize the time interval with a uniform time step $\delta t = \frac{T}{N}$, and let $t_n = n\delta t$. We use index n in the superscript $v^{(n)}$ to indicate a time dependent variable v corresponding to time step t_n. A backward Euler time discretization of Problem 4.2 gives the following formulation

Problem 3.2

Given solutions $\boldsymbol{u}^{(n-1)}, \boldsymbol{v}^{(n-1)} \in V$ *and* $\psi^{(n-1)} \in L^2(\Sigma_{\mathrm{f}})$ *for the previous time step* $t = t_{n-1}$*, find solutions* $\boldsymbol{u}^{(n)}, \boldsymbol{v}^{(n)} \in V$ *and* $\psi^{(n)} \in L^2(\Sigma_{\mathrm{f}})$ *for the current time step* $t = t_n$*, such that*

$$\begin{aligned}
&\frac{1}{\delta t}\big(\boldsymbol{v}^{(n)}\,,\,\boldsymbol{w}\big)_{L^2(\Omega;\rho^0)} - \frac{1}{4\pi G}\big(\nabla S(\boldsymbol{u}^{(n)})\,,\,\nabla S(\boldsymbol{w})\big)_{L^2(\mathbb{R}^3)} \\
&\qquad + \big(\boldsymbol{u}^{(n)}\,,\,\boldsymbol{w}\big)_{L^2(\Omega;\rho^0,\phi^0)} + \big(\nabla\boldsymbol{u}^{(n)}\,,\,\nabla\boldsymbol{w}\big)_{L^2(\Omega;\boldsymbol{\Lambda}^{\boldsymbol{T}^0})} + \gamma\big(\boldsymbol{v}^{(n)}\,,\,\boldsymbol{w}\big)_{H^1(\Omega)} \\
&\qquad + \big(\boldsymbol{F}^{\varepsilon}(\sigma^{(n)},\psi^{(n)},\boldsymbol{v}^{(n)},\boldsymbol{v}^{(n)})\,,\,T_{\mathrm{f}^{+}_{-}}(\boldsymbol{w})\big)_{L^2(\Sigma_{\mathrm{f}})} - \Big[\!\Big[\big(\boldsymbol{\tau}_2^{(n)}\,,\,\boldsymbol{w}\big)_{L^2(\Sigma_{\mathrm{f}})}\Big]\!\Big] \\
&\quad = \big(\boldsymbol{n}\cdot(\boldsymbol{T}^0 + \boldsymbol{T}_{\delta}^{(n)})\,,\,T_{\mathrm{f}^{+}_{-}}(\boldsymbol{w})\big)_{L^2(\Sigma_{\mathrm{f}})} + \frac{1}{\delta t}\big(\boldsymbol{v}^{(n-1)}\,,\,\boldsymbol{w}\big)_{L^2(\Omega;\rho^0)},
\end{aligned} \tag{3.62a}$$

$$\boldsymbol{\tau}_2^{(n)} + \nabla^{\Sigma}\cdot\big(\boldsymbol{u}^{(n)}(\boldsymbol{n}\cdot\boldsymbol{T}^0)\big) = 0, \tag{3.62b}$$

$$\sigma^{(n)} + \boldsymbol{n}\cdot\big\{\!\big\{\boldsymbol{\Lambda}^{\boldsymbol{T}^0} : \nabla\boldsymbol{u}^{(n)}\big\}\!\big\}\cdot\boldsymbol{n} + \boldsymbol{n}\cdot\boldsymbol{\tau}_2^{(n)} = -\boldsymbol{n}\cdot\big(\boldsymbol{T}^0 + \boldsymbol{T}_{\delta}^{(n)}\big), \tag{3.62c}$$

$$\boldsymbol{u}^{(n)} - \delta t\,\boldsymbol{v}^{(n)} = \boldsymbol{u}^{(n-1)}, \tag{3.62d}$$

$$\frac{1}{\delta t}\big(\psi^{(n)}\,,\,\varphi\big)_{L^2(\Sigma_{\mathrm{f}})} + \big(\mathcal{G}(|T_{\mathrm{f}^{+}_{-}}(\boldsymbol{v}^{(n)})|,\psi^{(n)}),\varphi\big)_{L^2(\Sigma_{\mathrm{f}})} = \frac{1}{\delta t}\big(\psi^{(n-1)}\,,\,\varphi\big)_{L^2(\Sigma_{\mathrm{f}})}. \tag{3.62e}$$

holds for all $\boldsymbol{w} \in V$ *and* $\varphi \in L^2(\Sigma_{\mathrm{f}})$*, with* $\varepsilon \to 0$*.*

The corresponding split coupling scheme is similar to the one in (3.40-3.43)

Problem 3.3

Given solutions $\boldsymbol{u}^{(n-1)}, \boldsymbol{v}^{(n-1)} \in V$ *and* $\psi^{(n-1)} \in L^2(\Sigma_\mathrm{f})$ *for the previous time step* $t = t_{n-1}$*, and solutions* $\boldsymbol{v}^{(n,k-1)} \in V$ *,* $\sigma^{(n,k-1)}, \boldsymbol{\tau}_2^{(n,k-1)} \in H^{-\frac{1}{2}}(\Sigma_\mathrm{f})$*, and* $\psi^{(n),k-1} \in L^2(\Sigma_\mathrm{f})$ *for the current time step* $t = t_n$ *at iteration* $k-1$*, find solutions* $\boldsymbol{u}^{(n,k)}, \boldsymbol{v}^{(n,k)} \in V$ *,* $\sigma^{(n,k)}, \boldsymbol{\tau}_2^{(n,k)} \in H^{-\frac{1}{2}}(\Sigma_\mathrm{f})$ *and* $\psi^{(n,k)} \in L^2(\Sigma_\mathrm{f})$ *at iteration* k*, such that*

$$\begin{aligned}
&\frac{1}{\delta t}\big(\boldsymbol{v}^{(n,k)}\,,\,\boldsymbol{w}\big)_{L^2(\Omega;\rho^0)} - \frac{1}{4\pi G}\big(\nabla S(\boldsymbol{u}^{(n,k-1)})\,,\,\nabla S(\boldsymbol{w})\big)_{L^2(\mathbb{R}^3)} \\
&\qquad + \big(\boldsymbol{u}^{(n,k)}\,,\,\boldsymbol{w}\big)_{L^2(\Omega;\rho^0,\phi^0)} + \big(\nabla \boldsymbol{u}^{(n,k)}\,,\,\nabla \boldsymbol{w}\big)_{L^2(\Omega;\boldsymbol{\Lambda}^{\boldsymbol{T}^0})} + \gamma\big(\boldsymbol{v}^{(n,k)}\,,\,\boldsymbol{w}\big)_{H^1(\Omega)} \\
&\qquad + \big(\boldsymbol{F}^{\varepsilon}(\sigma^{(n,k-1)}, \psi^{(n,k-1)}, \boldsymbol{v}^{(n,k)}, \boldsymbol{v}^{(n,k)})\,,\,T_{\mathrm{f}^+_-}(\boldsymbol{w})\big)_{L^2(\Sigma_\mathrm{f})} - \Big[\Big[\big(\boldsymbol{\tau}_2^{(n,k-1)}\,,\,\boldsymbol{w}\big)_{L^2(\Sigma_\mathrm{f})}\Big]\Big] \\
&\quad = \big(\boldsymbol{n}\cdot(\boldsymbol{T}^0 + \boldsymbol{T}_\delta^{(n)})\,,\,T_{\mathrm{f}^+_-}(\boldsymbol{w})\big)_{L^2(\Sigma_\mathrm{f})} + \frac{1}{\delta t}\big(\boldsymbol{v}^{(n-1)}\,,\,\boldsymbol{w}\big)_{L^2(\Omega;\rho^0)},
\end{aligned} \tag{3.63a}$$

$$\boldsymbol{\tau}_2^{(n,k)} + \nabla^{\Sigma}\cdot\big(\boldsymbol{u}^{(n,k)}(\boldsymbol{n}\cdot\boldsymbol{T}^0)\big) = 0, \tag{3.63b}$$

$$\sigma^{(n,k)} + \boldsymbol{n}\cdot\big\{\big\{\boldsymbol{\Lambda}^{\boldsymbol{T}^0} : \nabla \boldsymbol{u}^{(n,k)}\big\}\big\}\cdot\boldsymbol{n} + \big\{\big\{\boldsymbol{n}\cdot\boldsymbol{\tau}_2^{(n,k)}\big\}\big\} = -\boldsymbol{n}\cdot(\boldsymbol{T}^0 + \boldsymbol{T}_\delta^{(n)}), \tag{3.63c}$$

$$\boldsymbol{u}^{(n,k)} - \delta t\,\boldsymbol{v}^{(n,k)} = \boldsymbol{u}^{(n-1)}, \tag{3.63d}$$

$$\frac{1}{\delta t}\big(\psi^{(n,k)}\,,\,\varphi\big)_{L^2(\Sigma_\mathrm{f})} + \big(\mathcal{G}(|T_{\mathrm{f}^+_-}(\boldsymbol{v}^{(n,k)})|, \psi^{(n,k)}), \varphi\big)_{L^2(\Sigma_\mathrm{f})} = \frac{1}{\delta t}\big(\psi^{(n-1)}\,,\,\varphi\big)_{L^2(\Sigma_\mathrm{f})}. \tag{3.63e}$$

hold for all $\boldsymbol{w} \in V$ *and* $\varphi \in L^2(\Sigma_\mathrm{f})$*, with* $\varepsilon \to 0$*.*

In the remainder of this section, we prove that the solution of Problem 3.3 converges to the unique solution of Problem 4.3 under some restrictions on the model coefficients and a given convergence rate $\lambda^{-1} \in (0,1)$, with larger λ indicating faster convergence.

Theorem 3.3

Let the coefficients γ and δt satisfy

$$
\begin{aligned}
\frac{1}{\delta t} &\geq \lambda \frac{C^{\star\,2}_{\mathcal{F},\psi}}{2C_{\mathcal{F},s}} + \frac{C^{\star\,2}_{\mathcal{G},s}}{2C_{\mathcal{F},s}} - C_{\mathcal{G},\psi}, \\
\frac{\gamma}{\delta t} &\geq \sqrt{\lambda}\Big(C^{\star}_{\mathcal{F},\sigma}(C_I + C_I') + C_I' \Big) - C_{\boldsymbol{\Lambda}^{\boldsymbol{T}^0}}, \\
\frac{\gamma}{\delta t} + \frac{C_{\rho^0}}{\delta t^{\,2}} &\geq \sqrt{\lambda}\Big(\frac{C_S C^{\star}_{\rho^0}}{4\pi G} + C^{\star}_{\mathcal{F},\sigma}(C_I + C_I') + C_I' \Big) - C_{\phi^0}.
\end{aligned} \tag{3.64}
$$

*Then the solution of split coupling scheme (3.63*a-e*) is a contraction with convergence rate $\lambda^{-1} \in (0,1)$.*

Proof 3.3 We define the error vectors and scalars

$$
\boldsymbol{\eta}^k_{\boldsymbol{v}} := \boldsymbol{v}^{(n,k)} - \boldsymbol{v}^{(n)}, \quad \boldsymbol{\eta}^k_{\boldsymbol{\tau}_2} := \boldsymbol{\tau}_2^{(n,k)} - \boldsymbol{\tau}_2^{(n)}, \quad \eta^k_{\sigma} := \sigma^{(n,k)} - \sigma^{(n)}, \quad \eta^k_{\psi} := \psi^{(n,k)} - \psi^{(n)}
$$

and

$$
\begin{aligned}
\boldsymbol{\eta}^k_{\boldsymbol{F}^\varepsilon} &:= \boldsymbol{F}^\varepsilon(\sigma^{(n,k-1)}, \psi^{(n,k-1)}, \boldsymbol{v}^{(n,k)}, \boldsymbol{v}^{(n,k)}) - \boldsymbol{F}^\varepsilon(\sigma^{(n)}, \psi^{(n)}, \boldsymbol{v}^{(n)}, \boldsymbol{v}^{(n)}), \\
\eta^k_{\mathcal{F}} &:= \mathcal{F}(\sigma^{(n,k-1)}, |T_{\mathrm{f}^+_-}(\boldsymbol{v}^{(n,k)})|, \psi^{(n,k-1)}) - \mathcal{F}(\sigma^{(n)}, |T_{\mathrm{f}^+_-}(\boldsymbol{v}^{(n)})|, \psi^{(n)}), \\
\eta^k_{\mathcal{G}} &:= \mathcal{G}(|T_{\mathrm{f}^+_-}(\boldsymbol{v}^{(n,k)})|, \psi^{(n,k)}) - \mathcal{G}(|T_{\mathrm{f}^+_-}(\boldsymbol{v}^{(n)})|, \psi^{(n)}), \\
\eta^k_{s} &:= |T_{\mathrm{f}^+_-}(\boldsymbol{u}^{(n,k)})| - |T_{\mathrm{f}^+_-}(\boldsymbol{u}^{(n)})|.
\end{aligned}
$$

Similar to (3.47),

$$
\big\|\eta^k_s\big\|^2_{L^2(\Sigma_{\mathrm{f}})} \leq \Big\| T_{\mathrm{f}^+_-}(\boldsymbol{\eta}^k_{\boldsymbol{v}}) \Big\|^2_{L^2(\Sigma_{\mathrm{f}})} \leq \big\| T_{\mathrm{f}}(\boldsymbol{\eta}^k_{\boldsymbol{v}}) \big\|^2_{L^2(\Sigma_{\mathrm{f}})} \leq C_{\mathrm{f}} \big\|\boldsymbol{\eta}^k_{\boldsymbol{v}}\big\|^2_{H^1(\Omega)}. \tag{3.65}
$$

We eliminate $\boldsymbol{u}^{(n)}$ and $\boldsymbol{u}^{(n),k}$ with (3.62d) and (3.63d), and subtract (3.62a–c) from (3.63a–c) at iteration k to obtain the error estimate

$$
\begin{aligned}
&\frac{1}{\delta t}\big(\boldsymbol{\eta}^k_{\boldsymbol{v}}\,,\,\boldsymbol{w}\big)_{L^2(\Omega;\rho^0)} - \frac{\delta t}{4\pi G}\big(\nabla S(\boldsymbol{\eta}^{k-1}_{\boldsymbol{v}})\,,\,\nabla S(\boldsymbol{w})\big)_{L^2(\mathbb{R}^3)} \\
&\quad + \delta t\,\big(\boldsymbol{\eta}^k_{\boldsymbol{v}}\,,\,\boldsymbol{w}\big)_{L^2(\Omega;\rho^0,\phi^0)} + \delta t\,\big(\nabla\boldsymbol{\eta}^k_{\boldsymbol{v}}\,,\,\nabla\boldsymbol{w}\big)_{L^2(\Omega;\boldsymbol{\Lambda}^{\boldsymbol{T}^0})} + \gamma\big(\boldsymbol{\eta}^k_{\boldsymbol{v}}\,,\,\boldsymbol{w}\big)_{H^1(\Omega)} \\
&\quad + \big(\boldsymbol{\eta}^k_{\boldsymbol{F}^\varepsilon}\,,\,T_{\mathrm{f}^+_-}(\boldsymbol{w})\big)_{L^2(\Sigma_{\mathrm{f}})} - \Big[\!\!\Big[\big(\boldsymbol{\eta}^{k-1}_{\boldsymbol{\tau}_2}\,,\,\boldsymbol{w}\big)_{L^2(\Sigma_{\mathrm{f}})}\Big]\!\!\Big] = 0,
\end{aligned} \tag{3.66}
$$

$$\boldsymbol{\eta}^k_{\boldsymbol{\tau}_2} = -\delta t\, \Lambda'_{\boldsymbol{\Lambda T}^0,\rho^0,\phi^0}(\boldsymbol{\eta}^k_{\boldsymbol{v}}), \tag{3.67}$$

$$\eta^k_\sigma = -\delta t\, \boldsymbol{n}\cdot\big(\Lambda_{\boldsymbol{\Lambda T}^0,\rho^0,\phi^0} + \Lambda'_{\boldsymbol{\Lambda T}^0,\rho^0,\phi^0}\big)(\boldsymbol{\eta}^k_{\boldsymbol{v}}). \tag{3.68}$$

We let $\boldsymbol{w} = \boldsymbol{\eta}^k_{\boldsymbol{v}}$, so that (3.66) becomes

$$\begin{aligned}\frac{1}{\delta t}\big\|\boldsymbol{\eta}^k_{\boldsymbol{v}}\big\|^2_{L^2(\Omega;\rho^0)} &+ \delta t\,\big\|\boldsymbol{\eta}^k_{\boldsymbol{v}}\big\|^2_{L^2(\Omega;\rho^0,\phi^0)} + \delta t\,\big\|\nabla\boldsymbol{\eta}^k_{\boldsymbol{v}}\big\|^2_{L^2(\Omega;\boldsymbol{\Lambda T}^0)} + \gamma\big\|\boldsymbol{\eta}^k_{\boldsymbol{v}}\big\|^2_{H^1(\Omega)} \\ &= \frac{\delta t}{4\pi G}\big(\nabla S(\boldsymbol{\eta}^{k-1}_{\boldsymbol{v}})\,,\,\nabla S(\boldsymbol{\eta}^k_{\boldsymbol{v}})\big)_{L^2(\mathbb{R}^3)} - \big(\boldsymbol{\eta}^k_{\boldsymbol{F}^\varepsilon}\,,\,T_{\mathrm{f}^\pm_-}(\boldsymbol{\eta}^k_{\boldsymbol{v}})\big)_{L^2(\Sigma_\mathrm{f})} + \Big[\!\Big[\big(\boldsymbol{\eta}^{k-1}_{\boldsymbol{\tau}_2}\,,\,\boldsymbol{\eta}^k_{\boldsymbol{v}}\big)_{L^2(\Sigma_\mathrm{f})}\Big]\!\Big].\end{aligned} \tag{3.69}$$

We denote by J_1, J_2 and J_3 the terms on the right-hand side of (3.69), and similar as in (3.50-3.56),

$$J_1 \leq \frac{\delta t\, C_S C^\star_{\rho^0}}{8\pi G}\left(\frac{1}{\delta_6}\big\|\boldsymbol{\eta}^{k-1}_{\boldsymbol{v}}\big\|^2_{L^2(\Omega)} + \delta_6\big\|\boldsymbol{\eta}^k_{\boldsymbol{v}}\big\|^2_{L^2(\Omega)}\right), \tag{3.70}$$

$$J_2 \leq - C_{\mathcal{F},s}\big\|\eta^k_s\big\|^2_{L^2(\Sigma_\mathrm{f})} + C^\star_{\mathcal{F},\sigma}\big(|\eta^{k-1}_\sigma|\,,\,|\eta^k_s|\big)_{L^2(\Sigma_\mathrm{f})} + C^\star_{\mathcal{F},\psi}\big(|\eta^{k-1}_\psi|\,,\,|\eta^k_s|\big)_{L^2(\Sigma_\mathrm{f})}, \tag{3.71}$$

with

$$\big(|\eta^{k-1}_\sigma|\,,\,|\eta^k_s|\big)_{L^2(\Sigma_\mathrm{f})} \leq \delta t\,(C_I + C_I')\left(\frac{1}{2\delta_7}\big\|\boldsymbol{\eta}^{k-1}_{\boldsymbol{v}}\big\|^2_{H^1(\Omega)} + \frac{\delta_7}{2}\big\|\boldsymbol{\eta}^k_{\boldsymbol{v}}\big\|^2_{H^1(\Omega)}\right), \tag{3.72}$$

$$\big(|\eta^{k-1}_\psi|\,,\,|\eta^k_s|\big)_{L^2(\Sigma_\mathrm{f})} \leq \left(\frac{1}{2\delta_3}\big\|\eta^{k-1}_\psi\big\|^2_{L^2(\Sigma_\mathrm{f})} + \frac{\delta_3}{2}\big\|\eta^k_s\big\|^2_{L^2(\Sigma_\mathrm{f})}\right) \tag{3.73}$$

and

$$J_3 \leq \delta t\, C_I'\left(\frac{1}{2\delta_8}\big\|\boldsymbol{\eta}^{k-1}_{\boldsymbol{v}}\big\|^2_{H^1(\Omega)} + \frac{\delta_8}{2}\big\|\boldsymbol{\eta}^k_{\boldsymbol{v}}\big\|^2_{H^1(\Omega)}\right). \tag{3.74}$$

We also subtract (3.62e) from (3.63e) at step k, let $\varphi = \eta^k_\psi$ and obtain the estimate

$$\begin{aligned}\frac{1}{\delta t}\big\|\eta^k_\psi\big\|^2_{L^2(\Sigma_\mathrm{f})} = \big(\eta^k_{\mathcal{G}}\,,\,\eta^k_\psi\big)_{L^2(\Sigma_\mathrm{f})} &\leq \int_{\Sigma_\mathrm{f}}\big(C^\star_{\mathcal{G},s}|\eta^k_s| - C_{\mathcal{G},\psi}|\eta^k_\psi|\big)|\eta^k_\psi|\,\mathrm{d}\Sigma \\ &\leq \frac{C^\star_{\mathcal{G},s}}{2}\big(\frac{1}{\delta_5}\big\|\eta^k_\psi\big\|^2_{L^2(\Sigma_\mathrm{f})} + \delta_5\big\|\eta^k_s\big\|^2_{L^2(\Sigma_\mathrm{f})}\big) - C_{\mathcal{G},\psi}\big\|\eta^k_\psi\big\|^2_{L^2(\Sigma_\mathrm{f})}.\end{aligned} \tag{3.75}$$

We use the constants in (3.35) in (3.69), and combine (3.69)-(3.75) to obtain

$$\begin{aligned}
&\Big(\frac{C_{\rho^0}}{\delta t} + \delta t\, C_{\phi^0} - \frac{\delta t\, C_S C^\star_{\rho^0}\delta_6}{8\,\pi G}\Big)\big\|\boldsymbol{\eta}^k_{\boldsymbol{v}}\big\|^2_{L^2(\Omega)} + \delta t\, C_{\boldsymbol{\Lambda}\boldsymbol{T}^0}\big\|\nabla\boldsymbol{\eta}^k_{\boldsymbol{v}}\big\|^2_{L^2(\Omega)}\\
&\quad + \Big(\gamma - \frac{\delta t\ \delta_7\, C^\star_{\mathcal{F},\sigma}(C_I + C_I')}{2} - \frac{\delta t\ \delta_8\, C_I'}{2}\Big)\big\|\boldsymbol{\eta}^k_{\boldsymbol{v}}\big\|^2_{H^1(\Omega)}\\
&\quad + \Big(\frac{1}{\delta t} - \frac{C^\star_{\mathcal{G},s}}{2\delta_5} + C_{\mathcal{G},\psi}\Big)\big\|\eta^k_\psi\big\|^2_{L^2(\Sigma_{\mathrm{f}})} + \Big(C_{\mathcal{F},s} - \frac{\delta_3\, C^\star_{\mathcal{F},\psi}}{2} - \frac{\delta_5\, C^\star_{\mathcal{G},s}}{2}\Big)\big\|\eta^k_s\big\|^2_{L^2(\Sigma_{\mathrm{f}})}\\
&\leq \frac{\delta t\ C_S C^\star_{\rho^0}}{8\pi G\,\delta_6}\big\|\boldsymbol{\eta}^{k-1}_{\boldsymbol{v}}\big\|^2_{L^2(\Omega)} + \Big(\frac{\delta t\, C^\star_{\mathcal{F},\sigma}(C_I + C_I')}{2\delta_7} + \frac{\delta t\, C_I'}{2\delta_8}\Big)\big\|\boldsymbol{\eta}^{k-1}_{\boldsymbol{v}}\big\|^2_{H^1(\Omega)} + \frac{C^\star_{\mathcal{F},\psi}}{2\delta_3}\big\|\eta^{k-1}_\psi\big\|^2_{L^2(\Sigma_{\mathrm{f}})}.
\end{aligned} \tag{3.76}$$

When choosing $C^\star_{\mathcal{F},\psi}\delta_3 = C^\star_{\mathcal{G},s}\delta_5 = C_{\mathcal{F},s}$ and $\delta_6 = \delta_7 = \delta_8 = \sqrt{\lambda}$, (3.76) becomes

$$\begin{aligned}
&\Big(\frac{C_{\rho^0}}{\delta t} + \delta t\, C_{\phi^0} - \frac{\delta t\,\sqrt{\lambda} C_S C^\star_{\rho^0}}{8\,\pi G}\Big)\big\|\boldsymbol{\eta}^k_{\boldsymbol{v}}\big\|^2_{L^2(\Omega)} + \delta t\, C_{\boldsymbol{\Lambda}\boldsymbol{T}^0}\big\|\nabla\boldsymbol{\eta}^k_{\boldsymbol{v}}\big\|^2_{L^2(\Omega)}\\
&\quad + \Big(\gamma - \frac{\delta t\ \sqrt{\lambda}}{2}\,\big(C^\star_{\mathcal{F},\sigma}(C_I + C_I') + C_I'\big)\Big)\big\|\boldsymbol{\eta}^k_{\boldsymbol{v}}\big\|^2_{H^1(\Omega)} + \Big(\frac{1}{\delta t} - \frac{C^{\star\,2}_{\mathcal{G},s}}{2C_{\mathcal{F},s}} + C_{\mathcal{G},\psi}\Big)\big\|\eta^k_\psi\big\|^2_{L^2(\Sigma_{\mathrm{f}})}\\
&\leq \frac{\delta t\ C_S C^\star_{\rho^0}}{8\pi G\,\sqrt{\lambda}}\big\|\boldsymbol{\eta}^{k-1}_{\boldsymbol{v}}\big\|^2_{L^2(\Omega)} + \frac{\delta t}{2\sqrt{\lambda}}\big(C^\star_{\mathcal{F},\sigma}(C_I + C_I') + C_I'\big)\big\|\boldsymbol{\eta}^{k-1}_{\boldsymbol{v}}\big\|^2_{H^1(\Omega)} + \frac{C^{\star\,2}_{\mathcal{F},\psi}}{2C_{\mathcal{F},s}}\big\|\eta^{k-1}_\psi\big\|^2_{L^2(\Sigma_{\mathrm{f}})}.
\end{aligned} \tag{3.77}$$

It is clear that (3.77) is a contraction if (3.64) is satisfied, and a unique fixed point $(\boldsymbol{u}^{(n)}, \boldsymbol{v}^{(n)}, \psi^{(n)})$ in $V \times V \times L^2(\Sigma_{\mathrm{f}})$ can be obtained.

Remark 3.4

Theorem 4.2 indicates that γ can be chosen proportional to δt to ensure that the general time-discretized coupling problem converges to a unique solution.

Remark 3.5

In order to obtain a stable solution of the discretized problem over a finite simulation time, δt and γ must satisfy the conditions in both (3.45) and (3.64).

3.6 Conclusions

We establish a mathematical understanding of coupling spontaneous ruptures and seismic wave generation in a self-gravitating Earth by developing a splitting scheme. Using such a scheme we give an analysis of well-posedness. Thus we obtain a rigorous connection between regional earthquake sources and seismic body and surface waves, and ground motion. We present a framework for general rate- and state-dependent friction laws based on observations from experiments. We couple the nonlinear system of time-evolving friction with the elastic-gravitatational system of equations describing seismic waves via a fixed-point iteration. We show that an artificial viscosity term is necessary to guarantee the well-posedness of the coupled system, while the magnitude of artificial damping can be chosen small in accordance with rigorous conditions given in the theorems.

Our analysis elucidates a multi-rate time stepping strategy, which is helpful in numerical implementations dealing with the nonlinearity of the ordinary differential equation for state evolution. This evolution requires a significantly finer time step than the seismic wave propagation and scattering.

Chapter 4

Solving the spontaneous rupture problem with DG method: a nonlinear optimization approach

4.1 Introduction

The interaction of ruptures with seismic waves is of great practical interest in geophysical research and energy production, such as in reservoir characterization, hydraulic fracturing, induced seismicity, natural earthquake source mechanism, and many other implementations (*e.g.* [115, 165, 46, 105]). In particular, the nucleation and propagation of ruptures vary distinctively with both friction laws (*e.g.* [22, 21, 141, 6, 100, 167]) and rupture geometries (*e.g.* [129, 84, 108]). Numerical simulation of the rupture processes governed by general friction laws can be challenging due to ill-conditioning of the nonlinear feedback of traction and slip into the friction coefficient ([135, 175]). Various types of numerical methods have been used for the dynamic rupture problem, such as the boundary integral equation method (BIEM) (*e.g.* [63]), which is based on layer potentials derived from fundamental solutions of elastic waves, and thus restricts the rupture model to planar geometry and homogeneous material parameters on each side of the fault. Meanwhile, many other numerical approaches are designed for more general and realistic problems, allowing flexibility in the geometry of rupture surfaces and heterogeneity in material properties. A widely used numerical scheme is the finite difference (FD) method, with carefully designed curvilinear grids capturing the ground topography and rupture geometry (*e.g.* [160, 181, 56]). Beyond the standard FD methods for the wave equation, an external weak representation of boundary conditions properly describing the coupling with friction law is required. Commonly used methods of this category are summation by parts (SBP) difference operator (*e.g.* [98]), and hybridizing with numerical schemes with inherent boundary integrations (*e.g.* [120]).

The finite element (FE) method accommodates fully unstructured meshes with local refinements, allowing much more flexibility in characterizing the complex geometry of rupture surfaces. It relies on a weak formulation for the elastic system as well as the boundary conditions, where coupling with friction is imposed (*e.g.* [106, 79, 1]. Traditional FE methods use linear basis functions and shared nodal points, which result in non-diagonal mass matrices and require techniques like mass-lumping for efficient solutions, but may lead to nonphysical oscillation phenomena. The spectral element (SE) method addresses this problem by using tensor products of orthogonal polynomial basis functions. While sacrificing some of the freedom by choosing only hexahedral meshes, the SE method results in a diagonal mass matrix that can be trivially inverted, and provides high polynomial order accuracy in wavefield simulations (*e.g.* [61]). Both FE and SE methods require splitting nodes locally on the rupture surface that allow for displacement discontinuity (*e.g.* [86, 175]).

It is more natural to solve problems with discontinuities, such as rupture dynamic problems, by using methods that completely split the domain into elements. Such methods are well known as the finite volume (FV) method and the discontinuous Galerkin (DG) method, in which the nodes across the interface of two adjacent elements are distinct, and both the continuous and jumping boundary conditions are weakly imposed via numerical flux. In other words, algorithms for the standard elastic wave problems can be used in rupture dynamics without major issues. There are multiple choices for the numerical flux, including the central flux (*e.g.* [11, 158]), which is energy conservative, but requires artificial or physical viscosity to overcome the possible spurious oscillations. An upwind flux is obtained as the solution to the Riemann problem on the interface, which takes the friction law into account in a more concise and self-consistent manner (*e.g.* [52, 171, 123, 180]). Among other types of numerical fluxes are penalty-based schemes (*e.g.* [138, 49]), which avoid the difficulty of diagonalizing the system with anisotropic or poroelastic materials that come with heterogeneity.

Our method of solving the coupled system of seismicity and dynamic ruptures is based on our previous work on the DG method with modified penalty flux [177]. The novelty lies in three aspects. First, we avoid the usage of impedance, or the reliance on the Riemann solution of any kind. Instead, we directly impose the distinct parts of the nonlinear friction law, the slip rate and the frictional force, into the variational form as a slip boundary condition in a weak sense. The stability of this method is ensured by penalty terms as well as a viscosity coefficient, which is proportional to the time step that can be chosen small. Meanwhile, we consider the full Euler-Lagrange equation, which takes into account the impact of the prestress and the self-gravitation potential on the field of motion. A so-called "Cowling approximation" is used, with which the perturbation of gravitational potential induced by particle motion is ignored. Nevertheless, the complete solution of the Euler-Lagrange equation can be obtained by coupling a Poisson's equation of gravitational potential, which can be solved by infinite domain techniques (*e.g.* [19, 64]). Last but not least, we give the proof of well-posedness for the rupture dynamic problem based on a mix form of strain-velocity, on both continuous and discretized variational forms. We utilize a multi-rate iterative coupling scheme ([5]), which was developed for solving the problem of coupling flow with geomechanics by taking multiple finer time steps for the stiff part of flow within one coarse time step for the Biot model. In a similar manner, the elastic wave equation defined in the 3-D domain is separated from the rupture model defined on surface, which contains the nonlinear friction law as well as the ordinary differential equation (ODE) of the time-evolving rupture state, and takes the form of Schur-complements in the full nonlinear implicit system. We use higher order time integration techniques with smaller times steps for the state ODE, and set up a nonlinearly constrained optimization problem, which is solved by the Gauss–Newton method, where the gradient and Hessian matrix can be easily formed and factorized in each finite element. A fixed-point iteration is used (see also [128]), with the proof of stability given in section 4.5. The overall algorithm greatly reduced the computation of the large implicit nonlinear problem, and yields linear complexity.

While we are focusing on the spontaneous ruptures driven by prestress, it is worthwhile to mention the relevance to fracture problems, which also involve slip boundary conditions. Like the rate- and state-friction law, the fracture models also include a feedback from slip to boundary tractions, but further allow normal jumps on the particle velocity across the fracturing boundary. A well adopted law describing the fracture model is the linear slip (LS) boundary condition (*e.g.* [148, 131])

$$\begin{bmatrix} \kappa_1 & & \\ & \kappa_2 & \\ & & \kappa_3 \end{bmatrix} [\![\boldsymbol{v}]\!] = \dot{\boldsymbol{\tau}},$$

where $[\![\boldsymbol{v}]\!]$ and $\boldsymbol{\tau}$ are the velocity jump and boundary tractions, respectively (see Section 4.2 for definitions), and κ_i are positive constants. By taking $\kappa_1 = \infty$ and $\kappa_2 = \kappa_3 = \kappa$, the model turns into a linear slip-strengthening rupture problem, which is a simplified version of a rate- and state-friction model by taking the nonlinear functions

$\mathcal{F}(\sigma, s, \psi) = \psi$ and $\mathcal{G}(s, \psi) = \kappa s$ in (4.4) and (4.5). The general rate- and state-friction models, on the other hand, involve more complex nonlinear feedback mechanism, which accounts for the procedures of multi-physics. In the case of significant slip-weakening with nonlinearity, simple explicit algorithms can hardly give converging solutions, and nonlinear iterations are usually required (*e.g.* [128, 56]).

4.2 The nonlinear boundary value problem in a weak form

We consider a 3-dimensional bounded domain $\Omega \subset \mathbb{R}^3$ in an isolated space, which is an approximation of the Earth with fully elastic (and allowed to be generally anisotropic) material ignoring the effects of fluid or anelasticity. We further assume that Ω is a disjoint union of Lipschitz subdomains $\Omega = \bigcup_{k=1}^{k_0} \Omega_k$, with interior boundaries given by

$$\Sigma = \bigcup_{1 \leq k < k' \leq I} \partial\Omega_k \cap \partial\Omega_{k'} \setminus \partial\Omega.$$

We denote by Σ_{c} the non-slip solid–solid interfaces, and by Σ_{f} the cracked rupture surface. We choose $\boldsymbol{n} : \partial\Omega_k \to \mathbb{R}^3$ almost everywhere on $\Sigma \cup \partial\Omega$, as the unit normal vector of interior and exterior boundaries, which satisfies $\boldsymbol{n} \in L^\infty(\Sigma \cup \partial\Omega)^3$, and labels the two sides across Σ by " -" and " +". We denote by $[\![v]\!] := v^+ - v^-$ and $\{\!\{ v \}\!\} := \frac{1}{2}(v^+ + v^-)$ respectively the difference and average of any scalar or vector quantity v across Σ. We include the prestress tensor $\boldsymbol{T}^0$ and the static self-gravitational potential ϕ^0, but ignore the mass redistribution potential, the rotation, and the body sources other than the spontaneous ruptures. Prior to any rupture cracks, the system is in steady state with force equilibrium and zero particle velocity. The spontaneous rupture occurs when the material fails at some parts of the pre-existing fault plane, and the crack spreads catastrophically to adjacent regions, which is also called the "propagation" of rupture (*e.g.* [41, p. 187]). We assume that

$\Sigma_{\rm f}$ is given in the first place, with the slip boundary conditions applied on $\Sigma_{\rm f}$ throughout the simulation time. The consideration of time-variant $\Sigma_{\rm f}$ is a delicate issue that is outside the scope of this paper. We define several notations over the initial steady state as is shown in the following table:

ρ^0	the initial density	$\boldsymbol{T}^0$	the pre-stress tensor
Φ^0	the initial gravitational potential	$\boldsymbol{\Lambda}^{\boldsymbol{T}^0}$	the prestressed ealstic tensor

and time dependent quantities are list as follows:

$\boldsymbol{u}$	the particle displacement	$\boldsymbol{v}$	the particle velocity
$\boldsymbol{E}$	the strain tensor	$\boldsymbol{s}$	slip velocity on rupture $\Sigma_{\rm f}$
$\boldsymbol{\tau}_{\rm f}$	friction force on rupture $\Sigma_{\rm f}$	$\boldsymbol{n}^s$	instantaneous normal direction of Σ
$\boldsymbol{T}^s$	Eulerian Cauchy stress	$\boldsymbol{\tau}^s$	total traction ($\approx \boldsymbol{n}^s \cdot \boldsymbol{T}^s$ up to first order)

We note the gravitational relation

$$\Delta\Phi^0 = 4\pi G\rho^0,$$

where G stands for the gravitational constant, and the mechanical equilibrium without self-rotation

$$\nabla \cdot \boldsymbol{T}^0 = \rho^0 \nabla \Phi^0.$$

We write $\boldsymbol{\Lambda}^{\boldsymbol{T}^0}$ as the modified stiffness tensor depending on $\boldsymbol{T}^0$ and the *in situ* isentropic elastic stiffness tensor $\boldsymbol{C}$ by

$$\Lambda^{\boldsymbol{T}^0}_{ijkl} := C_{ijkl} + \tfrac{1}{2}\left(T^0_{ij}\delta_{kl} + T^0_{kl}\delta_{ij} + T^0_{ik}\delta_{jl} - T^0_{jl}\delta_{ik} - T^0_{jk}\delta_{il} - T^0_{il}\delta_{jk}\right)$$

such that $\boldsymbol{\Lambda}^{\boldsymbol{T}^0} : \boldsymbol{E}$ stands for the first Piola-Kirchhoff stress. We use the subscript notation "$(\boldsymbol{.})_{\|}$" for tangential component with regards to $\boldsymbol{n}$, such as the tangential particle velocity,

$$\boldsymbol{v}_{\|} := (\boldsymbol{I} - \boldsymbol{n}^{\mathrm{T}}\boldsymbol{n}) \cdot \boldsymbol{v} = \boldsymbol{v} - (\boldsymbol{n} \cdot \boldsymbol{v})\boldsymbol{n},$$

where $\boldsymbol{I}$ is 3×3 identity matrix. The slip velocity is then defined by

$$\boldsymbol{s} := [\![\boldsymbol{v}_{\|}]\!]. \tag{4.1}$$

4.2.1 Dynamic boundary conditions

The particle velocity and the Cauchy stress on Σ_{f} satisfy the non-open slip boundary conditions [41, (2.80) and (2.81)],

$$[\![\boldsymbol{n}^s \cdot \boldsymbol{u}]\!] = 0, \quad [\![\boldsymbol{\tau}^s]\!] = 0, \quad \text{on } \Sigma_{\mathrm{f}}. \tag{4.2}$$

The force balancing on the rupture surface requires that the tangential component of total traction equates the friction force, that is, $\boldsymbol{\tau}^s_{\|} = \boldsymbol{\tau}_{\mathrm{f}}$, whose direction is opposite to slip velocity, which yields (e.g. Day et al.(2005) [47, (4)], Moczo et al.(2014) [110, p. 60]),

$$|\boldsymbol{\tau}_{\mathrm{f}}|\, \boldsymbol{s} - |\boldsymbol{s}|\, \boldsymbol{\tau}_{\mathrm{f}} = 0. \tag{4.3}$$

To simplify the notation, we denote by $s := |\boldsymbol{s}\,|$ the amplitude of slip velocity, or "slip-rate", and by $\tau_{\mathrm{f}} := |\boldsymbol{\tau}_{\mathrm{f}}|$ the magnitude of friction force. We focus on the Dieterich–Ruina friction law discussed in Rice et al.(2001) [135] with the dependency on compressive stress, slip-rate and state variable by

$$\tau_{\mathrm{f}} = \mathcal{F}(\sigma, s, \psi), \tag{4.4}$$

in which ψ describes the maturity of rupture, and satisfies the ordinary differential relation

$$\dot{\psi} = \mathcal{G}(s, \psi). \tag{4.5}$$

We assume that both $\mathcal{F}$ and $\mathcal{G}$ are Lipschitz continuous (see also [178, section 2]), with the partial derivatives bounded by constants,

$$\begin{aligned}
&0 < C_{\mathcal{F},\sigma} \leq \frac{\partial \mathcal{F}(\sigma, s, \psi)}{\partial \sigma} \leq C^{\star}_{\mathcal{F},\sigma}, \quad 0 < C_{\mathcal{F},\psi} \leq \frac{\partial \mathcal{F}(\sigma, s, \psi)}{\partial \psi} \leq C^{\star}_{\mathcal{F},\psi}, \\
&0 < C_{\mathcal{F},s} \leq \frac{\partial \mathcal{F}(\sigma, s, \psi)}{\partial s} \leq C^{\star}_{\mathcal{F},s}, \quad \frac{\partial \mathcal{G}(s, \psi)}{\partial \psi} \geq C_{\mathcal{G},\psi} \geq 0, \quad \text{and} \quad \frac{\partial \mathcal{G}(s, \psi)}{\partial s} \leq C^{\star}_{\mathcal{G},s}.
\end{aligned} \tag{4.6}$$

We obtain the dynamic boundary conditions from (4.2) following the procedure in existing literatures (*e.g.* [41, p. 68], [18, p. 47]) that give (*cf.* [41, (3.73)])

$$[\![\boldsymbol{n} \cdot (\boldsymbol{\Lambda}^{\boldsymbol{T}^0} : \boldsymbol{E}) - \nabla^{\Sigma} \cdot (\boldsymbol{u}\,(\boldsymbol{n} \cdot \boldsymbol{T}^0))\,]\!] = 0. \quad [\![\boldsymbol{n} \cdot \boldsymbol{u}\,]\!] = 0, \quad \text{on } \Sigma_{\mathrm{f}}, \tag{4.7}$$

where $\nabla^{\Sigma} := \nabla - \boldsymbol{n}\partial_n$ is the surface gradient. For the completion of the discussion, we also write the dynamic boundary conditions on Σ_{c}, which is the solid-solid interface with standard continuity conditions on traction as well as particle velocity (*e.g.* [41, (2.79) and (3.65)])

$$[\![\boldsymbol{n} \cdot (\boldsymbol{\Lambda}^{\boldsymbol{T}^0} : \boldsymbol{E})\,]\!] = 0, \quad [\![\boldsymbol{u}\,]\!] = 0, \quad \text{on } \Sigma_{\mathrm{c}}. \tag{4.8}$$

The total traction $\boldsymbol{\tau}^s$ is then given by (*cf.* [18, p. 70])

$$\boldsymbol{\tau}^s = \boldsymbol{n} \cdot (\boldsymbol{\Lambda}^{\boldsymbol{T}^0} : \boldsymbol{E}) + \boldsymbol{n} \cdot \boldsymbol{T}^0 - \nabla^{\Sigma} \cdot (\boldsymbol{u}\,(\boldsymbol{n} \cdot \boldsymbol{T}^0)). \tag{4.9}$$

We assume that the rupture remains compressive, or in other words the compressive normal stress σ is positive throughout the time. Therefore, $\sigma = -\boldsymbol{n} \cdot \boldsymbol{T}^s \cdot \boldsymbol{n}$ if the trace of $\boldsymbol{T}^s$ is positive in tension.

4.2.2 Energy spaces and trace theorem

We first introduce the standard notations of functional analysis. We denote by

$$L^2(\Omega) = \left\{ v \,\middle|\, \sum_{i=1}^{I} \|v\|^2_{L^2(\Omega_i)} < \infty \right\}$$

the space of square integrable functions, and the corresponding Sobolev spaces $H^m(\Omega)$, particularly for $m = \pm 1, \pm \frac{1}{2}$.

We denote by $C^n([0,T];H)$ the space of real-valued n^{th} order continuously differentiable functions from the finite time interval $[0,T]$ to any Sobolev space H, for $n = 0, 1, 2, \cdots$, with the norm

$$\|v\|_{C^n([0,T];H)} := \sum_{i=0}^{n} \max_{t\in[0,T]} \left\| \Big(\frac{\mathrm{d}}{\mathrm{d}t}\Big)^n v(t) \right\|_H . \tag{4.10}$$

An equivalent norm in the space $C^n([0,T];H)$ is also introduced depending on any scalar $\beta > 0$ defined as

$$\|v\|^{\star}_{C^n([0,T];H)} = \max_{t\in[0,T]} e^{-\frac{t}{\beta}} \left\| \Big(\frac{\mathrm{d}}{\mathrm{d}t}\Big)^n v(t) \right\|_H .$$

We denote by $C([0,T];H)$ as an abbreviation of $C^0([0,T];H)$. We obtain the following lemma directly from the trace theorem.

Lemma 4.1

Let Ω be a Lipschitz composite domain and Σ_{f} be a subset of its Lipschitz continuous interior boundaries. There exists a linear continuous map $\boldsymbol{r}_{\mathrm{f}} : H^1(\Omega)^3 \to H^1(\Omega)^{3\times 3}$ such that

$$\int_{\Omega} \boldsymbol{r}_{\mathrm{f}}(\boldsymbol{v}) : \boldsymbol{H}\, \mathrm{d}\Omega = \int_{\Sigma_{\mathrm{f}}} [\![\boldsymbol{n}\cdot\boldsymbol{v}]\!] \,\{\{\boldsymbol{n}\cdot\boldsymbol{H}\cdot\boldsymbol{n}\}\}\, \mathrm{d}\Sigma, \quad \boldsymbol{H} \in H(\mathrm{div};\Omega)^{3\times 3}. \tag{4.11}$$

Proof 4.1 Following the trace theorem, we denote by $T_{\mathrm{f}}^{\pm} : H^1(\Omega) \to H^{\frac{1}{2}}(\Sigma_{\mathrm{f}})$ the trace operator and $R_{\mathrm{f}}^{\pm} : H^{\frac{1}{2}}(\Sigma_{\mathrm{f}}) \to H^1(\Omega)$. Both are linear continuous maps such that

$$T_{\mathrm{f}}^{\pm}(u) = u^{\pm}\big|_{\Sigma_{\mathrm{f}}}, \quad \forall u \in H^1(\Omega),$$

$$T_{\mathrm{f}}^{\pm} \circ R_{\mathrm{f}}^{\pm}(v) = v\big|_{\Sigma_{\mathrm{f}}}, \quad \forall v \in H^{\frac{1}{2}}(\Sigma_{\mathrm{f}}).$$

Clearly one can choose $\big(\boldsymbol{r}_{\mathrm{f}}(\boldsymbol{v})\big)_{ij} = \sum_{k=1}^{3} n_i n_j n_k (R_{\mathrm{f}}^{+} + R_{\mathrm{f}}^{-}) \circ (T_{\mathrm{f}}^{+} + T_{\mathrm{f}}^{-})\big(v_k\big)$ which satisfies (4.11). It immediately follows that

$$\begin{aligned} \|\boldsymbol{r}_{\mathrm{f}}(\boldsymbol{v})\|_{H^1(\Omega)}^2 &\leq \sum_{i,j,k=1}^{3} (n_i n_j n_k)^2 \big\|(R_{\mathrm{f}}^{+} + R_{\mathrm{f}}^{-}) \circ (T_{\mathrm{f}}^{+} + T_{\mathrm{f}}^{-})\big(v_k\big)\big\|_{H^1(\Omega)}^2 \\ &\leq C_1 \sum_{i,j,k=1}^{3} (n_i n_j n_k)^2 \big\|(T_{\mathrm{f}}^{+} + T_{\mathrm{f}}^{-})\big(v_k\big)\big\|_{H^{\frac{1}{2}}(\Sigma_{\mathrm{f}})}^2 \leq C_2 \sum_{i,j,k=1}^{3} (n_i n_j n_k)^2 \|v_k\|_{H^1(\Omega)}^2 \\ &\leq C_{\boldsymbol{r}} \|\boldsymbol{v}\|_{H^1(\Omega)}^2 \end{aligned} \tag{4.12}$$

We define the following weighted inner products

$$\begin{aligned} \big(\boldsymbol{v}, \boldsymbol{w}\big)_{L^2(\Omega;\rho^0)} &:= \sum_{k=1}^{k_0} \int_{\Omega_k} \rho^0 (\boldsymbol{v} \cdot \boldsymbol{w}) \, \mathrm{d}\Omega; \\ \big(\boldsymbol{v}, \boldsymbol{w}\big)_{L^2(\Omega;\rho^0,\phi^0)} &:= \sum_{k=1}^{k_0} \int_{\Omega_k} \rho^0 \boldsymbol{v} \cdot (\nabla\nabla\phi^0) \cdot \boldsymbol{w} \, \mathrm{d}\Omega; \\ \big(\boldsymbol{E}, \boldsymbol{H}\big)_{L^2(\Omega;\boldsymbol{\Lambda}^{\boldsymbol{T}^0})} &:= \sum_{k=1}^{k_0} \int_{\Omega_k} \boldsymbol{H} : (\boldsymbol{\Lambda}^{\boldsymbol{T}^0} : \boldsymbol{E}) \, \mathrm{d}\Omega. \end{aligned} \tag{4.13}$$

with the corresponding weighted norms that have the following equivalence

$$\begin{aligned} C_{\rho^0} \|\boldsymbol{u}\|_{L^2(\Omega)}^2 \;&\leq\; \|\boldsymbol{u}\|_{L^2(\Omega;\rho^0)}^2 \;\leq\; C_{\rho^0}^{\star} \|\boldsymbol{u}\|_{L^2(\Omega)}^2, \\ C_{\phi^0} \|\boldsymbol{u}\|_{L^2(\Omega)}^2 \;&\leq\; \|\boldsymbol{u}\|_{L^2(\Omega;\rho^0,\phi^0)}^2 \;\leq\; C_{\phi^0}^{\star} \|\boldsymbol{u}\|_{L^2(\Omega)}^2, \\ C_{\boldsymbol{\Lambda}^{\boldsymbol{T}^0}} \|\boldsymbol{E}\|_{L^2(\Omega)}^2 \;&\leq\; \|\boldsymbol{E}\|_{L^2(\Omega;\boldsymbol{\Lambda}^{\boldsymbol{T}^0})}^2 \;\leq\; C_{\boldsymbol{\Lambda}^{\boldsymbol{T}^0}}^{\star} \|\boldsymbol{E}\|_{L^2(\Omega)}^2. \end{aligned} \tag{4.14}$$

We give the space for weak solution as

$$\begin{aligned} V &= \Big\{ \boldsymbol{v} \in H^1(\Omega)^3 \;\Big|\; [\![\boldsymbol{v}]\!] = 0 \text{ on } \Sigma \setminus \Sigma_{\mathrm{f}} \Big\}, \\ E &= \Big\{ \boldsymbol{E} \in L^2(\Omega)^{3\times 3} \;\Big|\; \nabla \cdot (\boldsymbol{\Lambda}^{\boldsymbol{T}^0} : \boldsymbol{E}) \in L^2(\Omega)^3, \quad [\![\boldsymbol{n} \cdot (\boldsymbol{\Lambda}^{\boldsymbol{T}^0} : \boldsymbol{E})]\!] = 0 \text{ on } \Sigma \Big\}. \end{aligned} \tag{4.15}$$

4.2.3 Weak form of the coupled system

In the companion paper of this work [178], we assume the conformal variational form in representing the equation of motion coupled with rupturing interfaces. Here we introduce the mixed variational form by introducing the strain tensor $\boldsymbol{E}$, the gradient of particle displacement, as an unknown that allows us to compute the stress in a more direct way. We recall the strong form of particle motion with the cowling approximation as

$$\rho^0\big(\ddot{\boldsymbol{u}} + \boldsymbol{u}\cdot(\nabla\nabla\phi^0)\big) - \nabla\cdot\boldsymbol{T}^{\mathrm{PK1}} = 0. \tag{4.16}$$

Correspondingly, the first order hyperbolic system containing (5.2) as well as the equations on interior boundaries in (4.3)–(4.9) is reformulated weakly as follows.

Problem 4.1

Given $\boldsymbol{T}^0 \in H^m(\Omega)^{3\times3}$ *and* $\boldsymbol{T}_\delta(t) \in C([0,T], H^m(\Omega)^{3\times3})$ *with* $m > \frac{1}{2}$, *find* $\boldsymbol{u} \in C^2([0,T],V)$, $\boldsymbol{E} \in C^1([0,T],E)$ *and* $\psi \in C^1([0,T],L^2(\Sigma_{\mathrm{f}}))$ *such that*

$$\begin{aligned}
&\int_\Omega \rho^0\Big(\ddot{\boldsymbol{u}} + \boldsymbol{u}\cdot(\nabla\nabla\phi^0)\Big)\cdot\boldsymbol{w}\,\mathrm{d}\Omega + \int_\Omega (\boldsymbol{\Lambda}^{\boldsymbol{T}^0}\!:\boldsymbol{E}) : \nabla\boldsymbol{w}\,\mathrm{d}\Omega \\
&\quad + \boxed{\gamma\int_\Omega \Big((\dot{\boldsymbol{E}} : \nabla\boldsymbol{w}) + \frac{3}{4}(\dot{\boldsymbol{u}}\cdot\boldsymbol{w})\Big)\,\mathrm{d}\Omega} \\
&\quad + \int_{\Sigma_{\mathrm{f}}} \boldsymbol{\tau}_{\mathrm{f}}\cdot[\![\boldsymbol{w}_\parallel]\!]\,\mathrm{d}\Sigma - \int_{\Sigma_{\mathrm{f}}} \sigma\,[\![\boldsymbol{n}\cdot\boldsymbol{w}]\!]\,\mathrm{d}\Sigma - \int_{\Sigma_{\mathrm{f}}} [\![\boldsymbol{\tau}_2\cdot\boldsymbol{w}]\!]\,\mathrm{d}\Sigma \\
&\quad + \boxed{\alpha_{\mathrm{f}}\int_\Omega \boldsymbol{r}_{\mathrm{f}}\big(\boldsymbol{u}+\dot{\boldsymbol{u}}\big) : \boldsymbol{r}_{\mathrm{f}}\big(\boldsymbol{w}\big)\,\mathrm{d}\Omega} = \int_{\Sigma_{\mathrm{f}}} \big(\boldsymbol{n}\cdot(\boldsymbol{T}^0+\boldsymbol{T}_\delta)\big)\cdot[\![\boldsymbol{w}]\!]\,\mathrm{d}\Sigma,
\end{aligned} \tag{4.17a}$$

$$\begin{aligned}
&\int_\Omega \dot{\boldsymbol{E}} : \boldsymbol{H}\,\mathrm{d}\Omega + \int_\Omega \dot{\boldsymbol{u}}\cdot(\nabla\cdot\boldsymbol{H})\,\mathrm{d}\Omega + \int_{\Sigma_{\mathrm{f}}} \{\!\{\dot{\boldsymbol{u}}\}\!\}\cdot[\![\boldsymbol{n}\cdot\boldsymbol{H}]\!]\,\mathrm{d}\Sigma \\
&\quad + \int_{\Sigma_{\mathrm{f}}} \boldsymbol{s}\cdot\{\!\{\boldsymbol{n}\cdot\boldsymbol{H}\}\!\}\,\mathrm{d}\Sigma = 0,
\end{aligned} \tag{4.17b}$$

$$\int_{\Sigma_{\mathrm{f}}} \dot{\psi}\,\varphi\,\mathrm{d}\Sigma + \int_{\Sigma_{\mathrm{f}}} \mathcal{G}(s,\psi)\,\varphi\,\mathrm{d}\Sigma = 0, \tag{4.17c}$$

with

$$\boldsymbol{s} = [\![\dot{\boldsymbol{u}}_{\parallel}]\!], \quad s := |\boldsymbol{s}|, \tag{4.18a}$$

$$\boldsymbol{\tau}_2 + \nabla^{\Sigma} \cdot \big(\boldsymbol{u}(\boldsymbol{n} \cdot \boldsymbol{T}^0)\big) = 0, \tag{4.18b}$$

$$\sigma + \boldsymbol{n} \cdot \big(\boldsymbol{n} \cdot (\boldsymbol{T}^0 + \boldsymbol{T}_\delta + \{\!\{ \boldsymbol{\Lambda}^{\boldsymbol{T}^0} : \boldsymbol{E} \}\!\}) + \{\!\{ \boldsymbol{\tau}_2 \}\!\}\big) = 0, \tag{4.18c}$$

$$\mathcal{F}(\sigma, s, \psi)\boldsymbol{s} - s\boldsymbol{\tau}_{\mathrm{f}} = 0, \tag{4.18d}$$

holds for any $(\boldsymbol{w}, \boldsymbol{H}, \varphi) \in C^1([0,T], V \times E \times L^2(\Sigma_{\mathrm{f}}))$.

The boxed terms in (4.17a) are a viscous regularization term and a boundary penalty term, with the viscosity coefficient denoted by γ and the penalty coefficient by α_{f}, both of which are positive constants. We give in the next section the criterion for choosing γ and α_{f}.

4.2.4 A priori estimate

Here we prove the well-posedness of the weak form coupled with the nonlinear friction law.

Theorem 4.1

The coupled problem (4.17a)–(4.18d) is well-posed within a finite time interval $[0, T]$ *if* γ *and* α_{f} *satisfy*

$$\gamma \geq \frac{2}{3} {C'_I}^2 \beta \max\left(\frac{1}{C_{\phi^0}}, \frac{2}{C_{\boldsymbol{\Lambda}^{\boldsymbol{T}^0}}} \right), \quad \textit{and} \quad \alpha_{\mathrm{f}} \geq \max\Big(C_{\boldsymbol{\Lambda}^{\boldsymbol{T}^0}}, \gamma \Big), \tag{4.19}$$

for any given $\beta > 0$.

Proof 4.2 Taking (4.18a) into (4.17b) followed by integration by parts yields

$$\int_\Omega \Big(\dot{\boldsymbol{E}} - \nabla\dot{\boldsymbol{u}} + \boldsymbol{r}_{\mathrm{f}}(\dot{\boldsymbol{u}})\Big) : \boldsymbol{H}\,\mathrm{d}\Omega = 0. \tag{4.20}$$

By taking $\boldsymbol{H} = \dot{\boldsymbol{E}} + \nabla\dot{\boldsymbol{u}} + \boldsymbol{r}_{\mathrm{f}}\big(\dot{\boldsymbol{u}}\big)$ in (4.20), we obtain with Young's inequality,

$$\|\nabla\dot{\boldsymbol{u}}\|^2_{L^2(\Omega)} = \Big\|\dot{\boldsymbol{E}} + \boldsymbol{r}_{\mathrm{f}}\big(\dot{\boldsymbol{u}}\big)\Big\|^2_{L^2(\Omega)} \le (1+\delta_1)\Big\|\dot{\boldsymbol{E}}\Big\|^2_{L^2(\Omega)} + (1+\delta_1^{-1})\|\boldsymbol{r}_{\mathrm{f}}(\dot{\boldsymbol{u}})\|^2_{L^2(\Omega)}, \tag{4.21}$$

and by taking $\boldsymbol{H} = \dot{\boldsymbol{E}} - \nabla\dot{\boldsymbol{u}} - \boldsymbol{r}_{\mathrm{f}}\big(\dot{\boldsymbol{u}}\big)$ in (4.20), we obtain

$$\int_\Omega (\nabla\dot{\boldsymbol{u}}) : \dot{\boldsymbol{E}}\,\mathrm{d}\Omega = \frac{1}{2}\Big(\|\nabla\dot{\boldsymbol{u}}\|^2_{L^2(\Omega)} + \Big\|\dot{\boldsymbol{E}}\Big\|^2_{L^2(\Omega)} - \|\boldsymbol{r}_{\mathrm{f}}(\dot{\boldsymbol{u}})\|^2_{L^2(\Omega)}\Big). \tag{4.22}$$

We integrate (4.20) over time with the initial conditions $\boldsymbol{E}|_{t=0} = 0$ and $\boldsymbol{u}|_{t=0} = 0$, which yields

$$\int_\Omega \Big(\boldsymbol{E} - \nabla\boldsymbol{u} + \boldsymbol{r}_{\mathrm{f}}(\boldsymbol{u})\Big) : \boldsymbol{H}\,\mathrm{d}\Omega = 0, \tag{4.23}$$

and with $\boldsymbol{H} = \boldsymbol{E} + \nabla\boldsymbol{u} + \boldsymbol{r}_{\mathrm{f}}\big(\boldsymbol{u}\big)$, yields

$$\|\nabla\boldsymbol{u}\|^2_{L^2(\Omega)} \le (1+\delta_2)\|\boldsymbol{E}\|^2_{L^2(\Omega)} + (1+\delta_2^{-1})\|\boldsymbol{r}_{\mathrm{f}}(\boldsymbol{u})\|^2_{L^2(\Omega)}. \tag{4.24}$$

We let $\boldsymbol{w} = \dot{\boldsymbol{u}}$ and $\boldsymbol{H} = \boldsymbol{\Lambda}^{\boldsymbol{T}^0} : \boldsymbol{E}$, summarize (4.17a) and (4.20), and subtract (4.18c) and (4.22) to obtain

$$\begin{aligned} &\frac{1}{2}\frac{\mathrm{d}}{\mathrm{d}t}\Big(\|\dot{\boldsymbol{u}}\|^2_{L^2(\Omega;\rho^0)} + \|\boldsymbol{u}\|^2_{L^2(\Omega;\rho^0,\phi^0)} + \|\boldsymbol{E}\|^2_{L^2(\Omega;\boldsymbol{\Lambda}^{\boldsymbol{T}^0})} + \alpha_{\mathrm{f}}\|\boldsymbol{r}_{\mathrm{f}}(\boldsymbol{u})\|^2_{L^2(\Omega)}\Big) \\ &\qquad + \frac{\gamma}{2}\Big(\|\nabla\dot{\boldsymbol{u}}\|^2_{L^2(\Omega)} + \Big\|\dot{\boldsymbol{E}}\Big\|^2_{L^2(\Omega)} + \frac{3}{2}\|\dot{\boldsymbol{u}}\|^2_{L^2(\Omega)}\Big) + (\alpha_{\mathrm{f}} - \frac{\gamma}{2})\|\boldsymbol{r}_{\mathrm{f}}(\dot{\boldsymbol{u}})\|^2_{L^2(\Omega)} \\ &\quad = -\int_{\Sigma_{\mathrm{f}}} \big(\boldsymbol{\tau}_{\mathrm{f}} - \{\!\{\boldsymbol{\tau}_2\}\!\} - \boldsymbol{n}\cdot(\boldsymbol{T}^0 + \boldsymbol{T}^\delta)\big)\cdot\boldsymbol{s}\,\mathrm{d}\Sigma + \int_{\Sigma_{\mathrm{f}}} [\![\boldsymbol{\tau}_2]\!]\cdot\{\!\{\dot{\boldsymbol{u}}\}\!\}\,\mathrm{d}\Sigma. \end{aligned} \tag{4.25}$$

We mention some results from [178, section 4.2], namely

$$\int_\Omega \big(\{\!\{\boldsymbol{\tau}_2\}\!\}\cdot\boldsymbol{s} + [\![\boldsymbol{\tau}_2]\!]\cdot\{\!\{\dot{\boldsymbol{u}}\}\!\}\big)\,\mathrm{d}\Omega \;\le\; C_I'\Big(\frac{1}{2\delta_3}\|\boldsymbol{u}\|^2_{H^1(\Omega)} + \frac{\delta_3}{2}\|\dot{\boldsymbol{u}}\|^2_{H^1(\Omega)}\Big). \tag{4.26}$$

With Young's inequality,

$$\int_{\Sigma_{\mathrm{f}}} \boldsymbol{n}\cdot(\boldsymbol{T}^0 + \boldsymbol{T}^\delta)\cdot\boldsymbol{s}\,\mathrm{d}\Sigma \;\le\; \frac{1}{\delta_4}\big\|\boldsymbol{n}\cdot(\boldsymbol{T}^0 + \boldsymbol{T}^\delta)\big\|^2_{L^2(\Sigma_{\mathrm{f}})} + \delta_4\|s\|^2_{L^2(\Sigma_{\mathrm{f}})}. \tag{4.27}$$

We use the relation in (4.3), which leads to $\boldsymbol{\tau}_{\mathrm{f}} \cdot \boldsymbol{s} = \tau_{\mathrm{f}}\, s > 0$, and

$$\delta_4 = \Big(\int_{\Sigma_{\mathrm{f}}} \tau_{\mathrm{f}} s \,\mathrm{d}\Sigma\Big)/\|s\,\|^2_{L^2(\Sigma_{\mathrm{f}})} \geq C_{\mathcal{F},s}$$

in (4.27), and thus

$$\begin{aligned}
&-\int_{\Sigma_{\mathrm{f}}} (\boldsymbol{\tau}_{\mathrm{f}} - \boldsymbol{n}\cdot(\boldsymbol{T}^0+\boldsymbol{T}^\delta)\cdot \boldsymbol{s}\,\mathrm{d}\Sigma \\
&\qquad \leq \frac{1}{\delta_4}\big\|\boldsymbol{n}\cdot(\boldsymbol{T}^0+\boldsymbol{T}^\delta)\,\big\|^2_{L^2(\Sigma_{\mathrm{f}})} + \delta_4\|s\,\|^2_{L^2(\Sigma_{\mathrm{f}})} - \int_{\Sigma_{\mathrm{f}}} \tau_{\mathrm{f}} s\,\mathrm{d}\Sigma \\
&\qquad = \frac{1}{\delta_4}\big\|\boldsymbol{n}\cdot(\boldsymbol{T}^0+\boldsymbol{T}^\delta)\,\big\|^2_{L^2(\Sigma_{\mathrm{f}})} \leq \frac{1}{C_{\mathcal{F},s}}\big\|\boldsymbol{n}\cdot(\boldsymbol{T}^0+\boldsymbol{T}^\delta)\,\big\|^2_{L^2(\Sigma_{\mathrm{f}})}.
\end{aligned} \tag{4.28}$$

We eliminate the terms with $\boldsymbol{E}$ by taking (4.21) and (4.24) into (4.25) while letting $\delta_1 = \delta_2 = 1$, and use the results in (4.26)–(4.28), with $\delta_3 = \frac{3\gamma}{2C_I'}$ in (4.26), and give the energy estimate as

$$\begin{aligned}
&\frac{1}{2}\frac{\mathrm{d}}{\mathrm{d}t}\Big(C_{\rho^0}\|\dot{\boldsymbol{u}}\,\|^2_{L^2(\Omega)} + C_{\phi^0}\|\boldsymbol{u}\,\|^2_{L^2(\Omega)} + \frac{C_{\boldsymbol{\Lambda}\boldsymbol{T}^0}}{2}\|\nabla\boldsymbol{u}\,\|^2_{L^2(\Omega)} + (\alpha_{\mathrm{f}} - C_{\boldsymbol{\Lambda}\boldsymbol{T}^0})\|\boldsymbol{r}_{\mathrm{f}}(\boldsymbol{u})\,\|^2_{L^2(\Omega)}\Big) \\
&\qquad + \frac{3\gamma}{4}\|\dot{\boldsymbol{u}}\,\|^2_{H^1(\Omega)} + (\alpha_{\mathrm{f}} - \gamma)\|\boldsymbol{r}_{\mathrm{f}}(\dot{\boldsymbol{u}})\,\|^2_{L^2(\Omega)} - C_I'\Big(\frac{C_I'}{3\gamma}\|\boldsymbol{u}\,\|^2_{H^1(\Omega)} + \frac{3\gamma}{4C_I'}\|\dot{\boldsymbol{u}}\,\|^2_{H^1(\Omega)}\Big) \\
&\quad \leq \frac{1}{C_{\mathcal{F},s}}\big\|\boldsymbol{n}\cdot(\boldsymbol{T}^0+\boldsymbol{T}^\delta)\,\big\|^2_{L^2(\Sigma_{\mathrm{f}})}.
\end{aligned} \tag{4.29}$$

Multiply both sides of (4.25) by $e^{-\frac{t}{2\beta}}$, and integrate over $[0, T]$ to yield (see details in [178, section 4.2])

$$\begin{aligned}
&\frac{C_{\rho^0}}{2}\|\dot{\boldsymbol{u}}\,\|^{\star 2}_{C([0,T];L^2(\Omega))} + \Big(\frac{C_{\phi^0}}{2} - \frac{C_I'^{\,2}\beta}{3\gamma}\Big)\|\boldsymbol{u}\,\|^{\star 2}_{C([0,T];L^2(\Omega))} \\
&\qquad + \Big(\frac{C_{\boldsymbol{\Lambda}\boldsymbol{T}^0}}{4} - \frac{C_I'^{\,2}\beta}{3\gamma}\Big)\|\nabla\boldsymbol{u}\,\|^{\star 2}_{C([0,T];L^2(\Omega))} \\
&\qquad + \frac{1}{2}(\alpha_{\mathrm{f}} - C_{\boldsymbol{\Lambda}\boldsymbol{T}^0})\|\boldsymbol{r}_{\mathrm{f}}(\boldsymbol{u})\,\|^{\star 2}_{C([0,T];L^2(\Omega))} + \beta(\alpha_{\mathrm{f}} - \gamma)\|\boldsymbol{r}_{\mathrm{f}}(\dot{\boldsymbol{u}})\,\|^{\star 2}_{C([0,T];L^2(\Omega))} \\
&\quad \leq \frac{\beta}{C_{\mathcal{F},s}}\big\|\boldsymbol{n}\cdot(\boldsymbol{T}^0+\boldsymbol{T}^\delta)\,\big\|^{\star 2}_{C([0,T];L^2(\Sigma_{\mathrm{f}}))}.
\end{aligned} \tag{4.30}$$

Clearly, the solution of the system (4.17a)–(4.18d) is bounded if (4.19) is satisfied.

Remark 4.1

To properly define the energy, the parameter β should increase with the length of time interval T. For a long-time simulation, the overall time is subdivided into sufficiently small time invervals, namely,

$$[0, \delta t\,], [\delta t\,, 2\delta t\,], [2\delta t\,, 3\delta t\,], \cdots, [(N-1)\delta t\,, N\delta t\,], \quad \delta t\, := T/N,$$

and iterations are conducted within each time segment. In this way, a small β can be used in Theorem 4.1.

Remark 4.2

Since β can be chosen to be a sufficiently small positive number, then γ can be sufficiently small, which asymptotically approaches the original problem with pure elasticity.

4.3 The discontinuous Galerkin method with multi-rate implicit time discretization

We partition the domain Ω into tetrahedral finite elements, $\Omega = \bigcup \Omega^{\mathrm{e}}$, such that the unstructured tetrahedral mesh is coherent with geometry, that is, $\Sigma \subset \bigcup \partial\Omega^{\mathrm{e}}$. We distinguish the facets attached to the rupture plane with slip boundary conditions by $\Sigma_{\mathrm{f}}^{\mathrm{e}}$, and thus $\Sigma_{\mathrm{f}} = \bigcup \Sigma_{\mathrm{f}}^{\mathrm{e}}$. All other faces of the interior elements are denoted by $\Sigma_{\mathrm{c}}^{\mathrm{e}}$. We set

$$\begin{aligned}
V_h^p &= \Big\{ \boldsymbol{u} \in H^1(\Omega)^3 \,\Big|\, \big(v_i\big)\big|_{\Omega^{\mathrm{e}}} \in P^p\big(\Omega^{\mathrm{e}}\big), \quad i \in \{1,2,3\} \Big\}, \\
E_h^p &= \Big\{ \boldsymbol{E} \in L^2(\Omega)^{3\times 3} \,\Big|\, \big(E_{ij}\big)\big|_{\Omega^{\mathrm{e}}} \in P^p\big(\Omega^{\mathrm{e}}\big), \quad i,j \in \{1,2,3\} \Big\}, \\
\Xi_h^p &= \Big\{ \psi \in L^2(\Sigma_{\mathrm{f}}) \,\Big|\, \psi\big|_{\Omega^{\mathrm{e}}} \in P^p\big(\Omega^{\mathrm{e}}\big) \Big\},
\end{aligned} \tag{4.31}$$

where $P^p(\Omega^e)$ is the space of polynomial functions of degree at most $p \geq 1$ on Ω^e. To simplify the analysis, we assume that the elastic parameters are piecewise constant, that is,

$$\rho_h^0, \left(\boldsymbol{\Lambda}_h^{\boldsymbol{T}^0}\right)_{ijkl}, \left(\boldsymbol{T}_h^0\right)_{ij} \in \left\{\varphi \in L^\infty(\Omega) \,\middle|\, \varphi|_{\Omega^e} \in P^0\left(\Omega^e\right)\right\}, \quad i,j,k,l \in \{1,2,3\},$$

and that

$$\phi_h^0 \in \left\{\varphi \in H^2(\Omega) \,\middle|\, \varphi|_{\Omega^e} \in P^2\left(\Omega^e\right)\right\},$$

such that $\boldsymbol{K}_h := \nabla_h \nabla_h \phi_h^0$ is piecewise constant, with ∇_h is the gradient of polynomials within Ω^e. We give the semi-discretized DG formulation as follows.

Problem 4.2

Given the coefficient as above, and $\boldsymbol{T}_{\delta h}(t) \in C([0,T], E_h^p)$, find $\boldsymbol{u} \in C^2([0,T], V_h^p)$, $\boldsymbol{E} \in C^1([0,T], E_h^p)$ and $\psi \in C^1([0,T], \Xi_h^p)$ such that

$$\begin{aligned}
&\sum_{\Omega^e} \int_{\Omega^e} \Big(\big(\rho_h^0(\ddot{\boldsymbol{u}}_h + \boldsymbol{u}_h \cdot \boldsymbol{K}_h) + \frac{3\gamma^e}{4} \dot{\boldsymbol{u}}_h\big) \cdot \boldsymbol{w}_h + \big((\boldsymbol{\Lambda}_h^{\boldsymbol{T}^0} : \boldsymbol{E}_h + \gamma^e \dot{\boldsymbol{E}}_h) : \nabla \boldsymbol{w}_h\big)\Big)\, \mathrm{d}\Omega \\
&\quad + \sum_{\Sigma_f^e} \int_{\Sigma_f^e} \Big((\boldsymbol{\tau}_{\mathrm{f}\,h} - \sigma_h \boldsymbol{n}) \cdot [\![\boldsymbol{w}_h]\!] - [\![\boldsymbol{\tau}_{2\,h} \cdot \boldsymbol{w}_h]\!] + \alpha_f^e [\![\boldsymbol{n} \cdot (\boldsymbol{u}_h + \dot{\boldsymbol{u}}_h)]\!]\, [\![\boldsymbol{n} \cdot \boldsymbol{w}_h]\!] \Big)\, \mathrm{d}\Sigma \\
&\quad + \sum_{\Sigma_c^e} \int_{\Sigma_c^e} \left(\{\{\boldsymbol{n} \cdot (\boldsymbol{\Lambda}_h^{\boldsymbol{T}^0} : \boldsymbol{E}_h)\}\} + \alpha [\![\dot{\boldsymbol{u}}_h]\!] \right) \cdot [\![\boldsymbol{w}_h]\!]\, \mathrm{d}\Sigma \\
&\quad = \sum_{\Sigma_f^e} \int_{\Sigma_f^e} \left(\boldsymbol{n} \cdot (\boldsymbol{T}_h^0 + \boldsymbol{T}_{\delta h})\right) \cdot [\![\boldsymbol{w}_h]\!]\, \mathrm{d}\Sigma,
\end{aligned} \tag{4.32a}$$

$$\begin{aligned}
&\sum_{\Omega^e} \int_{\Omega^e} \Big(\dot{\boldsymbol{E}}_h : \boldsymbol{H}_h + \dot{\boldsymbol{u}}_h \cdot (\nabla \cdot \boldsymbol{H}_h) \Big)\, \mathrm{d}\Omega \\
&\quad + \sum_{\Sigma_f^e} \int_{\Sigma_f^e} \Big(\{\{\dot{\boldsymbol{u}}_h\}\} \cdot [\![\boldsymbol{n} \cdot \boldsymbol{H}_h]\!] + \boldsymbol{s}_h \cdot \{\{\boldsymbol{n} \cdot \boldsymbol{H}_h\}\} \Big)\, \mathrm{d}\Sigma \\
&\quad + \sum_{\Sigma_c^e} \int_{\Sigma_c^e} \left(\{\{\dot{\boldsymbol{u}}_h\}\} + \alpha [\![\boldsymbol{n} \cdot (\boldsymbol{\Lambda}_h^{\boldsymbol{T}^0} : \boldsymbol{E}_h)]\!] \right) \cdot [\![\boldsymbol{n} \cdot \boldsymbol{H}_h]\!]\, \mathrm{d}\Sigma = 0,
\end{aligned} \tag{4.32b}$$

$$\int_{\Sigma_{\mathrm{f}}^{\mathrm{e}}} \dot{\psi}_h \varphi_h \, \mathrm{d}\Sigma + \int_{\Sigma_{\mathrm{f}}^{\mathrm{e}}} \mathcal{G}(s_h, \psi_h) \varphi_h \, \mathrm{d}\Sigma = 0, \tag{4.32c}$$

$$\left\{ \begin{aligned} &\boldsymbol{\tau}_{2\,h} + \nabla^{\Sigma} \cdot (\boldsymbol{u}_h \, (\boldsymbol{n} \cdot \boldsymbol{T}_h^0)) = 0, \\ &\sigma_h + \boldsymbol{n} \cdot \Big(\boldsymbol{n} \cdot \big(\boldsymbol{T}_h^0 + \boldsymbol{T}_h^{\delta} + \{\{ \boldsymbol{\Lambda}_h^{\boldsymbol{T}^0} : \boldsymbol{E}_h \}\} \big) + \{\{ \boldsymbol{\tau}_{2\,h} \}\} \Big) = 0, \\ &\boldsymbol{s}_h = [[\dot{\boldsymbol{u}}_{h\,\|}]], \quad s_h := |\boldsymbol{s}_h|, \\ &\boldsymbol{s}_h \mathcal{F}\big(\sigma_h, \, s_h, \, \psi_h\big) - s_h \boldsymbol{\tau}_{\mathrm{f}\,h} = 0, \end{aligned} \right. \quad \textit{on } \Sigma_{\mathrm{f}}^{\mathrm{e}}. \tag{4.32d}$$

for arbitrary test functions $(\boldsymbol{H}_h, \boldsymbol{w}_h, \varphi_h) \in C^1([0,T], V_h^{\star} \times E_h^{\star} \times \Xi_h^{\star})$.

The constant $\alpha > 0$ in (4.32a) is the penalty coefficient that enforce the coercivity of the variational form with boundary conditions (see details in Ye et al.(2016) [177]). We use the particle velocity $\boldsymbol{v}_h = \dot{\boldsymbol{u}}_h$, and discretize the time interval with a uniform time step $\delta t = \frac{T}{N_T}$, and let $t_n = n\delta t$. We use index n in the superscript $v^{(n)}$ to indicate a time dependent variable v corresponding to t_n. We then rewrite Problem 4.2 as a discretized coupling system with backward Euler finite differencing in time, which is given as follows.

Problem 4.3

Given $(\boldsymbol{u}_h^{(n-1)}, \boldsymbol{E}_h^{(n-1)}, \psi_h^{(n-1)}) \in V_h$, *find* $(\boldsymbol{u}_h^{(n)}, \boldsymbol{E}_h^{(n)}, \psi_h^{(n)}) \in V_h$ *such that*

$$\begin{aligned}
&\sum_{\Omega^{\mathrm{e}}} \int_{\Omega^{\mathrm{e}}} \Big(\rho_h^0\big(\frac{1}{\delta t}\boldsymbol{v}_h^{(n)} + \boldsymbol{u}_h^{(n)} \cdot \boldsymbol{K}_h\big) + \frac{3\gamma^{\mathrm{e}}}{4}\boldsymbol{v}_h^{(n)}\Big) \cdot \boldsymbol{w}_h \,\mathrm{d}\Omega \\
&\quad + \sum_{\Omega^{\mathrm{e}}} \int_{\Omega^{\mathrm{e}}} \big(\boldsymbol{\Lambda}_h^{\boldsymbol{T}^0} \colon \boldsymbol{E}_h^{(n)} + \frac{\gamma^{\mathrm{e}}}{\delta t}\boldsymbol{E}_h^{(n)}\big) : \nabla \boldsymbol{w}_h \,\mathrm{d}\Omega \\
&\quad + \sum_{\Sigma_{\mathrm{f}}^{\mathrm{e}}} \int_{\Sigma_{\mathrm{f}}^{\mathrm{e}}} \Big((\boldsymbol{\tau}_{\mathrm{f}\,h}^{(n)} - \sigma_h^{(n)}\boldsymbol{n}) \cdot [\![\boldsymbol{w}_h]\!] - [\![\boldsymbol{\tau}_{2\,h}^{(n)} \cdot \boldsymbol{w}_h]\!]\Big) \,\mathrm{d}\Sigma \\
&\quad + \sum_{\Sigma_{\mathrm{f}}^{\mathrm{e}}} \alpha_{\mathrm{f}}^{\mathrm{e}} \int_{\Sigma_{\mathrm{f}}^{\mathrm{e}}} [\![\boldsymbol{n} \cdot (\boldsymbol{u}_h^{(n)} + \boldsymbol{v}_h^{(n)})]\!]\, [\![\boldsymbol{n} \cdot \boldsymbol{w}_h]\!] \,\mathrm{d}\Sigma \\
&\quad + \sum_{\Sigma_{\mathrm{c}}^{\mathrm{e}}} \int_{\Sigma_{\mathrm{c}}^{\mathrm{e}}} \Big(\{\{\boldsymbol{n} \cdot (\boldsymbol{\Lambda}_h^{\boldsymbol{T}^0} : \boldsymbol{E}_h^{(n)})\}\} + \alpha [\![\boldsymbol{v}_h^{(n)}]\!]\Big) \cdot [\![\boldsymbol{w}_h]\!] \,\mathrm{d}\Sigma \\
&= \frac{1}{\delta t} \sum_{\Omega^{\mathrm{e}}} \int_{\Omega^{\mathrm{e}}} \Big(\rho_h^0 \boldsymbol{v}_h^{(n-1)} \cdot \boldsymbol{w}_h + \gamma^{\mathrm{e}} \boldsymbol{E}_h^{(n-1)} : \nabla \boldsymbol{w}_h\Big) \,\mathrm{d}\Omega \\
&\quad + \sum_{\Sigma_{\mathrm{f}}^{\mathrm{e}}} \int_{\Sigma_{\mathrm{f}}^{\mathrm{e}}} \big(\boldsymbol{n} \cdot (\boldsymbol{T}_h^0 + \boldsymbol{T}_h^{\delta\,(n)})\big) \cdot [\![\boldsymbol{w}_h]\!] \,\mathrm{d}\Sigma
\end{aligned} \tag{4.33a}$$

$$\begin{aligned}
&\sum_{\Omega^{\mathrm{e}}} \int_{\Omega^{\mathrm{e}}} \Big(\frac{1}{\delta t}\boldsymbol{E}_h^{(n)} : \boldsymbol{H}_h + \boldsymbol{v}_h^{(n)} \cdot (\nabla \cdot \boldsymbol{H}_h)\Big) \,\mathrm{d}\Omega \\
&\quad + \sum_{\Sigma_{\mathrm{f}}^{\mathrm{e}}} \int_{\Sigma_{\mathrm{f}}^{\mathrm{e}}} \Big(\{\{\boldsymbol{v}_h^{(n)}\}\} \cdot [\![\boldsymbol{n} \cdot \boldsymbol{H}_h]\!] + \boldsymbol{s}_h^{(n)} \cdot \{\{\boldsymbol{n} \cdot \boldsymbol{H}_h\}\}\Big) \,\mathrm{d}\Sigma \\
&\quad + \sum_{\Sigma_{\mathrm{c}}^{\mathrm{e}}} \int_{\Sigma_{\mathrm{c}}^{\mathrm{e}}} \Big(\{\{\boldsymbol{v}_h^{(n)}\}\} + \alpha [\![\boldsymbol{n} \cdot (\boldsymbol{\Lambda}_h^{\boldsymbol{T}^0} : \boldsymbol{E}_h^{(n)})]\!]\Big) \cdot [\![\boldsymbol{n} \cdot \boldsymbol{H}_h]\!] \,\mathrm{d}\Sigma \\
&= \frac{1}{\delta t} \sum_{\Omega^{\mathrm{e}}} \int_{\Omega^{\mathrm{e}}} \boldsymbol{E}_h^{(n-1)} : \boldsymbol{H}_h \,\mathrm{d}\Omega,
\end{aligned} \tag{4.33b}$$

$$\int_{\Sigma_{\mathrm{f}}^{\mathrm{e}}} \psi_h^{(n)} \varphi_h \,\mathrm{d}\Sigma + \delta t \int_{\Sigma_{\mathrm{f}}^{\mathrm{e}}} \mathcal{G}(s_h^{(n)}, \psi_h^{(n)}) \varphi_h \,\mathrm{d}\Sigma = \int_{\Sigma_{\mathrm{f}}^{\mathrm{e}}} \psi_h^{(n-1)} \varphi_h \,\mathrm{d}\Sigma, \tag{4.33c}$$

with

$$\boldsymbol{\tau}_{2\,h}^{(n)} + \nabla^{\Sigma} \cdot (\boldsymbol{u}_h^{(n)}\, (\boldsymbol{n} \cdot \boldsymbol{T}_h^0)) = 0, \tag{4.34a}$$

$$\sigma_h^{(n)} + \boldsymbol{n} \cdot \big(\boldsymbol{n} \cdot \{\{\boldsymbol{\Lambda}_h^{\boldsymbol{T}^0} : \boldsymbol{E}_h^{(n)}\}\} + \{\{\boldsymbol{\tau}_{2\,h}^{(n)}\}\}\big) = -\,\boldsymbol{n} \cdot \big(\boldsymbol{T}_h^0 + \boldsymbol{T}_h^{\delta\,(n)}\big) \cdot \boldsymbol{n}, \tag{4.34b}$$

$$\boldsymbol{u}^{(n)} - \delta t\,\boldsymbol{v}^{(n)} = \boldsymbol{u}^{(n-1)}, \tag{4.34c}$$

$$\boldsymbol{s}_h^{(n)} - [\![\boldsymbol{v}_{h\,\|}^{(n)}]\!] = 0, \quad s_h^{(n)} = |\boldsymbol{s}_h^{(n)}|, \tag{4.34d}$$

$$\boldsymbol{s}_h^{(n)}\mathcal{F}\big(\sigma_h^{(n)},\, s_h^{(n)},\, \psi_h^{(n)}\big) - s_h^{(n)}\boldsymbol{\tau}_{\mathrm{f}\,h}^{(n)} = 0, \tag{4.34e}$$

for arbitrary test functions $(\boldsymbol{H}_h, \boldsymbol{w}_h, \varphi_h) \in V_h^\star$.

Alternative to (4.33c), we use N-stage implicit Runge-Kutta method for discretization (4.32c) in time, which generates the multi-rate scheme by

$$\begin{aligned} &\int_{\Sigma_\mathrm{f}^\mathrm{e}} \psi_h^{(n)}\varphi_h \,\mathrm{d}\Sigma + \delta t \sum_{i=1}^{N} b_i \int_{\Sigma_\mathrm{f}^\mathrm{e}} \theta_h^{(n),i}\varphi_h \,\mathrm{d}\Sigma = \int_{\Sigma_\mathrm{f}^\mathrm{e}} \psi_h^{(n-1)}\varphi_h \,\mathrm{d}\Sigma, \\ &\theta_h^{(n),i} = -\mathcal{G}\big(s_h^{(n),c_i},\, \psi_h^{(n-1)} + \delta t \sum_{j=1}^{N} a_{ij}\theta_h^{(n),j}\big), \end{aligned} \tag{4.35}$$

in which $s_h^{(n),c_i}$ is the linear interpolation defined by $s^{(n),c_i} := (1-c_i)s^{(n-1)} + c_i s^{(n)}$, with a_{ij}, b_i and c_i the elements of the Runge-Kutta matrix, weights and nodes, and $\theta_h^{(n),i}$ is the i^{th} intermediate stage of $\psi_h^{(n)}$. The coupling system (4.33–4.35) can be solved by a general nonlinear optimization approach such as Newton's method. This approach is computationally expensive however because of the factorization of global Hessian matrices. We therefore suggest the following iterative approach.

4.4 Iterative coupling

In order to obtain an accurate solution with affordable effort, we derive an alternative approach using fixed-point iteration, by separating the state ODE from the main part of the system, and conducting domain decomposition (*e.g.* [17, Section 6.1]) to separate the variables on $\Sigma_\mathrm{f}^\mathrm{e}$ from elsewhere.

We rewrite (4.33a,b) by moving surface integration terms on $\Sigma_\mathrm{c}^\mathrm{e}$ to the right-hand-sides, and construct a sequence of linear–nonlinear coupling problems for each time step $[t_{n-1}, t_n]$, which follows the iteration for $k = 1, 2, \cdots$, with $v^{(n,k)}$ representing the value at k^{th} iteration of a time dependent variable v corresponding to $t = t_n$. Therefore, we seek alternatively the solution of the following problem.

Problem 4.4

Given $(\boldsymbol{u}_h^{(n-1)}, \boldsymbol{E}_h^{(n-1)}, \psi_h^{(n-1)})$ *and* $(\boldsymbol{v}_h^{(n,k-1)}, \boldsymbol{E}_h^{(n,k-1)}, \cdot) \in V_h$,

find $(\boldsymbol{u}_h^{(n,k)}\ \boldsymbol{E}_h^{(n,k)}, \psi_h^{(n,k)}) \in V_h$ *such that*

$$
\begin{aligned}
&\sum_{\Omega^\mathrm{e}} \int_{\Omega^\mathrm{e}} \Big(\rho_h^0\big(\frac{1}{\delta t}\boldsymbol{v}_h^{(t,k)} + \boldsymbol{u}_h^{(t,k)} \cdot (\nabla\nabla\phi^0)_h\big) + \frac{3\gamma^\mathrm{e}}{4}\boldsymbol{v}_h^{(n)}\Big) \cdot \boldsymbol{w}_h \,\mathrm{d}\Omega \\
&\quad + \sum_{\Omega^\mathrm{e}} \int_{\Omega^\mathrm{e}} \big(\boldsymbol{\Lambda}_h^{\boldsymbol{T}^0} : \boldsymbol{E}_h^{(t,k)} + \frac{\gamma^\mathrm{e}}{\delta t}\boldsymbol{E}_h^{(t,k)}\big) : \nabla \boldsymbol{w}_h \,\mathrm{d}\Omega \\
&\quad + \sum_{\Sigma_\mathrm{f}^\mathrm{e}} \int_{\Sigma_\mathrm{f}^\mathrm{e}} \Big(\big(\boldsymbol{\tau}_{\mathrm{f}\,h}^{(t,k)} - \sigma_h^{(t,k)}\boldsymbol{n}\big) \cdot [\![\boldsymbol{w}_h]\!] - [\![\boldsymbol{\tau}_{2\,h}^{(t,k)} \cdot \boldsymbol{w}_h]\!]\Big) \,\mathrm{d}\Sigma \\
&\quad + \sum_{\Sigma_\mathrm{f}^\mathrm{e}} \alpha_\mathrm{f}^\mathrm{e} \int_{\Sigma_\mathrm{f}^\mathrm{e}} \Big([\![\boldsymbol{n} \cdot (\boldsymbol{u}_h^{(t,k)} + \boldsymbol{v}_h^{(t,k)})]\!]\,[\![\boldsymbol{n} \cdot \boldsymbol{w}_h]\!]\Big) \,\mathrm{d}\Sigma \qquad (4.36\mathrm{a}) \\
&= \frac{1}{\delta t} \sum_{\Omega^\mathrm{e}} \int_{\Omega^\mathrm{e}} \Big(\rho_h^0\big(\boldsymbol{v}_h^{(n-1)} + \gamma^\mathrm{e}\boldsymbol{E}_h^{(n-1)} : \nabla \boldsymbol{w}_h\Big) \,\mathrm{d}\Omega \\
&\quad - \sum_{\Sigma_\mathrm{c}^\mathrm{e}} \int_{\Sigma_\mathrm{c}^\mathrm{e}} \Big(\{\{\boldsymbol{n} \cdot (\boldsymbol{\Lambda}_h^{\boldsymbol{T}^0} : \boldsymbol{E}_h^{(t,k-1)})\}\} + \alpha\,[\![\boldsymbol{v}_h^{(t,k-1)}]\!]\Big) \cdot [\![\boldsymbol{w}_h]\!] \,\mathrm{d}\Sigma \\
&\quad + \sum_{\Sigma_\mathrm{f}^\mathrm{e}} \int_{\Sigma_\mathrm{f}^\mathrm{e}} \big(\boldsymbol{n} \cdot (\boldsymbol{T}_h^0 + \boldsymbol{T}_h^{\delta\,(n)})\big) \cdot [\![\boldsymbol{w}_h]\!] \,\mathrm{d}\Sigma
\end{aligned}
$$

$$
\begin{aligned}
&\sum_{\Omega^{\mathrm{e}}} \int_{\Omega^{\mathrm{e}}} \Big(\frac{1}{\delta t} \boldsymbol{E}_h^{(t,k)} : \boldsymbol{H}_h + \boldsymbol{v}_h^{(t,k)} \cdot \, (\nabla \cdot \boldsymbol{H}_h) \Big) \, \mathrm{d}\Omega \\
&\qquad + \sum_{\Sigma_{\mathrm{f}}^{\mathrm{e}}} \int_{\Sigma_{\mathrm{f}}^{\mathrm{e}}} \Big(\{\!\{ \boldsymbol{v}_h^{(t,k)} \}\!\} \cdot [\![\boldsymbol{n} \cdot \boldsymbol{H}_h]\!] + \boldsymbol{s}_h^{(t,k)} \cdot \{\!\{ \boldsymbol{n} \cdot \boldsymbol{H}_h \}\!\} \Big) \, \mathrm{d}\Sigma \\
&\quad = \frac{1}{\delta t} \sum_{\Omega^{\mathrm{e}}} \int_{\Omega^{\mathrm{e}}} \boldsymbol{E}_h^{(n-1)} : \boldsymbol{H}_h \, \mathrm{d}\Omega \\
&\qquad - \sum_{\Sigma_{\mathrm{c}}^{\mathrm{e}}} \int_{\Sigma_{\mathrm{c}}^{\mathrm{e}}} \Big(\{\!\{ \boldsymbol{v}_h^{(t,k-1)} \}\!\} + \alpha [\![\boldsymbol{n} \cdot (\boldsymbol{\Lambda}_h^{\boldsymbol{T}^0} : \boldsymbol{E}_h^{(t,k-1)})]\!] \Big) \cdot [\![\boldsymbol{n} \cdot \boldsymbol{H}_h]\!] \, \mathrm{d}\Sigma
\end{aligned}
\tag{4.36b}
$$

$$
\int_{\Sigma_{\mathrm{f}}^{\mathrm{e}}} \psi_h^{(t,k)} \varphi_h \, \mathrm{d}\Sigma + \delta t \int_{\Sigma_{\mathrm{f}}^{\mathrm{e}}} \mathcal{G}(s_h^{(t,k)}, \psi_h^{(t,k)}) \varphi_h \, \mathrm{d}\Sigma = \int_{\Sigma_{\mathrm{f}}^{\mathrm{e}}} \psi_h^{(n-1)} \varphi_h \, \mathrm{d}\Sigma, \tag{4.36c}
$$

with

$$
\boldsymbol{\tau}_{2\,h}^{(t,k)} + \nabla^{\Sigma} \cdot (\boldsymbol{u}_h^{(t,k)} \, (\boldsymbol{n} \cdot \boldsymbol{T}_h^0)) = 0, \tag{4.37a}
$$

$$
\sigma_h^{(n,k)} + \boldsymbol{n} \cdot \big(\boldsymbol{n} \cdot \{\!\{ \boldsymbol{\Lambda}_h^{\boldsymbol{T}^0} : \boldsymbol{E}_h^{(n,k)} \}\!\} + \{\!\{ \boldsymbol{\tau}_{2\,h}^{(n,k)} \}\!\} \big) = - \boldsymbol{n} \cdot \big(\boldsymbol{T}_h^0 + \boldsymbol{T}_h^{\delta\,(n)} \big) \cdot \boldsymbol{n}, \tag{4.37b}
$$

$$
\boldsymbol{u}_h^{(t,k)} - \delta t \, \boldsymbol{v}_h^{(t,k)} = \boldsymbol{u}_h^{(n-1)}, \tag{4.37c}
$$

$$
\boldsymbol{s}_h^{(t,k)} - [\![\boldsymbol{v}_{h\,\|}^{(t,k)}]\!] = 0, \quad s_h^{(t,k)} = |\boldsymbol{s}_h^{(t,k)}|, \tag{4.37d}
$$

$$
\boldsymbol{s}_h^{(t,k)} \mathcal{F}\big(\sigma_h^{(t,k)},\, s_h^{(t,k)},\, \psi_h^{(t,k)}\big) - s_h^{(t,k)} \boldsymbol{\tau}_{\mathrm{f}\,h}^{(t,k)} = 0, \tag{4.37e}
$$

for arbitrary test functions $(\boldsymbol{H}_h, \boldsymbol{w}_h, \varphi_h) \in V_h^{\star}$.

In (4.36c) we use the backward Euler scheme as a simplified example of (4.35). For the first iteration $k = 1$ the initial value of variables are obtained from the previous time step by

$$
\boldsymbol{v}_h^{(t,0)} = \boldsymbol{v}_h^{(n-1)}, \quad \boldsymbol{u}_h^{(t,0)} = \boldsymbol{u}_h^{(n-1)}, \quad \boldsymbol{E}_h^{(t,0)} = \boldsymbol{E}_h^{(n-1)}, \quad \psi_h^{(t,0)} = \psi_h^{(n-1)}. \tag{4.38}
$$

We solve the coupled nonlinear problem (4.36a–f) by defining a constrained optimization problem, in which the objective function

$$\mathfrak{L} := \tfrac{1}{2}\left\| \frac{\boldsymbol{s}_h^{(t,k)}}{s_h^{(t,k)}} \mathcal{F}\big(\sigma_h^{(t,k)},\, s_h^{(t,k)},\, \psi_h^{(t,k)}\big) - \boldsymbol{\tau}_{\mathrm{f}\,h}^{(t,k)} \right\|^2 \tag{4.39}$$

follows the normalized (4.37e), with the linear constraints (4.36a,b) and (4.36e,f), and the nonlinear constraint (4.36c). Compared with the original, implicitly discretized problem, the iterative problem is localized to each element, where the Hessian matrices become block-diagonal. Details of the numerical algorithm solving this problem using the Gauss-Newton's method are provided in 4.6.

4.5 Stability of the iterative coupling

We prove that the iterative coupling is a contraction under certain constraints on model coefficients, in parallel with the stability result for the second-order formulation of motion in Ye, et al.(2018)[178, section 5].

Theorem 4.2

The iterative coupling scheme (4.36a)–(4.36c) converges within each time step if γ^{e}, $\alpha_{\mathrm{f}}^{\mathrm{e}}$, α *and* δt *satisfy*

$$\begin{aligned}
&\gamma^{\mathrm{e}} \geq \delta t \, \max\left(\frac{4}{3}\Big(\big(C^{\star}_{\mathcal{F},\sigma}(C_I + C_I') + C_I' - C_{\phi^0}\big) - \frac{C_{\rho^0}}{\delta t^{\,2}} \Big), \frac{1}{2}\Big(3C^{\star}_{\mathcal{F},\sigma}(C_I + C_I') + 3C_I' - C_{\boldsymbol{\Lambda}\boldsymbol{T}^0} \Big) \right) \\
&\alpha_{\mathrm{f}}^{\mathrm{e}} \geq h^{-1}(\delta t \, + 1)^{-1} C_p \big(\delta t \, C_{\boldsymbol{\Lambda}\boldsymbol{T}^0} + \gamma^{\mathrm{e}} \big) \\
&\frac{1}{\delta t} \geq \frac{C^{\star\,2}_{\mathcal{F},\psi}}{2C_{\mathcal{F},s}} + \frac{C^{\star\,2}_{\mathcal{G},s}}{2C_{\mathcal{F},s}} - C_{\mathcal{G},\psi} \\
&C_p h^{-1} \big(\delta t \, C_{\boldsymbol{\Lambda}_h^{\boldsymbol{T}^0}} + \gamma^{\mathrm{e}} \big) \leq \alpha \leq C_p^{-1} h \big(\delta t \, C_{\boldsymbol{\Lambda}_h^{\boldsymbol{T}^0}} + \gamma^{\mathrm{e}} \big)^{-1}
\end{aligned} \tag{4.40}$$

Proof 4.3 We define the error vectors

$$\boldsymbol{\epsilon}_{\boldsymbol{v}}^{k} := \boldsymbol{v}_h^{(t,k)} - \boldsymbol{v}_h^{(n)}, \quad \boldsymbol{\epsilon}_{\boldsymbol{\tau}_2}^{k} := \boldsymbol{\tau}_{2\,h}^{(t,k)} - \boldsymbol{\tau}_{2\,h}^{(n)}, \quad \boldsymbol{\epsilon}_{\boldsymbol{\tau}_\mathrm{f}}^{k} := \boldsymbol{\tau}_{\mathrm{f}\,h}^{(t,k)} - \boldsymbol{\tau}_{\mathrm{f}\,h}^{(n)}, \quad \boldsymbol{\epsilon}_{\boldsymbol{s}}^{k} := \boldsymbol{s}_h^{(t,k)} - \boldsymbol{s}_h^{(n)},$$

$$\epsilon_{\sigma}^{k} := \sigma_h^{(t,k)} - \sigma_h^{(n)}, \quad \epsilon_{\psi}^{k} := \psi_h^{(t,k)} - \psi_h^{(n)}, \quad \epsilon_{\mathcal{F}}^{k} := \mathcal{F}(\sigma_h^{(t,k)}, s_h^{(t,k)}, \psi_h^{(t,k)}) - \mathcal{F}(\sigma_h^{(n)}, s_h^{(n)}, \psi_h^{(n)}),$$

$$\epsilon_{\mathcal{G}}^{k} := \mathcal{G}(s_h^{(t,k)}, \psi_h^{(t,k)}) - \mathcal{G}(s_h^{(n)}, \psi_h^{(n)}), \quad \epsilon_{s}^{k} := |\boldsymbol{s}_h^{(t,k)}| - |\boldsymbol{s}_h^{(n)}|.$$

We eliminate $\boldsymbol{u}_h^{(n)}$ and $\boldsymbol{u}_h^{(t,k)}$ by (4.34c) and (4.37c), and subtract (4.33a–d) from (4.36a–d) at iteration k to obtain the error estimate:

$$\begin{aligned}
&\sum_{\Omega^\mathrm{e}} \int_{\Omega^\mathrm{e}} \Big(\big(\rho_h^0 (\frac{1}{\delta t} \boldsymbol{\epsilon}_{\boldsymbol{v}}^{k} + \delta t\, \boldsymbol{\epsilon}_{\boldsymbol{v}}^{k} \cdot (\nabla\nabla\phi^0)_h) + \frac{3\gamma^\mathrm{e}}{4} \boldsymbol{\epsilon}_{\boldsymbol{v}}^{k}\big) \cdot \boldsymbol{w}_h + (\boldsymbol{\Lambda}_h^{\boldsymbol{T}^0} : \boldsymbol{\epsilon}_{\boldsymbol{E}}^{k} + \frac{\gamma^\mathrm{e}}{\delta t} \boldsymbol{\epsilon}_{\boldsymbol{E}}^{k}) : \nabla \boldsymbol{w}_h \Big) \,\mathrm{d}\Omega \\
&\qquad + \sum_{\Sigma_\mathrm{f}^\mathrm{e}} \int_{\Sigma_\mathrm{f}^\mathrm{e}} \Big(\big(\boldsymbol{\epsilon}_{\boldsymbol{\tau}_\mathrm{f}}^{k} - \epsilon_{\sigma}^{k} \boldsymbol{n}\big) \cdot [\![\boldsymbol{w}_h]\!] - [\![\boldsymbol{\epsilon}_{\boldsymbol{\tau}_2}^{k} \cdot \boldsymbol{w}_h]\!] + (\delta t\, + 1)\, \alpha_\mathrm{f}^\mathrm{e} [\![\boldsymbol{n} \cdot \boldsymbol{\epsilon}_{\boldsymbol{v}}^{k}]\!] [\![\boldsymbol{n} \cdot \boldsymbol{w}_h]\!] \Big) \,\mathrm{d}\Sigma \\
&\quad = - \sum_{\Sigma_\mathrm{c}^\mathrm{e}} \int_{\Sigma_\mathrm{c}^\mathrm{e}} \Big(\{\!\{ \boldsymbol{n} \cdot (\boldsymbol{\Lambda}_h^{\boldsymbol{T}^0} : \boldsymbol{\epsilon}_{\boldsymbol{E}}^{k-1}) \}\!\} + \alpha [\![\boldsymbol{\epsilon}_{\boldsymbol{v}}^{k-1}]\!] \Big) \cdot [\![\boldsymbol{w}_h]\!] \,\mathrm{d}\Sigma
\end{aligned} \tag{4.41a}$$

$$\begin{aligned}
&\sum_{\Omega^\mathrm{e}} \int_{\Omega^\mathrm{e}} \Big(\frac{1}{\delta t} \boldsymbol{\epsilon}_{\boldsymbol{E}}^{k} : \boldsymbol{H}_h \,\mathrm{d}\Omega + \boldsymbol{\epsilon}_{\boldsymbol{v}}^{k} \cdot\, (\nabla \cdot \boldsymbol{H}_h) \Big) \,\mathrm{d}\Omega \\
&\quad + \sum_{\Sigma_\mathrm{f}^\mathrm{e}} \int_{\Sigma_\mathrm{f}^\mathrm{e}} \Big(\{\!\{ \boldsymbol{\epsilon}_{\boldsymbol{v}}^{k} \}\!\} \cdot [\![\boldsymbol{n} \cdot \boldsymbol{H}_h]\!] + \boldsymbol{\epsilon}_{\boldsymbol{s}}^{k} \cdot \{\!\{ \boldsymbol{n} \cdot \boldsymbol{H}_h \}\!\} \Big) \,\mathrm{d}\Sigma \\
&\quad = - \sum_{\Sigma_\mathrm{c}^\mathrm{e}} \int_{\Sigma_\mathrm{c}^\mathrm{e}} \Big(\{\!\{ \boldsymbol{\epsilon}_{\boldsymbol{v}}^{k-1} \}\!\} + \alpha [\![\boldsymbol{n} \cdot (\boldsymbol{\Lambda}_h^{\boldsymbol{T}^0} : \boldsymbol{\epsilon}_{\boldsymbol{E}}^{k-1})]\!] \Big) \cdot [\![\boldsymbol{n} \cdot \boldsymbol{H}_h]\!] \,\mathrm{d}\Sigma
\end{aligned} \tag{4.41b}$$

$$\boldsymbol{\epsilon}_{\boldsymbol{\tau}_2}^{k} + \delta t\, \nabla^{\Sigma} \cdot (\boldsymbol{\epsilon}_{\boldsymbol{v}}^{k} (\boldsymbol{n} \cdot \boldsymbol{T}_h^0)) = 0, \tag{4.41c}$$

$$\epsilon_{\sigma}^{k} + \boldsymbol{n} \cdot \{\!\{ \boldsymbol{\Lambda}_h^{\boldsymbol{T}^0} : \boldsymbol{\epsilon}_{\boldsymbol{E}}^{k} \}\!\} \cdot \boldsymbol{n} + \boldsymbol{n} \cdot \{\!\{ \boldsymbol{\epsilon}_{\boldsymbol{\tau}_2}^{k} \}\!\} = 0. \tag{4.41d}$$

Integrating (4.41b) by parts yields

$$\begin{aligned}
&\sum_{\Omega^\mathrm{e}} \int_{\Omega^\mathrm{e}} \big(\frac{1}{\delta t} \boldsymbol{\epsilon}_{\boldsymbol{E}}^{k} - \nabla \boldsymbol{\epsilon}_{\boldsymbol{v}}^{k} \big) : \boldsymbol{H}_h \,\mathrm{d}\Omega + \sum_{\Sigma_\mathrm{f}^\mathrm{e}} \int_{\Sigma_\mathrm{f}^\mathrm{e}} [\![\boldsymbol{n} \cdot \boldsymbol{\epsilon}_{\boldsymbol{v}}^{k}]\!] \{\!\{ \boldsymbol{n} \cdot \boldsymbol{H}_h \cdot \boldsymbol{n} \}\!\} \,\mathrm{d}\Sigma \\
&\qquad + \sum_{\Sigma_\mathrm{c}^\mathrm{e}} \int_{\Sigma_\mathrm{c}^\mathrm{e}} \big([\![\boldsymbol{\epsilon}_{\boldsymbol{v}}^{k-1}]\!] + \alpha [\![\boldsymbol{n} \cdot (\boldsymbol{\Lambda}^{\boldsymbol{T}^0} : \boldsymbol{\epsilon}_{\boldsymbol{E}}^{k-1})]\!] \big) \{\!\{ \boldsymbol{n} \cdot \boldsymbol{H}_h \}\!\} \,\mathrm{d}\Sigma = 0.
\end{aligned} \tag{4.42}$$

We define linear continuous maps ("lifting operator", see Arnold et al.(2002) [8]), $\boldsymbol{r}^{\mathrm{e}}_{\mathrm{f}} : L^2(\Sigma^{\mathrm{e}}_{\mathrm{f}}) \to \mathcal{E}^p_h$ and $\boldsymbol{r}^{\mathrm{e}}_{\mathrm{c}} : L^2(\Sigma^{\mathrm{e}}_{\mathrm{c}})^3 \to \mathcal{E}^p_h$ by denoting $\mathcal{E}^p_h = \Big\{ \boldsymbol{E} \in L^2(\Omega)^{3\times 3} \Big| \big(E_{ij}\big)\big|_{\Omega^{\mathrm{e}}} \in P^p\big(\Omega^{\mathrm{e}}\big), \quad i,j \in \{1,2,3\} \Big\}$, such that

$$
\begin{aligned}
&\int_{\Omega^{\mathrm{e}\pm}} \boldsymbol{r}^{\mathrm{e}}_{\mathrm{f}}(v) : \boldsymbol{H}_h \,\mathrm{d}\Omega = \int_{\Sigma^{\mathrm{e}}_{\mathrm{f}}} v \,\big\{\!\big\{ \boldsymbol{n}\cdot \boldsymbol{H}_h \cdot \boldsymbol{n} \big\}\!\big\} \,\mathrm{d}\Sigma, \quad \text{for } \Sigma^{\mathrm{e}}_{\mathrm{f}} = \Omega^{\mathrm{e}^+} \cap \Omega^{\mathrm{e}^-}, \\
&\int_{\Omega^{\mathrm{e}\pm}} \boldsymbol{r}^{\mathrm{e}}_{\mathrm{c}}(\boldsymbol{v}) : \boldsymbol{H}_h \,\mathrm{d}\Omega = \int_{\Sigma^{\mathrm{e}}_{\mathrm{c}}} \boldsymbol{v}\cdot \big\{\!\big\{ \boldsymbol{n}\cdot \boldsymbol{H}_h \big\}\!\big\} \,\mathrm{d}\Sigma, \quad \text{for } \Sigma^{\mathrm{e}}_{\mathrm{c}} = \Omega^{\mathrm{e}^+} \cap \Omega^{\mathrm{e}^-}.
\end{aligned} \tag{4.43}
$$

It is suggested in Arnold et al.(2002) [8] that

$$
\begin{aligned}
&\| \boldsymbol{r}^{\mathrm{e}}_{\mathrm{f}}(v) \|^2_{L^2(\Omega^{\mathrm{e}\pm})} \le C_p h^{-1} \| v \|^2_{L^2(\Sigma^{\mathrm{e}}_{\mathrm{f}})}, \\
&\| \boldsymbol{r}^{\mathrm{e}}_{\mathrm{c}}(\boldsymbol{v}) \|^2_{L^2(\Omega^{\mathrm{e}\pm})} \le C_p h^{-1} \| \boldsymbol{v} \|^2_{L^2(\Sigma^{\mathrm{e}}_{\mathrm{c}})},
\end{aligned} \tag{4.44}
$$

with h the mesh size, and the positive constant $C_p = \mathcal{O}(p^2)$ if Ω^{e} is a tetrahedron (see Warburton and Hesthaven (2003) [170]). Therefore based on (4.42) and (4.43),

$$
\int_{\Omega^{\mathrm{e}}} \Big(\frac{1}{\delta t} \boldsymbol{\epsilon}^k_{\boldsymbol{E}} - \nabla \boldsymbol{\epsilon}^k_{\boldsymbol{v}} + \boldsymbol{r}^{\mathrm{e}}_{\mathrm{f}}\big([\![\boldsymbol{n}\cdot \boldsymbol{\epsilon}^k_{\boldsymbol{v}}]\!] \big) + \boldsymbol{r}^{\mathrm{e}}_{\mathrm{c}}\big([\![\boldsymbol{\epsilon}^{k-1}_{\boldsymbol{v}}]\!] + \alpha [\![\boldsymbol{n}\cdot (\boldsymbol{\Lambda}^{\boldsymbol{T}^0} : \boldsymbol{\epsilon}^{k-1}_{\boldsymbol{E}})]\!] \big) \Big) : \boldsymbol{H}_h \,\mathrm{d}\Omega = 0. \tag{4.45}
$$

By taking $\boldsymbol{H} = \frac{1}{\delta t} \boldsymbol{\epsilon}^k_{\boldsymbol{E}} + \nabla \boldsymbol{\epsilon}^k_{\boldsymbol{v}} + \boldsymbol{r}^{\mathrm{e}}_{\mathrm{f}}\big([\![\boldsymbol{n}\cdot \boldsymbol{\epsilon}^k_{\boldsymbol{v}}]\!] \big) + \boldsymbol{r}^{\mathrm{e}}_{\mathrm{c}}\big([\![\boldsymbol{\epsilon}^{k-1}_{\boldsymbol{v}}]\!] + \alpha [\![\boldsymbol{n}\cdot (\boldsymbol{\Lambda}^{\boldsymbol{T}^0} : \boldsymbol{\epsilon}^{k-1}_{\boldsymbol{E}})]\!] \big)$ in (4.45) while using Young's inequality,

$$
\begin{aligned}
\sum_{\Omega^{\mathrm{e}}} \| \nabla \boldsymbol{\epsilon}^k_{\boldsymbol{v}} \|^2_{L^2(\Omega^{\mathrm{e}})} \le \frac{3}{\delta t^2} \sum_{\Omega^{\mathrm{e}}} \| \boldsymbol{\epsilon}^k_{\boldsymbol{E}} \|^2_{L^2(\Omega^{\mathrm{e}})} + 3 C_p h^{-1} \sum_{\Sigma^{\mathrm{e}}_{\mathrm{f}}} \| [\![\boldsymbol{n}\cdot \boldsymbol{\epsilon}^k_{\boldsymbol{v}}]\!] \|^2_{L^2(\Sigma^{\mathrm{e}}_{\mathrm{f}})} \\
+ 3 C_p h^{-1} \sum_{\Sigma^{\mathrm{e}}_{\mathrm{c}}} \Big\| [\![\boldsymbol{\epsilon}^{k-1}_{\boldsymbol{v}}]\!] + \alpha [\![\boldsymbol{n}\cdot (\boldsymbol{\Lambda}^{\boldsymbol{T}^0} : \boldsymbol{\epsilon}^{k-1}_{\boldsymbol{E}})]\!] \Big\|^2_{L^2(\Sigma^{\mathrm{e}}_{\mathrm{c}})},
\end{aligned} \tag{4.46}
$$

and by taking $\boldsymbol{H} = \frac{1}{\delta t} \boldsymbol{\epsilon}^k_{\boldsymbol{E}} - \nabla \boldsymbol{\epsilon}^k_{\boldsymbol{v}} - \boldsymbol{r}^{\mathrm{e}}_{\mathrm{f}}\big([\![\boldsymbol{n}\cdot \boldsymbol{\epsilon}^k_{\boldsymbol{v}}]\!] \big) - \boldsymbol{r}^{\mathrm{e}}_{\mathrm{c}}\big([\![\boldsymbol{\epsilon}^{k-1}_{\boldsymbol{v}}]\!] + \alpha [\![\boldsymbol{n}\cdot (\boldsymbol{\Lambda}^{\boldsymbol{T}^0} : \boldsymbol{\epsilon}^{k-1}_{\boldsymbol{E}})]\!] \big)$ in (4.45),

$$
\begin{aligned}
\sum_{\Omega^{\mathrm{e}}} \int_{\Omega^{\mathrm{e}}} \boldsymbol{\epsilon}^k_{\boldsymbol{E}} : \nabla \boldsymbol{\epsilon}^k_{\boldsymbol{v}} \,\mathrm{d}\Omega \ge \frac{1}{2} \Big(\delta t \sum_{\Omega^{\mathrm{e}}} \| \nabla \boldsymbol{\epsilon}^k_{\boldsymbol{v}} \|^2_{L^2(\Omega^{\mathrm{e}})} + \frac{1}{\delta t} \sum_{\Omega^{\mathrm{e}}} \| \boldsymbol{\epsilon}^k_{\boldsymbol{E}} \|^2_{L^2(\Omega^{\mathrm{e}})} \Big) \\
- \frac{C_p}{2h} \delta t \Big(\sum_{\Sigma^{\mathrm{e}}_{\mathrm{f}}} \| [\![\boldsymbol{n}\cdot \boldsymbol{\epsilon}^k_{\boldsymbol{v}}]\!] \|^2_{L^2(\Sigma^{\mathrm{e}}_{\mathrm{f}})} + \sum_{\Sigma^{\mathrm{e}}_{\mathrm{c}}} \Big\| [\![\boldsymbol{\epsilon}^{k-1}_{\boldsymbol{v}}]\!] + \alpha [\![\boldsymbol{n}\cdot (\boldsymbol{\Lambda}^{\boldsymbol{T}^0} : \boldsymbol{\epsilon}^{k-1}_{\boldsymbol{E}})]\!] \Big\|^2_{L^2(\Sigma^{\mathrm{e}}_{\mathrm{c}})} \Big).
\end{aligned} \tag{4.47}
$$

Similar to (4.25), we let $\boldsymbol{w}_h = \boldsymbol{\epsilon}_{\boldsymbol{v}}^k$ in (4.41a) and $\boldsymbol{H}_h = \boldsymbol{\Lambda}^{\boldsymbol{T}^0} : \boldsymbol{\epsilon}_{\boldsymbol{E}}^k$ in (4.42), eliminate ϵ_{σ}^k by (4.41d), and use the result in (4.47) to obtain

$$
\begin{aligned}
&\sum_{\Omega^{\mathrm{e}}} \Big(\frac{1}{\delta t} \big\| \boldsymbol{\epsilon}_{\boldsymbol{v}}^k \big\|^2_{L^2(\Omega^{\mathrm{e}};\rho_h^0)} + \delta t \big\| \boldsymbol{\epsilon}_{\boldsymbol{v}}^k \big\|^2_{L^2(\Omega^{\mathrm{e}};\rho_h^0,\phi_h^0)} + \frac{3\gamma^{\mathrm{e}}}{4} \big\| \boldsymbol{\epsilon}_{\boldsymbol{v}}^k \big\|^2_{L^2(\Omega^{\mathrm{e}})} \\
&\qquad\qquad + \frac{1}{\delta t} \big\| \boldsymbol{\epsilon}_{\boldsymbol{E}}^k \big\|^2_{L^2(\Omega^{\mathrm{e}};\boldsymbol{\Lambda}_h^{\boldsymbol{T}^0})} + \frac{\gamma^{\mathrm{e}}}{2} \big\| \nabla \boldsymbol{\epsilon}_{\boldsymbol{v}}^k \big\|^2_{L^2(\Omega^{\mathrm{e}})} + \frac{\gamma^{\mathrm{e}}}{2\delta t^2} \big\| \boldsymbol{\epsilon}_{\boldsymbol{E}}^k \big\|^2_{L^2(\Omega^{\mathrm{e}})} \Big) \\
&\quad + \sum_{\Sigma_{\mathrm{f}}^{\mathrm{e}}} \big(\alpha_{\mathrm{f}}^{\mathrm{e}} (\delta t + 1) - \frac{\gamma^{\mathrm{e}}}{2h} C_p \big) \big\| [\![\boldsymbol{n} \cdot \boldsymbol{\epsilon}_{\boldsymbol{v}}^k]\!] \big\|^2_{L^2(\Sigma_{\mathrm{f}}^{\mathrm{e}})} \\
&= \sum_{\Sigma_{\mathrm{f}}^{\mathrm{e}}} \Big(- \int_{\Sigma_{\mathrm{f}}^{\mathrm{e}}} \big(\boldsymbol{\epsilon}_{\boldsymbol{\tau}_{\mathrm{f}}}^k - \{\!\{ \boldsymbol{\epsilon}_{\boldsymbol{\tau}_2}^k \}\!\} \big) \cdot \boldsymbol{\epsilon}_{\boldsymbol{s}}^k \,\mathrm{d}\Sigma + \int_{\Sigma_{\mathrm{f}}^{\mathrm{e}}} [\![\boldsymbol{\epsilon}_{\boldsymbol{\tau}_2}^k]\!] \cdot \{\!\{ \boldsymbol{\epsilon}_{\boldsymbol{v}}^k \}\!\} \,\mathrm{d}\Sigma \Big) \\
&\quad + \sum_{\Sigma_{\mathrm{c}}^{\mathrm{e}}} \Big(- \alpha \Big\| [\![\boldsymbol{n} \cdot (\boldsymbol{\Lambda}^{\boldsymbol{T}^0} : \boldsymbol{\epsilon}_{\boldsymbol{E}}^{k-1})]\!] \Big\|^2_{L^2(\Sigma_{\mathrm{c}}^{\mathrm{e}})} - \alpha \big\| [\![\boldsymbol{\epsilon}_{\boldsymbol{v}}^{k-1})]\!] \big\|^2_{L^2(\Sigma_{\mathrm{c}}^{\mathrm{e}})} \\
&\qquad\qquad + \frac{\gamma^{\mathrm{e}}}{2h} C_p \Big\| [\![\boldsymbol{\epsilon}_{\boldsymbol{v}}^{k-1}]\!] + \alpha [\![\boldsymbol{n} \cdot (\boldsymbol{\Lambda}^{\boldsymbol{T}^0} : \boldsymbol{\epsilon}_{\boldsymbol{E}}^{k-1})]\!] \Big\|^2_{L^2(\Sigma_{\mathrm{c}}^{\mathrm{e}})} \Big).
\end{aligned}
\tag{4.48}
$$

We also subtract (4.33c) from (4.36c) at step k, and let $\varphi = \epsilon_{\psi}^k$, such that

$$
\frac{1}{\delta t} \big\| \epsilon_{\psi}^k \big\|^2_{L^2(\Sigma_{\mathrm{f}}^{\mathrm{e}})} = - \int_{\Sigma_{\mathrm{f}}^{\mathrm{e}}} \epsilon_{\mathcal{G}}^k \, \epsilon_{\psi}^k \,\mathrm{d}\Sigma. \tag{4.49}
$$

Following the same procedure as [178, section 5], we get

$$
\begin{aligned}
- \int_{\Omega^{\mathrm{e}}} \boldsymbol{\epsilon}_{\boldsymbol{\tau}_{\mathrm{f}}}^k \cdot \boldsymbol{\epsilon}_{\boldsymbol{s}}^k \,\mathrm{d}\Omega \;&\leq\; - C_{\mathcal{F},s} \big\| \epsilon_s^k \big\|^2_{L^2(\Sigma_{\mathrm{f}}^{\mathrm{e}})} + C_{\mathcal{F},\sigma}^{\star} \delta t \,(C_I + C_I') \big\| \boldsymbol{\epsilon}_{\boldsymbol{v}}^k \big\|^2_{H^1(\Omega^{\mathrm{e}})} \\
&\quad + C_{\mathcal{F},\psi}^{\star} \big(\frac{1}{2\delta_7} \big\| \epsilon_{\psi}^k \big\|^2_{L^2(\Sigma_{\mathrm{f}}^{\mathrm{e}})} + \frac{\delta_7}{2} \big\| \epsilon_s^k \big\|^2_{L^2(\Sigma_{\mathrm{f}}^{\mathrm{e}})} \big), \\
\int_{\Omega^{\mathrm{e}}} \big(\{\!\{ \boldsymbol{\epsilon}_{\boldsymbol{\tau}_2}^k \}\!\} \cdot \boldsymbol{\epsilon}_{\boldsymbol{s}}^k + [\![\boldsymbol{\epsilon}_{\boldsymbol{\tau}_2}^k]\!] \cdot \{\!\{ \boldsymbol{\epsilon}_{\boldsymbol{v}}^k \}\!\} \big) \,\mathrm{d}\Omega \;&\leq\; \delta t \, C_I' \big\| \boldsymbol{\epsilon}_{\boldsymbol{v}}^k \big\|^2_{H^1(\Omega^{\mathrm{e}})}, \\
- \int_{\Sigma_{\mathrm{f}}^{\mathrm{e}}} \epsilon_{\mathcal{G}}^k \, \epsilon_{\psi}^k \,\mathrm{d}\Sigma \leq\; &C_{\mathcal{G},s}^{\star} \big(\frac{1}{2\delta_8} \big\| \epsilon_{\psi}^k \big\|^2_{L^2(\Sigma_{\mathrm{f}}^{\mathrm{e}})} + \frac{\delta_8}{2} \big\| \epsilon_s^k \big\|^2_{L^2(\Sigma_{\mathrm{f}}^{\mathrm{e}})} \big) - C_{\mathcal{G},\psi} \big\| \epsilon_{\psi}^k \big\|^2_{L^2(\Sigma_{\mathrm{f}}^{\mathrm{e}})}.
\end{aligned}
\tag{4.50}
$$

We let $C_{\mathcal{F},\psi}^{\star} \delta_7 = C_{\mathcal{G},s}^{\star} \delta_8 = C_{\mathcal{F},s}$ in (4.50), and plug (4.46) and (4.50) into (4.48) and

(4.49), such that

$$
\begin{aligned}
&\sum_{\Omega^{\mathrm{e}}} \left(\frac{C_{\rho^0}}{\delta t} + \delta t\, C_{\phi^0} + \frac{3\gamma^{\mathrm{e}}}{4} - \delta t\left(C^{\star}_{\mathcal{F},\sigma}(C_I + C_I') + C_I'\right)\right)\left\|\boldsymbol{\epsilon}^k_{\boldsymbol{v}}\right\|^2_{L^2(\Omega^{\mathrm{e}})} \\
&\quad + \sum_{\Omega^{\mathrm{e}}} \left(\frac{1}{3}C_{\boldsymbol{\Lambda}^{\boldsymbol{T}^0}}\delta t + \frac{2\gamma^{\mathrm{e}}}{3} - \delta t\left(C^{\star}_{\mathcal{F},\sigma}(C_I + C_I') + C_I'\right)\right)\left\|\nabla\boldsymbol{\epsilon}^k_{\boldsymbol{v}}\right\|^2_{L^2(\Omega^{\mathrm{e}})} \\
&\quad + \sum_{\Sigma^{\mathrm{e}}_{\mathrm{f}}} \left(\alpha^{\mathrm{e}}_{\mathrm{f}}(\delta t + 1) - \delta t\, h^{-1}C_pC_{\boldsymbol{\Lambda}^{\boldsymbol{T}^0}} - \gamma^{\mathrm{e}}h^{-1}C_p\right)\left\|[\![\boldsymbol{n}\cdot\boldsymbol{\epsilon}^k_{\boldsymbol{v}}]\!]\right\|^2_{L^2(\Sigma^{\mathrm{e}}_{\mathrm{f}})} \\
&\quad + \sum_{\Sigma^{\mathrm{e}}_{\mathrm{f}}} \left(\frac{1}{\delta t} + C_{\mathcal{G},\psi} - \frac{C^{\star\,2}_{\mathcal{F},\psi}}{2C_{\mathcal{F},s}} - \frac{C^{\star\,2}_{\mathcal{G},s}}{2C_{\mathcal{F},s}}\right)\left\|\epsilon^k_{\psi}\right\|^2_{L^2(\Sigma^{\mathrm{e}}_{\mathrm{f}})}. \\
&\leq -\sum_{\Sigma^{\mathrm{e}}_{\mathrm{c}}} \alpha^2\left(\frac{1}{\alpha} - C_ph^{-1}\left(\delta t\, C_{\boldsymbol{\Lambda}^{\boldsymbol{T}^0}_h} + \gamma^{\mathrm{e}}\right)\right)\left\|[\![\boldsymbol{n}\cdot(\boldsymbol{\Lambda}^{\boldsymbol{T}^0} : \boldsymbol{\epsilon}^{k-1}_{\boldsymbol{E}})]\!]\right\|^2_{L^2(\Sigma^{\mathrm{e}}_{\mathrm{c}})} \\
&\quad - \sum_{\Sigma^{\mathrm{e}}_{\mathrm{c}}} \left(\alpha - C_ph^{-1}\left(\delta t\, C_{\boldsymbol{\Lambda}^{\boldsymbol{T}^0}_h} + \gamma^{\mathrm{e}}\right)\right)\left\|[\![\boldsymbol{\epsilon}^{k-1}_{\boldsymbol{v}}]\!]\right\|^2_{L^2(\Sigma^{\mathrm{e}}_{\mathrm{c}})}.
\end{aligned}
\tag{4.51}
$$

Clearly, the solution is bounded for each (n, k) if (4.40) holds.

Remark 4.3

The value of γ^{e} can be chosen proportional to δt, which can be sufficiently small to asymptotically approach the original problem with pure elasticity. It can be also assigned elementwise, for example, with the value of 0 for elements that are not attached to the rupture surface.

4.6 The reduced problem of nonlinear friction with Newton's method

In this section we rewrite the iterative coupling system (4.36a–f) into the form of matrix–vector product, and derive the Hessian matrix of the Gauss-Newton's method. We write the unknown variables and test functions into local vectors based on each finite element or rupture facet, and into global vectors as unions of local vectors over elements. The notations are listed (with $i, j \in \{1, 2, 3\}$) as follows

variables in Ω or Σ_f	$(\boldsymbol{v}_h)_j$	$(\boldsymbol{w}_h)_j$	$(\boldsymbol{E}_h)_{ij}$	$(\boldsymbol{H}_h)_{ij}$	$(\boldsymbol{u}_h)_j$	$(\boldsymbol{s}_h)_j$	$(\boldsymbol{\tau}_{\mathrm{f}\,h})_j$	σ_h	ψ_h
local vectors in Ω^e	$\mathcal{V}_j^\mathrm{e}$	$\mathcal{W}_j^\mathrm{e}$	$\mathcal{E}_{ij}^\mathrm{e}$	$\mathcal{H}_{ij}^\mathrm{e}$	$\mathcal{U}_j^\mathrm{e}$				
local vectors on $\Sigma_\mathrm{f}^\mathrm{e}$	$\widetilde{\mathcal{V}}_j^\mathrm{e}$		$\widetilde{\mathcal{E}}_{ij}^\mathrm{e}$		$\widetilde{\mathcal{U}}_j^\mathrm{e}$	$\widetilde{\mathcal{S}}_j^\mathrm{e}$	$\widetilde{\mathcal{T}}_j^\mathrm{e}$	$\widetilde{\mathcal{N}}^\mathrm{e}$	$\widetilde{\Psi}^\mathrm{e}$
global vectors	$\mathcal{V}_j$	$\mathcal{W}_j$	$\mathcal{E}_{ij}$	$\mathcal{H}_{ij}$	$\mathcal{U}_j$				

where the notation " $\widetilde{\cdot}$ " denotes quantities on the surface.

We apply nodal expansion of order N to any space-dependent variables, based on 3-D Lagrange polynomials $\{\varphi_n^\mathrm{e}(\boldsymbol{x})\}_{n=1}^{N_p}$ defined on each element Ω^e, or on 2-D Lagrange polynomials $\{\widetilde{\varphi}_n^\mathrm{e}(\boldsymbol{x})\}_{n=1}^{\widetilde{N_p}}$ defined on each facet Σ^e, For example the j^th component particle velocity is expanded in Ω as

$$\boldsymbol{v}_j(\boldsymbol{x}) = \sum_\mathrm{e} \sum_{n=1}^{N_p} v_{jn}^\mathrm{e} \varphi_n^\mathrm{e}(\boldsymbol{x}), \quad \boldsymbol{x} \in \Omega\left(\mathbb{R}^3\right), \quad \mathcal{V}_j^\mathrm{e} := [\,\{v_{jn}\}_{n=1}^{N_p}\,]^\mathrm{T}, \tag{4.52}$$

and on Σ as

$$\boldsymbol{v}_j(\boldsymbol{x}) = \sum_\mathrm{e} \sum_{n=1}^{\widetilde{N_p}} \widetilde{v}_{jn}^\mathrm{e} \widetilde{\varphi}_n^\mathrm{e}(\boldsymbol{x}), \quad \boldsymbol{x} \in \Sigma\left(\mathbb{R}^3\right), \quad \widetilde{\mathcal{V}}_j^\mathrm{e} := [\,\{\widetilde{v}_{jn}\}_{n=1}^{\widetilde{N_p}}\,]^\mathrm{T}, \tag{4.53}$$

We define the global mass matrix $\mathcal{M}$ whose diagonal blocks are local mass matrix of dimension $N_p \times N_p$ on each element with

$$\mathcal{M}_{mn}^\mathrm{e} := \int_{\Omega^\mathrm{e}} \varphi_m^\mathrm{e} \varphi_n^\mathrm{e} \,\mathrm{d}\Omega.$$

We write the block diagonal derivative matrix $\mathcal{D}_j$, whose diagonal blocks are denoted by $\mathcal{D}_j^{\mathrm{e}}$ such that $\mathcal{D}_j^{\mathrm{e}}\mathcal{V}_i^{\mathrm{e}}$ spans $\partial \boldsymbol{v}_i/\partial \boldsymbol{x}_j$ on Ω^{e}, that is

$$\frac{\partial \boldsymbol{v}_i}{\partial \boldsymbol{x}_j}(\boldsymbol{x}) = \sum_{\mathrm{e}} \sum_{n=1}^{N} \left(\mathcal{D}_j^{\mathrm{e}}\mathcal{V}_i^{\mathrm{e}}\right)_n \varphi_n^{\mathrm{e}}(\boldsymbol{x}), \quad \boldsymbol{x} \in \Omega\left(\mathbb{R}^3\right). \tag{4.54}$$

We also define the local surface mass matrix $\widetilde{\mathcal{M}}^{\mathrm{e}}$ of dimension $\widetilde{N}_p \times \widetilde{N}_p$ in a similar manner on each triangle facets of elements. We define the matrix $\mathcal{P}^{\mathrm{e}}$, whose entries take the value of 0 or 1, that projects global vectors to local vectors in each Ω^{e} on the negative side of Σ with regard to $\boldsymbol{n}$, such as $\mathcal{V}_j^{\mathrm{e}} = \mathcal{P}^{\mathrm{e}}\mathcal{V}_j$, and $\widetilde{\mathcal{P}^{\mathrm{e}}}$ projecting global vectors to local vectors on the negative side of Σ^{e}, such as $\widetilde{\mathcal{V}}_j^{\mathrm{e}} = \widetilde{\mathcal{P}^{\mathrm{e}}}\mathcal{V}_j$. We use the notation "$\underline{\cdot}$" to denote the quantities on the positive side of Σ, and assume that each tetrahedral elements are connected to no more than one rupture facet, such that $\mathcal{P}^{\mathrm{e}}\Xi\underline{\widetilde{\mathcal{P}^{\mathrm{e}}}}^{\mathrm{T}} = \underline{\mathcal{P}^{\mathrm{e}}}\Xi\widetilde{\mathcal{P}^{\mathrm{e}}}^{\mathrm{T}} = 0$ for all elementwise block-diagonal matrices Ξ (in particular Ξ represents identity matrix, $\mathcal{M}$, or $\mathcal{D}_j^{\mathrm{T}}$). Also any global vector and its corresponding local vectors in Ω^{e} and Σ^{e} satisfy, for example

$$\widetilde{\mathcal{V}}_j^{\mathrm{e}} = \widetilde{\mathcal{P}^{\mathrm{e}}}\mathcal{V}_j = \widetilde{\mathcal{P}^{\mathrm{e}}}\mathcal{P}^{\mathrm{e}\mathrm{T}}\mathcal{V}_j^{\mathrm{e}}, \quad \underline{\widetilde{\mathcal{V}}_j^{\mathrm{e}}} = \underline{\widetilde{\mathcal{P}^{\mathrm{e}}}}\mathcal{V}_j = \underline{\widetilde{\mathcal{P}^{\mathrm{e}}}\mathcal{P}^{\mathrm{e}\mathrm{T}}\mathcal{V}_j^{\mathrm{e}}}.$$

We assume that the elastic parameters and prestress is piecewise constant, and define $\widetilde{\mathcal{Q}}_{ij}^{\mathrm{e}}$ such that $\widetilde{\mathcal{Q}}_{ij}^{\mathrm{e}}\mathcal{U}_j^{\mathrm{e}} = n_m\widetilde{\mathcal{P}^{\mathrm{e}}}\mathcal{P}^{\mathrm{e}\mathrm{T}}\big(\mathcal{D}_j^{\mathrm{e}} - n_j n_l \mathcal{D}_l^{\mathrm{e}}\big)\mathcal{P}^{\mathrm{e}}(T_{mi}^0\mathcal{U}_j)$, with $\boldsymbol{n} = [n_1, n_2, n_3]^{\mathrm{T}}$, for $i, j, l, m \in \{1, 2, 3\}$. To obtain an asymptotic solution for non-viscous problem, we let $\mathit{\Gamma}_{ijkl} = \gamma\delta_{ik}\delta_{jl}$, with γ sufficiently small (proportional to δt), and denote by $\Phi_{ij}^0 = \big(\frac{\partial^2}{\partial x_i \partial x_j}\phi^0\big)_h$. The equations (4.36a,b) and (4.36e,f) are rewritten in matrix form

$$
\begin{aligned}
&\mathcal{W}_i^{\mathrm{T}}\mathcal{M}\rho^0\,\mathcal{V}_i^{(t,k)} + \delta t\,\mathcal{W}_i^{T}\mathcal{M}\Phi^0_{ij}\mathcal{U}_j^{(t,k)} + \frac{3\gamma}{4}\delta t\,\mathcal{W}_i^{\mathrm{T}}\mathcal{M}\mathcal{V}_i^{(t,k)}\\
&\quad + \delta t\,\mathcal{W}_i^{\mathrm{T}}\mathcal{D}_j^{T}\mathcal{M}\mathit{\Lambda}^{\boldsymbol{T}^0}_{jilm}\mathcal{E}_{lm}^{(t,k)} + \gamma\mathcal{W}_i^{\mathrm{T}}\mathcal{D}_j^{T}\mathcal{M}\mathcal{E}_{ji}^{(t,k)}\\
&\quad + \delta t\,\mathcal{W}_i^{\mathrm{T}}\sum_{\Sigma_{\mathrm{f}}^{\mathrm{e}}}\Big((\underline{\widetilde{\mathcal{P}^{\mathrm{e}}}} - \widetilde{\mathcal{P}^{\mathrm{e}}})^{\mathrm{T}}\widetilde{\mathcal{M}^{\mathrm{e}}}(\widetilde{\mathcal{T}_i^{\mathrm{e}}} - n_i\widetilde{\mathcal{N}^{\mathrm{e}}}) + \underline{\widetilde{\mathcal{P}^{\mathrm{e}}}}^{\mathrm{T}}\widetilde{\mathcal{M}^{\mathrm{e}}}\,\underline{\widetilde{\mathcal{Q}^{\mathrm{e}}_{ij}}\mathcal{U}_j^{\mathrm{e}\,(t,k)}} - \widetilde{\mathcal{P}^{\mathrm{e}}}^{\mathrm{T}}\widetilde{\mathcal{M}^{\mathrm{e}}}\,\widetilde{\mathcal{Q}^{\mathrm{e}}_{ij}}\mathcal{U}_j^{\mathrm{e}\,(t,k)}\Big)\\
&\quad + \delta t\,\mathcal{W}_i^{\mathrm{T}}\Big(\sum_{\Sigma_{\mathrm{f}}^{\mathrm{e}}}\alpha_{\mathrm{f}}^{\mathrm{e}}n_in_j(\underline{\widetilde{\mathcal{P}^{\mathrm{e}}}} - \widetilde{\mathcal{P}^{\mathrm{e}}})^{\mathrm{T}}\widetilde{\mathcal{M}^{\mathrm{e}}}(\underline{\widetilde{\mathcal{P}^{\mathrm{e}}}} - \widetilde{\mathcal{P}^{\mathrm{e}}})\Big)(\mathcal{V}_j^{(t,k)} + \mathcal{U}_j^{(t,k)})\\
&= \delta t\,\mathcal{W}_i^{\mathrm{T}}\Big(\sum_{\Sigma_{\mathrm{f}}^{\mathrm{e}}}n_j(\underline{\widetilde{\mathcal{P}^{\mathrm{e}}}} - \widetilde{\mathcal{P}^{\mathrm{e}}})^{\mathrm{T}}\widetilde{\mathcal{M}^{\mathrm{e}}}\widetilde{\mathcal{P}^{\mathrm{e}}}\Big)(T^0_{ij} + T^{\delta\,(t)}_{ij}) + \mathcal{W}_i^{\mathrm{T}}\mathcal{M}\rho^0\,\mathcal{V}_i^{(t-\delta t)}\\
&\quad + \gamma\mathcal{W}_i^{\mathrm{T}}\mathcal{D}_j^{T}\mathcal{M}\mathcal{E}_{ji}^{(t-\delta t)} - \frac{\delta t}{2}\mathcal{W}_i^{\mathrm{T}}\Big(\sum_{\Sigma_{\mathrm{c}}^{\mathrm{e}}}n_j(\underline{\widetilde{\mathcal{P}^{\mathrm{e}}}} - \widetilde{\mathcal{P}^{\mathrm{e}}})^{\mathrm{T}}\widetilde{\mathcal{M}^{\mathrm{e}}}(\underline{\widetilde{\mathcal{P}^{\mathrm{e}}}} + \widetilde{\mathcal{P}^{\mathrm{e}}})\Big)\mathit{\Lambda}^{\boldsymbol{T}^0}_{jilm}\mathcal{E}_{lm}^{(t,k-1)}\\
&\quad - \alpha\delta t\,\mathcal{W}_i^{\mathrm{T}}\Big(\sum_{\Sigma_{\mathrm{c}}^{\mathrm{e}}}(\underline{\widetilde{\mathcal{P}^{\mathrm{e}}}} - \widetilde{\mathcal{P}^{\mathrm{e}}})^{\mathrm{T}}\widetilde{\mathcal{M}^{\mathrm{e}}}(\underline{\widetilde{\mathcal{P}^{\mathrm{e}}}} - \widetilde{\mathcal{P}^{\mathrm{e}}})\Big)\mathcal{V}_i^{(t,k-1)} - \delta t\,\mathcal{W}_i^{\mathrm{T}}\mathcal{M}\rho^0\,\mathcal{X}_i^{(t,k-1)}\\
&:= \mathcal{W}_i^{\mathrm{T}}\mathcal{M}\mathfrak{V}_i^{(t,k-1)}
\end{aligned}
\tag{4.55a}
$$

$$
\begin{aligned}
&\mathcal{H}_{ij}^{\mathrm{T}}\mathcal{M}\mathcal{E}_{ij}^{(t,k)} + \delta t\,\mathcal{H}_{ij}^{\mathrm{T}}\mathcal{D}_i^{T}\mathcal{M}\mathcal{V}_j^{(t,k)} + \frac{\delta t}{2}\mathcal{H}_{ij}^{\mathrm{T}}\Big(\sum_{\Sigma_{\mathrm{f}}^{\mathrm{e}}}n_i(\underline{\widetilde{\mathcal{P}^{\mathrm{e}}}} - \widetilde{\mathcal{P}^{\mathrm{e}}})^{\mathrm{T}}\widetilde{\mathcal{M}^{\mathrm{e}}}(\underline{\widetilde{\mathcal{P}^{\mathrm{e}}}} + \widetilde{\mathcal{P}^{\mathrm{e}}})\Big)\mathcal{V}_j^{(t,k)}\\
&\quad + \frac{\delta t}{2}\mathcal{H}_{ij}^{\mathrm{T}}\Big(\sum_{\Sigma_{\mathrm{f}}^{\mathrm{e}}}n_i(\underline{\widetilde{\mathcal{P}^{\mathrm{e}}}} + \widetilde{\mathcal{P}^{\mathrm{e}}})^{\mathrm{T}}\widetilde{\mathcal{M}^{\mathrm{e}}}\widetilde{\mathcal{S}}_j^{\mathrm{e}\,(t,k)}\Big)\\
&= \mathcal{H}_{ij}^{\mathrm{T}}\mathcal{M}\mathcal{E}_{ij}^{(t-\delta t)} - \frac{\delta t}{2}\mathcal{H}_{ij}^{\mathrm{T}}\Big(\sum_{\Sigma_{\mathrm{c}}^{\mathrm{e}}}n_i(\underline{\widetilde{\mathcal{P}^{\mathrm{e}}}} - \widetilde{\mathcal{P}^{\mathrm{e}}})^{\mathrm{T}}\widetilde{\mathcal{M}^{\mathrm{e}}}(\underline{\widetilde{\mathcal{P}^{\mathrm{e}}}} + \widetilde{\mathcal{P}^{\mathrm{e}}})\Big)\mathcal{V}_j^{(t,k-1)}\\
&\quad - \alpha\delta t\,\mathcal{H}_{ij}^{\mathrm{T}}\Big(\sum_{\Sigma_{\mathrm{c}}^{\mathrm{e}}}n_in_p(\underline{\widetilde{\mathcal{P}^{\mathrm{e}}}} - \widetilde{\mathcal{P}^{\mathrm{e}}})^{\mathrm{T}}\widetilde{\mathcal{M}^{\mathrm{e}}}(\underline{\widetilde{\mathcal{P}^{\mathrm{e}}}} - \widetilde{\mathcal{P}^{\mathrm{e}}})\Big)\mathit{\Lambda}^{\boldsymbol{T}^0}_{pjlm}\mathcal{E}_{lm}^{(t,k-1)}\\
&:= \mathcal{H}_{ij}^{\mathrm{T}}\mathcal{M}\mathfrak{E}_{ij}^{(t,k-1)}
\end{aligned}
\tag{4.55b}
$$

$$\begin{aligned}&\widetilde{\mathcal{N}}^{\mathrm{e}\,(t,k)} + \frac{n_i n_j}{2}\big(\widetilde{\underline{\mathcal{P}^{\mathrm{e}}}} + \widetilde{\mathcal{P}^{\mathrm{e}}}\big)\mathit{\Lambda}^{\boldsymbol{T}^0}_{ijlm}\mathcal{E}^{(t,k)}_{lm} - \frac{n_i}{2}\big(\underline{\widetilde{\mathcal{Q}}^{\mathrm{e}}_{ij}\mathcal{U}^{\mathrm{e}\,(t,k)}_j} + \widetilde{\mathcal{Q}}^{\mathrm{e}}_{ij}\mathcal{U}^{\mathrm{e}\,(t,k)}_j\big)\\ &\qquad = -n_i n_j \widetilde{\mathcal{P}^{\mathrm{e}}}\big(T^0_{ij}+T^{\delta\,(t)}_{ij}\big) := \widetilde{\mathfrak{N}}^{\mathrm{e}\,(t)}\end{aligned} \tag{4.55c}$$

$$\widetilde{\mathcal{S}}^{\mathrm{e}\,(t,k)}_i = (\delta_{ij} - n_i n_j)\big(\widetilde{\underline{\mathcal{P}^{\mathrm{e}}}} - \widetilde{\mathcal{P}^{\mathrm{e}}}\big)\mathcal{V}^{(t,k)}_j \tag{4.55d}$$

$$\mathcal{U}^{(t,k)}_i - \delta t\, \mathcal{V}^{(t,k)}_i = \mathcal{U}^{(t-\delta t)}_i \tag{4.55e}$$

We let $\mathcal{W}^{\mathrm{T}}_i\mathcal{M} = \mathcal{P}^{\mathrm{e}}$ and $\mathcal{H}^{\mathrm{T}}_{ij}\mathit{\Lambda}^{\boldsymbol{T}^0\mathrm{e}}_{jilm}\mathcal{M} = \mathcal{P}^{\mathrm{e}}$ in (4.55a) and (4.55b), which yields

$$\begin{aligned}&\big(\rho^{0\,\mathrm{e}} + \frac{3\gamma}{4}\delta t\,\big)\mathcal{V}^{\mathrm{e}\,(t,k)}_i + \delta t\,\Phi^{0\,\mathrm{e}}_{ij}\mathcal{U}^{\mathrm{e}\,(t,k)}_j + \overline{\mathcal{D}}^{\mathrm{e}}_j\big(\delta t\,\mathit{\Lambda}^{\boldsymbol{T}^0\mathrm{e}}_{jilm} + \gamma\delta_{jl}\delta_{im}\big)\mathcal{E}^{\mathrm{e}\,(t,k)}_{lm}\\ &\qquad - \delta t\,\mathcal{J}^{\mathrm{e}}\widetilde{\mathcal{T}}^{\mathrm{e}}_i + \delta t\, n_i\mathcal{J}^{\mathrm{e}}\widetilde{\mathcal{N}}^{\mathrm{e}} - \delta t\,\mathcal{J}^{\mathrm{e}}\widetilde{\mathcal{Q}}^{\mathrm{e}}_{ij}\mathcal{U}^{\mathrm{e}\,(t,k)}_j\\ &\qquad - \delta t\,\alpha^{\mathrm{e}}_{\mathrm{f}} n_i n_j\mathcal{J}^{\mathrm{e}}\big(\underline{\mathcal{L}^{\mathrm{e}}(\mathcal{V}^{\mathrm{e}\,(t,k)}_j + \mathcal{U}^{\mathrm{e}\,(t,k)}_j)} - \mathcal{L}^{\mathrm{e}}(\mathcal{V}^{\mathrm{e}\,(t,k)}_j + \mathcal{U}^{\mathrm{e}\,(t,k)}_j)\big) = \mathfrak{V}^{\mathrm{e}\,(t,k-1)}_i\end{aligned} \tag{4.56a}$$

$$\mathcal{E}^{\mathrm{e}\,(t,k)}_{ij} + \delta t\,\overline{\mathcal{D}}^{\mathrm{e}}_i\mathcal{V}^{\mathrm{e}\,(t,k)}_j - \frac{\delta t}{2}n_i\mathcal{J}^{\mathrm{e}}\left(\underline{\mathcal{L}^{\mathrm{e}}\mathcal{V}^{\mathrm{e}\,(t,k)}_j} + \mathcal{L}^{\mathrm{e}}\mathcal{V}^{\mathrm{e}\,(t,k)}_j - \widetilde{\mathcal{S}}^{\mathrm{e}\,(t,k)}_j\right) = \mathfrak{E}^{\mathrm{e}\,(t,k-1)}_{ij} \tag{4.56b}$$

where we define the abbreviative notation $\overline{\mathcal{D}}^{\mathrm{e}} := \mathcal{P}^{\mathrm{e}}\mathcal{M}^{-1}\mathcal{D}^{\mathrm{T}}\mathcal{M}$, $\mathcal{J}^{\mathrm{e}} := \mathcal{P}^{\mathrm{e}}\mathcal{M}^{-1}\widetilde{\mathcal{P}^{\mathrm{e}}}^{\mathrm{T}}\widetilde{\mathcal{M}}^{\mathrm{e}}$, $\mathcal{L}^{\mathrm{e}} := \widetilde{\mathcal{P}^{\mathrm{e}}}\mathcal{P}^{\mathrm{e}\,\mathrm{T}}$, $\underline{\mathcal{L}^{\mathrm{e}}} := \widetilde{\underline{\mathcal{P}^{\mathrm{e}}}}\underline{\mathcal{P}^{\mathrm{e}}}^{\mathrm{T}}$. We get similar equations on the other side of the rupture by applying $\mathcal{W}^{\mathrm{T}}_i\mathcal{M} = \underline{\mathcal{P}^{\mathrm{e}}}$ and $\mathcal{H}^{\mathrm{T}}_{ij}\mathit{\Lambda}^{\boldsymbol{T}^0\mathrm{e}}_{jilm}\mathcal{M} = \underline{\mathcal{P}^{\mathrm{e}}}$ to (4.55a) and (4.55b), and use the abbreviation $\underline{\overline{\mathcal{D}}^{\mathrm{e}}} := \underline{\mathcal{P}^{\mathrm{e}}}\mathcal{M}^{-1}\mathcal{D}^{\mathrm{T}}\mathcal{M}$ and $\underline{\mathcal{J}^{\mathrm{e}}} := \underline{\mathcal{P}^{\mathrm{e}}}\mathcal{M}^{-1}\underline{\widetilde{\mathcal{P}^{\mathrm{e}}}}^{\mathrm{T}}\widetilde{\mathcal{M}}$, such that

$$\begin{aligned}&\big(\underline{\rho^{0}} + \frac{3\gamma}{4}\delta t\,\big)\underline{\widetilde{\mathcal{V}}^{\mathrm{e}\,(t,k)}_i} + \delta t\,\underline{\Phi^{0\,\mathrm{e}}_{ij}\mathcal{U}^{\mathrm{e}\,(t,k)}_j} + \underline{\overline{\mathcal{D}}^{\mathrm{e}}_j}\big(\delta t\,\underline{\mathit{\Lambda}^{\boldsymbol{T}^0\mathrm{e}}_{jilm}} + \gamma\delta_{jl}\delta_{im}\big)\underline{\mathcal{E}^{\mathrm{e}\,(t,k)}_{lm}}\\ &\qquad + \delta t\,\underline{\mathcal{J}^{\mathrm{e}}}\widetilde{\mathcal{T}}^{\mathrm{e}}_i - \delta t\, n_i\underline{\mathcal{J}^{\mathrm{e}}}\widetilde{\mathcal{N}}^{\mathrm{e}} + \delta t\,\underline{\mathcal{J}^{\mathrm{e}}\widetilde{\mathcal{Q}}^{\mathrm{e}}_{ij}\mathcal{U}^{\mathrm{e}\,(t,k)}_j}\\ &\qquad + \delta t\,\alpha^{\mathrm{e}}_{\mathrm{f}} n_i n_j\underline{\mathcal{J}^{\mathrm{e}}}\big(\underline{\mathcal{L}^{\mathrm{e}}(\mathcal{V}^{\mathrm{e}\,(t,k)}_j + \mathcal{U}^{\mathrm{e}\,(t,k)}_j)} - \mathcal{L}^{\mathrm{e}}(\mathcal{V}^{\mathrm{e}\,(t,k)}_j + \mathcal{U}^{\mathrm{e}\,(t,k)}_j)\big) = \underline{\mathfrak{V}^{\mathrm{e}\,(t,k-1)}_i}\end{aligned} \tag{4.57a}$$

$$\underline{\widetilde{\mathcal{E}}^{\mathrm{e}\,(t,k)}_{ij}} + \delta t\,\underline{\overline{\mathcal{D}}^{\mathrm{e}}_i\mathcal{V}^{\mathrm{e}\,(t,k)}_j} + \frac{\delta t}{2}n_i\underline{\mathcal{J}^{\mathrm{e}}}\left(\underline{\mathcal{L}^{\mathrm{e}}\mathcal{V}^{\mathrm{e}\,(t,k)}_j} + \mathcal{L}^{\mathrm{e}}\mathcal{V}^{\mathrm{e}\,(t,k)}_j + \widetilde{\mathcal{S}}^{\mathrm{e}\,(t,k)}_j\right) = \underline{\mathfrak{E}^{\mathrm{e}\,(t,k-1)}_{ij}}. \tag{4.57b}$$

We also rewrite (4.55c–e) with local vectors,

$$\widetilde{\mathcal{N}}^{\mathrm{e}\,(t,k)} + \frac{n_i n_j}{2}\big(\underline{\mathcal{L}^{\mathrm{e}}\Lambda^{\boldsymbol{T}^0\mathrm{e}}_{ijlm}\mathcal{E}^{\mathrm{e}\,(t,k)}_{lm}} + \mathcal{L}^{\mathrm{e}}\Lambda^{\boldsymbol{T}^0\mathrm{e}}_{ijlm}\mathcal{E}^{\mathrm{e}\,(t,k)}_{lm}\big) - \frac{n_i}{2}\big(\underline{\widetilde{\mathcal{Q}}^{\mathrm{e}}_{ij}\mathcal{U}^{\mathrm{e}\,(t,k)}_j} + \widetilde{\mathcal{Q}}^{\mathrm{e}}_{ij}\mathcal{U}^{\mathrm{e}\,(t,k)}_j\big) = \widetilde{\mathfrak{N}}^{\mathrm{e}\,(t)} \tag{4.58a}$$

$$\mathcal{U}^{\mathrm{e}\,(t,k)}_i - \delta t\,\mathcal{V}^{\mathrm{e}\,(t,k)}_i = \mathcal{U}^{\mathrm{e}\,(t-\delta t)}_i, \quad \underline{\mathcal{U}^{\mathrm{e}\,(t,k)}_i} - \delta t\,\underline{\mathcal{V}^{\mathrm{e}\,(t,k)}_i} = \underline{\mathcal{U}^{\mathrm{e}\,(t-\delta t)}_i} \tag{4.58b}$$

$$\widetilde{\mathcal{S}}^{\mathrm{e}\,(t,k)}_i = (\delta_{ij} - n_i n_j)\big(\underline{\mathcal{L}^{\mathrm{e}}\mathcal{V}^{\mathrm{e}\,(t,k)}_j} - \mathcal{L}^{\mathrm{e}}\mathcal{V}^{\mathrm{e}\,(t,k)}_j\big) \tag{4.58c}$$

The above system is not full-rank because $\widetilde{\mathcal{S}}^{\mathrm{e}}_i$ and $\widetilde{\mathcal{T}}^{\mathrm{e}}_i$ has zeros normal components. We choose unit vectors $\boldsymbol{r} = [r_1, r_2, t_3]^{\mathrm{T}}$ and $\boldsymbol{t} = [t_1, t_2, t_3]^{\mathrm{T}}$ such that $[\boldsymbol{n}, \boldsymbol{r}, \boldsymbol{t}]$ forms an orthonormal matrix. We then denote by $\mathcal{K} = [\boldsymbol{r}, \boldsymbol{t}]^{\mathrm{T}}$ the matrix that projects vector variables to the tangential plane. We conclude (4.56a,b), (4.57a,b) and (4.58a–c) as a linear system that follows

$$\boldsymbol{\mathcal{A}}\boldsymbol{\mathcal{Y}} = \boldsymbol{\mathcal{Z}}, \tag{4.59}$$

where

$$\boldsymbol{\mathcal{Y}} = \left[\begin{array}{cccccc|ccc} \boldsymbol{\mathcal{U}} & \underline{\boldsymbol{\mathcal{U}}} & \boldsymbol{\mathcal{E}} & \underline{\boldsymbol{\mathcal{E}}} & \boldsymbol{\mathcal{V}} & \underline{\boldsymbol{\mathcal{V}}} & \widehat{\boldsymbol{\mathcal{S}}} & \widetilde{\boldsymbol{\mathcal{N}}} & \widehat{\boldsymbol{\mathcal{T}}} \end{array}\right]^{\mathrm{T}} := \left[\begin{array}{c} \boldsymbol{\mathcal{Y}}_1 \\ \hline\hline \boldsymbol{\mathcal{Y}}_2 \end{array}\right],$$

with

$$\begin{aligned}
\boldsymbol{\mathcal{U}} &:= \left[\mathcal{U}^{\mathrm{e}\,(t,k)}_1, \mathcal{U}^{\mathrm{e}\,(t,k)}_2, \mathcal{U}^{\mathrm{e}\,(t,k)}_3\right]^{\mathrm{T}}, \quad \boldsymbol{\mathcal{V}} := \left[\mathcal{V}^{\mathrm{e}\,(t,k)}_1, \mathcal{V}^{\mathrm{e}\,(t,k)}_2, \mathcal{V}^{\mathrm{e}\,(t,k)}_3\right]^{\mathrm{T}}, \\
\boldsymbol{\mathcal{E}} &:= \left[\mathcal{E}^{\mathrm{e}\,(t,k)}_{11}, \mathcal{E}^{\mathrm{e}\,(t,k)}_{21}, \mathcal{E}^{\mathrm{e}\,(t,k)}_{31}, \mathcal{E}^{\mathrm{e}\,(t,k)}_{12}, \mathcal{E}^{\mathrm{e}\,(t,k)}_{22}, \mathcal{E}^{\mathrm{e}\,(t,k)}_{32}, \mathcal{E}^{\mathrm{e}\,(t,k)}_{13}, \mathcal{E}^{\mathrm{e}\,(t,k)}_{23}, \mathcal{E}^{\mathrm{e}\,(t,k)}_{33}\right]^{\mathrm{T}}, \\
\widehat{\boldsymbol{\mathcal{S}}} &:= \left[\widehat{\mathcal{S}}^{\mathrm{e}\,(t,k)}_1, \widehat{\mathcal{S}}^{\mathrm{e}\,(t,k)}_2\right]^{T} = \mathcal{K}\left[\widetilde{\mathcal{S}}^{\mathrm{e}\,(t,k)}_1, \widetilde{\mathcal{S}}^{\mathrm{e}\,(t,k)}_2, \widetilde{\mathcal{S}}^{\mathrm{e}\,(t,k)}_3\right]^{\mathrm{T}}, \quad \widetilde{\boldsymbol{\mathcal{N}}} := \widetilde{\mathcal{N}}^{\mathrm{e}\,(t,k)}, \\
\widehat{\boldsymbol{\mathcal{T}}} &:= \left[\widehat{\mathcal{T}}^{\mathrm{e}\,(t,k)}_1, \widehat{\mathcal{T}}^{\mathrm{e}\,(t,k)}_2\right]^{T} = \mathcal{K}\left[\widetilde{\mathcal{T}}^{\mathrm{e}\,(t,k)}_1, \widetilde{\mathcal{T}}^{\mathrm{e}\,(t,k)}_2, \widetilde{\mathcal{T}}^{\mathrm{e}\,(t,k)}_3\right]^{\mathrm{T}},
\end{aligned}$$

and

$$\boldsymbol{\mathcal{Z}} = \left[\begin{array}{cccccc|cc} \boldsymbol{\mathfrak{U}} & \underline{\boldsymbol{\mathfrak{U}}} & \boldsymbol{\mathfrak{E}} & \underline{\boldsymbol{\mathfrak{E}}} & \boldsymbol{\mathfrak{V}} & \underline{\boldsymbol{\mathfrak{V}}} & \mathbf{0} & \widetilde{\boldsymbol{\mathfrak{N}}} \end{array}\right]^{\mathrm{T}} := \left[\begin{array}{c} \boldsymbol{\mathcal{Z}}_1 \\ \hline\hline \boldsymbol{\mathcal{Z}}_2 \end{array}\right],$$

with

$$\boldsymbol{\mathfrak{U}} := \left[\mathfrak{U}_1^{\mathrm{e}\,(t,k-1)}, \mathfrak{U}_2^{\mathrm{e}\,(t,k-1)}, \mathfrak{U}_3^{\mathrm{e}\,(t,k-1)}\right]^{\mathrm{T}}, \quad \boldsymbol{\mathfrak{V}} := \left[\mathfrak{V}_1^{\mathrm{e}\,(t,k-1)}, \mathfrak{V}_2^{\mathrm{e}\,(t,k-1)}, \mathfrak{V}_3^{\mathrm{e}\,(t,k-1)}\right]^{\mathrm{T}}, \quad \boldsymbol{\mathfrak{N}} = \widetilde{\mathfrak{N}}^{\mathrm{e}\,(t)},$$

$$\boldsymbol{\mathfrak{E}} := \left[\mathfrak{E}_{11}^{\mathrm{e}\,(t,k-1)}, \mathfrak{E}_{21}^{\mathrm{e}\,(t,k-1)}, \mathfrak{E}_{31}^{\mathrm{e}\,(t,k-1)}, \mathfrak{E}_{12}^{\mathrm{e}\,(t,k-1)}, \mathfrak{E}_{22}^{\mathrm{e}\,(t,k-1)}, \mathfrak{E}_{32}^{\mathrm{e}\,(t,k-1)}, \mathfrak{E}_{13}^{\mathrm{e}\,(t,k-1)}, \mathfrak{E}_{23}^{\mathrm{e}\,(t,k-1)}, \mathfrak{E}_{33}^{\mathrm{e}\,(t,k-1)}\right]^{\mathrm{T}},$$

and the linear operator

$$\boldsymbol{\mathcal{A}} = \left[\begin{array}{cc|cc|cc||c|c|c}
\boldsymbol{\mathcal{I}}_{3N_p} & & & & -\Delta t\,\boldsymbol{\mathcal{I}}_{3N_p} & & & & \\
 & \boldsymbol{\mathcal{I}}_{3N_p} & & & & -\Delta t\,\boldsymbol{\mathcal{I}}_{3N_p} & & & \\
\hline
 & & \boldsymbol{\mathcal{I}}_{9N_p} & & \Delta t\,\boldsymbol{\mathcal{D}}^{\dagger} - \frac{\Delta t}{2}\boldsymbol{\mathcal{R}}^{\mathrm{T}}\boldsymbol{\mathcal{J}}\widetilde{\boldsymbol{\mathcal{L}}} & -\frac{\Delta t}{2}\boldsymbol{\mathcal{R}}^{\mathrm{T}}\boldsymbol{\mathcal{J}}\underline{\widetilde{\boldsymbol{\mathcal{L}}}} & \frac{\Delta t}{2}\boldsymbol{\mathcal{R}}^{\mathrm{T}}\boldsymbol{\mathcal{J}}\widetilde{\boldsymbol{\mathcal{K}}}^{\mathrm{T}} & & \\
 & & & \boldsymbol{\mathcal{I}}_{9N_p} & \frac{\Delta t}{2}\boldsymbol{\mathcal{R}}^{\mathrm{T}}\underline{\boldsymbol{\mathcal{J}}}\widetilde{\boldsymbol{\mathcal{L}}} & \Delta t\,\underline{\boldsymbol{\mathcal{D}}}^{\dagger} + \frac{\Delta t}{2}\boldsymbol{\mathcal{R}}^{\mathrm{T}}\underline{\boldsymbol{\mathcal{J}}\widetilde{\boldsymbol{\mathcal{L}}}} & \frac{\Delta t}{2}\boldsymbol{\mathcal{R}}^{\mathrm{T}}\underline{\boldsymbol{\mathcal{J}}}\widetilde{\boldsymbol{\mathcal{K}}}^{\mathrm{T}} & & \\
\hline
\begin{array}{l}\Delta t\,\boldsymbol{\Phi} - \Delta t\,\boldsymbol{\mathcal{J}}\widetilde{\boldsymbol{\mathcal{Q}}} \\ \quad + \Delta t\,\alpha_{\mathrm{f}}^{\mathrm{e}}\boldsymbol{\mathcal{B}}^{\mathrm{T}}\boldsymbol{\mathcal{B}}\boldsymbol{\mathcal{J}}\widetilde{\boldsymbol{\mathcal{L}}}\end{array} & -\Delta t\,\alpha_{\mathrm{f}}^{\mathrm{e}}\boldsymbol{\mathcal{B}}^{\mathrm{T}}\boldsymbol{\mathcal{B}}\boldsymbol{\mathcal{J}}\underline{\widetilde{\boldsymbol{\mathcal{L}}}} & \Delta t\,\boldsymbol{\mathcal{D}}\boldsymbol{\Lambda} + \gamma\boldsymbol{\mathcal{D}} & & \begin{array}{l}(\rho^{0\,\mathrm{e}} + \frac{3\gamma}{4}\Delta t\,)\boldsymbol{\mathcal{I}}_{3N_p} \\ \quad + \Delta t\,\alpha_{\mathrm{f}}^{\mathrm{e}}\boldsymbol{\mathcal{B}}^{\mathrm{T}}\boldsymbol{\mathcal{B}}\boldsymbol{\mathcal{J}}\widetilde{\boldsymbol{\mathcal{L}}}\end{array} & -\Delta t\,\alpha_{\mathrm{f}}^{\mathrm{e}}\boldsymbol{\mathcal{B}}^{\mathrm{T}}\boldsymbol{\mathcal{B}}\boldsymbol{\mathcal{J}}\underline{\widetilde{\boldsymbol{\mathcal{L}}}} & & \Delta t\,\boldsymbol{\mathcal{J}}\widetilde{\boldsymbol{\mathcal{B}}}^{\mathrm{T}} & -\Delta t\,\boldsymbol{\mathcal{J}}\widetilde{\boldsymbol{\mathcal{K}}}^{\mathrm{T}} \\
-\Delta t\,\alpha_{\mathrm{f}}^{\mathrm{e}}\boldsymbol{\mathcal{B}}^{\mathrm{T}}\boldsymbol{\mathcal{B}}\underline{\boldsymbol{\mathcal{J}}}\widetilde{\boldsymbol{\mathcal{L}}} & \begin{array}{l}\Delta t\,\boldsymbol{\Phi} + \Delta t\,\underline{\boldsymbol{\mathcal{J}}\widetilde{\boldsymbol{\mathcal{Q}}}} \\ \quad + \Delta t\,\alpha_{\mathrm{f}}^{\mathrm{e}}\boldsymbol{\mathcal{B}}^{\mathrm{T}}\boldsymbol{\mathcal{B}}\underline{\boldsymbol{\mathcal{J}}\widetilde{\boldsymbol{\mathcal{L}}}}\end{array} & & \Delta t\,\underline{\boldsymbol{\mathcal{D}}\boldsymbol{\Lambda}} + \gamma\underline{\boldsymbol{\mathcal{D}}} & -\Delta t\,\alpha_{\mathrm{f}}^{\mathrm{e}}\boldsymbol{\mathcal{B}}^{\mathrm{T}}\boldsymbol{\mathcal{B}}\underline{\boldsymbol{\mathcal{J}}}\widetilde{\boldsymbol{\mathcal{L}}} & \begin{array}{l}(\underline{\rho}^{0\,\mathrm{e}} + \frac{3\gamma}{4}\Delta t\,)\boldsymbol{\mathcal{I}}_{3N_p} \\ \quad + \Delta t\,\alpha_{\mathrm{f}}^{\mathrm{e}}\boldsymbol{\mathcal{B}}^{\mathrm{T}}\boldsymbol{\mathcal{B}}\underline{\boldsymbol{\mathcal{J}}\widetilde{\boldsymbol{\mathcal{L}}}}\end{array} & & -\Delta t\,\underline{\boldsymbol{\mathcal{J}}}\widetilde{\boldsymbol{\mathcal{B}}}^{\mathrm{T}} & \Delta t\,\underline{\boldsymbol{\mathcal{J}}}\widetilde{\boldsymbol{\mathcal{K}}}^{\mathrm{T}} \\
\hline\hline
 & & & & \widetilde{\boldsymbol{\mathcal{K}}}\widetilde{\boldsymbol{\mathcal{L}}} & -\widetilde{\boldsymbol{\mathcal{K}}}\underline{\widetilde{\boldsymbol{\mathcal{L}}}} & \boldsymbol{\mathcal{I}}_{2\widetilde{N_p}} & & \\
\hline
-\frac{1}{2}\widetilde{\boldsymbol{\mathcal{B}}}\widetilde{\boldsymbol{\mathcal{Q}}} & -\frac{1}{2}\widetilde{\boldsymbol{\mathcal{B}}}\underline{\widetilde{\boldsymbol{\mathcal{Q}}}} & \frac{1}{2}\widetilde{\boldsymbol{\mathcal{B}}}\widetilde{\boldsymbol{\mathcal{L}}}\boldsymbol{\mathcal{R}}\boldsymbol{\Lambda} & \frac{1}{2}\widetilde{\boldsymbol{\mathcal{B}}}\underline{\widetilde{\boldsymbol{\mathcal{L}}}}\boldsymbol{\mathcal{R}}\underline{\boldsymbol{\Lambda}} & & & & \boldsymbol{\mathcal{I}}_{\widetilde{N_p}} &
\end{array}\right]$$

$$:= \left[\begin{array}{c|c} \boldsymbol{\mathcal{A}}_{11} & \boldsymbol{\mathcal{A}}_{12} \\ \hline \boldsymbol{\mathcal{A}}_{21} & \boldsymbol{\mathcal{A}}_{22} \end{array}\right],$$

in which $\mathcal{I}_N$ stands for $N \times N$ identity matrix, and the non-zero blocks are

$$\boldsymbol{\mathcal{B}} = \begin{bmatrix} n_1\boldsymbol{\mathcal{I}}_{N_p} \\ n_2\boldsymbol{\mathcal{I}}_{N_p} \\ n_3\boldsymbol{\mathcal{I}}_{N_p} \end{bmatrix}^{\mathrm{T}}, \quad \widetilde{\boldsymbol{\mathcal{B}}} = \begin{bmatrix} n_1\boldsymbol{\mathcal{I}}_{\widetilde{N_p}} \\ n_2\boldsymbol{\mathcal{I}}_{\widetilde{N_p}} \\ n_3\boldsymbol{\mathcal{I}}_{\widetilde{N_p}} \end{bmatrix}^{\mathrm{T}}, \quad \boldsymbol{\mathcal{R}} = \begin{bmatrix} \boldsymbol{\mathcal{B}} & . & . \\ . & \boldsymbol{\mathcal{B}} & . \\ . & . & \boldsymbol{\mathcal{B}} \end{bmatrix}, \quad \widetilde{\boldsymbol{\mathcal{K}}} = \begin{bmatrix} r_1\boldsymbol{\mathcal{I}}_{\widetilde{N_p}} & t_1\boldsymbol{\mathcal{I}}_{\widetilde{N_p}} \\ r_2\boldsymbol{\mathcal{I}}_{\widetilde{N_p}} & t_2\boldsymbol{\mathcal{I}}_{\widetilde{N_p}} \\ r_3\boldsymbol{\mathcal{I}}_{\widetilde{N_p}} & t_3\boldsymbol{\mathcal{I}}_{\widetilde{N_p}} \end{bmatrix}^{\mathrm{T}};$$

$$\boldsymbol{\mathcal{J}} = \begin{bmatrix} \mathcal{J}^{\mathrm{e}} & . & . \\ . & \mathcal{J}^{\mathrm{e}} & . \\ . & . & \mathcal{J}^{\mathrm{e}} \end{bmatrix}, \quad \widetilde{\boldsymbol{\mathcal{L}}} = \begin{bmatrix} \mathcal{L}^{\mathrm{e}} & . & . \\ . & \mathcal{L}^{\mathrm{e}} & . \\ . & . & \mathcal{L}^{\mathrm{e}} \end{bmatrix};$$

$$\underline{\boldsymbol{\mathcal{J}}} = \begin{bmatrix} \underline{\mathcal{J}}^{\mathrm{e}} & . & . \\ . & \underline{\mathcal{J}}^{\mathrm{e}} & . \\ . & . & \underline{\mathcal{J}}^{\mathrm{e}} \end{bmatrix}, \quad \underline{\widetilde{\boldsymbol{\mathcal{L}}}} = \begin{bmatrix} \underline{\mathcal{L}}^{\mathrm{e}} & . & . \\ . & \underline{\mathcal{L}}^{\mathrm{e}} & . \\ . & . & \underline{\mathcal{L}}^{\mathrm{e}} \end{bmatrix};$$

$$\boldsymbol{\mathcal{D}} = \begin{bmatrix} \mathcal{D} & . & . \\ . & \mathcal{D} & . \\ . & . & \mathcal{D} \end{bmatrix}, \text{ with } \mathcal{D} = \begin{bmatrix} \overline{\mathcal{D}}^{\mathrm{e}}_1 & \overline{\mathcal{D}}^{\mathrm{e}}_2 & \overline{\mathcal{D}}^{\mathrm{e}}_3 \end{bmatrix};$$

$$\boldsymbol{\mathcal{D}}^{\dagger} = \begin{bmatrix} \mathcal{D}^{\dagger} & . & . \\ . & \mathcal{D}^{\dagger} & . \\ . & . & \mathcal{D}^{\dagger} \end{bmatrix}, \text{ with } \mathcal{D}^{\dagger} = \begin{bmatrix} \overline{\mathcal{D}}^{\mathrm{e}}_1 \\ \overline{\mathcal{D}}^{\mathrm{e}}_2 \\ \overline{\mathcal{D}}^{\mathrm{e}}_3 \end{bmatrix};$$

$$\underline{\boldsymbol{\mathcal{D}}} = \begin{bmatrix} \underline{\mathcal{D}} & . & . \\ . & \underline{\mathcal{D}} & . \\ . & . & \underline{\mathcal{D}} \end{bmatrix}, \text{ with } \underline{\mathcal{D}} = \begin{bmatrix} \underline{\overline{\mathcal{D}}^{\mathrm{e}}_1} & \underline{\overline{\mathcal{D}}^{\mathrm{e}}_2} & \underline{\overline{\mathcal{D}}^{\mathrm{e}}_3} \end{bmatrix};$$

$$\underline{\boldsymbol{\mathcal{D}}^{\dagger}} = \begin{bmatrix} \underline{\mathcal{D}^{\dagger}} & . & . \\ . & \underline{\mathcal{D}^{\dagger}} & . \\ . & . & \underline{\mathcal{D}^{\dagger}} \end{bmatrix}, \text{ with } \underline{\mathcal{D}^{\dagger}} = \begin{bmatrix} \underline{\overline{\mathcal{D}}^{\mathrm{e}}_1} \\ \underline{\overline{\mathcal{D}}^{\mathrm{e}}_2} \\ \underline{\overline{\mathcal{D}}^{\mathrm{e}}_3} \end{bmatrix};$$

$$(\boldsymbol{\mathcal{Q}})_{ij} = \widetilde{\mathcal{Q}}^{\mathrm{e}}_{ij}, \quad (\underline{\boldsymbol{\mathcal{Q}}})_{ij} = \underline{\widetilde{\mathcal{Q}}^{\mathrm{e}}_{ij}}, \quad i, j \in \{1, 2, 3\};$$

$$
\begin{aligned}
\boldsymbol{\Lambda} \; &= \; \begin{bmatrix}
C_{11} & C_{16} & C_{15} & C_{16} & C_{12} & C_{14} & C_{15} & C_{14} & C_{13} \\
C_{16} & C_{66} & C_{56} & C_{66} & C_{26} & C_{46} & C_{56} & C_{46} & C_{36} \\
C_{15} & C_{56} & C_{55} & C_{56} & C_{25} & C_{45} & C_{55} & C_{45} & C_{35} \\
C_{16} & C_{66} & C_{56} & C_{66} & C_{26} & C_{46} & C_{56} & C_{46} & C_{36} \\
C_{12} & C_{26} & C_{25} & C_{26} & C_{22} & C_{24} & C_{25} & C_{24} & C_{23} \\
C_{14} & C_{46} & C_{45} & C_{46} & C_{24} & C_{44} & C_{45} & C_{44} & C_{34} \\
C_{15} & C_{56} & C_{55} & C_{56} & C_{25} & C_{45} & C_{55} & C_{45} & C_{35} \\
C_{14} & C_{46} & C_{45} & C_{46} & C_{24} & C_{44} & C_{45} & C_{44} & C_{34} \\
C_{13} & C_{36} & C_{35} & C_{36} & C_{23} & C_{34} & C_{35} & C_{34} & C_{33}
\end{bmatrix} \\
&+ \frac{1}{2} \left[\begin{array}{ccc|ccc|ccc}
0 & T^0_{12} & T^0_{13} & -T^0_{12} & T^0_{11}+T^0_{22} & T^0_{23} & -T^0_{13} & T^0_{23} & T^0_{11}+T^0_{33} \\
T^0_{21} & -T^0_{11}+T^0_{22} & T^0_{23} & -T^0_{11}-T^0_{22} & -T^0_{12} & -T^0_{13} & -T^0_{23} & -T^0_{13} & T^0_{12} \\
T^0_{31} & T^0_{32} & -T^0_{11}+T^0_{33} & -T^0_{23} & T^0_{13} & -T^0_{12} & -T^0_{11}-T^0_{33} & -T^0_{12} & -T^0_{13} \\
\hline
-T^0_{21} & -T^0_{22}-T^0_{11} & -T^0_{32} & T^0_{11}-T^0_{22} & T^0_{12} & T^0_{13} & -T^0_{23} & -T^0_{13} & T^0_{12} \\
T^0_{22}+T^0_{11} & -T^0_{21} & T^0_{31} & T^0_{21} & 0 & T^0_{23} & T^0_{13} & -T^0_{23} & T^0_{22}+T^0_{33} \\
T^0_{32} & -T^0_{31} & -T^0_{21} & T^0_{31} & T^0_{32} & -T^0_{22}+T^0_{33} & -T^0_{12} & -T^0_{22}-T^0_{33} & -T^0_{23} \\
\hline
-T^0_{31} & -T^0_{32} & -T^0_{33}-T^0_{11} & -T^0_{32} & T^0_{31} & -T^0_{21} & T^0_{11}-T^0_{33} & T^0_{12} & T^0_{13} \\
T^0_{32} & -T^0_{31} & -T^0_{21} & -T^0_{31} & -T^0_{32} & -T^0_{33}-T^0_{22} & T^0_{21} & T^0_{22}-T^0_{33} & T^0_{23} \\
T^0_{33}+T^0_{11} & T^0_{21} & -T^0_{31} & T^0_{21} & T^0_{33}+T^0_{22} & -T^0_{32} & T^0_{31} & T^0_{32} & 0
\end{array}\right],
\end{aligned}
$$

with C_{ij} the Voigt notation of elasticity tensor, while $\underline{\boldsymbol{\Lambda}}$ stands for the counterpart from neighbouring element. We conduct Gauss elimination, which yields

$$\overline{\boldsymbol{\mathcal{A}}}\boldsymbol{\mathcal{Y}}_2 = \overline{\boldsymbol{\mathcal{Z}}}, \tag{4.60}$$

where

$$\overline{\boldsymbol{\mathcal{A}}} = \boldsymbol{\mathcal{A}}_{22} - \boldsymbol{\mathcal{A}}_{21}\boldsymbol{\mathcal{A}}_{11}^{-1}\boldsymbol{\mathcal{A}}_{12} =: \left[\overline{\boldsymbol{\mathcal{A}}}_1 \,|\, \overline{\boldsymbol{\mathcal{A}}}_2\right], \tag{4.61}$$

with $\left(\overline{\boldsymbol{\mathcal{A}}}_1\right)_{3\widetilde{N_p}\times 2\widetilde{N_p}}$ and $\left(\overline{\boldsymbol{\mathcal{A}}}_2\right)_{3\widetilde{N_p}\times 3\widetilde{N_p}}$ submatrices of $\overline{\boldsymbol{\mathcal{A}}}$, and

$$\overline{\boldsymbol{\mathcal{Z}}} = \boldsymbol{\mathcal{Z}}_2 - \boldsymbol{\mathcal{A}}_{21}\boldsymbol{\mathcal{A}}_{11}^{-1}\boldsymbol{\mathcal{Z}}_1. \tag{4.62}$$

We denote

$$\overline{\overline{\boldsymbol{\mathcal{A}}}} := -\overline{\boldsymbol{\mathcal{A}}}_2^{-1}\overline{\boldsymbol{\mathcal{A}}}_1 = \left\{\overline{\overline{\mathcal{A}}}_{ij}\right\}_{i\in\{0,1,2\},\, j\in\{1,2\}}, \tag{4.63}$$

with each $\overline{\overline{\mathcal{A}}}_{ij}$ of dimension $\widetilde{N_p} \times \widetilde{N_p}$, thus

$$\left[\widetilde{\boldsymbol{\mathcal{N}}},\, \widehat{\boldsymbol{\mathcal{T}}}\right]^{\mathrm{T}} = \overline{\overline{\boldsymbol{\mathcal{A}}}}\widehat{\boldsymbol{\mathcal{S}}} + \overline{\boldsymbol{\mathcal{A}}}_2^{-1}\overline{\boldsymbol{\mathcal{Z}}}. \tag{4.64}$$

With a given nonlinear function F in (4.4), we formulate a minimization problem from (4.39),

$$\widehat{\boldsymbol{\mathcal{S}}} = \arg\min \mathfrak{L}(\widehat{\boldsymbol{\mathcal{S}}}), \quad \text{with} \quad \mathfrak{L} = \frac{1}{2}\left\| \frac{\widehat{\boldsymbol{\mathcal{S}}}}{|\widehat{\boldsymbol{\mathcal{S}}}|} F\big(\widetilde{\boldsymbol{\mathcal{N}}}, \widehat{\boldsymbol{\mathcal{S}}}, \widetilde{\Psi}\big) - \widehat{\boldsymbol{\mathcal{T}}} \right\|^2, \tag{4.65}$$

that is constrained by (4.59) and (4.35). We can therefore explicitly write the gradient

$$\mathfrak{G}_j := \frac{\partial \mathfrak{L}}{\partial \widehat{\mathcal{S}}_j} = \sum_{l=1}^{2} \Big(\frac{\widehat{\mathcal{S}}_l}{|\widehat{\mathcal{S}}|} F - \widehat{\mathcal{T}}_l\Big)\Big(\delta_{lj}\frac{F}{|\widehat{\mathcal{S}}|} + \frac{\widehat{\mathcal{S}}_l \widehat{\mathcal{S}}_j}{|\widehat{\mathcal{S}}|^3}\big((\frac{\partial F}{\partial s} + \frac{\partial F}{\partial \psi}\frac{\mathrm{d}\psi}{\mathrm{d}s})|\widehat{\mathcal{S}}| - F\big) + \frac{\widehat{\mathcal{S}}_l}{|\widehat{\mathcal{S}}|}\frac{\partial F}{\partial \sigma}\overline{\overline{\mathcal{A}}}_{0j} - \overline{\overline{\mathcal{A}}}_{lj}\Big), \tag{4.66}$$

and the Gauss-Newton Hessian

$$\begin{aligned}\mathfrak{H}_{ij} := \frac{\partial^2 \mathfrak{L}}{\partial \widehat{\mathcal{S}}_i \partial \widehat{\mathcal{S}}_j} \approx \sum_{l=1}^{2} \bigg(&\Big(\delta_{li}\frac{F}{|\widehat{\mathcal{S}}|} + \frac{\widehat{\mathcal{S}}_l \widehat{\mathcal{S}}_i}{|\widehat{\mathcal{S}}|^3}\big((\frac{\partial F}{\partial s} + \frac{\partial F}{\partial \psi}\frac{\mathrm{d}\psi}{\mathrm{d}s})|\widehat{\mathcal{S}}| - F\big) + \frac{\widehat{\mathcal{S}}_l}{|\widehat{\mathcal{S}}|}\frac{\partial F}{\partial \sigma}\overline{\overline{\mathcal{A}}}_{0i} - \overline{\overline{\mathcal{A}}}_{li}\Big)^{\mathrm{T}} \cdot \\ &\Big(\delta_{lj}\frac{F}{|\widehat{\mathcal{S}}|} + \frac{\widehat{\mathcal{S}}_l \widehat{\mathcal{S}}_j}{|\widehat{\mathcal{S}}|^3}\big((\frac{\partial F}{\partial s} + \frac{\partial F}{\partial \psi}\frac{\mathrm{d}\psi}{\mathrm{d}s})|\widehat{\mathcal{S}}| - F\big) + \frac{\widehat{\mathcal{S}}_l}{|\widehat{\mathcal{S}}|}\frac{\partial F}{\partial \sigma}\overline{\overline{\mathcal{A}}}_{0j} - \overline{\overline{\mathcal{A}}}_{lj}\Big).\end{aligned} \tag{4.67}$$

In the above, $\frac{\mathrm{d}\psi}{\mathrm{d}s}$ is evaluated by (4.35), that is

$$\mathrm{d}\psi = \delta t\, b_i\, \mathrm{d}\theta^{(i)}, \quad \mathrm{d}\theta^{(i)} = -\frac{\partial G}{\partial s}\big(s^{(c_i)}, \psi^{(c_i)}\big) c_i\, \mathrm{d}s - \frac{\partial G}{\partial \psi}\big(s^{(c_i)}, \psi^{(c_i)}\big)\delta t\, a_{ij}\, \mathrm{d}\theta^{(j)}$$

$$\text{with} \quad s^{(c_i)} := (1 - c_i)s^{(t-\delta t)} + c_i s, \quad \psi^{(c_i)} := \psi^{(t-\delta t)} + \delta t\, a_{ij}\theta^{(j)},$$

thus

$$\frac{\mathrm{d}\psi}{\mathrm{d}s} = -\delta t\, b_j\Big(\delta t\, \frac{\partial G}{\partial \psi}\big(s^{(c_i)}, \psi^{(c_i)}\big) a_{ij} + \delta_{ij}\Big)^{-1}\frac{\partial G}{\partial s}\big(s^{(c_i)}, \psi^{(c_i)}\big) c_i.$$

When using backward Euler scheme, we have a simplified version such as

$$\frac{\mathrm{d}\psi}{\mathrm{d}s} = -\delta t\, \frac{\partial G}{\partial s}\Big/\Big(\delta t\, \frac{\partial G}{\partial \psi} + 1\Big).$$

The complete procedure of spontaneous rupture solution follows Algorithm 1.

Algorithm 1 multi-rate iterative solution for spontaneous rupture problem

initiate rupture geometry and materials

form matrix $\boldsymbol{\mathcal{A}}$ in (4.59)

compute matrix $\overline{\boldsymbol{\mathcal{A}}}$ following (4.61) and $\overline{\overline{\boldsymbol{\mathcal{A}}}}$ following (4.63)

for time steps $t = t_0 + m\delta t$, $m = 1, 2, 3, \cdots$ **do**

if $\boldsymbol{T}_0$ perturbs **then**

update matrix $\boldsymbol{\mathcal{A}}$ and recompute matrix $\overline{\boldsymbol{\mathcal{A}}}$ and $\overline{\overline{\boldsymbol{\mathcal{A}}}}$

end if

compute the right-hand-side $\boldsymbol{\mathcal{Z}}$ in (4.59)

obtain initial guess of $\widehat{\boldsymbol{\mathcal{S}}}$ from previous time step

for coupling iteration $k = 1, 2, 3, \cdots$ **do**

compute $\overline{\boldsymbol{\mathcal{Z}}}$ following (4.62)

for Newton's iteration $i = 1, 2, \cdots$ **do**

compute $\widehat{\boldsymbol{\mathcal{T}}}$ and $\widetilde{\mathcal{N}}$ following (4.64)

update rupture state variable $\widetilde{\boldsymbol{\Psi}}$ following (4.35)

if $\mathfrak{L} \leq \epsilon$ **then**

converges and exits the loop

end if

form gradient and Hessian matrices following (4.66) and (4.67)

update slip velocity via $\widehat{\boldsymbol{\mathcal{S}}}^{(i)} = \widehat{\boldsymbol{\mathcal{S}}}^{(i-1)} - \mathfrak{H}^{-1}\mathfrak{G}$

end for

update the wavefield by $\boldsymbol{\mathcal{Y}}_1 = \boldsymbol{\mathcal{A}}_{11}^{-1}\big(\boldsymbol{\mathcal{Z}}_1 - \boldsymbol{\mathcal{A}}_{12}\boldsymbol{\mathcal{Y}}_2\big)$ follwing (4.59)

end for

end for

4.7 Computational experiments

4.7.1 Planar fault with homogeneous material

We verify our numerical algorithm by testing it on the benchmark problem "TPV102" designed by SCEC/USGS Spontaneous Rupture Code Verification Project (SRCVP) [72], which has been used in recent dynamic rupture studies (*e.g.* [56]). The model takes the range of [-18km , 18km] $\times$ [-18km , 0km] $\times$ [-12km , 12km], where the depth is along the direction of x_2, and $x_2 = 0$ represents the ground surface, with a traction-free boundary condition. The planar strike-slip rupture is located on $x_3 = 0$, on which the friction parameters are set to be slip-weakening within the central portion [-15km , 15km] $\times$ [-15km , 0km], with smooth transition into a slip-strengthening condition at positions close to the boundary of the model. The nonlinear dependency of friction magnitude upon normal stress, slip rate and state variable is given by

$$\mathcal{F}(\sigma, s, \psi) = a\,\sigma\,\mathrm{arcsinh}\left(\frac{s}{2s_0}\exp\left(\frac{f_0 + b\ln(s_0\psi/L)}{a}\right)\right),$$

while the state ODE is written as

$$\mathcal{G}(s, \psi) = -1 + \frac{s}{L}\psi.$$

The coefficients of material and components of prestress tensor are shown in Table 4.1, where the coefficient a as well as the initial value of the state variable are assigned by a function depending on position, and satisfy the quasi-static assumptions.

The nucleation of cracking takes place with a time-variant perturbation in stress $\boldsymbol{T}^\delta$ in a ball region centered at (0.0km,-7.5km,0.0km) with radius r_0 =3km, following the

V_p	V_s	ρ	ψ_{ini}
6.0km/s	3.464km/s	2.67g/cm^3	$1.606 \times 10^{9\sim13}\text{s}$
a	b	L	s_0
$0.008 \sim 0.016$	0.012	2cm	$1\mu\text{m/s}$
f_0	s_c	$(\boldsymbol{T}_0)_{13}$	$(\boldsymbol{T}_0)_{33}$
0.6	$10^{-6}\mu\text{m/s}$	75MPa	-120MPa

Table 4.1 : Material parameters, rupture coefficients and prestress in the homogeneous-elastic planar rupture model TPV102. The components of $\boldsymbol{T}_0$ not listed take the value 0. The quantity s_c is an aseismic (creeping) velocity that keeps s away from 0.

scalar function

$$T_{13}^{\delta}(r,t) = T_{31}^{\delta}(r,t) = \delta\tau\, g(r)\, h(t-0),$$

$$g(r) = \begin{cases} \exp\left(\frac{r^2}{r^2-r_0^2}\right) & , \text{ if } r < r_0 \\ 0 & , \text{ if } r \geq r_0 \end{cases} \quad , \quad h(t) = \begin{cases} \exp\left(\frac{(t-1)^2}{t(t-2)}\right) & , \text{ if } 0 < t < 1 \\ 1 & , \text{ if } t \geq 1 \end{cases}$$

where r is the distance of any spatial point in the model to the hypocenter, and $\delta\tau = 25$MPa.

We extend the model to [-20km , 20km] $\times$ [-20km , 0km] $\times$ [-12km , 12km], with extra layers for absorbing boundary, and discretize the computational domain using a fully unstructured tetrahedral mesh with 1,912,556 elements, generated by DistMesh [126] and Tetgen [154]. The rupture plane is properly aligned by subdomain interfaces, and the triangle facets on rupture have a mean area of 0.015km^2, as is shown in Figure 4.7.1. In the numerical simulation we used elements with polynomial order from 1 to 3. The viscosity coefficient is assigned elementwise, which takes a constant value of $4.0, 2.0$ and 1.0×10^{-7}GPa·s within the elements attached to the rupture plane, respectively for polynomial order 1,2 and 3, and 0 in the rest ones. We conducted domain decomposition and ran the simulation on distributed memory machines using 256 cores. We show the snapshots at t=4.5, 5.5 and 6.5 seconds for the order 2 simulation, with the three components of particle velocity in the volume listed in Figure 4.7.2. The propagation of rupture, and the time variations of friction force, normal stress, as well as state variable are also shown in Figure 4.7.4.

We benchmark our numerical result with the ones using a spectral element (SE) method ([87]) and a finite element (FE) method (PyLith [2]), by comparing the seismograms of stations located on the fault plane as well as the ground surface, as is shown in Figure 4.7.5 and Figure 4.7.6 respectively. Clearly, all the physical quantities obtained form the DG simulations match the reference data produced by existing

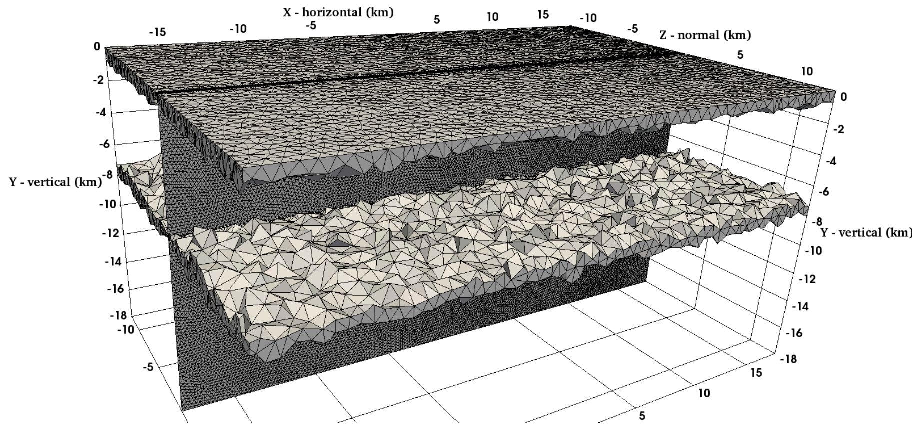

Figure 4.7.1 : Visualization of "TPV102" model with unstructured tetrahedral mesh,

softwares within apt tolerance, even with a coarser mesh compared with the ones used by FE or SE (both using a semi-regular mesh with size of 0.1km, and the SE modeling uses 5^{th} order elements). The numerical results between SE method and DG method with $p \geq 2$ shows very good agreements. In general, numerical results generated by lower-ordered schemes (FE, DG with order 1) show slightly slower propagation speeds of rupture. It can be intuitively related to the intrinsic dissipation of the numerical methods, which affects the solution in a similar manner as artificial viscosity (see also discussions in 4.7.4). For higher order schemes (SE, higher-ordered DG) with smaller numerical dissipation and artificial viscosity, and correspondingly smaller time steps required by stability conditions, the numerical solutions of rupture approach uniformly one with relatively fast propagation speed, which can be interpreted as an appropriate approximation of the physical phenomenon.

4.7.2 Planar fault with bi-material

We modify the strong contrast bi-material model "TPV6" designed by SCEC/USGS SRCVP, by replacing the linear slip-weakening friction law with the rate- and state-

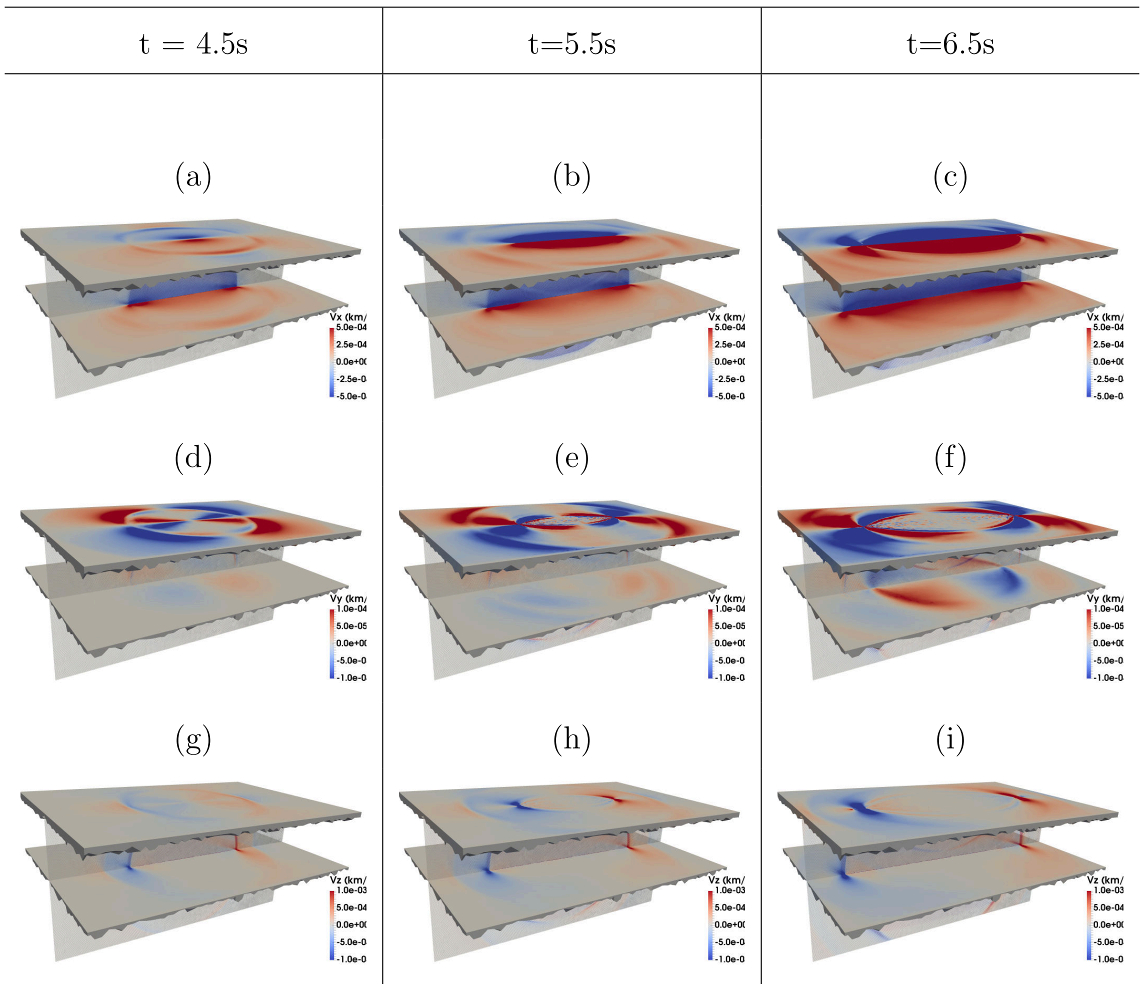

Figure 4.7.2 : Snapshots of particle velocities for “TPV102” model at t = 4.5, 5.5, 6.5 seconds with (a, e, h) horizontal component, (c, f, i) vertical component, (d, g, j) normal component, computed by DG method with polynomial order 2.

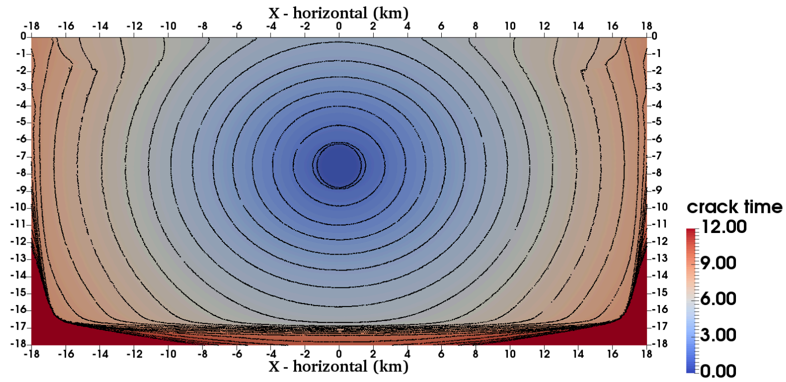

Figure 4.7.3 : Contour of cracking time (when the slip-rate exceeds 1mm/s) on the rupture plane of “TPV102” model, with interval step of 0.5 second.

friction law given in section 4.7.1. The material parameters are listed in Table 4.2. The dimension of the model is [-18km , 18km] $\times$ [-18km , 0km] $\times$ [-10km , 10km]. The location of the rupture and the free-surface, as well as the space-time dependency of stress perturbation $\boldsymbol{T}^{\delta}$ are the same as the “TPV102” model in section 4.7.1. For the sake of computation efficiency, we discretize the model using a quasi-regular tetrahedral mesh with 1,058,400 elements, which is also locally refined, and the fault plane is decomposed to uniform triangles with 1.125×10^{-2} km^2 in area, as is shown in Figure 4.7.7. We also construct a finer mesh with 1,617,408 elements, and on the fault plane the uniform triangles with 7.812×10^{-3} km^2 in area.

In the numerical simulation we use polynomial order 1 and 2, and compute the wavefields till $t = 15.0$ second. We assign elementwise constant viscosity coefficient, which is 2.0×10^{-4}GPa·s in the elements attached to the rupture plane, and 0 in the rest ones. We show the snapshots at $t = 5.0, 6.0$ and 7.0 second, with the three components of particle velocity in the volume listed in Figure 4.7.8 (a)–(i). The propagation of rupture, and the time variations of friction force, normal stress as well as state variable are also shown in Figure 4.7.10. We observe the asymmetric

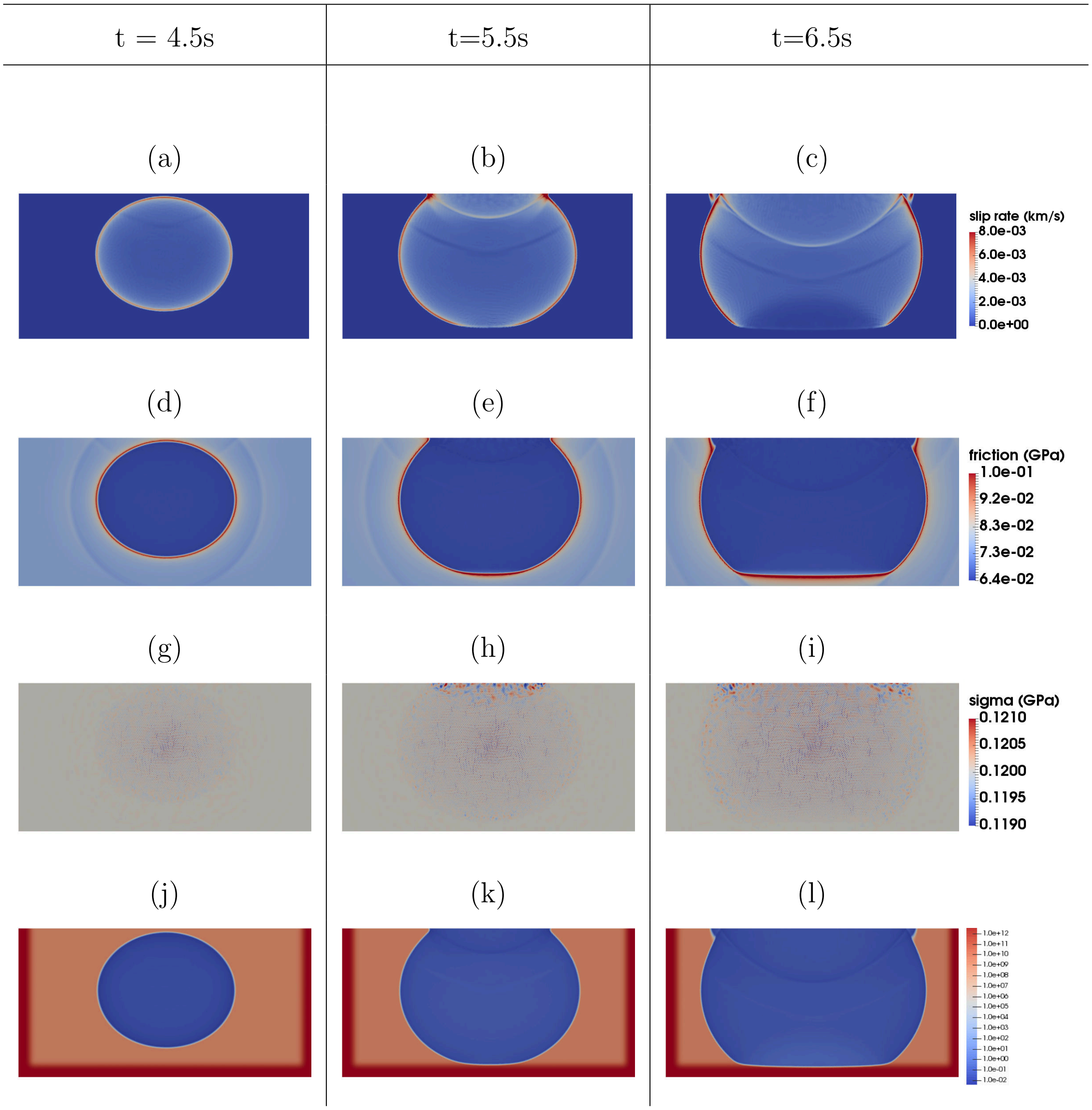

Figure 4.7.4 : Visualization on the rupture plane of "TPV102" model with (a, b, c) the slip rate, (d, e, f) the magnitude of friction force, (g, h, i) the compressive normal stress, (j, k, l) the state variable ("age" of rupture with unit of second), at time t = 4.5, 5.5, 6.5 seconds.

(a)

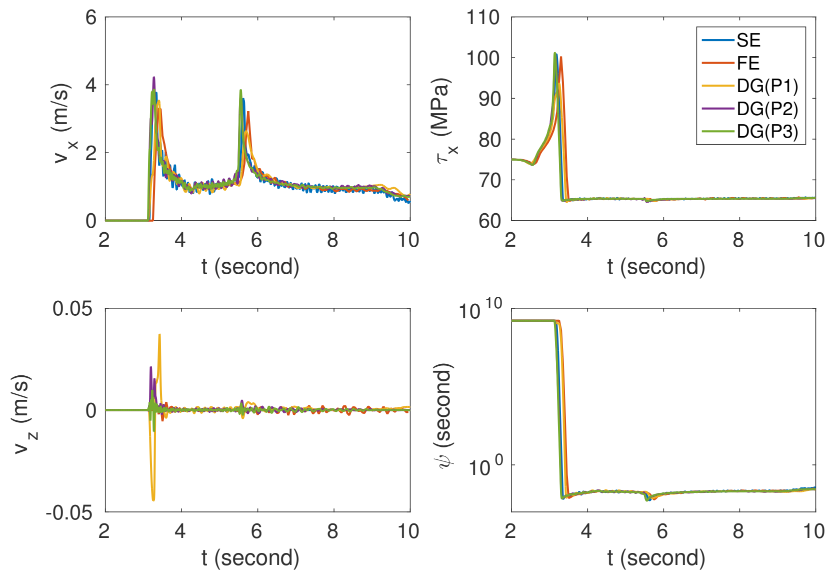

(b)

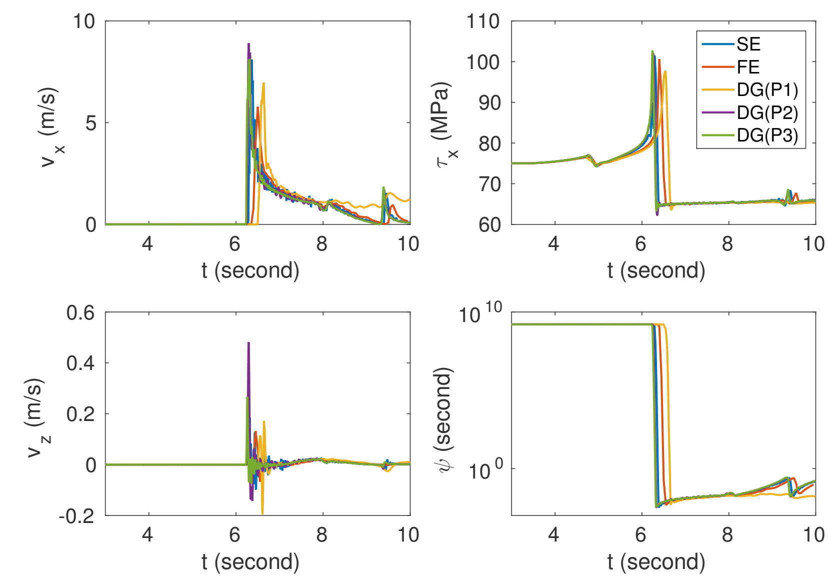

Figure 4.7.5 : Benchmark of the iterative coupling DG method for polynomial order 1,2 and 3, denoted respectively by “DG(P1)”, “DG(P2)” and “DG(P3)” respectively in the legend, with the spectral element (SE) method and the finite element (FE) method on TPV102 with on–fault stations located at (a) [0.0 , 3.0 , 0.0] km, and (b) [12.0 , 12.0 , 0.0] km, showing the horizontal slip rate v_x, horizontal shear stress τ_x, vertical slip rate v_z and state-variable ψ.

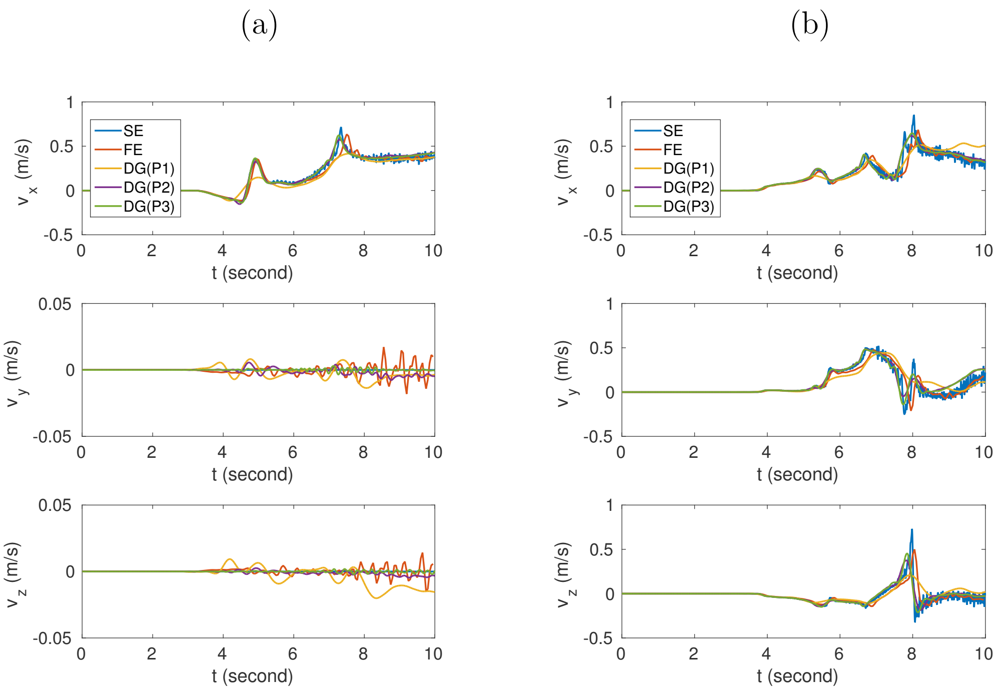

Figure 4.7.6 : Benchmark of the iterative coupling DG method for polynomial order 1,2 and 3, denoted respectively by “DG(P1)”, “DG(P2)” and “DG(P3)” respectively in the legend, with the spectral element (SE) method and the finite element (FE) method on TPV102 with on–ground stations located at (a) [0.0 , 0.0 , 9.0] km and (b) [12.0 , 0.0 , 6.0] km, showing the horizontal velocity v_x, normal velocity v_y, and vertical velocity v_z.

V_{p1}	V_{s1}	ρ_1	V_{p2}	V_{s2}
3.750km/s	2.165km/s	2.225g/cm^3	6.0km/s	3.464km/s
ρ_2	ψ_{ini}	a	b	L
2.67g/cm^3	$1.606 \times 10^{9\sim13}$s	$0.008 \sim 0.016$	0.012	2cm
s_0	f_0	s_c	$(\boldsymbol{T}_0)_{13}$	$(\boldsymbol{T}_0)_{33}$
1μm/s	0.6	$10^{-6}\mu$m/s	75MPa	-120MPa

Table 4.2 : Material parameters, rupture coefficients and prestress in the modified bi-material model with planar rupture. The components of $\boldsymbol{T}_0$ not listed take the value 0. The quantity s_c is an aseismic (creeping) velocity that keeps s away from 0.

propagation speed of rupture that is typical in bi-material models. We show the comparison of seismograms generated by different mesh sizes and polynomial orders in Figure 4.7.11, which demonstrate the convergence of numerical results with *hp*-refinements. Nevertheless, the difference among the seismograms are much more significant than the homogeneous test example, which can be intuitively related to the nonlinear feedback of time-variant normal stress.

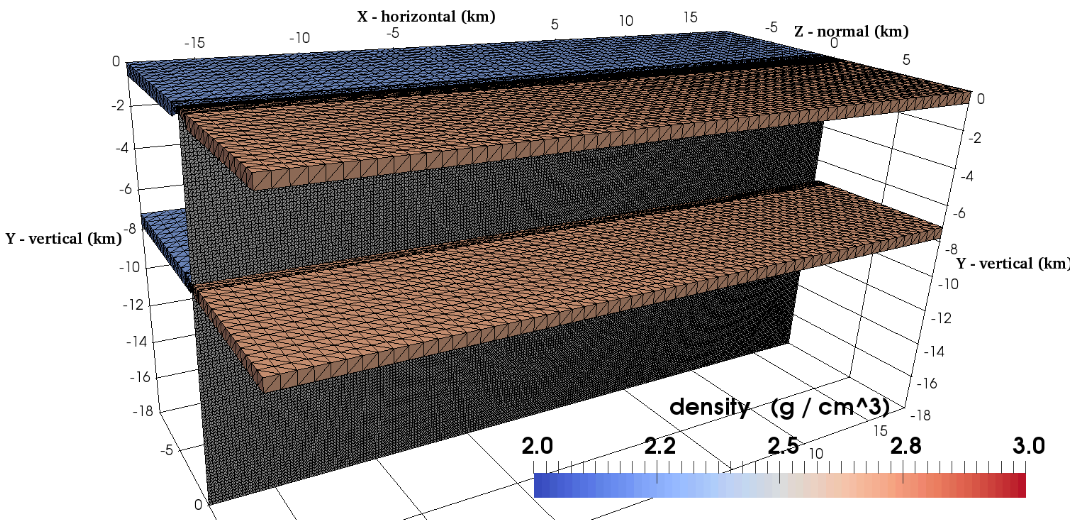

Figure 4.7.7 : Visualization of modified “TPV6” model in a quasi-regular tetrahedral mesh locally refined around rupture with local mesh size $h = 30$m.

4.7.3 Non-planar fault with homogeneous material

A realistic fault has commonly complex geometries, such as bending, step-over, and branching. Here, we consider two stepping-over fault planes with offset of 1.5 km, connected by a third fault plane, forming dihedral angles of 166°. The material parameters are chosen to be almost the same as the “TPV102” model, except for the components of the prestress tensor, as listed in Table 4.3, and the state variable is computed accordingly based on the quasi-static assumption. The dimension of the model is [-20km , 20km] × [-20km , 0km] × [-12km , 12km]. The free-surface boundary condition is applied at x_3 = 0km. The space-time dependency of stress perturbation $\boldsymbol{T}^{\delta}$ are mostly the same as the “TPV102” model in section 4.7.1, except that the hypocenter is placed alternatively at (-9.0km,-7.5km,0.0km).

We discretize the model using a fully unstructured, and sufficiently refined, tetrahedral mesh with 2,101,840 elements, while the rupture planes are discretized by

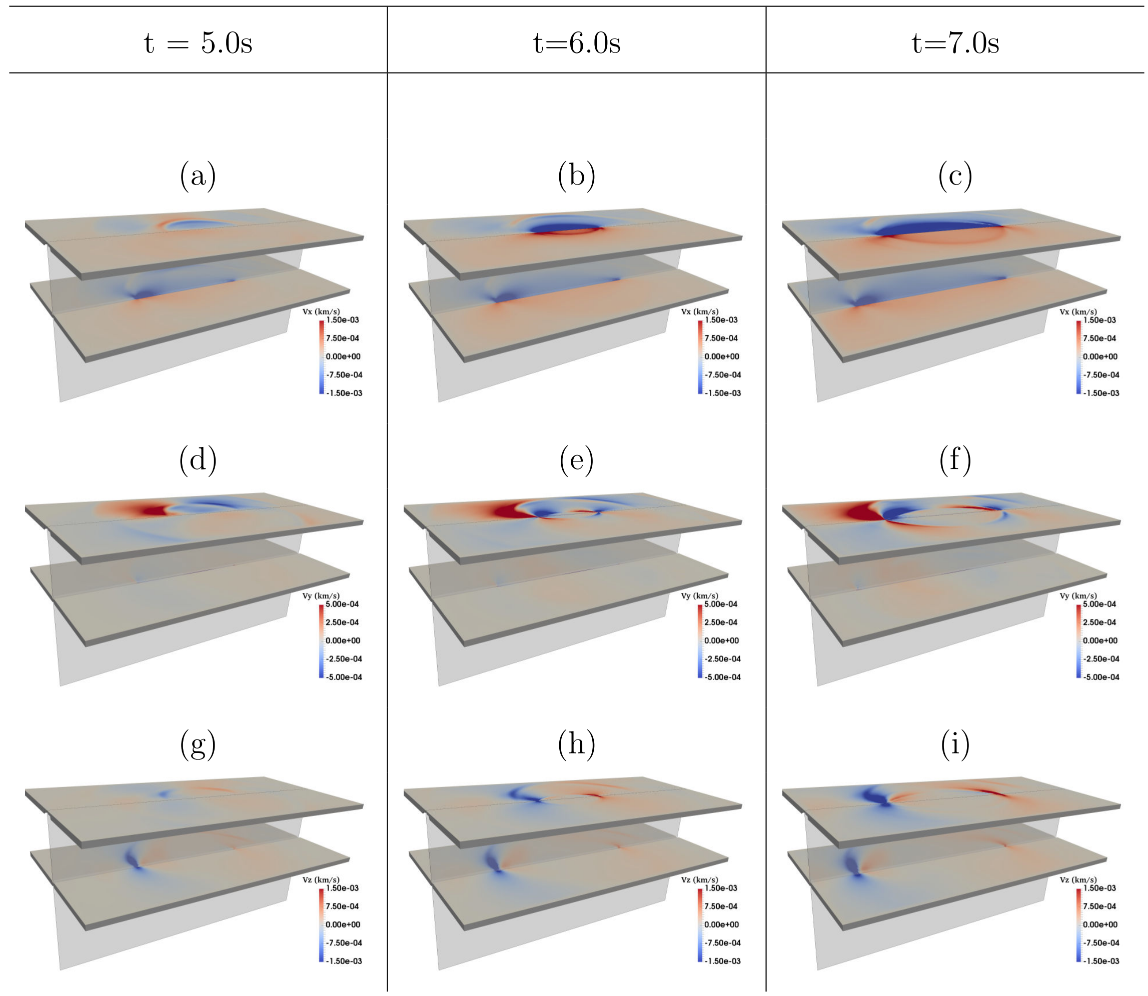

Figure 4.7.8 : Visualization of particle velocities in the modified “TPV6” model at t = 5.0, 6.0, 7.0 seconds with (a, b, c) horizontal component, (d, e, f) vertical component, (g, h, i) normal component, computed by DG method with polynomial order 2 and $h = 30$m.

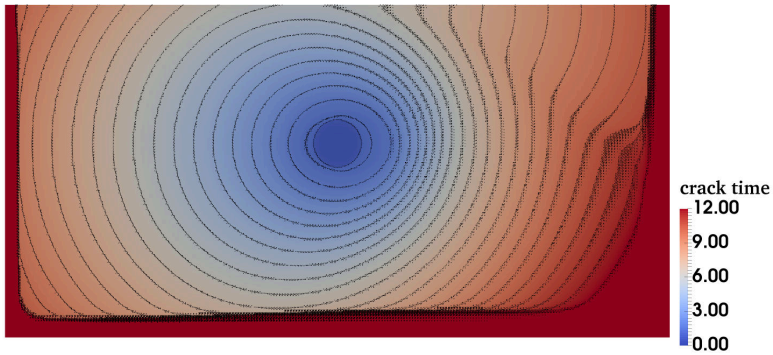

Figure 4.7.9 : Contour of cracking time (when the slip-rate exceeds 1mm/s) on the rupture plane of "TPV102" model, with interval step of 0.5 second.

52,340 triangles, with varying sizes based on the material coefficients (see Figure 4.7.13). In the numerical simulation we use polynomial order 1. We choose the viscosity coefficient elementwise, taking a constant value of 4.0×10^{-7}GPa·s within the elements attached to the rupture plane, and 0 in the rest ones. We show the snapshots at $t = 4.0 \sim 11.0$ seconds during simulation, with the 3 components of particle velocity in the volume listed in Figure 4.7.15–4.7.17. The propagation of rupture, and the time variations of friction force, normal stress as well as state variable are also shown in Figure 4.7.14, Figure 4.7.18 and Figure 4.7.19. We mention the consistency of our numerical result with that shown in relevant researches [108], both indicating the reduction of rupture speed when propagating through a kink.

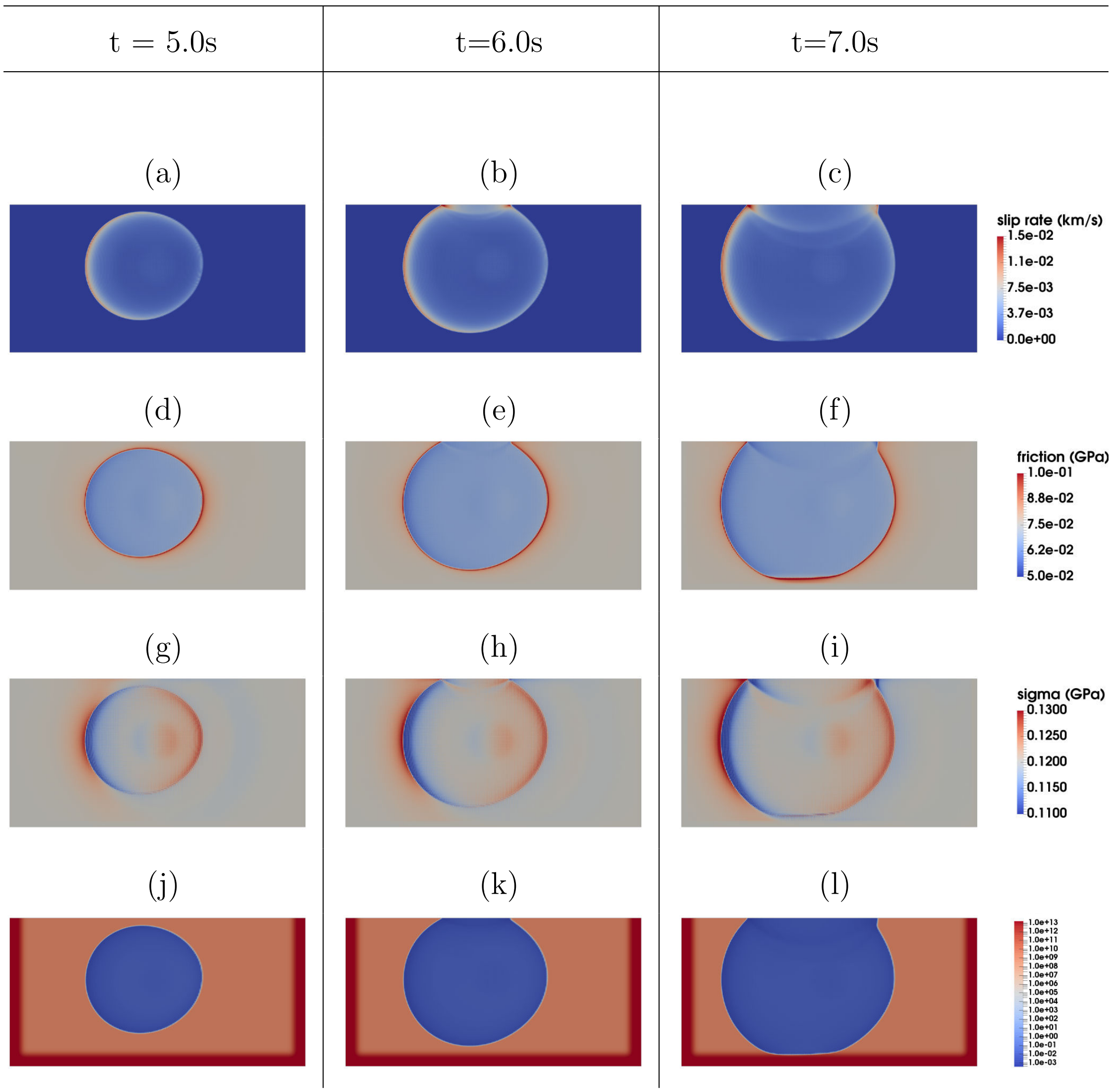

Figure 4.7.10 : Visualization on the rupture plane of modified "TPV6" model with (a, b, c) the slip rate, (d, e, f) the magnitude of friction force, (g, h, i) the compressive normal stress, (j, k, l) the state variable ("age" of rupture with unit of second), at time t = 5.0, 6.0, 7.0 seconds, computed by DG method with polynomial order 2 and $h = 30$m.

(a)

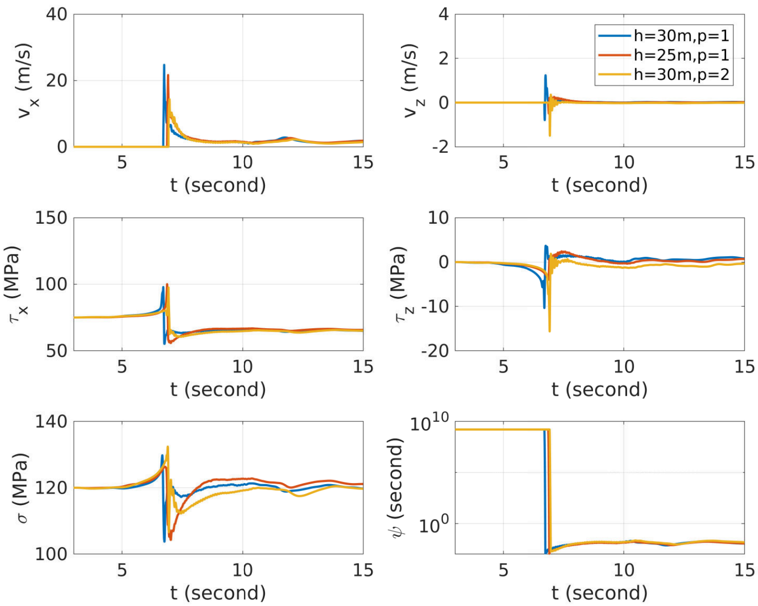

(b)

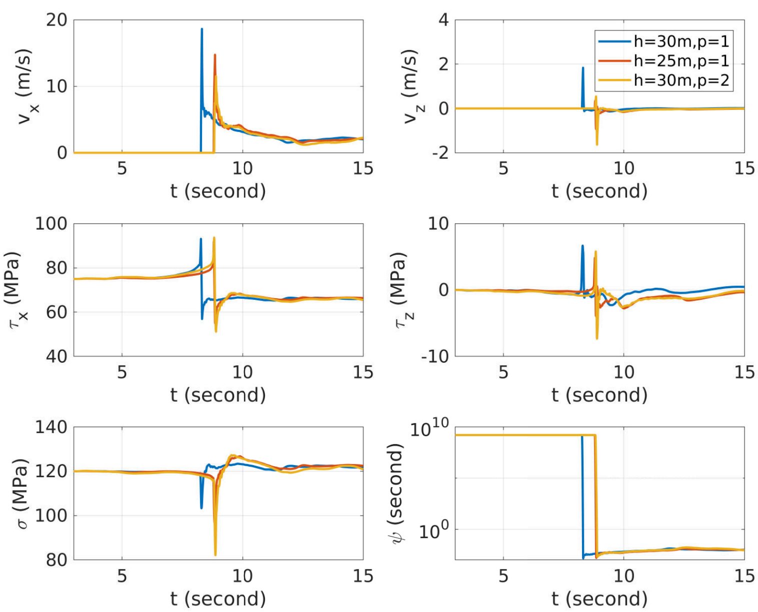

Figure 4.7.11 : Comparison of seismograms at on–fault stations located at (a) $[-12.0\,,\,-12.0\,,\,0.0]$ km, and (b) $[12.0\,,\,-3.0\,,\,0.0]$ km of the modified "TPV6" model with variant mesh size and polynomial order, showing the horizontal and vertical slip rate v_x and v_z, horizontal and vertical shear stress τ_x and τ_z, compressive normal stress σ and state-variable ψ.

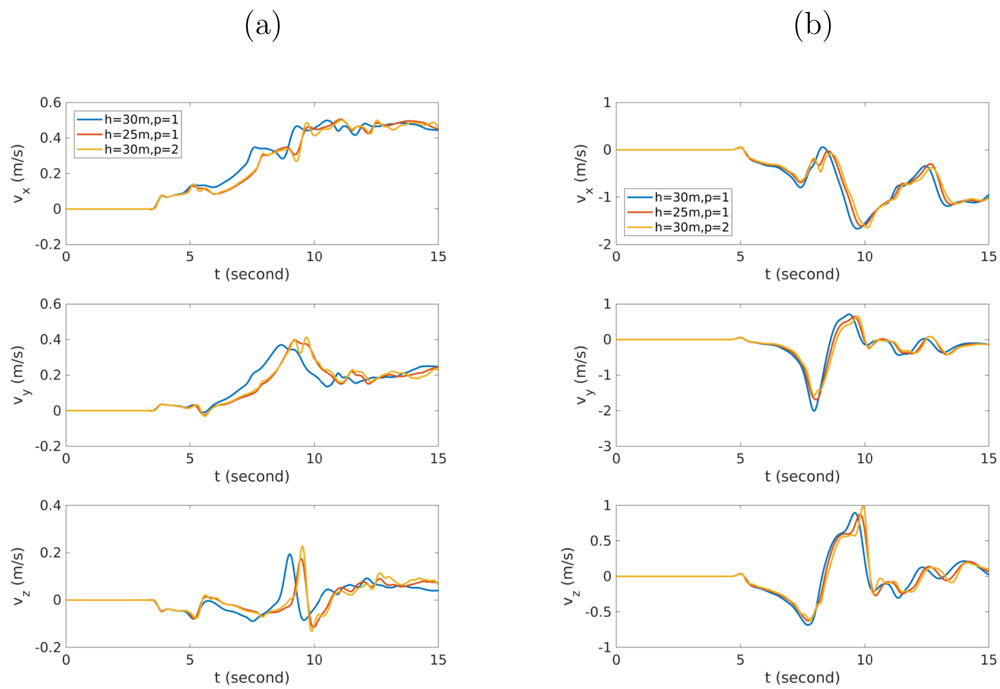

Figure 4.7.12 : Comparison of seismograms at on–ground stations located at (a) [12.0 , 0.0 , 6.0] km, and (b) [−12.0 , 0.0 , −6.0] km of the modified “TPV6” model with variant mesh size and polynomial order, showing the horizontal velocity v_x, normal velocity v_y, and vertical velocity v_z.

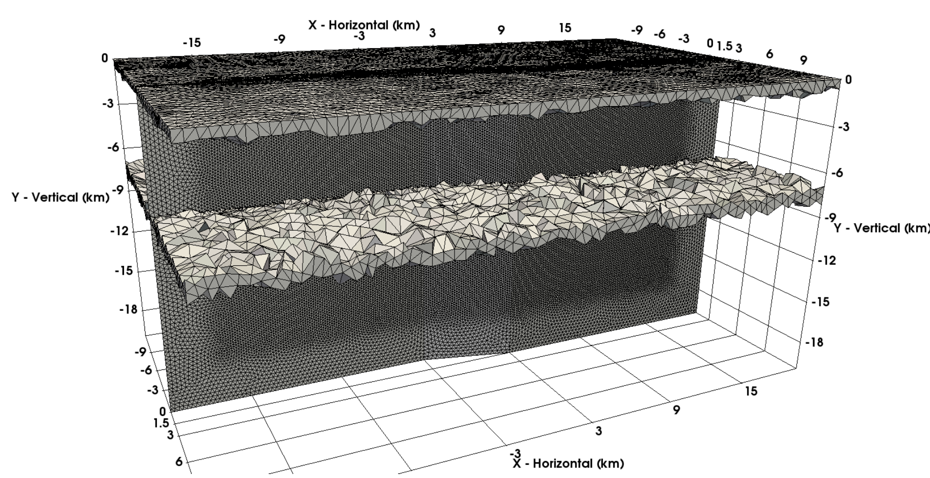

Figure 4.7.13 : Visualization of stepping-over fault model with unstructured tetrahedral mesh.

V_p	V_s	ρ	s_c
6.0km/s	3.464km/s	$2.67\mathrm{g/cm}^3$	$10^{-6}\mu\mathrm{m/s}$
a	b	L	s_0
$0.008 \sim 0.016$	0.012	2cm	$1\mu\mathrm{m/s}$
f_0	$(\boldsymbol{T}_0)_{11}$	$(\boldsymbol{T}_0)_{13}$	$(\boldsymbol{T}_0)_{33}$
0.6	−255MPa	75MPa	−120MPa

Table 4.3 : Material parameters, rupture coefficients and prestress in the homogeneous-elastic stepping-over rupture model. The components of $\boldsymbol{T}_0$ not listed take the value 0. The quantity s_c is an aseismic (creeping) velocity that keeps s away from 0.

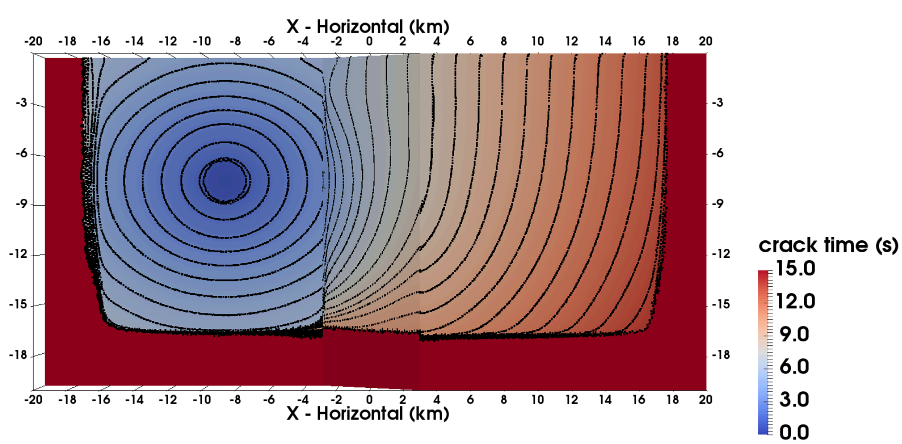

Figure 4.7.14 : Contour of cracking time (when the slip-rate exceeds 1mm/s) on the rupture surface of the stepping-over fault model, with interval step of 0.5 second.

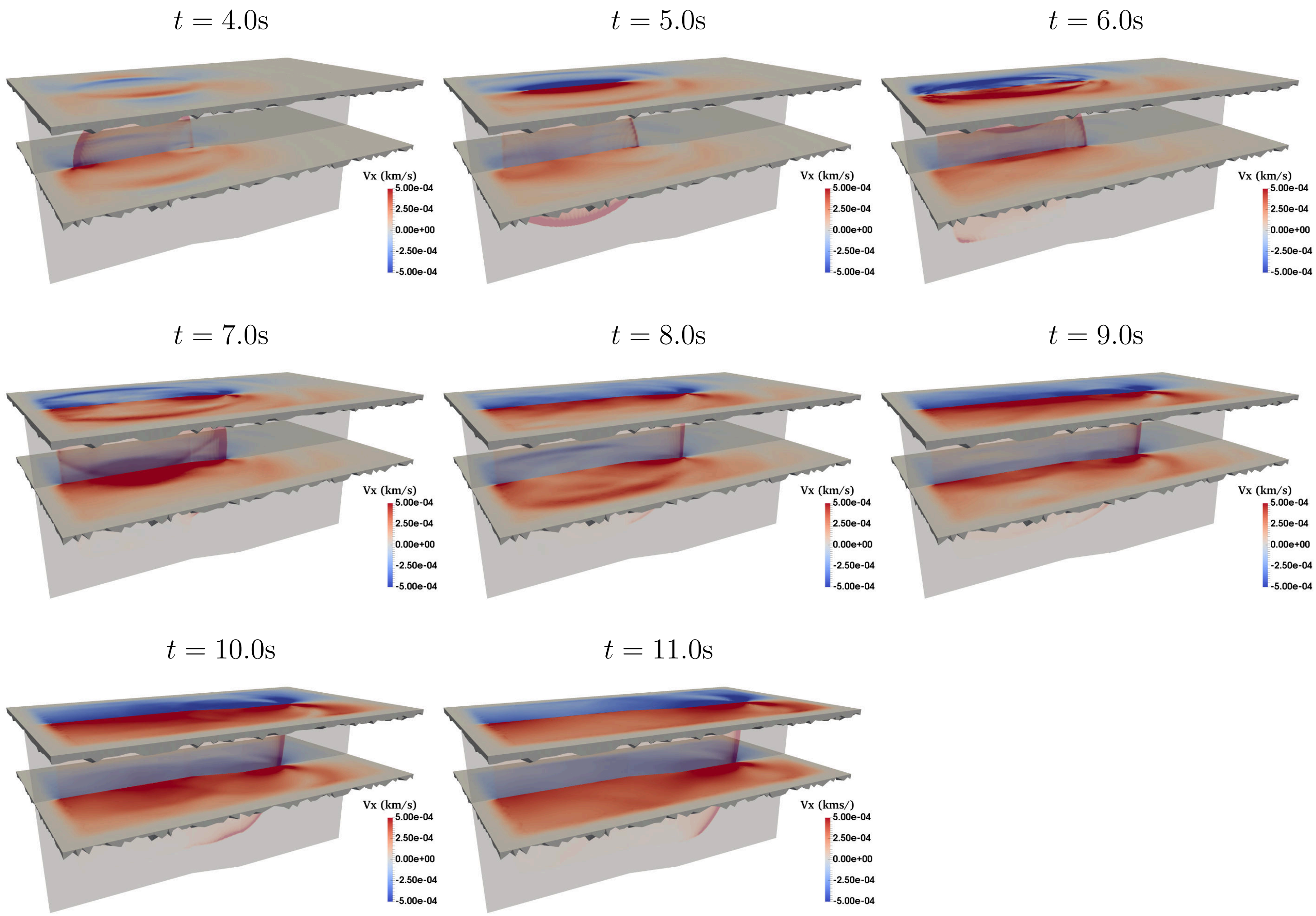

Figure 4.7.15 : Snapshots of the particle velocity with the horizontal component (respect to the two main planes) during the simulation of the stepping-over fault model, at time $t = 4.0 \sim 11.0$s.

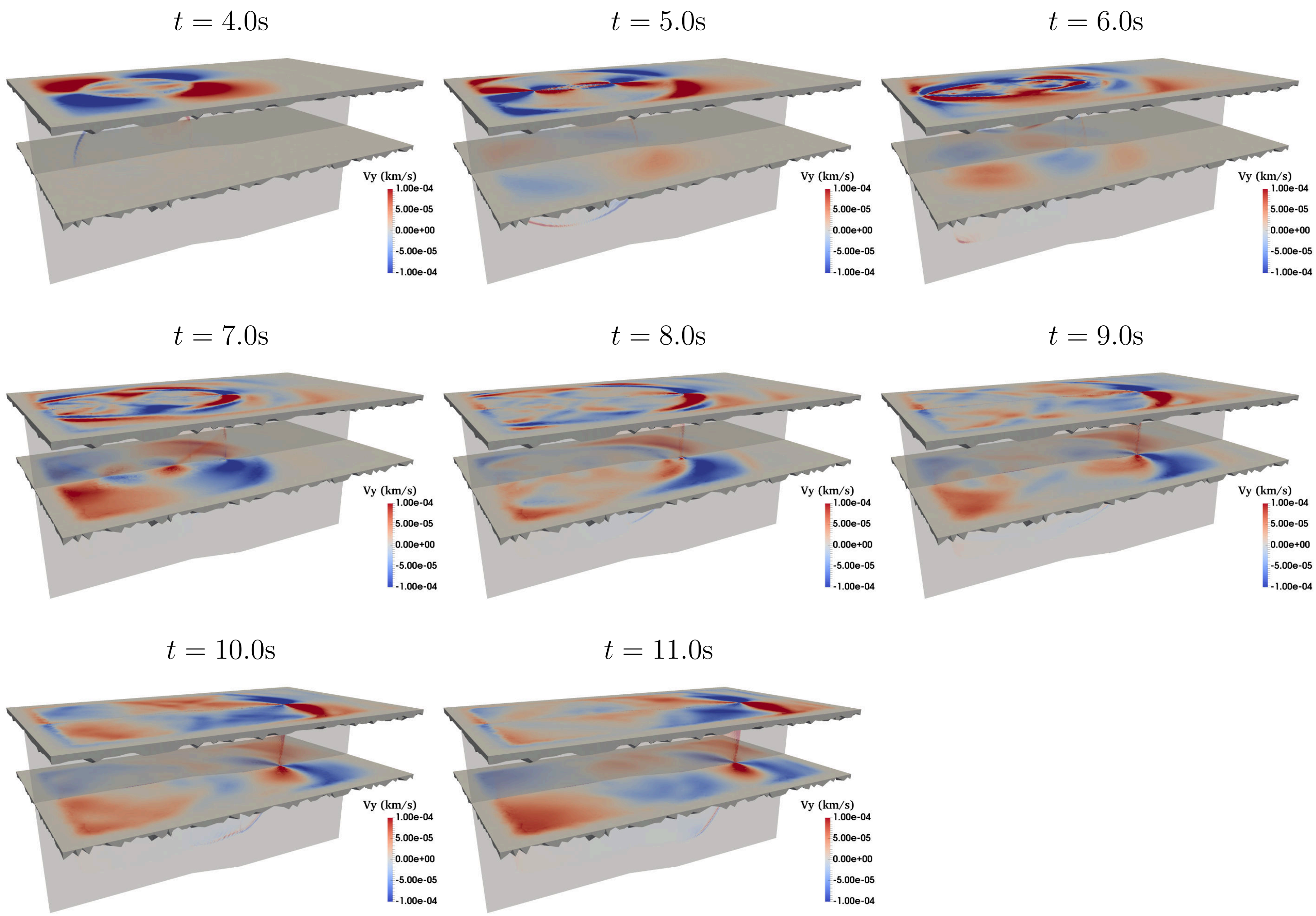

Figure 4.7.16 : Snapshots of the particle velocity with the vertical component during the simulation of the stepping-over fault model, at time $t = 4.0 \sim 11.0$s.

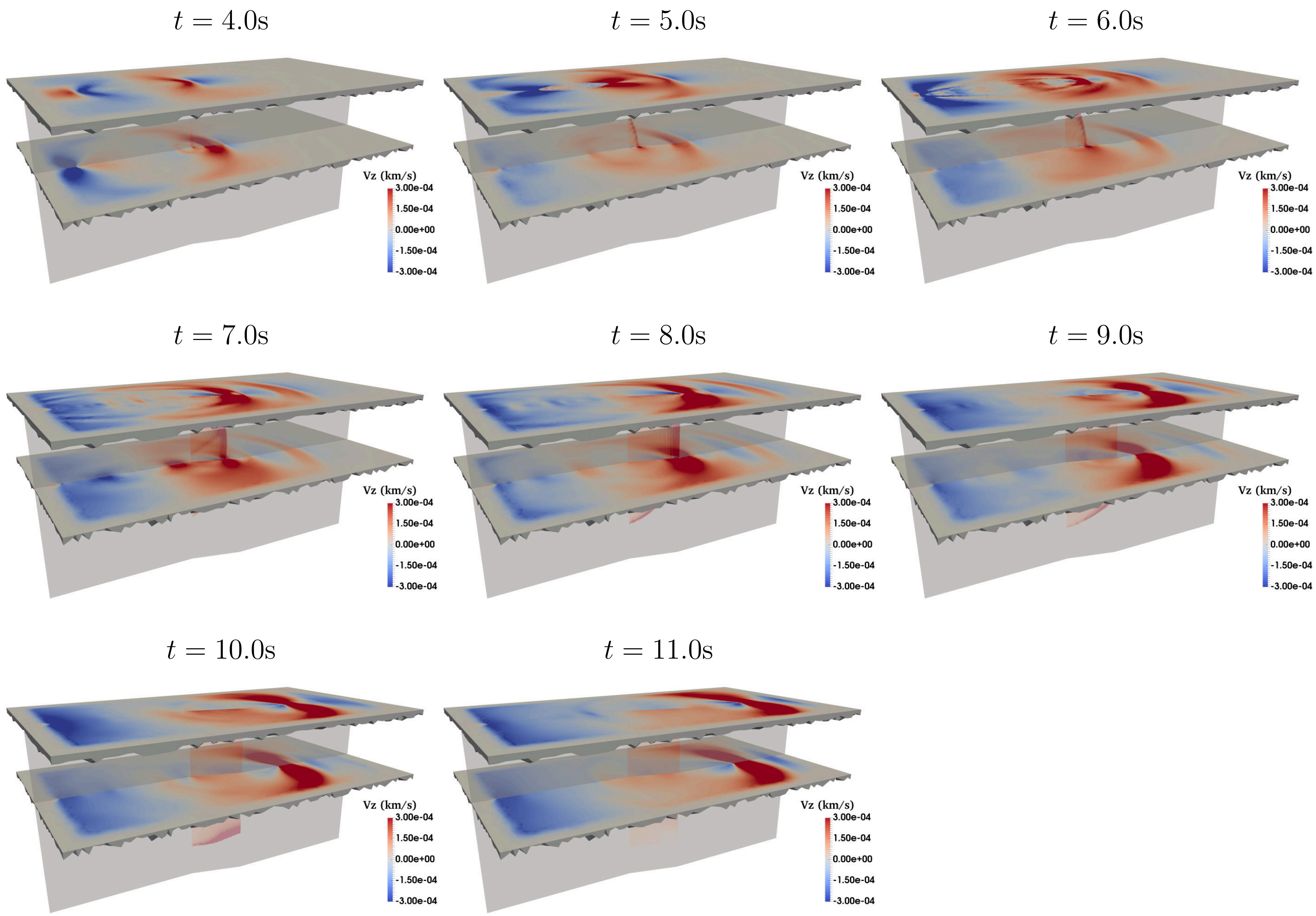

Figure 4.7.17 : Snapshots of the particle velocity with the normal component (respect to the two main planes) during the simulation of the stepping-over fault model, at time $t = 4.0 \sim 11.0$s.

(a)

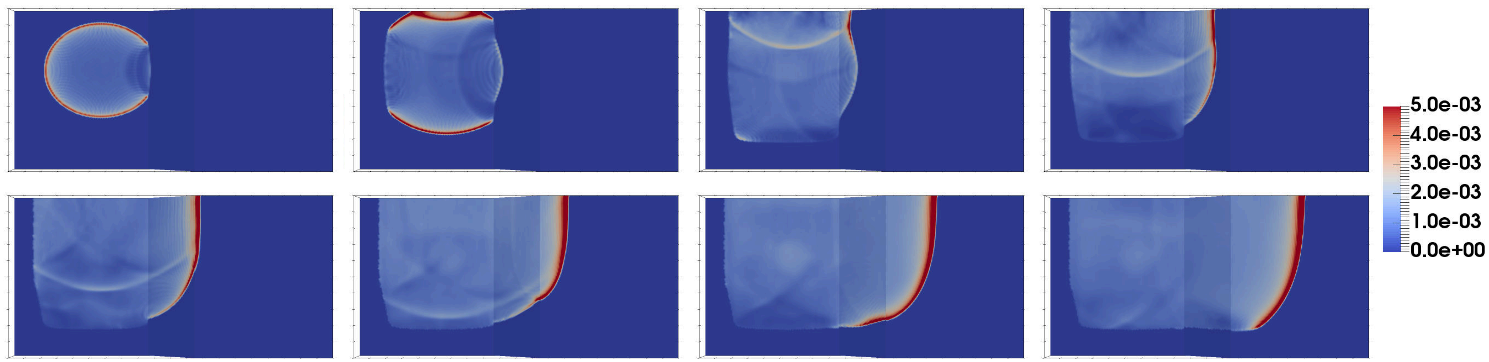

(b)

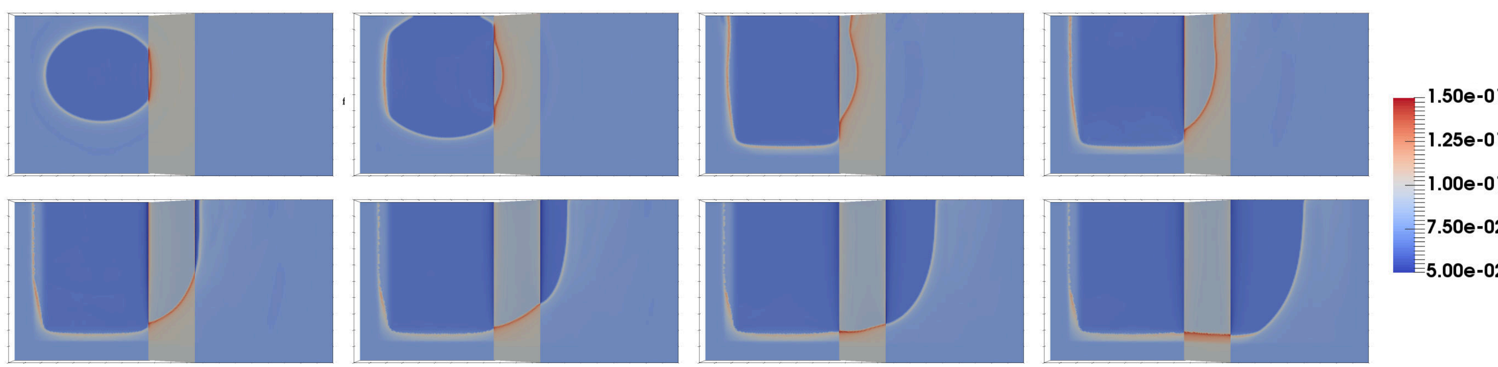

Figure 4.7.18 : Visualization on the rupture surface of the stepping-over fault model with (a) the slip rate, (b) the magnitude of friction force, at time $t = 4.0 \sim 11.0$ seconds with interval of 1.0 second.

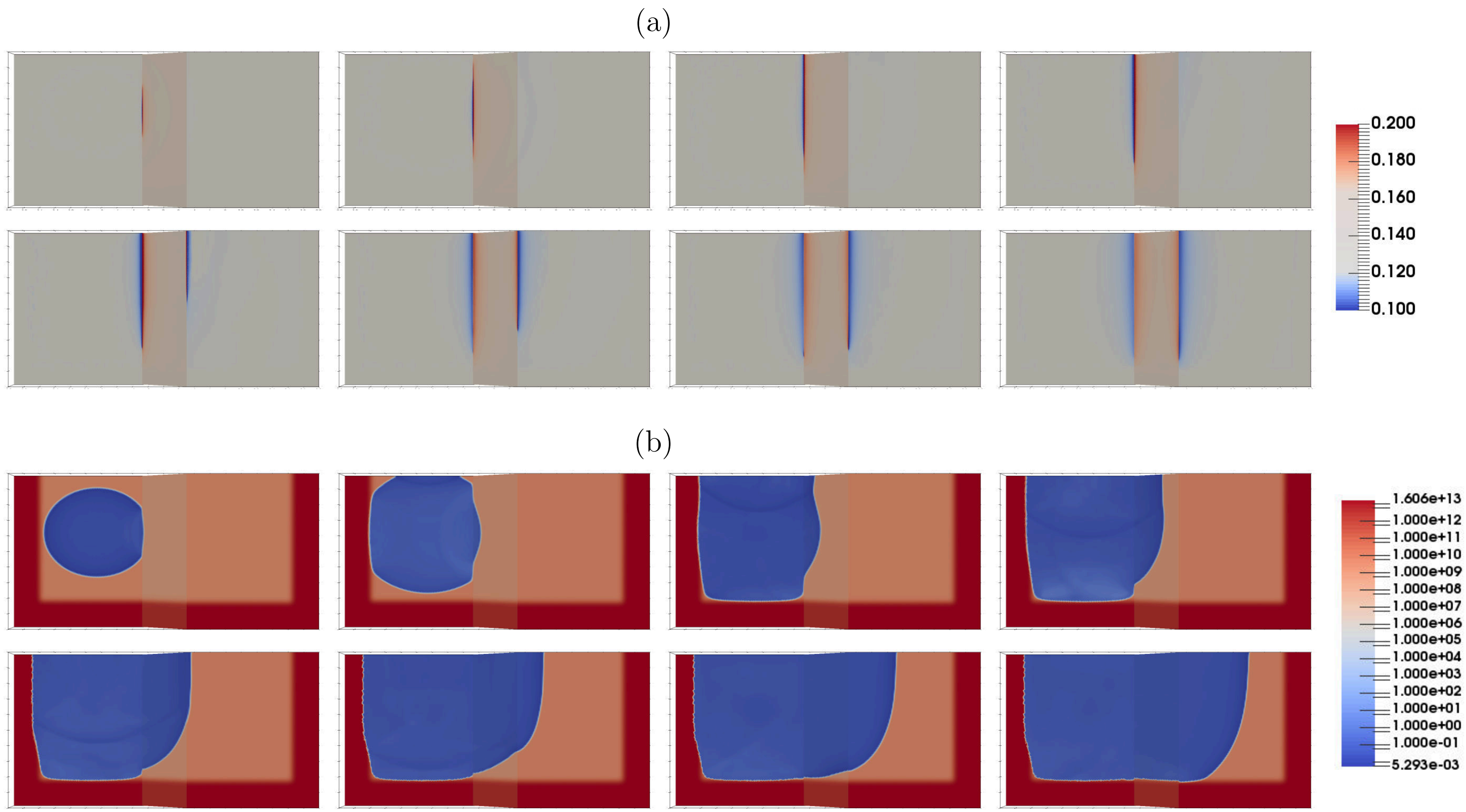

Figure 4.7.19 : Visualization on the rupture surface of the stepping-over fault model with (a) the compressive normal stress, and (b) the state variable ("age" of rupture with unit of second), at time $t = 4.0 \sim 11.0$ seconds with interval of 1.0 second.

4.7.4 The impact of artificial viscosity on rupture propagation

In Theorem 4.1 and Theorem 4.2, lower-bounds of the viscosity coefficient for stability are given. On the other hand, relatively large viscosity coefficients provide sufficient convergence stability, might however change the physical problem. The general impacts of viscosity on the evolution of rupture dynamics are outside the scope of this paper. Nevertheless, we show an example demonstrating the importance of choosing an appropriate value of viscosity coefficient that is sufficient for stability, while not too large to maintain the physical properties of the original problem.

We consider the non-planar rupture problem described in section 4.7.3, while alternatively choose a series of larger viscosity coefficients, namely 2.0×10^{-5}, 4.0×10^{-5} and 4.0×1.0^{-4}GPa·s, within the elements attached to the rupture surface, and 0 in the rest ones. We show the snapshots of slip rate at $t = 6.0s$, when the rupture propagates across the first intersection corner, for different values of viscosity in Figure 4.7.20. The comparison of crack time is shown in Figure 4.7.21. As a general observation from the numerical results, the propagation speed of rupture decreases with increasing viscosity. Moreover, the impact of viscosity can be significant for rupture surface with non-planar geometry, and result in distinct propagation pattern. In particular, the viscosity tends to buffer the change of normal stress (see also [129, section 2.1.1]). In other words, the artificial viscosity must be chosen sufficiently small to properly approximate the real physics, which also sets an upper bound for time stepping of friction modeling based on the stability conditions.

$\gamma = 4.0 \times 10^{-7}$GPa·s

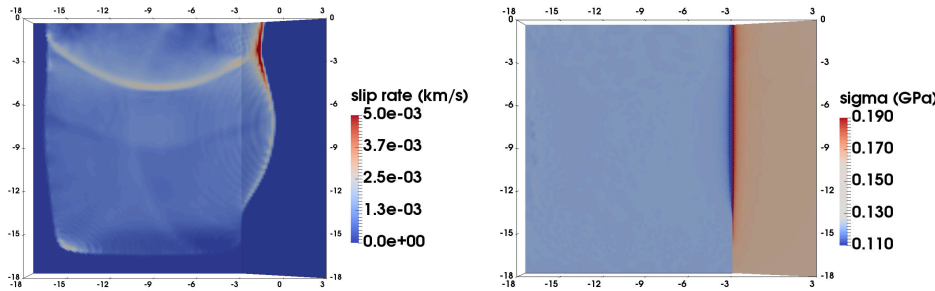

$\gamma = 2.0 \times 10^{-5}$GPa·s

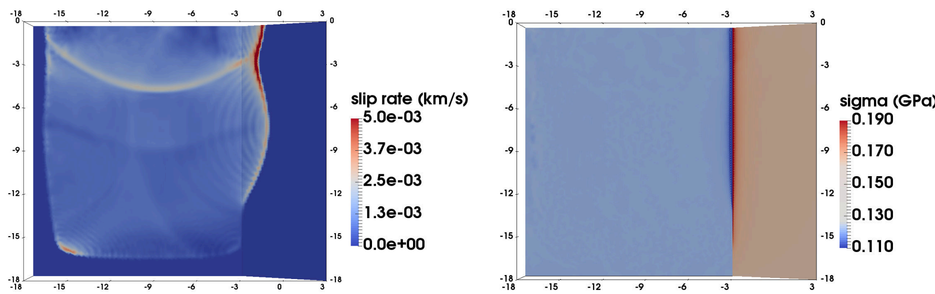

$\gamma = 4.0 \times 10^{-5}$GPa·s

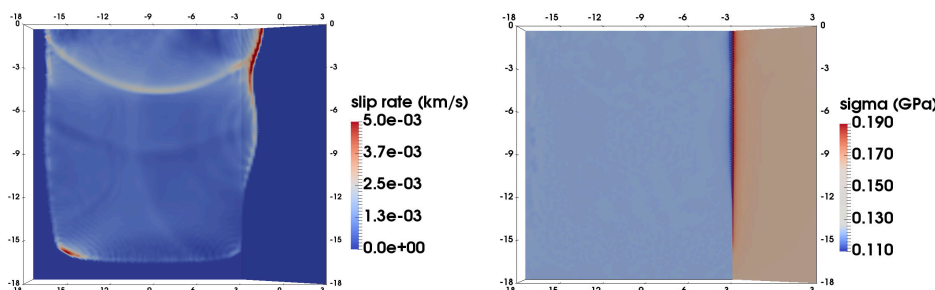

$\gamma = 1.0 \times 10^{-4}$GPa·s

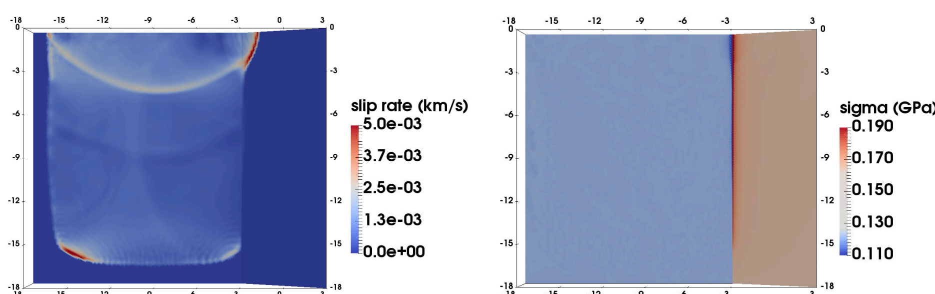

Figure 4.7.20 : Visualization of slip rate (left column) and normal compressive stress (right column) at the rupture surface of the stepping-over fault model at time $t = 6.0$s with different viscosity coefficients.

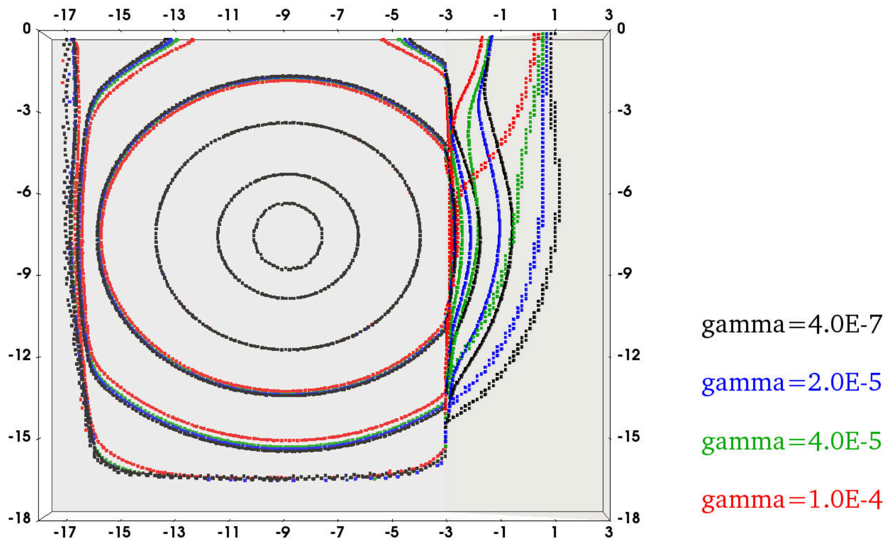

Figure 4.7.21 : Comparison of crack time at the rupture surface of the stepping-over fault model with different values of the viscosity coefficient: $\gamma = 4.0 \times 10^{-7}$GPa·s (black), 2.0×10^{-5}GPa·s (blue), 4.0×10^{-5}GPa·s (green), 1.0×10^{-4}GPa·s (red). Contours are plotted from 1.0 to 7.0 seconds with the interval of 1.0 second.

4.8 Conclusion

We introduce a novel multi-rate iterative coupling scheme for the dynamic system of seismic waves interacting with nonlinear rate- and state-frictional interfaces. We give the full Euler-Lagrange formulation with pre-stress, and the corresponding interior boundary conditions on the rupture surfaces. We use a modified penalty based discontinuous Galerkin method, in which the friction law is integrated in the weak form of particle motion as numerical flux.

Our choice for the iterative scheme is motivated by a robust and flexible solution strategy for the nonlinear coupled model. The time scale for the friction model may not be the same as the elasticity equation in the matrix. In our split approach, the friction model being a differential-algebraic system (DAEs), we take higher order time integration techniques while taking different time steps and integration technique for the elasticity equation. The splitting approach also allows for using appropriate linear solvers for the individual parts such as the elasticity equation, which is otherwise difficult when using an implicit approach such as Gauss-Newton for the fully coupled system. The splitting strategy also simplifies the numerical implementation as it does not require assembling the off-diagonal terms in the linear system. As the analysis shows, this splitting is a contraction in appropriate norms and hence, also robust.

We have tested our numerical algorithm on several spontaneous rupture problems with a rate- and state-dependent friction law, which are simulated in three dimensions with unstructured tetrahedral meshes. We have shown the propagation of rupture on the fault surface as well as the elastic waves in the near-fault region. We have also shown converging results with polynomial refinements, and benchmarks with existing softwares.

Chapter 5

Simulation of elastic-gravitational system of equations

5.1 Introduction

In full-band seismic simulations, acousto-elastic waves propagate in materials which are generally anisotropic, scatter on arbitrary shaped interfaces with solid-solid, fluid-fluid and fluid-solid interactions, and are subjected to rotation and self-gravitation of the Earth. The gravitational field is perturbed by the redistribution of mass induced by particle motions, which has significant impact on relatively low eigenfrequencies of the earth. A strong formulation for the equation of motion with self-gravitation and boundary conditions on slipping interfaces can be obtained from Euler-Lagrange equations [38, 41]. However, the linearization encounters problem in the derivation of its weak form due to the presence of fluid-solid interfaces, generating so-called "eigenvalue pollution" and spurious modes. Treatments are given by Chaljub and Valette (2003) [27], and then by de Hoop et al.(2015) [50] in a broader mathematical framework, where a Brunt-Väisälä frequency is introduced to consider the non-seismic modes in the fluid regions (outer-core and ocean).

The perturbation of gravitation field induced by seismicity is becoming an interesting topic recently as Vallée et al.[164] observes the signals of gravity perturbation of the 2011, Mw=9.1, Tohoku earthquake, in broadband seismometers. The gravity changes instantaneously at the nucleation of rupture with significant motion of mass lumps, This observation provides opportunity in real-time magnitude assesment. Nevertheless, this potential technique relies on the analysis of weak-amplitude perturbation of signals on pre-arrival seismogram, which requires on one hand, state-of-art instruments for accurately collecting seismic data, and on the other, in-depth mathematical understanding on the coupling of seismic waves with mass-redistribution potential, which is the main purpose of this paper.

In most implementations so far, a "Cowling approximation" is employed [41, 27, 94], which only accounts for the unperturbed reference gravitational field, while ignoring the perturbation. However, for long period waves (greater than $\sim$100s) and free oscillation of the earth, this simplification is not valid, and one has to solve a Poisson's equation to account for the mass redistribution potential. There are a few implementations where the perturbations of the gravitational field are either solved using the Dirichlet-to-Neumann map on spherical harmonic expansions [27], or by the infinite-element method [64], both coupled with the spectral-element method. Nevertheless, a boundary integral method (BIM) hybrid with finite-element-type methods are widely used for various geophysical problems in regular unbounded domains [36, 66], and thus it can be a candidate for the problem considered here, despite the drawback of inverting a large dense matrix.

We introduce a new discretization and algorithm, based on the discontinuous Galerkin method, that is capable of solving a broad range of seismological problems including regional and global wave propagations and dynamic ruptures. Unlike the spectral-element method and many others, it is based on a first-order strain/pressure – displacement/velocity formulation, which presents a unique way of dealing with various boundary conditions accounting for discontinuities. A modified penalty flux scheme is used to ensure the coercivity of the coupling fluid-solid system [177], which achieves a similar stability result as upwind flux based on a Riemann solution [171], while having broader implementations [153]. When solving the unbounded domain Poisson's equation, a domain decomposition strategy is introduced, where an interior penalty discontinuous Galerkin (IPDG) method [139] is involved in solving the boundary value problem of the interior subdomain. This elliptic subproblem can be solved by a parallel geometric multifrontal solver using a hierarchically semiseparable structure (HSS) [173, 174], while the exterior solution is represented by integration of a Green's function (kernel), which can be numerically computed by the fast-multipole method (FMM) [68, 32]. The two subdomains are coupled via a Robin boundary condition, whose well-posedness for the Poisson's problem is justified (*e.g.* [112]). The well-posedness of the overall system, the bilinear wave equation coupled with the Poisson's equation, is addressed in this paper, with implementations using an iterative coupling scheme.

5.2 The elastic-gravitational system of equations

We follow the notations in [50], in which a bounded set $\tilde{X} \subset \mathbb{R}^3$ is considered representing the interior of the earth, with Lipschitz continuous external boundary $\partial\tilde{X}$. The set $\tilde{X}$ is divided into fluid and solid regions, denoted by Ω_{F} and Ω_{S} respectively. The union of Lipschitz continuous interior surfaces dividing the solid and fluid regions is denoted by Σ^{FS}. In reality, the fluid region Ω_{F} contains the ocean layer as well as the liquid outer core, while the solid region Ω_{S} represents the union of the inner core, the mantle, and the crust. The fluid-solid interfaces correspond to the ocean bottom, the core-mantle boundary and the inner-outer core boundary. The external boundary $\partial\tilde{X}$ is also divided into the continental surface $\partial\tilde{X}^{\text{S}}$ and the ocean top $\partial\tilde{X}^{\text{F}}$. Both Ω_{S} and Ω_{F} can be further divided into subregions with Lipschitz continuous boundaries, that is

$$\Omega_{\mathrm{S}} = \bigcup_{i=1}^{n} \Omega_i^{\mathrm{S}}, \quad \Omega_{\mathrm{F}} = \bigcup_{j=1}^{m} \Omega_j^{\mathrm{F}}.$$

We denote by Σ^{SS} the union of the interfaces in the interior of $\overline{\Omega_{\mathrm{S}}}$, that is, in between two inner solid regions, and by Σ^{FF} the union of all the interfaces in the interior of $\overline{\Omega_{\mathrm{F}}}$, that is, in between two inner fluid regions. We denote by Σ the union of all inner interfaces, including $\Sigma^{\mathrm{SS}}, \Sigma^{\mathrm{FF}}$ and Σ^{FS}. We also write Σ^{F} for the union of all interfaces involving a fluid. In conclusion,

$$\begin{aligned} \tilde{X} =& \Omega_{\mathrm{S}} \cup \Omega_{\mathrm{F}} \cup \Sigma \cup \partial\tilde{X}, \\ \partial\tilde{X} =& \partial\tilde{X}^{\mathrm{S}} \cup \partial\tilde{X}^{\mathrm{F}}, \\ \Sigma =& \Sigma^{\mathrm{SS}} \cup \Sigma^{\mathrm{FF}} \cup \Sigma^{\mathrm{FS}}, \\ \Sigma^{\mathrm{F}} =& \Sigma^{\mathrm{FF}} \cup \Sigma^{\mathrm{FS}}. \end{aligned} \tag{5.1}$$

We impose further restrictions on the above model for the purpose of a well-posedness result. In our model, the earth is assumed to be made up of "onion-like" layers of the solid subregions Ω_i^{S} and fluid subregions Ω_j^{F} (see Figure 5.2.1, for example). We also assume that the boundaries and interfaces of different types listed above do not intersect one another in the interior. The inner interfaces in the fluid regions Σ^{FF} are assumed to be C^1 continuous. Different subregions are glued together following boundary conditions as discussed in subsection 5.2.1.

5.2.1 The strong form of the equation of motion

Prior to the occurrence of an earthquake, the earth is assumed to be in a state of mechanical equilibrium by which the static momentum equation (5.7) is satisfied throughout $\tilde{X}$. In the fluid region Ω_{F}, the static momentum equation can also take the special form of (5.8). Moreover, a "perfect fluid" assumption characterized by

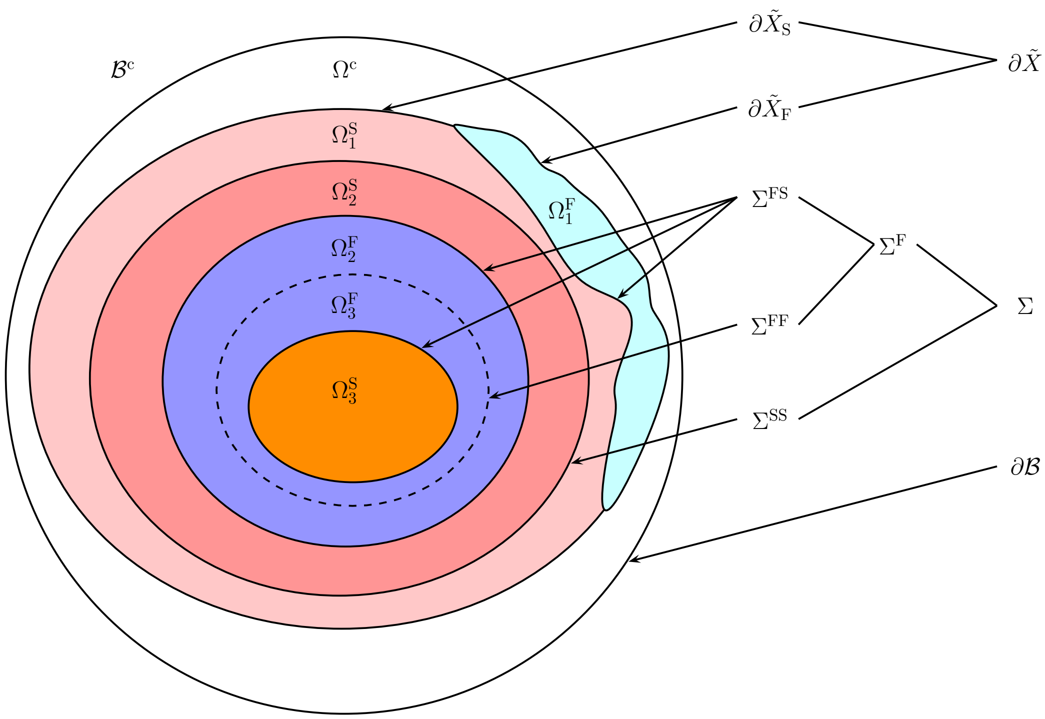

Figure 5.2.1 : Cartoon of a simplified "onion-like" earth model, with Ω_1^{S} the crust and upper mantle, Ω_2^{S} the lower mantle, Ω_3^{S} the solid inner–core, Ω_1^{F} the ocean layer, $\Omega_2^{\mathrm{F}}, \Omega_3^{\mathrm{F}}$ the fluid outer–core that has two subregions with different parameters. $\mathcal{B}$ is a ball that covers the whole earth (see Section 5.3), and Ω^{c} is the gap between the earth and the sphere $\partial\mathcal{B}$.

(5.21) is adopted within the fluid region.

We denote by $\boldsymbol{u} = \boldsymbol{u}(t, \boldsymbol{x})$ the displacement which takes values in $\mathbb{C}^3$. The existence and uniqueness are expected for the solutions to the following equation of motion (5.2) modelling the oscillations of an elastic and self-gravitating earth, imposed with boundary and interface conditions listed in Table 5.1,

$$\rho^0[\ddot{\boldsymbol{u}} + 2\boldsymbol{R_\Omega} \cdot \dot{\boldsymbol{u}}] + \rho^0 \boldsymbol{u} \cdot \nabla\nabla(\Phi^0 + \Psi^s) + \rho^0 \nabla \Phi^1 - \nabla \cdot \boldsymbol{T}^{\mathrm{PK1}} = \rho^0 \boldsymbol{f}. \tag{5.2}$$

Here, $\boldsymbol{f} \in \mathbb{R}^3$ is the body source, which typically represents a rupture process. $\boldsymbol{R_\Omega} \cdot \dot{\boldsymbol{u}}$ represents the induced Coriolis force, while $\Psi^s(x)$ is the corresponding (spatial) centrifugal potential given by (5.3). Φ^0 is the gravitational potential of the reference state given by (5.4), and Φ^1 is the mass redistribution potential given by (5.12). $\boldsymbol{T}^{\mathrm{PK1}}$ stands for the first Piola-Kirchhoff stress. Details about the physical meaning of the parameters and variables in (5.2) are described separately below.

Earth's rotation

With $\boldsymbol{\Omega} \in \mathbb{R}^3$ denoting the angular velocity of the earth's rotation, the induced Coriolis force is given by

$$\boldsymbol{R_\Omega} \cdot \dot{\boldsymbol{u}} = \boldsymbol{\Omega} \times \dot{\boldsymbol{u}} \quad \text{with } \boldsymbol{R_\Omega} := \left(\sum_{j=1}^{3} \epsilon_{ijk} \Omega_j \right)_{i,k=1}^{3} .$$

Remark that $\boldsymbol{R_\Omega}$ is skew symmetric, and that $\left(\boldsymbol{R_\Omega} \cdot \dot{\boldsymbol{u}}\right) \cdot \dot{\boldsymbol{u}} = 0$. The (spatial) centrifugal potential Ψ^s is given by

$$\Psi^s(\boldsymbol{x}) := -\tfrac{1}{2} \left(|\boldsymbol{\Omega}|^2 |\boldsymbol{x}|^2 - (\boldsymbol{\Omega} \cdot \boldsymbol{x})^2 \right). \tag{5.3}$$

Initial prestressed state

Φ^0 is the reference gravitational potential and ρ^0 is the reference density. The reference state of Earth oscillation corresponds to these quantities which satisfy the relation

$$\Delta \Phi^0 = 4\pi G \rho^0, \tag{5.4}$$

where G is the gravitational constant. We assume that $\rho^0 \in L^\infty(\tilde{X})$ and thus $\Phi^0 \in H^2(\mathbb{R}^3)$ by elliptic regularity. In fact for well-posedness ρ^0 is required to be in the space $W^{1,\infty}(\tilde{X} \backslash \Sigma)$ and to be bounded from below by a positive constant. Remark that $W^{1,\infty}$ is the space of C^0 functions whose weak gradient is in L^∞, or equivalently the space of uniformly Lipschitz functions. Thus, $W^{1,\infty}(\tilde{X} \setminus \Sigma)$ is the space of functions which are uniformly Lipschitz in $\tilde{X}$ except for possibly having jumps across some of the interfaces in Σ. Since $\Phi^0 \in H^2(\mathbb{R}^3)$, Φ^0 is continuous across all of the boundaries Σ. The sum $\Phi^0 + \Psi^s$ is referred to as the geopotential.

Denote by p^0 the initial hydrostatic pressure,

$$p^0 := \begin{cases} \text{hydrostatic pressure} & \text{in } \Omega_{\mathrm{F}} \\ -\frac{1}{3}\mathrm{tr}(\boldsymbol{T}^0) & \text{in } \Omega_{\mathrm{S}} \end{cases}, \tag{5.5}$$

by $\boldsymbol{T}^0$ the initial static stress,

$$\boldsymbol{T}^0 = \begin{cases} -p^0 \boldsymbol{I}_d & \text{in } \Omega_{\mathrm{F}} \\ -p^0 \boldsymbol{I}_d + \boldsymbol{\tau}^0 & \text{in } \Omega_{\mathrm{S}} \end{cases}, \tag{5.6}$$

which is decomposed into its isotropic and deviatoric parts respectively as $-p^0 \boldsymbol{I}_{\mathrm{d}}$ and $\boldsymbol{\tau}^0$, and that from these definitions $\mathrm{tr}(\tau^0) = 0$. It is important to note that (5.6) includes the physical assumption that the prestress is hydrostatic in Ω_{F}. Also remark that T^0 has the symmetry

$$T^0_{ij} = T^0_{ji}.$$

Mechanical equilibrium

For a uniformly rotating earth model prior to the occurrence of an earthquake, the earth is assumed to be in a state of mechanical equilibrium, that is, at rest with respect to a set of Cartesian coordinates $\boldsymbol{x} \in \mathbb{R}^3$ which are rotating uniformly with angular velocity $\boldsymbol{\Omega}$ [41]. The mechanical equilibrium condition is given by the static momentum equation, satisfied throughout Ω_{S} and Ω_{F}.

$$\text{Mechanical equilibrium :} \quad \nabla \cdot \boldsymbol{T}^0 = \rho^0 \nabla(\mathit{\Phi}^0 + \mathit{\Psi}^s) =: \rho^0 \boldsymbol{g}_0'. \tag{5.7}$$

Here, we are making the definition $\boldsymbol{g}_0' := \nabla(\mathit{\Phi}^0 + \mathit{\Psi}^s)$, and we recall that $\mathit{\Phi}^0$ is the gravitational potential of the reference state given by (5.4), and Ψ^s is the centrifugal potential given by (5.3). It is important to note that not all components of the deviatoric initial static stress, $\boldsymbol{\tau}_0$, in the solid regions are determined by (5.7). Indeed, the equations (with appropriate boundary conditions given by (5.9) below) only constrain three out of six independent components of $\boldsymbol{T}_0$. In the fluid region, the static momentum equation (5.7) assumes the following form,

$$\text{Hydrostatic equilibrium in } \Omega_{\mathrm{F}} : \qquad \nabla p^0 = -\rho^0 \boldsymbol{g}_0'. \tag{5.8}$$

Taking the limit at the boundaries and interfaces, the equilibrium conditions take the form of the

$$\text{Traction Continuity Condition :} \begin{cases} \partial\tilde{X} & : \quad \boldsymbol{\nu} \cdot \boldsymbol{T}^0 = 0 \\ \Sigma^{\mathrm{SS}} \cup \Sigma^{\mathrm{FF}} \cup \Sigma^{\mathrm{FS}} & : \quad [\![\boldsymbol{\nu} \cdot \boldsymbol{T}^0]\!] = 0 \end{cases} \tag{5.9}$$

where $\boldsymbol{\nu}$ is a unit normal to the relevant surface oriented from the "negative side" to the "positive side". The notation $[\![\cdot]\!]$ indicates the difference between the limits from each size of an interface (that is, the limit from the positive side minus the limit from the negative side). For the interior interfaces, a choice of which side is positive and which is negative must be made for every interface in a consistent way, but the boundary conditions do not depend on these choices. Along Σ^{FF} and Σ^{SS}, the choice we will take is so that the normal vector fields along these interfaces point outward. For the exterior interfaces (that is, along $\partial\tilde{X}$) we take the interior of $\tilde{X}$ to be the negative side and the exterior to be the positive side so that $\boldsymbol{\nu}$ is the outward pointing unit normal vector on $\partial\tilde{X}$. For the fluid-solid interface Σ^{FS}, we take the positive side to be the solid region and the negative side to be the fluid region so that $\boldsymbol{\nu}$ points from the fluid toward the solid. Following [50, Lemma 2.1], ρ_0, p^0, and $\boldsymbol{g}_0'$ are assumed to be in C^1 up to the boundary on each component of Ω_{F} and satisfy (5.8) in Ω_{F}. Therefore,

$$\nabla\rho^0 \big|\big| \boldsymbol{g}_0' \big|\big| \nabla p^0 \tag{5.10}$$

holds on Ω_{F}, with the notation $\big|\big|$ meaning that the two vectors are parallel. Moreover, on any C^1 portion of Σ^{FF} across which ρ^0 is not continuous,

$$\nabla\rho^0_{\pm} \big|\big| \nabla p^0_{\pm} \big|\big| (\boldsymbol{g}_0')_{\pm} \big|\big| \boldsymbol{\nu}, \tag{5.11}$$

where $\nabla\rho^0_{\pm}$ denotes respectively the limit of $\nabla\rho^0$ from either the positive or negative side of Σ^{FF}.

Mass redistribution potential

$\mathit{\Phi}^1$ denotes the perturbation of the gravitational potential caused by the redistribution of mass. This is the Eulerian perturbation of the Newtonian potential associated to the field of displacement $\boldsymbol{u}$. We have

$$\Delta\mathit{\Phi}^1 = -4\pi G \nabla \cdot (\rho^0 \boldsymbol{u}). \tag{5.12}$$

Note that the divergence in this formula is taken in the weak sense since ρ^0 may not be continuous across the interfaces Σ.

First Piola-Kirchhoff stress and incremental Lagrangian stress

In (5.2), the first Piola-Kirchhoff stress tensor, T^{PK1}, satisfies

$$\boldsymbol{T}^{\mathrm{PK1}} = \boldsymbol{\Lambda}^{\boldsymbol{T}^0} : \nabla \boldsymbol{u},$$

where $\boldsymbol{\Lambda}^{\boldsymbol{T}^0}$ is the modified stiffness tensor defined by

$$\Lambda^{\boldsymbol{T}^0}_{ijkl} = \Xi_{ijkl} + T^0_{ik}\delta_{jl} \tag{5.13}$$

with $\boldsymbol{T}^0$ the initial static stress appearing in (5.6) and $\Xi_{ijkl} \in L^\infty(\tilde{X})$ is the stiffness tensor coming from the linearization of the constitutive function. The stiffness tensor possesses the classical symmetries [41]

$$\Xi_{ijkl} = \Xi_{jikl} = \Xi_{ijlk} = \Xi_{klij} \tag{5.14}$$

On the other hand, the first Piola-Kirchhoff stress tensor $\boldsymbol{T}^{\mathrm{PK1}}$ is not symmetric. We also mention the perturbation of Lagrangian stressi, $\boldsymbol{T}^{\mathrm{L1}}$, related to the First Piola-Kirchhoff stress by a first-order approximation

$$\boldsymbol{T}^{\mathrm{L1}} \approx \boldsymbol{T}^{\mathrm{PK1}} + \boldsymbol{T}^0 \cdot (\nabla \boldsymbol{u})^{\mathrm{T}} - \boldsymbol{T}^0(\nabla \cdot \boldsymbol{u}) = \boldsymbol{\Gamma}^{\boldsymbol{T}^0} : \nabla \boldsymbol{u}, \tag{5.15}$$

where

$$\Gamma^{\boldsymbol{T}^0}_{ijkl} = \Lambda^{\boldsymbol{T}^0}_{ijkl} + T^0_{jk}\delta_{il} - T^0_{ij}\delta_{kl}. \tag{5.16}$$

Following the discussion in [41, Section 3.6.2], one can introduce the alternate representations,

$$\begin{aligned} \Lambda^{\boldsymbol{T}^0}_{ijkl} =& \Gamma_{ijkl} + a(T^0_{ij}\delta_{kl} + T^0_{kl}\delta_{ij}) + (1+b)T^0_{ik}\delta_{jl} + b(T^0_{jk}\delta_{il} + T^0_{il}\delta_{jk} + T^0_{jl}\delta_{ik}), \\ \Gamma^{\boldsymbol{T}^0}_{ijkl} =& \Gamma_{ijkl} + (a-1)T^0_{ij}\delta_{kl} + aT^0_{kl}\delta_{ij}) + (1+b)(T^0_{ik}\delta_{jl} + T^0_{jk}\delta_{il}) + b(T^0_{il}\delta_{jk} + T^0_{jl}\delta_{ik}). \end{aligned} \tag{5.17}$$

Each choice of scalars a, b defines a possible tensor $\mathbf{\Gamma}$ possessing the symmetries (5.14). $\boldsymbol{\Xi}$ in (5.13) is the elastic tensor with $a = b = 0$, which is also the choice of [162]. Another choice adopted by [38] is $a = \frac{1}{2}, b = -\frac{1}{2}$, which renders $\boldsymbol{T}^{\mathrm{L1}}$ independent of $p^0 = -\frac{1}{3}\mathrm{tr}(\boldsymbol{T}^0)$. We use $\mathbf{\Gamma}$ to denote from now on this choice of elasticity tensor (that is, with $a = -b = \frac{1}{2}$) so that the modified stiffness tensor is given by

$$\begin{aligned} \Lambda^{\boldsymbol{T}^0}_{ijkl} =& \mathit{\Gamma}_{ijkl} + \tfrac{1}{2}(T^0_{ij}\delta_{kl} + T^0_{kl}\delta_{ij} + T^0_{ik}\delta_{jl} - T^0_{jk}\delta_{il} - T^0_{il}\delta_{jk} - T^0_{jl}\delta_{ik}), \\ \mathit{\Gamma}^{\boldsymbol{T}^0}_{ijkl} =& \mathit{\Gamma}_{ijkl} + \tfrac{1}{2}(-T^0_{ij}\delta_{kl} + T^0_{kl}\delta_{ij} + T^0_{ik}\delta_{jl} + T^0_{jk}\delta_{il} - T^0_{il}\delta_{jk} - T^0_{jl}\delta_{ik}). \end{aligned} \tag{5.18}$$

Now, the definition of an isotropic solid given in [41] is of the form

$$\mathit{\Gamma}_{ijkl} = (\lambda - \tfrac{2}{3}\mu)\,\delta_{ij}\delta_{kl} + \mu\,(\delta_{ik}\delta_{jl} + \delta_{il}\delta_{jk}), \tag{5.19}$$

where λ is the isentropic incompressibility (or bulk modulus) and μ is the rigidity (or shear modulus). In the fluid regions Ω_{F}, $\mathbf{\Gamma}$ is isotropic and the rigidity is identically zero so we have

$$\mathit{\Gamma}_{ijkl} = \lambda\,\delta_{ij}\delta_{kl}. \tag{5.20}$$

Using (5.20) and the relationship between $\mathit{\Xi}_{ijkl}$ and $\mathit{\Gamma}_{ijkl}$, which can be found by equating the right hand sides of (5.13) and (5.18), we obtain

$$\begin{aligned} \text{Perfect fluid } \Omega_{\mathrm{F}}: \quad \mathit{\Xi}_{ijkl} &= -p^0\,(\delta_{ij}\delta_{kl} - \delta_{jk}\delta_{il} - \delta_{ik}\delta_{jl}) + \lambda\,\delta_{ij}\delta_{kl} \\ &= p^0(\gamma - 1)\delta_{ij}\delta_{kl} + p^0\delta_{ik}\delta_{jl} + p^0\delta_{jk}\delta_{il}, \end{aligned} \tag{5.21}$$

where γ is the adiabatic index of the fluid. Using (5.21) we also find that in the fluid regions

$$T^{PK1}_{ij} = p^0(\gamma - 1)\delta_{ij}(\nabla\cdot\boldsymbol{u}) + p^0(\nabla\boldsymbol{u})_{ij}. \tag{5.22}$$

Boundary conditions

The equations of motion (5.2) are accompanied by linearized kinematic, dynamic and gravitational conditions on the boundaries and interfaces $\partial\tilde{X} \cup \Sigma^{\mathrm{SS}} \cup \Sigma^{\mathrm{FF}} \cup \Sigma^{\mathrm{FS}}$. The discussion here follows partly from [41, Section 3.4] although we will use [162] for the dynamic boundary condition along Σ^{FS}, which is (5.26). We also comment that the boundaries are required to have at least C^1 regularity.

We recall that the jump across a boundary between two regions Ω^- and Ω^+ will be written as $[\![u]\!] := u^+ - u^-$ where $\boldsymbol{\nu}$ is the unit normal oriented from Ω^- to Ω^+. Along Σ^{FS}, we chose the unit normal $\boldsymbol{\nu}$ that points from Ω_{F} to Ω_{S}, so in this case Ω_{S} is Ω^+ and Ω_{F} is Ω^-. On the earth's free surface, $\partial\tilde{X}$, $\boldsymbol{\nu}$ will denote the outward pointing unit normal.

1. The Kinematic Boundary Conditions require that there is no slip along the welded solid-solid interfaces, which means that

$$[\![\boldsymbol{u}]\!] = 0 \text{ across } \Sigma^{\text{SS}}. \tag{5.23}$$

Along the fluid-solid and fluid-fluid interfaces, tangential slip is allowed but it is required that there is no separation or interpenetration [41]. This is assured by the linearized continuity condition

$$[\![\boldsymbol{u} \cdot \boldsymbol{\nu}]\!] = 0 \text{ across } \Sigma^{\text{F}} = \Sigma^{\text{FF}} \cup \Sigma^{\text{FS}}. \tag{5.24}$$

We call this the first-order tangential slip condition.

2. The Dynamic Boundary Conditions require that juxtaposed particles on either side of a welded or solid-solid boundary at time $t = 0$ must remain juxtaposed [41]. This condition can be written in terms of $\boldsymbol{T}^{\text{PK1}}$ and $\boldsymbol{T}^{\text{L1}}$ as

$$[\![\boldsymbol{\nu} \cdot \boldsymbol{T}^{\text{PK1}}]\!] = [\![\boldsymbol{\nu} \cdot \boldsymbol{T}^{\text{L1}}]\!] = 0, \quad \text{across } \Sigma^{\text{SS}}.$$

On the outer free surface $\partial\tilde{X}$

$$\boldsymbol{\nu} \cdot \boldsymbol{T}^{\text{PK1}} = 0. \tag{5.25}$$

To model the case in which there is an applied traction force at the surface, the right hand side of (5.25) can be made nonzero although we will not consider this here. Along Σ^{FS} and Σ^{FF}, since there may be tangential slip, juxtaposed particles on either side of the boundary need not remain juxtaposed after deformation. However, it is required that there is no shear traction along $\Sigma^{\text{F}} = \Sigma^{\text{FF}} \cup \Sigma^{\text{FS}}$. To model this requirement we use the condition

$$[\![\boldsymbol{\nu} \cdot \boldsymbol{T}^{\text{PK1}}]\!] = -\boldsymbol{\nu}\nabla^{\Sigma} \cdot (p^0 [\![\boldsymbol{u}]\!]) - p^0 W [\![\boldsymbol{u}]\!] \tag{5.26}$$

where $\nabla^{\Sigma}\cdot$ is the surface divergence and W is the Weingarten operator for the surface (see [50, Appendix A]. Meanwhile, by taking (5.15) into (5.26), and with zero deviatoric stress $\boldsymbol{\tau}^0$ at all surface involving fluid Σ^{F}, we can obatin

$$[\![\boldsymbol{\nu} \cdot \boldsymbol{T}^{\text{L1}}]\!] = 0, \quad \text{across } \Sigma^{\text{F}} = \Sigma^{\text{FS}} \cup \Sigma^{\text{FF}}. \tag{5.27}$$

We comment that (5.26) corresponds precisely with formula (3.81) in [41]. Furthermore, [41] includes an extra condition at the fluid-solid boundary given by [41, Formula (3.82)]. It can be checked that this extra condition is automatically satisfied when Ξ_{ijkl} takes the form (5.21) in the fluid region.

3. Gravitational Boundary Conditions: The following continuity conditions are satisfied on all $\partial\tilde{X} \cup \Sigma^{\text{SS}} \cup \Sigma^{\text{FF}} \cup \Sigma^{\text{FS}}$,

$$[\![\Phi^1]\!] = 0,$$
$$[\![\boldsymbol{\nu} \cdot \nabla \Phi^1 + 4\pi G \rho^0 (\boldsymbol{u} \cdot \boldsymbol{\nu})]\!] = 0.$$

For a summary of all the boundary conditions including the conditions (5.23) to (5.25) and the traction continuity condition at the boundaries (5.9) see table 5.1.

Table 5.1 : Linearized Boundary Conditions satisfied by $\boldsymbol{u}$ and $\boldsymbol{T}^0$

Boundary Type	**Linearized Boundary Conditions**
Earth's free surface, $\partial\tilde{X}$	$\boldsymbol{\nu}\cdot\boldsymbol{T}^0 = 0;\quad \boldsymbol{\nu}\cdot\boldsymbol{T}^{\mathrm{L1}} = 0;\quad \boldsymbol{\nu}\cdot\boldsymbol{T}^{\mathrm{PK1}} = 0$
Solid - Solid, Σ^{SS}	$[\![\boldsymbol{\nu}\cdot\boldsymbol{T}^0]\!] = 0;\quad [\![\boldsymbol{\nu}\cdot\boldsymbol{T}^{\mathrm{L1}}]\!] = 0;$ $[\![\boldsymbol{\nu}\cdot\boldsymbol{T}^{\mathrm{PK1}}]\!] = 0;\ [\![\boldsymbol{u}]\!] = 0$
Fluid involved interface, $\Sigma^{\mathrm{F}} := \Sigma^{\mathrm{FF}} \cup \Sigma^{\mathrm{FS}}$	$[\![\boldsymbol{\nu}\cdot\boldsymbol{T}^0]\!] = 0;\quad [\![\boldsymbol{\nu}\cdot\boldsymbol{T}^{\mathrm{L1}}]\!] = 0;\quad [\![\boldsymbol{\nu}\cdot\boldsymbol{u}]\!] = 0;$ $[\![\boldsymbol{\nu}\cdot\boldsymbol{T}^{\mathrm{PK1}}]\!] = -\boldsymbol{\nu}\nabla^{\Sigma}\cdot(p^0[\![\boldsymbol{u}]\!]) - p^0 W[\![\boldsymbol{u}]\!]$
All boundaries and interfaces $\partial\tilde{X}\cup\Sigma^{\mathrm{SS}}\cup\Sigma^{\mathrm{FF}}\cup\Sigma^{\mathrm{FS}}$	$[\![\Phi^1]\!] = 0;\quad [\![\boldsymbol{\nu}\cdot\nabla\Phi^1 + 4\pi G\rho^0\boldsymbol{\nu}\cdot\boldsymbol{u}]\!] = 0$

5.2.2 Equivalent weak formulations

Since it is not always possible to obtain a classical solution, one must explore various notions of a weak solution. Coercivity is the crucial ingredient in any approach to proving existence and uniqueness of weak, or classical, solutions of (5.2). We thus briefly review the concept of coercivity. Let H and E be Hilbert spaces with $E \hookrightarrow H$ a dense and continuous embedding, and E' be the Banach dual of E. A continuous sesquilinear form a over $E \times E$ is said to be E coercive relative to H if there exist $c_\alpha > 0$ and $c_\beta \in \mathbb{R}$ so that

$$a(u,u) \geq c_\alpha \|v\|_E^2 - c_\beta \|v\|_H^2, \quad \forall \;\; v \in E.$$

This definition also carries over to the unbounded operator A defined on the triple (E, H, a), which corresponds to $a(\cdot,\cdot)$ in the sense that

$$(a + c_\beta)(u,w) = \big\langle (A + c_\beta\, \boldsymbol{I}_d)u, w \big\rangle_{E',E} \quad , \quad \forall u, w \in E,$$

where $\langle \cdot,\cdot \rangle_{E',E}$ is the duality paring between E' and E. By [45, Theorem XVII.3.3], if coercivity of A holds, then A is the infinitesimal generator of a semigroup of class $\mathcal{C}^0$ in H. From this result, [10] gives the well-posedness for the Cauchy problem $u_t + Au = f$, $u(0) = g$. This is called the semi-group approach, which is also useful in the proof of convergence of the discretized problem in section 5.5.2. In the following sections, we define proper spaces in which the coercivity of the bilinear form in the weak formulation related to the problem (5.2) with boundary conditions in table 5.1 can be obtained.

Definition of space

We define the following weighted L^2 Hilbert space with inner product

$$\begin{aligned} L^2(\tilde{X};\rho^0) &:= \left\{ \boldsymbol{u} \in L^2(\tilde{X})^3 \Big| \int_{\tilde{X}} \rho^0 |\boldsymbol{u}|^2 \,\mathrm{d}\Omega < \infty \right\}, \\ \big(\boldsymbol{u},\boldsymbol{w}\big)_{L^2(\tilde{X};\rho^0)} &:= \int_{\tilde{X}} \rho^0\, \boldsymbol{u}\cdot\boldsymbol{w}\,\mathrm{d}\Omega. \end{aligned} \tag{5.28}$$

For Ω a bounded domain with Lipschitz boudary $\partial\Omega$, denote by $\boldsymbol{\nu}$ the outward unit normal on $\partial\Omega$, and we define the following Hilbert space with innter product

$$\begin{aligned} H^{\mathrm{div}}(\Omega) &:= \big\{ \boldsymbol{u} \in L^2(\Omega)^3 \big| \nabla\cdot\boldsymbol{u} \in L^2(\Omega) \big\} \\ \big(\boldsymbol{u},\boldsymbol{w}\big)_{H^{\mathrm{div}}(\Omega)} &:= \big(\boldsymbol{u},\boldsymbol{w}\big)_{L^2(\Omega)} + \big(\nabla\cdot\boldsymbol{u},\nabla\cdot\boldsymbol{w}\big)_{L^2(\Omega)} \end{aligned} \tag{5.29}$$

$$\begin{aligned} H^{\mathrm{div}}\big(\Omega, L^2(\partial\Omega)\big) &:= \big\{ \boldsymbol{u} \in L^2(\Omega)^3 \big| \nabla\cdot\boldsymbol{u} \in L^2(\Omega), \boldsymbol{u}|_{\partial\Omega}\cdot\boldsymbol{\nu} \in L^2(\partial\Omega) \big\} \\ \big(\boldsymbol{u},\boldsymbol{w}\big)_{H^{\mathrm{div}}(\Omega,L^2(\partial\Omega))} &:= \big(\boldsymbol{u},\boldsymbol{w}\big)_{L^2(\Omega)} + \big(\nabla\cdot\boldsymbol{u},\nabla\cdot\boldsymbol{w}\big)_{L^2(\Omega)} + \big(\boldsymbol{u}|_{\partial\Omega},\boldsymbol{w}|_{\partial\Omega}\big)_{L^2(\partial\Omega)} \end{aligned} \tag{5.30}$$

We can then define the following space E equipped with inner product $(\cdot,\cdot)_E$ as follows

$$\begin{aligned} E &= \left\{ \boldsymbol{u} \in L^2(\tilde{X};\rho^0) : \begin{cases} \boldsymbol{u}|_{\Omega_{\mathrm{S}}} \in H^1(\Omega_{\mathrm{S}})^3, \\ \boldsymbol{u}|_{\Omega_{\mathrm{F}}} \in H^{\mathrm{div}}\big(\Omega_{\mathrm{F}},\ L^2(\partial\Omega_{\mathrm{F}})\big), \\ \big[\!\big[\boldsymbol{\nu}\cdot\boldsymbol{u}\big]\!\big] = 0 \ \text{ along } \Sigma^{\mathrm{FS}} \cup \Sigma^{\mathrm{FF}} \end{cases} \right\}; \\ (\boldsymbol{u},\boldsymbol{w})_E &:= (\boldsymbol{u}|_{\Omega_{\mathrm{S}}},\boldsymbol{w}|_{\Omega^S})_{H^1(\Omega_{\mathrm{S}})} + (\boldsymbol{u}|_{\Omega_{\mathrm{F}}},\boldsymbol{w}|_{\Omega_{\mathrm{F}}})_{H^{\mathrm{div}}\left(\Omega_{\mathrm{F}},\, L^2(\Sigma^{\mathrm{FF}}\cup\partial\tilde{X}^{\mathrm{F}})\right)}. \end{aligned} \tag{5.31}$$

Based on [162, Proposition 14, p.104], E is a separable Hilbert space which is dense in $L^2(\tilde{X};\rho^0)$, and the injective inclusion of E into $L^2(\tilde{X};\rho^0)$ is continuous. As a result, we have the setting of a Hilbert triple

$$E \hookrightarrow L^2(\tilde{X};\rho^0) \hookrightarrow E',$$

where each space is continuously, densely and injectively embedded in the next, denoted by $\hookrightarrow$.

Equivalent weak form based on $\boldsymbol{T}^{\mathrm{PK1}}$

We review the weak form of the elastic-gravitational problem given by [50] as follows.

Problem 5.1

Find $\boldsymbol{u} \in E$ and $\Phi^1 \in H_0^1(\mathbb{R}^3)$ such that

$$\frac{\mathrm{d}}{\mathrm{d}t}\int_{\tilde{X}} \rho^0\Big(\dot{\boldsymbol{u}} + 2\boldsymbol{\Omega}\times\dot{\boldsymbol{u}} + \nabla\Phi^1\Big)\cdot\boldsymbol{w}\,\mathrm{d}\Omega + a_3(\boldsymbol{u},\boldsymbol{w}) = \int_{\tilde{X}} \rho^0 \boldsymbol{f}\cdot\boldsymbol{w}\,\mathrm{d}\Omega, \tag{5.32}$$

$$\frac{1}{4\pi G}\int_{\mathbb{R}^3} \nabla\Phi^1\cdot\nabla\varphi\,\mathrm{d}\Omega + \int_{\tilde{X}} \rho^0\boldsymbol{u}\cdot\nabla\varphi\,\mathrm{d}\Omega = 0, \tag{5.33}$$

with

$$\begin{aligned}
a_3(\boldsymbol{u},\boldsymbol{w}) = &\int_{\Omega_{\mathrm{S}}} (\boldsymbol{\Lambda}^{\boldsymbol{T}^0} : \nabla\boldsymbol{u}) : \nabla\boldsymbol{w}\,\mathrm{d}\Omega \\
&- \int_{\Omega_{\mathrm{S}}} \mathfrak{S}\Big\{(\boldsymbol{u}\cdot\boldsymbol{g}_0')(\boldsymbol{w}\cdot\nabla\rho^0) + \rho^0(\boldsymbol{u}\cdot\boldsymbol{g}_0')(\nabla\cdot\boldsymbol{w}) + \rho^0\boldsymbol{u}\cdot(\nabla\boldsymbol{w})\cdot\boldsymbol{g}_0'\Big\}\,\mathrm{d}\Omega \\
&+ \int_{\Omega_{\mathrm{F}}} \Big(\frac{\lambda}{(\rho^0)^2}\big(\nabla\cdot(\rho^0\boldsymbol{u}) - \boldsymbol{s}\cdot\boldsymbol{u}\big)\big(\nabla\cdot(\rho^0\boldsymbol{w}) - \boldsymbol{s}\cdot\boldsymbol{w}\big) + \rho^0 N^2\frac{(\boldsymbol{u}\cdot\boldsymbol{g}_0')(\boldsymbol{w}\cdot\boldsymbol{g}_0')}{\|\boldsymbol{g}_0'\|^2}\Big)\,\mathrm{d}\Omega \\
&- \int_{\Sigma^{\mathrm{SS}}} \mathfrak{S}\Big\{[[\rho^0]](\boldsymbol{u}\cdot\boldsymbol{g}_0')(\boldsymbol{w}\cdot\boldsymbol{\nu})\Big\}\,\mathrm{d}\Sigma - \int_{\Sigma^{\mathrm{FF}}} [[\rho^0]](\boldsymbol{g}_0'\cdot\boldsymbol{\nu})(\boldsymbol{u}\cdot\boldsymbol{\nu})(\boldsymbol{w}\cdot\boldsymbol{\nu})\,\mathrm{d}\Sigma \\
&+ \int_{\Sigma^{\mathrm{FS}}} p^0\mathfrak{S}\Big\{\big[\boldsymbol{u}\cdot\nabla\boldsymbol{w}\cdot\boldsymbol{\nu} - (\boldsymbol{\nu}\cdot\boldsymbol{u})\nabla\cdot\boldsymbol{w}\big]^+\Big\}\,\mathrm{d}\Sigma \\
&- \int_{\Sigma^{\mathrm{FS}}} \mathfrak{S}\Big\{[[\rho^0]](\boldsymbol{u}^+\cdot\boldsymbol{g}_0')(\boldsymbol{w}\cdot\boldsymbol{\nu})\Big\}\,\mathrm{d}\Sigma + \int_{\partial\tilde{X}} \mathfrak{S}\Big\{\rho^0(\boldsymbol{u}\cdot\boldsymbol{g}_0')(\boldsymbol{w}\cdot\boldsymbol{\nu})\Big\}\,\mathrm{d}\Sigma.
\end{aligned} \tag{5.34}$$

for any $\boldsymbol{w} \in E$ and $\varphi \in H_0^1(\mathbb{R}^3)$.

In the above, we denote by $\mathfrak{S}$ a symmetrization operation for any bilinear expression $L(\boldsymbol{u},\boldsymbol{w})$, such that

$$\mathfrak{S}\big\{L(\boldsymbol{u},\boldsymbol{w})\big\} := \frac{1}{2}\big(L(\boldsymbol{u},\boldsymbol{w}) + L(\boldsymbol{w},\boldsymbol{u})\big),$$

and the vector function $\boldsymbol{s}$ is defined by

$$\boldsymbol{s} := \nabla\rho^0 + \frac{(\rho^0)^2\boldsymbol{g}_0'}{\lambda}, \tag{5.35}$$

which is related to the Brunt-Väisälä frequency by

$$N^2 = -\frac{1}{\rho^0}\boldsymbol{s}\cdot\boldsymbol{g}_0'. \tag{5.36}$$

The second term in (5.32) represents the induced Coriolis force, while the third term takes into account the mass-redistribution potential, which will vanish under the Cowling approximation. The bilinear form a_3 considers the general prestress that allows non-zero deviatoric stress within the solid region Ω_{S}. We recall that

$$a_2(\boldsymbol{u},\boldsymbol{w}) = a_3(\boldsymbol{u},\boldsymbol{w}) - \frac{1}{4\pi G}\int_{\mathbb{R}^3}\nabla S(\boldsymbol{u})\cdot\nabla S(\boldsymbol{w})\,\mathrm{d}\Omega$$

corresponds to the bilinear form of same notation defined in [50, section 4], and remark that a_2 and a_3 have the same coercivity. Therefore, most results discussed in [50] about a_2 can be applied to a_3 without any issues. We also remark that a surface term $\int_{\Sigma\cup\partial\tilde{X}}[\![\boldsymbol{\nu}\cdot(\nabla\Phi^1+4\pi G\rho^0\boldsymbol{u})]\!]\,\mathrm{d}\Sigma$ which has been generated from integration by parts in (5.33) vanishes, based on the last boundary condition in table 5.1.

Equivalent weak form based on $\boldsymbol{T}^{\mathrm{L1}}$

We combine (5.35) and (5.36) with (5.34), which yields

$$\begin{aligned}
a_3(\boldsymbol{u},\boldsymbol{w}) = {}& \int_{\Omega_{\mathrm{S}}}(\boldsymbol{\Lambda}^{\boldsymbol{T}^0}:\nabla\boldsymbol{u}):\nabla\boldsymbol{w}\,\mathrm{d}\Omega + \int_{\Omega_{\mathrm{F}}}\lambda(\nabla\cdot\boldsymbol{u})(\nabla\cdot\boldsymbol{w})\,\mathrm{d}\Omega\\
&- \int_{\Omega_{\mathrm{S}}}\mathfrak{S}\Big\{(\boldsymbol{u}\cdot\boldsymbol{g}_0')(\boldsymbol{w}\cdot\nabla\rho^0) + \rho^0(\boldsymbol{u}\cdot\boldsymbol{g}_0')(\nabla\cdot\boldsymbol{w}) + \rho^0\boldsymbol{u}\cdot(\nabla\boldsymbol{w})\cdot\boldsymbol{g}_0'\Big\}\,\mathrm{d}\Omega\\
&- \int_{\Omega_{\mathrm{F}}}\Big(\rho^0(\boldsymbol{w}\cdot\boldsymbol{g}_0')(\nabla\cdot\boldsymbol{u}) + \rho^0(\boldsymbol{u}\cdot\boldsymbol{g}_0')(\nabla\cdot\boldsymbol{w}) + \varrho^0(\boldsymbol{u}\cdot\boldsymbol{g}_0')(\boldsymbol{w}\cdot\boldsymbol{g}_0')\Big)\,\mathrm{d}\Omega\\
&- \int_{\Sigma^{\mathrm{SS}}}\mathfrak{S}\Big\{[\![\rho^0]\!](\boldsymbol{u}\cdot\boldsymbol{g}_0')(\boldsymbol{w}\cdot\boldsymbol{\nu})\Big\}\,\mathrm{d}\Sigma - \int_{\Sigma^{\mathrm{FF}}}[\![\rho^0]\!](\boldsymbol{g}_0'\cdot\boldsymbol{\nu})(\boldsymbol{u}\cdot\boldsymbol{\nu})(\boldsymbol{w}\cdot\boldsymbol{\nu})\,\mathrm{d}\Sigma\\
&+ \int_{\Sigma^{\mathrm{FS}}}p^0\mathfrak{S}\Big\{\big[\boldsymbol{u}\cdot\nabla\boldsymbol{w}\cdot\boldsymbol{\nu} - (\boldsymbol{\nu}\cdot\boldsymbol{u})(\nabla\cdot\boldsymbol{w})\big]^+\Big\}\,\mathrm{d}\Sigma\\
&- \int_{\Sigma^{\mathrm{FS}}}\mathfrak{S}\Big\{[\![\rho^0]\!](\boldsymbol{u}^+\cdot\boldsymbol{g}_0')(\boldsymbol{w}\cdot\boldsymbol{\nu})\Big\}\,\mathrm{d}\Sigma + \int_{\partial\tilde{X}}\mathfrak{S}\Big\{\rho^0(\boldsymbol{u}\cdot\boldsymbol{g}_0')(\boldsymbol{w}\cdot\boldsymbol{\nu})\Big\}\,\mathrm{d}\Sigma,
\end{aligned} \tag{5.37}$$

with $\varrho^0 := (\boldsymbol{g}_0' \cdot \nabla\rho^0)/\|\boldsymbol{g}_0'\|^2$. We remark the following integration by parts using the boundary conditions in table 5.1

$$
\begin{aligned}
&\int_{\Omega_{\mathrm{S}}} \mathfrak{S}\Big\{(\boldsymbol{u}\cdot\boldsymbol{g}_0')(\boldsymbol{w}\cdot\nabla\rho^0)\Big\}\,\mathrm{d}\Omega = \\
&\qquad -\int_{\Omega_{\mathrm{S}}} \rho^0\mathfrak{S}\Big\{\boldsymbol{w}\cdot\nabla\boldsymbol{u}\cdot\boldsymbol{g}_0' + \boldsymbol{w}\cdot\nabla\boldsymbol{g}_0'\cdot\boldsymbol{u} + (\boldsymbol{u}\cdot\boldsymbol{g}_0')(\nabla\cdot\boldsymbol{w})\Big\}\,\mathrm{d}\Omega \\
&\qquad -\int_{\Sigma^{\mathrm{SS}}} \mathfrak{S}\Big\{[\![\rho^0]\!](\boldsymbol{u}\cdot\boldsymbol{g}_0')(\boldsymbol{w}\cdot\boldsymbol{\nu})\Big\}\,\mathrm{d}\Sigma \\
&\qquad -\int_{\Sigma^{\mathrm{FS}}} \mathfrak{S}\Big\{\,[\rho^0\,]^+(\boldsymbol{u}^+\cdot\boldsymbol{g}_0')(\boldsymbol{w}\cdot\boldsymbol{\nu})\Big\}\,\mathrm{d}\Sigma + \int_{\partial\tilde{X}^{\mathrm{S}}} \mathfrak{S}\Big\{\rho^0(\boldsymbol{u}\cdot\boldsymbol{g}_0')(\boldsymbol{w}\cdot\boldsymbol{\nu})\Big\}\,\mathrm{d}\Sigma.
\end{aligned}
\tag{5.38}
$$

On the other hand, based on (5.11),

$$
\begin{aligned}
\int_{\partial\tilde{X}} \mathfrak{S}\{\rho^0(\boldsymbol{u}\cdot\boldsymbol{g}_0')(\boldsymbol{w}\cdot\boldsymbol{\nu})\}\,\mathrm{d}\Sigma &= \int_{\partial\tilde{X}^{\mathrm{S}}} \mathfrak{S}\{\rho^0(\boldsymbol{u}\cdot\boldsymbol{g}_0')(\boldsymbol{w}\cdot\boldsymbol{\nu})\}\,\mathrm{d}\Sigma \\
&\quad + \int_{\partial\tilde{X}^{\mathrm{F}}} \rho^0(\boldsymbol{g}_0'\cdot\boldsymbol{\nu})(\boldsymbol{u}\cdot\boldsymbol{\nu})(\boldsymbol{w}\cdot\boldsymbol{\nu})\,\mathrm{d}\Sigma,
\end{aligned}
\tag{5.39}
$$

and based on (5.6) and (5.18),

$$
\begin{aligned}
&\int_{\Omega_{\mathrm{S}}} (\boldsymbol{\Lambda}^{\boldsymbol{T}^0} : \nabla\boldsymbol{u}) : \nabla\boldsymbol{w}\,\mathrm{d}\Omega \\
&\quad = \int_{\Omega_{\mathrm{S}}} \Big((\boldsymbol{\Gamma} : \nabla\boldsymbol{u}) : \nabla\boldsymbol{w} + \tfrac{1}{2}(\boldsymbol{T}^0\cdot\nabla\boldsymbol{u} - \nabla\boldsymbol{u}\cdot\boldsymbol{T}^0) : \nabla\boldsymbol{w}\Big)\,\mathrm{d}\Omega \\
&\qquad + \int_{\Omega_{\mathrm{S}}} \mathfrak{S}\Big\{\big((\nabla\cdot\boldsymbol{u})\boldsymbol{T}^0 - (\nabla\boldsymbol{u})^{\mathrm{T}}\cdot\boldsymbol{T}^0\big) : \nabla\boldsymbol{w}\Big\}\,\mathrm{d}\Omega \\
&\quad = \int_{\Omega_{\mathrm{S}}} (\boldsymbol{\tau}^0\cdot\nabla\boldsymbol{u} - \nabla\boldsymbol{u}\cdot\boldsymbol{\tau}^0) : \nabla\boldsymbol{w}\,\mathrm{d}\Omega \\
&\qquad + \int_{\Omega_{\mathrm{S}}} \mathfrak{S}\Big\{(\boldsymbol{u}\cdot\nabla p^0)(\nabla\cdot\boldsymbol{w}) - (\boldsymbol{u}\cdot\nabla\boldsymbol{\tau}^0) : \nabla\boldsymbol{w} + \rho^0\boldsymbol{u}\cdot\nabla\boldsymbol{w}\cdot\boldsymbol{g}_0'\Big\}\,\mathrm{d}\Omega \\
&\qquad + \int_{\Sigma^{\mathrm{FS}}} p^0\mathfrak{S}\Big\{(\boldsymbol{\nu}\cdot\boldsymbol{u})(\nabla\cdot\boldsymbol{w}) - \boldsymbol{u}\cdot(\nabla\boldsymbol{w})\cdot\boldsymbol{\nu}\Big\}\,\mathrm{d}\Sigma.
\end{aligned}
\tag{5.40}
$$

The boundary continuities at solid-solid interfaces (listed in Table 5.1) indicate that all surface terms on Σ^{SS} vanish when conducting integration by parts in the above equation (see also [18, section 4.4.4]), and the second equality is derived by

$$
\begin{aligned}
&\int_{\Omega_\mathrm{S}} \mathfrak{S}\Big\{(\partial_i u_i)T^0_{jk}(\partial_j w_k) - (\partial_j u_i)T^0_{jk}(\partial_i w_k)\Big\}\,\mathrm{d}\Omega \\
&\qquad = -\int_{\Omega_\mathrm{S}} \mathfrak{S}\Big\{u_i(\partial_i T^0_{jk})(\partial_j w_k) - u_i(\partial_j T^0_{jk})(\partial_i w_k)\Big\}\,\mathrm{d}\Omega \\
&\qquad\quad - \int_{\Sigma^\mathrm{FS}} \mathfrak{S}\Big\{\,\big[\,\nu_i u_i T^0_{jk}(\partial_j w_k) - \nu_j u_i T^0_{jk}(\partial_i w_k)\,\big]^+\Big\}\,\mathrm{d}\Sigma \\
&\qquad = \int_{\Omega_\mathrm{S}} \mathfrak{S}\Big\{(u_i\partial_i p)(\partial_j w_j) - u_i(\partial_i \tau^0_{jk})(\partial_j w_k) + \rho u_i(g_0')_k(\partial_i w_k)\Big\}\,\mathrm{d}\Omega \\
&\qquad\quad + \int_{\Sigma^\mathrm{FS}} p^0\mathfrak{S}\Big\{\nu_i u_i(\partial_j w_j) - \nu_j u_i(\partial_i w_j)\Big\}\,\mathrm{d}\Sigma.
\end{aligned}
\tag{5.41}
$$

Substituting (5.38) – (5.40) from (5.37) yields a new bilinear form

$$
\begin{aligned}
\tilde{a}_3(\boldsymbol{u},\boldsymbol{w}) =: &\int_{\Omega_\mathrm{S}} (\boldsymbol{\Gamma} : \nabla\boldsymbol{u}) : \nabla\boldsymbol{w}\,\mathrm{d}\Omega + \int_{\Omega_\mathrm{F}} \lambda(\nabla\cdot\boldsymbol{u})(\nabla\cdot\boldsymbol{w})\,\mathrm{d}\Omega \\
&+ \int_{\Omega_\mathrm{S}} \tfrac{1}{2}\boldsymbol{\tau}^0 : \big(\nabla\boldsymbol{u}\cdot(\nabla\boldsymbol{w})^\mathrm{T} - (\nabla\boldsymbol{u})^\mathrm{T}\cdot\nabla\boldsymbol{w}\big)\,\mathrm{d}\Omega \\
&+ \int_{\Omega_\mathrm{S}} \mathfrak{S}\Big\{\boldsymbol{u}\cdot(\nabla\cdot\boldsymbol{\tau}^0)(\nabla\cdot\boldsymbol{w}) - (\boldsymbol{u}\cdot\nabla\boldsymbol{\tau}^0) : \nabla\boldsymbol{w}\Big\}\,\mathrm{d}\Omega \\
&+ \int_{\Omega_\mathrm{S}} \rho^0\mathfrak{S}\Big\{\boldsymbol{u}\cdot\nabla\boldsymbol{g}_0'\cdot\boldsymbol{w} + \boldsymbol{u}\cdot\mathrm{dev}(\nabla\boldsymbol{w})\cdot\boldsymbol{g}_0'\Big\}\,\mathrm{d}\Omega \\
&- \int_{\Omega_\mathrm{F}} \Big(\rho^0(\boldsymbol{w}\cdot\boldsymbol{g}_0')(\nabla\cdot\boldsymbol{u}) + \rho^0(\boldsymbol{u}\cdot\boldsymbol{g}_0')(\nabla\cdot\boldsymbol{w}) + \varrho^0(\boldsymbol{u}\cdot\boldsymbol{g}_0')(\boldsymbol{w}\cdot\boldsymbol{g}_0')\Big)\,\mathrm{d}\Omega \\
&+ \int_{\Sigma^\mathrm{FS}} \mathfrak{S}\Big\{\rho^{0\,-}(\boldsymbol{u}^+\cdot\boldsymbol{g}_0')(\boldsymbol{w}\cdot\boldsymbol{\nu})\Big\}\,\mathrm{d}\Sigma - \int_{\Sigma^\mathrm{FF}} [\![\rho^0]\!](\boldsymbol{g}_0'\cdot\boldsymbol{\nu})(\boldsymbol{u}\cdot\boldsymbol{\nu})(\boldsymbol{w}\cdot\boldsymbol{\nu})\,\mathrm{d}\Sigma \\
&+ \int_{\partial\tilde{X}^\mathrm{F}} \rho^0(\boldsymbol{g}_0'\cdot\boldsymbol{\nu})(\boldsymbol{u}\cdot\boldsymbol{\nu})(\boldsymbol{w}\cdot\boldsymbol{\nu})\,\mathrm{d}\Sigma.
\end{aligned}
\tag{5.42}
$$

Indeed, $\tilde{a}_3(\boldsymbol{u},\boldsymbol{w})$ is equivalent to $a_3(\boldsymbol{u},\boldsymbol{w})$ within the space of E, due to the enforcement of $[\![\boldsymbol{\nu}\cdot\boldsymbol{u}]\!] = 0$ along $\Sigma^\mathrm{F} = \Sigma^\mathrm{FF}\cup\Sigma^\mathrm{FS}$.

Weak formulation of first order system

We introduce the strain tensor $\boldsymbol{E} := \nabla\boldsymbol{u}$ in the solid domain Ω_S, and the incremental pressure $P := \lambda(\nabla\cdot\boldsymbol{u})$ in the fluid domain as a scalar variable. With the definition of space E, it is clear that $\boldsymbol{E} \in L^2(\Omega_{\mathrm{S}})^{3\times 3}$ and $P \in L^2(\Omega_{\mathrm{F}})$. We combine the variables as

$$\boldsymbol{q} = \big(\, \boldsymbol{u}, \boldsymbol{E}, P, \Phi^1 \,\big)^{\mathrm{T}}, \tag{5.43}$$

and introduce the space of solution for $\boldsymbol{q}$ as follows

$$\mathcal{E} := E \times L^2(\Omega_{\mathrm{S}})^{3\times 3} \times L^2(\Omega_{\mathrm{F}}) \times H^1_0(\mathbb{R}^3), \tag{5.44}$$

with the inner product

$$\begin{aligned} (\boldsymbol{q}, \boldsymbol{p})_{\mathcal{E}} := (\boldsymbol{u}, \boldsymbol{w})_E + (\boldsymbol{E}, \boldsymbol{H})_{L^2(\Omega_{\mathrm{S}})} + (P, Q)_{L^2(\Omega_{\mathrm{F}})} + (\nabla \Phi^1, \nabla \varphi)_{L^2(\mathbb{R}^3)}, \\ \text{for all } \boldsymbol{q} := \big(\boldsymbol{u}, \boldsymbol{E}, P, \Phi^1\big)^{\mathrm{T}} \text{ and } \boldsymbol{p} := \big(\boldsymbol{w}, \boldsymbol{H}, Q, \varphi\big)^{\mathrm{T}} \in \mathcal{E}. \end{aligned} \tag{5.45}$$

We introduce a bilinear form

$$b(\cdot,\cdot) : \mathcal{E} \times \mathcal{E} \to \mathbb{C},$$

and reformulate Problem 5.1 as follows.

Problem 5.2

Find $\boldsymbol{q} = (\boldsymbol{u}, \boldsymbol{E}, P, \Phi^1)^T \in \mathcal{E}$ *that satisfy*

$$\frac{\mathrm{d}}{\mathrm{d}t} \int_{\tilde{X}} \rho^0 \dot{\boldsymbol{u}} \cdot \boldsymbol{w} \, \mathrm{d}\Omega + \int_{\tilde{X}} 2\rho^0 (\boldsymbol{\Omega} \times \dot{\boldsymbol{u}}) \cdot \boldsymbol{w} \, \mathrm{d}\Omega + b\big(\boldsymbol{q}, \boldsymbol{p}\big) = \int_{\tilde{X}} \rho^0 \boldsymbol{f} \cdot \boldsymbol{w} \, \mathrm{d}\Omega, \tag{5.46}$$

for any $\boldsymbol{p} = (\boldsymbol{w}, \boldsymbol{H}, Q, \varphi)^{\mathrm{T}} \in \mathcal{E}$, *where*

$$\begin{aligned} b\big(\boldsymbol{q}, \boldsymbol{p}\big) := \tilde{a}_3(\boldsymbol{u}, \boldsymbol{w}) + \kappa \int_{\Omega_{\mathrm{S}}} (\boldsymbol{E} - \nabla \boldsymbol{u}) : (\boldsymbol{\Gamma} : \boldsymbol{H}) \, \mathrm{d}\Omega + \kappa \int_{\Omega_{\mathrm{F}}} (P - \lambda \nabla \cdot \boldsymbol{u}) \, Q \, \mathrm{d}\Omega \\ + \frac{1}{4\pi G} \int_{\mathbb{R}^3} (\nabla \Phi^1) \cdot (\nabla \varphi) \, \mathrm{d}\Omega + \int_{\tilde{X}} \rho^0 (\nabla \Phi^1) \cdot \boldsymbol{w} \, \mathrm{d}\Omega + \int_{\tilde{X}} (\rho^0 \boldsymbol{u}) \cdot (\nabla \varphi) \, \mathrm{d}\Omega. \end{aligned} \tag{5.47}$$

In the following theorem, we show the coercivity of $b(\cdot,\cdot)$ in the space $\mathcal{E}$.

Theorem 5.1

With the assumptions listed in [50, Theorem 5.7], there exist $c_\alpha, c_\beta, c_\kappa > 0$ *such that*

$$\begin{aligned} b(\boldsymbol{q},\boldsymbol{q}) \geq c_\alpha \|\boldsymbol{u}\|_E^2 + c_\kappa\big(\|\boldsymbol{E}\|^2_{L^2(\Omega_{\mathrm{S}})}\|P\|^2_{L^2(\Omega_{\mathrm{F}})}\big\|\nabla\mathit{\Phi}^1\big\|^2_{L^2(\mathbb{R}^3)}\big) - c_\beta\|\boldsymbol{u}\|^2_{L^2(\tilde{X};\rho)}, \\ \forall \boldsymbol{q} := (\boldsymbol{u},\boldsymbol{E},P,\mathit{\Phi}^1)^T \in \mathcal{E}. \end{aligned} \tag{5.48}$$

Proof 5.1 We assume the upper and lower bound on the coefficients

$$C_\rho \leq \big\|\rho^0\big\| \leq C_\rho^*, \quad C_\mathit{\Gamma} \leq \|\boldsymbol{\Gamma}\| \leq C_\mathit{\Gamma}^*, \quad C_\lambda \leq \|\lambda\| \leq C_\lambda^*. \tag{5.49}$$

Using Young's inequality, (5.47) yields

$$\begin{aligned} b(\boldsymbol{q},\boldsymbol{q}) \geq{}& a_3(\boldsymbol{u},\boldsymbol{u}) + \kappa\big(C_\mathit{\Gamma} - \delta\frac{C_\mathit{\Gamma}^*}{2}\big)\|\boldsymbol{E}\|^2_{L^2(\Omega_{\mathrm{S}})} + \kappa\big(1-\delta\frac{C_\lambda^*}{2}\big)\|P\|^2_{L^2(\Omega_{\mathrm{F}})} \\ &+ \frac{1}{8\pi G}\big\|\nabla\mathit{\Phi}^1\big\|^2_{L^2(\mathbb{R}^3)} - \kappa\frac{C_\mathit{\Gamma}^*}{2\delta}\|\nabla\boldsymbol{u}\|^2_{L^2(\Omega_{\mathrm{S}})} \\ &- \kappa\frac{C_\lambda^*}{2\delta}\|\nabla\cdot\boldsymbol{u}\|^2_{L^2(\Omega_{\mathrm{F}})} - 8\pi G C_\rho^*\|\boldsymbol{u}\|^2_{L^2(\tilde{X};\rho)}. \end{aligned}$$

Based on the coercivity of a_3 following [50, Theorem 5.7], it is clear that by choosing sufficiently small δ and κ, the theorem holds.

Problem 5.2 can also be written in the following equivalent form, which highlights the relavence to the conventional first-order wave equations.

Problem 5.3

Find $\boldsymbol{q} := (\boldsymbol{u},\boldsymbol{E},P,\mathit{\Phi}^1)^T \in \mathcal{E}$ *that satisfy* (5.46), *namely*

$$\frac{\mathrm{d}}{\mathrm{d}t}\int_{\tilde{X}}\rho^0\dot{\boldsymbol{u}}\cdot\boldsymbol{w}\,\mathrm{d}\Omega + \int_{\tilde{X}}2\rho^0(\boldsymbol{\Omega}\times\dot{\boldsymbol{u}})\cdot\boldsymbol{w}\,\mathrm{d}\Omega + b\big(\boldsymbol{q},\boldsymbol{p}\big) = \int_{\tilde{X}}\rho^0\boldsymbol{f}\cdot\boldsymbol{w}\,\mathrm{d}\Omega,$$

for any $\boldsymbol{p} := (\boldsymbol{w},\boldsymbol{H},Q,\varphi)^{\mathrm{T}} \in \mathcal{E}$, *where*

$$\begin{aligned} b(\boldsymbol{q},\boldsymbol{p}) :={}& \mathfrak{W}^a\big(\,\boldsymbol{u},\boldsymbol{E},P,\mathit{\Phi}^1\ ;\ \boldsymbol{w}\,\big) + \mathfrak{W}^b\big(\,\boldsymbol{u},\boldsymbol{E}\ ;\ \boldsymbol{l}_{\mathrm{S}}[\kappa](\boldsymbol{w},\boldsymbol{H})\,\big) \\ &+ \mathfrak{W}^c\big(\boldsymbol{u},\boldsymbol{E},P,\mathit{\Phi}^1\ ;\ \boldsymbol{w}\big) + \mathfrak{W}^d\big(\,\boldsymbol{u},P\ ;\ l_{\mathrm{F}}[\kappa](\boldsymbol{w},Q)\,\big) + \mathfrak{Y}\big(\,\boldsymbol{u},\mathit{\Phi}^1\ ;\ \varphi\,\big), \end{aligned} \tag{5.50}$$

with the linear maps defined by

$$\begin{aligned}\mathfrak{W}^a\big(\boldsymbol{u}, \boldsymbol{E}, P, \varPhi^1\ ;\ \boldsymbol{w}\big) &:= \int_{\Omega_\mathrm{S}} (\boldsymbol{\Gamma} : \boldsymbol{E}) : \nabla \boldsymbol{w}\,\mathrm{d}\Omega \\ &\quad + \int_{\Omega_\mathrm{S}} \rho^0 \nabla \varPhi^1 \cdot \boldsymbol{w}\,\mathrm{d}\Omega + \int_{\Omega_\mathrm{S}} \tfrac{1}{2}(\boldsymbol{\tau}^0 \cdot \boldsymbol{E} - \boldsymbol{E}\cdot\boldsymbol{\tau}^0) : \nabla \boldsymbol{w}\,\mathrm{d}\Omega \\ &\quad + \int_{\Omega_\mathrm{S}} \mathfrak{S}\Big\{\boldsymbol{u}\cdot(\nabla\cdot\boldsymbol{\tau}^0)(\nabla\cdot\boldsymbol{w}) - (\boldsymbol{u}\cdot\nabla\boldsymbol{\tau}^0) : \nabla\boldsymbol{w}\Big\}\,\mathrm{d}\Omega \\ &\quad + \int_{\Omega_\mathrm{S}} \rho^0 \mathfrak{S}\Big\{\boldsymbol{u}\cdot\nabla\boldsymbol{g}_0'\cdot\boldsymbol{w} + \boldsymbol{u}\cdot\mathrm{dev}(\nabla\boldsymbol{w})\cdot\boldsymbol{g}_0'\Big\}\,\mathrm{d}\Omega \\ &\quad + \int_{\Sigma^\mathrm{FS}} \mathfrak{S}\Big\{\rho^{0\,-}(\boldsymbol{u}^+\cdot\boldsymbol{g}_0')(\boldsymbol{w}\cdot\boldsymbol{\nu})\Big\}\,\mathrm{d}\Sigma,\end{aligned} \tag{5.51a}$$

$$\mathfrak{W}^b\big(\boldsymbol{u}, \boldsymbol{E}\ ;\ \boldsymbol{H}\big) := \int_{\Omega_\mathrm{S}} \boldsymbol{E} : \boldsymbol{H}\,\mathrm{d}\Omega - \int_{\Omega_\mathrm{S}} (\nabla\boldsymbol{u}) : \boldsymbol{H}\,\mathrm{d}\Omega, \tag{5.51b}$$

$$\begin{aligned}\mathfrak{W}^c\big(\boldsymbol{u}, \boldsymbol{E}, P, \varPhi^1\ ;\ \boldsymbol{w}\big) &:= \int_{\Omega_\mathrm{F}} P\,(\nabla\cdot\boldsymbol{w})\,\mathrm{d}\Omega + \int_{\Omega_\mathrm{F}} \rho^0\nabla\varPhi^1\cdot\boldsymbol{w}\,\mathrm{d}\Omega \\ &\quad - \int_{\Omega_\mathrm{F}} 2\rho^0\mathfrak{S}\Big\{(\boldsymbol{u}\cdot\boldsymbol{g}_0')(\nabla\cdot\boldsymbol{w})\Big\}\,\mathrm{d}\Omega - \int_{\Omega_\mathrm{F}} \varrho^0(\boldsymbol{u}\cdot\boldsymbol{g}_0')(\boldsymbol{w}\cdot\boldsymbol{g}_0')\,\mathrm{d}\Omega \\ &\quad - \int_{\Sigma^\mathrm{FF}} [\![\rho^0]\!](\boldsymbol{g}_0'\cdot\boldsymbol{\nu})\{\!\{\boldsymbol{u}\cdot\boldsymbol{\nu}\}\!\}\{\!\{\boldsymbol{w}\cdot\boldsymbol{\nu}\}\!\}\,\mathrm{d}\Sigma + \int_{\partial\tilde{X}^\mathrm{F}} \rho^0(\boldsymbol{g}_0'\cdot\boldsymbol{\nu})(\boldsymbol{u}\cdot\boldsymbol{\nu})(\boldsymbol{w}\cdot\boldsymbol{\nu})\,\mathrm{d}\Sigma,\end{aligned} \tag{5.51c}$$

$$\mathfrak{W}^d\big(\boldsymbol{u}, P\ ;\ Q\big) := \int_{\Omega_\mathrm{F}} \lambda^{-1}\,P\,Q\,\mathrm{d}\Omega - \int_{\Omega_\mathrm{F}} (\nabla\cdot\boldsymbol{u})\,Q\,\mathrm{d}\Omega, \tag{5.51d}$$

$$\mathfrak{Y}\big(\boldsymbol{u}, \varPhi^1\ ;\ \varphi\big) := \frac{1}{4\pi G}\int_{\mathbb{R}^3} (\nabla\varPhi^1)\cdot(\nabla\varphi)\,\mathrm{d}\Omega + \int_{\tilde{X}} (\rho^0\boldsymbol{u})\cdot(\nabla\varphi)\,\mathrm{d}\Omega \tag{5.51e}$$

$$\boldsymbol{l}_\mathrm{S}[\kappa](\boldsymbol{w}, \boldsymbol{H}) := \boldsymbol{\Gamma} : \big(\kappa\boldsymbol{H} - \nabla\boldsymbol{w}\big) - \tfrac{1}{2}\big(\boldsymbol{\tau}^0\cdot\nabla\boldsymbol{w} - \nabla\boldsymbol{w}\cdot\boldsymbol{\tau}^0\big) \tag{5.51f}$$

$$l_\mathrm{F}[\kappa](\boldsymbol{w}, Q) := \lambda\big(\kappa Q - \nabla\cdot\boldsymbol{w}\big). \tag{5.51g}$$

Problem 5.2 and 5.3 equivalently consider the complete acousto-elastic self-gravitational system of the rotating Earth. Nevertheless, we remark some simplifications that are commonly applied in practice.

The prestress tensor $\boldsymbol{T}^0$ is non-determinant based on (5.7), and a *hydrostatic assumption* can be applied by extensively using the equations (5.8) in the whole domain of $\tilde{X}$. In other words, the deviatoric initial stress $\boldsymbol{\tau}^0$ vanishes and $\nabla p^0 = -\rho^0 \boldsymbol{g}_0'$ is satisfied everywhere. With this assumption, Problem 5.2 is simplified by omitting terms containing $\boldsymbol{\tau}^0$, namely the second and third lines of $\tilde{a}_3$ in (5.42). Another approximation that is usually applied independently is the non-rotating earth assumption, in which the Coriolis term $2\rho^0(\boldsymbol{\Omega} \times \dot{\boldsymbol{u}})$ is removed from (5.46), and the field of geopotentiala $\boldsymbol{g}_0'$ is replaced everywhere in (5.42) or in (5.51a,c) by the initial gravitational field $\boldsymbol{g}_0 := \nabla \Phi^0$. A third independent simplification is the so-called "Cowling" approximation, in which the impact of mass-redistribution potential is omitted. One removes the $\nabla \Phi^1$ term from $b(\cdot, \cdot)$, namely the second line of (5.47), and eliminates the coupling with Poisson's equation on an infinite domain within this approximation. Finally, a non-gravitating and non-rotating approximation can be applied upon the simplifications mentioned above, by furthermore assuming $\boldsymbol{g}_0' \equiv 0$ in $b(\cdot, \cdot)$, which also indicates that $\boldsymbol{T}^0 \equiv 0$ due to the maximum principle of Poisson's equation. This final simplification corresponds to the widely implemented high-frequency approximation of seismic wave modelling, for example in [177].

5.3 The boundary integral method for the mass-redistribution potential

In this section, we discuss the solution to (5.12) or equivalently (5.33) for the mass-redistribution potential Φ^1, while the solution to (5.4) for Φ^0, the gravitational potential of the reference state, takes the same manner.

We use the boundary integral method, also known as the layer potential method, to eliminate the solution in the complement of a bounded subset. We conduct a domain decomposition by introducing a ball $B_{(0,R)}$ with sufficiently large radius R such that $\tilde{X} \subset B_{(0,R)}$, and that $\tilde{X} \cap \partial B_{(0,R)} = \emptyset$. In other words, a thin complementary layer is appended between $\tilde{X}$ and the ball sphere $\partial B_{(0,R)}$, denoted by $\Omega^{\mathrm{c}} = B_{(0,R)} \setminus \tilde{X}$ (see Figure 5.2.1). Without causing ambiguity, we use the notation $\mathcal{B}$ to represent $B_{(0,R)}$, and denote $\mathcal{B}^{\mathrm{c}} = \mathbb{R}^3 \setminus \mathcal{B}$. We denote the outer normal direction of $\partial\mathcal{B}$ as $\boldsymbol{n} = \frac{\boldsymbol{x}}{|\boldsymbol{x}|}, \forall \boldsymbol{x} \in \partial\mathcal{B}$. The "internal" and "external" solutions of the the original problem (5.33) is coupled via a Robin boundary condition

$$\boldsymbol{n} \cdot \nabla \Phi^1 + \vartheta \Phi^1 = \mathfrak{f} \quad \text{on } \partial\mathcal{B}, \tag{5.52}$$

with ϑ a positive constant.

The external Laplacian problem

The weak formulation of the subproblem in $\mathcal{B}^{\mathrm{c}}$ can be written as

$$\int_{\mathcal{B}^{\mathrm{c}}} \nabla \Phi^1 \cdot \nabla \varphi \, \mathrm{d}\Omega - \int_{\partial\mathcal{B}} (\vartheta \Phi^1 - \mathfrak{f}) \varphi \, \mathrm{d}\Omega = 0. \tag{5.53}$$

We use the Poisson kernal to compute the external solution, and notice that both ρ^0 and $\boldsymbol{u}$ vanish outside $\tilde{X}$. Therefore, with integration by parts,

$$\begin{aligned}\varPhi^1(\boldsymbol{x}) &= -4\pi G \int_{\tilde{X}} \frac{\nabla \cdot (\rho^0 \boldsymbol{u})}{|\boldsymbol{x}-\boldsymbol{y}|}\,\mathrm{d}\Omega \\ &= 4\pi G \int_{\tilde{X}} \rho^0 \boldsymbol{u} \cdot \frac{(\boldsymbol{x}-\boldsymbol{y})}{|\boldsymbol{x}-\boldsymbol{y}|^3}\,\mathrm{d}\Omega + 4\pi G \int_{\Sigma} \frac{[\![\rho^0]\!]\,(\boldsymbol{\nu}\cdot\boldsymbol{u})}{|\boldsymbol{x}-\boldsymbol{y}|}\,\mathrm{d}\Sigma - 4\pi G \int_{\partial\tilde{X}} \frac{\rho^0(\boldsymbol{\nu}\cdot\boldsymbol{u})}{|\boldsymbol{x}-\boldsymbol{y}|}\,\mathrm{d}\Sigma, \\ &\quad \text{for } \boldsymbol{x} \in \overline{\mathcal{B}_{\mathrm{c}}}.\end{aligned} \tag{5.54}$$

We can therefore compute the Robin boundary condition as

$$\mathfrak{f}(\boldsymbol{x}) = \int_{\tilde{X}} \rho^0 \boldsymbol{u} \cdot \boldsymbol{\varUpsilon}_1(\boldsymbol{y};\boldsymbol{x})\,\mathrm{d}\Omega + \int_{\Sigma} [\![\rho^0]\!]\,(\boldsymbol{\nu}\cdot\boldsymbol{u})\,\varUpsilon_2(\boldsymbol{y};\boldsymbol{x})\,\mathrm{d}\Sigma - \int_{\partial\tilde{X}} \rho^0(\boldsymbol{\nu}\cdot\boldsymbol{u})\,\varUpsilon_2(\boldsymbol{y};\boldsymbol{x})\,\mathrm{d}\Sigma \quad \text{for } \boldsymbol{x} \in \partial\mathcal{B}, \tag{5.55}$$

with

$$\begin{aligned}\boldsymbol{\varUpsilon}_1(\boldsymbol{x},\boldsymbol{y}) =& 4\pi G\Big(\frac{\vartheta(\boldsymbol{x}-\boldsymbol{y})}{|\boldsymbol{x}-\boldsymbol{y}|^3} + \frac{\boldsymbol{x}}{|\boldsymbol{x}|(|\boldsymbol{x}-\boldsymbol{y}|)^3} - \frac{3\big(\boldsymbol{x}\cdot(\boldsymbol{x}-\boldsymbol{y})\big)(\boldsymbol{x}-\boldsymbol{y})}{|\boldsymbol{x}|(|\boldsymbol{x}-\boldsymbol{y}|)^5}\Big), \\ \varUpsilon_2(\boldsymbol{x},\boldsymbol{y}) =& 4\pi G\Big(\frac{\vartheta}{|\boldsymbol{x}-\boldsymbol{y}|} - \frac{\boldsymbol{x}\cdot(\boldsymbol{x}-\boldsymbol{y})}{|\boldsymbol{x}||\boldsymbol{x}-\boldsymbol{y}|^3}\Big).\end{aligned} \tag{5.56}$$

The interior Poisson's problem

The weak formulation of the interior problem in $\mathcal{B}$ can be written as

$$\begin{aligned}&\frac{1}{4\pi G}\int_{\mathcal{B}} \nabla\varPhi^1 \cdot \nabla\varphi\,\mathrm{d}\Omega + \int_{\tilde{X}} \rho^0 \boldsymbol{u}\cdot\nabla\varphi\,\mathrm{d}\Omega + \frac{1}{4\pi G}\int_{\partial\mathcal{B}} (\vartheta\varPhi^1 - \mathfrak{f})\varphi\,\mathrm{d}\Omega = 0, \\ &\qquad \forall \varPhi^1,\ \varphi \in H^1(\mathcal{B}).\end{aligned} \tag{5.57}$$

We remark that the interior boundary conditions regarding $\varPhi^1$ and $\nabla\varPhi^1$ in Table 5.1 have already been imposed in (5.57).

5.4 Preparation for the DG method

5.4.1 The Hilbert spaces without boundary conditions and modified trace operator

The definition of the space E in (5.31), which includes continuous boundary conditions over the normal component of particle velocity across fluid-solid interfaces, puts extra restrictions on the space of test functions. The choice of a polynomial basis will be nontrivial in this situation when implementing the DG method. We introduce an alternative space of solutions $\hat{E}$ without implying the continuity condition on fluid-solid and fluid-fluid interfaces, which is given as follows with an inner product

$$\hat{E} = \left\{ \boldsymbol{u} \in L^2(\tilde{X};\rho^0) : \begin{cases} \boldsymbol{u}|_{\Omega_{\mathrm{S}}} \in H^1(\Omega_{\mathrm{S}})^3, \\ \boldsymbol{u}|_{\Omega_{\mathrm{F}}} \in H^{\mathrm{div}}\big(\Omega_{\mathrm{F}},\ L^2(\partial\Omega_{\mathrm{F}})\big) \end{cases} \right\}; \tag{5.58}$$

$$(\boldsymbol{u},\boldsymbol{w})_{\hat{E}} := (\boldsymbol{u}|_{\Omega_{\mathrm{S}}},\boldsymbol{w}|_{\Omega_{\mathrm{S}}})_{H^1(\Omega_{\mathrm{S}})} + (\boldsymbol{u}|_{\Omega_{\mathrm{F}}},\boldsymbol{w}|_{\Omega_{\mathrm{F}}})_{H^{\mathrm{div}}\left(\Omega_{\mathrm{F}},\, L^2(\Sigma^{\mathrm{FF}}\cup\partial\tilde{X}^{\mathrm{F}})\right)}.$$

It is clear that $E \subset \hat{E}$. We also introduce the space for the combination of variables $\boldsymbol{q} := (\boldsymbol{u},\boldsymbol{E},P,\Phi^1)^{\mathrm{T}}$ as

$$\hat{\mathcal{E}} := \hat{E} \times L^2(\Omega_{\mathrm{S}})^{3\times3} \times L^2(\Omega_{\mathrm{F}}) \times H^1(\mathcal{B}), \tag{5.59}$$

with the inner product

$$(\boldsymbol{q},\boldsymbol{p})_{\hat{\mathcal{E}}} := (\boldsymbol{u},\boldsymbol{w})_E + (\boldsymbol{E},\boldsymbol{H})_{L^2(\Omega_{\mathrm{S}})} + (P,Q)_{L^2(\Omega_{\mathrm{F}})} + (\nabla\Phi^1,\nabla\varphi)_{L^2(\mathcal{B})} + (\Phi^1,\varphi)_{L^2(\partial\mathcal{B})},$$
$$\text{for all } \boldsymbol{q} := \big(\boldsymbol{u},\boldsymbol{E},P,\Phi^1\big)^{\mathrm{T}} \text{ and } \boldsymbol{p} := \big(\boldsymbol{w},\boldsymbol{H},Q,\varphi\big)^{\mathrm{T}} \in \hat{\mathcal{E}}. \tag{5.60}$$

We consider the boundary conditions in Table 5.1 by introducing a new bilinear form

$$\hat{b}(\cdot,\cdot) : \hat{\mathcal{E}} \times \hat{\mathcal{E}} \to \mathbb{C},$$

which contains penalty terms over the jumps of normal displacements over $\Sigma^{\mathrm{F}} = \Sigma^{\mathrm{FF}} \cup \Sigma^{\mathrm{FS}}$ in the sense of trace. Before writing the formulation of $\hat{b}$, we introduce the following modified trace operator, which is defined by the jump of quantities across the interface in the sense of trace, and honors the boundary conditions in table 5.1, with the lemma directly obtained from a general trace theorem (see also [8, 179]).

Lemma 5.1

There exist linear continous maps $\boldsymbol{r}_{\text{SF}} : L^2(\Sigma^{\text{FS}})^3 \to H^1(\Omega_{\text{S}})^3$, $r_{\text{FS}} : L^2(\Sigma^{\text{FS}})^3 \to H^{\text{div}}(\Omega_{\text{F}})$, *and* $r_{\text{FF}} : L^2(\Sigma^{\text{FF}})^3 \to H^{\text{div}}(\Omega_{\text{F}})$, *such that*

$$\begin{aligned}\int_{\Omega_{\text{S}}} \boldsymbol{r}_{\text{SF}}(\boldsymbol{v}) : \boldsymbol{H} \, \mathrm{d}\Omega &= \int_{\Sigma^{\text{FS}}} \tfrac{1}{2} [\![\boldsymbol{v} \cdot \boldsymbol{\nu}]\!] (\boldsymbol{\nu} \cdot \boldsymbol{H}^+ \cdot \boldsymbol{\nu}) \, \mathrm{d}\Sigma, \\ \int_{\Omega_{\text{F}}} r_{\text{FS}}(\boldsymbol{v}) \, Q \, \mathrm{d}\Omega &= \int_{\Sigma^{\text{FS}}} \tfrac{1}{2} [\![\boldsymbol{v} \cdot \boldsymbol{\nu}]\!] Q^- \, \mathrm{d}\Sigma, \\ \int_{\Omega_{\text{F}}} r_{\text{FF}}(\boldsymbol{v}) \, Q \, \mathrm{d}\Omega &= \int_{\Sigma^{\text{FF}}} [\![\boldsymbol{v} \cdot \boldsymbol{\nu}]\!] \{\!\{ Q \}\!\} \, \mathrm{d}\Sigma, \quad \forall \boldsymbol{H} \in L^2(\Omega_{\text{S}})^3, \quad Q \in L^2(\Omega_{\text{F}}).\end{aligned} \tag{5.61}$$

We also denote by $\mathfrak{F} : L^2(\tilde{X}; \rho^0) \to L^2(\partial\mathcal{B})$ a linear continuous map such that $\mathfrak{F}(\boldsymbol{u}) = \mathfrak{f}$ with $\mathfrak{f}$ defined by (5.55).

5.4.2 Weak formulation with interior penalty over traces

Since the boundary condition $[\![\boldsymbol{\nu} \cdot \boldsymbol{u}]\!] = 0$ along $\Sigma^{\text{FS}} \cup \Sigma^{\text{FF}}$ is not implied in test space, some surface terms do not vanish when doing an integration by parts. We restore these boundary terms with corresponding penalties in the system described in Problem 5.3 which yields the following modified equations.

Problem 5.4

Find $\boldsymbol{q} := (\boldsymbol{u}, \boldsymbol{E}, P, \Phi^1)^T \in \hat{\mathcal{E}}$ *that satisfy*

$$\frac{\mathrm{d}}{\mathrm{d}t} \int_{\tilde{X}} \rho^0 \dot{\boldsymbol{u}} \cdot \boldsymbol{w} \, \mathrm{d}\Omega + \int_{\tilde{X}} 2\rho^0 (\boldsymbol{\Omega} \times \dot{\boldsymbol{u}}) \cdot \boldsymbol{w} \, \mathrm{d}\Omega + \hat{b}(\boldsymbol{q}, \boldsymbol{p}) - \frac{1}{4\pi G} \int_{\partial\mathcal{B}} \mathfrak{F}(\boldsymbol{u}) \, \varphi \, \mathrm{d}\Sigma = \int_{\tilde{X}} \rho^0 \boldsymbol{f} \cdot \boldsymbol{w} \, \mathrm{d}\Omega, \tag{5.62}$$

where

$$\hat{b}\big(\boldsymbol{q},\boldsymbol{p}\big) := \hat{\mathfrak{W}}^a\big(\,\boldsymbol{u},\boldsymbol{E},P,\Phi^1\ ;\ \boldsymbol{w}\,\big) + \hat{\mathfrak{W}}^b\big(\,\boldsymbol{u},\boldsymbol{E}\ ;\ \boldsymbol{l}_{\mathrm{S}}[\kappa](\boldsymbol{w},\boldsymbol{H})\,\big) \\ + \hat{\mathfrak{W}}^c\big(\boldsymbol{u},\boldsymbol{E},P,\Phi^1\ ;\ \boldsymbol{w}\big) + \hat{\mathfrak{W}}^d\big(\,\boldsymbol{u},P\ ;\ l_{\mathrm{F}}[\kappa](\boldsymbol{w},Q)\,\big) + \hat{\mathfrak{Y}}\big(\,\boldsymbol{u},\Phi^1\ ;\ \varphi\,\big), \tag{5.63}$$

for any $\boldsymbol{p} := (\boldsymbol{w},\boldsymbol{H},Q,\varphi)^{\mathrm{T}} \in \hat{\mathcal{E}}$, *with the linear maps defined by*

$$\hat{\mathfrak{W}}^a\big(\boldsymbol{u},\boldsymbol{E},P,\Phi^1\ ;\ \boldsymbol{w}\big) := \int_{\Omega_{\mathrm{S}}} (\boldsymbol{\Gamma} : \boldsymbol{E}) : \nabla\boldsymbol{w}\,\mathrm{d}\Omega \\ + \int_{\Omega_{\mathrm{S}}} \rho^0\nabla\Phi^1\cdot\boldsymbol{w}\,\mathrm{d}\Omega + \int_{\Omega_{\mathrm{S}}} \tfrac{1}{2}(\boldsymbol{\tau}^0\cdot\boldsymbol{E} - \boldsymbol{E}\cdot\boldsymbol{\tau}^0) : \nabla\boldsymbol{w}\,\mathrm{d}\Omega \\ + \int_{\Omega_{\mathrm{S}}} \mathfrak{S}\Big\{\boldsymbol{u}\cdot(\nabla\cdot\boldsymbol{\tau}^0)(\nabla\cdot\boldsymbol{w}) - (\boldsymbol{u}\cdot\nabla\boldsymbol{\tau}^0) : \nabla\boldsymbol{w}\Big\}\,\mathrm{d}\Omega \\ + \int_{\Omega_{\mathrm{S}}} \rho^0\mathfrak{S}\Big\{\boldsymbol{u}\cdot\nabla\boldsymbol{g}_0'\cdot\boldsymbol{w} + \boldsymbol{u}\cdot\mathrm{dev}(\nabla\boldsymbol{w})\cdot\boldsymbol{g}_0'\Big\}\,\mathrm{d}\Omega \\ + \int_{\Sigma^{\mathrm{FS}}} \tfrac{1}{2}\big(\boldsymbol{\nu}\cdot(\boldsymbol{\Gamma}:\boldsymbol{E})^+\cdot\boldsymbol{\nu} + P^-\big)(\boldsymbol{\nu}\cdot\boldsymbol{w}^+)\,\mathrm{d}\Sigma + \alpha\int_{\Omega_{\mathrm{S}}} \boldsymbol{r}_{\mathrm{SF}}(\boldsymbol{u}) : \boldsymbol{r}_{\mathrm{SF}}(\boldsymbol{w})\,\mathrm{d}\Omega, \tag{5.64a}$$

$$\hat{\mathfrak{W}}^b\big(\boldsymbol{u},\boldsymbol{E}\ ;\ \boldsymbol{H}\big) := \int_{\Omega_{\mathrm{S}}} \boldsymbol{E} : \boldsymbol{H}\,\mathrm{d}\Omega - \int_{\Omega_{\mathrm{S}}} (\nabla\boldsymbol{u}) : \boldsymbol{H}\,\mathrm{d}\Omega - \int_{\Sigma^{\mathrm{FS}}} \tfrac{1}{2}\big[\!\big[\boldsymbol{\nu}\cdot\boldsymbol{u}\big]\!\big]\,(\boldsymbol{\nu}\cdot\boldsymbol{H}^+\cdot\boldsymbol{\nu})\,\mathrm{d}\Sigma, \tag{5.64b}$$

$$\hat{\mathfrak{W}}^c\big(\boldsymbol{u},\boldsymbol{E},P,\Phi^1\ ;\ \boldsymbol{w}\big) := \int_{\Omega_{\mathrm{F}}} P\,(\nabla\cdot\boldsymbol{w})\,\mathrm{d}\Omega \\ + \int_{\Omega_{\mathrm{F}}} \rho^0\nabla\Phi^1\cdot\boldsymbol{w}\,\mathrm{d}\Omega - \int_{\Omega_{\mathrm{F}}} 2\rho^0\mathfrak{S}\Big\{(\boldsymbol{u}\cdot\boldsymbol{g}_0')(\nabla\cdot\boldsymbol{w})\Big\}\,\mathrm{d}\Omega \\ - \int_{\Omega_{\mathrm{F}}} \varrho^0(\boldsymbol{u}\cdot\boldsymbol{g}_0')(\boldsymbol{w}\cdot\boldsymbol{g}_0')\,\mathrm{d}\Omega + \int_{\Sigma^{\mathrm{FS}}} \mathfrak{S}\Big\{\rho^{0\,-}(\boldsymbol{u}^+\cdot\boldsymbol{g}_0')(\boldsymbol{w}^-\cdot\boldsymbol{\nu})\Big\}\,\mathrm{d}\Sigma \\ - \int_{\Sigma^{\mathrm{FF}}} (\boldsymbol{g}_0'\cdot\boldsymbol{\nu})\big[\!\big[\rho^0(\boldsymbol{u}\cdot\boldsymbol{\nu})(\boldsymbol{w}\cdot\boldsymbol{\nu})\big]\!\big]\,\mathrm{d}\Sigma + \int_{\partial\tilde{X}^{\mathrm{F}}} \rho^0(\boldsymbol{g}_0'\cdot\boldsymbol{\nu})(\boldsymbol{u}\cdot\boldsymbol{\nu})(\boldsymbol{w}\cdot\boldsymbol{\nu})\,\mathrm{d}\Sigma \\ - \int_{\Sigma^{\mathrm{FS}}} \tfrac{1}{2}\Big(\boldsymbol{\nu}\cdot(\boldsymbol{\Gamma}:\boldsymbol{E})^+\cdot\boldsymbol{\nu} + P^-\Big)(\boldsymbol{\nu}\cdot\boldsymbol{w}^-)\,\mathrm{d}\Sigma + \alpha\int_{\Omega_{\mathrm{F}}} r_{\mathrm{FS}}(\boldsymbol{u})\,r_{\mathrm{FS}}(\boldsymbol{w})\,\mathrm{d}\Omega \\ + \int_{\Sigma^{\mathrm{FF}}} \{\!\{P\}\!\}\,\big[\!\big[\boldsymbol{\nu}\cdot\boldsymbol{w}\big]\!\big]\,\mathrm{d}\Sigma + \alpha\int_{\Omega_{\mathrm{F}}} r_{\mathrm{FF}}(\boldsymbol{u})\,r_{\mathrm{FF}}(\boldsymbol{w})\,\mathrm{d}\Omega, \tag{5.64c}$$

$$\hat{\mathfrak{W}}^{d}\big(\boldsymbol{u},P\;;\;Q\big):=\int_{\Omega_{\mathrm{F}}}\lambda^{-1}\,P\,Q\,\mathrm{d}\Omega-\int_{\Omega_{\mathrm{F}}}(\nabla\cdot\boldsymbol{u})\,Q\,\mathrm{d}\Omega$$
$$-\int_{\Sigma^{\mathrm{FS}}}\tfrac{1}{2}\big[\!\big[\boldsymbol{\nu}\cdot\boldsymbol{u}\big]\!\big]\,Q^{-}\,\mathrm{d}\Sigma-\int_{\Sigma^{\mathrm{FF}}}\big[\!\big[\boldsymbol{\nu}\cdot\boldsymbol{u}\big]\!\big]\,\big\{\!\big\{Q\big\}\!\big\}\,\mathrm{d}\Sigma, \tag{5.64d}$$

$$\hat{\mathfrak{Y}}\big(\boldsymbol{u},\Phi^{1}\;;\;\varphi\big):=\frac{1}{4\pi G}\int_{\mathcal{B}}(\nabla\Phi^{1})\cdot(\nabla\varphi)\,\mathrm{d}\Omega+\int_{\tilde{X}}(\rho^{0}\boldsymbol{u})\cdot(\nabla\varphi)\,\mathrm{d}\Omega+\frac{\vartheta}{4\pi G}\int_{\partial\mathcal{B}}\Phi^{1}\,\varphi\,\mathrm{d}\Sigma, \tag{5.64e}$$

and $\boldsymbol{l}_{\mathrm{S}}, l_{\mathrm{F}}$ defined in (5.51fg).

We subtract (5.64a–e) and (5.61) from (5.63), which gives

$$\begin{aligned}\hat{b}\big(\boldsymbol{q},\boldsymbol{p}\big):=\;&\tilde{a}_3'(\boldsymbol{u},\boldsymbol{w})+\frac{1}{4\pi G}\int_{\mathcal{B}}(\nabla\mathit{\Phi}^{1})\cdot(\nabla\varphi)\,\mathrm{d}\Omega\\
&+\int_{\tilde{X}}\rho^{0}(\nabla\mathit{\Phi}^{1})\cdot\boldsymbol{w}\,\mathrm{d}\Omega+\int_{\tilde{X}}(\rho^{0}\boldsymbol{u})\cdot(\nabla\varphi)\,\mathrm{d}\Omega+\frac{\vartheta}{4\pi G}\int_{\partial\mathcal{B}}\mathit{\Phi}^{1}\,\varphi\,\mathrm{d}\Sigma\\
&+\kappa\int_{\Omega_{\mathrm{S}}}(\boldsymbol{E}-\nabla\boldsymbol{u}):(\boldsymbol{\Gamma}:\boldsymbol{H})\,\mathrm{d}\Omega+\int_{\Omega_{\mathrm{S}}}(\boldsymbol{\Gamma}:\boldsymbol{E}):\boldsymbol{r}_{\mathrm{SF}}(\boldsymbol{w})\,\mathrm{d}\Omega\\
&-\int_{\Omega_{\mathrm{S}}}\boldsymbol{r}_{\mathrm{SF}}(\boldsymbol{u}):\Big(\boldsymbol{\Gamma}:\big(\kappa\boldsymbol{H}-\nabla\boldsymbol{w}\big)-\tfrac{1}{2}\big(\boldsymbol{\tau}^{0}\cdot\nabla\boldsymbol{w}-\nabla\boldsymbol{w}\cdot\boldsymbol{\tau}^{0}\big)\Big)\,\mathrm{d}\Omega\\
&+\kappa\int_{\Omega_{\mathrm{F}}}\big(P-\lambda(\nabla\cdot\boldsymbol{u})\big)\,Q\;\mathrm{d}\Omega-\int_{\Omega_{\mathrm{F}}}\big(r_{\mathrm{FS}}(\boldsymbol{u})+r_{\mathrm{FF}}(\boldsymbol{u})\big)\,\lambda(\kappa Q-\nabla\cdot\boldsymbol{w})\,\mathrm{d}\Omega\\
&+\int_{\Omega_{\mathrm{F}}}P\,\big(r_{\mathrm{FS}}(\boldsymbol{w})+r_{\mathrm{FF}}(\boldsymbol{w})\big)\,\mathrm{d}\Omega-\int_{\Sigma^{\mathrm{FS}}}\mathfrak{S}\Big\{\rho^{0\,-}(\boldsymbol{u}^{+}\cdot\boldsymbol{g}_0')\big[\!\big[\boldsymbol{w}\cdot\boldsymbol{\nu}\big]\!\big]\Big\}\,\mathrm{d}\Sigma\\
&+\alpha\bigg(\int_{\Omega_{\mathrm{S}}}\boldsymbol{r}_{\mathrm{SF}}(\boldsymbol{u}):\boldsymbol{r}_{\mathrm{SF}}(\boldsymbol{w})\,\mathrm{d}\Omega+\int_{\Omega_{\mathrm{F}}}r_{\mathrm{FS}}(\boldsymbol{u})\,r_{\mathrm{FS}}(\boldsymbol{w})\,\mathrm{d}\Omega+\int_{\Omega_{\mathrm{F}}}r_{\mathrm{FF}}(\boldsymbol{u})\,r_{\mathrm{FF}}(\boldsymbol{w})\,\mathrm{d}\Omega\bigg),\end{aligned} \tag{5.65}$$

where

$$
\begin{aligned}
\tilde{a}_3'(\boldsymbol{u},\boldsymbol{w}) := & \int_{\Omega_{\mathrm{S}}} (\boldsymbol{\Gamma} : \nabla \boldsymbol{u}) : \nabla \boldsymbol{w} \,\mathrm{d}\Omega + \int_{\Omega_{\mathrm{F}}} \lambda (\nabla \cdot \boldsymbol{u})(\nabla \cdot \boldsymbol{w}) \,\mathrm{d}\Omega \\
& + \int_{\Omega_{\mathrm{S}}} (\nabla \boldsymbol{u}) : \Big(\tfrac{1}{2} \big(\boldsymbol{\tau}^0 \cdot \nabla \boldsymbol{w} - \nabla \boldsymbol{w} \cdot \boldsymbol{\tau}^0 \big) \Big) \,\mathrm{d}\Omega \\
& + \int_{\Omega_{\mathrm{S}}} \mathfrak{S} \Big\{ \boldsymbol{u} \cdot (\nabla \cdot \boldsymbol{\tau}^0)(\nabla \cdot \boldsymbol{w}) - (\boldsymbol{u} \cdot \nabla \boldsymbol{\tau}^0) : \nabla \boldsymbol{w} \Big\} \,\mathrm{d}\Omega \\
& + \int_{\Omega_{\mathrm{S}}} \rho^0 \mathfrak{S} \Big\{ \boldsymbol{u} \cdot \nabla \boldsymbol{g}_0' \cdot \boldsymbol{w} + \boldsymbol{u} \cdot \mathrm{dev}(\nabla \boldsymbol{w}) \cdot \boldsymbol{g}_0' \Big\} \,\mathrm{d}\Omega \\
& - \int_{\Omega_{\mathrm{F}}} 2\rho^0 \mathfrak{S} \Big\{ (\boldsymbol{u} \cdot \boldsymbol{g}_0')(\nabla \cdot \boldsymbol{w}) \Big\} \,\mathrm{d}\Omega - \int_{\Omega_{\mathrm{F}}} \varrho^0 (\boldsymbol{u} \cdot \boldsymbol{g}_0')(\boldsymbol{w} \cdot \boldsymbol{g}_0') \,\mathrm{d}\Omega \\
& + \int_{\Sigma^{\mathrm{FS}}} \mathfrak{S} \Big\{ \rho^{0\,-} (\boldsymbol{u}^+ \cdot \boldsymbol{g}_0')(\boldsymbol{w}^+ \cdot \boldsymbol{\nu}) \Big\} \,\mathrm{d}\Sigma - \int_{\Sigma^{\mathrm{FF}}} (\boldsymbol{g}_0' \cdot \boldsymbol{\nu}) [\![\rho^0]\!] \{\!\{ (\boldsymbol{u} \cdot \boldsymbol{\nu})(\boldsymbol{w} \cdot \boldsymbol{\nu}) \}\!\} \,\mathrm{d}\Sigma \\
& + \int_{\partial \tilde{X}^{\mathrm{F}}} \rho^0 (\boldsymbol{g}_0' \cdot \boldsymbol{\nu})(\boldsymbol{u} \cdot \boldsymbol{\nu})(\boldsymbol{w} \cdot \boldsymbol{\nu}) \,\mathrm{d}\Sigma.
\end{aligned}
\tag{5.66}
$$

We show that Problem 5.4 is well-posed by proving the coercivity of $\hat{b}(\cdot,\cdot)$.

Theorem 5.2

With the assumptions listed in [50, Theorem 5.7], and sufficiently large α, there exist $\hat{c}_\alpha, \hat{c}_\beta, \hat{c}_\kappa > 0$ such that

$$
\begin{aligned}
\hat{b}(\boldsymbol{q},\boldsymbol{q}) \geq & \ \hat{c}_\alpha \|\boldsymbol{u}\|_{\hat{E}}^2 + \hat{c}_\kappa \big(\|\boldsymbol{E}\|_{L^2(\Omega_{\mathrm{S}})}^2 + \|P\|_{L^2(\Omega_{\mathrm{F}})}^2 \big) \\
& + \frac{1}{8\pi G} \big\| \nabla \mathit{\Phi}^1 \big\|_{L^2(\mathcal{B})}^2 + \frac{\vartheta}{8\pi G} \big\| \mathit{\Phi}^1 \big\|_{L^2(\partial\mathcal{B})}^2 - \hat{c}_\beta \|\boldsymbol{u}\|_{L^2(\tilde{X};\rho^0)}^2, \\
& \forall \boldsymbol{q} := (\boldsymbol{u}, \boldsymbol{E}, P, \mathit{\Phi}^1)^T \in \hat{\mathcal{E}}.
\end{aligned}
\tag{5.67}
$$

Proof 5.2 We let $\boldsymbol{p} = \boldsymbol{q}$, that is, $\boldsymbol{w} = \boldsymbol{u}, \boldsymbol{H} = \boldsymbol{E}, Q = P$ and $\varphi = \mathit{\Phi}^1$, in (5.65), which yields

$$
\begin{aligned}
\hat{b}\big(\boldsymbol{q},\boldsymbol{q}\big) &:= \tilde{a}_3'(\boldsymbol{u},\boldsymbol{u}) \\
&\quad + \frac{1}{4\pi G}\big\|\nabla\mathit{\Phi}^1\big\|^2_{L^2(\mathcal{B})} + \frac{\vartheta}{4\pi G}\big\|\mathit{\Phi}^1\big\|^2_{L^2(\partial\mathcal{B})} + 2\int_{\tilde{X}}\rho^0(\nabla\mathit{\Phi}^1)\cdot\boldsymbol{u}\,\mathrm{d}\Omega \\
&\quad + \kappa\int_{\Omega_{\mathrm{S}}}\boldsymbol{E}:(\boldsymbol{\Gamma}:\boldsymbol{E})\,\mathrm{d}\Omega - \kappa\int_{\Omega_{\mathrm{S}}}\big(\nabla\boldsymbol{u}+\boldsymbol{r}_{\mathrm{SF}}(\boldsymbol{u})\big):(\boldsymbol{\Gamma}:\boldsymbol{E})\,\mathrm{d}\Omega + \int_{\Omega_{\mathrm{S}}}(\boldsymbol{\Gamma}:\boldsymbol{E}):\boldsymbol{r}_{\mathrm{SF}}(\boldsymbol{u})\,\mathrm{d}\Omega \\
&\quad + \int_{\Omega_{\mathrm{S}}}\boldsymbol{r}_{\mathrm{SF}}(\boldsymbol{u}):(\boldsymbol{\Gamma}:\nabla\boldsymbol{u})\,\mathrm{d}\Omega + \int_{\Omega_{\mathrm{S}}}\tfrac{1}{2}\big(\boldsymbol{\tau}^0\cdot\nabla\boldsymbol{u}-\nabla\boldsymbol{u}\cdot\boldsymbol{\tau}^0\big):\boldsymbol{r}_{\mathrm{SF}}(\boldsymbol{u})\,\mathrm{d}\Omega \\
&\quad + \kappa\|P\|^2_{L^2(\Omega_{\mathrm{F}})} - \kappa\int_{\Omega_{\mathrm{F}}}\lambda\big(\nabla\cdot\boldsymbol{u}+r_{\mathrm{FS}}(\boldsymbol{u})+r_{\mathrm{FF}}(\boldsymbol{u})\big)\,P\,\mathrm{d}\Omega \\
&\quad + \int_{\Omega_{\mathrm{F}}}\big(P+\lambda\nabla\cdot\boldsymbol{u}\big)\big(r_{\mathrm{FS}}(\boldsymbol{u})+r_{\mathrm{FF}}(\boldsymbol{u})\big)\,\mathrm{d}\Omega - \int_{\Sigma^{\mathrm{FS}}}\rho^{0\,-}(\boldsymbol{u}^+\cdot\boldsymbol{g}_0')\,[\![\boldsymbol{u}\cdot\boldsymbol{\nu}]\!]\,\mathrm{d}\Sigma \\
&\quad + \alpha\Big(\|\boldsymbol{r}_{\mathrm{SF}}(\boldsymbol{u})\|^2_{L^2(\Omega_{\mathrm{S}})} + \|r_{\mathrm{FS}}(\boldsymbol{u})\|^2_{L^2(\Omega_{\mathrm{F}})} + \|r_{\mathrm{FF}}(\boldsymbol{u})\|^2_{L^2(\Omega_{\mathrm{F}})}\Big).
\end{aligned}
\tag{5.68}
$$

We remark that $\tilde{a}_3'$ yields the same coercivity result as $\tilde{a}_3$ by following the same procedure as proof of [50, Theorem 5.7].

We consider the terms containing $\mathit{\Phi}^1$, namely, the second line of (5.68), which yields

$$
\begin{aligned}
2\int_{\tilde{X}}\rho^0(\nabla\mathit{\Phi}^1)\cdot\boldsymbol{u}\,\mathrm{d}\Omega \geq & -\frac{1}{8\pi G}\big\|\nabla\mathit{\Phi}^1\big\|^2_{L^2(\tilde{X})} - 8\pi G\big\|\rho^0\boldsymbol{u}\big\|^2_{L^2(\tilde{X})} \\
\geq & -\frac{1}{8\pi G}\big\|\nabla\mathit{\Phi}^1\big\|^2_{L^2(\mathcal{B})} - 8\pi G C_{\rho^0}\|\boldsymbol{u}\|^2_{L^2(\tilde{X};\rho^0)}.
\end{aligned}
\tag{5.69}
$$

For the volume integration terms within Ω_{S}, obviously with Young's inequality

$$
\kappa\int_{\Omega_{\mathrm{S}}}\boldsymbol{E}:(\boldsymbol{\Gamma}:\boldsymbol{E})\,\mathrm{d}\Omega \geq \kappa C_{\boldsymbol{\Gamma}}\|\boldsymbol{E}\|^2_{L^2(\Omega_{\mathrm{S}})},
\tag{5.70}
$$

$$
\begin{aligned}
-\kappa\int_{\Omega_{\mathrm{S}}}\big(\nabla\boldsymbol{u}+\boldsymbol{r}_{\mathrm{SF}}(\boldsymbol{u})\big):(\boldsymbol{\Gamma}:\boldsymbol{E})\,\mathrm{d}\Omega \geq & \\
& -\kappa C^*_{\boldsymbol{\Gamma}}\Big(\frac{1}{\delta}\|\nabla\boldsymbol{u}\|^2_{L^2(\Omega_{\mathrm{S}})} + \frac{1}{\delta}\|\boldsymbol{r}_{\mathrm{SF}}(\boldsymbol{u})\|^2_{L^2(\Omega_{\mathrm{S}})} + \frac{\delta}{2}\|\boldsymbol{E}\|^2_{L^2(\Omega_{\mathrm{S}})}\Big),
\end{aligned}
\tag{5.71}
$$

$$
\int_{\Omega_{\mathrm{S}}}(\boldsymbol{\Gamma}:\boldsymbol{E}):\boldsymbol{r}_{\mathrm{SF}}(\boldsymbol{u})\,\mathrm{d}\Omega \geq -C^*_{\boldsymbol{\Gamma}}\Big(\frac{1}{2\kappa\delta}\|\boldsymbol{r}_{\mathrm{SF}}(\boldsymbol{u})\|^2_{L^2(\Omega_{\mathrm{S}})} + \frac{\kappa\delta}{2}\|\boldsymbol{E}\|^2_{L^2(\Omega_{\mathrm{S}})}\Big),
\tag{5.72}
$$

$$\int_{\Omega_{\mathrm{S}}} \boldsymbol{r}_{\mathrm{SF}}(\boldsymbol{u}) : (\boldsymbol{\Gamma} : \nabla \boldsymbol{u}) \, \mathrm{d}\Omega \geq - C^*_{\boldsymbol{\Gamma}} \Big(\frac{1}{2\delta} \| \boldsymbol{r}_{\mathrm{SF}}(\boldsymbol{u}) \|^2_{L^2(\Omega_{\mathrm{S}})} + \frac{\delta}{2} \| \nabla \boldsymbol{u} \|^2_{L^2(\Omega_{\mathrm{S}})} \Big), \tag{5.73}$$

$$\begin{aligned} \int_{\Omega_{\mathrm{S}}} \tfrac{1}{2} \big(\boldsymbol{\tau}^0 \cdot \nabla \boldsymbol{u} - \nabla \boldsymbol{u} \cdot \boldsymbol{\tau}^0 \big) : \boldsymbol{r}_{\mathrm{SF}}(\boldsymbol{u}) \, \mathrm{d}\Omega \geq & \\ - \big\| \boldsymbol{\tau}^0 \big\|_{L^\infty(\Omega_{\mathrm{S}})} \Big(\frac{1}{2\delta} \| \boldsymbol{r}_{\mathrm{SF}}(\boldsymbol{u}) \|^2_{L^2(\Omega_{\mathrm{S}})} + \frac{\delta}{2} \| \nabla \boldsymbol{u} \|^2_{L^2(\Omega_{\mathrm{S}})} \Big). & \end{aligned} \tag{5.74}$$

For the volume integration terms within Ω_{F}, obviously with Young's inequality

$$\begin{aligned} -\kappa \int_{\Omega_{\mathrm{F}}} \lambda \big(\nabla \cdot \boldsymbol{u} + r_{\mathrm{FS}}(\boldsymbol{u}) + r_{\mathrm{FF}}(\boldsymbol{u}) \big) \, P \, \mathrm{d}\Omega \geq & \\ - \kappa C^*_\lambda \Big(\frac{1}{\delta} \| \nabla \cdot \boldsymbol{u} \|^2_{L^2(\Omega_{\mathrm{F}})} + \frac{2}{\delta} \| r_{\mathrm{FS}}(\boldsymbol{u}) \|^2_{L^2(\Omega_{\mathrm{F}})} + \frac{2}{\delta} \| r_{\mathrm{FF}}(\boldsymbol{u}) \|^2_{L^2(\Omega_{\mathrm{F}})} + \frac{\delta}{2} \| P \|^2_{L^2(\Omega_{\mathrm{F}})} \Big), & \end{aligned} \tag{5.75}$$

$$\begin{aligned} \int_{\Omega_{\mathrm{F}}} \big(P + \lambda \nabla \cdot \boldsymbol{u} \big) \big(r_{\mathrm{FS}}(\boldsymbol{u}) + r_{\mathrm{FF}}(\boldsymbol{u}) \big) \, \mathrm{d}\Omega \geq & \\ - \Big(\frac{1}{\kappa} \| r_{\mathrm{FS}}(\boldsymbol{u}) \|^2_{L^2(\Omega_{\mathrm{F}})} + \frac{1}{\kappa} \| r_{\mathrm{FF}}(\boldsymbol{u}) \|^2_{L^2(\Omega_{\mathrm{F}})} + \frac{\kappa}{2} \| P \|^2_{L^2(\Omega_{\mathrm{F}})} \Big) & \\ - C^*_\lambda \Big(\frac{1}{\delta} \| r_{\mathrm{FS}}(\boldsymbol{u}) \|^2_{L^2(\Omega_{\mathrm{F}})} + \frac{1}{\delta} \| r_{\mathrm{FF}}(\boldsymbol{u}) \|^2_{L^2(\Omega_{\mathrm{F}})} + \frac{\delta}{2} \| \nabla \cdot \boldsymbol{u} \|^2_{L^2(\Omega_{\mathrm{F}})} \Big). & \end{aligned} \tag{5.76}$$

For the surface integration terms on Σ^{FS}, we use trace inequality such that

$$- \int_{\Sigma^{\mathrm{FS}}} \rho^{0\,-} (\boldsymbol{u}^+ \cdot \boldsymbol{g}_0') \big[\!\big[\boldsymbol{u} \cdot \boldsymbol{\nu} \big]\!\big] \, \mathrm{d}\Sigma \geq - C_{\boldsymbol{g}_0'} \Big(\delta \| \boldsymbol{u} \|^2_{L^2(\Omega_{\mathrm{S}})} + \frac{1}{\delta} \| \boldsymbol{r}_{\mathrm{SF}}(\boldsymbol{u}) \|^2_{L^2(\Omega_{\mathrm{S}})} \Big). \tag{5.77}$$

Summarizing (5.69)–(5.77) yields

$$\begin{aligned} \hat{b}(\boldsymbol{q}, \boldsymbol{q}) - \tilde{a}_3'(\boldsymbol{u}, \boldsymbol{u}) \geq & \frac{1}{8\pi G} \big\| \nabla \varPhi^1 \big\|^2_{L^2(\mathcal{B})} + \frac{\vartheta}{8\pi G} \big\| \varPhi^1 \big\|^2_{L^2(\partial\mathcal{B})} \\ & + \kappa (C_{\boldsymbol{\Gamma}} - C_1 \delta) \| \boldsymbol{E} \|^2_{L^2(\Omega_{\mathrm{S}})} + \kappa (\tfrac{1}{2} - C_2 \delta) \| P \|^2_{L^2(\Omega_{\mathrm{F}})} \\ & - (C_3 \frac{\kappa}{\delta} + C_4 \delta) \| \nabla \boldsymbol{u} \|^2_{L^2(\Omega_{\mathrm{S}})} - (C_5 \frac{\kappa}{\delta} + C_6 \delta) \| \nabla \cdot \boldsymbol{u} \|^2_{L^2(\Omega_{\mathrm{F}})} \\ & + \Big(\alpha - C_7 \big(\frac{\kappa}{\delta} + \frac{1}{\kappa\delta} + \frac{1}{\delta} \big) \Big) \| \boldsymbol{r}_{\mathrm{SF}}(\boldsymbol{u}) \|^2_{L^2(\Omega_{\mathrm{S}})} \\ & + \Big(\alpha - C_8 \big(\frac{\kappa}{\delta} + \frac{1}{\kappa} + \frac{1}{\delta} \big) \Big) \Big(\| r_{\mathrm{SF}}(\boldsymbol{u}) \|^2_{L^2(\Omega_{\mathrm{F}})} + \| r_{\mathrm{FF}}(\boldsymbol{u}) \|^2_{L^2(\Omega_{\mathrm{F}})} \Big). \end{aligned} \tag{5.78}$$

Clearly, by taking sufficiently small δ, κ and correspondingly sufficiently large α, the coercivity result holds.

5.5 Numerical approximation using DG method with iterative coupling

We conduct a domain partitioning for $\tilde{X} \cup \Omega^{\mathrm{c}}$ into a finite element mesh, $\bigcup \Omega^{\mathrm{e}}$, and denote by $\Omega^{\mathrm{e}}_{\mathrm{S}}$ the elements in the solid regions, by $\Omega^{\mathrm{e}}_{\mathrm{F}}$ the elements in the fluid regions, and by $\Omega^{\mathrm{e}}_{\mathrm{c}}$ the elements outside the physical domain of earth while inside the extended ball $\mathcal{B}$. We also denote by $\Sigma^{\mathrm{e}}_{\mathrm{SS}}, \Sigma^{\mathrm{e}}_{\mathrm{FF}}, \Sigma^{\mathrm{e}}_{\mathrm{FS}}, \Sigma^{\mathrm{e}}_{\mathrm{Sb}}, \Sigma^{\mathrm{e}}_{\mathrm{Fb}}$ and $\Sigma^{\mathrm{e}}_{\mathcal{B}}$ the facets located on solid-solid, fluid-fluid, fluid-solid interfaces, Earth land $\partial\tilde{X}^{\mathrm{S}}$, ocean surface $\partial\tilde{X}^{\mathrm{F}}$ and the boundary of the extended ball $\partial\mathcal{B}$ respectively. We further denote the union of $\Omega^{\mathrm{e}}_{\mathrm{S}}$ and $\Omega^{\mathrm{e}}_{\mathrm{F}}$ by $\Omega^{\mathrm{e}}_{\tilde{X}}$, the union of $\Sigma^{\mathrm{e}}_{\mathrm{SS}}, \Sigma^{\mathrm{e}}_{\mathrm{FF}}$ and $\Sigma^{\mathrm{e}}_{\mathrm{FS}}$ by Σ^{e}, and the union of $\Sigma^{\mathrm{e}}_{\mathrm{Sb}}$ and $\Sigma^{\mathrm{e}}_{\mathrm{Fb}}$ by $\Sigma^{\mathrm{e}}_{\mathrm{b}}$. The summations over elements and facets mentioned above are implied in the discretized formulations in this section.

We denote by $V^p_h(\Omega)$ the space of polynomials in Ω with order less than or equal to p. We introduce the following space of polynomial solutions in the finite elements,

$$\hat{E}^p_h = \left\{ \boldsymbol{u} \in L^2(\tilde{X};\rho^0) : \begin{cases} \boldsymbol{u}|_{\Omega^{\mathrm{e}}_{\mathrm{S}}} \in \left(H^1(\Omega^{\mathrm{e}}_{\mathrm{S}}) \cap V^p_h(\Omega^{\mathrm{e}}_{\mathrm{S}})\right)^3, \\ \boldsymbol{u}|_{\Omega^{\mathrm{e}}_{\mathrm{F}}} \in \left(H^{\mathrm{div}}\big(\Omega^{\mathrm{e}}_{\mathrm{F}},\ L^2(\Sigma^{\mathrm{e}}_{\mathrm{FF}} \cup \Sigma^{\mathrm{e}}_{\mathrm{Fb}})\big) \cap V^p_h(\Omega^{\mathrm{e}}_{\mathrm{F}})\right)^3 \end{cases} \right\}, \tag{5.79}$$

with inner product

$$\begin{aligned}(\boldsymbol{u},\boldsymbol{w})_{\hat{E}_h} :=& \left(\boldsymbol{u}|_{\Omega^{\mathrm{e}}_{\mathrm{S}}}, \boldsymbol{w}|_{\Omega^{\mathrm{e}}_{\mathrm{S}}}\right)_{H^1(\Omega^{\mathrm{e}}_{\mathrm{S}})} + \left(\boldsymbol{u}|_{\Omega^{\mathrm{e}}_{\mathrm{F}}}, \boldsymbol{w}|_{\Omega^{\mathrm{e}}_{\mathrm{F}}}\right)_{H^{\mathrm{div}}(\Omega^{\mathrm{e}}_{\mathrm{F}})} \\ &+ \left(\boldsymbol{u}|_{\Sigma^{\mathrm{e}}_{\mathrm{FF}}\cup\Sigma^{\mathrm{e}}_{\mathrm{Fb}}}, \boldsymbol{w}|_{\Sigma^{\mathrm{e}}_{\mathrm{FF}}\cup\Sigma^{\mathrm{e}}_{\mathrm{Fb}}}\right)_{L^2(\Sigma^{\mathrm{e}}_{\mathrm{FF}}\cup\Sigma^{\mathrm{e}}_{\mathrm{Fb}})}.\end{aligned} \tag{5.80}$$

We denote by

$$\boldsymbol{q}_h := \left(\boldsymbol{u}_h, \boldsymbol{E}_h, P_h, \Phi^1_h\right)^{\mathrm{T}} \text{ and } \boldsymbol{p}_h := \left(\boldsymbol{w}_h, \boldsymbol{H}_h, Q_h, \varphi_h\right)^{\mathrm{T}} \tag{5.81}$$

the array of solutions and test functions in polynomial space, and by $\hat{\mathcal{E}}^p_h$ the polynomial solution space for $\boldsymbol{q}_h$ which is a subspace of $\hat{\mathcal{E}}$, as

$$\hat{\mathcal{E}}_h^p := \hat{E}_h^p \times \Big(L^2(\Omega_{\mathrm{S}}^{\mathrm{e}}) \cap V_h^p(\Omega_{\mathrm{S}}^{\mathrm{e}})\Big)^{3\times 3} \times \Big(L^2(\Omega_{\mathrm{F}}^{\mathrm{e}}) \cap V_h^p(\Omega_{\mathrm{F}}^{\mathrm{e}})\Big) \times \Big(H^1(\Omega^{\mathrm{e}}) \cap V_h^p(\Omega^{\mathrm{e}})\Big), \tag{5.82}$$

with the corresponding inner product

$$\begin{aligned}(\boldsymbol{q}_h, \boldsymbol{p}_h)_{\hat{\mathcal{E}}_h} :=& (\boldsymbol{u}_h, \boldsymbol{w}_h)_{\hat{E}_h} + (\boldsymbol{E}_h, \boldsymbol{H}_h)_{L^2(\Omega_{\mathrm{S}}^{\mathrm{e}})} + (P_h, Q_h)_{L^2(\Omega_{\mathrm{F}}^{\mathrm{e}})} \\ &+ (\nabla \varPhi_h^1, \nabla \varphi_h)_{L^2(\Omega^{\mathrm{e}})} + (\varPhi_h^1, \varphi_h)_{L^2(\Sigma_{\mathcal{B}}^{\mathrm{e}})}, \\ &\text{for all } \boldsymbol{q}_h := \big(\boldsymbol{u}_h, \boldsymbol{E}_h, P_h, \varPhi_h^1\big)^{\mathrm{T}} \text{ and } \boldsymbol{p}_h := \big(\boldsymbol{w}_h, \boldsymbol{H}_h, Q_h, \varphi_h\big)^{\mathrm{T}} \in \hat{E}_h.\end{aligned} \tag{5.83}$$

Based on the *Weierstrass approximation theorem*, $\bigcup_{p=1}^{\infty} \hat{\mathcal{E}}_h^p$ is dense in $\hat{\mathcal{E}}$.

We also introduce the following lemmas that can be directly obtained from the discrete trace theorem with polynomials (see also [8, 170]).

Lemma 5.2

There exist linear continous maps $\boldsymbol{r}_{\mathrm{SS}}^{\mathrm{e}} : L^2(\Sigma_{\mathrm{SS}}^{\mathrm{e}})^3 \to \mathcal{V}_{h,p}^{\mathrm{S}}$, $\boldsymbol{r}_{\mathrm{SF}}^{\mathrm{e}} : L^2(\Sigma_{\mathrm{FS}}^{\mathrm{e}})^3 \to \mathcal{V}_{h,p}^{\mathrm{S}}$, $r_{\mathrm{FS}}^{\mathrm{e}} : L^2(\Sigma_{\mathrm{FS}}^{\mathrm{e}})^3 \to \mathcal{V}_{h,p}^{\mathrm{F}}$, *and* $r_{\mathrm{FF}}^{\mathrm{e}} : L^2(\Sigma_{\mathrm{FF}}^{\mathrm{e}})^3 \to \mathcal{V}_{h,p}^{\mathrm{F}}$, *for*

$$\begin{aligned}\mathcal{V}_{h,p}^{\mathrm{S}} :=& \Big\{ \boldsymbol{E} \in L^2(\Omega_{\mathrm{S}})^{3\times 3} \Big| \boldsymbol{E}_{ij}|_{\Omega_{\mathrm{S}}^{\mathrm{e}}} \in V_h^p, \quad i,j \in \{1,2,3\} \Big\}, \\ \mathcal{V}_{h,p}^{\mathrm{F}} :=& \Big\{ P \in L^2(\Omega_{\mathrm{S}}) \Big| P|_{\Omega_{\mathrm{S}}^{\mathrm{e}}} \in V_h^p \Big\},\end{aligned}$$

such that

$$\begin{aligned}\int_{\Omega_{\mathrm{S}}^{\mathrm{e}}} \boldsymbol{r}_{\mathrm{SS}}^{\mathrm{e}}(\boldsymbol{v}_h) : \boldsymbol{H}_h \,\mathrm{d}\Omega &= \int_{\Sigma_{\mathrm{SS}}^{\mathrm{e}}} [\![\boldsymbol{v}_h]\!] \cdot \{\!\{\boldsymbol{\nu} \cdot \boldsymbol{H}_h\}\!\} \,\mathrm{d}\Sigma, \\ \int_{\Omega_{\mathrm{S}}^{\mathrm{e}}} \boldsymbol{r}_{\mathrm{SF}}^{\mathrm{e}}(\boldsymbol{v}_h) : \boldsymbol{H}_h \,\mathrm{d}\Omega &= \int_{\Sigma_{\mathrm{FS}}^{\mathrm{e}}} \tfrac{1}{2} [\![\boldsymbol{v}_h \cdot \boldsymbol{\nu}]\!] (\boldsymbol{\nu} \cdot \boldsymbol{H}_h^+ \cdot \boldsymbol{\nu}) \,\mathrm{d}\Sigma, \\ \int_{\Omega_{\mathrm{F}}^{\mathrm{e}}} r_{\mathrm{FS}}^{\mathrm{e}}(\boldsymbol{v}_h)\, Q_h \,\mathrm{d}\Omega &= \int_{\Sigma_{\mathrm{FS}}^{\mathrm{e}}} \tfrac{1}{2} [\![\boldsymbol{v}_h \cdot \boldsymbol{\nu}]\!] Q_h^- \,\mathrm{d}\Sigma, \\ \int_{\Omega_{\mathrm{F}}^{\mathrm{e}}} r_{\mathrm{FF}}^{\mathrm{e}}(\boldsymbol{v}_h)\, Q_h \,\mathrm{d}\Omega &= \int_{\Sigma_{\mathrm{FF}}^{\mathrm{e}}} [\![\boldsymbol{v}_h \cdot \boldsymbol{\nu}]\!] \{\!\{Q_h\}\!\} \,\mathrm{d}\Sigma.\end{aligned} \tag{5.84}$$

The linear maps $\boldsymbol{r}^{\mathrm{e}}_{*}$ are also known as "lifting operators". We mention the trace inequality in finite elements as follows.

Lemma 5.3

With the linear continuous maps defined in Lemma 5.1, there exist a bounded constant $C_p > 0$ *depending on polynomial order* p*, such that*

$$\begin{aligned}
\|\boldsymbol{r}^{\mathrm{e}}_{\mathrm{SS}}(\boldsymbol{u}_h)\|^2_{L^2(\Omega^{\mathrm{e}}_{\mathrm{S}})} &\leq C_p h^{-1} \| [\![\boldsymbol{u}_h]\!] \|^2_{L^2(\Sigma^{\mathrm{e}}_{\mathrm{SS}})}, \\
\|\boldsymbol{r}^{\mathrm{e}}_{\mathrm{SF}}(\boldsymbol{u}_h)\|^2_{L^2(\Omega^{\mathrm{e}}_{\mathrm{S}})} &\leq C_p h^{-1} \| [\![\boldsymbol{\nu} \cdot \boldsymbol{u}_h]\!] \|^2_{L^2(\Sigma^{\mathrm{e}}_{\mathrm{FS}})}, \\
\|\boldsymbol{r}^{\mathrm{e}}_{\mathrm{FS}}(\boldsymbol{u}_h)\|^2_{L^2(\Omega^{\mathrm{e}}_{\mathrm{F}})} &\leq C_p h^{-1} \| [\![\boldsymbol{\nu} \cdot \boldsymbol{u}_h]\!] \|^2_{L^2(\Sigma^{\mathrm{e}}_{\mathrm{FS}})}, \\
\|\boldsymbol{r}^{\mathrm{e}}_{\mathrm{FF}}(\boldsymbol{u}_h)\|^2_{L^2(\Omega^{\mathrm{e}}_{\mathrm{F}})} &\leq C_p h^{-1} \| [\![\boldsymbol{\nu} \cdot \boldsymbol{u}_h]\!] \|^2_{L^2(\Sigma^{\mathrm{e}}_{\mathrm{FF}})},
\end{aligned} \tag{5.85}$$

with h *the mesh size.*

In the following subsection, we introduce the bilinear form $\hat{b}_h$, which is $\hat{E}^p_h$ coercive with respect to $L^2(\tilde{X}; \rho^0)$, and based on that, give an error estimate for the semidiscretized DG scheme.

5.5.1 The DG method with penalty flux

We introduce a DG formulation with penalty flux, where α_h is a positive constant penalty coefficiet, that yields a semi-discretized form derived from (5.62)–(5.64) as follows.

Problem 5.5

Find $\boldsymbol{q}_h := \left(\boldsymbol{u}_h, \boldsymbol{E}_h, P_h, \Phi^1_h\right)^{\mathrm{T}} \in \hat{E}^p_h$ *such that*

$$\begin{aligned}
&\frac{\mathrm{d}}{\mathrm{d}t} \int_{\Omega^{\mathrm{e}}} \rho^0 \dot{\boldsymbol{u}}_h \cdot \boldsymbol{w}_h \,\mathrm{d}\Omega + \int_{\Omega^{\mathrm{e}}} 2\rho^0 (\boldsymbol{\Omega} \times \dot{\boldsymbol{u}}_h) \cdot \boldsymbol{w}_h \,\mathrm{d}\Omega - \frac{1}{4\pi G} \int_{\Sigma^{\mathrm{e}}_{\mathcal{B}}} \mathfrak{F}(\boldsymbol{u}_h)\, \varphi_h \,\mathrm{d}\Sigma \\
&\qquad + \hat{b}_h(\boldsymbol{q}_h, \boldsymbol{p}_h) = \int_{\Omega^{\mathrm{e}}} \rho^0 \boldsymbol{f}_h \cdot \boldsymbol{w}_h \,\mathrm{d}\Omega,
\end{aligned} \tag{5.86}$$

for any $\boldsymbol{p}_h := \big(\boldsymbol{w}_h, \boldsymbol{H}_h, Q_h, \varphi_h\big)^{\mathrm{T}} \in \hat{E}_h^p$, *where*

$$\begin{aligned}\hat{b}_h\big(\boldsymbol{q}_h, \boldsymbol{p}_h\big) := {}& \hat{\mathfrak{W}}_h^a\big(\boldsymbol{u}_h, \boldsymbol{E}_h, P_h, \Phi_h^1\ ;\ \boldsymbol{w}_h\big) + \hat{\mathfrak{W}}_h^b\big(\boldsymbol{u}_h, \boldsymbol{E}_h\ ;\ \boldsymbol{l}_{\mathrm{S}}[\kappa](\boldsymbol{w}_h, \boldsymbol{H}_h)\big) \\ & + \hat{\mathfrak{W}}_h^c\big(\boldsymbol{u}_h, \boldsymbol{E}_h, P_h, \Phi_h^1\ ;\ \boldsymbol{w}_h\big) + \hat{\mathfrak{W}}_h^d\big(\boldsymbol{u}_h, P_h\ ;\ l_{\mathrm{F}}[\kappa](\boldsymbol{w}_h, Q_h)\big) + \hat{\mathfrak{Y}}_h\big(\boldsymbol{u}_h, \Phi_h^1\ ;\ \varphi_h\big),\end{aligned} \tag{5.87}$$

with the linear operators

$$\begin{aligned}\hat{\mathfrak{W}}_h^a\big(\boldsymbol{u}_h, \boldsymbol{E}_h, P_h, \Phi_h^1\ ;\ \boldsymbol{w}_h\big) = {}& \int_{\Omega_{\mathrm{S}}^{\mathrm{e}}} (\boldsymbol{\Gamma} : \boldsymbol{E}_h) : \nabla \boldsymbol{w}_h \,\mathrm{d}\Omega \\ & + \int_{\Omega_{\mathrm{S}}^{\mathrm{e}}} \rho^0 \nabla \Phi_h^1 \cdot \boldsymbol{w}_h \,\mathrm{d}\Omega + \int_{\Omega_{\mathrm{S}}^{\mathrm{e}}} \tfrac{1}{2}(\boldsymbol{\tau}^0 \cdot \boldsymbol{E}_h - \boldsymbol{E}_h \cdot \boldsymbol{\tau}^0) : \nabla \boldsymbol{w}_h \,\mathrm{d}\Omega \\ & + \int_{\Omega_{\mathrm{S}}^{\mathrm{e}}} \mathfrak{S}\Big\{\boldsymbol{u}_h \cdot (\nabla \cdot \boldsymbol{\tau}^0)(\nabla \cdot \boldsymbol{w}_h) - (\boldsymbol{u}_h \cdot \nabla \boldsymbol{\tau}^0) : \nabla \boldsymbol{w}_h\Big\} \,\mathrm{d}\Omega \\ & + \int_{\Omega_{\mathrm{S}}^{\mathrm{e}}} \rho^0 \mathfrak{S}\Big\{\boldsymbol{u}_h \cdot \nabla \boldsymbol{g}_0' \cdot \boldsymbol{w}_h + \boldsymbol{u}_h \cdot \mathrm{dev}(\nabla \boldsymbol{w}_h) \cdot \boldsymbol{g}_0'\Big\} \,\mathrm{d}\Omega \\ & + \int_{\Sigma_{\mathrm{FS}}^{\mathrm{e}}} \tfrac{1}{2}\big(\boldsymbol{\nu} \cdot (\boldsymbol{\Gamma} : \boldsymbol{E}_h)^+ \cdot \boldsymbol{\nu} + P_h^-\big)(\boldsymbol{\nu} \cdot \boldsymbol{w}_h^+) \,\mathrm{d}\Sigma + \alpha_h \int_{\Sigma_{\mathrm{FS}}^{\mathrm{e}}} [\![\boldsymbol{\nu} \cdot \boldsymbol{u}_h]\!] \big(\boldsymbol{\nu} \cdot \boldsymbol{w}_h^+\big) \,\mathrm{d}\Sigma \\ & + \int_{\Sigma_{\mathrm{SS}}^{\mathrm{e}}} \{\!\{\boldsymbol{\nu} \cdot (\boldsymbol{\Gamma} : \boldsymbol{E}_h)\}\!\} \cdot [\![\boldsymbol{w}_h]\!] \,\mathrm{d}\Sigma + \alpha_h \int_{\Sigma_{\mathrm{SS}}^{\mathrm{e}}} [\![\boldsymbol{u}_h]\!] \cdot [\![\boldsymbol{w}_h]\!] \,\mathrm{d}\Sigma,\end{aligned} \tag{5.88a}$$

$$\begin{aligned}\hat{\mathfrak{W}}_h^b\big(\boldsymbol{u}_h, \boldsymbol{E}_h\ ;\ \boldsymbol{H}_h\big) = {}& \int_{\Omega_{\mathrm{S}}^{\mathrm{e}}} \boldsymbol{E}_h : \boldsymbol{H}_h \,\mathrm{d}\Omega - \int_{\Omega_{\mathrm{S}}^{\mathrm{e}}} (\nabla \boldsymbol{u}_h) : \boldsymbol{H}_h \,\mathrm{d}\Omega \\ & - \int_{\Sigma_{\mathrm{FS}}^{\mathrm{e}}} \tfrac{1}{2}[\![\boldsymbol{\nu} \cdot \boldsymbol{u}_h]\!]\,(\boldsymbol{\nu} \cdot \boldsymbol{H}_h^+ \cdot \boldsymbol{\nu}) \,\mathrm{d}\Sigma - \int_{\Sigma_{\mathrm{SS}}^{\mathrm{e}}} [\![\boldsymbol{u}_h]\!] \cdot \{\!\{\boldsymbol{\nu} \cdot \boldsymbol{H}_h\}\!\} \,\mathrm{d}\Sigma,\end{aligned} \tag{5.88b}$$

$$\hat{\mathfrak{W}}^c_h\big(\boldsymbol{u}_h, \boldsymbol{E}_h, P_h, \varPhi^1_h \;;\; \boldsymbol{w}_h\big) = \int_{\Omega^{\mathrm{e}}_{\mathrm{F}}} P_h\,(\nabla\cdot\boldsymbol{w}_h)\,\mathrm{d}\Omega$$
$$+ \int_{\Omega^{\mathrm{e}}_{\mathrm{F}}} \rho^0\nabla\varPhi^1_h\cdot\boldsymbol{w}_h\,\mathrm{d}\Omega - \int_{\Omega^{\mathrm{e}}_{\mathrm{F}}} 2\rho^0\mathfrak{S}\Big\{(\boldsymbol{u}_h\cdot\boldsymbol{g}'_0)(\nabla\cdot\boldsymbol{w}_h)\Big\}\,\mathrm{d}\Omega$$
$$- \int_{\Omega^{\mathrm{e}}_{\mathrm{F}}} \varrho^0(\boldsymbol{u}_h\cdot\boldsymbol{g}'_0)(\boldsymbol{w}_h\cdot\boldsymbol{g}'_0)\,\mathrm{d}\Omega + \int_{\Sigma^{\mathrm{e}}_{\mathrm{FS}}} \mathfrak{S}\Big\{\rho^{0\,-}(\boldsymbol{u}^+_h\cdot\boldsymbol{g}'_0)(\boldsymbol{w}^-_h\cdot\boldsymbol{\nu})\Big\}\,\mathrm{d}\Sigma$$
$$- \int_{\Sigma^{\mathrm{e}}_{\mathrm{FF}}} (\boldsymbol{g}'_0\cdot\boldsymbol{\nu})\,[\![\rho^0(\boldsymbol{u}_h\cdot\boldsymbol{\nu})(\boldsymbol{w}_h\cdot\boldsymbol{\nu})\,]\!]\,\mathrm{d}\Sigma + \int_{\Sigma^{\mathrm{e}}_{\mathrm{Fb}}} \rho^0(\boldsymbol{g}'_0\cdot\boldsymbol{\nu})(\boldsymbol{u}_h\cdot\boldsymbol{\nu})(\boldsymbol{w}_h\cdot\boldsymbol{\nu})\,\mathrm{d}\Sigma$$
$$- \int_{\Sigma^{\mathrm{e}}_{\mathrm{FS}}} \tfrac{1}{2}\Big(\boldsymbol{\nu}\cdot(\boldsymbol{\Gamma}:\boldsymbol{E}_h)^+\cdot\boldsymbol{\nu} + P^-_h\Big)(\boldsymbol{\nu}\cdot\boldsymbol{w}^-_h)\,\mathrm{d}\Sigma - \alpha\int_{\Sigma^{\mathrm{e}}_{\mathrm{FS}}} [\![\boldsymbol{\nu}\cdot\boldsymbol{u}_h\,]\!]\,(\boldsymbol{\nu}\cdot\boldsymbol{w}^-_h)\,\mathrm{d}\Sigma$$
$$+ \int_{\Sigma^{\mathrm{e}}_{\mathrm{FF}}} \{\!\{P_h\}\!\}\;[\![\boldsymbol{\nu}\cdot\boldsymbol{w}_h\,]\!]\,\mathrm{d}\Sigma + \alpha\int_{\Sigma^{\mathrm{e}}_{\mathrm{FF}}} [\![\boldsymbol{\nu}\cdot\boldsymbol{u}_h\,]\!]\;[\![\boldsymbol{\nu}\cdot\boldsymbol{w}_h\,]\!]\,\mathrm{d}\Sigma, \tag{5.88c}$$

$$\begin{aligned}\hat{\mathfrak{W}}^d_h\big(\boldsymbol{u}_h, P_h \;;\; Q_h\big) &= \int_{\Omega^{\mathrm{e}}_{\mathrm{F}}} \lambda^{-1}_h\,P_h\,Q_h\,\mathrm{d}\Omega - \int_{\Omega^{\mathrm{e}}_{\mathrm{F}}} (\nabla\cdot\boldsymbol{u}_h)\,Q_h\,\mathrm{d}\Omega \\ &- \int_{\Sigma^{\mathrm{e}}_{\mathrm{FS}}} \tfrac{1}{2}[\![\boldsymbol{\nu}\cdot\boldsymbol{u}_h\,]\!]\,Q^-_h\,\mathrm{d}\Sigma - \int_{\Sigma^{\mathrm{e}}_{\mathrm{FF}}} [\![\boldsymbol{\nu}\cdot\boldsymbol{u}_h\,]\!]\;\{\!\{Q_h\}\!\}\,\mathrm{d}\Sigma,\end{aligned} \tag{5.88d}$$

$$\begin{aligned}\hat{\mathfrak{Y}}_h\big(\boldsymbol{u}_h, \Phi^1_h \;;\; \varphi_h\big) &:= \frac{1}{4\pi G}\int_{\Omega^{\mathrm{e}}} (\nabla\Phi^1_h)\cdot(\nabla\varphi_h)\,\mathrm{d}\Omega + \int_{\Omega^{\mathrm{e}}} (\rho^0\boldsymbol{u}_h)\cdot(\nabla\varphi_h)\,\mathrm{d}\Omega \\ &+ \frac{\vartheta}{4\pi G}\int_{\Sigma^{\mathrm{e}}_{\mathcal{B}}} \Phi^1_h\,\varphi_h\,\mathrm{d}\Sigma + \frac{\alpha'_h}{4\pi G}\int_{\Sigma^{\mathrm{e}}} [\![\Phi^1_h\,]\!]\;[\![\varphi_h\,]\!]\,\mathrm{d}\Sigma\end{aligned} \tag{5.88e}$$

$$\mathfrak{F}(\boldsymbol{u}_h) := \int_{\Omega^{\mathrm{e}}} \rho^0\boldsymbol{u}_h\cdot\boldsymbol{\varUpsilon}_1\,\mathrm{d}\Omega + \int_{\Sigma^{\mathrm{e}}} [\![\rho^0\,]\!]\,\{\!\{\boldsymbol{\nu}\cdot\boldsymbol{u}_h\}\!\}\,\varUpsilon_2\,\mathrm{d}\Sigma - \int_{\Sigma^{\mathrm{e}}_{\mathrm{b}}} \rho^0(\boldsymbol{\nu}\cdot\boldsymbol{u}_h)\,\varUpsilon_2\,\mathrm{d}\Sigma, \tag{5.88f}$$

and $\boldsymbol{l}_{\mathrm{S}}, l_{\mathrm{F}}$ *defined in (5.47fg).*

The scalar α_h in (5.88) is a constant penalty coefficient that depends on the mesh size [139]. We remark that the linear functions $\boldsymbol{\varUpsilon}_1(\boldsymbol{x},\boldsymbol{y})$ and $\varUpsilon_2(\boldsymbol{x},\boldsymbol{y})$ are defined in (5.56), which satisfy far-field approximation when $|\boldsymbol{x}-\boldsymbol{y}|$ is sufficiently large. Therefore, a low-rank approximation can be used in computing the integration within $\mathfrak{F}$. Details of the matrix formulation for computing (5.88f) can be found in section 5.6.2. Clearly, $\hat{b}_h$ can be equivalently written as

$$
\begin{aligned}
\hat{b}_h\big(\boldsymbol{q}_h, \boldsymbol{p}_h\big) := {} & a_h(\boldsymbol{u}_h, \boldsymbol{w}_h) + \frac{1}{4\pi G}\int_{\Omega^{\mathrm{e}}} (\nabla \mathit{\Phi}_h^1)\cdot(\nabla\varphi_h)\,\mathrm{d}\Omega + \frac{\alpha_h'}{4\pi G}\int_{\Sigma^{\mathrm{e}}} [\![\mathit{\Phi}_h^1]\!]\,[\![\varphi_h]\!]\,\mathrm{d}\Sigma \\
& + \int_{\Omega^{\mathrm{e}}_{\tilde{X}}} \rho^0(\nabla\mathit{\Phi}_h^1)\cdot\boldsymbol{w}_h\,\mathrm{d}\Omega + \int_{\Omega^{\mathrm{e}}_{\tilde{X}}} (\rho^0\boldsymbol{u}_h)\cdot(\nabla\varphi_h)\,\mathrm{d}\Omega + \frac{\vartheta}{4\pi G}\int_{\Sigma^{\mathrm{e}}_{\mathcal{B}}} \mathit{\Phi}_h^1\,\varphi_h\,\mathrm{d}\Sigma \\
& + \kappa\int_{\Omega^{\mathrm{e}}_{\mathrm{S}}} (\boldsymbol{E}_h - \nabla\boldsymbol{u}_h) : (\boldsymbol{\Gamma} : \boldsymbol{H}_h)\,\mathrm{d}\Omega + \int_{\Omega^{\mathrm{e}}_{\mathrm{S}}} (\boldsymbol{\Gamma} : \boldsymbol{E}_h) : \big(\boldsymbol{r}^{\mathrm{e}}_{\mathrm{SS}}(\boldsymbol{w}_h) + \boldsymbol{r}^{\mathrm{e}}_{\mathrm{SF}}(\boldsymbol{w}_h)\big)\,\mathrm{d}\Omega \\
& - \int_{\Omega^{\mathrm{e}}_{\mathrm{S}}} \big(\boldsymbol{r}^{\mathrm{e}}_{\mathrm{SS}}(\boldsymbol{u}_h) + \boldsymbol{r}^{\mathrm{e}}_{\mathrm{SF}}(\boldsymbol{u}_h)\big) : \Big(\boldsymbol{\Gamma} : \big(\kappa\boldsymbol{H}_h - \nabla\boldsymbol{w}_h\big) - \tfrac{1}{2}\big(\boldsymbol{\tau}^0\cdot\nabla\boldsymbol{w}_h - \nabla\boldsymbol{w}_h\cdot\boldsymbol{\tau}^0\big)\Big)\,\mathrm{d}\Omega \\
& + \kappa\int_{\Omega^{\mathrm{e}}_{\mathrm{F}}} \big(P_h - \lambda_h(\nabla\cdot\boldsymbol{u}_h)\big)\,Q_h\,\mathrm{d}\Omega - \int_{\Omega^{\mathrm{e}}_{\mathrm{F}}} \big(r^{\mathrm{e}}_{\mathrm{FS}}(\boldsymbol{u}_h) + r^{\mathrm{e}}_{\mathrm{FF}}(\boldsymbol{u}_h)\big)\,\lambda(\kappa Q_h - \nabla\cdot\boldsymbol{w}_h)\,\mathrm{d}\Omega \\
& + \int_{\Omega^{\mathrm{e}}_{\mathrm{F}}} P_h\,\big(r^{\mathrm{e}}_{\mathrm{FS}}(\boldsymbol{w}_h) + r^{\mathrm{e}}_{\mathrm{FF}}(\boldsymbol{w}_h)\big)\,\mathrm{d}\Omega - \int_{\Sigma^{\mathrm{e}}_{\mathrm{FS}}} \mathfrak{S}\Big\{\rho^{0\,-}(\boldsymbol{u}_h^+\cdot\boldsymbol{g}_0')\,[\![\boldsymbol{w}_h\cdot\boldsymbol{\nu}]\!]\Big\}\,\mathrm{d}\Sigma \\
& + \alpha\int_{\Sigma^{\mathrm{e}}_{\mathrm{SS}}} [\![\boldsymbol{u}_h]\!] : [\![\boldsymbol{w}_h]\!]\,\mathrm{d}\Omega + \alpha\int_{\Sigma^{\mathrm{e}}_{\mathrm{FF}}} [\![\boldsymbol{\nu}\cdot\boldsymbol{u}_h]\!]\,[\![\boldsymbol{\nu}\cdot\boldsymbol{w}_h]\!]\,\mathrm{d}\Omega \\
& + \alpha\int_{\Sigma^{\mathrm{e}}_{\mathrm{FS}}} [\![\boldsymbol{\nu}\cdot\boldsymbol{u}_h]\!]\,[\![\boldsymbol{\nu}\cdot\boldsymbol{w}_h]\!]\,\mathrm{d}\Omega
\end{aligned}
\tag{5.89}
$$

where

$$
\begin{aligned}
a_h(\boldsymbol{u}_h, \boldsymbol{w}_h) := {} & \int_{\Omega^{\mathrm{e}}_{\mathrm{S}}} (\boldsymbol{\Gamma} : \nabla\boldsymbol{u}_h) : \nabla\boldsymbol{w}\,\mathrm{d}\Omega + \int_{\Omega^{\mathrm{e}}_{\mathrm{F}}} \lambda(\nabla\cdot\boldsymbol{u}_h)(\nabla\cdot\boldsymbol{w}_h)\,\mathrm{d}\Omega \\
& + \int_{\Omega^{\mathrm{e}}_{\mathrm{S}}} (\nabla\boldsymbol{u}_h) : \Big(\tfrac{1}{2}\big(\boldsymbol{\tau}^0\cdot\nabla\boldsymbol{w}_h - \nabla\boldsymbol{w}_h\cdot\boldsymbol{\tau}^0\big)\Big)\,\mathrm{d}\Omega \\
& + \int_{\Omega^{\mathrm{e}}_{\mathrm{S}}} \mathfrak{S}\Big\{\boldsymbol{u}_h\cdot(\nabla\cdot\boldsymbol{\tau}^0)(\nabla\cdot\boldsymbol{w}_h) - (\boldsymbol{u}_h\cdot\nabla\boldsymbol{\tau}^0) : \nabla\boldsymbol{w}_h\Big\}\,\mathrm{d}\Omega \\
& + \int_{\Omega^{\mathrm{e}}_{\mathrm{S}}} \rho^0\mathfrak{S}\Big\{\boldsymbol{u}_h\cdot\nabla\boldsymbol{g}_0'\cdot\boldsymbol{w}_h + \boldsymbol{u}_h\cdot\mathrm{dev}(\nabla\boldsymbol{w}_h)\cdot\boldsymbol{g}_0'\Big\}\,\mathrm{d}\Omega \\
& - \int_{\Omega^{\mathrm{e}}_{\mathrm{F}}} 2\rho^0\mathfrak{S}\Big\{(\boldsymbol{u}_h\cdot\boldsymbol{g}_0')(\nabla\cdot\boldsymbol{w}_h)\Big\}\,\mathrm{d}\Omega - \int_{\Omega^{\mathrm{e}}_{\mathrm{F}}} \varrho^0(\boldsymbol{u}_h\cdot\boldsymbol{g}_0')(\boldsymbol{w}_h\cdot\boldsymbol{g}_0')\,\mathrm{d}\Omega \\
& + \int_{\Sigma^{\mathrm{e}}_{\mathrm{FS}}} \mathfrak{S}\Big\{\rho^{0\,-}(\boldsymbol{u}_h^+\cdot\boldsymbol{g}_0')(\boldsymbol{w}_h^+\cdot\boldsymbol{\nu})\Big\}\,\mathrm{d}\Sigma + \int_{\Sigma^{\mathrm{e}}_{\mathrm{Fb}}} \rho^0(\boldsymbol{g}_0'\cdot\boldsymbol{\nu})(\boldsymbol{u}_h\cdot\boldsymbol{\nu})(\boldsymbol{w}_h\cdot\boldsymbol{\nu})\,\mathrm{d}\Sigma \\
& - \int_{\Sigma^{\mathrm{e}}_{\mathrm{FF}}} (\boldsymbol{g}_0'\cdot\boldsymbol{\nu})\,[\![\rho^0]\!]\,\{\{(\boldsymbol{u}_h\cdot\boldsymbol{\nu})(\boldsymbol{w}_h\cdot\boldsymbol{\nu})\}\}\,\mathrm{d}\Sigma.
\end{aligned}
\tag{5.90}
$$

5.5.2 The convergence analysis of semi-discretized system

First of all, We show that the bilinear operator $\hat{b}_h$ is $\hat{\mathcal{E}}_h$ coercive relative to $L^2(\tilde{X};\rho^0)$ within $\hat{\mathcal{E}}_h^p \times \hat{\mathcal{E}}_h^p$ by the following theorem.

Theorem 5.3

With the assumptions given in Theorem 5.2, for sufficiently large penalty coefficient α, there exist $\hat{c}'_\alpha, \hat{c}'_\beta, \hat{c}'_\kappa > 0$ such that

$$\begin{aligned}\hat{b}_h(\boldsymbol{q}_h, \boldsymbol{q}_h) \geq\ & \hat{c}'_\alpha \|\boldsymbol{u}_h\|^2_{\hat{E}_h} + \hat{c}'_\kappa \big(\|\boldsymbol{E}_h\|^2_{L^2(\Omega^{\mathrm{e}}_{\mathrm{S}})} + \|P_h\|^2_{L^2(\Omega^{\mathrm{e}}_{\mathrm{F}})}\big) \\ & + \frac{1}{8\pi G}\big\|\nabla \mathit{\Phi}^1_h\big\|^2_{L^2(\Omega^{\mathrm{e}})} + \frac{\vartheta}{8\pi G}\big\|\mathit{\Phi}^1_h\big\|^2_{L^2(\Sigma^{\mathrm{e}}_{\mathcal{B}})} - \hat{c}'_\beta \|\boldsymbol{u}_h\|^2_{L^2(\Omega^{\mathrm{e}}_{\tilde{X}};\rho^0)}, \\ & \forall \boldsymbol{q}_h := (\boldsymbol{u}_h, \boldsymbol{E}_h, P_h, \mathit{\Phi}^1_h)^T \in \hat{\mathcal{E}}^p_h.\end{aligned} \tag{5.91}$$

Proof 5.3 Due to the same structure of $\hat{b}_h$ with $\hat{b}$, we can follow the same procedure of proving Theorem 5.2 and obtain

$$\begin{aligned}\hat{b}_h(\boldsymbol{q}_h, \boldsymbol{q}_h) \geq\ & a_h(\boldsymbol{u}_h, \boldsymbol{u}_h) + \frac{1}{8\pi G}\big\|\nabla \mathit{\Phi}^1_h\big\|^2_{L^2(\Omega^{\mathrm{e}})} + \frac{\vartheta}{8\pi G}\big\|\mathit{\Phi}^1_h\big\|^2_{L^2(\Sigma^{\mathrm{e}}_{\mathcal{B}})} + \frac{\alpha'_h}{8\pi G}\big\|[\![\mathit{\Phi}^1_h]\!]\big\|^2_{L^2(\Sigma^{\mathrm{e}})} \\ & + \hat{c}'_\kappa \Big(\|\boldsymbol{E}_h\|^2_{L^2(\Omega^{\mathrm{e}}_{\mathrm{S}})} + \|P_h\|^2_{L^2(\Omega^{\mathrm{e}}_{\mathrm{F}})}\Big) - C\delta\Big(\|\nabla \boldsymbol{u}_h\|^2_{L^2(\Omega^{\mathrm{e}}_{\mathrm{S}})} + \|\nabla\cdot \boldsymbol{u}_h\|^2_{L^2(\Omega^{\mathrm{e}}_{\mathrm{F}})}\Big) \\ & + \alpha\Big(\big\|[\![\boldsymbol{u}_h]\!]\big\|^2_{L^2(\Sigma^{\mathrm{e}}_{\mathrm{SS}})} + \big\|[\![\boldsymbol{\nu}\cdot\boldsymbol{u}_h]\!]\big\|^2_{L^2(\Sigma^{\mathrm{e}}_{\mathrm{FS}})} + \big\|[\![\boldsymbol{\nu}\cdot\boldsymbol{u}_h]\!]\big\|^2_{L^2(\Sigma^{\mathrm{e}}_{\mathrm{FF}})}\Big) \\ & - \frac{1}{d(\delta)}\Big(\|\boldsymbol{r}^{\mathrm{e}}_{\mathrm{SS}}(\boldsymbol{u}_h)\|^2_{L^2(\Omega^{\mathrm{e}}_{\mathrm{S}})} + \|\boldsymbol{r}^{\mathrm{e}}_{\mathrm{SF}}(\boldsymbol{u}_h)\|^2_{L^2(\Omega^{\mathrm{e}}_{\mathrm{S}})} + \|r^{\mathrm{e}}_{\mathrm{FS}}(\boldsymbol{u}_h)\|^2_{L^2(\Omega^{\mathrm{e}}_{\mathrm{F}})} + \|r^{\mathrm{e}}_{\mathrm{FF}}(\boldsymbol{u}_h)\|^2_{L^2(\Omega^{\mathrm{e}}_{\mathrm{F}})}\Big),\end{aligned} \tag{5.92}$$

with $d(\delta) > 0$ depends continuously on $\delta > 0$ and $C > 0$ a constant. We remark that a_h has the same coercivity as $\tilde{a}'_3$. We choose sufficiently small δ, and based on Lemma 5.3, choose $\alpha \geq \frac{2C_p h^{-1}}{d(\delta)}$, thus Theorem 5.3 holds.

We also remark that $\hat{b}_h$ is bounded within $\hat{\mathcal{E}} \times \hat{\mathcal{E}}$ by the following Lemma.

Lemma 5.4

With the assumptions given in Theorem 5.2, there exist $C > 0$ such that

$$|\hat{b}_h(\boldsymbol{q}, \boldsymbol{p})| \leq C \|\boldsymbol{q}\|_{\hat{\mathcal{E}}_h} \|\boldsymbol{p}\|_{\hat{\mathcal{E}}_h}, \quad \forall \boldsymbol{q}, \boldsymbol{p} \in \hat{\mathcal{E}}. \tag{5.93}$$

Proof of Lemma 5.4 can be obtained following [50, Lemma5.6], and by using Trace inequality.

We can now prove the convergence of the discretized formulation in Problem 5.5 via a semi-group approach, following [50, section 5.3]. Define

$$\hat{b}'_h(\boldsymbol{q}_h, \boldsymbol{p}_h) := \hat{b}_h(\boldsymbol{q}_h, \boldsymbol{p}_h) + \hat{c}'_\beta(\boldsymbol{u}_h, \boldsymbol{w}_h)_{L^2(\Omega^{\mathrm{e}}_{\tilde{X}};\rho^0)} - \frac{\vartheta}{16\pi G}(\mathit{\Phi}^1_h, \varphi_h)_{L^2(\Sigma^{\mathrm{e}}_{\mathcal{B}})}, \tag{5.94}$$

Obviously both $\hat{b}_h$ and $\hat{b}'_h$ are Hermitian. It is also clear from Theorem 5.3 that

$$\begin{aligned} \hat{b}'_h(\boldsymbol{q}_h, \boldsymbol{q}_h) \geq & \hat{c}'_\alpha \|\boldsymbol{u}_h\|^2_{\hat{E}_h} + \hat{c}'_\kappa \big(\|\boldsymbol{E}_h\|^2_{L^2(\Omega^{\mathrm{e}}_{\mathrm{S}})} + \|P_h\|^2_{L^2(\Omega^{\mathrm{e}}_{\mathrm{F}})}\big) \\ & + \frac{1}{8\pi G}\big\|\nabla \mathit{\Phi}^1_h\big\|^2_{L^2(\Omega^{\mathrm{e}})} + \frac{\vartheta}{16\pi G}\big\|\mathit{\Phi}^1_h\big\|^2_{L^2(\Sigma^{\mathrm{e}}_{\mathcal{B}})} \\ \geq & \hat{c}' \|\boldsymbol{q}_h\|^2_{\hat{\mathcal{E}}_h}. \end{aligned} \tag{5.95}$$

In other words, $\hat{b}'_h$ is a bounded sesquilinear form on $\hat{\mathcal{E}}^p_h \times \hat{\mathcal{E}}^p_h$ and is $\hat{\mathcal{E}}_h$ coercive. We define the following product space

$$\mathcal{H}_h := H \times \hat{\mathcal{E}}_h; \quad H = L^2(\Omega^{\mathrm{e}}_{\tilde{X}}, \rho^0), \tag{5.96}$$

equipped with the product $(\cdot,\cdot)_{\mathcal{H}}$ defined by

$$\left(\begin{pmatrix} \boldsymbol{u}_1 \\ \boldsymbol{q}_2 \end{pmatrix}, \begin{pmatrix} \boldsymbol{w}_1 \\ \boldsymbol{p}_2 \end{pmatrix} \right)_{\mathcal{H}_h} = (\boldsymbol{u}_1, \boldsymbol{w}_1)_H + (\boldsymbol{q}_2, \boldsymbol{p}_2)_{\hat{\mathcal{E}}_h}. \tag{5.97}$$

We therefore rewrite (5.86) by

$$\begin{aligned} \frac{\mathrm{d}}{\mathrm{d}t}\big(\dot{\boldsymbol{u}}_h, \boldsymbol{w}_h\big)_H + \hat{b}'_h\big(\boldsymbol{q}_h, \boldsymbol{p}_h\big) - \hat{c}'_\beta\big(\boldsymbol{u}_h, \boldsymbol{w}_h\big)_H + \frac{\vartheta}{16\pi G}\big(\mathit{\Phi}^1_h, \varphi_h\big)_{L^2(\Sigma^{\mathrm{e}}_{\mathcal{B}})} \\ + 2\big(\boldsymbol{R}_{\boldsymbol{\Omega}} \cdot \dot{\boldsymbol{u}}_h, \boldsymbol{w}_h\big)_H - \frac{1}{4\pi G}\big(\mathfrak{F}(\boldsymbol{u}_h), \varphi_h\big)_{L^2(\Sigma^{\mathrm{e}}_{\mathcal{B}})} = \big(\boldsymbol{f}_h, \boldsymbol{w}_h\big)_H. \end{aligned} \tag{5.98}$$

We consider the true solutions $\boldsymbol{q} = (\boldsymbol{u}, \boldsymbol{E}, P, \mathit{\Phi}^1)^{\mathrm{T}} \in \hat{\mathcal{E}}$ for Problem 5.5, and the numerical solution $\boldsymbol{q}_h = (\boldsymbol{u}_h, \boldsymbol{E}_h, P_h, \mathit{\Phi}_h^1)^{\mathrm{T}} \in \hat{\mathcal{E}}_h^p$, and denote by π_h^p the H-orthogonal projection onto $\hat{\mathcal{E}}_h^p$. We define the following quantities of error:

$$\begin{aligned}
\boldsymbol{\varepsilon_u} &:= \boldsymbol{u} - \boldsymbol{u}_h, & \varepsilon_\Phi &:= \Phi^1 - \Phi_h^1, & \boldsymbol{\varepsilon_q} &:= \boldsymbol{q} - \boldsymbol{q}_h,\\
\boldsymbol{\epsilon_u} &:= (1-\pi_h^p)\boldsymbol{u}, & \epsilon_\Phi &:= (1-\pi_h^p)\Phi^1, & \boldsymbol{\epsilon_q} &:= (1-\pi_h^p)\boldsymbol{q},\\
\boldsymbol{\eta_u} &:= \boldsymbol{u}_h - \pi_h^p\boldsymbol{u}, & \eta_\Phi &:= \Phi_h^1 - \pi_h^p\Phi^1, & \boldsymbol{\eta_q} &:= \boldsymbol{q}_h - \pi_h^p\boldsymbol{q},
\end{aligned}$$

and remark that $\boldsymbol{\varepsilon}_\star = \boldsymbol{\epsilon}_\star - \boldsymbol{\eta}_\star$. By projection approximation, we have $\|\boldsymbol{\epsilon_q}\| \leq Ch^{p+1}\|\boldsymbol{q}\|$. To simplify the discussion, we assume that the body source, prestress and material coefficients are piecewise constant. The numerical error is orthogonal to the polynomial basis, that is

$$\begin{aligned}
&\frac{\mathrm{d}}{\mathrm{d}t}\big(\dot{\boldsymbol{\varepsilon}}_{\boldsymbol{u}}, \boldsymbol{w}_h\big)_H + \hat{b}_h'\big(\,\boldsymbol{\varepsilon_q}, \boldsymbol{p}_h\,\big) - \hat{c}_\beta'\big(\boldsymbol{\varepsilon_u}, \boldsymbol{w}_h\big)_H + \frac{\vartheta}{16\pi G}\big(\boldsymbol{\varepsilon}_{\mathit{\Phi}}, \varphi_h\big)_{L^2(\Sigma_{\mathcal{B}}^{\mathrm{e}})}\\
&\qquad + 2\big(\boldsymbol{R_\Omega}\cdot\dot{\boldsymbol{\varepsilon}}_{\boldsymbol{u}}, \boldsymbol{w}_h\big)_H - \frac{1}{4\pi G}\big(\mathfrak{F}(\boldsymbol{\varepsilon_u}), \varphi_h\big)_{L^2(\Sigma_{\mathcal{B}}^{\mathrm{e}})} = 0, \qquad (5.99)\\
&\quad \forall \boldsymbol{p}_h := (\boldsymbol{w}_h, \boldsymbol{H}_h, Q_h, \varphi_h)^{\mathrm{T}} \in \hat{\mathcal{E}}_h^p.
\end{aligned}$$

We let $\boldsymbol{p}_h = \dot{\boldsymbol{\eta}}_{\boldsymbol{q}}$, which also implies that $\boldsymbol{w}_h = \dot{\boldsymbol{\eta}}_{\boldsymbol{u}}$ and $\varphi_h = \dot{\boldsymbol{\eta}}_{\mathit{\Phi}}$, and use $\boldsymbol{\varepsilon}_\star = \boldsymbol{\epsilon}_\star - \boldsymbol{\eta}_\star$ in (5.99) to obtain

$$\begin{aligned}
&\frac{\mathrm{d}}{\mathrm{d}t}\Big(\|\dot{\boldsymbol{\eta}}_{\boldsymbol{u}}\|_H^2 + \hat{b}_h'\big(\,\boldsymbol{\eta_q}, \boldsymbol{\eta_q}\,\big) + \frac{\vartheta}{16\pi G}\|\boldsymbol{\eta}_{\mathit{\Phi}}\|^2_{L^2(\Sigma_{\mathcal{B}}^{\mathrm{e}})} - \big(\dot{\boldsymbol{\epsilon}}_{\boldsymbol{u}}, \dot{\boldsymbol{\eta}}_{\boldsymbol{u}}\big)_H\Big)\\
&\quad = \frac{\vartheta}{16\pi G}\big(\boldsymbol{\epsilon}_{\mathit{\Phi}}, \dot{\boldsymbol{\eta}}_{\mathit{\Phi}}\big)_{L^2(\Sigma_{\mathcal{B}}^{\mathrm{e}})} + \frac{1}{4\pi G}\big(\mathfrak{F}(\boldsymbol{\eta_u}), \dot{\boldsymbol{\eta}}_{\mathit{\Phi}}\big)_{L^2(\Sigma_{\mathcal{B}}^{\mathrm{e}})} + \hat{c}_\beta'\big(\boldsymbol{\eta_u}, \dot{\boldsymbol{\eta}}_{\boldsymbol{u}}\big)_H \qquad (5.100)\\
&\qquad + 2\big(\boldsymbol{R_\Omega}\cdot\dot{\boldsymbol{\epsilon}}_{\boldsymbol{u}}, \dot{\boldsymbol{\eta}}_{\boldsymbol{u}}\big)_H - \frac{1}{4\pi G}\big(\mathfrak{F}(\boldsymbol{\epsilon_u}), \dot{\boldsymbol{\eta}}_{\mathit{\Phi}}\big)_{L^2(\Sigma_{\mathcal{B}}^{\mathrm{e}})} + \hat{b}_h\big(\,\boldsymbol{\epsilon_q}, \dot{\boldsymbol{\eta}}_{\boldsymbol{q}}\,\big).
\end{aligned}$$

In the above, we use the skew symmetry of $\boldsymbol{R}_{\boldsymbol{\Omega}}$, with $\big(\boldsymbol{R}_{\boldsymbol{\Omega}}\cdot\dot{\boldsymbol{\eta}}_{\boldsymbol{u}},\dot{\boldsymbol{\eta}}_{\boldsymbol{u}}\big)_H=0$. Integration over the time interval $[0,t]$ yields

$$\begin{aligned}\|\dot{\boldsymbol{\eta}}_{\boldsymbol{u}}\|_H^2&+\hat{b}'_h\big(\boldsymbol{\eta}_{\boldsymbol{q}},\boldsymbol{\eta}_{\boldsymbol{q}}\big)+\frac{\vartheta}{16\pi G}\|\boldsymbol{\eta}_{\Phi}\|^2_{L^2(\Sigma^{\mathrm{e}}_{\mathcal{B}})}=\big(\dot{\boldsymbol{\epsilon}}_{\boldsymbol{u}},\dot{\boldsymbol{\eta}}_{\boldsymbol{u}}\big)_H+\hat{b}_h\big(\boldsymbol{\epsilon}_{\boldsymbol{q}},\boldsymbol{\eta}_{\boldsymbol{q}}\big)\\&+\frac{1}{4\pi G}\Big(\frac{\vartheta}{4}\big(\boldsymbol{\epsilon}_{\Phi},\boldsymbol{\eta}_{\Phi}\big)_{L^2(\Sigma^{\mathrm{e}}_{\mathcal{B}})}+\big(\mathfrak{F}(\boldsymbol{\eta}_{\boldsymbol{u}}),\boldsymbol{\eta}_{\Phi}\big)_{L^2(\Sigma^{\mathrm{e}}_{\mathcal{B}})}-\big(\mathfrak{F}(\boldsymbol{\epsilon}_{\boldsymbol{u}}),\boldsymbol{\eta}_{\Phi}\big)_{L^2(\Sigma^{\mathrm{e}}_{\mathcal{B}})}\Big)\\&-\frac{1}{4\pi G}\int_0^t\Big(\frac{\vartheta}{4}\big(\dot{\boldsymbol{\epsilon}}_{\Phi},\boldsymbol{\eta}_{\Phi}\big)_{L^2(\Sigma^{\mathrm{e}}_{\mathcal{B}})}+\big(\mathfrak{F}(\dot{\boldsymbol{\eta}}_{\boldsymbol{u}}),\boldsymbol{\eta}_{\Phi}\big)_{L^2(\Sigma^{\mathrm{e}}_{\mathcal{B}})}-\big(\mathfrak{F}(\dot{\boldsymbol{\epsilon}}_{\boldsymbol{u}}),\boldsymbol{\eta}_{\Phi}\big)_{L^2(\Sigma^{\mathrm{e}}_{\mathcal{B}})}\Big)\,\mathrm{d}s\\&+\int_0^t\Big(\hat{c}'_\beta\big(\boldsymbol{\eta}_{\boldsymbol{u}},\dot{\boldsymbol{\eta}}_{\boldsymbol{u}}\big)_H+2\big(\boldsymbol{R}_{\boldsymbol{\Omega}}\cdot\dot{\boldsymbol{\epsilon}}_{\boldsymbol{u}},\dot{\boldsymbol{\eta}}_{\boldsymbol{u}}\big)_H-\hat{b}_h\big(\dot{\boldsymbol{\epsilon}}_{\boldsymbol{q}},\boldsymbol{\eta}_{\boldsymbol{q}}\big)\Big)\,\mathrm{d}s.\end{aligned}\tag{5.101}$$

We remark that $\mathfrak{F}:H\to L^2(\partial\mathcal{B})$ is a linear continuous map, thus with Cauchy-Schwartz inequality followed by Young's inequality,

$$\big(\mathfrak{F}(\boldsymbol{w}),\varphi\big)_{L^2(\Sigma^{\mathrm{e}}_{\mathcal{B}})}\le C'_1\|\boldsymbol{w}\|_H\|\varphi\|_{L^2(\Sigma^{\mathrm{e}}_{\mathcal{B}})}\le\delta C_1\|\boldsymbol{w}\|_H^2+\frac{1}{\delta}\|\varphi\|^2_{L^2(\Sigma^{\mathrm{e}}_{\mathcal{B}})}.\tag{5.102}$$

Using Lemma 5.4 followed by Young's inequality,

$$|\hat{b}_h(\boldsymbol{q},\boldsymbol{p})|\le\frac{C_2}{\delta}\|\boldsymbol{q}\|^2_{\hat{\mathcal{E}}_h}+\delta\|\boldsymbol{p}\|^2_{\hat{\mathcal{E}}_h}.\tag{5.103}$$

Also, $\boldsymbol{R}_{\boldsymbol{\Omega}}$ is bounded, thus

$$\big(\boldsymbol{R}_{\boldsymbol{\Omega}}\cdot\boldsymbol{u},\boldsymbol{w}\big)_H\le C'_3\|\boldsymbol{u}\|_H\|\boldsymbol{w}\|_H\le\frac{C_3}{\delta}\|\boldsymbol{u}\|_H^2+\delta\|\boldsymbol{w}\|_H^2.\tag{5.104}$$

The constant δ in (5.102)–(5.104) can be asigned with any positive value. Using (5.95) and (5.102)–(5.104), (5.101) therefore yields

$$\begin{aligned}\|\dot{\boldsymbol{\eta}}_{\boldsymbol{u}}\|_H^2&+\hat{c}'\big\|\boldsymbol{\eta}_{\boldsymbol{q}}\big\|^2_{\hat{\mathcal{E}}_h}+\frac{\vartheta}{16\pi G}\|\boldsymbol{\eta}_{\Phi}\|^2_{L^2(\Sigma^{\mathrm{e}}_{\mathcal{B}})}\le\frac{1}{2\delta}\|\dot{\boldsymbol{\epsilon}}_{\boldsymbol{u}}\|_H^2+\frac{\delta}{2}\|\dot{\boldsymbol{\eta}}_{\boldsymbol{u}}\|_H^2+\frac{C_2}{\delta}\|\boldsymbol{\epsilon}_{\boldsymbol{q}}\|^2_{\hat{\mathcal{E}}_h}+\delta\big\|\boldsymbol{\eta}_{\boldsymbol{q}}\big\|^2_{\hat{\mathcal{E}}_h}\\&+\frac{1}{4\pi G}\Big(\frac{\vartheta}{8}\|\boldsymbol{\epsilon}_{\Phi}\|^2_{L^2(\Sigma^{\mathrm{e}}_{\mathcal{B}})}+\frac{\vartheta}{8}\|\boldsymbol{\eta}_{\Phi}\|^2_{L^2(\Sigma^{\mathrm{e}}_{\mathcal{B}})}+\delta C_1\|\boldsymbol{\eta}_{\boldsymbol{u}}\|_H^2+\delta C_1\|\boldsymbol{\epsilon}_{\boldsymbol{u}}\|_H^2+\frac{2}{\delta}\|\boldsymbol{\eta}_{\Phi}\|^2_{L^2(\Sigma^{\mathrm{e}}_{\mathcal{B}})}\Big)\\&+\frac{1}{4\pi G}\int_0^t\Big(\frac{\vartheta}{8}\|\dot{\boldsymbol{\epsilon}}_{\Phi}\|^2_{L^2(\Sigma^{\mathrm{e}}_{\mathcal{B}})}+\frac{\vartheta}{8}\|\boldsymbol{\eta}_{\Phi}\|^2_{L^2(\Sigma^{\mathrm{e}}_{\mathcal{B}})}+C_1\|\dot{\boldsymbol{\eta}}_{\boldsymbol{u}}\|_H^2+C_1\|\dot{\boldsymbol{\epsilon}}_{\boldsymbol{u}}\|_H^2+2\|\boldsymbol{\eta}_{\Phi}\|^2_{L^2(\Sigma^{\mathrm{e}}_{\mathcal{B}})}\Big)\,\mathrm{d}s\\&+\int_0^t\Big(\frac{\hat{c}'_\beta}{2}\|\boldsymbol{\eta}_{\boldsymbol{u}}\|_H^2+\frac{\hat{c}'_\beta}{2}\|\dot{\boldsymbol{\eta}}_{\boldsymbol{u}}\|_H^2+2C_3\|\dot{\boldsymbol{\epsilon}}_{\boldsymbol{u}}\|_H^2+2\|\dot{\boldsymbol{\eta}}_{\boldsymbol{u}}\|_H^2+C_2\|\dot{\boldsymbol{\epsilon}}_{\boldsymbol{q}}\|^2_{\hat{\mathcal{E}}_h}+\big\|\boldsymbol{\eta}_{\boldsymbol{q}}\big\|^2_{\hat{\mathcal{E}}_h}\Big)\,\mathrm{d}s.\end{aligned}\tag{5.105}$$

Reorganizing (5.105) yields

$$\begin{aligned}
&\big(1-\frac{\delta}{2}\big)\|\dot{\boldsymbol{\eta}}_{\boldsymbol{u}}\|_H^2+\big(\hat{c}'-\delta\big)\big\|\boldsymbol{\eta}_{\boldsymbol{q}}\big\|_{\hat{\mathcal{E}}_h}^2-\frac{\delta C_1}{4\pi G}\|\boldsymbol{\eta}_{\boldsymbol{u}}\|_H^2+\frac{1}{4\pi G}\big(\frac{\vartheta}{8}-\frac{2}{\delta}\big)\|\boldsymbol{\eta}_{\Phi}\|_{L^2(\Sigma_{\mathcal{B}}^{\mathrm{e}})}^2\\
&\quad\le\int_0^t\Big(\big(\frac{C_1}{4\pi G}+\frac{\hat{c}_\beta'}{2}+2\big)\|\dot{\boldsymbol{\eta}}_{\boldsymbol{u}}\|_H^2+\frac{(\vartheta+16)}{32\pi G}\|\boldsymbol{\eta}_{\Phi}\|_{L^2(\Sigma_{\mathcal{B}}^{\mathrm{e}})}^2+\frac{\hat{c}_\beta'}{2}\|\boldsymbol{\eta}_{\boldsymbol{u}}\|_H^2+\big\|\boldsymbol{\eta}_{\boldsymbol{q}}\big\|_{\hat{\mathcal{E}}_h}^2\Big)\,\mathrm{d}s\\
&\qquad+\frac{1}{2\delta}\|\dot{\boldsymbol{\epsilon}}_{\boldsymbol{u}}\|_H^2+\frac{C_2}{\delta}\|\boldsymbol{\epsilon}_{\boldsymbol{q}}\|_{\hat{\mathcal{E}}_h}^2+\frac{1}{4\pi G}\Big(\frac{\vartheta}{8}\|\boldsymbol{\epsilon}_{\Phi}\|_{L^2(\Sigma_{\mathcal{B}}^{\mathrm{e}})}^2+\delta C_1\|\boldsymbol{\epsilon}_{\boldsymbol{u}}\|_H^2\Big)\\
&\qquad+\int_0^t\Big(\frac{\vartheta}{32\pi G}\|\dot{\boldsymbol{\epsilon}}_{\Phi}\|_{L^2(\Sigma_{\mathcal{B}}^{\mathrm{e}})}^2+\frac{C_1}{4\pi G}\|\dot{\boldsymbol{\epsilon}}_{\boldsymbol{u}}\|_H^2+C_2\|\dot{\boldsymbol{\epsilon}}_{\boldsymbol{q}}\|_{\hat{\mathcal{E}}_h}^2+2C_3\|\dot{\boldsymbol{\epsilon}}_{\boldsymbol{u}}\|_H^2\Big)\,\mathrm{d}s.
\end{aligned}\tag{5.106}$$

Remark that

$$\|\boldsymbol{u}_h\|_H^2\le\|\boldsymbol{u}_h\|_H^2+\big\|\Phi_h^1\big\|_{L^2(\Sigma_{\mathcal{B}}^{\mathrm{e}})}^2\le C\|\boldsymbol{q}_h\|_{\hat{\mathcal{E}}_h}^2,\quad\text{for } \boldsymbol{q}_h=(\boldsymbol{u}_h,\boldsymbol{E}_h,P_h,\Phi_h^1)^{\mathrm{T}}$$

with some constant $C>0$. Therefore by choosing sufficiently small δ and correspondingly sufficiently large ϑ, (5.106) yields

$$c_1\left\|\begin{pmatrix}\dot{\boldsymbol{\eta}}_{\boldsymbol{u}}\\ \boldsymbol{\eta}_{\boldsymbol{q}}\end{pmatrix}\right\|_{\mathcal{H}_h}^2\le c_2\int_0^t\left\|\begin{pmatrix}\dot{\boldsymbol{\eta}}_{\boldsymbol{u}}\\ \boldsymbol{\eta}_{\boldsymbol{q}}\end{pmatrix}\right\|_{\mathcal{H}_h}^2\mathrm{d}s+c_3\Big(\|\dot{\boldsymbol{\epsilon}}_{\boldsymbol{u}}\|_H^2+\|\boldsymbol{\epsilon}_{\boldsymbol{q}}\|_{\hat{\mathcal{E}}_h}^2+\int_0^t\|\dot{\boldsymbol{\epsilon}}_{\boldsymbol{q}}\|_{\hat{\mathcal{E}}_h}^2\,\mathrm{d}s\Big).\tag{5.107}$$

The error estimate is then obtained by applying a modified *Gronwall's lemma* [169] as

$$\left\|\begin{pmatrix}\dot{\boldsymbol{\eta}}_{\boldsymbol{u}}\\ \boldsymbol{\eta}_{\boldsymbol{q}}\end{pmatrix}\right\|_{\mathcal{H}_h}^2\le C\int_0^t\Big(\|\dot{\boldsymbol{\epsilon}}_{\boldsymbol{u}}\|_H^2+\|\boldsymbol{\epsilon}_{\boldsymbol{q}}\|_{\hat{\mathcal{E}}_h}^2+\|\dot{\boldsymbol{\epsilon}}_{\boldsymbol{q}}\|_{\hat{\mathcal{E}}_h}^2\Big)\,\mathrm{d}s.\tag{5.108}$$

5.6 The iterative coupling method for the overall system

Here we describe the numerical implementation of Problem 5.5. To simplify the discussion, we use backward Euler scheme to discretize the time, which can be easily extened to higher-ordered numerical algorithms such as implicit-explicit Runge-Kutta (IMEXRK) method [125].

5.6.1 Time discretization and the iterative coupling scheme

We introduce the notation $\boldsymbol{v}_h := \dot{\boldsymbol{u}}_h$ that denotes the particle velocity, and remark that $\begin{pmatrix} \boldsymbol{v}_h \\ \boldsymbol{q}_h \end{pmatrix} \in \mathcal{H}_h$, with $\mathcal{H}_h$ defined in (5.96). We discretize the time interval $[0, T]$ uniformly by $\delta t = \frac{T}{N_T}$, with $t_n = n\delta t$. We use the superscript notation $v^{(n)}$ to indicate a time dependent variable v corresponding to t_n. We apply the backward Euler scheme along with an iterative coupling method within each time step (see also [178]), for iterations $k = 1, 2, \cdots$, with the notation $v^{(n,k)}$ standing for the k^{th} iteration of the time dependent variable v corresponding to t_n. We then rewrite the overall Problem 5.5 as follows.

Problem 5.6
Given $\begin{pmatrix} \boldsymbol{v}_h^{(n-1)} \\ \boldsymbol{q}_h^{(n-1)} \end{pmatrix}, \begin{pmatrix} \boldsymbol{v}_h^{(n,k-1)} \\ \boldsymbol{q}_h^{(n,k-1)} \end{pmatrix} \in \mathcal{H}_h$, *and* $\boldsymbol{f}_h^{(n)} \in H$, *find* $\begin{pmatrix} \boldsymbol{v}_h^{(n,k)} \\ \boldsymbol{q}_h^{(n,k)} \end{pmatrix} \in \mathcal{H}_h$, *such that*

$$\begin{aligned}
&\frac{1}{\delta t}\int_{\Omega^{\mathrm{e}}} \rho^0 \boldsymbol{v}_h^{(n,k)} \cdot \boldsymbol{w}_h \,\mathrm{d}\Omega + \int_{\Omega^{\mathrm{e}}} 2\rho^0 (\boldsymbol{\Omega} \times \boldsymbol{v}_h^{(n,k)}) \cdot \boldsymbol{w}_h \,\mathrm{d}\Omega + \hat{b}_h^{\mathrm{IM}}\big(\, \boldsymbol{q}_h^{(n,k)}, \boldsymbol{p}_h \,\big) \\
&\qquad + \hat{b}_h^{\mathrm{EX}}\big(\, \boldsymbol{q}_h^{(n,k-1)}, \boldsymbol{p}_h \,\big) - \frac{1}{4\pi G}\int_{\Sigma^{\mathrm{e}}_{\mathcal{B}}} \mathfrak{F}(\boldsymbol{u}_h^{(n,k-1)})\, \varphi_h \,\mathrm{d}\Sigma \\
&\quad = \frac{1}{\delta t}\int_{\Omega^{\mathrm{e}}} \rho^0 \boldsymbol{v}_h^{(n-1)} \cdot \boldsymbol{w}_h \,\mathrm{d}\Omega + \int_{\Omega^{\mathrm{e}}} \rho^0 \boldsymbol{f}_h^{(n)} \cdot \boldsymbol{w}_h \,\mathrm{d}\Omega,
\end{aligned} \tag{5.109}$$

$$\boldsymbol{u}^{(n,k)} = \delta t\, \boldsymbol{v}^{(n,k)} + \boldsymbol{u}^{(n-1)}, \tag{5.110}$$

for any $\begin{pmatrix} \boldsymbol{w}_h \\ \boldsymbol{p}_h \end{pmatrix} \in \mathcal{H}_h$, *with* $\boldsymbol{p}_h = \big(\boldsymbol{w}_h, \boldsymbol{H}_h, Q_h, \varphi_h\big)^{\mathrm{T}}$, *where*

$$\begin{aligned}
\hat{b}_h^{\mathrm{IM}}\big(\boldsymbol{q}_h, \boldsymbol{p}_h\big) :=\ & a_h(\boldsymbol{u}_h, \boldsymbol{w}_h) + \frac{1}{4\pi G}\int_{\Omega^{\mathrm{e}}} (\nabla \varPhi_h^1)\cdot(\nabla\varphi_h)\,\mathrm{d}\Omega \\
& + \int_{\Omega^{\mathrm{e}}_{\tilde{X}}} \rho^0 (\nabla \varPhi_h^1)\cdot \boldsymbol{w}_h\,\mathrm{d}\Omega + \int_{\Omega^{\mathrm{e}}_{\tilde{X}}} (\rho^0 \boldsymbol{u}_h)\cdot(\nabla\varphi_h)\,\mathrm{d}\Omega + \frac{\vartheta}{4\pi G}\int_{\Sigma^{\mathrm{e}}_{\mathcal{B}}} \varPhi_h^1\,\varphi_h\,\mathrm{d}\Sigma \\
& + \kappa\int_{\Omega^{\mathrm{e}}_{\mathrm{S}}} (\boldsymbol{E}_h - \nabla\boldsymbol{u}_h) : (\boldsymbol{\Gamma} : \boldsymbol{H}_h)\,\mathrm{d}\Omega + \kappa\int_{\Omega^{\mathrm{e}}_{\mathrm{F}}} \big(P_h - \lambda_h(\nabla\cdot\boldsymbol{u}_h)\big)\,Q_h\,\mathrm{d}\Omega \\
& - \int_{\Sigma^{\mathrm{e}}_{\mathrm{FS}}} \mathfrak{S}\Big\{\rho^{0\,-}(\boldsymbol{u}_h^{+}\cdot\boldsymbol{g}_0')\,[\![\boldsymbol{w}_h\cdot\boldsymbol{\nu}]\!]\Big\}\,\mathrm{d}\Sigma,
\end{aligned} \tag{5.111}$$

and

$$\begin{aligned}
\hat{b}_h^{\mathrm{EX}}\big(\boldsymbol{q}_h, \boldsymbol{p}_h\big) :=\ & \frac{\alpha_h'}{4\pi G}\int_{\Sigma^{\mathrm{e}}} [\![\varPhi_h^1]\!]\,[\![\varphi_h]\!]\,\mathrm{d}\Sigma + \int_{\Omega^{\mathrm{e}}_{\mathrm{S}}} (\boldsymbol{\Gamma} : \boldsymbol{E}_h) : \big(\boldsymbol{r}^{\mathrm{e}}_{\mathrm{SS}}(\boldsymbol{w}_h) + \boldsymbol{r}^{\mathrm{e}}_{\mathrm{SF}}(\boldsymbol{w}_h)\big)\,\mathrm{d}\Omega \\
& - \int_{\Omega^{\mathrm{e}}_{\mathrm{S}}} \big(\boldsymbol{r}^{\mathrm{e}}_{\mathrm{SS}}(\boldsymbol{u}_h) + \boldsymbol{r}^{\mathrm{e}}_{\mathrm{SF}}(\boldsymbol{u}_h)\big) : \Big(\boldsymbol{\Gamma} : \big(\kappa\boldsymbol{H}_h - \nabla\boldsymbol{w}_h\big) - \tfrac{1}{2}\big(\boldsymbol{\tau}^0\cdot\nabla\boldsymbol{w}_h - \nabla\boldsymbol{w}_h\cdot\boldsymbol{\tau}^0\big)\Big)\,\mathrm{d}\Omega \\
& - \int_{\Omega^{\mathrm{e}}_{\mathrm{F}}} \big(r^{\mathrm{e}}_{\mathrm{FS}}(\boldsymbol{u}_h) + r^{\mathrm{e}}_{\mathrm{FF}}(\boldsymbol{u}_h)\big)\,\lambda(\kappa Q_h - \nabla\cdot\boldsymbol{w}_h)\,\mathrm{d}\Omega + \int_{\Omega^{\mathrm{e}}_{\mathrm{F}}} P_h\,\big(r^{\mathrm{e}}_{\mathrm{FS}}(\boldsymbol{w}_h) + r^{\mathrm{e}}_{\mathrm{FF}}(\boldsymbol{w}_h)\big)\,\mathrm{d}\Omega \\
& + \alpha\int_{\Sigma^{\mathrm{e}}_{\mathrm{SS}}} [\![\boldsymbol{u}_h]\!] : [\![\boldsymbol{w}_h]\!]\,\mathrm{d}\Omega + \alpha\int_{\Sigma^{\mathrm{e}}_{\mathrm{FF}}} [\![\boldsymbol{\nu}\cdot\boldsymbol{u}_h]\!]\,[\![\boldsymbol{\nu}\cdot\boldsymbol{w}_h]\!]\,\mathrm{d}\Omega \\
& + \alpha\int_{\Sigma^{\mathrm{e}}_{\mathrm{FS}}} [\![\boldsymbol{\nu}\cdot\boldsymbol{u}_h]\!]\,[\![\boldsymbol{\nu}\cdot\boldsymbol{w}_h]\!]\,\mathrm{d}\Omega,
\end{aligned} \tag{5.112}$$

with $\boldsymbol{q}_h = \big(\boldsymbol{u}_h, \boldsymbol{E}_h, P_h, \varPhi_h^1\big)^{\mathrm{T}}$.

At the beginning of each time step, the unknowns are assigned with the value of the previous step, that is, $\boldsymbol{v}_h^{(n,0)} = \boldsymbol{v}_h^{(n-1)}$ and $\boldsymbol{q}_h^{(n,0)} = \boldsymbol{q}_h^{(n-1)}$. The stop criterion of the iteration is that no significant updates are applied to the solution. For example, at k^{th} iteration, with

$$\left\| \begin{pmatrix} \boldsymbol{v}_h^{(n,k)} \\ \boldsymbol{q}_h^{(n,k)} \end{pmatrix} - \begin{pmatrix} \boldsymbol{v}_h^{(n,k-1)} \\ \boldsymbol{q}_h^{(n,k-1)} \end{pmatrix} \right\|^2_{\mathcal{H}_h} \leq \varepsilon, \tag{5.113}$$

for ε some small constant, the final solution of current time step is assigned by $\boldsymbol{v}_h^{(n)} = \boldsymbol{v}_h^{(n,k)}$ and $\boldsymbol{q}_h^{(n)} = \boldsymbol{q}_h^{(n,k)}$. The stability of iterative coupling can be obtained by following the same procedure in [178, section 5], in which the contraction of iteration can be obtained with sufficiently small time step δt.

5.6.2 The matrix formulation of the coupled problem

To compute $\mathfrak{f}_h := \mathfrak{F}(\boldsymbol{u}_h)$ as defined in (5.88f), we expand $\boldsymbol{\Upsilon}_1(\boldsymbol{y};\boldsymbol{x})$ and $\Upsilon_2(\boldsymbol{y};\boldsymbol{x})$ with regard to the first position variable $\boldsymbol{y}$ by a set of 3-D Lagrange basis $\left\{\ell_i^{\mathrm{e}}\right\}_{i=1}^{N_p}$ in each $\Omega_{\tilde{X}}^{\mathrm{e}} \in \left\{\Omega_{\mathrm{S}}^{\mathrm{e}}, \Omega_{\mathrm{F}}^{\mathrm{e}}\right\}$, and by a set of 2-D Lagrange basis $\left\{\tilde{\ell}_i^{\mathrm{e}}\right\}_{i=1}^{\tilde{N}_p}$ in each $\Sigma^{\mathrm{e}} \in \left\{\Sigma_{\mathrm{SS}}^{\mathrm{e}}, \Sigma_{\mathrm{FF}}^{\mathrm{e}}, \Sigma_{\mathrm{FS}}^{\mathrm{e}}, \Sigma_{\mathrm{b}}^{\mathrm{e}}\right\}$, that is

$$\boldsymbol{\Upsilon}_{1\,h}(\boldsymbol{y};\boldsymbol{x})\big|_{\boldsymbol{y}\in\Omega_{\tilde{X}}^{\mathrm{e}}} \approx \sum_{i=1}^{N_p} \hat{\boldsymbol{\Upsilon}}^{\mathrm{e}}_{1\,i}(\boldsymbol{x})\ell_i^{\mathrm{e}}(\boldsymbol{y}), \quad \hat{\boldsymbol{\Upsilon}}^{\mathrm{e}}_{1\,i}(\boldsymbol{x}) := \boldsymbol{\Upsilon}_1(\boldsymbol{y}_i^{\mathrm{e}};\boldsymbol{x}),$$

$$\boldsymbol{y}_i^{\mathrm{e}}: \text{ the } i^{\text{th}} \text{ nodal point of } \Omega_{\tilde{X}}^{\mathrm{e}};$$

$$\Upsilon_{2\,h}(\boldsymbol{y};\boldsymbol{x})\big|_{\boldsymbol{y}\in\Sigma^{\mathrm{e}}} \approx \sum_{i=1}^{\tilde{N}_p} \tilde{\Upsilon}^{\mathrm{e}}_{2\,i}(\boldsymbol{x})\tilde{\ell}_i^{\mathrm{e}}(\boldsymbol{y}), \quad \tilde{\Upsilon}^{\mathrm{e}}_{2\,i}(\boldsymbol{x}) := \Upsilon_2(\tilde{\boldsymbol{y}}_i^{\mathrm{e}};\boldsymbol{x}),$$

$$\tilde{\boldsymbol{y}}_i^{\mathrm{e}}: \text{ the } i^{\text{th}} \text{ nodal point of } \Sigma^{\mathrm{e}}.$$

We also write the polynomial expansion of $\rho^0\boldsymbol{u}_h$ in each $\Omega_{\tilde{X}}^{\mathrm{e}}$ and Σ^{e} as

$$\rho^0(\boldsymbol{y})\boldsymbol{u}_h(\boldsymbol{y})\big|_{\boldsymbol{y}\in\Omega_{\tilde{X}}^{\mathrm{e}}} \approx \sum_{i=1}^{N_p} \hat{\rho}_i^{0\,\mathrm{e}}\hat{\boldsymbol{u}}_i^{\mathrm{e}}\ell_i^{\mathrm{e}}(\boldsymbol{y}), \quad \hat{\rho}_i^{0\,\mathrm{e}} := \rho^0(\boldsymbol{y}_i^{\mathrm{e}}), \quad \hat{\boldsymbol{u}}_i^{\mathrm{e}} := \boldsymbol{u}(\boldsymbol{y}_i^{\mathrm{e}});$$

$$\rho^0(\boldsymbol{y})\boldsymbol{u}_h(\boldsymbol{y})\big|_{\boldsymbol{y}\in\Sigma^{\mathrm{e}}} \approx \sum_{i=1}^{\tilde{N}_p} \tilde{\rho}_i^{0\,\mathrm{e}}\tilde{\boldsymbol{u}}_i^{\mathrm{e}}\tilde{\ell}_i^{\mathrm{e}}(\boldsymbol{y}), \quad \tilde{\rho}_i^{0\,\mathrm{e}} := \rho^0(\tilde{\boldsymbol{y}}_i^{\mathrm{e}}), \quad \tilde{\boldsymbol{u}}_i^{\mathrm{e}} := \boldsymbol{u}(\tilde{\boldsymbol{y}}_i^{\mathrm{e}}).$$

We can therefore write $\mathfrak{f}_h = \mathfrak{F}(\boldsymbol{u}_h)$ in nodal expansion as $\mathfrak{f}_h(\boldsymbol{x})\big|_{\boldsymbol{x}\in\Sigma_{\mathcal{B}}^{\mathrm{e}}} = \sum_{i=1}^{N_p} \hat{\mathfrak{f}}_i^{\mathrm{e}}\tilde{\ell}_i^{\mathrm{e}}(\boldsymbol{x})$, with

$$\hat{\mathfrak{f}}_i^{\mathrm{e}} = \sum_{\Omega_{\tilde{X}}^{\mathrm{e}}} \sum_{j,m=1}^{N_p} M_{jm}^{\mathrm{e}}\hat{\rho}_j^{0\,\mathrm{e}}\left(\hat{\boldsymbol{u}}_j^{\mathrm{e}} \cdot \hat{\boldsymbol{\Upsilon}}^{\mathrm{e}}_{1\,m}(\boldsymbol{x}_i^{\mathrm{e}})\right) + \sum_{\Sigma^{\mathrm{e}}} \sum_{j,m=1}^{\tilde{N}_p} \tilde{M}_{jm}^{\mathrm{e}}[\![\tilde{\rho}_j^{0\,\mathrm{e}}]\!]\{\{\boldsymbol{\nu}\cdot\tilde{\boldsymbol{u}}_j^{\mathrm{e}}\}\}\,\tilde{\Upsilon}^{\mathrm{e}}_{2\,m}(\tilde{\boldsymbol{x}}_i^{\mathrm{e}}), \tag{5.114}$$

where $M^{\mathrm{e}}_{ij} := \int_{\Omega^{\mathrm{e}}_{\tilde{X}}} \ell^{\mathrm{e}}_i \ell^{\mathrm{e}}_j \,\mathrm{d}\Omega$ and $\tilde{M}^{\mathrm{e}}_{ij} := \int_{\Sigma^{\mathrm{e}}} \tilde{\ell}^{\mathrm{e}}_i \tilde{\ell}^{\mathrm{e}}_j \,\mathrm{d}\Sigma$ are volume and surface mass matrices.

We consider the array of unknown

$$\mathsf{q} := \big(\boldsymbol{v}_h, \boldsymbol{q}_h, \mathfrak{f}_h \big)^{\mathrm{T}},$$

and therefore rewrite (5.109) in matrix form,

$$\mathcal{A}\mathsf{q}^{(n,k)} = \mathcal{B}\mathsf{q}^{(n,k-1)} + \mathcal{C}\mathsf{q}^{(n-1)} + \mathcal{F}, \tag{5.115}$$

with

$$\mathcal{A} = \begin{pmatrix} A_{11} & A_{12} & A_{13} \\ A_{21} & A_{22} & 0 \\ 0 & 0 & A_{33} \end{pmatrix} \tag{5.116}$$

$$\mathcal{B} = \begin{pmatrix} B_{11} & B_{12} & 0 \\ B_{21} & B_{22} & 0 \\ B_{31} & 0 & 0 \end{pmatrix} \tag{5.117}$$

$$\mathcal{C} = \begin{pmatrix} C_{11} & 0 & 0 \\ 0 & C_{22} & 0 \\ 0 & 0 & 0 \end{pmatrix} \tag{5.118}$$

$$\mathcal{F} = \big(\boldsymbol{f}_h, 0, 0\big)^{\mathrm{T}}. \tag{5.119}$$

In the above, A_{ij} and C_{ij} are block diagonal matrices, $B_{11}, B_{12}, B_{21}, B_{22}$ are sparse matrices, and B_{31} is a low-rank dense matrix. One can use the structured matrices techniques (*e.g.*, HSS matrices [173, 174]) to compress B_{31}, and yield $N^{\partial\mathcal{B}}_{\mathrm{dof}}\,\mathcal{O}\big(\log(N^{\tilde{X}}_{\mathrm{dof}})\big)$ computation and storage costs, with $N^{\partial\mathcal{B}}_{\mathrm{dof}}$ the degree of freedom on $\partial\mathcal{B}$, and $N^{\tilde{X}}_{\mathrm{dof}}$ the degree of freedom in $\tilde{X}$.

We write the procedure of solving Problem 5.6 in Figure 5.6.2.

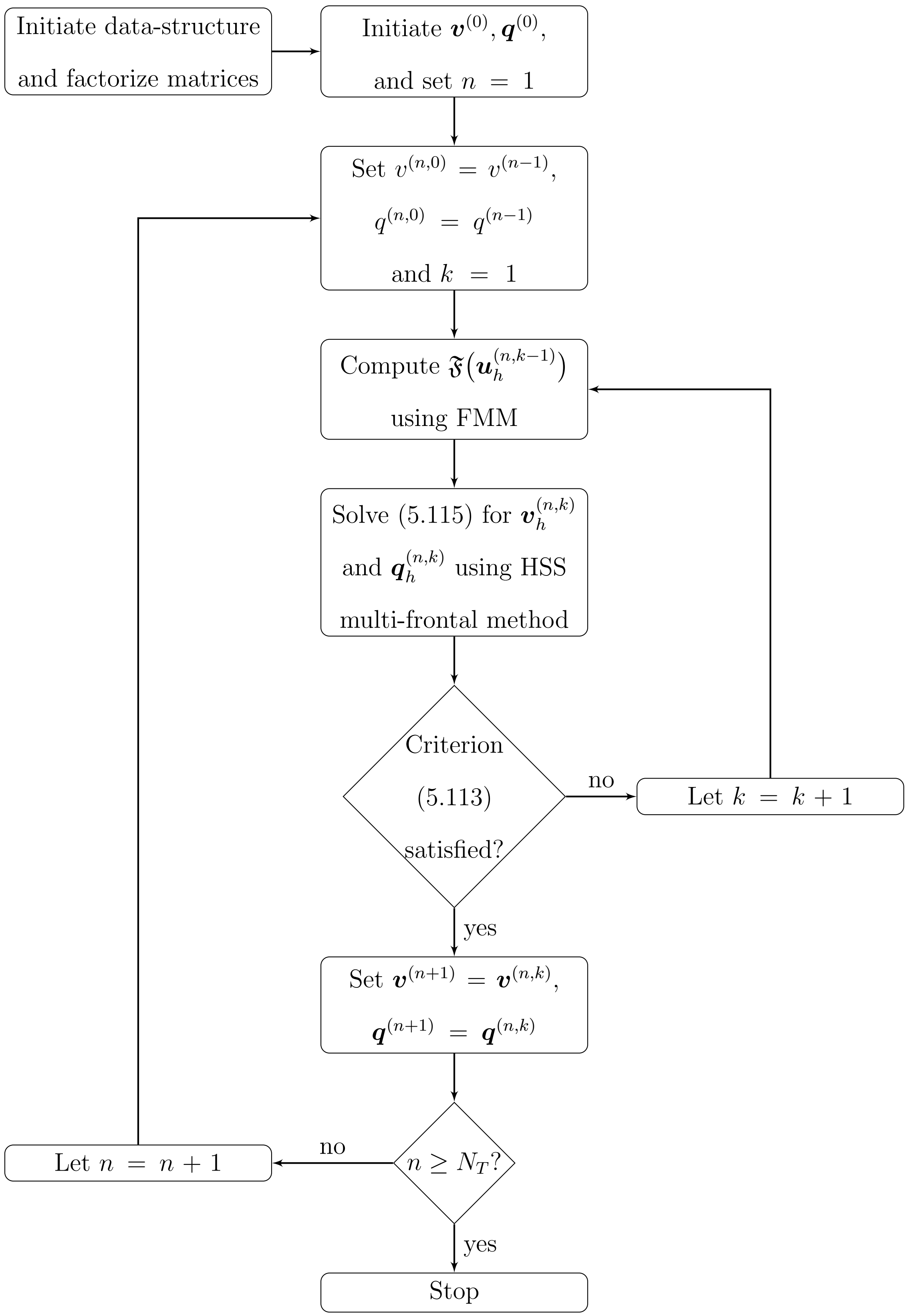

Figure 5.6.2 : Procedure of solving Problem 5.6.

5.7 Conclusion

Based on the analysis of the linear equations of motion for a uniformly rotating, elastic and self-gravitating earth model, we present the weak formulation that is well-posed, and ready for numerical implementation. We repeat the proof for the coercivity of the coupled system, allow it in an alternative space where boundary conditions are not enfored on test functions. We introduce penalty terms for boundary jumps in the bilinear form as a precurser to the implementation of the DG method, and ensure that the coercivity property gets preserved. We apply the DG method together with the iterative coupling scheme, which allows us to compute the wave motion and the perturbation of the geophysical potential separately using distinct numerical techniques such as the structured matrix factorization dealing with low-rank Poisson matrices.

Chapter 6

Deforming a tetrahedral mesh constrainted by shape optimization of interior polyhedral boundaries with physics-based regularization

6.1 Introduction

We consider the recovery of an unstructured tetrahedral mesh using vertices as the data. We develop an iterative reconstruction method derived from Hausdorff warping. This problem is motivated by a recent result in the analysis of inverse boundary problems for the Helmholtz equation. Let the wavespeed be piecewise constant on an unknown (unstructured) tetrahedral mesh with the values of the wavespeeds belonging to a known finite set. Then the tetrahedral mesh can be stably recovered from the Dirichlet-to-Neumann map as the data [12]. Our primary application is full-waveform inversion (FWI) in exploration and global seismology, representing the material properties of Earth's interior, partitioned into a tetrahedral mesh, by piecewise constant parameters. The key contribution of this chapter is the development of an automated framework of techniques ensuring that, in the mesh updating the conditions on the mesh for the above mentioned result to hold remain satisfied, and of procedures for local multi-scale refinement. The techniques are adapted from ones used in computer vision. Following a multi-level approach, the meshes enable sparse model representations, that is, effective hierarchical compression, which is an important component in enlarging the radii of convergence of multi-level iterative schemes [50].

Hale [71] introduced atomic meshing for reservoir modelling constrained by seismic images. Kononov *et al.* [97] presented a 3D mesh generator designed for seismic problems. Rueger and Hale [142] considered meshing of wavespeed models specifically for the purpose of seismic ray tracing. For sparse representations on tetrahedral meshes using wavelets, see the work of Dahmen and Stevenson [42]. The approach of updating a domain partition in FWI was introduced by Shin [152]. Hinz and Bradford [76] used an adaptive mesh in Ground-Penetrating-Radar reflection attenuation tomography. Unstructured meshing has also been developed in the GOCAD research group; for recent results and applications in remote sensing, see Caumon and Collon-Drouaillet [25]. Unstructured meshes adapt well to geotectonic features such as fault planes, salt domes but also sedimentary layering are naturally captured as interior boundaries, and their shapes are optimized in the process of mesh recovery. In earlier work [70], we introduced a comprehensive segmentation procedure to obtain triangulated interior boundaries from a seismic image (or data misfit gradient) which were then used to generate a consistent unstructured tetrahedral mesh. This procedure can guide us to obtain an initial mesh.

Techniques of mesh deformation appear widely in CFD problems, where interfaces are driven by the physical laws of fluid dynamics (see, for example, Cristini *et al.* [37]), and in biomedical imaging, where the surface shape is governed by cortical surface data obtained from magnetic resonance imaging (as in Dassi *et al.* [44]). For surface mesh deformation and quality control, we refer to the generalized Lagrangian gradient flows on discretized surfaces developed by Eckstein *et al.* [57], which depend on the choice of functional with multiple options of inner-product spaces. We also mention surface meshing techniques, such as Delaunay triangulation, surface mesh simplification [62, 78, 77, 119, 85, 44] and topology optimization [3].

Variational approaches, to which our procedure belongs, include constrained Delaunay tetrahedralization [151], and advancing front methods [147]. The Delaunay method reveals hidden deficiencies in tetrahedral meshes by generating flat sliver tetrahedral elements with squeezed volumes [150]. A sliver removal technique can be found in [33]. The advancing front methods conform with interfaces, but generate tetrahedra with quality depending on the shape [113]. Also, these methods face challenges when a near-contact surface mesh appears, which occurs frequently in our application. Furthermore, we mention the body-centered cubic meshing technique based on level sets [159] as a candidate remeshing tool, with desired quality control and boundary matching.

We study problems in which a target mesh, which we view as the "true" domain partition, is given. This domain partition is typically sufficiently fine to capture the structure of Earth's subsurface. The shapes of the unstructured meshes are governed by the relevant vertices, which are regarded as the "data" in the recovery. We start the iterative reconstruction with an initial mesh. This mesh can be quite dissimilar from the target mesh, and is not required to have either the same number of vertices, or a similar number of facets. The initial mesh is typically coarse. The misfit or energy functional is derived from an approximation of the Hausdorff distance [31]. Indeed, the Hausdorff distance appears in the Lipschitz stability estimate for the inverse boundary value problem mentioned above. We incorporate a multi-level approach with local refinement facilitating a gradual growth of the number of tetrahedra. A direct deformation for updating typically leads to the (unpredictable) generation of ill-conditioned elements and hidden deficiencies such as an artificial change in topology. To mitigate these complications, we constrain our mesh updating by updating a set of interior boundaries. We invoke the following techniques: the non-uniform mesh refinement, the local mesh coarsening, the mesh warping, and the level set method. The surrounding mesh deformation is then regularized based on elastic deformation. Thus we preserve the mesh quality and above mentioned conditions.

The outline of this chapter is as follows. In Section 2, we introduce unstructured tetrahedral meshes and polyhedral interior boundaries and state our key assumptions which are essentially related to quality control. In Section 3 we introduce the pseudo-Hausdorff distance, the energy functional and its Gateaux derivative. In Section 4 we introduce the constraining interior boundary shape optimization. We discuss the multi-level, multi-scale refinement and the simplification approach for local element modification in Section 5. The key components of our algorithm are given in Section 6, namely the optimization of mesh quality metrics. We present computational experiments in Section 7.

6.2 Unstructured tetrahedral mesh with interior polyhedral boundaries

We consider a bounded domain Ω segmented and partitioned into subdomains $\{\hat{\Omega}_i\}$, which are connected sets of tetrahedra: $\hat{\Omega}_i = \bigcup_{j=1}^{N_{\mathcal{T}}^{\hat{\Omega}}} \mathcal{T}_j$, where $\mathcal{T}$ denotes a tetrahedron. We also define the following notation: τ as a triangular facet or surface element, $\mathcal{E}$ as an edge and $\mathcal{V}$ as a vertex (or its location). To ensure proper behaviors during deformation, we make the following assumptions for a valid regular tetrahedral mesh:

- the boundary for each subdomain $\partial\hat{\Omega}_i$ is a triangulated two-dimensional manifold;
- no tetrahedron may have all four vertices on the boundary; and
- no interior edge may connect two boundary nodes.

Any two distinct tetrahedra in a regular volume mesh have one of four possible types of relations. They are either isolated, or share a common vertex, a common edge or a common facet. We distinguish the last relation as neighbouring (or adjacent) tetrahedra.

We also denote the interior boundaries $\{\hat{\Gamma}_i\}$, each is a manifold containing all triangle facets that belong to two distinct subdomains as $\hat{\Gamma}_i := \bigcup_{j=1}^{N_\tau^{\hat{\Gamma}}} \tau_j$. In other words, an interior interface is the intersection of two adjacent subdomains $\hat{\Omega}_{i_1}$ and $\hat{\Omega}_{i_2}$, that is $\hat{\Gamma}_i = \hat{\Omega}_{i_1} \cap \hat{\Omega}_{i_2}$. For each triangle $\tau_j \in \hat{\Gamma}_i$, there exists exactly one pair of tetrahedra $\mathcal{T}_{j_1} \in \hat{\Omega}_{i_1}$ and $\mathcal{T}_{j_2} \in \hat{\Omega}_{i_2}$ such that $\tau_j = \mathcal{T}_{j_1} \cap \mathcal{T}_{j_2}$. Three types of relations exist for two distinct triangles in each $\hat{\Gamma}_i$: they are either isolated, or share a common vertex or a common edge. In the last case, we will say the triangles are neighbouring (or adjacent). We also say an edge is adjacent to a tetrahedron or a triangle if it is one of its edges. To ensure a properly behaved surface, we propose the self-nonintersecting assumptions:

- no triangles may intersect with each other in all boundaries $\{\hat{\Gamma}_i\}$; and
- no edge may be adjacent to more than two triangles in each boundary surface $\hat{\Gamma}_i$.

Based on these assumptions, we immediately obtain the relationship between the total number of triangles ($N_\tau^{\hat{\Gamma}_i}$), the total number of edges ($N_{\mathcal{E}}^{\hat{\Gamma}_i}$) and the number of boundary edges ($N_{\tilde{\mathcal{E}}}^{\hat{\Gamma}_i}$, which can be zero if $\hat{\Gamma}_i$ is closed), as

$$3N_\tau^{\hat{\Gamma}_i} = 2N_{\mathcal{E}}^{\hat{\Gamma}_i} - N_{\tilde{\mathcal{E}}}^{\hat{\Gamma}_i}. \tag{6.1}$$

Violating this relation indicates that topological changes occur to $\hat{\Gamma}_i$ during mesh evolution. We consider the inverse problem of recovery of a tetrahedral mesh with the vertices of the true mesh as the "data". Our reconstruction scheme is derived from Hausdorff warping. We begin with introducing an unstructured tetrahedral mesh $\hat{\Omega} = \bigcup_i \hat{\Omega}_i$ with interior boundaries $\hat{\Gamma} = \bigcup_i \hat{\Gamma}_i$. We denote the set of vertices contained in $\hat{\Omega}$ as $\{\mathcal{V}_j\}_{j=1}^{N_{\mathcal{V}}^{\hat{\Omega}}}$. We describe the mesh deformation, that is, evolution in the iterative reconstruction by the motion of vertices. This motion is represented by a piecewise linear vector field, that is, $\boldsymbol{x} + t\hat{\boldsymbol{v}}(\boldsymbol{x})$. Such a vector field is defined by

$$\hat{\boldsymbol{v}}(\boldsymbol{x}) = \sum_j \boldsymbol{v}_j \phi_j(\boldsymbol{x})$$

with linear interpolating basis functions ϕ_j satisfying $\sum_j \phi_j(\boldsymbol{x}) = 1$. Thus

$$\hat{\boldsymbol{v}}(\mathcal{V}_j) = \boldsymbol{v}_j$$

and the motion at each vertex, $\mathcal{V}_j$, is given by $\mathcal{V}_j + t\boldsymbol{v}_j$, $j = 1, 2, \cdots, N_{\mathcal{V}}^{\hat{\Omega}}$. We write $V = \{\boldsymbol{v}_j\}_{j=1}^{N_{\mathcal{V}}^{\hat{\Omega}}}$. We obtain the inner product

$$(\hat{\boldsymbol{u}}, \hat{\boldsymbol{v}})_{\hat{\Omega}} = U^T M^{\hat{\Omega}} V,$$

where $M^{\hat{\Omega}}$ is the symmetric positive definite mass matrix

$$M_{jk}^{\hat{\Omega}} = I_{3\times 3} \int_{\hat{\Omega}} \phi_j(\boldsymbol{x}) \phi_k(\boldsymbol{x})\, \mathrm{d}\boldsymbol{x}, \quad j, k = 1, 2, \cdots, N_{\mathcal{V}}^{\hat{\Omega}}, \tag{6.2}$$

with $I_{3\times 3}$ the three-by-three identity matrix. Note that M is sparse, but not diagonal. A classical approximation, simplifying computations considerably with limited accuracy loss, is to use mass lumping which turns $M^{\hat{\Omega}}$ into a diagonal matrix $\hat{M}^{\hat{\Omega}}$, where $\hat{M}_{jj}^{\hat{\Omega}}$ is the volume of j^{th} Voronoi dual cell times $I_{3\times 3}$. We define the analogous deformation of polyhedral interior boundaries, with the vertices on each surface $\hat{\Gamma}$ as $\{\mathcal{V}_j\}_{j=1}^{N_{\mathcal{V}}^{\hat{\Gamma}}}$, and the corresponding lumped diagonal mass matrix denoted by $\hat{M}^{\hat{\Gamma}}$.

6.3 Energy functional derived from the Hausdorff distance

The energy functional to be minimized is a measure of dissimilarity between the evolving mesh and a target mesh. This measure is based on the Hausdorff distance. We use a differentiable approximation of the well-known Hausdorff distance, as proposed in Charpiat et al. (2005) [31].

6.3.1 Pseudo-Hausdorff distance and similarity measure

We consider a shape warping problem from a candidate tetrahedral mesh to a given target mesh. We define the distance function from a spatial point $\boldsymbol{x}$ to a subset (or shape) $\hat{\Omega}_i$ as

$$d_{\hat{\Omega}_i}(\boldsymbol{x}) = \inf_{\boldsymbol{y}\in\hat{\Omega}_i} |\boldsymbol{x}-\boldsymbol{y}| = \inf_{\boldsymbol{y}\in\hat{\Omega}_i} d(\boldsymbol{x},\boldsymbol{y}), \quad \hat{\Omega}_i \neq \emptyset \tag{6.3}$$

where $d(\boldsymbol{x},\boldsymbol{y})$ is the $l^2(\mathbb{R}^3)$ distance between two spatial locations $\boldsymbol{x}$ and $\boldsymbol{y}$. Concerning the distance functions, these are Lipschitz continuous with a Lipschitz constant equal to 1. Consequently, the distance functions are differentiable almost everywhere and the magnitudes of their gradients, when they exist, are less than or equal to 1.

If we assume that Ω_1, Ω_2 are contained in a bounded set D, we can introduce the similarity measure which is the $C(D)$ norm of the difference of distance functions,

$$\rho_D := \left\| d_{\hat{\Omega}_1} - d_{\hat{\Omega}_2} \right\|_{C(D)} = \sup_{\boldsymbol{x}\in D} |d_{\hat{\Omega}_1}(\boldsymbol{x}) - d_{\hat{\Omega}_2}(\boldsymbol{x})|. \tag{6.4}$$

This measure is defined on equivalence classes of sets. The corresponding topology is equivalent to the one induced by the standard Hausdorff metric. In Equation (6.4) one can replace the $C(D)$ norm by the $W^{1,2}(D)$ norm defining a complete metric structure, since the set of $C_d(D)$ distance functions is closed in $W^{1,2}(D)$.

We now consider the Hausdorff distance betweeen two meshes $\hat{\Omega}_1$ and $\hat{\Omega}_2$, which is given by Eckstein et al. (2007) [57]:

$$\rho_{\mathcal{H}}(\hat{\Omega}_1, \hat{\Omega}_2) = \max\left(\max_{\mathcal{V}_j \in \hat{\Omega}_1} \min_{\mathcal{V}_k \in \hat{\Omega}_2} \|\mathcal{V}_j - \mathcal{V}_k\|, \max_{\mathcal{V}_k \in \hat{\Omega}_2} \min_{\mathcal{V}_j \in \hat{\Omega}_1} \|\mathcal{V}_j - \mathcal{V}_k\| \right). \tag{6.5}$$

We introduce smooth approximations of the Hausdorff distance, between two meshes

$$\widetilde{\rho}_{\mathcal{H}}(\hat{\Omega}_1, \hat{\Omega}_2) = \left(\frac{1}{N_{\mathcal{V}}^{\hat{\Omega}_1}} \sum_{j=1}^{N_{\mathcal{V}}^{\hat{\Omega}_1}} \hat{M}_{jj}^{\hat{\Omega}_1} f_j^{-1} + \frac{1}{N_{\mathcal{V}}^{\hat{\Omega}_2}} \sum_{k=1}^{N_{\mathcal{V}}^{\hat{\Omega}_1}} \hat{M}_{kk}^{\hat{\Omega}_2} g_k^{-1} \right)^{\frac{1}{2\alpha}}. \tag{6.6}$$

In the above

$$\begin{aligned} f_j =& \frac{1}{N_{\mathcal{V}}^{\hat{\Omega}_2}} \sum_{k=1}^{N_{\mathcal{V}}^{\hat{\Omega}_2}} \hat{M}_{kk}^{\hat{\Omega}_2} (d(\mathcal{V}_j, \mathcal{V}_k)^2 + \epsilon^2)^{-\alpha}, \\ g_k =& \frac{1}{N_{\mathcal{V}}^{\hat{\Omega}_1}} \sum_{j=1}^{N_{\mathcal{V}}^{\hat{\Omega}_1}} \hat{M}_{jj}^{\hat{\Omega}_1} (d(\mathcal{V}_j, \mathcal{V}_k)^2 + \epsilon^2)^{-\alpha}, \end{aligned} \tag{6.7}$$

with $\epsilon > 0$ small. To prove that the above expression converges to the Hausdorff distance between the two meshes when the sampling of the two meshes increases and $\alpha \to \infty$, we can follow the continuous proof of Charpiat et al. (2005). Here, it is used that

$$\lim_{\alpha \to +\infty} \left(\frac{1}{N} \sum_{i=1}^{N} \xi_i^{\alpha} \right)^{\frac{1}{\alpha}} = \max_{i \le i \le N} \xi_i.$$

The energy functional regarding the target mesh $\hat{\Omega}_{\dagger}$ and evolving mesh $\hat{\Omega}$ is then chosen to be

$$\mathcal{E}(\hat{\Omega}) = \tfrac{1}{2} \widetilde{\rho}_{\mathcal{H}}(\hat{\Omega}, \hat{\Omega}^{\dagger})^2. \tag{6.8}$$

6.3.2 Gradient flow

In general, one models the space of admissible deformations as an inner product space $(F, \langle \cdot, \cdot \rangle)$. If there exists a deformation field $\boldsymbol{u} \in F$ such that

$$\forall \boldsymbol{v} \in F \ : \ \delta\mathcal{E}[\hat{\Omega}](\boldsymbol{v}) = \langle \boldsymbol{u}, \boldsymbol{v} \rangle_F,$$

then $\boldsymbol{u}$ is called the gradient of $\mathcal{E}$ relative to the inner product. Here, we let $F = L^2$.

We obtain the gradient

$$\boldsymbol{u}(\mathcal{V}_j) = (\hat{M}^{\hat{\Omega}})^{-1} \frac{\partial \mathcal{E}}{\partial \mathcal{V}_j}, \tag{6.9}$$

where

$$\frac{\partial \mathcal{E}}{\partial \mathcal{V}_j} = \widetilde{\rho}_{\mathcal{H}}(\hat{\Omega}, \hat{\Omega}^{\dagger}) \frac{\partial \widetilde{\rho}_{\mathcal{H}}}{\partial \mathcal{V}_j}, \tag{6.10}$$

in which

$$\frac{\partial \widetilde{\rho}_{\mathcal{H}}(\hat{\Omega}, \hat{\Omega}^{\dagger})}{\partial \mathcal{V}_j} = (\widetilde{\rho}_{\mathcal{H}}(\hat{\Omega}, \hat{\Omega}^{\dagger}) + \epsilon)^{1-2\alpha} \frac{\hat{M}^{\hat{\Omega}}_{jj}}{N^{\hat{\Omega}}_{\mathcal{V}} N^{\hat{\Omega}^{\dagger}}_{\mathcal{V}}} \sum_{k=1}^{N^{\hat{\Omega}^{\dagger}}_{\mathcal{V}}} \frac{\mathcal{V}_j - \mathcal{V}^{\dagger}_k}{d(\mathcal{V}_j, \mathcal{V}^{\dagger}_k)^{2\alpha+2}} \hat{M}^{\hat{\Omega}^{\dagger}}_{kk} (f_j^{-2} + g_k^{-2}), \tag{6.11}$$

with f_j and g_k defined in (6.7).

The complexity of computing the Hausdorff distance or its gradient is can be prohibitive when using large datasets. In practice, we restrict the sums in f_i and g_i to only the ϵ-nearest neighbor pairs (found in constant time using a uniform partitioning of the domain), without a noticeable loss of accuracy. The use of multi-resolution is natural in the iterative reconstruction and also reduces the computational cost.

The L^2 gradient descent follows to be chosen along the negative gradient

$$\begin{aligned} \frac{\mathrm{d}\mathcal{V}_j}{\mathrm{d}t} &= -\,\boldsymbol{u}(\mathcal{V}_j) \\ &= -\,(\hat{M}^{\hat{\Omega}}_{jj})^{-1} \widetilde{\rho}_{\mathcal{H}}(\hat{\Omega}, \hat{\Omega}^{\dagger}) \frac{\partial \widetilde{\rho}_{\mathcal{H}}}{\partial \mathcal{V}_j}, \end{aligned} \tag{6.12}$$

with which the vertices evolve in the steepest direction of reducing the energy.

6.3.3 Interior boundary only recovery

We consider here a single polyhedral interior boundary or interface $\hat{\Gamma}_i$. The velocity $\boldsymbol{v}$ is then defined on $\hat{\Gamma}_i$. Again, we consider an energy derived from the Hausdorff distance, replacing $\hat{\Omega}$ by $\hat{\Gamma}_i$. We redefine the mass matrix as the inner product of basis functions $\phi_j(\boldsymbol{v})$, now on $\hat{\Gamma}_i$ instead of $\hat{\Omega}$, as

$$M_{ij}^{\hat{\Gamma}_i} = I_{3\times 3}\int_{\hat{\Gamma}_i}\phi_j(\boldsymbol{x})\phi_k(\boldsymbol{x})\,\mathrm{d}\boldsymbol{x}, \quad j,k = 1,2,\cdots,N_{\mathcal{V}}^{\hat{\Gamma}_i}, \tag{6.13}$$

and lumped to diagonal matrix $\hat{M}^{\hat{\Gamma}_i}$. The corresponding L^2 gradient descent has the same form as in the case of volumetric meshes obtained in (6.12)

$$\frac{\mathrm{d}\mathcal{V}_j}{\mathrm{d}t} = -(\hat{M}_{jj}^{\hat{\Gamma}_i})^{-1}\widetilde{\rho}_{\mathcal{H}}(\hat{\Gamma}_i,\hat{\Gamma}_i^{\dagger})\frac{\partial\widetilde{\rho}_{\mathcal{H}}}{\mathcal{V}_j},\ \mathcal{V}_j\in\hat{\Gamma}_i, \tag{6.14}$$

in which

$$\widetilde{\rho}_{\mathcal{H}}(\hat{\Gamma}_i,\hat{\Gamma}_i^{\dagger}) = \left(\frac{1}{N_{\mathcal{V}}^{\hat{\Gamma}_i}}\sum_{j=1}^{N_{\mathcal{V}}^{\hat{\Gamma}_i}}\hat{M}_{jj}^{\hat{\Gamma}_i}f_j^{-1} + \frac{1}{N_{\mathcal{V}}^{\hat{\Gamma}_i^{\dagger}}}\sum_{k=1}^{N_{\mathcal{V}}^{\hat{\Gamma}_i^{\dagger}}}\hat{M}_{kk}^{\hat{\Gamma}_i^{\dagger}}g_k^{-1}\right)^{\frac{1}{2\alpha}}, \tag{6.15}$$

$$f_j = \frac{1}{N_{\mathcal{V}}^{\hat{\Gamma}_i^{\dagger}}}\sum_{k=1}^{N_{\mathcal{V}}^{\hat{\Gamma}_i^{\dagger}}}\hat{M}_{kk}^{\hat{\Gamma}_i^{\dagger}}(d(\mathcal{V}_j,\mathcal{V}_k^{\dagger})^2+\epsilon^2)^{-\alpha}, \tag{6.16}$$

$$g_k = \frac{1}{N_{\mathcal{V}}^{\hat{\Gamma}_i}}\sum_{j=1}^{N_{\mathcal{V}}^{\hat{\Gamma}_i}}\hat{M}_{jj}^{\hat{\Gamma}_i}(d(\mathcal{V}_j,\mathcal{V}_k^{\dagger})^2+\epsilon^2)^{-\alpha},\ \mathcal{V}_j\in\hat{\Gamma}_i,\ \mathcal{V}_k^{\dagger}\in\hat{\Gamma}_i^{\dagger}, \tag{6.17}$$

and

$$\frac{\partial\widetilde{\rho}_{\mathcal{H}}(\hat{\Gamma})}{\partial\mathcal{V}_j} = (\widetilde{\rho}_{\mathcal{H}}(\hat{\Gamma},\hat{\Gamma}^{\dagger})+\epsilon)^{1-2\alpha}\frac{\hat{M}_{jj}^{\hat{\Gamma}}}{N_{\mathcal{V}}^{\hat{\Gamma}}N_{\mathcal{V}}^{\hat{\Gamma}^{\dagger}}}\sum_{k=1}^{N_{\mathcal{V}}^{\hat{\Gamma}^{\dagger}}}\frac{\mathcal{V}_j-\mathcal{V}_k^{\dagger}}{d(\mathcal{V}_j,\mathcal{V}_k^{\dagger})^{2\alpha+2}}\hat{M}_{kk}^{\hat{\Gamma}^{\dagger}}(f_j^{-2}+g_k^{-2}). \tag{6.18}$$

We interpolate the piecewise linear gradient flow as

$$\boldsymbol{V}(\boldsymbol{x}) = \sum_j\frac{\mathrm{d}\mathcal{V}_j}{\mathrm{d}t}\phi_j(\boldsymbol{x}). \tag{6.19}$$

We write the linearized shape deformation scheme based on (6.14) as

$$\mathcal{V}_j^t = \mathcal{V}_j - t\boldsymbol{V}(\mathcal{V}_j), \quad j = 1,2,\cdots,N_{\mathcal{V}}^{\hat{\Gamma}}, \tag{6.20}$$

with t some proper step size, which can be adaptively obtained using a backtracking line search for each deformation step.

6.4 Interior boundaries: topological optimization with regularization

There are some practical challenges for minimizing the volume based Hausdorff distance or related objective functionals. The complexity for computing $\widetilde{\rho}_{\mathcal{H}}(\hat{\Omega}, \hat{\Omega}^{\dagger})$ is $\mathcal{O}(N_{\mathcal{V}}^{\hat{\Omega}} \times N_{\mathcal{V}}^{\hat{\Omega}^{\dagger}})$, which is significant for large scale 3D models or greatly refined models in later iterations. Moreover, moving the vertices in the volume mesh directly without proper regularization can result in a severely distorted tetrahedral mesh with a large number of poor-quality elements. We alternatively conduct the interior boundary recovery by deriving similar energy functionals and gradients based on interior surfaces $\hat{\Gamma}$, and use the level sets and finite element method based on physical laws as regularization for the evolution of volume mesh.

6.4.1 Levels sets enabling repicking of interior boundaries

A level set is an implicit representation for a subdomain and its boundary (Sussman et al. (1994) [156]). Since we have explicit representation of interior boundaries as surface mesh, we do not need the level sets everywhere. We only adopt it for topological change problems, which can be challenging for purely mesh-based techniques, while can be naturally dealt with by level set methods. We use more general level sets rather than the standard signed distance function (eg. Osher & Fedkiw, (2003) [122]), defined as piecewise linear distributions based on the tetrahedral mesh for each subdomain $\hat{\Omega}_i$ as

$$\hat{\psi}_i(\boldsymbol{x}) = \sum_j \psi_i(\mathcal{V}_j)\phi_j(\boldsymbol{x}), \tag{6.21}$$

where

$$\psi_i(\boldsymbol{x}) = \begin{cases} 1, & \boldsymbol{x} \in \hat{\Omega}_i^c \\ -1, & \boldsymbol{x} \in \hat{\Omega}_i \\ 0, & \boldsymbol{x} \in \partial\hat{\Omega}_i \end{cases} . \tag{6.22}$$

and the basis function ϕ is defined in Section 6.2. In our approach, the mesh deformation is driven by the gradient flow on vertices and physics constraints. The level set is not regarded as a motivator for mesh deformation any more, but a "domain identifier" to determine whether each node is inside or outside the subdomain $\hat{\Omega}_i$, or on the interior boundary. The update of the level sets follows the mesh evolution by updating the values of $\psi_i(\mathcal{V}_j)$ on some of the vertices $\mathcal{V}_j$ in the neighbourhood of interior boundary, and reinterpolating into the whole space by (6.21).

We describe the updating from $\hat{\psi}_i(\mathcal{V}_j)$ to the new level set $\hat{\psi}_i^t(\mathcal{V}_j)$ as follows. For each tetrahedron $\mathcal{T}$, we denote the centeroid $\boldsymbol{x}_{\mathcal{T}}$. We find the map from each facet τ_k in the neighbourhood of interior boundary to two tetrahedra $\mathcal{T}_{k_1}$ and $\mathcal{T}_{k_2}$. We then let

$$\psi_i^t(\mathcal{V}_j) = 0, \qquad \text{for any } \mathcal{V}_j \in \tau_k = \mathcal{T}_{k_1} \cap \mathcal{T}_{k_2} \text{ if } \hat{\psi}_i(\boldsymbol{x}_{\mathcal{T}_{k_1}})\hat{\psi}_i(\boldsymbol{x}_{\mathcal{T}_{k_2}}) < 0.$$

Otherwise,

$$\psi_i^t(\mathcal{V}_j) = \operatorname{sign}(\hat{\psi}_i(\boldsymbol{x}_{\mathcal{T}_k})), \text{ for any } \mathcal{V}_j \in \mathcal{T}_k.$$

Thus the updated level set

$$\hat{\psi}_i^t(\boldsymbol{x}) = \sum_j \psi_i^t(\mathcal{V}_j)\phi_j(\boldsymbol{x}).$$

This process is conducted at the end of each deformation step for repick the interior boundary surface from the deformed volume mesh. An example is demonstrated in lower dimension in Fig. 6.4.1 where the piecewise linear level set is defined and updated along with mesh deformation and modification. We discuss this "feed-back"

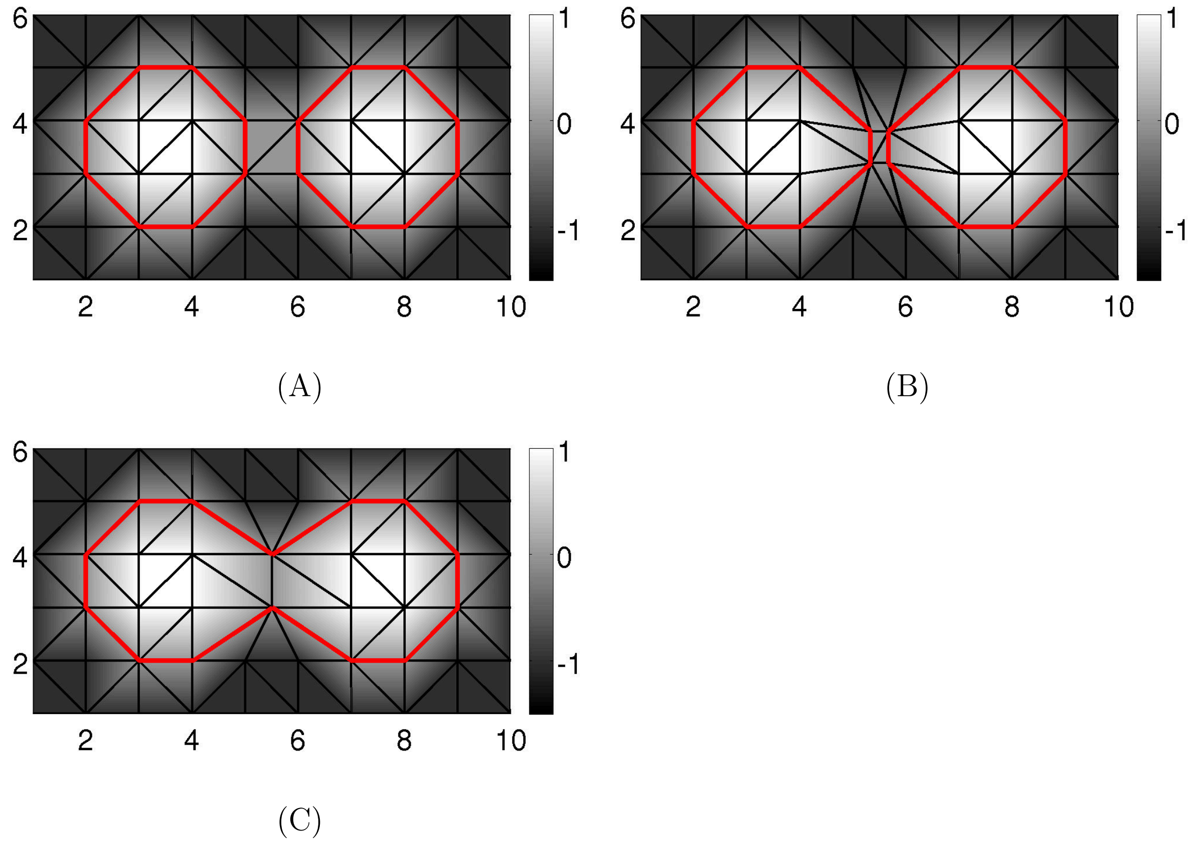

Figure 6.4.1 : Demonstration of polyhedra-based piecewise linear level sets in two-dimension: (A) level sets based on mesh; (B) updated level sets after mesh deformation by vertex movement; (C) updated level sets after edge collapse, with contacting topology change. The red lines highlight the subdomain boundaries.

mechanism from volume mesh to surface mesh in details for dealing with topological change in Subsections 6.6.1 and 6.6.2.

6.4.2 Elastic-deformation based regularization

We outfit our mesh with a deformable model based on the finite element method. An alternative method based on masses and springs is discussed in Teran et al. (2005) [159]. The two techniques differ in how the external forces are computed, but both have equilibrium positions that try to maintain high quality tetrahedra.

We discretize the equations of continuum mechanics with the finite element method. The equations of elasticity are a more natural and more flexible way of encoding a quasi-material response to distortion. In discretized finite element form, they resist the three-dimensional distortion of elements. A big advantage of finite element techniques over mass spring networks is the versatility provided by the framework.

To discretize these constitutive models, we use finite elements with linear basis functions in each tetrahedron. The displacement of material is a linear function of the tetrahedron's four nodes. From the nodal locations and velocities we obtain the Jacobian of this linear mapping and its derivative, and use them to compute the partical displacements on the nodes. A detailed matrix formulation of the finite element method for the linear elasticity deformation problem is presented in 6.4.3. When the displacement vector $\boldsymbol{u}_I$ is obtianed from (6.28), we conduct a one-time redistribution for the interior node locations via

$$\mathcal{V}_j^t = \mathcal{V}_j + \boldsymbol{u}_I(\mathcal{V}_j).$$

This process provides necessary regularization on the deformation of interiors of each subdomain and ensures that its volume mesh exactly conforms its deformed boundary. One can obtain optimal redistribution of interior nodes via replacing the boundary condition of (6.24) by Neumann (force) boundary condition (as in Teran et al. [159]) and apply an iterative scheme, which is not necessary and can be overwhelmed by the mesh quality optimization presented in Section 6.6.

6.4.3 Energy of elastic volume deformation and elliptic BVP

We consider a bounded subdomain $\hat{\Omega}$ partitioned into tetrahedral elements, and we denote its boundaries by $\hat{\Gamma}$ for the interior boundary and $\partial\hat{\Omega} \setminus \hat{\Gamma}$ as the external boundary. The elastic material is represented by Lamé parameters λ and μ. We denote the vector field $\boldsymbol{u}$ as the particle displacement, and let

$$\varepsilon = \tfrac{1}{2}(\nabla \boldsymbol{u} + \nabla \boldsymbol{u}^T)$$

be the strain. Based on Hooke's law, the elastic stress tensor is obtained as

$$\sigma = \lambda \mathrm{Tr}(\varepsilon) + 2\mu\varepsilon.$$

The energy of deformation is defined (see Fuchs et al. (2009) [60]):

$$E(\boldsymbol{u}) = \int_\Omega \left(\lambda(\sum_{i=1}^{3} \varepsilon_{ii})^2 + 2\mu \sum_{j,k=1}^{3} \varepsilon_{jk}^2 \right) \mathrm{d}\Omega. \tag{6.23}$$

Since

$$\varepsilon_{ij} = \tfrac{1}{2}(\frac{\partial \boldsymbol{u}_i}{\partial \boldsymbol{x}_j} + \frac{\partial \boldsymbol{u}_j}{\partial \boldsymbol{x}_i}),$$

we have the stationary equation

$$\begin{aligned} \frac{\partial E}{\partial u_i} =& \lambda \frac{\partial}{\partial x_i} \left(\sum_{j=1}^{3} \varepsilon_{jj} \right) + 2\mu \sum_{k=1}^{3} \left(\frac{\partial}{\partial x_k} \varepsilon_{ik} \right) \\ =& \lambda \frac{\partial}{\partial x_i} \left(\sum_{j=1}^{3} \frac{\partial u_j}{\partial x_j} \right) + \mu \sum_{k=1}^{3} \left(\frac{\partial^2 u_i}{\partial x_k^2} + \frac{\partial^2 u_k}{\partial x_i \partial x_k} \right) = 0. \end{aligned} \tag{6.24}$$

The deformation only occurs on interior boundaries, and the external boundary remains fixed. We obtain the boundary conditions from the gradient flow (6.19) over the interior boundary surfaces, as a Dirichlet condition

$$\boldsymbol{u}|_{\boldsymbol{x}\in\hat{\Gamma}} = \boldsymbol{f}, \quad \boldsymbol{u}|_{\boldsymbol{x}\in\partial\hat{\Omega}\backslash\hat{\Gamma}} = 0,$$

where

$$\boldsymbol{f} = \alpha \boldsymbol{V}(\boldsymbol{x}), \quad \boldsymbol{x} \in \hat{\Gamma},$$

following (6.20). We derive the weak form of Equation 6.24 by introducing a test function $\boldsymbol{w}$ in $L^2(\hat{\Omega})$ and taking advantage of the homogeneous Dirichlet boundary condition of $\boldsymbol{u}$,

$$\lambda \sum_{j=1}^{3} \left(\frac{\partial u_j}{\partial x_j}, \frac{\partial w_i}{\partial x_i} \right) + \mu \sum_{k=1}^{3} \left(\frac{\partial u_k}{\partial x_i} + \frac{\partial u_i}{\partial x_k}, \frac{\partial w_i}{\partial x_k} \right) = 0. \tag{6.25}$$

We discretize Eq. 6.25 into finite element space in 3D, obtaining the matrix formulation:

$$\begin{pmatrix} \beta K_{11} + \mu(K_{22} + K_{33}) & \lambda K_{12} + \mu K_{21} & \lambda K_{13} + \mu K_{31} \\ \lambda K_{21} + \mu K_{12} & \beta K_{22} + \mu(K_{11} + K_{33}) & \lambda K_{23} + \mu K_{32} \\ \lambda K_{31} + \mu K_{13} & \lambda K_{32} + \mu K_{23} & \beta K_{33} + \mu(K_{11} + K_{22}) \end{pmatrix} \begin{pmatrix} u_1 \\ u_2 \\ u_3 \end{pmatrix} = \begin{pmatrix} 0 \\ 0 \\ 0 \end{pmatrix} \tag{6.26}$$

where M is the mass matrix defined in (6.2) for $\hat{\Omega}$,

$$K_{ij} = \int_{\hat{\Omega}} \nabla \phi_i(\boldsymbol{x}) \otimes \nabla \phi_j(\boldsymbol{x}) \, \mathrm{d}\boldsymbol{x}, \tag{6.27}$$

and $\beta = \lambda + 2\mu$ is the P-wave modulus. We rewrite Eq. 6.26 as

$$\boldsymbol{A}\boldsymbol{u} = 0.$$

We note that that $K_{ij} = K_{ji}^T$, thus the global matrix $\boldsymbol{A}$ is symmetric. We divide $\boldsymbol{u}$ into $\boldsymbol{u}_I$ and $\boldsymbol{u}_B$, which denote for the particle displacement of interior points and points contained in $\partial\hat{\Omega}$, respectively. We split $\boldsymbol{A}$ correspondingly and include the boundary condition described in Eq. 6.24 by Lagrange multiplier $\boldsymbol{u}_\lambda$, which yields

$$\begin{pmatrix} \boldsymbol{A}_{BB} & \boldsymbol{A}_{BI} & \boldsymbol{I} \\ \boldsymbol{A}_{IB} & \boldsymbol{A}_{II} & 0 \\ \boldsymbol{I} & 0 & 0 \end{pmatrix} \begin{pmatrix} \boldsymbol{u}_B \\ \boldsymbol{u}_I \\ \boldsymbol{u}_\lambda \end{pmatrix} = \begin{pmatrix} 0 \\ 0 \\ \boldsymbol{g} \end{pmatrix}, \tag{6.28}$$

where $\boldsymbol{g} = \begin{pmatrix} \boldsymbol{f} \\ 0 \end{pmatrix}$, and $\boldsymbol{I}$ is identity matrics.

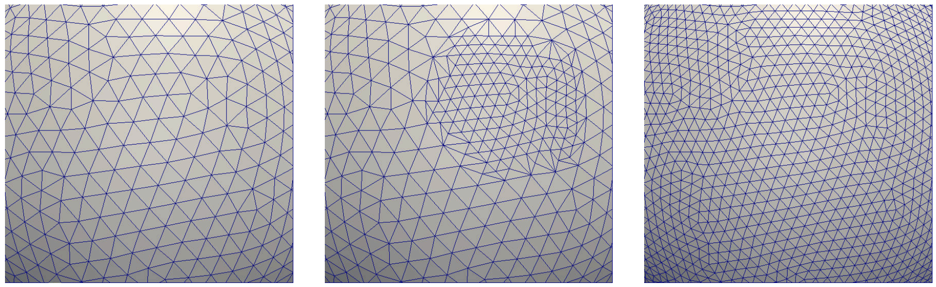

Figure 6.5.2 : Demonstration of triangulated surface refinement, with (A) the original surface mesh, (B) the locally refined mesh, and (C) the globally refined mesh.

6.5 Multi-scale, multi-level refinement

A local/global refinement algorithm is crucial for the adaptive evolution of an unstructured mesh. We propose a multi-level approach during mesh evolution. Within each level, a local refining approach is applied for the purpose of mesh quality control. When approaching the next level, a global mesh refinement is conducted in which all edges are divided uniformly into two by adding new center nodes. Examples of local and global refinement can be found in Fig. 6.5.2. We adaptively conduct the local and global refinements on both the surface mesh and volume mesh, whenever an increase of resolution is required.

6.5.1 Surface mesh refinement based on edge spliting

In terms of mesh refinements for both triangulated surface and tetrahedral volume meshes, we define the notions of edge split following the work in Hoppe et al. (1993) [77], as is shown in Fig. 6.5.3. A split operation on edge $\mathcal{E}(\mathcal{V}_i, \mathcal{V}_j)$ adds a new vertex $\mathcal{V}_k$ on the center of the edge $\frac{1}{2}(\mathcal{V}_i + \mathcal{V}_j)$, and divides all the elements (triangles in surface mesh, and tetrahedra in volume mesh) into smaller elements, and the per-

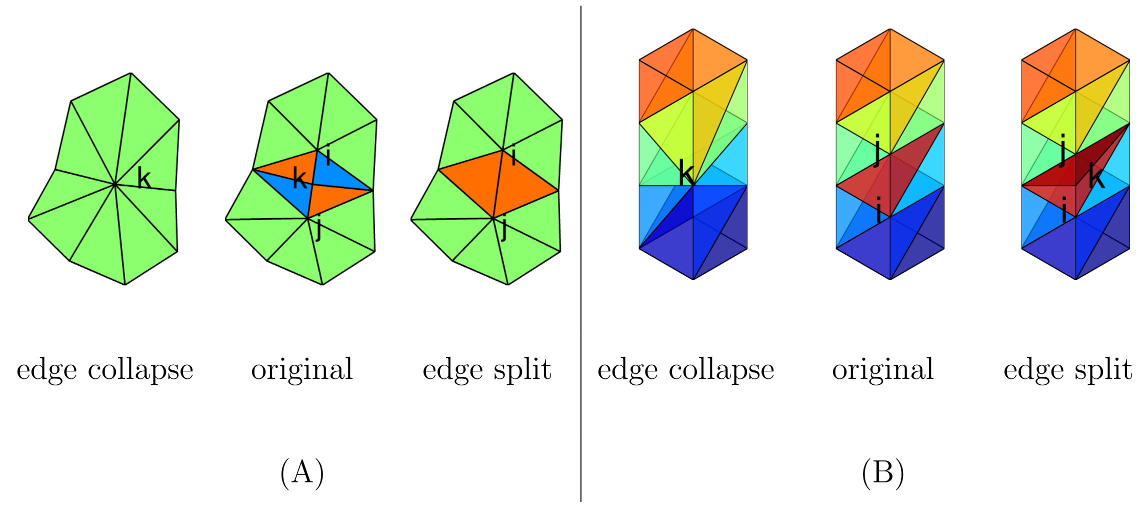

Figure 6.5.3 : Illustration of edge split and collapse for (A) triangulated surface, and (B) tetrahedral volume mesh.

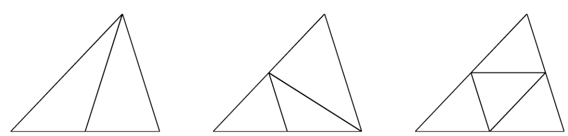

Figure 6.5.4 : Three valid patterns for triangle refinement.

mutation of vertices for each new element remains the same as the original elements. The adjacency graph of the mesh changes after each split or collapse operation. We implement our refining and coarsening algorithm for both surface and volume mesh based on these two primary operations. Our refinement approach is a one-time operation, that is, all edges that match the refining criterion will be picked out and split simultaneously. A trivial penalty can be applied by placing an upper bound $l_{\mathcal{E}}^{\max}$ on edge length in order to find low-sampled areas. The refinement over each triangle follows the three given patterns listed in Fig. 6.5.4, dividing the triangle into two, three or four pieces. We note that the second division has a mirror symmetric pattern, and the choice between the two is determined by the interior angles of the triangle.

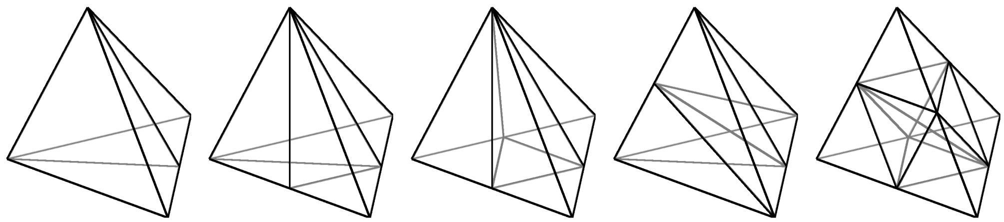

Figure 6.5.5 : Five valid patterns for triangle refinement. The second type of division is only allowed in joint refinement with interior boundary surfaces; the last one corresponds to the "red" refinement procedure and the remaining patterns are denoted as "green" refinements by Teran et al. (2005) [159]

6.5.2 Non-uniform tetrahedra refinements

We propose a joint algorithm for refining the tetrahedral mesh coherently with the interior boundary surfaces. Similar to the operation for the surface mesh, the refinement over the volume mesh is conducted via edge splitting. We allow five types of tetrahedral dividing patterns as is shown in Fig. 6.5.5. The second type of division can only be conducted jointly with the interior boundary triangular element refinement, as it can easily damage the topology by generating a non-conforming mesh (see Fig. 6.5.6). The remaining four patterns correspond to the red and green hierarchical refinements discribed in Teran et al. (2005) [159], which regularly (red) refines any tetrahedron where more resolution is required, and then irregularly (green) refines tetrahedra to restore the mesh to a valid simplicial complex. Instead of a one-time operation as surface refinements, the volume mesh refining process may require several iterations, depending on the complexity of adjacency graph of refinable tetrahedra.

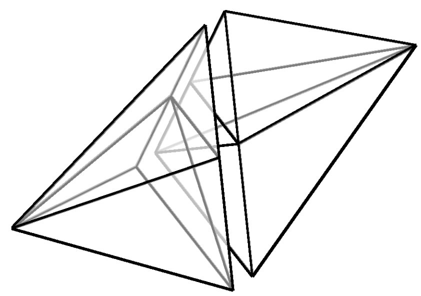

Figure 6.5.6 : Demonstration of topological change generated by non-conforming refinement.

6.5.3 Local coarsening: counter-action to the refinement

The general mesh deformation procedure not only generates low-resolution areas that require refinement, but also over-sampled regions where elements are squeezed with tiny volumes or areas. These regions can be predicted by the result of finite-element based regularization, as they usually come with large compression stress. A one-way mesh refinement scheme can hardly remedy this problem. We introduce the counter-action to the refinement as the local coarsening that simplifies the unstructured mesh representation by removing undesired vertices. The operation is conducted by edge collapse [77], as in Fig. 6.5.3, where the edge $\mathcal{E}(\mathcal{V}_i, \mathcal{V}_j)$ is removed by collapses $\mathcal{V}_j$ and $\mathcal{V}_i$ into intermediate node $\mathcal{V}_k$, with all elements connected to $\mathcal{E}(\mathcal{V}_i, \mathcal{V}_j)$ vanishing. This operation can cause topological distortion such as inverted triangles (Fig. 6.5.7). For a surface mesh the topology disordering can be quickly detected by Equation 6.1, and we can fix the topology by removing the flipped triangle facets (e.g., T_1'' in Fig. 6.5.7(B)). For the volume mesh we check the disordering of mesh topology using the similar equation regarding the total number of tetrahedra $N_{\mathcal{T}}^{\hat{\Omega}}$, the total number of

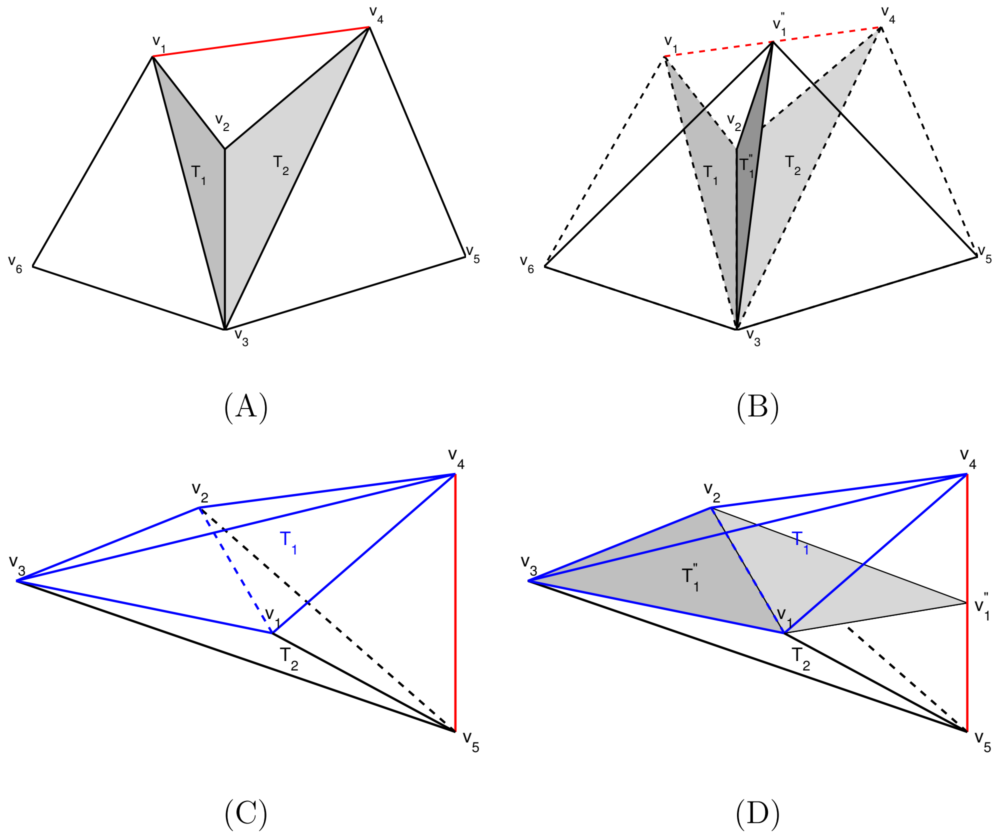

Figure 6.5.7 : Demonstration of inverted triangles generated by edge collapse, in triangulated surface mesh from (A) to (B), and in tetrahedral volume mesh from (C) to (D).

triangular facets $N_{\tau}^{\hat{\Omega}}$ and the number of boundary triangles $N_{\tilde{\tau}}^{\hat{\Omega}}$ as

$$4N_{\mathcal{T}}^{\hat{\Omega}} = 2N_{\tau}^{\hat{\Omega}} - N_{\tilde{\tau}}^{\hat{\Omega}}. \tag{6.29}$$

6.6 Optimization of mesh quality metrics

Considering the stability of mesh deformation iterations, the tetrahedra in a partitioned domain are required to be non-degenerate. In particular, there exist positive numbers e_1, β_1, and r_1 such that for each tetrahedron in the mesh,

- the edge lengths are greater than e_1,

- the internal angles of triangular facets are greater than β_1, and
- the insphere radius is greater than r_1.

We also invoke a mesh quality estimate for the triangulated surface $\hat{\Gamma}$ with the existance of positive numbers d_1, a_1, and α_1 such that for each τ_j in $\hat{\Gamma}$,

- the length of edges are greater than d_1,
- the internal angles are greater than α_1, and
- the area is greater than a_1.

We note that the area of a triangle can be a negative value, determined by the permutation of three vertices. As an additional step, alternating with physics-based regularization, we directly optimize mesh quality metrics, based on the above assumptions. The procedure is conducted via joint refinement-coarsening operations, depending on the type of bad elements we are going to remove. The triangular surface can be well regularized by penalizing the edges. We remove the edges with tiny length or opposite to small interior angles. For a tetrahedral mesh we describe three types of bad elements, based on edges' length and facet interior angles, demonstrated in Fig. 6.6.8. Each of them requires a different type of treatment:

- Type 1: tetrahedra with short edges are dealt with by edge collapse;
- Type 2: tetrahedra with no short edges but small inter-facet angles are refined into two elements, both become Type 1 and are eliminated by edge collapse;
- Type 3: tetrahedra with no short edges or small inter-facet angles are refined into four elements, all of which become Type 1 and are eliminated by edge collapse.

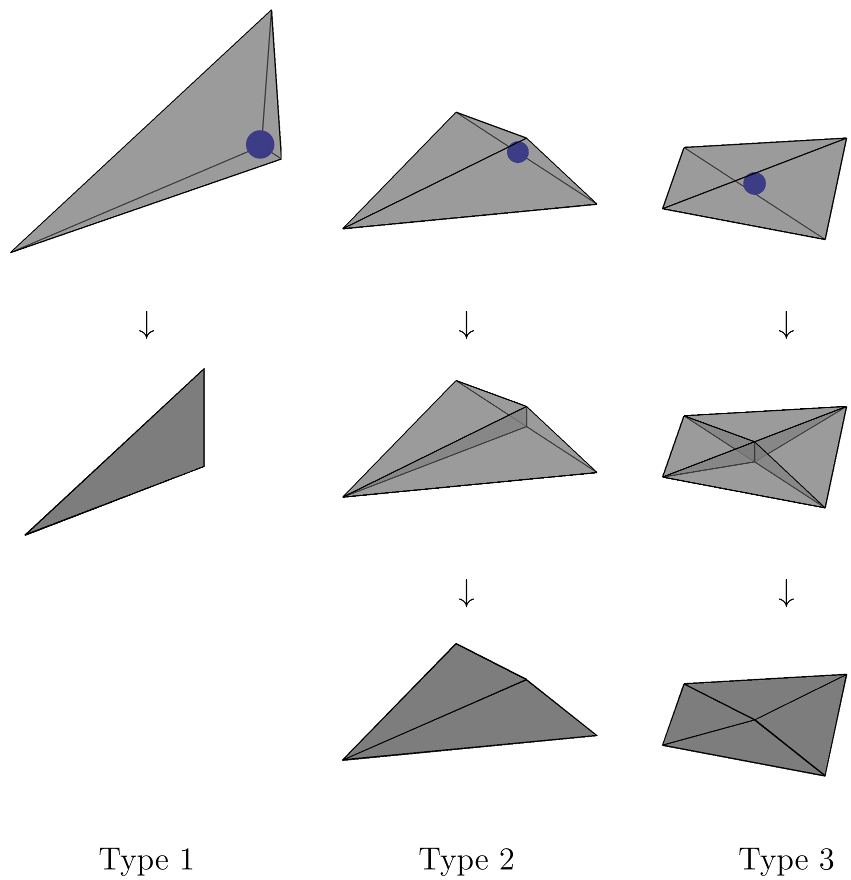

Figure 6.6.8 : Demonstration of poor-quality tetrahedra with high circumscribed radius / subscribed radius ratio, with: Type 1: one or more short edges; Type 2: no short edges but small interior angles in facets; and Type 3: no short edges or small inter-facet angles. The blue balls are inscribed shperes of the three tetrahedra. The modified mesh after edge collapse is listed below each case, where poor-quality tetrahedra become facets.

For the edge-collapse operation, removable short edges can be collapsed simultaneously as long as they are isolated from each other, that is, any two of they neither share a common vertex, nor belong to the same tetrahedron. Such a simultaneous operation is far more efficient than conducting each edge removal sequentially.

The mesh quality control coincides with topological corrections. Conventional techniques usually have difficulty dealing with topological optimization problems in the absence of smoothness assumptions. We introduce a feed-back mechanism in joint volume and surface mesh evolution, with the connection provided by level sets. We discuss two particular types of topological change: subdomain contacting and break-up.

6.6.1 Near-contacting prediction and topology correction

With the absence of smoothness or convexity assumptions in our study, we seek reasonable alternative penalty conditions for the stability of mesh evolution. A non-oscillating assumption is applied, which indicates that we can find a sufficiently large lower bound for the dihedral angle of two adjacent facets, which, on the other hand, provides a regularization for the quality of tetrahedral volume mesh. With this assumption, we define "bad" edges as ones with small dihedral angles, which we aim to remove. This approach is essential, and it is efficient to predict and prevent the occurrence of artificial topological changes beforehand rather than fix them after they appear. One such situation is a convexity artifact. When an actual local topology is convex while the current mesh is locally non-convex, an intersection is likely to occur in next deformation steps, especially with refinement. Meanwhile, we would like to preserve the non-convexity for locally non-convex regions. The local convexity of the current mesh can be determined by the dihedral angle between two adjacent facets, and the true local convexity can be predicted by the direction of gradient flow. If both the local mesh is non-convex and the out-going gradient flow occurs, we conduct a convexity fix as is demonstrated in Fig. 6.6.9, which is also defined as an edge warping operation in [77]. Otherwise, an edge-removal approach will be conducted.

When an actual contacting comes with topological change, such as the formation of a torus or a hole from a simply connected subdomain, we need to evolve the level sets and regenerate interior boundary surfaces. There are multiple ways of detecting the intersection of facets [114], removing them and remeshing the hole [149] in two-dimension manifolds. Unlike these conventional mesh optimization processes, we evolve the surface coherently with volume mesh modification, incorporating the piecewise linear level sets. The contacting of surfaces always comes with collapsed or inverted volume elements. The effects that removing these poor-quality tetrahedra might have upon the interior boundaries are listed as follows:

- the vertices' movement does not affect either the the number of triangles, or connection of the adjacency graph;
- the local and global refinement changes the number of triangles, but does not influence the connection of the adjacency graph;
- the local coarsening changes the number of triangles, and possibly modifies the connection of the adjacency graph.

The third effect is considered as a feed-back of volume mesh correction to the interior surface. As the volume elements between the two parts of approaching surface boundaries are squeezed and eliminated by the edge collapse operation, the basis functions of the level set supported on these elements are also removed from the frame. New connected facets are formed, connecting these two partial surfaces, and if the values of the level set between the two sides of facets have the same sign, the facets are removed from $\hat{\Gamma}$. This process creates a new connection between two partial surfaces, which results in topological change in the subdomains. We repick $\hat{\Gamma}$ from the global set of facets based on the value of the level set $\hat{\psi}$, with its topological information if the contaction occurs. A lower-dimentional example can be found in Fig. 6.4.1 (C), where a surface mesh topology automatically updates after volume mesh evolution.

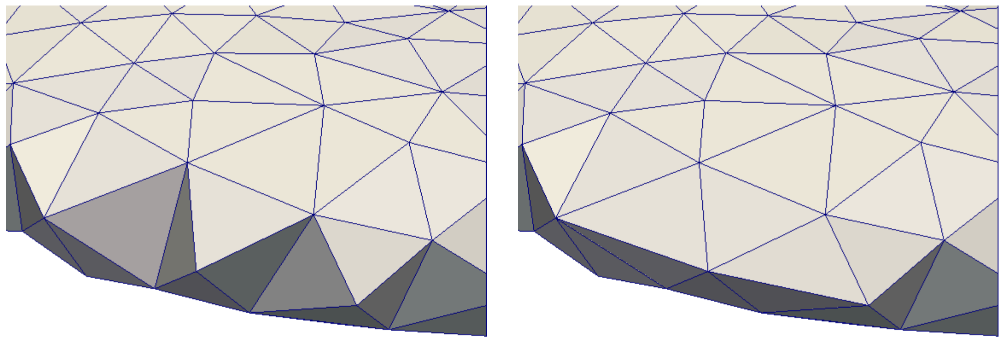

(A) (B)

Figure 6.6.9 : Demonstration of convex surface restoration from original non-convex surface (A) to convexity relaxed surface (B).

6.6.2 The break-up topology change

In break-up geometry, the triangular elements at the necking region of interior boundaries collapse into each other, which results in two or more sets of simply connected triangulated surfaces, connected to each other by isolated vertices or edges. Regarding the two sets of iso-surfaces connected by edges, one will violate the relation (6.1) (See Fig. 6.6.10 as an example). When the situation described above happens, we implement a marching scheme based on the adjacency graph, and distinguish triangles in two distinct set of surfaces. In the iterations that follow, we consider the two surfaces separately for their deformations, as they characterize two isolated subdomains. The break-up process also comes with the updating of level sets and the feed-back between volume mesh and interior triangular surfaces. An artificial break-up geometry automatically heals with mesh quality control in later iterations, and the valid break-ups evolve to the actually isolated bodies (see Fig. 6.6.11).

We conclude our scheme for surface mesh evolution in Algorithm 2, and the joint volume-surface mesh evolution in Algorithm 6.6.2.

Algorithm 2 Surface mesh evolution

start with initial triangle isosurface
set initial $l_{\mathcal{E}}^{\max}$ and $l_{\mathcal{E}}^{\min}$
set initial stepsize
for level $= 1, 2, 3, \cdots$ **do**
    for step $= 1, 2, 3, \cdots$ **do**
        set refinement criterion as edges $\geq l_{\mathcal{E}}^{\max}$ and call **SurfRefine**(nodes, triangles, criterions)
        set coarsening criterion as edges $\leq l_{\mathcal{E}}^{\min}$ and call **SurfCoarsen**(nodes, triangles, criterions)
        calculate gradient flow $\boldsymbol{V}(\mathcal{V}_j)$ from (6.19)
        $\mathcal{V}_j^t = \mathcal{V}_j + t\boldsymbol{V}(\mathcal{V}_j)$
        while not satisfying surface convexity penalty condition **do**
            call **SurfConvexity**(nodes, triangles, $\boldsymbol{V}$)
        end while
    end for
    set refinement criterion as all edges selected and call proc(surface edge refinement)
    reduce $l_{\mathcal{E}}^{\max}$ by factor 2
end for

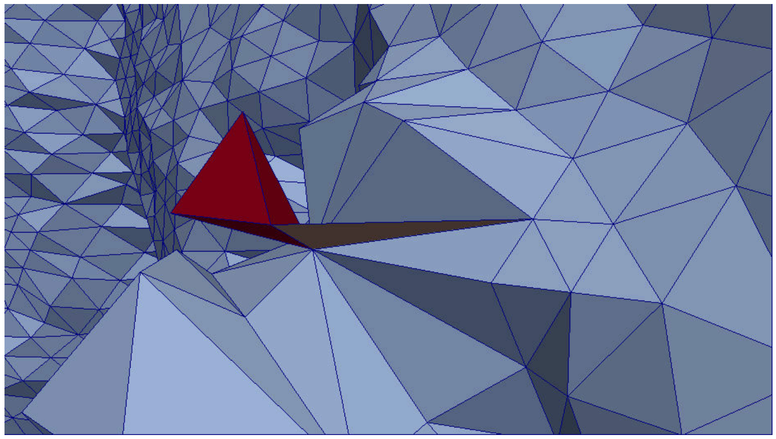

Figure 6.6.10 : Demonstration of an artificial topological change during surface mesh deformation. Three simply connected triangulated surface are detected as the main one in light blue, a collapsed one in dark gray and a closed one with only four triangles in red.

Algorithm 3 volume mesh evolution with surface mesh

generate volume mesh based on initial triangle isosurface
for level $= 1, 2, 3, \cdots$ **do**
    for step $= 1, 2, 3, \cdots$ **do**
        evolve the interior surface boundary
        jointly refine and coarsen the tetrahedral mesh with surface mesh
        solve the linear system (6.28) for $\boldsymbol{u}_I$
        $\mathcal{V}_j^t = \mathcal{V}_j + \boldsymbol{u}_I(\mathcal{V}_j)$
        refine interior tetrahedral mesh inside each subdomain
        simplify tetrahedral mesh inside each subdomain based on element quality control
        repick new interior surface boundary from piecewise linear level sets
    end for
    refine tetrahedral mesh along with surface edge refinement
end for

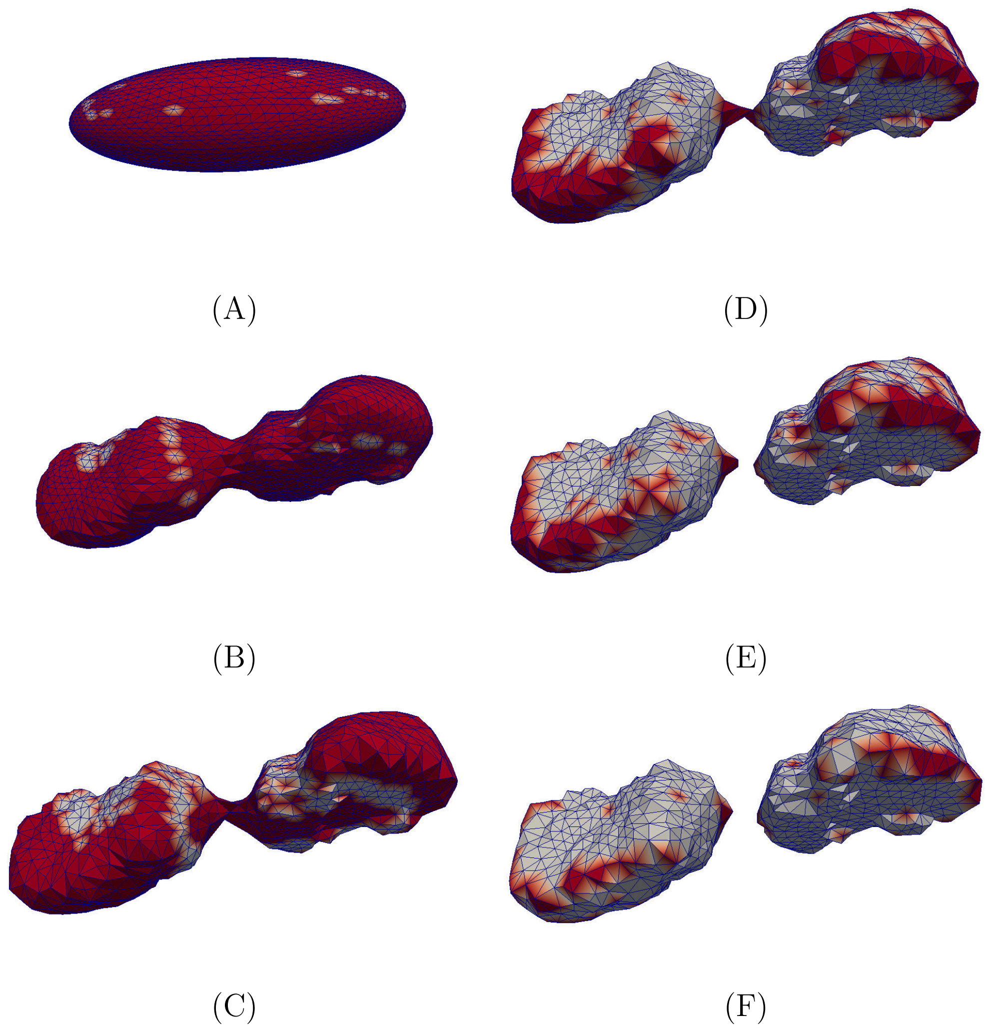

Figure 6.6.11 : Demonstration of a single subdomain in (A) breaking up into two isolated subdomains in (F). Intermediates (B) through (E) show the break-up process.

Algorithm 4 Surface edge refinement

```
function SurfRefine(nodes, triangles, criterions)
    get edges information from triangles
    find refinable edges based on refinement criterions
    determine refinement type based on number of refinable edges within each triangle
    generate new nodes at the center of each refinable edge
    pick out non-refinable triangles and save them in output triangle list
    for refine type = 1, 2, 3 do
        pick out the triangles of each refine type
        permute the vertices and generate new triangles
        save the new triangles in output triangle list
    end for
    return updated nodes and triangles
end function
```

Algorithm 5 Surface edge coarsening

```
function SurfCoarsen(nodes, triangles, criterions)
    get edges information from triangles and mark boundary vertices
    while not satisfying termination criterions do
        find collapsible edges based on coarsening criterion
        pick a largest possible subset of collapsible edges, such that any two of them are not connected to each other
        if no collapsible edges found then
            break the while loop
        end if
        for each removable edge E(V_j, V_k) in the subset do
            if V_j is a boundary vertex while V_k is not then
                replace V_k by V_j in triangles and edges
            else if V_k is a boundary vertex while V_j is not then
                replace V_j by V_k in triangles and edges
            else
                if both V_j and V_k are boundary vertices then
                    save V_k into boundary update information
                end if
                change the coordinate of V_j by the center point 1/2(V_j + V_k)
                replace V_k by V_j in triangles and edges
            end if
        end for
        update triangle and edge list
    end while
    return updated nodes, triangles, and boundary update information
end function
```

Algorithm 6 Surface convexity correction

function SURFCONVEXITY(nodes, triangles, gradient flow $\boldsymbol{V}$)
    get edges information from triangles
    initiate an empty list of irremovable edges
    while not satisfying termination criterion **do**
        find an edge $\mathcal{E}(\mathcal{V}_j, \mathcal{V}_k)$ relevant to a non-convex dihedral angle while not in the irremovable edge list
        if no such edge found **then**
            break the while loop
        end if
        backup the nodes and triangles
        find the out-normal direction $\boldsymbol{n}$ of $\hat{\Gamma}$ at edge center $\mathcal{V}_{\mathcal{E}} := \frac{1}{2}(\mathcal{V}_j + \mathcal{V}_k)$
        if $\boldsymbol{n}(\mathcal{V}_{\mathcal{E}}) \cdot \boldsymbol{V}(\mathcal{V}_{\mathcal{E}}) < -\mathrm{TOL}$ **then** conduct an edge warping
        elsecollapse the edge $\mathcal{E}(\mathcal{V}_j, \mathcal{V}_k)$
        end if
        if topological artifact occurs **then**
            restore the nodes and triangles before correction
            add $\mathcal{E}(\mathcal{V}_j, \mathcal{V}_k)$ to irremovable edge list
        end if
    end while
    refine the edges in the irremovable edge list
    return updated nodes and triangles
end function

6.7 Numerical examples

We verify our numerical scheme with two experiments. Both are relatively complex and realistic geological models. The first one contains a single salt body with generally non-smooth shapes, and the second involves multiple subdomains and interior boundaries interacting with each other, which require a joint deformation iterative scheme.

6.7.1 Recovery of a single body

We use the SEG/EAGE 3D salt model as our test target. The model ranges $13.5 \times 13.5 \times 4.0$km, and salt body is located at the center of the model and is roughly 6.0km in diameter. We start with an ellipsoid whose center roughly overlays the center of salt body, and run the shape optimizations for 20 iterations, in two levels with one global refinement. We control the edge length of the surface mesh representing the salt boundary with an upper bound of 0.6km and a lower bound of 0.06km. We conduct a global refinement after 10 steps of deformation. The result is shown in Fig. 6.7.12. The deformation of the corresponding volume mesh is also demonstrated, in the right column in Fig. 6.7.12, where most deformed elements are located close to the salt body, while elements far away from the deforming surface stay unchanged. We calculate the functional as the square of Hausdorff distance. The decay of the energy functional is plotted in Fig. 6.7.13.

6.7.2 Intersecting interfaces: recovery of a fault geometry

The immediate technical challenge of recovering a fault geometry is that we can neither consider the intersecting interfaces as a single isorsurface, nor regard them as isolated surfaces because they are governed by the intersecting line, which is as

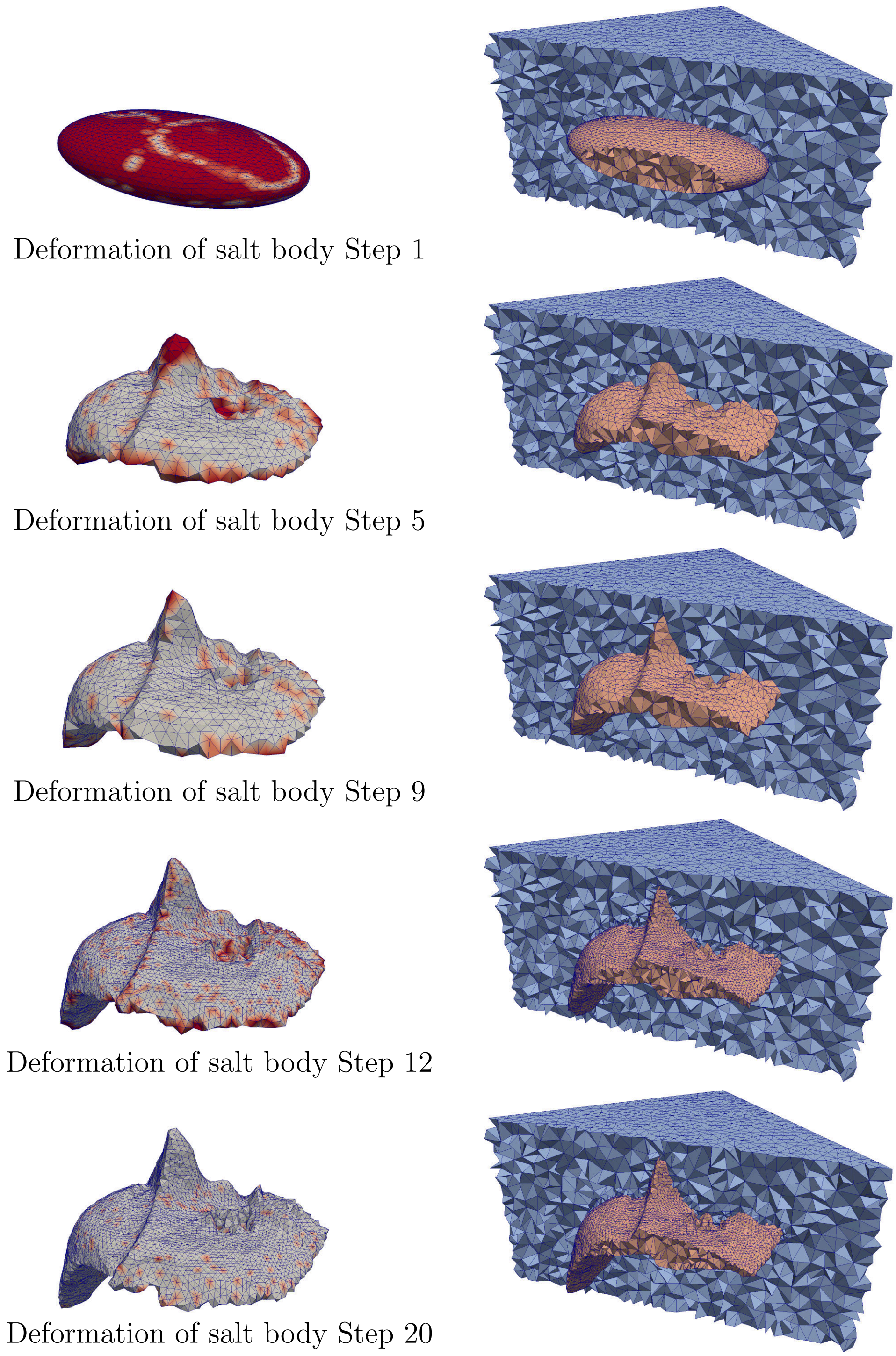

Figure 6.7.12 : Demonstration of SEG/EAGE 3D salt body deformation. Red color on salt surface represents misfit to true shape.

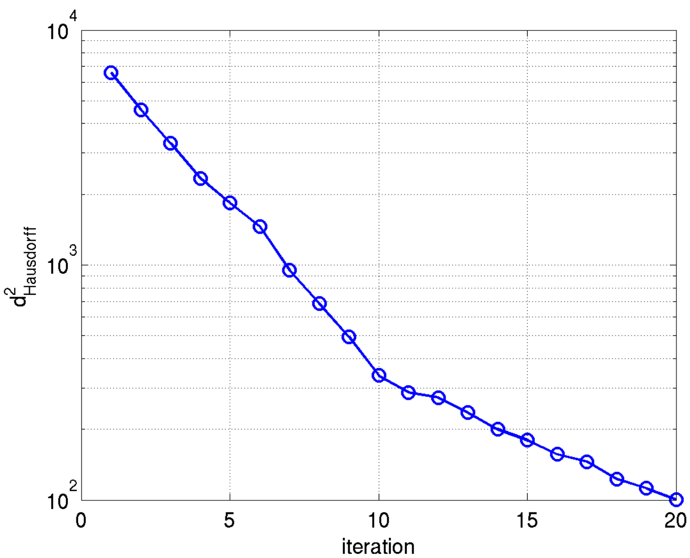

Figure 6.7.13 : The evolution of functional with defromation iterations for salt body.

crucial as a “boundary condition” in determing the shape. Here we present our joint algorithm for the evolution of pairs of intersecting isosurfaces, which can properly deal with this representational challenge and preserve the geometry.

For a particular fault geometry (see Fig. 6.7.14), we consider the intersection line **L** as a separator dividing the segment layer **A** from the fault plane, and partitioning the fault plane into two subplanes noted by **B** and **C**. In the joint algorithm, we calculate the Hausdorff distance as well as the gradient flow respectively for **L**, **A**, **B** and **C**, and update the location of their vertices separately. In the mesh modification step, we first conduct the refinement-coarsening operation for **L**, and modify the triangles attached to **L** in **A**, **B** and **C** correspondingly. Afterwards we can conduct the refinement-coarsening for each of the subplanes by considering them separately from each other. The previously developed edge split-collapse based algorithm can be implemented thereafter, with the only modification that we preserve the boundary vertices and edges for each subset of triangular surface. The volume mesh deformation algorithm does not change either. A numerical example is shown in Fig. 6.7.14 and the decaying objective function in Fig. 6.7.15.

6.8 Discussion

We developed a framework for the iterative reconstruction of unstructured tetrahedral meshes derived from Hausdorff warping. We constrain the reconstruction by shape optimization of interior boundaries and invoke a physics based regularization. The iterative reconstruction or evolution of the shape of interior boundaries makes, in part, use of level sets. We choose to use elastic deformation as regularization. Alternatively, we can connect the regularization to more general equations from geodynamics. Our energy functional is derived from the Hausdorff distance. This distance appears in the Lipschitz stability estimate for the recovery of a mesh representing a domain partition for the wavespeed in the inverse boundary value problem for the Helmholtz equation. The introduction of the associated Gateaux derivative, which is derived from the one used in this chapter, will be part of future work. A key component of our work is the development of procedures guaranteeing that the assumptions on the regularity of the mesh remain satisfied during the iteration.

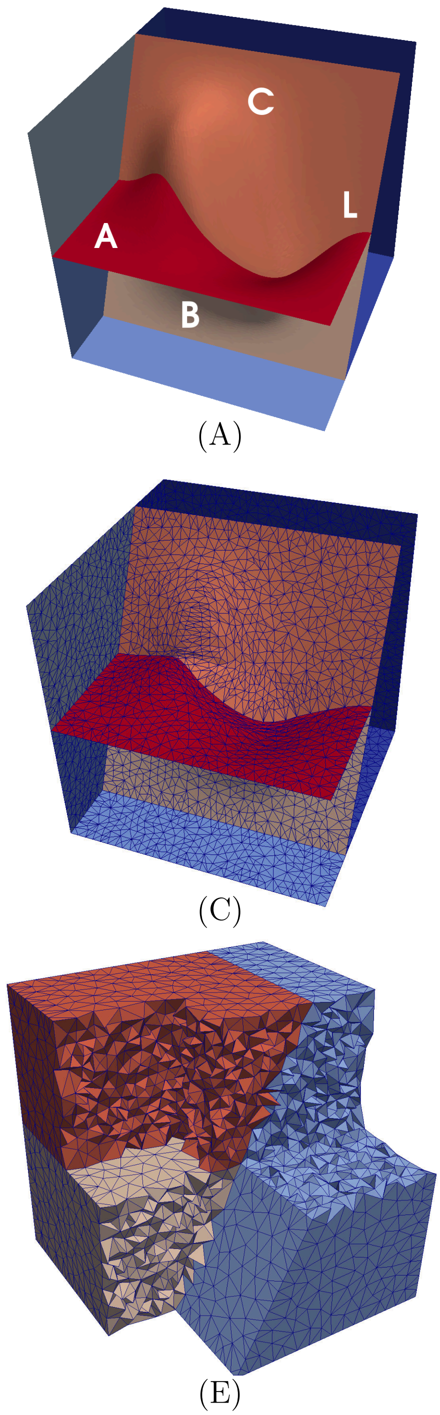

Figure 6.7.14 : Demonstration of fault geometry in (A) target shape and (B) starting mesh. The intersecting line is denoted as **L** dividing the tri-intersecting subplanes **A**, **B** and **C**. The evolving mesh at 10$^{\text{th}}$ step and final step after 40 iterations are shown in (C) and (D) respectively. The volume mesh of starting model and final iteration is visualized in (E) and (F).

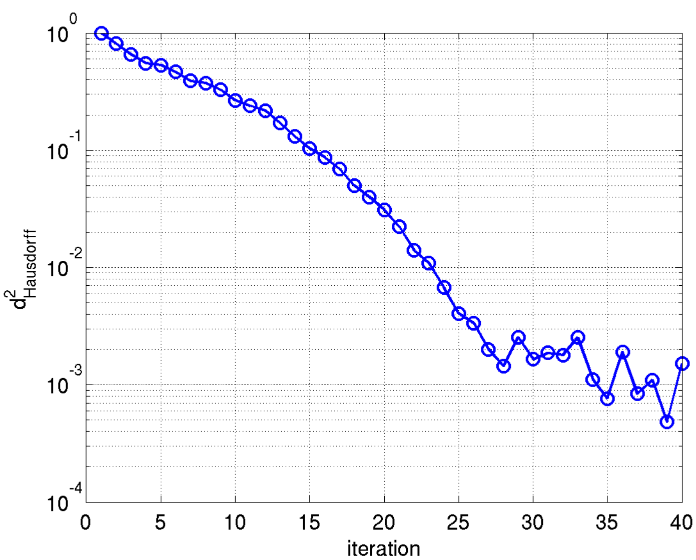

Figure 6.7.15 : The evolution of functional with defromation iterations for fault planes.

Bibliography

[1] B. T. Aagaard, G. Anderson, and K. W. Hudnut, *Dynamic rupture modeling of the transition from thrust to strike-slip motion in the 2002 denali fault earthquake, alaska*, Bulletin of the Seismological Society of America, 94 (2004), pp. S190–S201.

[2] B. T. Aagaard, M. G. Knepley, and C. A. Williams, *A domain decomposition approach to implementing fault slip in finite-element models of quasi-static and dynamic crustal deformation*, Journal of Geophysical Research: Solid Earth, 118 (2013), pp. 3059–3079.

[3] N. Aage, T. H. Poulsen, A. Gersborg-Hansen, and O. Sigmund, *Topology optimization of large scale stokes flow problems*, Structural and Multidisciplinary Optimization, 35 (2008), pp. 175–180.

[4] J. D. Achenbach, *Wave propagation in elastic solids*, vol. 16, North-Holland Amsterdam, 1973.

[5] T. Almani, K. Kumar, A. Dogru, G. Singh, and M. Wheeler, *Convergence analysis of multirate fixed-stress split iterative schemes for coupling flow with geomechanics*, Computer Methods in Applied Mechanics and Engineering, 311 (2016).

[6] J.-P. Ampuero and A. M. Rubin, *Earthquake nucleation on rate and state faults–aging and slip laws*, Journal of Geophysical Research: Solid Earth, 113

(2008).

[7] D. Appelö and N. A. Petersson, *A stable finite difference method for the elastic wave equation on complex geometries with free surfaces*, Communications in Computational Physics, 5 (2009), pp. 84–107.

[8] D. N. Arnold, F. Brezzi, B. Cockburn, and L. D. Marini, *Unified analysis of discontinuous galerkin methods for elliptic problems*, SIAM journal on numerical analysis, 39 (2002), pp. 1749–1779.

[9] U. M. Ascher, S. J. Ruuth, and R. J. Spiteri, *Implicit-explicit Runge-Kutta methods for time-dependent partial differential equations*, Applied Numerical Mathematics, 25 (1997), pp. 151–167.

[10] J. Ball, *Strongly continuous semigroups, weak solutions, and the variation of constants formula*, Proceedings of the American Mathematical Society, 63 (1977), pp. 370–373.

[11] M. Benjemaa, N. Glinsky-Olivier, V. Cruz-Atienza, and J. Virieux, *3-d dynamic rupture simulations by a finite volume method*, Geophysical Journal International, 178 (2009), pp. 541–560.

[12] E. Beretta, M. V. de Hoop, E. Francini, and S. Vessella, *Stable determination of polyhedral interfaces from boundary data for the helmholtz equation*, arXiv preprint arXiv:1408.1569, (2014).

[13] E. Beretta, M. V. de Hoop, E. Francini, S. Vessella, and J. Zhai, *Uniqueness and lipschitz stability of an inverse boundary value problem for time-harmonic elastic waves*, Inverse Problems, 33 (2017), p. 035013.

[14] E. Beretta, M. V. de Hoop, L. Qiu, and O. Scherzer, *Inverse boundary value problem for the helmholtz equation: multi-level approach and iterative reconstruction*, arXiv preprint arXiv:1406.2391, (2014).

[15] A. Bermúdez, L. Hervella-Nieto, and R. Rodriguez, *Finite element computation of three-dimensional elastoacoustic vibrations*, Journal of Sound and Vibration, 219 (1999), pp. 279–306.

[16] K. D. Blazek, C. Stolk, and W. W. Symes, *A mathematical framework for inverse wave problems in heterogeneous media*, Inverse Problems, 29 (2013), p. 065001.

[17] J. Bogers, *Transport in fractured media: Well-posedness, upscaling and numerical schemes for problems involving a nonlinear transmission condition*, master's thesis, Eindhoven University of Technology, 2011.

[18] K. Brazda, M. V. de Hoop, and G. Hörmann, *Variational formulation of the earth's elastic-gravitational deformations under low regularity conditions,*, Cambridge University Press, 2017.

[19] D. Brunner, M. Junge, P. Rapp, M. Bebendorf, and L. Gaul, *Comparison of the fast multipole method with hierarchical matrices for the helmholtz-bem*, Computer Modeling in Engineering & Sciences(CMES), 58 (2010), pp. 131–160.

[20] L. Bureau, T. Baumberger, and C. Caroli, *Shear response of a frictional interface to a normal load modulation*, Physical Review E, 62 (2000), p. 6810.

[21] M. Campillo, P. Favreau, I. R. Ionescu, and C. Voisin, *On the effective friction law of a heterogeneous fault*, Journal of Geophysical Research: Solid

Earth, 106 (2001), pp. 16307–16322.

[22] M. Campillo and I. R. Ionescu, *Initiation of antiplane shear instability under slip dependent friction*, Journal of Geophysical Research: Solid Earth, 102 (1997), pp. 20363–20371.

[23] J. M. Carcione, *The wave equation in generalized coordinates*, Geophysics, 59 (1994), pp. 1911–1919.

[24] L. Carrington, D. Komatitsch, M. Laurenzano, M. M. Tikir, D. Michéa, N. Le Goff, A. Snavely, and J. Tromp, *High-frequency simulations of Global seismic wave propagation using SPECFEM3D_GLOBE on 62K processors*, (2008), pp. 60:1–60:11.

[25] G. Caumon and P. Collon-Drouaillet, *Special issue on three-dimensional structural modeling*, Mathematical Geosciences, 46 (2014), pp. 905–908.

[26] E. Chaljub, Y. Capdeville, and J.-P. Vilotte, *Solving elastodynamics in a fluid–solid heterogeneous sphere: a parallel spectral element approximation on non-conforming grids*, Journal of Computational Physics, 187 (2003), pp. 457–491.

[27] E. Chaljub and B. Valette, *Spectral element modelling of three-dimensional wave propagation in a self-gravitating Earth with an arbitrarily stratified outer core*, Geophysical Journal International, 158 (2004), pp. 131–141.

[28] J. Chan, R. J. Hewett, and T. Warburton, *Weight-adjusted discontinuous galerkin methods: curvilinear meshes*, SIAM Journal on Scientific Comput-

ing, 39 (2017), pp. A2395–A2421.

[29] ——, *Weight-adjusted discontinuous galerkin methods: wave propagation in heterogeneous media*, SIAM Journal on Scientific Computing, 39 (2017), pp. A2935–A2961.

[30] J. Chan, Z. Wang, A. Modave, J.-F. Remacle, and T. Warburton, *Gpu-accelerated discontinuous galerkin methods on hybrid meshes*, Journal of Computational Physics, 318 (2016), pp. 142–168.

[31] G. Charpiat, O. Faugeras, and R. Keriven, *Approximations of shape metrics and application to shape warping and empirical shape statistics*, Foundations of Computational Mathematics, 5 (2005), pp. 1–58.

[32] H. Cheng, L. Greengard, and V. Rokhlin, *A fast adaptive multipole algorithm in three dimensions*, Journal of computational physics, 155 (1999), pp. 468–498.

[33] S.-W. Cheng, T. K. Dey, H. Edelsbrunner, M. A. Facello, and S.-H. Teng, *Silver exudation*, Journal of the ACM (JACM), 47 (2000), pp. 883–904.

[34] E. T. Chung and B. Engquist, *Optimal discontinuous Galerkin methods for wave propagation*, SIAM Journal on Numerical Analysis, 44 (2006), pp. 2131–2158.

[35] B. Cockburn and C.-W. Shu, *Runge–Kutta discontinuous Galerkin methods for convection-dominated problems*, Journal of scientific computing, 16 (2001), pp. 173–261.

[36] M. Costabel and E. P. Stephan, *Coupling of finite and boundary element methods for an elastoplastic interface problem*, SIAM Journal on Numerical Analysis, 27 (1990), pp. 1212–1226.

[37] V. Cristini, J. Bławzdziewicz, and M. Loewenberg, *An adaptive mesh algorithm for evolving surfaces: simulations of drop breakup and coalescence*, Journal of Computational Physics, 168 (2001), pp. 445–463.

[38] F. Dahlen, *Elastic dislocation theory for a self-gravitating elastic configuration with an initial static stress field*, Geophysical Journal International, 28 (1972), pp. 357–383.

[39] ——, *Elastic dislocation theory for a self-gravitating elastic configuration with an initial static stress field ii. energy release*, Geophysical Journal International, 31 (1973), pp. 469–484.

[40] ——, *The balance of energy in earthquake faulting*, Geophysical Journal International, 48 (1977), pp. 239–261.

[41] F. Dahlen and J. Tromp, *Theoretical Global seismology*, Princeton university press, 1998.

[42] W. Dahmen and R. Stevenson, *Element-by-element construction of wavelets satisfying stability and moment conditions*, SIAM journal on numerical analysis, 37 (1999), pp. 319–352.

[43] L. A. Dalguer and S. M. Day, *Staggered-grid split-node method for spontaneous rupture simulation*, Journal of Geophysical Research: Solid Earth, 112 (2007).

[44] F. Dassi, B. Ettinger, S. Perotto, and L. M. Sangalli, *A mesh simplification strategy for a spatial regression analysis over the cortical surface of the brain*, Applied Numerical Mathematics, 90 (2015), pp. 111–131.

[45] R. Dautray, J.-L. Lions, C. Dewitt-Morette, and E. Myers, *Mathematical analysis and numerical methods for science and technology*, Physics Today, 44 (1991), p. 72.

[46] R. Davies, G. Foulger, A. Bindley, and P. Styles, *Induced seismicity and hydraulic fracturing for the recovery of hydrocarbons*, Marine and Petroleum Geology, 45 (2013), pp. 171–185.

[47] S. M. Day, L. A. Dalguer, N. Lapusta, and Y. Liu, *Comparison of finite difference and boundary integral solutions to three-dimensional spontaneous rupture*, Journal of Geophysical Research: Solid Earth, 110 (2005).

[48] J. D. De Basabe, M. K. Sen, and M. F. Wheeler, *The interior penalty discontinuous Galerkin method for elastic wave propagation: grid dispersion*, Geophysical Journal International, 175 (2008), pp. 83–93.

[49] ——, *Elastic wave propagation in fractured media using the discontinuous galerkin method*, Geophysics, 81 (2016), pp. T163–T174.

[50] M. V. de Hoop, S. Holman, and H. Pham, *On the system of elastic-gravitational equations describing the oscillations of the earth*, arXiv preprint arXiv:1511.03200, (2015).

[51] J. de la Puente, J.-P. Ampuero, and M. Käser, *Dynamic rupture modeling on unstructured meshes using a discontinuous galerkin method*, Journal of Geophysical Research: Solid Earth, 114 (2009).

[52] ——, *Dynamic rupture modeling on unstructured meshes using a discontinuous galerkin method*, Journal of Geophysical Research: Solid Earth, 114 (2009).

[53] J. H. Dieterich, *Modeling of rock friction: 1. experimental results and constitutive equations*, Journal of Geophysical Research: Solid Earth, 84 (1979), pp. 2161–2168.

[54] M. Dumbser and M. Käser, *An arbitrary high-order discontinuous Galerkin method for elastic waves on unstructured meshes–II. the three-dimensional isotropic case*, Geophysical Journal International, 167 (2006), pp. 319–336.

[55] E. M. Dunham, D. Belanger, L. Cong, and J. E. Kozdon, *Earthquake ruptures with strongly rate-weakening friction and off-fault plasticity, part 1: Planar faults*, Bulletin of the Seismological Society of America, 101 (2011), pp. 2296–2307.

[56] K. Duru and E. M. Dunham, *Dynamic earthquake rupture simulations on nonplanar faults embedded in 3d geometrically complex, heterogeneous elastic solids*, Journal of Computational Physics, 305 (2016), pp. 185–207.

[57] I. Eckstein, J.-P. Pons, Y. Tong, C.-C. Kuo, and M. Desbrun, *Generalized surface flows for mesh processing*, in Proceedings of the fifth Eurographics symposium on Geometry processing, Eurographics Association, 2007, pp. 183–192.

[58] V. Etienne, E. Chaljub, J. Virieux, and N. Glinsky, *An hp-adaptive discontinuous Galerkin finite-element method for 3-D elastic wave modelling*, Geophysical Journal International, 183 (2010), pp. 941–962.

[59] M. Fehler and P. J. Keliher, *SEAM Phase 1: Challenges of Subsalt Imaging in Tertiary Basins, with Emphasis on Deepwater Gulf of Mexico*, Society of Exploration Geophysicists Tulsa, 2011.

[60] M. Fuchs, B. Jüttler, O. Scherzer, and H. Yang, *Shape metrics based on elastic deformations*, Journal of Mathematical Imaging and Vision, 35 (2009), pp. 86–102.

[61] P. Galvez, J.-P. Ampuero, L. Dalguer, S. Somala, and T. Nissen-Meyer, *Dynamic earthquake rupture modelled with an unstructured 3-d spectral element method applied to the 2011 m9 tohoku earthquake*, Geophysical Journal International, 198 (2014), pp. 1222–1240.

[62] M. Garland and P. S. Heckbert, *Surface simplification using quadric error metrics*, in Proceedings of the 24th annual conference on Computer graphics and interactive techniques, ACM Press/Addison-Wesley Publishing Co., 1997, pp. 209–216.

[63] P. H. Geubelle and J. R. Rice, *A spectral method for three-dimensional elastodynamic fracture problems*, Journal of the Mechanics and Physics of Solids, 43 (1995), pp. 1791–1824.

[64] H. N. Gharti and J. Tromp, *A spectral-infinite-element solution of poisson's equation: an application to self gravity*, arXiv preprint arXiv:1706.00855, (2017).

[65] V. Girault, K. Kumar, and M. F. Wheeler, *Convergence of iterative coupling of geomechanics with flow in a fractured poroelastic medium*, Computational Geosciences, 20 (2016), pp. 997–1011.

[66] E. Grasso, J. Semblat, S. Chaillat, and M. Bonnet, *Modelling damped seismic waves by coupling the finite element method and the fast multipole boundary element method*, in 15th World Conf. on Earthquake Eng, 2012.

[67] R. W. Graves, *Simulating seismic wave propagation in 3d elastic media using staggered-grid finite differences*, Bulletin of the Seismological Society of America, 86 (1996), pp. 1091–1106.

[68] L. Greengard and V. Rokhlin, *A new version of the fast multipole method for the laplace equation in three dimensions*, Acta numerica, 6 (1997), pp. 229–269.

[69] M. J. Grote, A. Schneebeli, and D. Schötzau, *Discontinuous Galerkin finite element method for the wave equation*, SIAM Journal on Numerical Analysis, 44 (2006), pp. 2408–2431.

[70] Z. Guo, M. V. de Hoop, et al., *Shape optimization and level set method in full waveform inversion with 3d body reconstruction*, in 2013 SEG Annual Meeting, Society of Exploration Geophysicists, 2013.

[71] D. Hale, *Atomic meshes: from seismic imaging to reservoir simulation*, in Proceedings of the 8th European Conference on the Mathematics of Oil Recovery, Citeseer, 2002.

[72] R. Harris, M. Barall, R. Archuleta, E. Dunham, B. Aagaard, J. Ampuero, H. Bhat, V. Cruz-Atienza, L. Dalguer, P. Dawson, et al., *The scec/usgs dynamic earthquake rupture code verification exercise*, Seismological Research Letters, 80 (2009), pp. 119–126.

[73] R. A. Harris, *Large earthquakes and creeping faults*, Reviews of Geophysics, 55 (2017), pp. 169–198.

[74] A. Henderson, *ParaView Guide, A Parallel Visualization Application*, Kitware Inc., 2007.

[75] J. S. Hesthaven and T. Warburton, *Nodal discontinuous Galerkin methods: algorithms, analysis, and applications*, vol. 54, Springer, 2007.

[76] E. A. Hinz and J. H. Bradford, *Ground-penetrating-radar reflection attenuation tomography with an adaptive mesh*, Geophysics, 75 (2010), pp. WA251–WA261.

[77] H. Hoppe, T. DeRose, T. Duchamp, J. McDonald, and W. Stuetzle, *Mesh optimization*, in Proceedings of the 20th annual conference on Computer graphics and interactive techniques, ACM, 1993, pp. 19–26.

[78] F.-C. Huang, B.-Y. Chen, and Y.-Y. Chuang, *Progressive deforming meshes based on deformation oriented decimation and dynamic connectivity updating*, in Proceedings of the 2006 ACM SIGGRAPH/Eurographics symposium on Computer animation, Eurographics Association, 2006, pp. 53–62.

[79] H. Huang and F. Costanzo, *On the use of space-time finite elements in the solution of elasto-dynamic fracture problems*, International Journal of Fracture, 127 (2004), pp. 119–146.

[80] H. Igel, *Wave propagation in three-dimensional spherical sections by the Chebyshev spectral method*, Geophysical Journal International, 136 (1999), pp. 559–566.

[81] I. R. Ionescu, *Viscosity solutions for dynamic problems with slip-rate dependent friction*, Quarterly of Applied Mathematics, 60 (2002), pp. 461–476.

[82] I. R. Ionescu, Q.-L. Nguyen, and S. Wolf, *Slip-dependent friction in dynamic elasticity*, Nonlinear Analysis: Theory, Methods & Applications, 53 (2003), pp. 375–390.

[83] I. R. Ionescu and J.-C. Paumier, *On the contact problem with slip displacement dependent friction in elastostatics*, International journal of engineering science, 34 (1996), pp. 471–491.

[84] N. Kame, J. R. Rice, and R. Dmowska, *Effects of prestress state and rupture velocity on dynamic fault branching*, Journal of Geophysical Research: Solid Earth, 108 (2003).

[85] T. Kanaya, Y. Teshima, K.-i. Kobori, and K. Nishio, *A topology-preserving polygonal simplification using vertex clustering*, in Proceedings of the 3rd international conference on Computer graphics and interactive techniques in Australasia and South East Asia, ACM, 2005, pp. 117–120.

[86] Y. Kaneko and N. Lapusta, *Variability of earthquake nucleation in continuum models of rate-and-state faults and implications for aftershock rates*, Journal of Geophysical Research: Solid Earth, 113 (2008).

[87] Y. Kaneko, N. Lapusta, and J.-P. Ampuero, *Spectral element modeling of spontaneous earthquake rupture on rate and state faults: Effect of velocity-strengthening friction at shallow depths*, Journal of Geophysical Research: Solid Earth, 113 (2008).

[88] A. Kanevsky, M. H. Carpenter, D. Gottlieb, and J. S. Hesthaven, *Application of implicit-explicit high order Runge–Kutta methods to discontinuous-Galerkin schemes*, Journal of Computational Physics, 225 (2007), pp. 1753 – 1781.

[89] M. Käser and M. Dumbser, *A highly accurate discontinuous Galerkin method for complex interfaces between solids and moving fluids*, Geophysics, 73 (2008), pp. T23–T35.

[90] A. A. Kaufman and A. L. Levshin, *Acoustic and elastic wave fields in geophysics*, vol. 3, Elsevier, 2005.

[91] A. Klarbring, A. Mikelić, and M. Shillor, *Frictional contact problems with normal compliance*, International Journal of Engineering Science, 26 (1988), pp. 811–832.

[92] D. Komatitsch, C. Barnes, and J. Tromp, *Wave propagation near a fluid-solid interface: A spectral-element approach*, Geophysics, 65 (2000), pp. 623–631.

[93] D. Komatitsch and R. Martin, *An unsplit convolutional perfectly matched layer improved at grazing incidence for the seismic wave equation*, Geophysics, 72 (2007), pp. SM155–SM167.

[94] D. Komatitsch and J. Tromp, *Spectral-element simulations of global seismic wave propagation – I. validation*, Geophysical Journal International, 149 (2002), pp. 390–412.

[95] D. Komatitsch, S. Tsuboi, and J. Tromp, *The spectral-element method in seismology*, Geophysical Monograph Series, 157 (2005), pp. 205–227.

[96] D. Komatitsch and J.-P. Vilotte, *The spectral element method: An efficient tool to simulate the seismic response of 2D and 3D geological structures*, Bulletin of the seismological society of America, 88 (1998), pp. 368–392.

[97] A. Kononov, S. Minisini, E. Zhebel, and W. Mulder, *A 3d tetrahedral mesh generator for seismic problems*, in 74th EAGE Conference and Exhibition incorporating EUROPEC 2012, 2012.

[98] J. E. Kozdon, E. M. Dunham, and J. Nordström, *Interaction of waves with frictional interfaces using summation-by-parts difference operators: Weak enforcement of nonlinear boundary conditions*, Journal of Scientific Computing, 50 (2012), pp. 341–367.

[99] ——, *Simulation of dynamic earthquake ruptures in complex geometries using high-order finite difference methods*, Journal of Scientific Computing, 55 (2013), pp. 92–124.

[100] S. Latour, M. Campillo, C. Voisin, I. Ionescu, J. Schmedes, and D. Lavallée, *Effective friction law for small-scale fault heterogeneity in 3d dynamic rupture*, Journal of Geophysical Research: Solid Earth, 116 (2011).

[101] W. Li, C. L. Petrovitch, and L. J. Pyrak-Nolte, *The effect of fabric-controlled layering on compressional and shear wave propagation in carbonate rock*, International Journal of the JCRM, 4 (2009), pp. 79–85.

[102] M. Linker and J. Dieterich, *Effects of variable normal stress on rock friction: Observations and constitutive equations*, Journal of Geophysical Research: Solid Earth, 97 (1992), pp. 4923–4940.

[103] B. Lombard and J. Piraux, *Numerical treatment of two-dimensional interfaces for acoustic and elastic waves*, Journal of Computational Physics, 195 (2004), pp. 90–116.

[104] B. Lombard, J. Piraux, C. Gélis, and J. Virieux, *Free and smooth boundaries in 2-D finite-difference schemes for transient elastic waves*, Geophysical Journal International, 172 (2008), pp. 252–261.

[105] J. C. Lozos, R. A. Harris, J. R. Murray, and J. J. Lienkaemper, *Dynamic rupture models of earthquakes on the bartlett springs fault, northern california*, Geophysical Research Letters, 42 (2015), pp. 4343–4349.

[106] S. Ma, R. J. Archuleta, and M. T. Page, *Effects of large-scale surface topography on ground motions, as demonstrated by a study of the san gabriel mountains, los angeles, california*, Bulletin of the Seismological Society of America, 97 (2007), pp. 2066–2079.

[107] R. Madariaga, *Dynamics of an expanding circular fault*, Bulletin of the Seismological Society of America, 66 (1976), pp. 639–666.

[108] R. Madariaga, J. Ampuero, and M. Adda-Bedia, *Seismic radiation from simple models of earthquakes*, Earthquakes: radiated Energy and the Physics of Faulting, (2006), pp. 223–236.

[109] J. Martins and J. Oden, *Existence and uniqueness results for dynamic contact problems with nonlinear normal and friction interface laws*, Nonlinear Analysis: Theory, Methods & Applications, 11 (1987), pp. 407–428.

[110] P. Moczo, J. Kristek, and M. Gális, *The finite-difference modelling of earthquake motions: Waves and ruptures*, Cambridge University Press, 2014.

[111] A. Modave, A. Atle, J. Chan, and T. Warburton, *A gpu-accelerated nodal discontinuous galerkin method with high-order absorbing boundary conditions and corner/edge compatibility*, International Journal for Numerical Methods in Engineering, 112 (2017), pp. 1659–1686.

[112] A. Mohammed and A. Tuffaha, *On boundary control of the poisson equation with the third boundary condition*, Journal of Mathematical Analysis and Applications, 459 (2018), pp. 217–235.

[113] P. Möller and P. Hansbo, *On advancing front mesh generation in three dimensions*, International Journal for Numerical Methods in Engineering, 38 (1995), pp. 3551–3569.

[114] T. Möller, *A fast triangle-triangle intersection test*, Journal of graphics tools, 2 (1997), pp. 25–30.

[115] M. Möllhoff and C. J. Bean, *Validation of elastic wave measurements of rock fracture compliance using numerical discrete particle simulations*, Geophysical Prospecting, 57 (2009), pp. 883–895.

[116] H. Noda, E. M. Dunham, and J. R. Rice, *Earthquake ruptures with thermal weakening and the operation of major faults at low overall stress levels*, Journal of Geophysical Research: Solid Earth, 114 (2009).

[117] R. Nurmi, M. Charara, M. Waterhouse, and R. Park, *Heterogeneities in carbonate reservoirs: detection and analysis using borehole electrical imagery*, Geological Society, London, Special Publications, 48 (1990), pp. 95–111.

[118] T. Ohminato and B. A. Chouet, *A free-surface boundary condition for*

including 3D topography in the finite-difference method, Bulletin of the Seismological Society of America, 87 (1997), pp. 494–515.

[119] C. Ollivier-Gooch and C. Boivin, *Guaranteed-quality simplical mesh generation with cell size and grading control*, Engineering with Computers, 17 (2001), pp. 269–286.

[120] O. O'Reilly, J. Nordström, J. E. Kozdon, and E. M. Dunham, *Simulation of earthquake rupture dynamics in complex geometries using coupled finite difference and finite volume methods*, Communications in Computational Physics, 17 (2015), pp. 337–370.

[121] M. Oristaglio, *SEAM Phase II–land seismic challenges*, The Leading Edge, 31 (2012), pp. 264–266.

[122] S. Osher and R. Fedkiw, *Level set methods and dynamic implicit surfaces*, vol. 153, Springer Science & Business Media, 2003.

[123] C. Pelties, J. Puente, J.-P. Ampuero, G. B. Brietzke, and M. Käser, *Three-dimensional dynamic rupture simulation with a high-order discontinuous galerkin method on unstructured tetrahedral meshes*, Journal of Geophysical Research: Solid Earth, 117 (2012).

[124] H. Perfettini, J. Schmittbuhl, J. R. Rice, and M. Cocco, *Frictional response induced by time-dependent fluctuations of the normal loading*, Journal of Geophysical Research: Solid Earth, 106 (2001), pp. 13455–13472.

[125] P.-O. Persson, *High-order LES simulations using implicit-explicit Runge–Kutta schemes*, in Proceedings of the 49th AIAA Aerospace Sciences Meeting and Exhibit, AIAA, vol. 684, 2011.

[126] P.-O. Persson and G. Strang, *A simple mesh generator in matlab*, SIAM review, 46 (2004), pp. 329–345.

[127] E. Pipping, *Existence of long-time solutions to dynamic problems of viscoelasticity with rate-and-state friction*, arXiv preprint arXiv:1703.04289, (2017).

[128] E. Pipping, O. Sander, and R. Kornhuber, *Variational formulation of rate-and state-dependent friction problems*, ZAMM-Journal of Applied Mathematics and Mechanics/Zeitschrift für Angewandte Mathematik und Mechanik, 95 (2015), pp. 377–395.

[129] A. N. Poliakov, R. Dmowska, and J. R. Rice, *Dynamic shear rupture interactions with fault bends and off-axis secondary faulting*, Journal of Geophysical Research: Solid Earth, 107 (2002).

[130] V. Prakash, *Frictional response of sliding interfaces subjected to time varying normal pressures*, Journal of Tribology, 120 (1998), pp. 97–102.

[131] L. J. Pyrak-Nolte, L. R. Myer, and N. G. Cook, *Transmission of seismic waves across single natural fractures*, Journal of Geophysical Research: Solid Earth, 95 (1990), pp. 8617–8638.

[132] A. Quarteroni and A. Valli, *Numerical approximation of partial differential equations*, vol. 23, Springer Science & Business Media, 2008.

[133] J. Rice and A. Ruina, *Stability of steady frictional slipping*, Journal of applied mechanics, 50 (1983), pp. 343–349.

[134] J. R. Rice, *Constitutive relations for fault slip and earthquake instabilities*, Pure and applied geophysics, 121 (1983), pp. 443–475.

[135] J. R. Rice, N. Lapusta, and K. Ranjith, *Rate and state dependent friction and the stability of sliding between elastically deformable solids*, Journal of the Mechanics and Physics of Solids, 49 (2001), pp. 1865–1898.

[136] E. Richardson and C. Marone, *Effects of normal stress vibrations on frictional healing*, J. geophys. Res, 104 (1999), pp. 28859–28878.

[137] B. Rivière and M. F. Wheeler, *A discontinuous Galerkin method applied to nonlinear parabolic equations*, in Discontinuous Galerkin Methods, Springer, 2000, pp. 231–244.

[138] B. Riviere and M. F. Wheeler, *Discontinuous finite element methods for acoustic and elastic wave problems*, Contemporary Mathematics, 329 (2003), pp. 271–282.

[139] B. Rivière, M. F. Wheeler, and V. Girault, *Improved energy estimates for interior penalty, constrained and discontinuous galerkin methods for elliptic problems. part i*, Computational Geosciences, 3 (1999), pp. 337–360.

[140] J. O. Robertsson, *A numerical free-surface condition for elastic/viscoelastic finite-difference modeling in the presence of topography*, Geophysics, 61 (1996), pp. 1921–1934.

[141] A. Rubin and J.-P. Ampuero, *Earthquake nucleation on (aging) rate and state faults*, Journal of Geophysical Research: Solid Earth, 110 (2005).

[142] A. Rüger and D. Hale, *Meshing for velocity modeling and ray tracing in complex velocity fields*, Geophysics, 71 (2006), pp. U1–U11.

[143] A. Ruina, *Slip instability and state variable friction laws*, Journal of Geophysical Research: Solid Earth, 88 (1983), pp. 10359–10370.

[144] A. L. Ruina, *Friction laws and instabilities: A quasistatic analysis of some dry frictional behavior*, PhD thesis, Brown University, 1981.

[145] M. Salo, *Calderón problem*, Lecture Notes, (2008).

[146] S. V. Schmitt, P. Segall, and E. M. Dunham, *Nucleation and dynamic rupture on weakly stressed faults sustained by thermal pressurization*, Journal of Geophysical Research: Solid Earth, 120 (2015), pp. 7606–7640.

[147] J. Schöberl, *Netgen an advancing front 2d/3d-mesh generator based on abstract rules*, Computing and visualization in science, 1 (1997), pp. 41–52.

[148] M. Schoenberg, *Elastic wave behavior across linear slip interfaces*, The Journal of the Acoustical Society of America, 68 (1980), pp. 1516–1521.

[149] W. J. Schroeder, J. A. Zarge, and W. E. Lorensen, *Decimation of triangle meshes*, in ACM Siggraph Computer Graphics, vol. 26, ACM, 1992, pp. 65–70.

[150] J. R. Shewchuk, *Tetrahedral mesh generation by delaunay refinement*, in Proceedings of the fourteenth annual symposium on Computational geometry, ACM, 1998, pp. 86–95.

[151] ——, *Constrained delaunay tetrahedralizations and provably good boundary recovery.*, in IMR, Citeseer, 2002, pp. 193–204.

[152] C.-S. Shin, *Nonlinear elastic wave inversion by blocky representation*, PhD thesis, University of Oklahoma, 1988.

[153] K. Shukla, P. Jaiswal, M. de Hoop, and R. Ye, *A discontinuous Galerkin method with a modified penalty flux for broadband Biot's equation*, 2017, pp. 4080–4085.

[154] H. Si, *TetGen, a Delaunay-based quality tetrahedral mesh generator*, ACM Trans. Math. Softw., 41 (2015), pp. 11:1–11:36.

[155] T. M. Smith, S. S. Collis, C. C. Ober, J. R. Overfelt, and H. F. Schwaiger, *Elastic wave propagation in variable media using a discontinuous Galerkin method*, SEG Epanded Abstracts, 29 (2010), pp. 2982–2987.

[156] M. Sussman, P. Smereka, and S. Osher, *A level set approach for computing solutions to incompressible two-phase flow*, Journal of Computational physics, 114 (1994), pp. 146–159.

[157] W. Symes and T. Vdovina, *Interface error analysis for numerical wave propagation*, Computational Geosciences, 13 (2009), pp. 363–371.

[158] J. Tago, V. M. Cruz-Atienza, J. Virieux, V. Etienne, and F. J. Sánchez-Sesma, *A 3d hp-adaptive discontinuous galerkin method for modeling earthquake dynamics*, Journal of Geophysical Research: Solid Earth, 117 (2012).

[159] J. Teran, N. Molino, R. Fedkiw, and R. Bridson, *Adaptive physics based tetrahedral mesh generation using level sets*, Engineering with computers, 21 (2005), pp. 2–18.

[160] E. Tessmer, D. Kosloff, and A. Behle, *Elastic wave propagation simulation in the presence of surface topography*, Geophysical Journal International, 108 (1992), pp. 621–632.

[161] M. Y. Thomas, J.-P. Avouac, and N. Lapusta, *Rate-and-state friction properties of the longitudinal valley fault from kinematic and dynamic modeling of seismic and aseismic slip*, Journal of Geophysical Research: Solid Earth, 122 (2017), pp. 3115–3137. 2016JB013615.

[162] B. Valette, *About the influence of pre-stress upon adiabatic perturbations of the earth*, Geophysical Journal International, 85 (1986), pp. 179–208.

[163] B. Valette, *Spectre des oscillations libres de la terre: aspects mathématiques et géophysiques (spectrum of the free oscillations of the earth: mathematical and geophysical aspects)*, 1987.

[164] M. Vallée, J. P. Ampuero, K. Juhel, P. Bernard, J.-P. Montagner, and M. Barsuglia, *Observations and modeling of the elastogravity signals preceding direct seismic waves*, Science, 358 (2017), pp. 1164–1168.

[165] J. Vermylen, M. D. Zoback, et al., *Hydraulic fracturing, microseismic magnitudes, and stress evolution in the barnett shale, texas, usa*, in SPE Hydraulic Fracturing Technology Conference, Society of Petroleum Engineers, 2011.

[166] J. Virieux, *P-SV wave propagation in heterogeneous media: Velocity-stress finite-difference method*, Geophysics, 51 (1986), pp. 889–901.

[167] Y. Wang and S. M. Day, *Seismic source spectral properties of crack-like and pulse-like modes of dynamic rupture*, Journal of Geophysical Research: Solid Earth, (2017).

[168] T. Warburton, *An explicit construction of interpolation nodes on the simplex*, Journal of Engineering Mathematics, 56 (2006), pp. 247–262.

[169] ——, *A low-storage curvilinear Discontinuous Galerkin method for wave problems*, SIAM Journal on Scientific Computing, 35 (2013), pp. A1987–A2012.

[170] T. Warburton and J. S. Hesthaven, *On the constants in hp-finite element trace inverse inequalities*, Computer methods in applied mechanics and engineering, 192 (2003), pp. 2765–2773.

[171] L. C. Wilcox, G. Stadler, C. Burstedde, and O. Ghattas, *A high-order discontinuous Galerkin method for wave propagation through coupled elastic–acoustic media*, Journal of Computational Physics, 229 (2010), pp. 9373–9396.

[172] J. Woodhouse and F. Dahlen, *The effect of a general aspherical perturbation on the free oscillations of the earth*, Geophysical Journal International, 53 (1978), pp. 335–354.

[173] J. Xia, *On the complexity of some hierarchical structured matrix algorithms*, SIAM Journal on Matrix Analysis and Applications, 33 (2012), pp. 388–410.

[174] Z. Xin, J. Xia, M. V. de Hoop, S. Cauley, and V. Balakrishnan, *A distributed-memory randomized structured multifrontal method for sparse direct solutions*, SIAM Journal on Scientific Computing, 39 (2017), pp. C292–C318.

[175] S. Xu, Y. Ben-Zion, J.-P. Ampuero, and V. Lyakhovsky, *Dynamic ruptures on a frictional interface with off-fault brittle damage: feedback mechanisms and effects on slip and near-fault motion*, Pure and Applied Geophysics, 172 (2015), pp. 1243–1267.

[176] Z. Xu, X.-Y. Chen, and Y. Liu, *A new runge–kutta discontinuous galerkin*

method with conservation constraint to improve cfl condition for solving conservation laws, Journal of computational physics, 278 (2014), pp. 348–377.

[177] R. Ye, M. V. de Hoop, C. L. Petrovitch, L. J. Pyrak-Nolte, and L. C. Wilcox, *A discontinuous galerkin method with a modified penalty flux for the propagation and scattering of acousto-elastic waves*, Geophysical Journal International, (2016).

[178] R. Ye, K. Kumar, M. V. de Hoop, and M. Campillo, *A multi-rate iterative coupling scheme for dynamic ruptures generating seismic waves in a self-gravitating earth and well-posedness*, Mathematical Models and Methods in Applied Sciences, (2018). Submitted.

[179] R. Ye, K. Kunmar, M. V. de Hoop, and M. Campillo, *A multi-rate iterative coupling scheme for dynamic ruptures and seismic waves generation in the self-gravitating earth: the discontinuous galerkin method*, Journal of Computational Physics, (2018). Submitted.

[180] Q. Zhan, Q. Sun, Q. Ren, Y. Fang, H. Wang, and Q. H. Liu, *A discontinuous galerkin method for simulating the effects of arbitrary discrete fractures on elastic wave propagation*, Geophysical Journal International, (2017). submitted.

[181] Z. Zhang, W. Zhang, and X. Chen, *Three-dimensional curved grid finite-difference modelling for non-planar rupture dynamics*, Geophysical Journal International, 199 (2014), pp. 860–879.

[182] O. Zienkiewicz and P. Bettess, *Fluid-structure dynamic interaction and wave forces. an introduction to numerical treatment*, International Journal for

Numerical Methods in Engineering, 13 (1978), pp. 1–16.

[183] D. W. Zingg, *Comparison of high-accuracy finite-difference methods for linear wave propagation*, SIAM Journal on Scientific Computing, 22 (2000), pp. 476–502.

[184] D. W. Zingg, H. Lomax, and H. Jurgens, *High-accuracy finite-difference schemes for linear wave propagation*, SIAM Journal on Scientific Computing, 17 (1996), pp. 328–346.